Number 5 Volume 17 October 2011 Journal of Engineering

THERMAL BUCKLING OF RECTANGULAR PLATES WITH DIFFERENT TEMPERATURE DISTRIBUTION USING STRAIN ENERGY METHOD

Dr.Wael R. Abdul-Majeed
University of Baghdad
Al-Khwarazimi Eng. Coll.
Mechatronics Eng. Dpt.

Prof. Dr. Muhsin J. Jweeg
University of Al-Nahrain
Engineering College

Ass. Prof. Dr. Adnan N. Jameel
University of Baghdad
Engineering College
Mech. Eng . Dpt.

ABSTRACT:

By using governing differential equation and the Rayleigh-Ritz method of minimizing the total potential energy of a thermoelastic structural system of isotropic thermoelastic thin plates, thermal buckling equations were established for rectangular plate with different fixing edge conditions and with different aspect ratio. The strain energy stored in a plate element due to bending, mid-plane thermal force and thermal bending was obtained. Three types of thermal distribution have been considered these are: uniform temperature, linear distribution and non-linear thermal distribution across thickness. It is observed that the buckling strength enhanced considerably by additional clamping of edges. Also, the thermal buckling temperatures and thermal buckling load have lowest values at first mode of buckling for all types of ends condition and with all values of aspect ratios.

Key words: **Thermal bulking, Strain energy, Thin plate, Ends condition, Buckling mode**

الخلاصة :

باستخدام المعادلات التفاضلية الرئيسية الخاصة وطريقة ريلي-رتز لخفض الطاقة الكامنة تم استحداث معادلات خاصة بالانبعاج الحراري الخاص بالصفائح المستطيلة المتجانسة الرقيقة متضمنة مختلف حالات النهايات مع مختلف نسب الأبعاد. تم إيجاد طاقة الانفعال المخزونة الناتجة من الانحناء في عنصر الصفيحة والقوى والعزوم الحرارية في المستوي الوسطي للصفيح بالإضافة إلى درجة الحرارة الخاصة بالانبعاج القلق .تم اعتماد ثلاثة أنواع مختلفة من التوزيع الحراري وهي:درجة حرارة منتظمة، وتوزيع درجة حرارة خطية عبر السمك وتوزيع درجة حرارة لا خطية عبر السمك. لوحظ أن مقاومة الانبعاج تزداد مع تثبيت النهايات كما أن قوى الانبعاج الحراري تملك اقل قيم لها في الطور الأول للانبعاج لكل أنواع تثبيت النهايات ومع كل نسب الأبعاد.

Dr.Wael R. Abdul-Majeed
Prof. Dr. Muhsin J. Jweeg
Ass. Prof. Dr. Adnan N. Jameel

INTRODUCTION:

Thermoelastic buckling of beam-plates and plates has long been of vivid interest to researchers. Perfectly isotropic beams and plates, which are fixed from motion in their plane, are found to exhibit bifurcation buckling at a critical temperature when they are exposed to a homogeneous temperature field (i.e., the plate will remain flat during increasing temperature until a critical temperature is reached at which point the magnitude of transverse deflection becomes indeterminate [Shariat, & Eslami 2006]

When a plate is compressed in its midplane, it becomes unstable and begins to buckle at ascertain critical *value* of the in-plane force. Buckling of plates is qualitatively similar to column buckling [Chen& Virgin 2006]. However; a buckling analysis of the former case is not performed as readily as for the latter. Plate-buckling solutions usually involve considerable difficulty and subtlety [Matsunaga 2006] and the condition that result in the lowest eigenvalue, or the actual buckling load, are not at all obvious in many situations. This is especially true in plates having other than simply supported edges.

For a plate, the in-plane load that results in an elastic instability, as in the case of a beam-column, is independent of the lateral loading. Thin plates or sheets, although quite capable of carrying tensile loadings, are poor in resisting compression. Usually, buckling or wrinkling phenomena observed in compressed plates (and shells) takes place rather suddenly and are very dangerous. However, a change in temperature may also induce instability of a thin Structure, such as bifurcation buckling, snap-through buckling, or 'just' unacceptable large out-of-plane deflections of the structure [Timoshenko & Krieger 1959]. The present work takes theoretical approach to determine the buckling temperature and buckling mode for a flat, rectangular plate with various types of thermal loads and edge conditions, buckling eigenvalue problem

ANALYTICAL STUDY:

The plate analyzed usually has been assumed to be composed of a single homogeneous and isotropic material with shape and dimensions as in **Fig. (1)** [Ko 95].

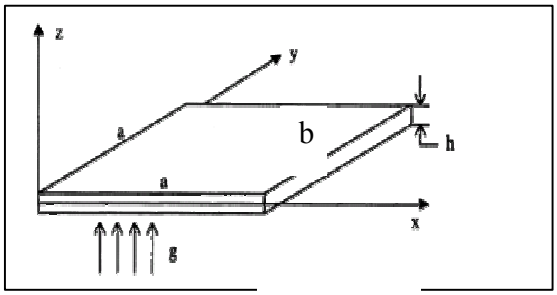

Fig. (1) Schematic Diagram of Thin Plate

Thermal Distribuation Types:

Three types of thermal distribution on plate have been considered

A- Uniform heating of plate ,the whole plate been warmed up to specificic temperature then

$$\Delta T = Tc$$

B- Linear temperature distribution across the plate thickness h then

$$\Delta T = T_{0l} + zT_{1l} \quad (1)$$

C-Temperature field across the plate thickness is assumed in nonlinear form as

$$\Delta T = T_{0n} + zT_{1n} + z^2T_{2n} \quad (2)$$

Boundary Conditions:

General closed – form solutions are given of a thermoelastiuc rectangular plate with different aspect ratio (a/b) and various elementary boundary conditions on each of the four edges. appendix A collect some important combinations of end boundary conditions. [Let the plate be placed in a coordinate system with the origin at it center and the edge width (a) be

parallel to x – axis and and the edge width (b) be parallel to y as in **Fig. (1)**

Strain Energy Methods:

As an alternative to the equilibrium methods, the analysis of deformation and stress in an elastic body can be accomplished by employing energy methods. These two techniques are respectively, the newtonian and lagrangian approaches to mechanics. The latter is predicted upon the fact that the governing equation of a deformed elastic body is derivable by minimizing the energy associated with deformation and loading. Applications of energy methods are effective in situations involving irregular shapes, non-uniform loads, variable cross sections, and anisotropic materials [Langhaar 1962]. We shall begin our discussion of energy techniques by treating the case of loaded thin plates. The strain energy stored in an elastic body, for a general state of stress, is given by [Lee 2002]

$$\Pi_b = \frac{1}{2}\iiint_V (\sigma_x\varepsilon_x + \sigma_y\varepsilon_y + \sigma_z\varepsilon_z + \tau_{xy}\gamma_{xy} + \tau_{xz}\gamma_{xz} + \tau_{yz}\gamma_{yz})dxdydz \quad (3)$$

Integration extends over the entire body volume. Based upon the assumptions of thin plates $\sigma_x, \gamma_{xz}, \gamma_{yz}$ can be omitted. Thus, introducing Hook's law, the above expression reduces to the following form involving only stresses and elastic constants:

$$\Pi_b = \frac{1}{2}\iiint_V \{(\sigma_x^2 + \sigma_y^2 - 2\nu\sigma_x\sigma_y)/E + \tau_{xy}^2/G)\}dxdydz \quad (4)$$

For a plate of uniform thickness, Eq. (4) may be written in terms of deflection w as follows

$$\Pi_b = \frac{1}{2}\iint_A D\left\{\left(\frac{\partial^2 w}{\partial x^2} + \frac{\partial^2 w}{\partial y^2}\right)^2 - 2(1-\nu)\left[\frac{\partial^2 w}{\partial x^2}\frac{\partial^2 w}{\partial y^2} - \left(\frac{\partial^2 w}{\partial x \partial y}\right)^2\right]\right\}dxdy \quad (5)$$

Where A is the area of the plate surface .The strain energy associated with in plane forces is given by

$$\Pi_N = -\frac{1}{2}\iint_A \left[N_x\left(\frac{\partial w}{\partial x}\right)^2 + N_y\left(\frac{\partial w}{\partial y}\right)^2 + 2N_{xy}\left(\frac{\partial w}{\partial x}\right)\left(\frac{\partial w}{\partial x}\right)\right]dxdy \quad (6)$$

Also the strain energy of thermal moments will have the form

$$\Pi_M = \iint_A \frac{M_t}{(1-\nu)}\left(\frac{\partial^2 w}{\partial x^2} + \frac{\partial^2 w}{\partial y^2}\right)dxdy \quad (7)$$

The total potential energy will equal to

$$\Pi_{strain} = \Pi_b + \Pi_N + \Pi_M \quad (8)$$

The expression $\frac{\partial^2 w}{\partial x^2}\frac{\partial^2 w}{\partial y^2} - \left(\frac{\partial^2 w}{\partial x \partial y}\right)^2$ represents the Gaussian curvature of the deformed surface and for the plate with general three types of ends conditions will have been studied; all edges are simply supported, all edges are clamped and two opposite edges are simply supported and the another's are clamped, then the Gaussian curvature becomes zero[Bhat 1985] . As a result the bending strain energy expression simplified to

$$\Pi_b = \frac{1}{2}\iint_A D\left\{\left(\frac{\partial^2 w}{\partial x^2} + \frac{\partial^2 w}{\partial y^2}\right)^2\right\}dxdy$$

Where $D = \frac{Eh^3}{12(1-\upsilon^2)}$, here the quantities

$$N_t = \alpha E \int_{-h/2}^{h/2} (\Delta T)dz$$

$$M_t = \alpha E \int_{-h/2}^{h/2} (\Delta T) z dz \qquad (9)$$

Are termed the thermal stress resultants.

Uniform Heating of Plate:

The whole plate been warmed up to specificic temperature then $\Delta T = Tc$ then there is no thermal moments developed in plate $\Pi_M = 0$ then the total strain will become

$\Pi_{strain} = \Pi_b + \Pi_N$

Assuming all edges are restrained then

$$N_x = N_y = -\frac{N_t}{1-\upsilon}$$

$$N_{xy} = 0 \qquad (10)$$

In Ritz method we minimize the Eq. (8) with respect to the arbitrary parameter w_{ij} i.e.

$$w(x,y) = \sum_{i=1}^{m}\sum_{j=1}^{n} A_{ij} X_i(x) Y_j(y)$$

Assuming $\frac{\partial \Pi_{strain}}{\partial A_{ij}} = 0 \qquad (11)$

Substituting w(x, y) into Ritz formula with in plane thermal force of Eq. (11) then

$$\sum_{k=1}^{m}\sum_{j=1}^{n}\left[D\int_0^a\int_0^b \left((X'')^2Y^2 + 2X''XY''Y + X^2(Y'')^2\right)dxdy + \frac{N_t}{(1-v)}\int_0^a\int_0^b \left((X')^2Y^2 + X^2(Y')^2\right) dxdy \right] A_{ij} = 0 \qquad (12)$$

Assume that $A_{ij} \neq 0$ then

$$N_{tcr} = -\frac{(1-v)D\int_0^a\int_0^b \left((X'')^2Y^2 + 2X''XY''Y + X^2(Y'')^2\right)dxdy}{\int_0^a\int_0^b \left((X')^2Y^2 + X^2(Y')^2\right)dxdy} \qquad (13)$$

In terms of temperature critical thermal buckling temperature Tc_{cr}

$$Tc_{cr} = -\frac{h^2\int_0^a\int_0^b \left((X'')^2Y^2 + 2X''XY''Y + X^2(Y'')^2\right)dxdy}{12(1+v)\alpha\int_0^a\int_0^b \left((X')^2Y^2 + X^2(Y')^2\right)dxdy} \qquad (14)$$

If edges at x=0, a are restrained and edges at y=0, b are unrestrained .Then Eq. (8) will have the form

$$\Pi_N = \frac{N_t}{2(1-v)}\int_0^a\int_0^b \left(\frac{\partial w}{\partial x}\right)^2 dxdy \qquad (15)$$

Assume the same w(x, y) as in Eqs. (11) taking the same procedure of the previous example then the critical thermal buckling force will introduce as

$$N_{tcr} = -\frac{(1-v)D\int_0^a\int_0^b \left((X'')^2Y^2 + 2X''XY''Y + X^2(Y'')^2\right)dxdy}{\int_0^a\int_0^b \left((X')^2Y^2\right)dxdy} \qquad (16)$$

In terms of critical buckling temperature

$$Tc_{cr} = -\frac{h^2\int_0^a\int_0^b \left((X'')^2Y^2 + 2X''XY''Y + X^2(Y'')^2\right)dxdy}{12(1+v)\alpha\int_0^a\int_0^b \left((X')^2Y^2\right)dxdy} \qquad (17)$$

Linear Temperature Distribution :

Assume the temperature across the plate thickness h have the form $\Delta T = T_{0l} + zT_{1l}$ .In Ritz method we minimize the Eq. (8) with respect to the arbitrary parameter w_{mn}

$$\frac{\partial \Pi_b}{\partial A_{ij}} + \frac{\partial \Pi_N}{\partial A_{ij}} + \frac{\partial \Pi_M}{\partial A_{ij}} = 0 \qquad (18)$$

Assuming all edges are restrained taking the form of deflection as in Eq. (11) and substituting w(x, y) into Ritz formula with in plane thermal force and thermal moments then Eq. (18) will be

$$\sum_{k=1}^{m}\sum_{j=1}^{n}\left[D\int_0^a\int_0^b \left((X'')^2Y^2 + 2X''XY''Y + X^2(Y'')^2\right)dxdy + \frac{N_t}{(1-v)}\int_0^a\int_0^b \left((X')^2Y^2 + X^2(Y')^2\right)dxdy\right]A_{ij} + \sum_{i=1}^{m}\sum_{j=1}^{n}\frac{M_t}{(1-v)}\int_0^a\int_0^b (X''Y + XY'')dxdy = 0 \qquad (19)$$

Finding A_{ij} from Eq. (19)

$$A_{ij} = -\frac{M_t\int\int (X''Y + XY'')dxdy}{(1-v)D\int\int\left((X'')^2Y^2 + 2XXYY + X^2(Y'')^2\right)dxdy + N_t\int\int\left((X')^2Y^2 + X^2(Y')^2\right)dxdy} \qquad (20)$$

Then the deflection

$$w(x,y) = -\sum_{i=1}^{m}\sum_{j=1}^{n}\left\{\frac{M_t\int_0^a\int_0^b (X''Y + XY'')dxdy}{(1-v)D\int_0^a\int_0^b\left((X'')^2Y^2 + 2X''XY''Y + X^2(Y'')^2\right)dxdy + N_t\int_0^a\int_0^b\left((X')^2Y^2 + X^2(Y')^2\right)dxdy}\right\}X_iY_j \qquad (21)$$

In terms of temperatures substituting Eqs. (9) in (21) then

$$w(x,y) = -\sum_{i=1}^{m}\sum_{j=1}^{n}\left\{\frac{\alpha Eh^2T_{ij}\int_0^a\int_0^b (X''Y + XY'')dxdy}{12\left[(1-v)D\int_0^a\int_0^b\left((X'')^2Y^2 + 2X''XY''Y + X^2(Y'')^2\right)dxdy + \alpha EhT_{ij}\int_0^a\int_0^b\left((X')^2Y^2 + X^2(Y')^2\right)dxdy\right]}\right\}X_iY_j \qquad (22)$$

From Eqs. (21)& (22), the deflection w(x, y) tends to infinity when the critical thermal forces and critical thermal buckling temperature satisfy the following condition:

$$N_{tcr} = -\frac{(1-v)D\int\int\left((X'')^2Y^2 + 2X''XY''Y + X^2(Y'')^2\right)dxdy}{\int\int\left((X')^2Y^2 + X^2(Y')^2\right)dxdy} \qquad (23)$$

$$T_{0tcr} = \left[\left[-\frac{h^2\int\int\left[\left((X'')^2Y^2 + 2X''XY''Y + X^2(Y'')^2\right)dxdy\right]}{12(1+v)\alpha\int\int\left((X')^2Y^2 + X^2(Y')^2\right)dxdy}\right]\right] \qquad (24)$$

Assume the same w(x, y) as in Eqs. (11) Substituting it into Ritz formula with in plane thermal force and thermal moments with edges at (x=0, a) are restrained and edges at (y=0, b) are unrestrained then Eq. (19) will be

$$\sum_{k=1}^{m}\sum_{j=1}^{n}\left[D\int_0^a\int_0^b \left((X'')^2Y^2 + 2X''XY''Y + X^2(Y'')^2\right)dxdy + \frac{N_t}{(1-v)}\int_0^a\int_0^b \left((X')^2Y^2\right)dxdy\right]A_{ij} + \sum_{i=1}^{m}\sum_{j=1}^{n}\frac{M_t}{(1-v)}\int_0^a\int_0^b (X''Y + XY'')dxdy = 0 \qquad (25)$$

then

$$A_{ij} = -\frac{M_t \int\int (X''Y + XY'')dxdy}{(1-v)D\int\int\left((X'')^2Y^2 + 2XXYY + X^2(Y'')^2\right)dxdy + N_t\int\int\left((X')^2Y^2\right)dxdy} \quad (26)$$

Then the deflection

$$w(x,y) = -\sum_{i=1}^{m}\sum_{j=1}^{n}\left\{\frac{M_t\int_0^a\int_0^b (X''Y + XY'')dxdy}{(1-v)D\int_0^a\int_0^b\left((X'')^2Y^2 + 2X''XY''Y + X^2(Y'')^2\right)dxdy + N_t\int_0^a\int_0^b\left((X')^2Y^2\right)dxdy}\right\}X_iY_j \quad (27)$$

In terms of temperatures substituting Eq. (7) in Eq. (25) then

$$w(x,y) = -\sum_{i=1}^{m}\sum_{j=1}^{n}\left\{\frac{\alpha Eh^3T_{1l}\int_0^a\int_0^b (X''Y + XY'')dxdy}{12\left\{(1-v)D\int_0^a\int_0^b\left((X'')^2Y^2 + 2X''XY''Y + X^2(Y'')^2\right)dxdy + \alpha EhT_{0l}\int_0^a\int_0^b\left((X')^2Y^2\right)dxdy\right\}}\right\}X_iY_j \quad (28)$$

From Eqs. (26) & (27), the critical thermal forces and critical thermal buckling temperature as the deflection tends to infinity will develop as

$$N_{tcr} = -\frac{(1-v)D\int\int\left((X'')^2Y^2 + 2X''XY''Y + X^2(Y'')^2\right)dxdy}{\int\int\left((X')^2Y^2\right)dxdy} \quad (29)$$

$$T_{0lcr} = -\frac{h^2\int\int\left((X'')^2Y^2 + 2X''XY''Y + X^2(Y'')^2\right)dxdy}{12(1+v)\alpha\int\int\left((X')^2Y^2\right)dxdy} \quad (30)$$

Non- Linear Temperature Distribution :

Temperature field across the plate thickness is assumed in nonlinear form as in Eq.(2)

$$\Delta T = T_{0n} + zT_{1n} + z^2T_{2n}$$

The total strain energy and Ritz formulas in terms of in plane thermal forces and thermal moment will have the same form as in case of linear temperature distribution Eqs.(20),(21) and(22). But they different when taking the thermal forces and moments as a functions of temperatures, therefore, when all edges are restrained then the deflection in terms of temperatures will be

$$w(x,y) = -\sum_{i=1}^{m}\sum_{j=1}^{n}\left\{\frac{\alpha Eh^3T_{1n}\int_0^a\int_0^b (X''Y + XY'')dxdy}{12\left\{(1-v)D\int_0^a\int_0^b\left((X'')^2Y^2 + 2X''XY''Y + X^2(Y'')^2\right)dxdy + \alpha Eh(T_{0n} + h^2T_{2n}/12)\int_0^a\int_0^b\left((X')^2Y^2 + X^2(Y')^2\right)dxdy\right\}}\right\}X_iY_j \quad (31)$$

Then the deflection tends to infinity when the critical thermal buckling temperature have this magnitude

$$(T_{0n} + h^2T_{2n}/12)_{cr} = -\frac{h^2\int\int\left((X'')^2Y^2 + 2X''XY''Y + X^2(Y'')^2\right)dxdy}{12(1+v)\alpha\int\int\left((X')^2Y^2 + X^2(Y')^2\right)dxdy} \quad (32)$$

Again when edge at(x=0, a) are restrained and edges at (y=0, b) are unrestrained then Eq. (31) will be

$$w(x,y)=$$

$$-\sum_{i=1}^{m}\sum_{j=1}^{n}\frac{\alpha E h^3 T_{1n}\int_0^a\int_0^b (X''Y+XY'')dxdy}{12(1-\nu)D\int_0^a\int_0^b\left((X'')^2Y^2+2X''XY''Y+X^2(Y'')^2\right)dxdy+\alpha Eh(T_{0n}+h^2T_{2n}/12)\int_0^a\int_0^b\left((X')^2Y^2\right)dxdy}\{X_iY_j \quad (33)$$

And the critical thermal buckling temperature will be

$$(T_{0n}+h^2T_{2n}/12)_{cr}=-\frac{h^2\int\int\left((X'')^2Y^2+2X''XY''Y+X^2(Y'')^2\right)dxdy}{12(1+\nu)\alpha\int\int\left((X')^2Y^2\right)dxdy} \quad (34)$$

Thermal Buckling Temperature for Uniform Temperature :

Uniform heating of plate have been considerd ,the whole plate been warmed up to specificic temperature then $\Delta T = Tc$. The corresponding strain components are identically zero all over the domain. Then, the resultant forces are given as

$$N_x = N_y = -\frac{N_t}{1-\upsilon} \quad ,$$

$$N_{xy}=0 \quad N_t=\alpha EhT_c$$

$$M_t=0 \quad (35)$$

Substituting X_i and Y_j from Eq. (11) with help of appendix C the critical thermal buckling temperature for SSSS ends condition with edges at (x=0, a) are restrained and edges at y=0,b are unrestrained will be:

$$Tc_{cr}(m,n)=\frac{D\pi^2(1-\nu)(m^2+r^2n^2)^2}{E\alpha hm^2a^2} \quad (36)$$

For CCCC ends condition with edges at (x=0, a) are restrained and edges at y=0,b are unrestrained the critical thermal buckling temperature as

$$Tc_{cr}=\frac{h^2(\alpha_1^4+2r^2\alpha_2+r^4\alpha_3^4)}{12(1+\nu)a^2\alpha_1^2} \quad (37)$$

For CSCS ends condition with edges at (x=0, a) are restrained and edges at y=0,b are unrestrained the critical thermal buckling temperature will be

$$Tc_{cr}=\frac{h^2(\beta_1^4+2r^2\beta_2+r^4\beta_3^4)}{12(1+\nu)a^2\beta_1^2} \quad (38)$$

Thermal Buckling Temperature for Linear Temperature Distribution :

Assume the temperature across the plate thickness h have the form as in Eq.(1) $\Delta T = T_{0l} + zT_{1l}$ So that

$$N_t=\alpha Eh(T_{0n}+h^2T_{2n}/12) \quad \text{and}$$

$$M_t=\frac{\alpha Eh^3T_{1n}}{12} \quad (39)$$

Substituting X_i and Y_j from Eq. (11) with the help of appendix C. For SSSS ends condition when edges at (x=0, a) are restrained and edges at (y=0, b) are unrestrained the critical thermal buckling temperature will be

$$T_{0lcr}(m,n)=\frac{h^2\pi^2(m^2+n^2r^2)^2}{12(1+\nu)\alpha m^2a^2} \quad (40)$$

For CCCC with edges at (x=0, a) are restrained and edges at (y=0, b) are unrestrained

$$T_{0lcr} = \frac{h^2(\alpha_1^4 + 2r^2\alpha_2 + r^4\alpha_3^4)}{12(1+v)a^2\alpha_1^2} \quad (41)$$

And for CSCS with edges at (x=0, a) are restrained and edges at (y=0, b) are unrestrained

$$T_{0lcr} = \frac{h^2(\beta_1^4 + 2r^2\beta_2 + r^4\beta_3^4)}{12(1+v)a^2\beta_1^2} \quad (42)$$

Thermal Buckling Temperature For Non - Linear Temperature Distribution :

Assume the temperature across the plate thickness h have the formas in Eq.(2)

$\Delta T = T_{0n} + zT_{1n} + z^2T_{2n}$ so that

$N_t = \alpha Eh(T_{0n} + h^2T_{2n}/12)$ and

$$M_t = \frac{\alpha Eh^3T_{1n}}{12} \quad (43)$$

Substituting X_i and Y_j from Eq. (11) with the help of appendix C. with edges at(x=0, a) are restrained and edges at (y=0, b) are unrestrained

For SSSS

$$(T_{0n} + h^2T_{2n}/12)_{cr} =$$

$$\frac{D\pi^2(1-v)(m^2 + r^2n^2)^2}{E\alpha hm^2a^2} \quad (44)$$

For CCCC

$$(T_{0n} + h^2T_{2n}/12)_{cr} =$$

$$\frac{h^2(\alpha_1^4 + 2r^2\alpha_2 + r^4\alpha_3^4)}{12(1+v)a^2\alpha_1^2} \quad (45)$$

And For CSCS

$$(T_{0n} + h^2T_{2n}/12)_{cr} =$$

$$\frac{h^2(\beta_1^4 + 2r^2\beta_2 + r^4\beta_3^4)}{12(1+v)a^2\beta_1^2} \quad (46)$$

RESULTS AND DISCUSSIONS:

The sample of calculations was made on Aluminum 1060-H18 rectangular plate which has the mechanical and thermal properties given in appendix A respectively. Rectangular plate with three different aspect ratio a/b (2, 1.5, and 1.2). And three different dimensional ratio φ (16, 80 and 60) where $\varphi = a/h$ and owing constant magnitude of a=0.12 m have been studied

Tables (1) to (9) listed the first four buckling temperatures for SSSS, CCCC and CSCS plates which edges are restrained at x=0, a and unrestrained at y=0, b at different aspect ratios r (1.2, 1.5 and 2) and different φ (16, 80 and 60) from these results finding that the thermal buckling temperatures increased with increase the thickness to span ratio of the plates for all ends conditions. For each type of Ends condition the thermal buckling temperature increased when the aspect ratio (r) increased for the same end condition.

The CSCS ends condition have the lowest thermal buckling temperatures and the CCCC ends condition have the highest thermal buckling temperatures and the SSSS ends thermal buckling temperatures are between as shown in **figures (2) to (4).**

The CSCS ends thermal buckling temperatures will tends to be close to the thermal buckling temperatures of SSSS ends condition when the values of aspect ratio (r) increase, as shown in **figures (2) to (4).**

Finally thermal buckling temperatures and thermal buckling load have lowest values at first mode of buckling (1, 1) for all types of Ends condition and with all values of aspect ratios (r and φ).

It is observed that the minimum value of Nt occur when n=1 for SSSS case. Thus, for SSSS rectangular plate panels will buckle into several half-waves (m) in the loading direction, and only one half-wave (n) in the transverse direction, when the simply supported plate buckles the buckling mode can only be one half sine wave, $\sin(\pi y/b)$, across the span, while several have waves in the direction of (compression) restrained edges can occur thus

$$N_{tcr} = F\frac{(1-v)\pi^2 D}{b^2}$$

Where $F = (\frac{m}{r} + \frac{r}{m})^2$

To ascertain the aspect ratio r at which the critical thermal load is a minimum we set $\frac{\partial N_{tcr}}{\partial r} = 0$ and the result will be r = m, this provides the following minimum value of the critical thermal load where F=4 at r=1,2,3 and 4 as shown in **Fig. (5),** therefore no thermal buckling taking place when

$$N_{tcr} < \frac{4(1-v)\pi^2 D}{b^2}$$

The intersection point for the curves $m = 1$ and $m = 2$ is given from $\left(\frac{1}{r} + \frac{r}{1}\right) = \left(\frac{2}{r} + \frac{r}{2}\right) \Rightarrow r = 1.414$ Similarly the intersection points for the curves m=2 and m=3, etc., can be obtained as 2.449, 3.464 etc. as shown in **Fig. (5)** these results are similar to mechanical buckling of SSSS plate with uniaxial load only mentioned in references [McFarland et al. 1975].

For CCCC case It is observed that the minimum value of *Nt* occur when j=1 when the CCCC plate buckles the buckling mode can only be first mode appendix C

Across the span b, while several have waves in the direction of compression can occur thus

$$N_{tcr} = F\frac{(1-v)D}{b^2}$$

Where $F = \frac{\alpha_1^4 + 2\alpha_2 r^2 + \alpha_3^4 r^4}{\alpha_1^2 r^2}$

To ascertain the aspect ratio r at which the critical thermal load is a minimum we set $\frac{\partial N_{tcr}}{\partial r} = 0$ and the result will be $r = 0.2114\alpha_1$, this provides the following minimum value of the critical thermal load where F=58.2711 at r=1 and 4 as shown in **Fig. (6)** ,therefore no thermal buckling taking place for CCCC case when

$$N_{tcr} < \frac{58.2711(1-v)D}{b^2}$$

The intersection point for the curves *i* = 1 and *i* = *2* is r=1.3556 and is driven as for SSSS case. similarly the intersection points for the curves *i*=2 and *i*=3 can be obtained as *r*=2.0228 , and for curves *i*=3 and *i*=4 the intersection point will be at *r*=2.694 as shown in **Fig. (6).**

For CSCS case It is observed that the minimum value of *Nt* occur when j=1 when the plate buckles the buckling mode can only be first mode, the buckling mode can only be one half sine wave ,$\sin(\pi y/b)$,across the span b ,while several have waves in the direction of compression can occur thus

$$N_{tcr} = F\frac{(1-v)D}{b^2}$$

Where $F = \frac{\beta_1^4 + 2\beta_2 r^2 + \beta_3^4 r^4}{\beta_1^2 r^2}$

To ascertain the aspect ratio r at which the critical thermal load is a minimum we set $\frac{\partial N_{tcr}}{\partial r} = 0$ and the result will be $r = \alpha_1/\pi$, this provides the following minimum value of the critical thermal load where F=71.437 at r=1.5056 and as shown in **Fig. (7)**, therefore no

thermal buckling taking place for CSCS case when

$$N_{tcr} < \frac{71.437(1-v)D}{b^2}$$

The intersection point for the curves *i* = 1 and *i* = *2* is r=2.228 and is driven as for SSSS case. similarly the intersection points for the curves *i*=2 and *i*=3 can be obtained as *r*=3.149, and for curves *i*=3 and *i*=4 the intersection point will be at *r*=4.229 as shown in **Fig. (7)** .Therefore for SSSS and CCCC at r=1.2 the uniaxial thermal compression load buckles at mode 1 and for r= 1.5 and 2 the buckles at mode 2. In CSCS case the uniaxial thermal compression load buckles at mode 1 for r=1.2 and 1.5 and buckles at mode 2 for r=2 the intervals between two intersection points are very useful to determine the lowest thermal buckling mode .

CONCLUSIONS:

Following the main summarized conclusions raised by this paper are:

1- The buckling strength could be enhanced considerably by additional clamping of edges (i.e. from SSSS and CSCS cases to CCCC case) .
2- Thermal buckling temperatures and thermal buckling load have lowest values at first mode of buckling for all types of ends condition and with all values of aspect ratios (r and φ).
3- Thermal loads on plate induced thermal stresses when the edges are restrained. It has been found that a compression stress will developed when the temperature are uniform at the direction perpendicular to restrained edges with no deflection but at non uniform temperature thermal bending will appear and lateral deflection will occur.
4- Thermal buckling temperature and thermal stresses of thermoelastic plate affected by dimensional aspect ratios, temperature distributions and boundary conditions.

REFERENCES:

B.A. Samsam Shariat, M.R. Eslami "THERMAL BUCKLING OF IMPERFECT FUNCTIONALLY GRADED PLATES " International Journal of Solids and Structures. Volume 43, Issues 14-15, July 2006, Pages 4082-4096

D. McFarland , B. L. Smith, and W. D. Bernhart "ANALYSIS OF PLATES", Spartan Books, 1975.

Hiroyuki Matsunaga "THERMAL BUCKLING OF ANGLE-PLY LAMINATED COMPOSITE AND SANDWICH PLATES ACCORDING TO A GLOBAL HIGHER-ORDER DEFORMATION THEORY" Composite Structures 72 (2006) 177–192

H. L. Langhaar "ENERGY METHODS IN APPLIED MECHANICS", Wiley, 1962.

Hui Chen, Lawrence N. Virgin " FINITE ELEMENT ANALYSIS OF POST-BUCKLING DYNAMICS IN PLATES PART I: AN ASYMPTOTIC APPROACH" International Journal of Solids and Structures 43 (2006) 3983–4007

J. Lee, "COMPARISON OF THE TWO FORMULATIONS OF *w-u-v* AND *w-F* IN NONLINEAR PLATE ANALYSIS", Brief Notes, Journal of Applied mechanics, ASME,Vol. 69, JULY 2002.

R. B. Bhat "NATURAL FREQUANCES OF RECTANGULAR PLATES USING CHARAVHTERISTICS POLYNOMIALS IN RAYLIEGH-RITZ METHOD " J. Sound & Vib. Vol.102, 1985 p.493

S. P. Timoshenko and S. Woinowsky -krieger, "THEORY OF PLATES AND SHELLS" McGraw-Hill, 1959.

William L. Ko "PREDICTIONS OF THERMAL BUCKLING STRENGTHS OF HYPERSONIC AIRCRAFT SANDWICH PANELS USING MINIMUM POTENTIAL ENERGY AND FINITE ELEMENT METHODS ", NASA Technical Memorandum 4643, May 1995

Table (1) Four Lowest Critical Buckling Temperature for SSSS, Ends at x=0, a are Restrained and Ends at y=0, b are Unrestrained with r=1.2

r=1.2	Thermal critical temperature Tc_{cr} C^0		
Mode number	φ =16	φ =80	φ =60
1,1	11.1783	25.1512	44.729
2,1	13.8910	31.2548	55.5641
3,1	22.7382	51.1609	90.9526
4,1	35.6919	80.3068	142.7676

Table (2) Four Lowest Critical Buckling Temperature for SSSS, Ends at x=0, a are Restrained and Ends at y=0, b are Unrestrained with r=1.5

r=1.5	thermal critical temperature Tc_{cr} C^0		
Mode number	φ =16	φ =80	φ =60
1,1	19.8319	44.6217	79.3275
2,1	18.3357	41.2553	73.3427
3,1	26.4034	59.4076	105.631
4,1	39.0843	87.9397	156.3373

Table (3) Four Lowest Critical Buckling Temperature for SSSS, Ends at x=0, a are Restrained and Ends at y=0, b are Unrestrained with r=2

r=2	Thermal critical temperature Tc_{cr} C^0		
Mode number	φ =16	φ =80	φ =60
1,1	46.9393	105.631	187.7573
2,1	30.0412	67.5926	16.1647
3,1	35.2566	79.3275	141.0266
4,1	46.9393	105.631	187.7573

Table (4) Four Lowest Critical Buckling Temperature for CCCC, Ends at x=0, a are Restrained and Ends at y=0, b are Unrestrained with r=1.2

r=1.2	Thermal critical temperature Tc_{cr} C^0		
Mode number	φ =16	φ =80	φ =60
1,1	16.7869	37.7706	67.1477
2,1	19.9588	44.9072	79.8350
3,1	30.1467	67.8300	16.5866
4,1	44.7944	100.7875	179.1777

Table (5) Four Lowest Critical Buckling Temperature for CCCC, Ends at x=0, a are Restrained and Ends at y=0, b are Unrestrained with r=1.5

r=1.5	Thermal critical temperature Tc_{cr} C^0		
Mode number	φ =16	φ =80	φ =60
1,1	31.5924	71.0828	22.3694
2,1	27.3981	61.6457	5.5924
3,1	35.6019	80.1043	142.4076
4,1	49.4729	7.3140	197.8916

Table (6) Four Lowest Critical Buckling Temperature for CCCC, Ends at x=0, a are Restrained and Ends at y=0, b are Unrestrained with r=2

r=2	Thermal critical temperature Tc_{cr} C^0		
Mode No.	φ =16	φ =80	φ =60
1,1	82.6470	185.9558	330.5882
2,1	50.3865	9.3697	201.5461
3,1	50.9164	10.5619	203.6655
4,1	61.7152	34.8592	246.8608

Table (7) Four Lowest Critical Buckling Temperature for CSCS, Ends at x=0, a are Restrained and Ends at y=0, b are Unrestrained with r=1.2

r=1.2	Thermal critical temperature Tc_{cr} C^0		
Mode number	φ =16	φ =80	φ =60
1,1	8.9465	20.257	35.7861
2,1	16.3882	36.8734	65.5528
3,1	27.7419	62.4194	6.9678
4,1	42.8555	96.4249	171.4221

Table (8) Four Lowest Critical Buckling Temperature for CSCS, Ends at x=0, a are Restrained and Ends at y=0, b are Unrestrained with r=1.5

r=1.5	Thermal critical temperature Tc_{cr} C^0		
Mode number	φ =16	φ =80	φ =60
1,1	13.0944	29.4624	52.3775
2,1	19.5532	43.9947	78.224
3,1	30.6885	69.0491	18.7539
4,1	45.7440	102.9240	182.9761

Table (9) Four Lowest Critical Buckling Temperature for CSCS, Ends at x=0, a are Restrained and Ends at y=0, b are Unrestrained with r=2

r=2	Thermal critical temperature Tc_{cr} (C^0)		
Mode number	φ =16	φ =80	φ =60
1,1	25.7665	57.9745	103.0659
2,1	27.7370	62.4083	6.9482
3,1	37.7411	84.9174	150.9643
4,1	52.4000	13.8999	209.5999

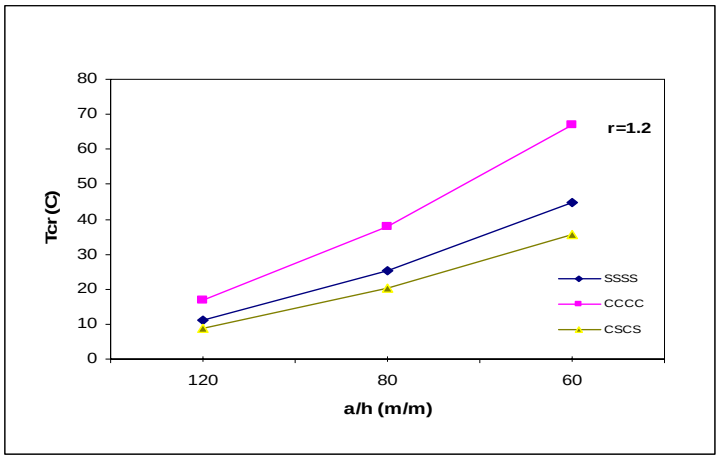

Fig. (2) Critical Thermal Buckling Temperatures at Different End Conditions, Ends are Restrained only at x=0, a. with Different φ Values at Constant Aspect Ratio (r=1. 2)

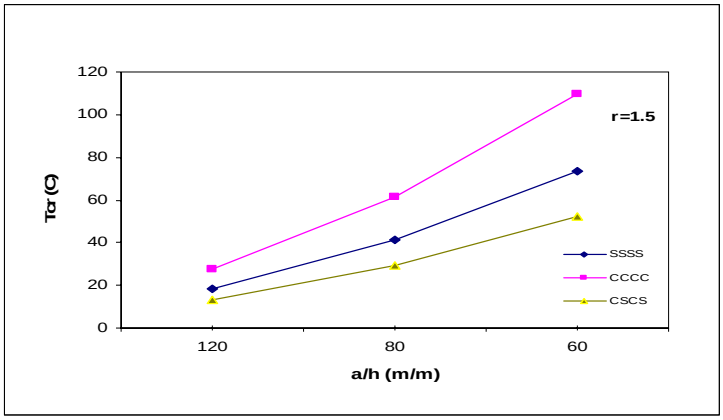

Fig. (3) Critical Thermal Buckling Temperatures at Different End Conditions, Ends are Restrained only at x=0, a with Different φ Values at Constant Aspect Ratio (r=1. 5)

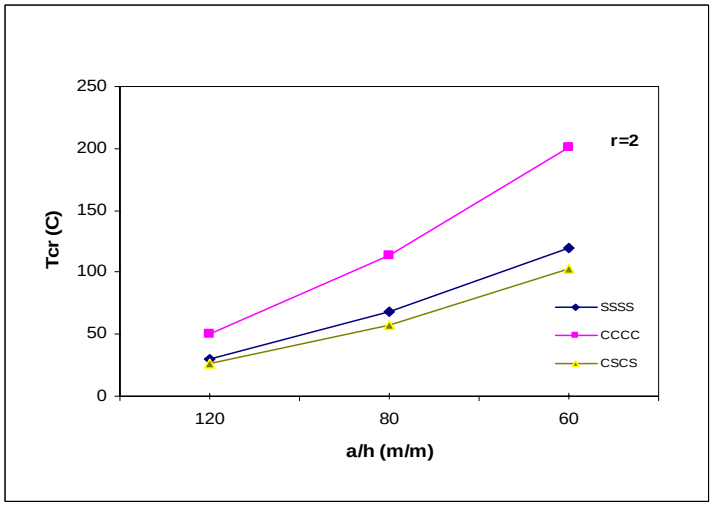

Fig. (4) Critical Thermal Buckling Temperatures at Different End Conditions, Ends are Restrained only at x=0, a with Different φ Values at Constant Aspect Ratio (r=2)

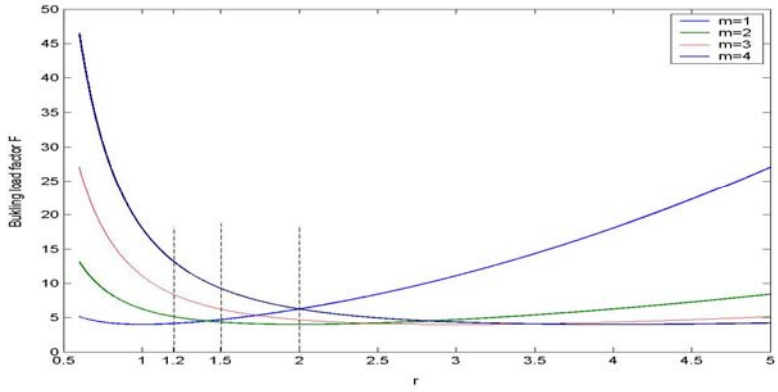

Fig. (5) Thermal Load vs. Aspect Ratio (r) for SSSS End Conditions, Ends are Restrained only at x=0, a

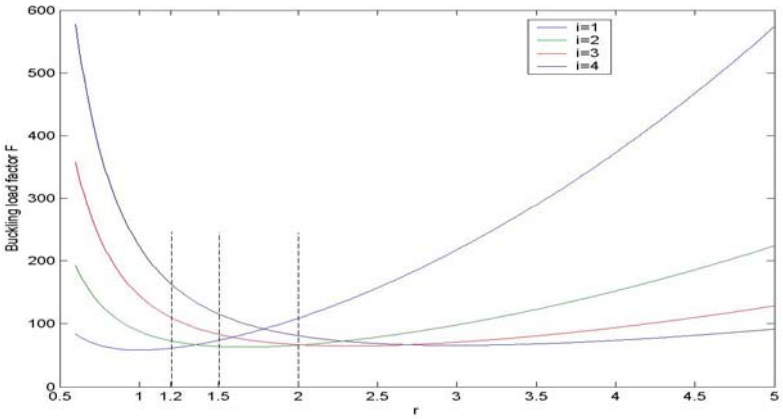

Fig. (6) Thermal Load vs. Aspect Ratio (r) for CCCC End Conditions, Ends are Restrained only at x=0, a.

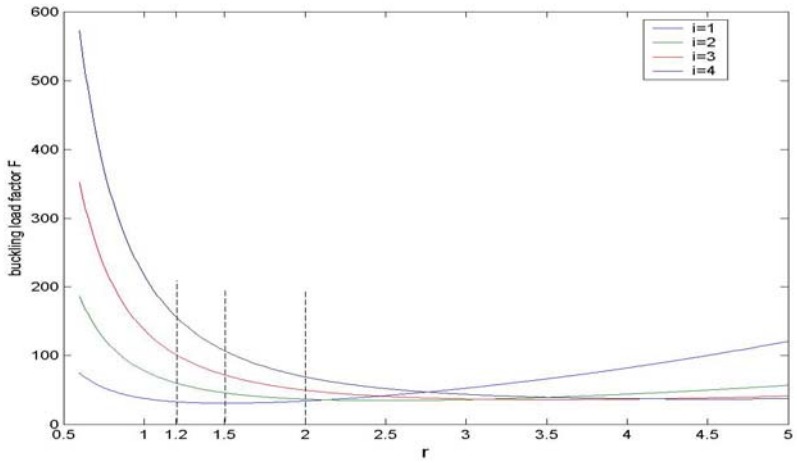

Fig. (7) Thermal Load Factor vs. Aspect Ratio (r) for CSCS End Conditions, Ends are Restrained only at x=0, a.

APPENDICES

Appendix A:

Some Combinations of End Boundary Conditions

deflection	mid—plane deformation	symbol
clamped	restrained	
	unrestrained	
supported	restrained	
	unrestrained	
free	restrained	
	unrestrained	

Appendix B :

Mechanical Properties of Aluminum 1060-H18

Density	**2705 kg/m³**
Hardness, Brinell	**35**
Ultimate Tensile Strength	**27 MPa**
Tensile Yield Strength	**20 MPa**
Elongation at Break	**6 %**
Modulus of Elasticity	**69 GPa**
Poisson's Ratio	**0.3**
Fatigue Strength	**44.8 MPa**
Machinability	**30 %**
Shear Modulus	**26 GPa**
Shear Strength	**75.8 MPa**

Thermal Properties of Aluminum 1060-H18

Heat Capacity	**0.9 J/g °C**
Thermal Conductivity	**233 W/m °C**
Coefficient of Thermal expansion	**2.34e-5/°C**
Convection Coefficient	**2.5 W/m² °C**

Appendix C:

For SSSS ends condition

$$X_i = \sin \mu_i x \ , \ Y_j = \sin \mu_j y$$

$$w_{x=0} = w_{x=a} = 0 \quad , \quad w_{y=0} = w_{y=b} = 0 \quad , \quad \frac{\partial^2 w_{x=0}}{\partial x^2} = \frac{\partial^2 w_{x=a}}{\partial x^2} = 0 , \quad \frac{\partial^2 w_{y=0}}{\partial y^2} = \frac{\partial^2 w_{y=b}}{\partial y^2} = 0$$

For CCCC ends condition

$$X_i = \sin \mu_i x - \sinh \mu_i x - \eta_i (\cos \mu_i x - \cosh \mu_i x)$$

$$\eta_i = (\sin \mu_i a - \sinh \mu_i a)/(\cos \mu_i a - \cosh \mu_i a)$$

$$Y_j = \sin \mu_j y - \sinh \mu_j y - \eta_j (\cos \mu_j y - \cosh \mu_j y)$$

$$\eta_j = (\sin \mu_j b - \sinh \mu_j b)/(\cos \mu_j b - \cosh \mu_j b)$$

$$w_{x=0} = w_{x=a} = 0 , \quad w_{y=0} = w_{y=b} = 0 \quad , \quad \frac{\partial w_{x=0}}{\partial x} = \frac{\partial w_{x=a}}{\partial x} = 0 , \quad \frac{\partial w_{y=0}}{\partial y} = \frac{\partial w_{y=b}}{\partial y} = 0$$

For SCSC ends condition

$$X_i = \sin \mu_i x - \sinh \mu_i x - \eta_i (\cos \mu_i x - \cosh \mu_i x)$$

$$\eta_i = (\sin \mu_i a - \sinh \mu_i a)/(\cos \mu_i a - \cosh \mu_i a) \quad , \quad Y_j = \sin \mu_j y$$

$$w_{x=0} = w_{x=a} = 0 \quad , \quad w_{y=0} = w_{y=b} = 0 \quad , \quad \frac{\partial w_{x=0}}{\partial x} = \frac{\partial w_{x=a}}{\partial x} = 0 , \quad \frac{\partial^2 w_{y=0}}{\partial y^2} = \frac{\partial^2 w_{y=b}}{\partial y^2} = 0$$

Where $\mu_i a$ and $\mu_j b$ are the roots of the above equations

The roots of SSSS ends condition are;

$$\mu_i = \frac{m\pi}{a} \quad , \quad \mu_i = \frac{n\pi}{b}$$

The roots of CCCC ends condition are;

$\alpha_1 = \alpha_3 = 4.73$
$\alpha_2 = 151.3$ For i=1 , j=1

$\alpha_1 = 4.73$
$\alpha_3 = (j+0.5)\pi$
$\alpha_2 = 123\alpha_3(\alpha_3 - 2)$ For i=1 , j=2,3,4,….

$\alpha_1 = (i+0.5)\pi$
$\alpha_3 = 4.37$
$\alpha_2 = 12.3\alpha_1(\alpha_1 - 2)$ For i=2,3,4,… j=1

$\alpha_1 = (i+0.5)\pi$
$\alpha_3 = (j+0.5)\pi$
$\alpha_2 = \alpha_1(\alpha_1 - 2)\alpha_3(\alpha_3 - 2)$ For i=2,3,4,. j=2,3,4,….\

$\alpha_1 = (i+0.5)\pi$
$\alpha_3 = (j+0.5)\pi$
$\alpha_2 = \alpha_1(\alpha_1 - 2)\alpha_3(\alpha_3 - 2)$ For i=2,3,4,. j=2,3,4,….

The roots of CSCS ends condition are

$\beta_1 = 4.73$
$\beta_3 = j\pi$
$\beta_2 = 12.3\, j^2\pi^2$ For i=1 , j=1, 2, 3,..

$\beta_1 = (i+0.5)\pi$
$\beta_3 = j\pi$
$\beta_2 = \alpha_1(\alpha_1 - 2)\, j^2\pi^2$ For i=2,3,4,… j=1,2,3….

NOMENCLATURE

Latin Symbols:

A	**Area (mm^2)**
a, b	**Plate side length (mm)**
D	**Flexural rigidity of an isotropic plate (N.mm)**
E	**Modulus of elasticity of isotropic material (N/mm^2)**
G	**Shear modulus of isotropic material (N/mm^2)**
h	**Plate thickness (mm)**
i ,j	**Integer**
Mt	**Thermal bending moment (N.m)**
m,n	**Integer**
Nx, Ny	**Edge forces per unit length (N/m)**
Nxy	**Shearing forces per unit length (N/m)**
Nt	**Thermal forces per unit length (N/m)**
r	**Dimensional aspect ratio a/b (m/m)**
T	**Temperature (C^0), Kinetic energy of the element (J)**
T_0	**Initial reference temperature (C^0)**
u, v, w	**Displacement components in x,y,z directions**
x, y, z	**Cartesian coordinates**

Greek Symbols:

V	**Poisson's ratio**
$\sigma_x, \sigma_y, \sigma_z$	**Normal stresses parallel to x, y, z axes (N/mm^2)**

$\tau_{xy}, \tau_{xz}, \tau_{yz}$	**Shear stresses component xy, xz, yz plain (N/mm^2)**
$\varepsilon_x, \varepsilon_y, \varepsilon_z$	**Direct strain in x, y, z directions**
$\gamma_{xy}, \gamma_{xz}, \gamma_{yz}$	**Shear strain component**
Π_{strain}	**Strain energy stored in complete plate (J)**
Π_b	**Strain energy stored due to bending (J)**
Π_N	**Strain energy stored due to mid-plane thermal forces (J)**
Π_M	**Strain energy stored due to thermal bending (J)**
φ	**Dimensional aspect ratio side / thickness (m/m)**
α	**Coefficient of thermal expansion ($1/C^0$)**
w	**Deflection (mm)**

Abbreviations Symbols:

CCCC	**Clamped-Clamped-Clamped-Clamped**
CSCS	**Clamped-Simply-Clamped-Simply**
SSSS	**Simply-Simply-Simply-Simply**

IMPLEMENTATION OF GYPSEOUS SOIL-ASPHALT STABILIZATION TECHNIQUE FOR BASE COURSE CONSTRUCTION

Prof.Saad I. Sarsam **Ass.prof.Dr. A′amal A. Al- Saidi** **Ban H. Al – Khayat**

Department of Civil Engineering, College of Engineering, University of Baghdad.

ABSTRACT

The aim of this research work is to study the effect of stabilizing gypseous soil, which covers vast areas in the middle, west and south parts of Iraq, using liquid asphalt on its strength properties to be used as a base course layer replacing the traditional materials of coarse aggregate and broken stones which are scarce at economical prices and hauling distances.

Gypseous soil brought from Al-Ramadi City, west of Iraq, with gypsum content of 66.65%, medium curing cutback asphalt (MC-30), and hydrated lime are used in this study.

The conducted tests on untreated and treated gypseous soil with different percentages of medium curing cutback asphalt (MC-30), water, and lime were: unconfined compression strength, and one dimensional confined compression under both dry and absorbed test conditions.

The test results showed that stabilizing gypseous soil using the optimum fluid content of 16% (5% cutback asphalt+11% water) have improved the unconfined compressive strength, compressibility, rebound consolidation, and waterproofing of gypseous soil, but under absorbed condition the stabilized gypseous soil using cutback asphalt only did not satisfy the requirements for base course construction, therefore it was decided to use lime additive to improve the properties of soil-cutback mixture under absorbed condition.

Keywords: Gypseous soil, Cutback asphalt, Asphalt stabilization, Unconfined compressive strength**,** Rebound consolidation.

الخلاصة

يتضمن هذا البحث دراسة تأثير تثبيت التربة الجبسية والتي تغطي مساحات شاسعة من وسط، غرب ، وجنوب العراق بأستعمال الأسفلت السائل على خواص القوة للتربة الجبسية و ذلك لغرض أستعمال مزيج التربة والأسفلت في انشاء طبقة الاساس للطرق كبديل لأستعمال الحجر المكسر أو الحصى الخابط التي تستعمل عادة لأنشاء أساس الطرق (base course layer) والتي يندر وجودها بأسعار مناسبة ومسافات حمل اقتصادية.

لغرض الدراسة تم اختيار تربة جبسية من مدينة الرمادي، غربي العراق ذات محتوى جبسي بنسبة 66.65% وتم استعمال أسفلت سائل متوسط التصلب (medium curing cutback asphalt) (MC-30) ومادة النورة.

تضمنت الدراسة اجراء فحوصات الانضغاط غير المحصور والانضغاط احادي المحور حيث اجريت جميع هذه الفحوصات للتربة غير المعالجة والمعالجة بنسب مختلفة من الاسفلت السائل متوسط التصلب , الماء والنورة في حالتي الجفاف والتشبع بالماء.

أوضحت النتائج ان تثبيت التربة الجبسية بأستعمال نسبة المعالجة المثلى وهي 16% (5% من الاسفلت السائل المتوسط التصلب+ 11% من الماء) ساعدت على تحسين قوة الانضغاط، الانضغاط المسترجع، وعزل الماء لكن بعد اشباع التربة الجبسية المثبتة بالأسفلت السائل بالماء أصبح مزيج التربة والاسفلت غير مناسب لتصميم طبقة أساس الطريق لهذا تم في المرحلة الثامنة من برنامج العمل اضافة مادة النورة لتحسين خواص مزيج التربة والاسفلت في حالة التشبع بالماء.

1. INTRODUCTION

Soil stabilization is a process of improvement in both strength and durability of a soil in such a manner as to maintain, alter or improve the performance of the soil as a construction material (Kadiyali and Lal, 2006). The process may include the blending of soils to achieve a desired gradation or the mixing of commercially available additives that may alter the gradation, texture or plasticity, or act as a binder for cementation of the soil (Stafen, 1994).

In the selection of a stabilizer, the factors that must be considered are the type of soil to be stabilized, the purpose for which the stabilized layer will be used, the type of soil improvement desired, the required strength, durability of the stabilized layer, the cost and environmental conditions (Stafen, 1994).

The purpose of stabilization are generally satisfied if one or more of the following changes in soil properties are accomplished by the agent or additive (Building Research Advisory Board, 1969) :

1. Increased strength.
2. Reduction in swelling properties.
3. Improved compactibility.
4. Reduced permeability.

2. MATERIALS

2.1 Gypseous Soil

The soil of this investigation was taken from Al-Ramadi city, Al-Anbar Governorate, west of Iraq. A shovel was used to remove the top soil and gypseous soil was obtained from a depth of 0.5m up to 1.0 m depth. Due to the presence of gypsum in a macrocrystalline form in the soil under study, a suitable sizing process has been performed using a plastic hammer then soil was sieved through sieve No.4, and the portion passing was oven dried at 45°c. **Table (1)** summarizes the chemical properties of gypseous soil and **Table (2)** presents the physical properties of gypsies soil, while **Fig. (1)** shows the grain size distribution of the soil.

2.2 Liquid Asphalt

Medium curing cutback asphalt (MC-30) "manufactured at al-Dora refinery" by one-step:

91.2 %[(40-50) Asphalt cement] +8.8% [Kerosene] → (MC-30)

Properties of cutback asphalt (MC-30) used are given in **Table (3)**.

2.3 Water

Ordinary tap water is used throughout this study in preparing the specimens.

2.4 Lime

In this study, hydrated lime manufactured at "Tang Fani" factory in Iran was used. The chemical composition of lime is given in **Table (4)**.

3. SPECIMENS PREPARATION

3.1 Mixing Technique

To prepare the specimen, the pulverized and homogenous gypseous soil passing No.4 sieve was oven dried at a temperature of (45°) then thoroughly mixed with the required percentage of water by hand until the water dispersed throughout the mixture, then the required percentage of cutback asphalt was added and mixed by rubbing the mixture between palms for two minutes so that the mixture has a homogenous character, and a proper coating of soil particles with asphalt

occurred. When lime additive was added to the soil cutback mixture to improve the properties of the soil cutback mixture under absorbed condition the required amount of lime additive was first mixed with the oven dried passing No. 4 sieve gypseous soil. Then the optimum water content of 11% was added to the soil-lime mixture and mixed thoroughly by hand. Then cutback asphalt was added and mixed by rubbing the mixture between palms for two minutes so that the mixture has a homogenous character.

3.2 Unconfined Compression test Specimens' Preparation and Testing

After mixing soil with the required amount of fluid content (cutback asphalt and water). The predetermined weight of the mix which gives the maximum modified dry unit weight of 19.8 (kN/m^3), was statically compacted in a cylindrical mould of a split type of 3.8 cm in diameter, and 7.6 cm in height in three equal layers according to the (ASTM D 5102 – 96). Specimens were allowed to cure for four days at room temperature of 25± 3ºC and the average value of the unconfined compressive strength for each duplicate specimens was calculated and considered for analysis. The unconfined compression test was carried out according to the (ASTM D 2166 – 00) standard, using a constant strain compression machine with a loading rate of 1.52 mm per minute. To determine the effect of water absorption on the unconfined compressive strength of the soil asphalt mixture the prepared unconfined compression test specimens were weighted then placed in the absorption apparatus which consisted of a container of size 35×25×16 cm depth, filled with 8 cm thickness of fully saturated sand passing 6 mm sieve, this sand layer was kept saturated throughout the absorption period with distilled water by visual inspection then the whole tank was covered by polythene sheets tightly to retain the moisture in the sand and specimens. This was done for 24 hours to allow the water to reach the samples by capillary action. This procedure was adopted to simulate the field conditions, the sand layer representing the subbase material, the polythene sheets representing the bituminous surfacing and the specimens representing the stabilized base course. After an absorption period of 9 days, the unconfined compressive strength of specimens was tested.

3.3 One-Dimensional Confined Compression Test Specimens' Preparation and Testing

This test is carried out on specimens of natural soil and on specimens prepared at the optimum fluid content of 16%; additional specimens were prepared with 1% variation of fluid content as 15% and 17% to check the effect of fluid content on the consolidation properties. Another group of specimens were prepared at the optimum fluid content of 16% mixed with the optimum lime content of 7%. After mixing the soil with the required amount of fluid content, the predetermined weight of the stabilized soil that gives the maximum standard dry unit weight of 17.7 (kN/m^3) was compacted in a mould of 75mm diameter and 20mm height using static compaction. Specimens were allowed to cure in the ring for (7) days at room temperature of 25±3 ºC, to maintain the specimen's shape, then specimen was withdrawn from the ring.

The test was conducted according to the procedure of (ASTM D 2435 – 96). The prepared specimens were divided into two groups, the first group was tested in dry condition, while the second group was flooded with water for (24) hrs. One dimensional confined compression test was conducted using the consolidation test apparatus. Each specimen was subjected to successive load increments of 25, 50, 100, 200, 400, and 800 kPa during 24 hours and the consolidation readings were recorded. The load was doubled after each increment and the

time was also doubled before making the next observation. After recording the consolidation at a load of 400 kPa, the load was released to 200 kPa to allow for strain rebound and the first rebound strain was recorded after two hours release period, then load was applied again and raised to 800 kPa. The consolidation was recorded at this load, then another unloading process was conducted by releasing the load to 200 kPa, the final rebound strain was recorded after a two hour release period.

4. ANALYSIS AND DISCUSSION OF TEST RESULTS

4.1 Unconfined Compression Test

It was found as shown in **Fig. (2)** that the unconfined compressive strength increases with increasing cutback asphalt content, this increase may be attributed to the gain in cohesion which is provided by continuous film of asphalt coating the soil particles. The unconfined compressive strength reaches a maximum value at 16% fluid content (5% cutback asphalt + 11% water) which may represent the optimum particle coating, but the unconfined compressive strength decreases as the cutback asphalt content increases, this may be attributed to the increases in thickness of bitumen films surrounding the soil particles and the fluid content is such to fill the voids completely preventing the particle interlock, this causes a high reduction in friction, which in turn leads to a reduction in the compressive strength. Such results are in agreement with many researchers work (TRRL, 1974), (Al-Kawaaz, 1990), (Al- Safarani, 2007), and (Taha, et. al., 2008).

Fig. (3) indicates that the absorption of the test specimens after 9 days absorption greatly reduces the compressive strength as compared to dry condition. This reduction may be attributed to the adhesion failure or a weaking of the cohesive bond between the asphalt-particles system. This result was well confirmed with (TRRL, 1974), (Al-Kawaaz, 1990), and (Taha, et. al, 2008).After adding lime additive in different percentages to the soil cutback mixture it was found as shown in **Fig. (4)**, that the unconfined compressive strength increases with increasing lime content. This behavior may be attributed to the to the role of the reaction of lime additive with soil in improvement of the cementation and water proofing action of the soil cutback mixture thus effect of water damage on soil cutback mixture is reduced.

4.2 One-Dimensional Confined Compression Test

As illustrated in **Fig. (5)** and **Fig. (6)** at both dry and soaked test conditions the strain decreases with increasing the cutback asphalt content up to the cutback asphalt content of 5%, then strain increases with increasing cutback asphalt content. This behavior may be attributed to that the cementation between soil particles increases with increasing cutback asphalt content up to optimum cutback asphalt content of 5% then, further increase in cutback asphalt content results in a lubrication action causes the soil particles will to slide over each other and that will increases the strain. Same behavior was observed by (Al-Kawaaz, 1990), (Al-Sharrad 2007), and (Al-Safarani, 2007). Additional reduction in strain was observed when the optimum lime additive of 7% was added to the soil cutback mixture as shown in **Fig. (7)**.

It's also shown in **Fig. (5)** that that when the applied load of 400 kPa is unloaded to 200 kPa at the first rebound cycle, and when load is reduced from 800 kPa to 200 kPa in the second rebound cycle the strain was increased which indicates the formation of certain type of elastic properties and rebound consolidation in the soil cutback mixture tested under dry condition and it can be noticed that when cutback asphalt content has

increased the percent of rebound consolidation has increased up to the optimum cutback asphalt content of 5% then percent of the rebound consolidation decreased with increasing cutback asphalt content, on the other hand as shown in **Fig. (6)** for specimens tested under soaked condition no significant strain change was observed(Al-Kawaaz, 1990), and (Sarsam and Ibrahim, 2008).

5. CONCLUSIONS

Based on the limited testing program, the following conclusions could be drawn:

1. The unconfined compressive strength of the soil-cutback mixture under dry and absorbed test conditions increases with increasing cutback asphalt content up to the optimum cutback asphalt content of 5%, then decreases.
2. There is a high reduction in the unconfined compressive strength of the soil-cutback mixture under absorbed condition as compared to the dry test condition. When lime additive is added to the soil-cutback mixture, the unconfined compressive strength under absorbed condition improves and increases with increasing lime content.
3. Soaking of pure gypseous soil in water causes a high increase in the volumetric strain. Addition of cutback asphalt to gypseous soil causes a reduction in the volumetric strain to the optimum cutback asphalt content of 5% then increase, additional reduction is observed when lime is added to the soil-cutback asphalt mixture.
4. Under dry test condition the addition of cutback asphalt to gypseous soil creates a type of elastic properties and rebound consolidation in the soil – cutback mixture at high stress application, and the permanent strain reduces.

REFERNCES

Al-Kawaaz, N., 1990. "Characteristics of Soil Asphalt Mixture" M. Sc. Thesis, College of Engineering, University of Baghdad.

Al-Safarani, M. G., 2007. "Improvement Ability of Gypseous Soil Characteristics Using Cutback Aasphalt and Lime" M. Sc. Thesis, Civil Engineering Department, University of Al – Mustansiria.

Al-Sharrad, S. I., 2007. "Effect of Cut-back MC-60 on Permeability and Compressibility of Gypseous Soil" IJCE-7th Issue, (p 16-26).

Building Research Advisory Board Study for Federal Housing Administration, 1969. "Chemical Soil Stabilization" National Academy of Sciences, Washington D. C.

Head, K.H., 1980. "Manual of Soil Laboratory Testing" Volume 1, Prentch, Press, London.

Head, K.H., 1982. "Manual of Soil Laboratory Testing" Volume 2, Prentch, Press, London.

Kadiyali, T. M. and Lal, N. B., 2006. "Principles and Practices of Highway Engineering" Third Edition. Khanna Publishers, New Delhi.

Sarsam, S. I. and Ibrahim, S. W., 2008. "Contribution of Liquid Asphalt in Shear Strength and Rebound Consolidation of Gypseous Soil" Engineering and Technology, Vol. 26, No. 4.

Stafen, M., 1994. "Soil stabilization for pavements" technical manual, No. 5-822-14, Air force manual, No 32- 1 0 19.

Taha, M.Y., Al-Obaydi, A.H.and Taha, O.M., 2008. "The Use of Liquid Asphalt to Improve Gypseous Soils" Al-Rafidain Engineering, Vol. 16, No. 4, (p 38-48).

Transport and Road Research Laboratory (TRRL), 1974. "Soil Mechanics for Road Engineers" London: Her Majesty's Stationery Office. (HMSO).

Table (1) Chemical composition of the natural soil

Organic content (%)	0.064
Gypsum content ($CaSO_4$) (%)	66.65
Carbonate content ($CaCo_3$) (%)	21.97
Total soluble salts (T.S.S.) (%)	58.1
Total (SO_3) (%)	31
pH value	8

Table (2) Physical properties of the natural soil

Physical property	**Test result**
Specific gravity	G_S = 2.42
Atterberg limits Liquid limit (%) Plastic limit (%) Plasticity index (%)	 L.L. = 33 P.L. = Non plastic P.I. = Non plastic
Standard compaction properties Max. standard unit weight Optimum moisture content (%)	 $\gamma_{d\ max}$=1.81 (gm/cm^3) = 17.7 (kN/m^3) O.M.C. =12 (%)
Modified compaction properties Max. modified unit weight Optimum moisture content (%)	 $\gamma_{d\ max}$=2.02(gm/cm^3) = 19.8 (kN/m^3) O.M.C. =11.6 (%)
Maximum dry unit weight (kN/m^3)	$\gamma_{max.}$ =20.17
Minimum dry unit weight (kN/m^3)	γ_{min} =12.4
% passing sieve No. 200	4.69
Coefficient of curvature	C_c =0.6
Coefficient of uniformity	C_u =8
Unified classification system	SP
Group index	0
AASHTO classification system	A-3

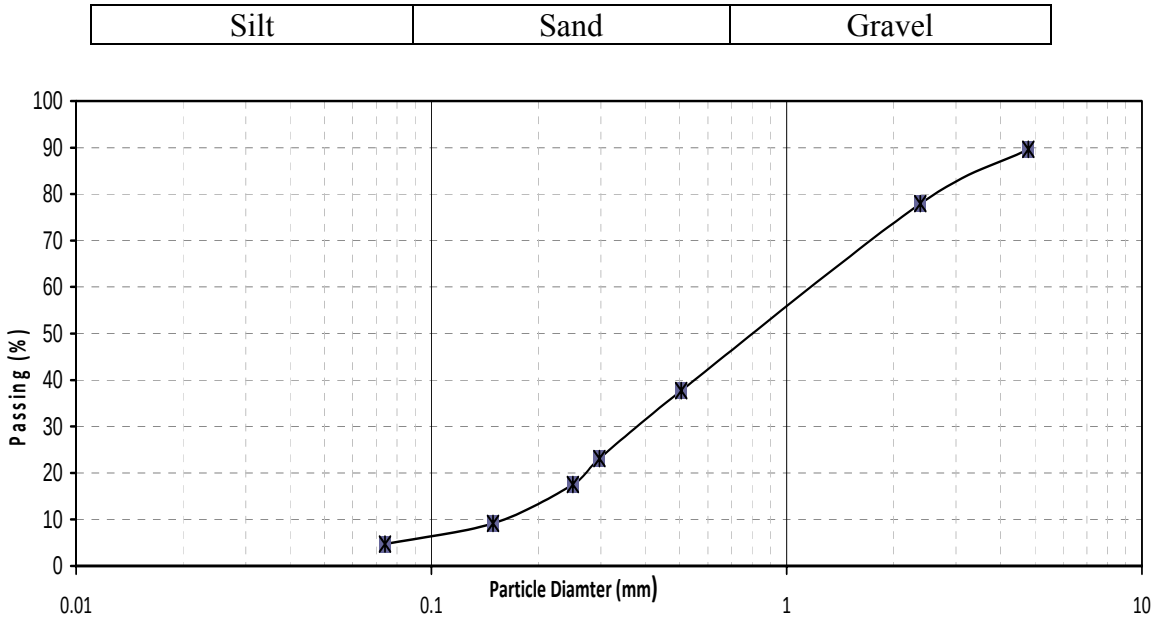

Fig. (1) Grain size distribution curve for the tested soil (ASTM D422-63).

Table (3) Properties of cutback asphalt (MC-30)*

Properties	Test results
Kinematic viscosity at 60ºC (c.stroke)	33
Specific gravity	0.99
Distillation Distillate % vol. of total distillate to 360ºC. To 225ºC To 260ºC To 315ºC Residue from distillation to 360ºC %vol. By difference	 25 max. 40-70 75-93 50 min.
Tests on residue from distillation Penetration at 25ºC (100gm, 5 sec.) Ductility at 25ºC (5cm/min) Solubility in carbon tetrachloride CCl_4 % wt.min	 120-300 100 min. 99.5 min.

*After Dora Refinery Lab/Baghdad

Table (4) Chemical composition of lime

The composition	Percent by weight
SiO_2	0.74
Fe_2O_3	0.19
Al_2O_3	0.5
CaO	64.23
MgO	1.17
L.O.I. (Loss On Ignition)	29.94
Percent passing No. 200 sieve	69.9

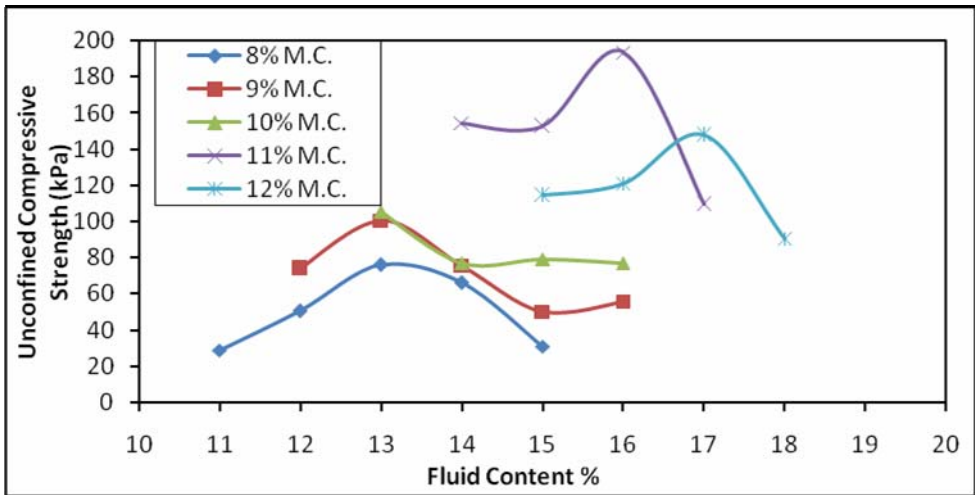

Fig. (2) Unconfined compressive strength-fluid content (%) relationship.

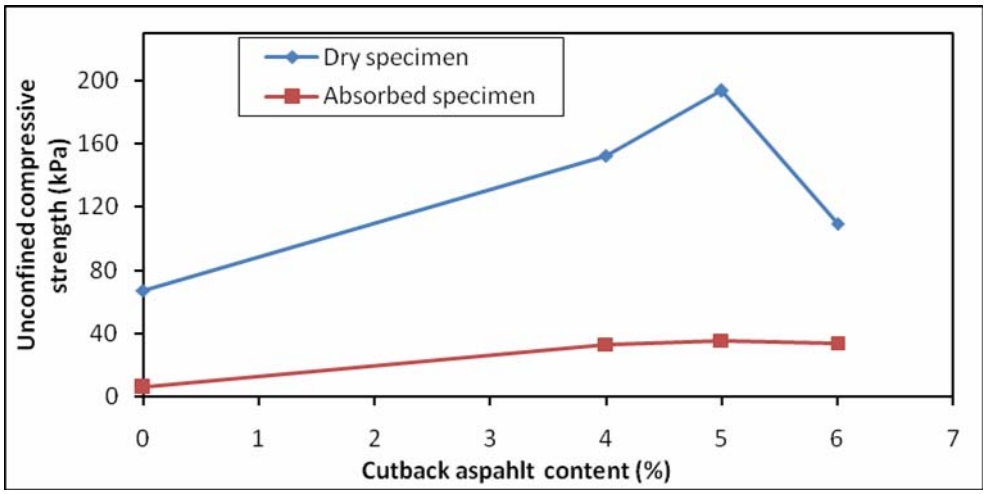

Fig. (3) Effect of water absorption on the unconfined compressive strength.

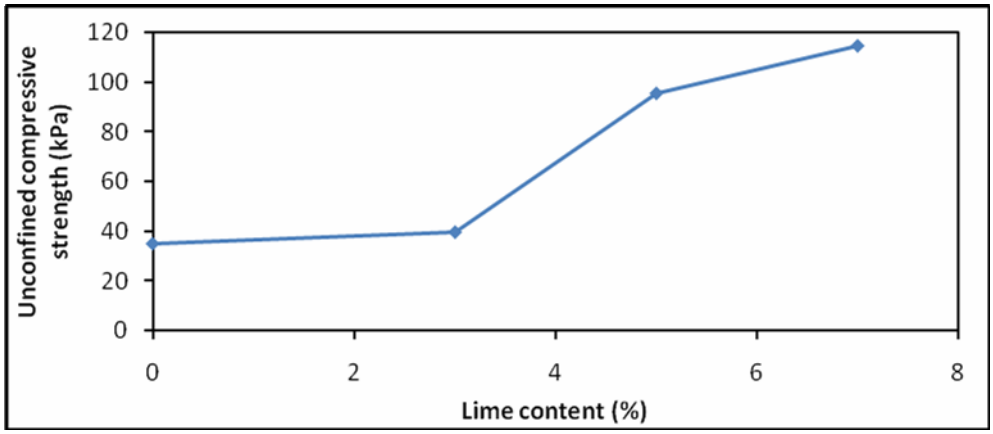

Fig. (4) Effect of lime additive content on the unconfined compressive strength of the soil cutback mixture.

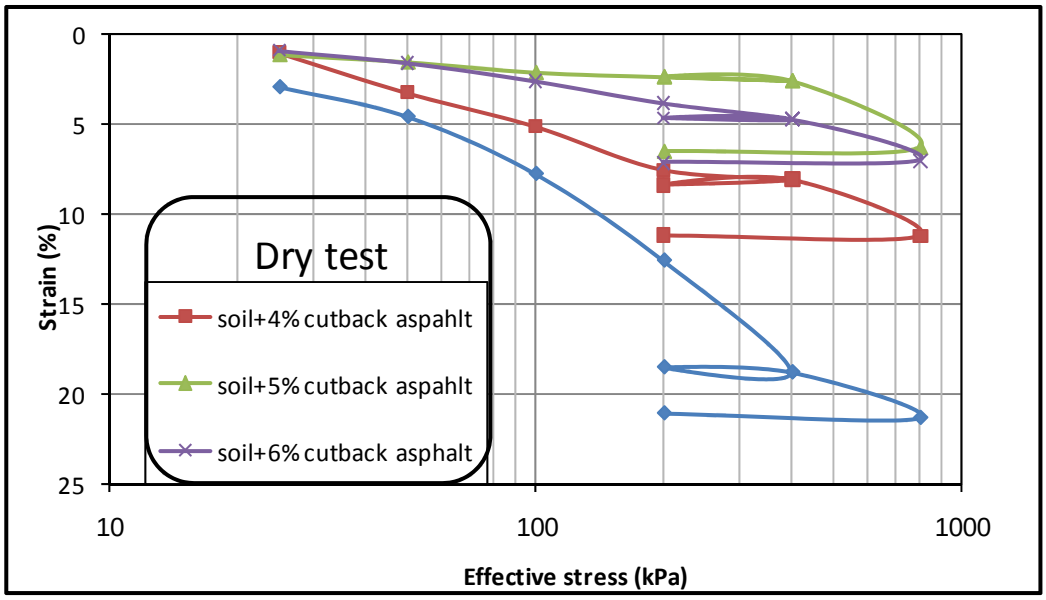

Fig. (5) Stress-strain relationship of one-dimensional compression test (dry condition).

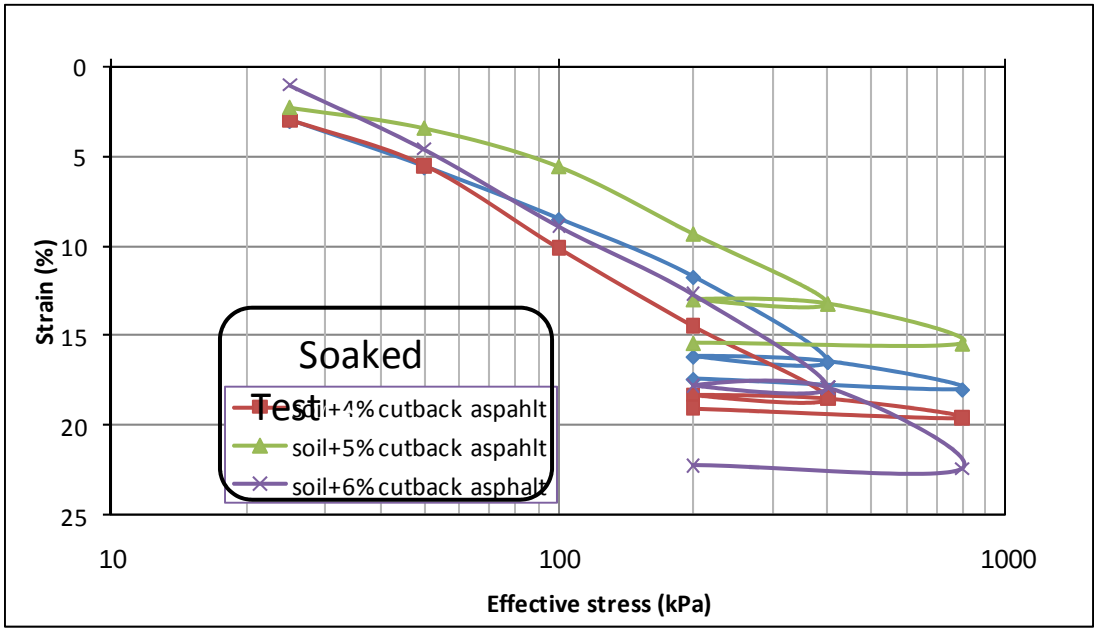

Fig. (6) Stress-strain relationship of one-dimensional compression test (soaked condition).

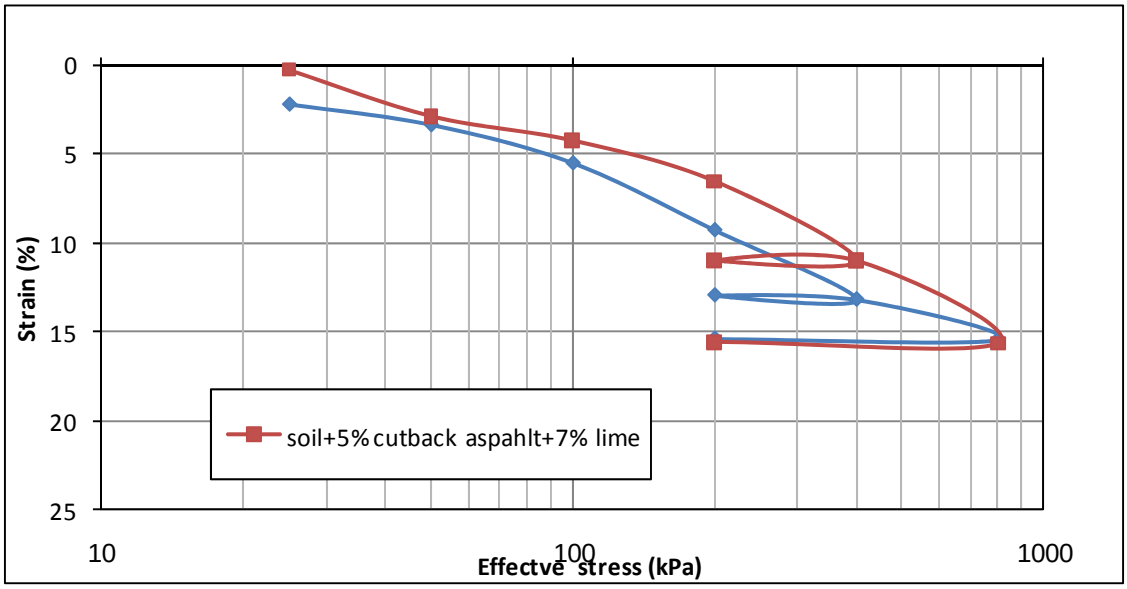

Fig. (7) Stress-strain relationship of one-dimensional compression test (soaked condition).

EMBEDDED LENGTH OF STEEL BARS IN SELF COMPACTED CONCRETE (SCC)

Dr. Amer F. Izzat
Lecturer in
Civil Engineering Depart.
AmerFarouk@yahoo.com

Dr. Ali I. Salahaldin
Lecturer in
Civil Engineering Depart.
ali_salahaldin@yahoo.com

ABSTRACT:

Experimental research was carried out on eight reinforced concrete beams to study the embedded length of the longitudinal reinforcement. Six beams were casted using self compacted concrete, and the two other beams were casted using normal concrete. The test was carried out on beams subjected to two point loads. The strain and the slip of the main reinforcement have been measured by using grooves placed during casting the beams at certain places. The measured strain used to calculate the longitudinal stresses (bond stress) surrounding the bar reinforcement,

The study was investigated the using of self compacted concrete SCC on the embedded length of reinforcing bars, and comparing the results with normal concrete.

The test results show that using SCC improve the concrete properties like the compressive strength and the tensile strength which mainly affected the bond strength and the splitting of the concrete cover failure. The testes show that with increasing concrete strength the bond strength increased.

Key word: SCC, Bond strength, Bond stress, Embedded length and Shear span,

الخلاصة:

دراسة عملية اجريت على ثمان عتبات خرسانية مسلحة لدراسة طول الطمر لقضبان حديد التسليح الموضوع في الخرسانة.ست نماذج استخدمت فيها الخرسانة ذاتية الرص ونموذجان استخدم فيهما خرسانة اعتيادية. الفحوصات اجريت على عتبات حملت بنقطتي تحميل. وباستخدام فراغات معينة وضعت في اثناء الصب داخل النماذج لقياس الانفعالات في قضبان حديد التسليح وكذلك لقياس الانزلاق الذي من الممكن ان يحدث، تم قياس اجهاد القص المحيط بقضبان حديد التسليح والمسبب للفشل وانسحاب قضبان حديد التسليح. الدراسة ركزت على عاملين رئيسيين هما:

- قوة تحمل الخرسانة.
- وطول الطمر المتاح لقضبان حديد التسليح.

لايجاد كيفية تاثيرهما على قيم اطوال الطمر في حالة استخدام خرسانة ذاتية الرص. وكذلك مقارنة النتائج مع الخرسانة الاعتيادية. اظهرت النتائج تحسن في خواص الخرسانة في حالة استخدام الخرسانة ذاتية الرص من ناحية مقاومة الانضغاط ومقاومة الشد الذي يؤثر تاثير مباشر على مقاومة الترابط وفشل الغطاء الخرساني وتهشمه.

INTRODUCTION:

The relationship between the workability of concrete against the stability of concrete matrix is specifying the durability and strength of concrete, because the loss of stability will lead to developing cracks in the concrete, which will increase the bond failure between the concrete contents [Foroughi et al 2008].

The self compacted concrete SCC has a high workability with acceptable stability, because the properties of concrete are affected by cementations matrix, aggregate and the transition zone between these two phases. Reducing the water cement (w/c) ratio and the addition of pozzolanic admixtures like silica fume are often used to modify the microstructure of the matrix and to optimize the transition zone [Caijin and Yanzahong 2005]. The reduction of the w/c ratio results in a decrease in porosity and refinement of capillary pores in a matrix. On the other hand, reducing w/c ratio may negatively influence the flowing ability of the fresh concrete, so a high range water reducing admixture must be used to keep an acceptable flowing ability. The effect of the pozzolanic admixtures can be explained by their pozzolanic reaction with calcium hydroxide released from cement hydration and by their filling effect in the voids among cement or other powder materials particles [Timo 2003].

MATERIAL PROPERTIES:

- The cement used in this study was Ordinary Portland Cement complying with ASTM C150-02. The test results are shown in **Tables 1** and **2** for the chemical and physical properties respectively.
- The coarse aggregate used was natural aggregate with 4.74-19mm nominal size of aggregate. The grading obtained from the results of sieve analysis of the aggregate lies within the range defined by ASTM C33-03.
- The results of the sieve analysis which was carried out on fine aggregate lies also within the range defined by ASTM C33-03. The chemical and physical test results for gravel and sand are shown in **Tables 3** and **4** respectively.
- Glenium 51: (modified polycarboxylic ether) was used as a water reducing agent plus stabilizing agent with a specific gravity of 1.1, at 20°C, PH = 6.5 as issued by the producer.
- Silica fume mineral admixture or micro silica**:** composed of ultrafine, amorphous glassy spheres of silicon dioxide (SiO_2), produced by Crosfield Chemicals, Warrington, England,

CONCRETE MIX PROPERTIES:

Several trial mixes were used. The final mix proportions used is 1:1.5:1.6 with various water cement ratio, the amount of glenium-51 admixture for each 100kg of cement and the content of silica fume. The mixture proportions are summarized in **Table 5**.

The slump flow test was carried out to measure the flowability of the SCC concrete mixes, while the ordinary slump test was carried out in case of using ordinary concrete.

The longitudinal steel reinforcement bars were deformed. Their tensile properties were determined according to ASTM 615-05a. The results are shown in **Table 6**

Table (1): Chemical cement test results

Chemical composition	
Composition	Quantity%
SO_3	1.24
MgO	2.80
C_3A	8.60
SIO_2	21.2
Al_2O_3	5.4
L.O.I	3.34
C_3S	35.1
CaO	52.5

*Chemical analysis was conducted by National Center for Construction Laboratories and Researches

Table (2): Physical cement test results

Physical properties	
Compressive strength, MPa (3 days) (7 days)	 32.6 39.4
Setting time (Vicate apparatus), Initial setting, h:min Final setting, h:min	 2:35 4:40
Specific surface area (Blaine method), m^2/kg	472
Soundness (Auto Clave) method, %	0.24

*Physical tests was conducted by National Center for Construction Laboratories and Researches

Table (3): Chemical and physical gravel test results

Properties	Test results
Absorption %	0.70
Specific gravity	2.60
Dry loose-unit weight kg/m^3	1582
Sulfate content as SO_3 %	0.42
Materials finer than 75μm%	2.80

* Tests was conducted by National Center for Construction Laboratories and Researches

Table (4): Chemical and physical sand test results.

Properties	Test results
Absorption %	0.54
Specific gravity	2.54
Sulfate content	0.07

* Tests was conducted by National Center for Construction Laboratories and Researches

Table (5): Concrete mix proportions

Beam designation		B1 & B2	B3 & B4	B5 & B6	B7 & B8
Water / powder (W/P)		0.6	0.5	0.4	0.5
Water	Kg/m^3	240	200	160	200
Superplasticizer	lit./100Kg(powder)	2	3	4	-
Cement	Kg/m^3	392	392	392	400
Silica Fume	Kg/m^3	8	8	8	-
Total Powder	Kg/m3	400	400	400	400
Gravel	Kg/m3	640	640	640	640
Sand	Kg/m3	600	600	600	600
Slump flow	(mm)	720	705	695	120*

* Slump test

Table (6): Properties of steel bars

Bar diameter (mm)	Modulus of elasticity (GPa)	Yield stress (MPa)	Strain at yield stress (microstrain)	Ultimate stress (MPa)
6	195	510	2615	650
16	192	480	2500	580

Mixing of concrete was carried out in a tilting pan type mixer. Aggregates and cement were first mixed dry for about 90seconds, water, silica fume and the superplasticizer together were mixed externally in a pan then were added to the pan mixer, after that mixing continued, for a further 90seconds.
For each test beam the following specimens were cast to determine the properties of the hardened concrete:

3-150mm diam. x 300mm long cylinders for compressive strength.
3-150mm diam. x 300mm long cylinders for indirect tensile strength.

EXPERIMENTAL PROGRAM:

Eight simply supported beams were tested; with clear span of 1000mm. Each beam is 100mm wide and 180mm depth as shown in **Fig. 1**. The main variables were the concrete strength and the embedment length, as shown in **Table 7**. Load was applied by using electric hydraulic jack.

Slip of reinforcing bar at the end of concrete beam has been measured by fixing a small steel angle at the face of each free end of the beam to support a dial gage of 0.002mm/div sensitivity, as shown in **Fig. 1b** (this called free end slip).

To specify the free end of the embedded length the bar was wrapped by a thick strip of an adhesive tape as tube spreader between the concrete and bar surface and at the other end of the shear span, groove was made by using pieces of cork placed at the mold and tied by the longitudinal bar.

In the groove zone, a 6mm bar diameter and 30mm long was welded on the longitudinal reinforcement before casting the concrete to fix the dial gage which was 0.002mm/div. sensitivity, and by fixing piece of steel plate at the face of the groove side toward the shear span, the slip under point load was measured, (this called loaded end slip) as shown in **Fig. 1b**. On the other side of the longitudinal bar reinforcement at the groove zone, two bars of 12mm diameter were welded at a space of 50mm, before casting the concrete, to fix the demec discs, to measure the strain in the longitudinal bar reinforcement by using the extensometer with 0.002mm/div. sensitivity. **Fig. 2** shows test set up of beam B1.

Table (7): Details of the beams specimens

Beam designation	Concrete strength	Bar diameter	Embedded length	Type of concrete*
B1	32	16	200	SCC
B2	30	16	250	SCC
B3	43	16	200	SCC
B4	45	16	250	SCC
B5	51	16	200	SCC
B6	53	16	250	SCC
B7	26	16	200	NC
B8	27	16	250	NC

- SCC: self compacted concrete
- . NC: normal concrete

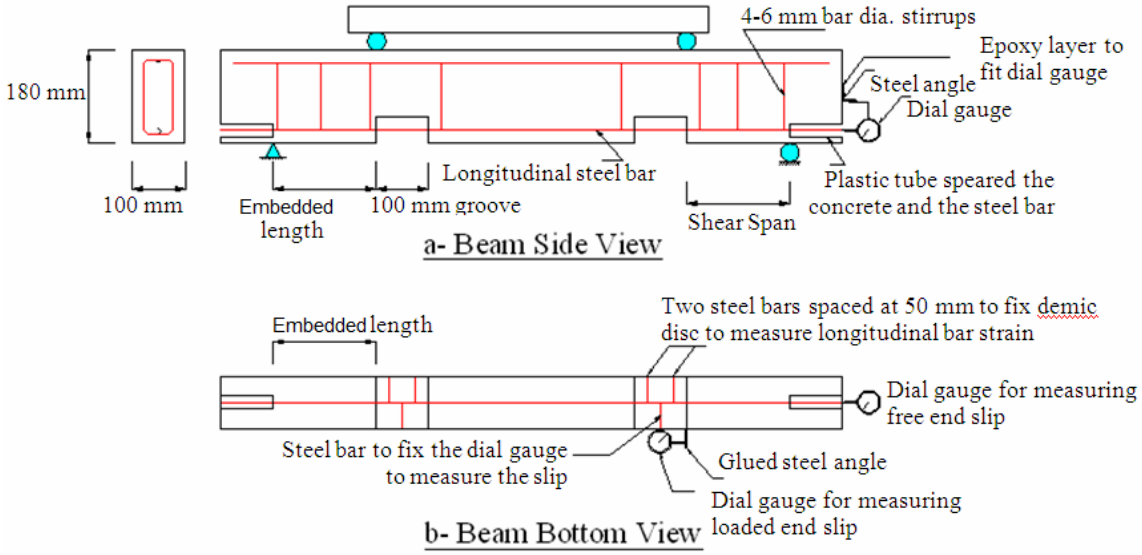

Figure (1): Details of the beam specimens

Figure (2): Test set up of beam B1

RESULTS AND DISCUSSIONS:

Some researchers define the bond strength failure as bond strength where the slippage at the reinforcement reaches a specific value such as 0.25mm [Foroughi et al 2008] while others define the bond strength failure by the ultimate bond strength (maximum average bond stress) where many cracks will appear and the reinforcement will pull out i.e. separation occurs between the reinforcing bar and the surrounding concrete cover [Ferguson et al 1954]. Obviously using a specific slippage is more conservative or the second one is over estimated.

Bond stress (u) in the test was calculated by using the strain which was measured by the extensometer and converted by using the modulus of elasticity of the reinforcement.

$$l_d \ \pi \ d_b \ u = A_b \ f \Rightarrow$$

$$u = \frac{d_b \ f_s}{4 \ l_d} \qquad \text{Eq (1)}$$

Table 8 shows the steel bar stress near failure, the bond stress and the mode of failure. As shown in this table with increasing compressive strength of the concrete the mode of failure enhancing by delaying the bond failure (splitting of concrete cover) till reaching the reinforcement to the higher stresses (yielding of the reinforcement). Splitting cylinder tension test was carried out by using 300mm x 150mm cylinders to find the concrete tensile strength. Because shear and bond strength are dependent on the tensile strength of the concrete [Holm 1994]. **Table 9** shows the tensile test and the ACI-code equation results. The test results show improvements in the tensile strength in case of using *SCC* as compared to the *NC*. Also, it shows the ratio of splitting tensile strength to compressive strength (f'_{ct} / f'_c) to be ranging from 8 to11, in agreement with [Avram et al 1981]. They found that (f'_{ct} / f'_c) ranges from about 6 to 20. Also the table shows that, the increase in compressive strength is higher than that in the tensile strength. So, the ratio (f'_{ct} / f'_c) approximately deceases with increasing in compressive strength. This observation watches that of [Mindess et al 2003] where they show that as the compressive strength increases the ratio (f'_{ct} / f'_c) decreases. Also,

comparing the test results with that of the ACI-code (the ratio of measured /calculated tensile strength) shows that, the ratio was more than one and it increased with increasing the SCC compressive strength i.e. the ACI-code results were underestimated in case of using SCC, in contradict, the ratio was less than one for normal concrete.

Crack patterns: all beams show typical crack patterns. During loading steps, a longitudinal main crack appeared from the groove zone at the beam tension face and extended towards the beam free end. During that with increasing the applied load, transverse cracks were observed and gradually extended upward to the beam sides (in the shear span) and growing diagonally toward the loading point, but the shear reinforcement prevents shear failure. Also, some diagonal cracks were observed at the beam bottom face. These cracks propagated, growing and joining together to cause the splitting of the concrete cover at the beam bottom face. The main difference between the beam crack patterns, were that, with increasing of the compressive strength the transverse cracks were concentrated in a few numbers than that for the beams with less compressive strength, where many cracks were observed. This can be seen in **Fig. 3** and **Fig. 4** for beams B2 and B3 respectively.

Loaded end slip: (the dial gauge under the loading point).

1 - All beams shows that at earlier loading stages, no slip to occur at the loaded end slip (the dial gauge at the groove zone), because the whole concrete section works in both tension and compression together to resist the applied load. When the cracks began to appear at the bottom face of the shear span, slip was recorded. Beams with NC recorded slightly earlier slip than beams with SCC**,** for the similar bond stress, the earlier loaded end slip increased as the concrete strength decrease, and at the latest loading steps it will increase, as shown in **Figs 5** and **6**.

2 - The experimental results in **Figs 7** and **8** show, for the beams of approximately equal concrete strength, the loaded end slip was similar but with slightly differs near failure, with increasing the embedded length by 25% the loaded end slip increased by about 20%. This tendency to occur because the bond failure is progressively starting from the loaded end toward the free end and as the embedded length increased this will delay the bond failure (concrete splitting) and allow to record more loaded end slip. **Table 10** shows the ratio of the loaded end slip of SCC beams to NC beams (which they had same embedded length but with different concrete strength) i.e. beams B1, B2 and B3 to B7 (which they had same l_d = *200mm)* the ratios were 25%, 36% and 157% respectively and for B2, B4 and B6 to B8 (which they had same l_d = *250mm)* the ratios were 18%, 21% and 116% this due to the same reason above (the bond failure is progressively starting from the loaded end toward the free end and as the embedded length increased this will delay the bond failure).

Free end slip: (The last point of the shear span toward the beam end)

1- The free end slip was less than that for loaded end slip at all loading steps, and comparing beams having same embedded length but with different concrete strength as shown in **Figs 9 and 10**, the free end slip decrease with increasing the concrete strength, this because of the enhancing in the concrete properties especially the tensile strength of the concrete (concrete surrounding the reinforcement bar). **Table 10** shows with increasing the compressive strength the free end slip will decreases.

2- **Figs 11** and **12** shows, increasing the embedded length will decrease the free end slip, because the bond stress is not uniformly distributed along the

embedded length, its highest value at the loaded end and gradually decreases or vanished near the free end. This was visible in the crack patterns. They were forming and propagating from the loaded end toward the free end during the loading stages, so, the bond failure is progressive process. Many researchers had the same observation and they connect between the bond strength and the square root of the concrete strength [Ferguson 1962], [Untrauer and Henry 1965] and [Kemp and Wilhelm 1997] when the other factors are constant, while [Orangun et al 1975] study the lap splices, they assume that the strain variation along the splice approximately linear.

CONCLUSIONS:

1. Using SCC improves concrete strength (compressive strength and the tensile strength) as a result, resistance of the concrete to prevent pull out the reinforcement bar, compared to the NC, this was observed by enhancing in the mode of failure from bond failure (pull out) to bond with yielding the reinforcement bar.
2. The loaded and free ends slip for the SCC beams were less than that for the beams with NC at the similar loading stag (bond stress).
3. Beams with similar embedded length, increasing the concrete strength will decrease the earlier loaded end slip and increasing the loaded end slip near the failure.
4. While for the similar concrete strength, increasing the embedded length will increase the loaded end slip, and decreasing the free end slip near the failure.
5. The cracks propagates from the loading point extended towered the free end, this means that , the bond stress is not uniformly distributed along the embedded length, it reaches the maximum value at the loading point and decreases or vanished near the free end .
6. The bond failure depends on the free end slip, because it's the last resisting point of the embedded length, and increasing the embedded length will decrease the free end slip or delaying the bond failure.

Table (8): Beams test results.

Beam designation	Embedded Length * (mm)	Compressive strength (MPa)	Steel stress (MPa)	Bond Stress *u* (MPa)	Mode of failure
B1	205	32	337	6.57	Bond
B2	250	30	384	6.14	Bond
B3	204	43	427	8.37	Bond
B4	246	45	496	8.06	Bond with yield
B5	204	51	489	9.58	Bond with yield
B6	252	53	520	8.24	Bond with yield
B7	200	26	238	4.76	Bond
B8	250	27	247	3.95	Bond

* The embedded length was measured for the failed side.
(All beams with the same bar diameter.)

Table (9): Beams tensile strength results.

Beam designation	f'_{ct}* (MPa)	f'_{ct}/f'_c	ACI-code equation	Measured/calculated Tensile strength
B1	3.12	9.7	3.16	0.98
B2	3.02	10.1	3.06	0.99
B3	3.70	8.6	3.67	1.01
B4	3.71	8.24	3.76	0.99
B5	4.76	9.33	4.00	1.18
B6	4.83	9.11	4.08	1.18
B7	2.48	9.5	2.86	0.86
B8	2.41	8.9	2.91	0.83

- Concrete tensile strength by indirect test.
- The ACI 05-code equation $f'_{ct} = 0.56\sqrt{f'_c}$ (R11.2.1.1)

Table (10): results of loaded end and free end slip.

Beam designation	Loaded end slip (mm)	(SCC/NC) % of loaded end slip*	Free end slip (mm)	(SCC/NC) % of free end slip*
B1	0.58	28	0.46	13
B2	0.73	18	0.35	34
B3	0.61	36	0.28	85
B4	0.75	21	0.22	113
B5	1.16	157	0.20	160
B6	1.34	116	0.15	213
B7	0.45	100	0.52	100
B8	0.62	100	0.47	100

* Ratio of (SCC/NC) loaded end slip for the same embedded length i.e. (B1, 3, 5/B7 and B2, 4, 6/B8)

Figure (3): Crack patterns for beam specimen B2 with compressive strength 30MPa

Figure (4): Crack patterns for beam specimen B6 with compressive strength 53MPa

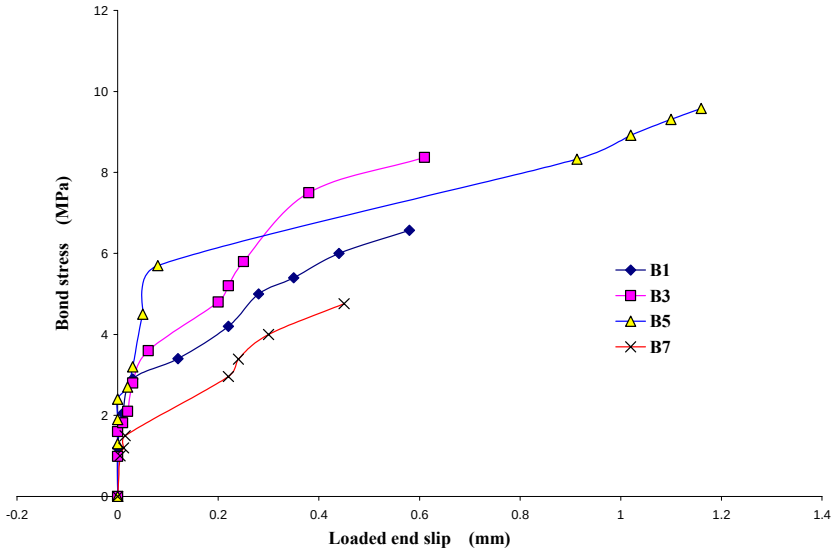

Figure (5): Bond stress-loaded end slip for beams had same embedded length (l_d = 200mm) and different compressive strength

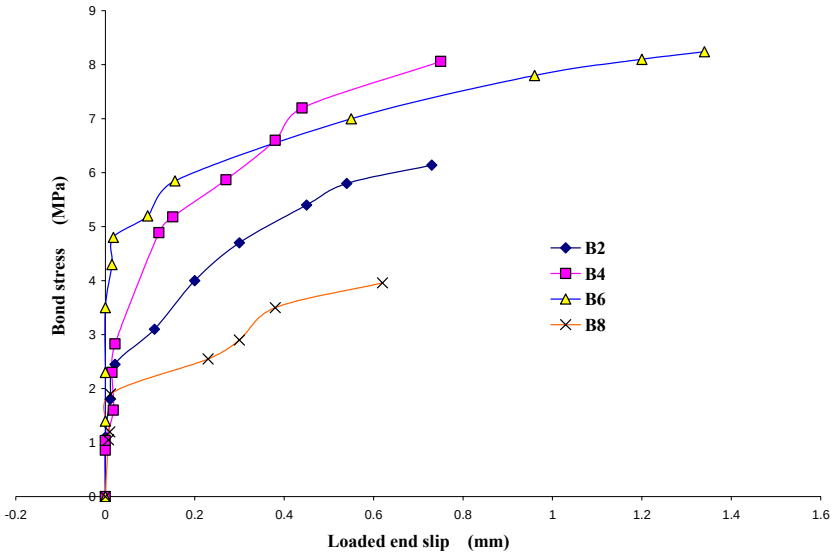

Figure (6): Bond stress-loaded end slip for beams had same embedded length (l_d = 250mm) and different compressive strength

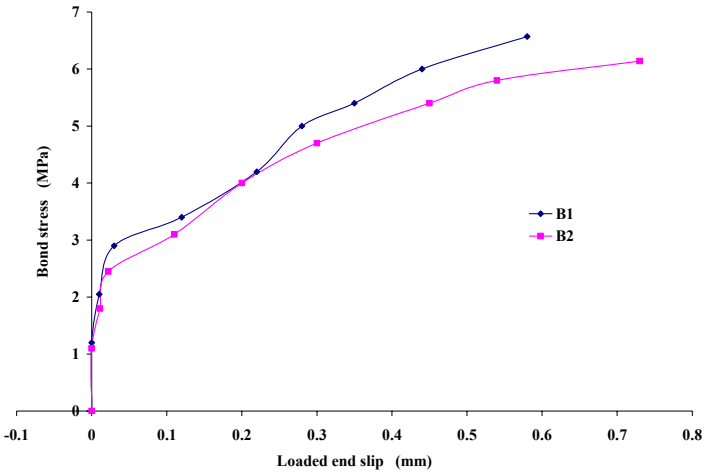

Figure (7): Bond stress-loaded end slip for beams had same compressive strength ($f_c' \cong 30$MPa) and different embedded length

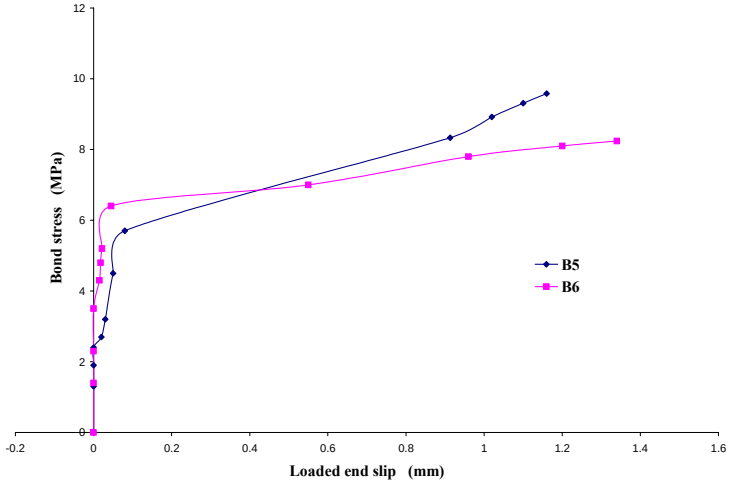

Figure (8): Bond stress-loaded end slip for beams had same compressive strength ($f_c' \cong$ 52MPa)and different embedded length

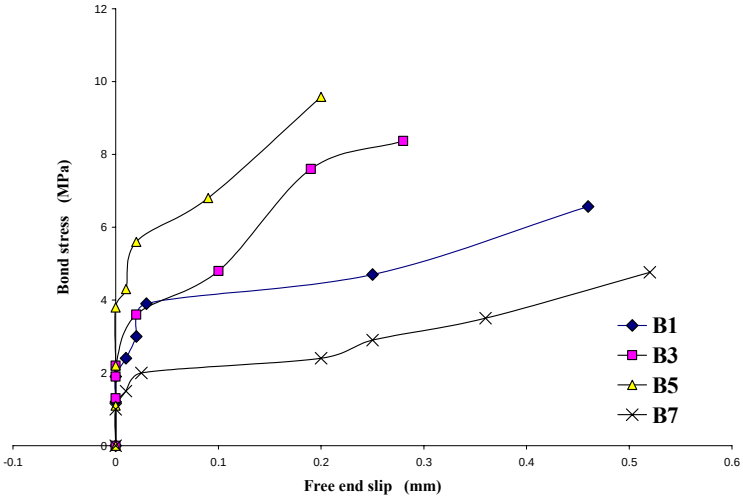

Figure (9): Bond stress-free end slip for beams had same embedded length (l_d = 200mm) and different compressive strength

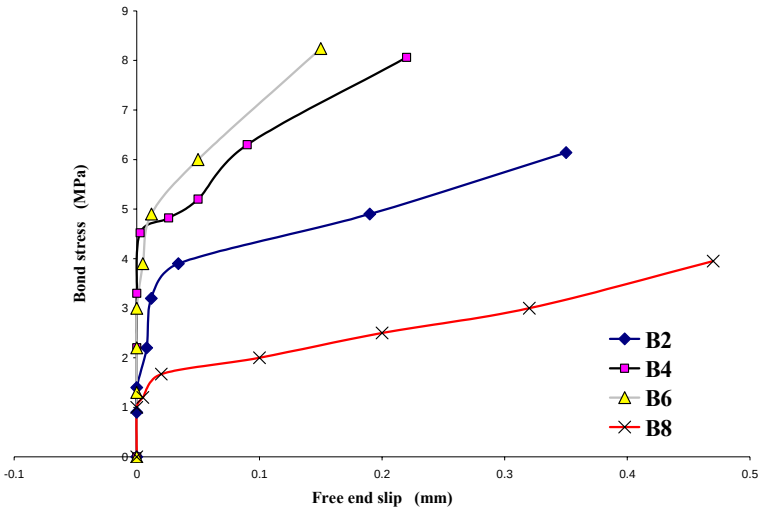

Figure (10): Bond stress-free end slip for beams had same embedded length (l_d = 250mm) and different compressive strength

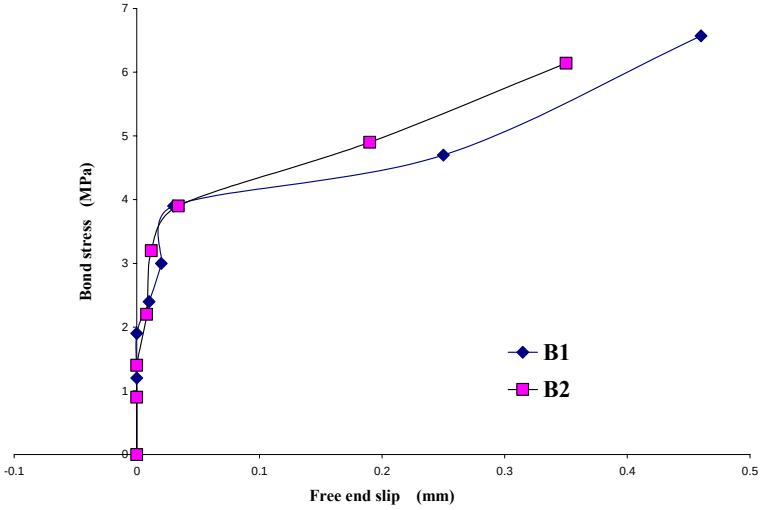

Figure (11): Bond stress-free end slip for beams had same compressive strength ($f_c' \cong 30$MPa) and different embedded length

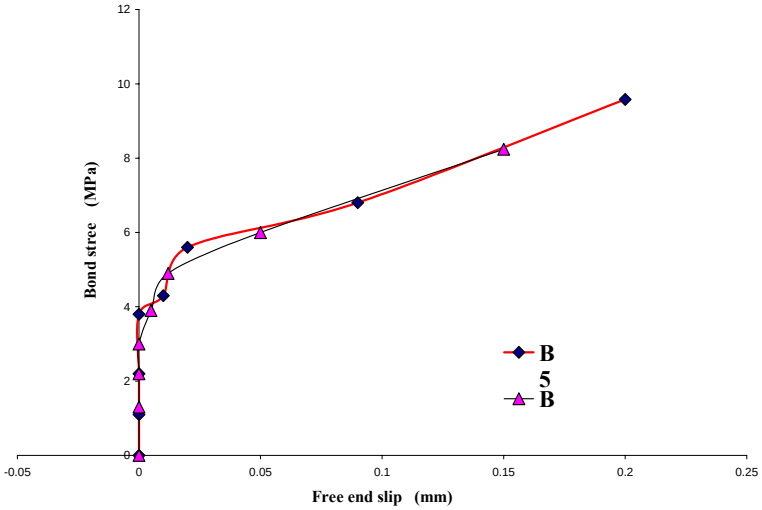

Figure (12): Bond stress-free end slip for had same compressive strength ($f_c' \cong$ 52MPa)and different embedded length

REFFRENCES:

- A. Foroughi-Asl, S. Dilmaghani. and H. Famili "Bond Strength of Reinforcement Steel in Self Compacted Concrete", International Journal of Civil Engineering, Vol.6, No. 1, March 2008. pp. 24-33.
- ASTM Designation C150-02"Standard Specification for Portland Cement " 2002 Annual Book of ASTM Standard, American Society for Testing and Material, Philadelphia Pennsylvania, Section4,Vol. 4.02. pp. 89-93.
- ASTM Designation C33-03"Standard Specification for Concrete Aggregate" 2002 Annual Book of ASTM Standard, American Society for Testing and Material, Philadelphia Pennsylvania, Section4, Vol. 4.02, pp. 10-16.
- ASTM Designation A615-05a"Standard Specification for Testing Method and Definitions for Mechanical Testing of Steel Products "2002 Annual Book of ASTM Standard, American Society for Testing and Material, Philadelphia Pennsylvania, Section4, Vol. 1.01, pp. 248-287C.
- C. Avram, I. Facaorau,O. Mirsu, I. Filimon and I. Tertea" Concrete strength and strains", Elsevier Scientific Publishing Company, pp. 105-133, 1981
- E. L. Kemp, andW. J. Wilhelm, "Investigation of the Parameters Influencing Bond Cracking" ACI Journal, Proceedings V. 76, No. 1, Jan. 1979, PP 47-72.
- C. O. Orangun, J. O. Jirsa, and J. E. Breen "The Strength of Anchoraged Bars: A Reevaluation of Test Data on Development Length and Splices", Research Report No. 154-3F, Centre for Highway Research, The University of Texas at Austin, Jan. 1975, pp78.
- P. M. Ferguson, R. D. Turpin, and J. N. Thompson" Minimum Bar Spacing as a Function of Bond and Shear Strength", ACI Journal, Proceedings V.50, No.10,June 1954, pp. 869-887.
- P. M. Ferguson, and J.N. Thompson, "Development Length of High Strength Reinforcing Bars in Bond", ACI Journal, Proceedings V. 59, No. 7, July 1962, pp887-992
- R. E. Untrauer, and R. L. Henry, "Influence of Normal Pressure on Bond Strength", ACI Journal, Proceedings V. 62, No. 5, May 1965, pp. 577-586.
- S. Mindess, J. F. Young, and D. Darwin, "Concrete Design", Second Edition, Prentice Hall, 2003.
- S. Caijin, and W. Yanzahong, "Mixture Proportioning and Properties of Self-Consolidating Lightweight Concrete Containing Glass Powder", ACI Materials Journal, Vol. 102, No. 5, Sep./Oct. 2005, pp. 355-363.
- Timo Wüstholz, "Fresh Properties of Self-Compacting Concrete", Otto-Graf-Journal, Vol. 14, 2003, pp. 179-188.
- T. A. Holm, "Light Weight Concrete and Aggregates", Standard technical Publication 169C, 1994.
- W. Zhu, M. Sonebi and P.J.M. Bartos "Bond and Interfacial Properties of Reinforcement in-Self Compacted Concrete", Advanced Concrete and Masonry Cement, University of Paisley, PA12BE, Scotland, UK, 2000 pp. 442-448.

NOTATIONS:

A : Bar cross-section area (mm^2)

d_b : Bar diameter (mm)

l_d : Effective embeddedlength (mm)

f_s : Steel stress (MPa)

SCC: Self compacted concrete

u : Bond stress (MPa)

INFLUENCE OF AMBIENT TEMPERATURE ON STIFFNESS OF ASPHALT PAVING MATERIALS

Prof. Hamed M. H. AL-
(Civil Eng. Dept.) / Baghdad Univ.
eng_mariam1985@yahoo.com

Maryam S. Makki , M.Sc.,
(Civil Eng. Dept.) / Baghdad Univ.
Email: profhamedalani@yahoo.com Email:

ABSTRACT

Asphalt pavement properties in Iraq are highly affected by elevated summer air temperatures. One of these properties is stiffness (resilient modulus).To explain the effect of air temperatures on stiffness of asphalt concrete, it is necessary to determine the distribution of temperatures through the pavement asphalt concrete layers. In this study, the distribution of pavement temperatures at three depths (2cm ,7cm, 10cm) below the pavement surface is determined by using the temperature data logger instrument .

A relationship for determining pavement temperature as related to depth and air temperature has been suggested.

To achieve the objective of this thesis,the prepared specimens have been tested for indirect tension in accordance with ASTM D4123, using the pnuematic repeated load apparatus , in order to determine the values of resilient modulus at three different temperatures (10, 25, 40) ˚C.

From results of testing, it is observed that the resilient modulus decreases with increase in test temperature by a rate of 8.78×10^3 Psi/C˚ for asphalt concrete wearing courses.

An increase in optimum asphalt content by 0.1% (by weight of total mixture) causes a decrease in resilient modulus by 22% at a temperature of 40C˚.

A statistical model for the prediction of resilient modulus has been developed depending on mixture variables of: asphalt content , asphalt binder viscosity , surface area of combined aggregates , air voids of compacted mixture and test temperature.

Key words: Ambient temperature , Stiffness

الخلاصه

خواص التبليط الاسفلتي في العراق تتأثر بدرجة كبيرة بدرجات حرارة الهواء المرتفعة خلال فصل الصيف.وانه أحد هذه الخواص هو معامل الجساءة و لبيان تأثير درجات حرارة الهواء على معامل الجساءة للخرسانة الاسفلتية فأنه من الضروري تحديد توزيع درجات الحرارة خلال طبقات الخرسانة الاسفلتية للتبليط.

في هذه الدراسة توزيع درجات حرارة التبليط على ثلاثة اعماق(2سم ،7سم ،10 سم) تحت سطح التبليط تم تحديده بأستخدام جهاز تسجيل بيانات درجات الحرارة.

لقد تم اقتراح علاقة رياضية لتحديد درجة حرارة التبليط نسبة الى العمق ودرجة حرارة الهواء.

و لتحقيق الهدف من هذا البحث العينات المحضرة تم فحصها للشد الغير مباشر وفقآ (ASTM D4123)بأستخدام جهاز الاحمال المتكررة لأيجاد معامل المرونة بثلاث درجات حرارة مختلفة هي (10, 25 ،40) درجة مئوية.

ومن نتائج الفحص لوحظ ان معامل المرونة يتناقص بزيادة درجة حرارة الفحص بنسبة 8.78×10^3 Psi/C˚ للطبقات السطحية للخرسانة الاسفلتية.

وأن الزيادة في محتوى الاسفلت المثالي بمقدار 0.1% من وزن الخلطة الكلية يسبب نقصان في معامل المرونة بمقدار 22% عند درجة حرارة 40 مئوي.

وقد تم تطوير علاقة احصائية لتنبأ معامل المرونة وفقآ لمتغيرات الخلطة الاسفلتية: محتوى الاسفلت ’ لزوجة الاسفلت ’المساحة السطحية للركام ’نسبة الفجوات الهوائية للخلطة المرصوصة ودرجة حرارة الفحص.

INTRODUCTION

Asphalt concrete pavements are physical structures responding in a complex way to the influence of many factors (i.e., loads, material, variables, environmental conditions, etc.) and their interactions.

Temperature is one of the most important environmental factors affecting the design, performance, and distress of pavement structures.
Temperature affects many physical properties in asphalt concrete pavement including material stiffness. Generally, the stiffness (resilient modulus) of a pavement is a measure of materials performance and their ability to spread the applied traffic loading over a specified area.

The resilient modulus Mr, is defined as the elastic modulus based on the recoverable strain under repeated Loading:

$$Mr = \frac{\sigma}{\varepsilon_r}$$

σ: Repeated diametral stress

ε_r: Vertical resilient strain

Because the applied load is usually small, the resilient modulus test is considered as a nondestructive test and the same sample can be used for other tests.

The resilient modulus is a major parameters in design of pavement structures, overlay thickness determination, and for the assessment of other rehabilitation needs. In design, the properties of materials must be specified, so that the response of the pavement, such as stresses, strains, and displacements, in the critical components, can be determined (Huang, 1993).

REVIEW OF LITERATURE

Increase in the temperature of asphalt layer is one of the major factors of failure in asphalt pavements in tropic zones. In these areas, high air temperature and severe radiation of solar ray cause increase in asphalt layer temperature. It has been shown that the modulus of elasticity can strongly depend on the temperature **Figure (1).**
The surface of the pavement varies with time during the day, which in turn changes the temperature in the pavement section. For instance, temperature variation in a flexible pavement section in Los Angeles (**Ongel and Harvey 2004**) is shown in **Figure (2).**
Thus, to determine in-situ strength characteristics of flexible pavement, it is necessary to predict the temperature distribution within the HMA layers. There exist several developed models for the prediction of the pavement temperature based on air temperature in the literature (**Witczak, 1972; Fatani et al. (1990),SHRP, 1994)** are shown in eq. (1) and (2), (3)respectively.

$$T_{pave} = T_{air}\left(1 + \frac{76.2}{Z + 304.8}\right) - \frac{84.7}{Z + 304.8} + 3.3 \quad (1)$$

Where:
Tpave = pavement temperature (˚C)
Tair = air temperature (˚C)
Z= depth below the pavement surface (cm)

$$T(d) = 3.714 + 1.006\ T(a) - 0.146\ d \quad (2)$$

Where:
T(d) = pavement temperature at depth d, °C
T(a) = air temperature, °C
d = depth from pavement surface, cm

$$T_{pave} = [T_{air} - 0.00618\,(latitude)^2 + 0.22891\,(latitude) + 42.2]0.9594 - 17.78 \quad (3)$$

Where:
Tpave = pavement temperature at the 2 cm depth below the surface (°C)
Tair = air temperature (°C)

Diefenderfer et al. (2003) linear models are developed for predicting daily maximum and minimum temperatures based on data collected at the Virginia Smart Road. Data are used from three depths within the pavement for model development: 0.038, 0.063, and 0.188m below the surface.
The model is developed to predict maximum daily pavement temperatures, Tpmax , is as follows:

$$Tpmax = 3.2935 + 0.6356Tmax + 0.1061Y - 27.7975Pd \quad (4)$$

The RMSE for this model is 3.54 and the adjusted R^2 value is 91.36%. The model is developed to predict minimum daily pavement temperatures, Tpmin, is as follows:

$$Tpmin = 1.6472 + 0.6504Tmin + 0.0861Y + 7.2385Pd \quad (5)$$

The RMSE for this model is 2.79 and the adjusted R^2 is found to be 91.41%. These values indicate that the model for predicting the minimum daily pavement temperature is slightly more accurate than the model for predicting the maximum daily pavement temperature. **Figure (5)** presents the actual maximum daily pavement temperature and the predicted maximum daily pavement temperature at a depth of 0.038m for this model validation time period. **Figure(6)** presents the actual minimum daily pavement temperature and the predicted minimum daily pavement temperature at a depth of 0.038m for this model validation time period.

(Algibury,2008) develops two models to predict the resilient modulus of asphalt pavement layers (surface, binder, base) layers.R^2 for model no. (6) and model no.(7) are 0.957 , 0.955 .

$$M_r = 322342.7 - 47368.7(T^{0.310683} + P_8^{0.310683}) - 4341.74P_s + 8913.09P_{200} + 11055.16\sin(-577.43Av - 28.083) \quad (6)$$

$$M_r = 10249376 - 38888.4(T^{0.365504} + P_8^{0.365504}) - 5996.61P_s + 11115.29P_{200} - 0.000181EXP(0.000122Av + 24.72744) \quad (7)$$

Where:
Mr : Resilient Modulus (psi)
T : Test Temperature (°C)
Av : Percent Air Voids
P_S : Percent Volume of Effective Asphalt
P_8 : Percent Passing Sieve No. 8
P_{200} : Percent Passing by weight of Filler Content

Tpmax= 3.2935 + 0.6356Tmax + 0.1061Y – 27.7975Pd

EXPERIMENTAL WORK

Indirect Tension Repeated Load Test

The indirect tension repeated load test specified by **ASTM D4123** "Standard Test Method for Indirect Tension Test for Resilient Modulus of Bituminous Mixtures ", are conducted by using the pneumatic repeated load system (PRLS), (Al-Bayati, 2006). In these tests, repetitive diametral loading is applied to the specimen and the resilient vertical strain is measured under load repetitions. Diametral loading is applied with a constant loading frequency of 60 cycles per minute and loading sequence of 0.1 sec load duration and 0.9 sec rest period .Three temperatures 10C , 25C , 40C are used in the tests, and the applied stress level is 20 psi.

The IDT repeated load test procedures used in this study is summarized as follows:

- Place the specimen in the testing chamber for two hours at the desired testing temperature to bring it to test temperature and to allow for a uniform temperature distribution within the specimen.
- The LVDT (Linear Variable Differential Transformer) is set to zero reading after completion of the specimen "setup" in the testing equipment. The pressure actuator is adjusted to the specified stress level. The timer (both loading port and rest port) is also set to the required load and rest durations.
- The experiment is commenced by application of repeated indirect tensile stress and the resilient strain is measured.
- The test is completed after number of load repetitions when the resilient strain reading is reached to its suitable value or small difference between two readings that can be neglected.

Figure (8) shows the IDT test apparatus. The resilient strain (ε_r) and resilient modulus (Mr) are calculated as follows:

Resilient strain:

$$\varepsilon_r = (rd*Fc)/h \qquad (8)$$

Where:
ε_r: Vertical resilient strain (mm/mm).
rd: Reading of LVDT for voltage in volt unit.

Fc= calibration factor to convert the reading of LVDT from voltage in (volt unit) to distance in (mm) unit . Shown in Figure(9)
h: specimen diameter (mm).

Resilient modulus:

$$Mr = \frac{\sigma}{\varepsilon_r} \qquad (9)$$

Where:
Mr: Resilient modulus (psi).
σ: Repeated diametral stress (psi).

Predictive Model for Resilient Modulus

The resilient modulus is a key parameter in the pavement design and performance prediction system, so it is desirable to have a statistical model capable for the prediction of the resilient modulus of asphalt concrete.

Linear regression is used to develop model for prediction the resilient modulus of asphalt concrete as a function of mixture properties(asphalt content , viscosity at 135C° , air voids, surface area) and test temperature.

This model has an R^2 value of 0.849 .

$$MR=763480.93-173341.49AC+16835.719\eta-3793.643Av-8778.963T+88084.523S.A \qquad (10)$$

Where:
MR : Resilient Modulus (psi)
T : Test Temperature (°C)
Av : Percent Air Voids
%AC: Percent by Weight of Effective Asphalt
Ŋ= Viscosity of binder at 135°C (Pa.sec)
S.A=Surface Area (m^2/kg)

Field Measurements

In this study,the **µlogger 4R** - For measuring Temperature with a thermistor or resistance is used. This model of µlogger (pronounced micro-logger) has four resistance channels; usually for connecting to our high quality thermistor based temperature sensors but can be connected to any sensor that produces a 100 - 50k Ohm output.

The supplied software allows the µlogger to be configured before leaving it at the logging site. At the end of the logging period your data is offloaded and can be displayed and analysed using the same software.
Three metal sensors are embedded in the pavement at the depths of 2, 7 and 10 cm, representing the depth of the first three layers of asphalt concrete. One sensor is seperated from three sensors collects the air temperature data.

Model Development

Linear regression is used to develop model for prediction of pavement temperature as a function of the air temperature and the depth below the pavement surface. The developed statistical model is shown below in equation (11). This model has an R^2 value of 0.923 and SE of 2.7725. The figures (13) to (15) show the relationships between air temperatures and pavement temperatures at three depths below the pavement surface.

T_{Pave} =3.17 5+0.0 4866Z+ 0.946 T_{air} (11)

Where :
T_{Pave} = Pavement Temperature °C
Z =Depth below the pavement surface (cm)
T_{air}= Air Temperature °C

Based on the diagnostic plots shown in figures (16) to (18), the model is rational. The residual plots of this model do not indicate any unusual pattern and normally distributed.

Conclusions

Within the limitations of materials and testing program used in this work, the following principal conclusions are made based on the findings of the investigations:

1. Based on the indirect tensile test results employing the pneumatic repeated load apparatus, a model is developed to predict the resilient modulus of the asphalt concrete for different test conditions and mix properties, in the following form:

M_R=763480.93-173341.49AC+16835.719

ŋ-3793.643Av-8778.963T+88084.523S.A

2. The resilient modulus values of the two types of asphalt paving mixtures used in local specifications for wearing and Leveling courses (mid gradation limit, 40-50 grade binder, optimum asphalt content) are as shown at different temperatures:

Asphalt Concrete Layers	Resilient Modulus (psi) at Temperatures		
	10C°	25C°	40C°
Wearing course	342328	210643	78959
Leveling course	346891	215206	85522

3. The average rate of decrease in resilient modulus as affected by increase in temperature is equal to 8.78×10^3 Psi/C° for wearing course and 8.72×10^3 Psi/C° for Leveling course.

4. The resilient modulus is adversely affected by change in asphalt cement content from optimum value. An increase in asphalt content by 0.1% (by weight of total mixture) causes a decrease in resilient modulus by : 5.1% at 10 C°, 8.3% at 25 C° and 22% at 40 C°.

5. From Local field work , using the temperature data logger instrument the following model is developed according to air temperatures and depths below the pavement surface:-

T_{Pave} = 3.175+ 0.04866Z +0 .946 T_{air}

REFERENCES

- Algibury, T.(2008)." Prediction of Resilient Modulus in Asphalt Paving Mixture", M.Sc. Thesis, Civil Engineering , University of Babylon.
- Alkasawneh, W., E. Pan ,F. Han, R. Zhu and R. Green." Effect of temperature variation on pavement responses using3D multilayered elastic analysis" Computer Modeling and Simulation Group, Department of Civil Engineering, The University of Akron, Akron, OH 44325-3905, USA‡Ohio Department of Transportation, 1980 West Broad Street, Columbus, OH 43223, USA. International Journal of Pavement Engineering,Vol. 8, No. 3, September 2007, 203–212.
- Diefenderfer,B. K.,I. L. Al-Qadi, S. D. Reubush and T. E. Freeman. "Development And Validation Of A model To Predict Pavement Temperature Profile".TRB(2003) Annual Meeting CD-ROM.
- Fatani, M. N., Al-Abdul Wahhab, H. I., Balghunaim, F. A., Bubshait, A., and Al- Dhubeeb, I. (1990). "Evaluation of permanent deformation of asphalt concrete pavement in Saudi Arabia." *Progress Rep. No. 6* on Nat. Res. Project, King Abdulaziz City for Sci. and Technol. (KACST), Riyadh, Saudi Arabia.
- Huang H. Yang , " Pavement Analysis and Design " , University of Kentucky, 1993.
- Ongel, A. and Harvey, J., "Analysis of 30 years of pavement temperatures using the enhanced integrated climate model (EICM)", Pavement Research Centre, University of California Davis ,2004.
- Strategic Highway Research Program, SHRP (1994), "The Superpave Mix Design Manual for New Construction and Overlays", SHRP-A-407, National Research Council, Washington, D. C..USA.
- Witczak, M. (1972). "Design of Full Depth Air Field Pavement", Proceedings, Third International Conference on the Structural Design of Asphalt Pavements, London.

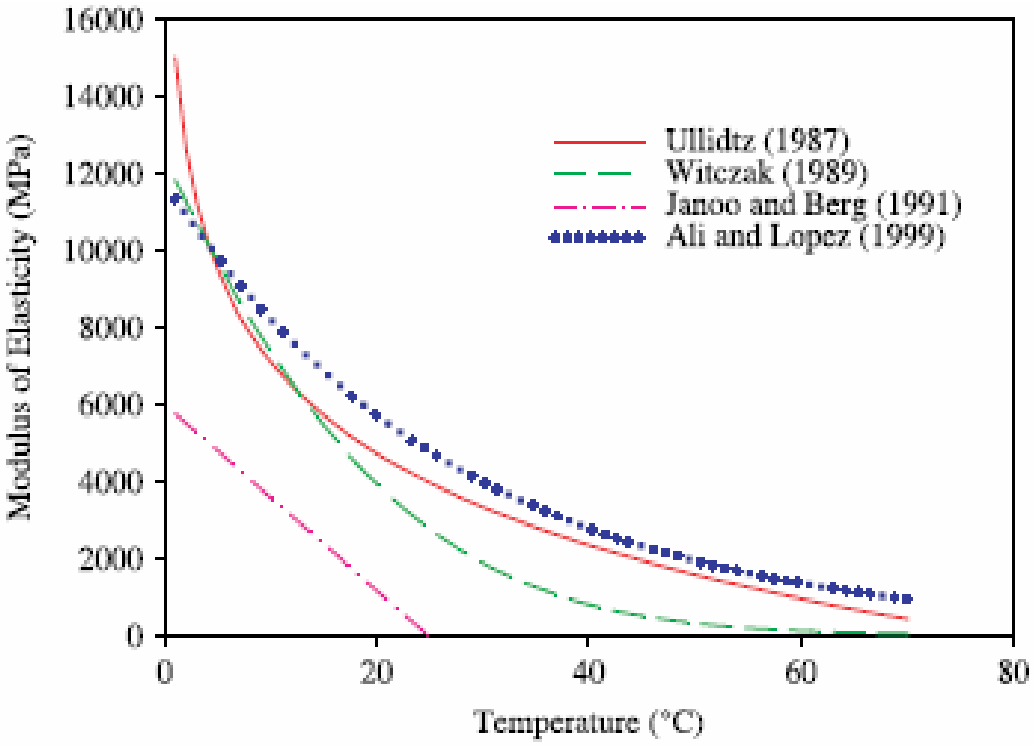

Figure (1) Resilient Modulus vs. Temperature (Alkasawneh et.al ,2007)

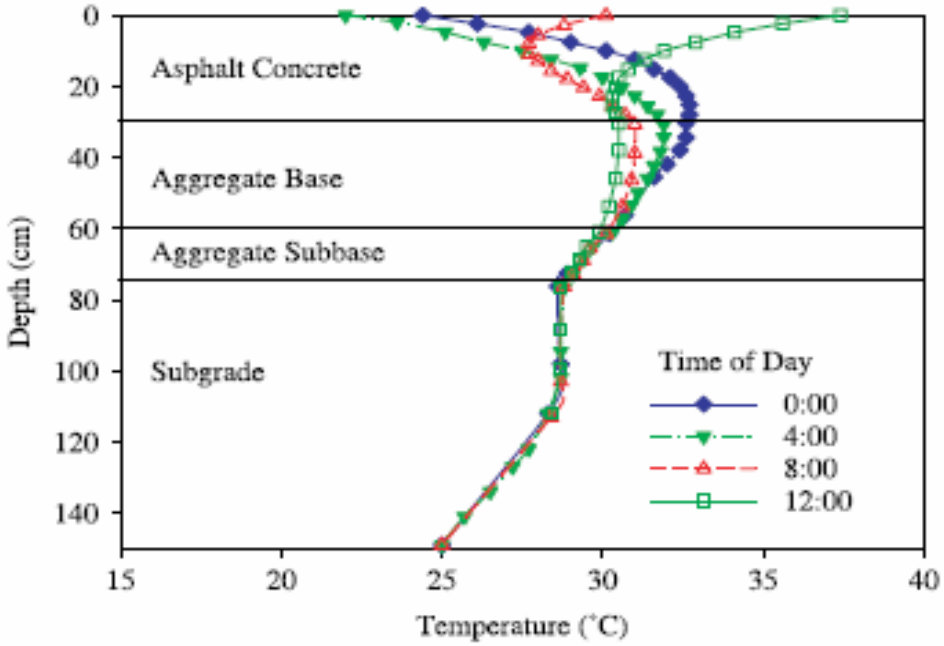

Figure (2) Daily Temperature Variation (modified by Ongel and Harvey 2004)

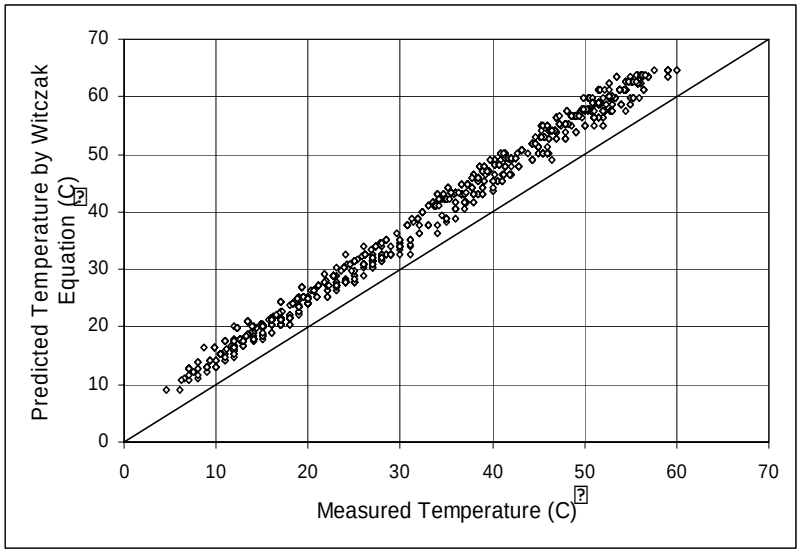

Figure (3) Comparison between Measured Pavement Temperature and That Predicted By Witczak Equation (Witczak, 1972)

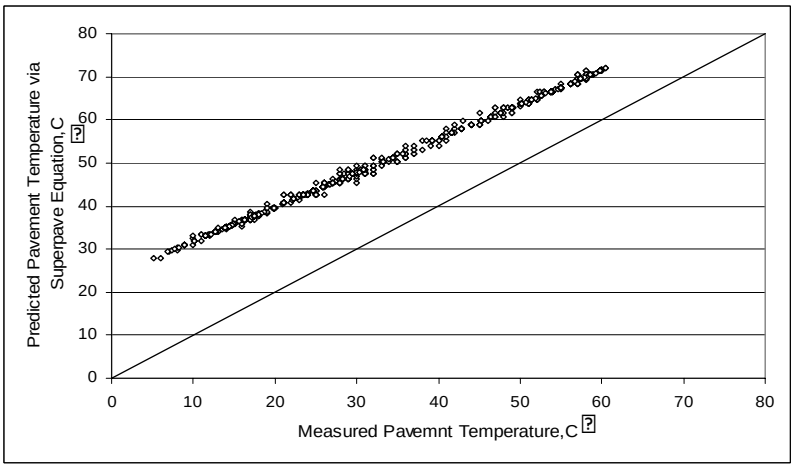

Figure (4) Comparison between Pavement Temperatures Predicted Via Superpave Equation and That Measured at Depth 2 Cm (SHRP, 1994)

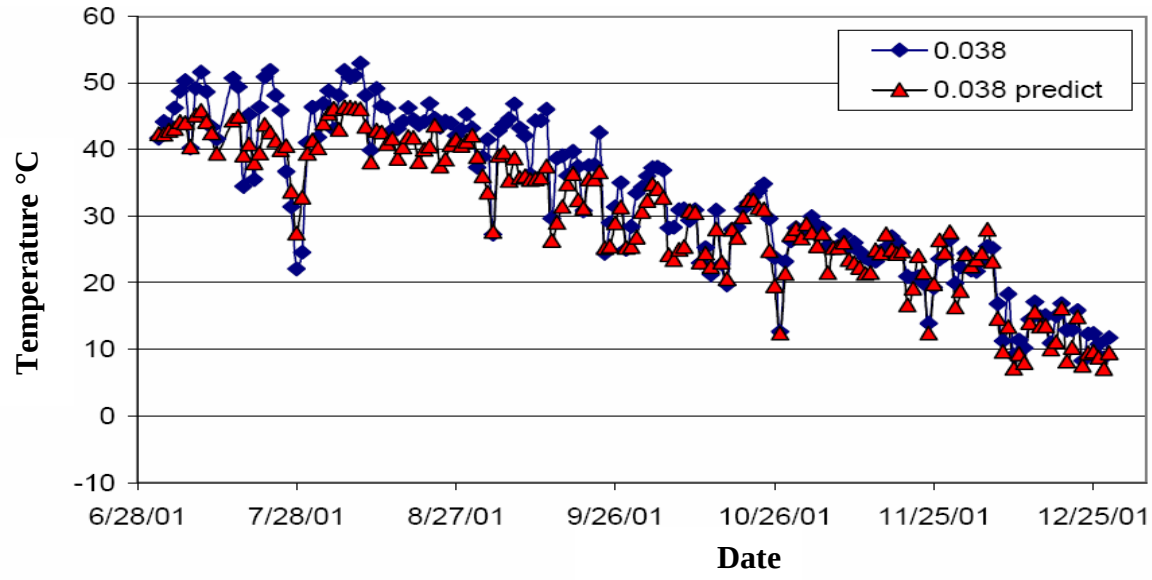

Figure (5) Maximum Daily Pavement Temperature Utilizing Day of Year at 0.038m Depth (Diefenderfer et al. 2003)

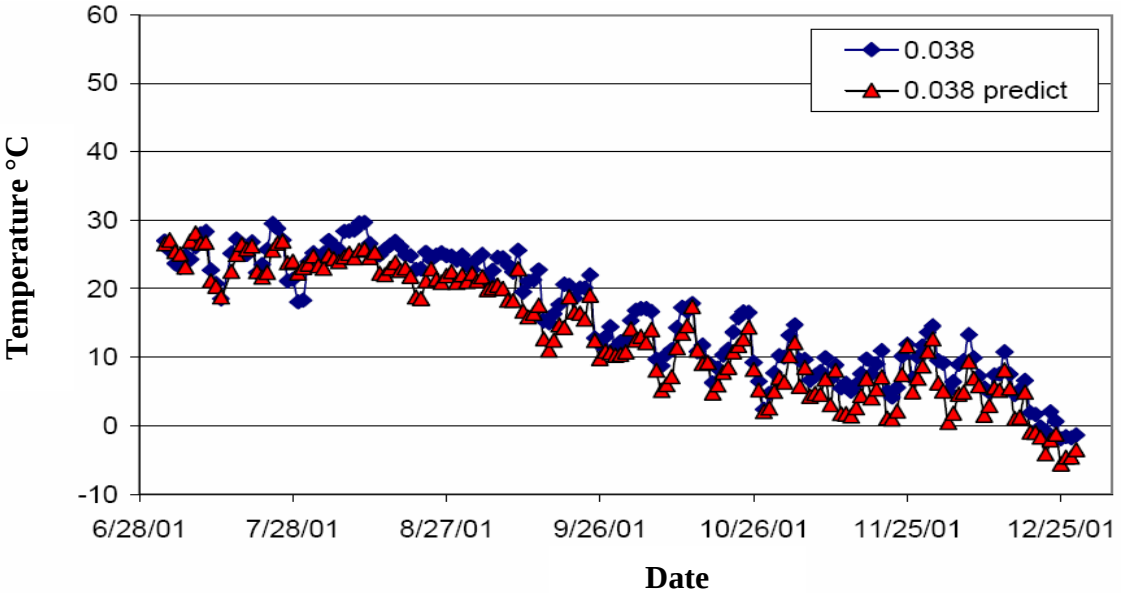

Figure (6) Minimum Daily Pavement Temperature Utilizing Day of Year at 0.038m Depth (Diefenderfer et al. 2003)

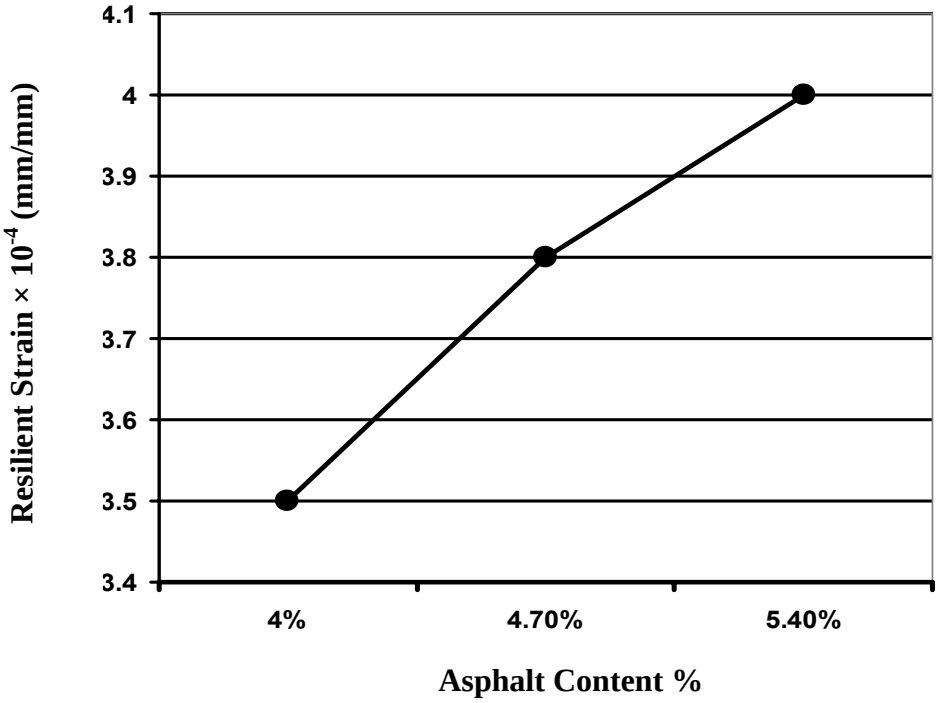

Figure (7) Effect of Asphalt Content on Resilient Strain (Algibury, 2008)

Figure (8) Indirect Tension Test Apparatus

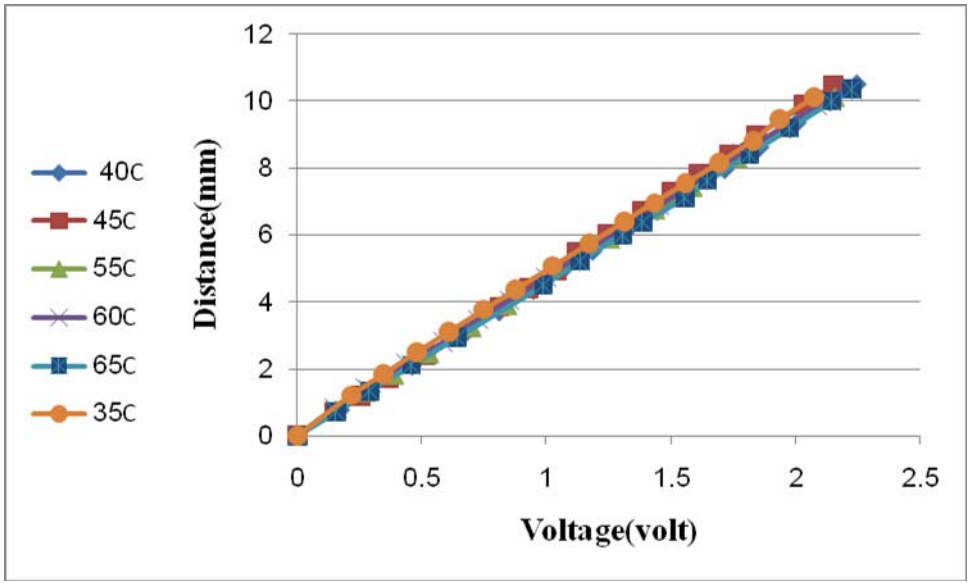

Figure (9) The Average Calibration Factor for LVDT at Different Temperatures

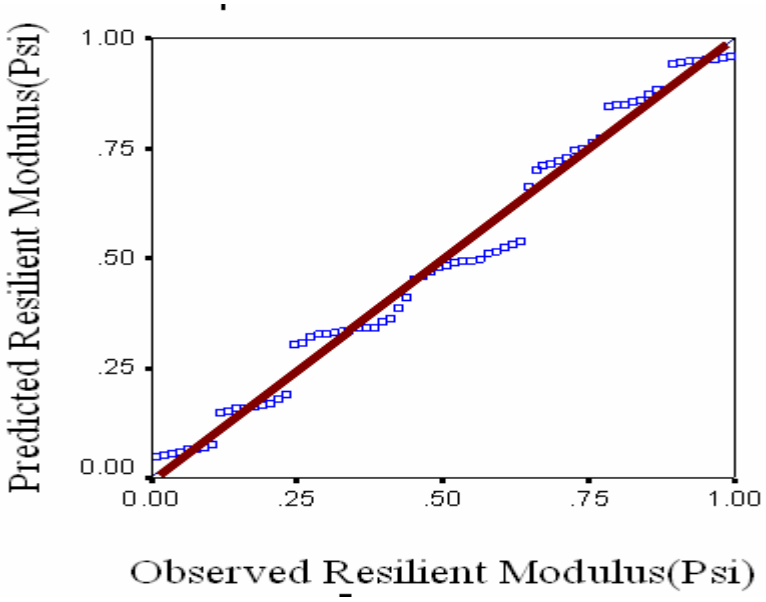

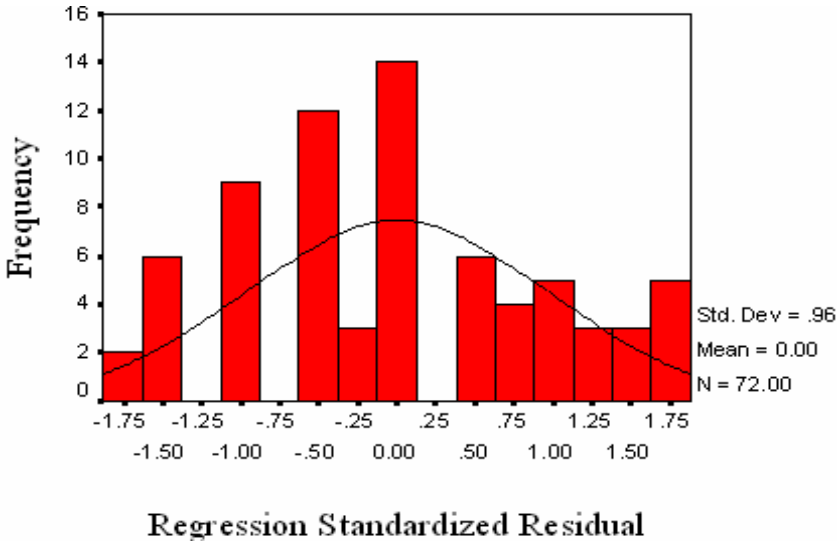

Figure (10) Diagnostic Plots for Resilient Modulus

Table (1) Indirect Tensile Test Data

%AC	Viscosity(Pa.s)	AV	Temperature C^{o}	M_R (psi)	S.A(m^2/kg)
4.9	0.516	4.84	10	430108	5.97
5.2	0.516	4.08	10	215054	5.97
4.6	0.516	3.47	10	430385	5.97
4.9	0.516	2.67	10	430108	5.97
5.2	0.516	2.47	10	215054	5.97
4.6	0.516	2.94	10	430385	5.97
4.9	0.516	3.9	10	430108	5.98
5.2	0.516	2.31	10	215054	5.98
4.6	0.516	3.47	10	430385	5.98
4.9	0.516	4.19	10	430108	5.98
5.2	0.516	3.26	10	215054	5.98
4.6	0.516	5.23	10	430385	5.98
5.2	0.400	4.54	10	215054	5.97
4.6	0.400	3.81	10	430385	5.97
4.9	0.400	3.62	10	430108	5.97
4.9	0.400	2.96	10	430108	5.97
5.2	0.400	4.00	10	215054	5.97
4.6	0.400	3.72	10	430385	5.97
4.9	0.400	4.27	10	430108	5.98
5.2	0.400	3.05	10	215054	5.98
4.6	0.400	5.07	10	430385	5.98
4.9	0.400	2.63	10	430108	5.98
5.2	0.400	3.92	10	215054	5.98
4.6	0.400	2.5	10	430385	5.98
4.9	0.516	3.08	25	215031	5.97

5.2	0.516	2.84	25	143369	5.97
4.6	0.516	3.59	25	215054	5.97
4.6	0.400	4.46	25	215054	5.97
4.9	0.400	4.19	25	215031	5.97
5.2	0.400	3.26	25	143369	5.97
4.6	0.400	3.97	25	215054	5.97
4.9	0.400	2.79	25	215031	5.97
5.2	0.400	2.72	25	143369	5.97
4.6	0.400	2.95	25	215054	5.98
4.9	0.400	2.75	25	215031	5.98
5.2	0.400	5.49	25	143369	5.98
4.6	0.400	3.72	25	215054	5.98
4.9	0.400	2.01	25	215031	5.98
5.2	0.400	4.70	25	143369	5.98
4.6	0.516	3.8	25	215054	5.97
4.9	0.516	3.45	25	215031	5.97
5.2	0.516	2.51	25	143369	5.97
4.6	0.516	4.25	25	215054	5.98
4.9	0.516	2.87	25	215031	5.98
5.2	0.516	3.50	25	143369	5.98
4.6	0.516	4.49	25	215054	5.98
4.9	0.516	2.3	25	215031	5.98
5.2	0.516	4.37	25	143369	5.98
4.9	0.516	4.27	40	86014	5.97
5.2	0.516	3.63	40	85837	5.97
4.6	0.516	5.07	40	107538	5.97
4.6	0.400	4.95	40	107538	5.97
4.9	0.400	3.20	40	86207	5.97
5.2	0.400	2.48	40	86014	5.97
4.6	0.400	4.3	40	86022	5.97
4.9	0.400	2.34	40	86014	5.97
5.2	0.400	2.81	40	86003	5.97
4.6	0.400	3.93	40	107527	5.98
4.9	0.400	2.47	40	86014	5.98
5.2	0.400	4.91	40	85837	5.98
4.6	0.400	4.99	40	107518	5.98
4.9	0.400	3.12	40	86014	5.98
5.2	0.400	4.99	40	85837	5.98
4.6	0.516	4.94	40	107538	5.97
4.9	0.516	4.31	40	107527	5.97
5.2	0.516	4.40	40	86014	5.97
4.6	0.516	4.21	40	107527	5.98
4.9	0.516	3.69	40	86014	5.98
5.2	0.516	3.09	40	85837	5.98
4.6	0.516	5.47	40	107538	5.98
4.9	0.516	3.08	40	107516	5.98
5.2	0.516	3.13	40	86022	5.98

Figure (11) The µlogger 4R (Temperature Data Logger)

Figure (12) The µlogger 4R with Four Channels

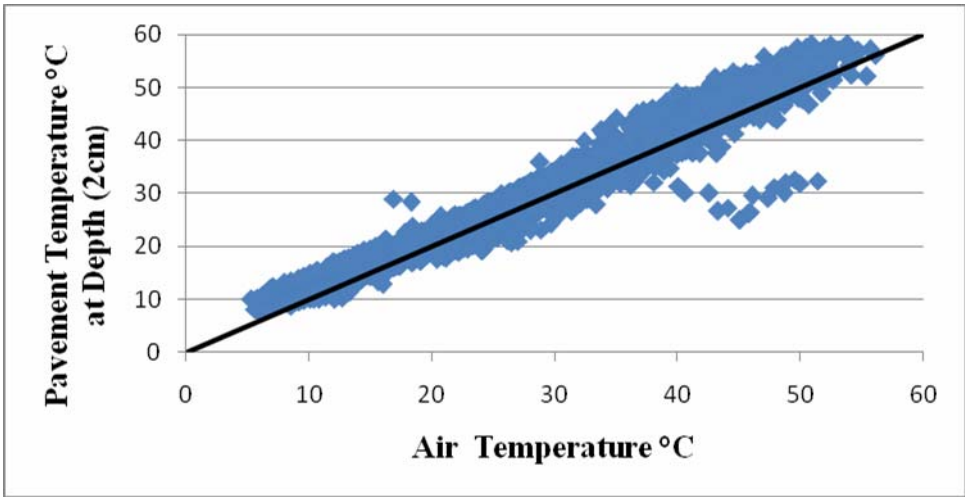

Figure (13) Effect of Air Temperature on Pavement Temperature at Depth 2cm

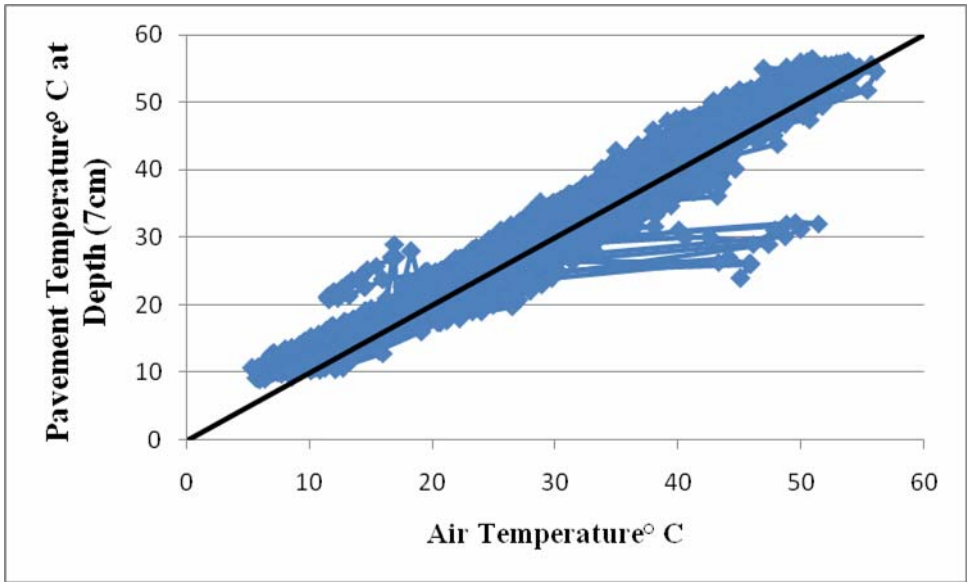

Figure (14)Effect of Air Temperature on Pavement Temperature at Depth 7cm

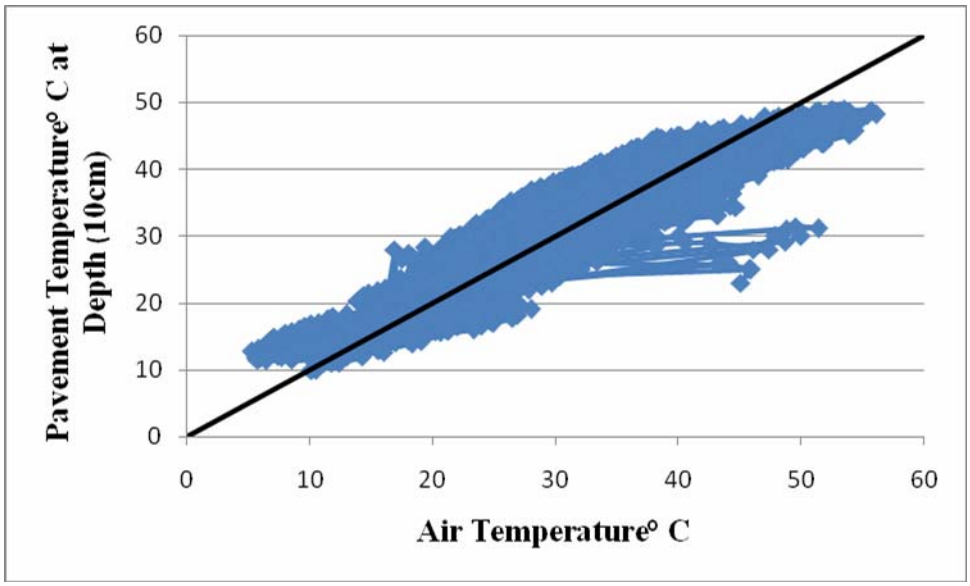

Figure (15) Effect of Air Temperature on Pavement Temperature at Depth 10cm

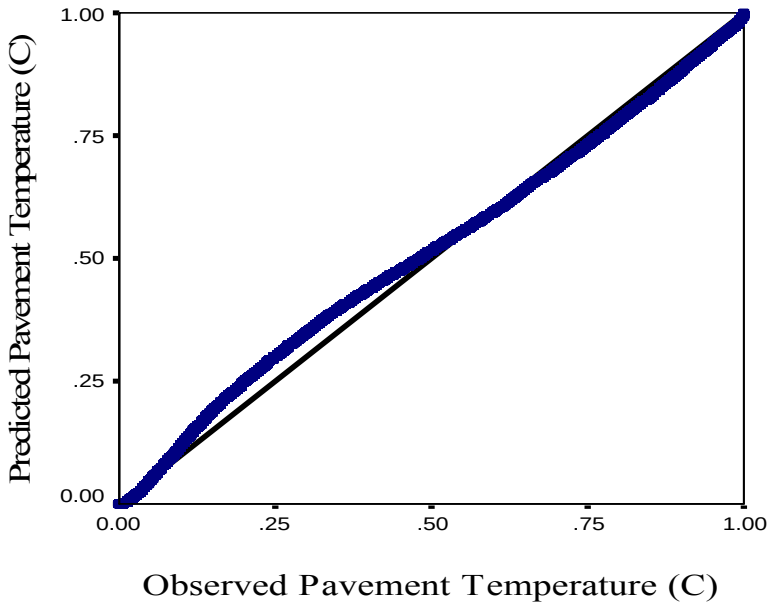

Figure (16) Predicted Versus Observed Pavement Temperature

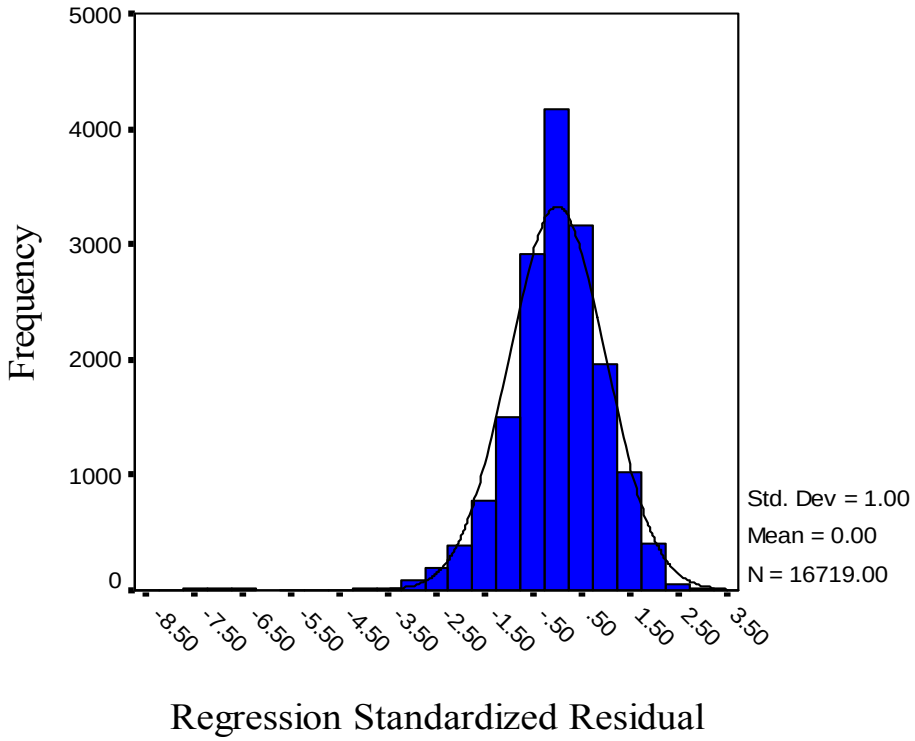

Figure (17) Frequency Versus Regression Standardized Residual for Pavement Temperature Model

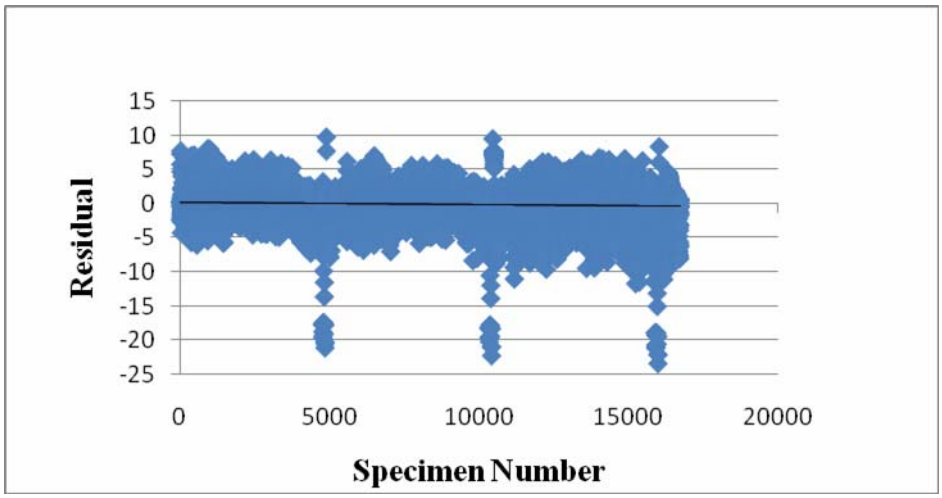

Figure (18) Residual Versus Specimen Number for Pavement Temperature Model

Table (2) Part of Pavement Temperature Data

Date and Time	Tpave(2cm)	Tpave(10cm)	Tpave(7cm)	air temperatures C°
Mon 27 of Apr at 12:07:23 2009	43.3	32.9	41.1	34.6
Mon 27 of Apr at 13:07:23 2009	44.7	34.6	42.6	37.7
Mon 27 of Apr at 14:07:23 2009	44.1	35.6	42.8	35
Mon 27 of Apr at 15:07:23 2009	42.2	35.4	40.8	36.2
Mon 27 of Apr at 16:07:23 2009	37.1	34.5	36.9	35.5
Mon 27 of Apr at 17:07:23 2009	34.6	33.3	34.4	35.6
Mon 27 of Apr at 18:07:23 2009	31.7	32.2	32.2	29.8
Mon 27 of Apr at 19:07:23 2009	29.1	31	29.9	26.9
Mon 27 of Apr at 20:07:23 2009	27.2	29.8	28.1	25.5
Mon 27 of Apr at 21:07:23 2009	26	28.8	26.9	24.4
Mon 27 of Apr at 22:07:23 2009	24.9	28	25.8	23.3

NOMENCLATURE

ASTM	American Society for Testing and Materials
Mr	resilient Modulus
σ	Repeated Diametral Stress
ε_r	Vertical Resilient Strain
Tpave	Pavement Temperature
Tair	Air Temperature
Z	Depth below Pavement Surface
Tpmax	Predict Maximum Daily Pavement Temperatures
Tpmin	Predict Minimum Daily Pavement Temperatures
Tmax	Maximum Daily Ambient Temperature
Tmin	Minimum Daily Ambient Temperature
Y	Day of Year
Pd	Depth Within The Pavement

T	Test Temperature
Av	Percent Air Voids
P_S	Percent Volume of Effective Asphalt
P_8	Percent Passing Sieve No. 8
P_{200}	Percent Passing by weight of Filler Content
PRLS	Pneumatic Repeated Load System
rd	Reading of LVDT
Fc	Calibration Factor
h	Specimen Diameter
LVDT	Linear Variable Differential Transformer
%AC	Percent by Weight of Effective Asphalt
Ŋ	Viscosity of Binder
S.A	Surface Area

THE EFFECT OF CUTOFF WALL ANGLE ON SEEPAGE UNDER DAMS

Zainal, Abdul Kareem Esmat

ABSTRACT

Flow of water under concrete dams generates uplift pressure under the dam, which may cause the dam to function improperly, in addition to the exit gradient that may cause piping if exceeded a safe value.

Cutoff walls usually used to minimize the effect of flow under dams. It is required to 1)minimize the flow quantity to conserve water in the reservoir, it is also required to 2)minimize the uplift pressure under the dam to maintain stability of the dam, and it is required to 3) minimize the exit gradient to prevent quick condition to occur at the toe of the dam where piping may occur and may cause erosion of the soil.

Varying the angle of cutoff walls affects its influence on the factors aforementioned that are required to be minimized.

In this paper, the cutoff wall angle was varied from 0° to 180° using GeoStudio 2007 SEEP/W computer program, and the variations of the three factors were studied and analyzed.

The results shows that the best angle to minimize the water flow is about 60°, the best angle to minimize the uplift pressure was about 120° to 135°, and the best angle to minimize the exit gradient was about 45° to 75°.

The case where two cutoff walls were used one with angle 60°, the other with an angle 120° were investigated. The results indicated where the minimum values for all factors may be obtained.

الخلاصة

ان عملية جريان الماء تحت السدود الخرسانية تولد ضغط للمياه تحت السد، ومن الممكن لهذا الضغط ان يقلل من الاداء الصحيح للسد، اضافة الى ما يسببه انحدار الخروج من جرف للتربة في نهاية السد اذا ما زادت عن حدها المسموح به.

لذا تستخدم الجدران القاطعة للتقليل من تاثيرات جريان المياه تحت السد. حيث انه من المطلوب 1) تقليل كمية المياه التي تجري تحت السد وذلك للمحافظة على كمية المياه في الخزان امام السد، كذلك من المطلوب 2) تقليل ضغط المياه تحت السد للمحافظة على استقرارية السد، اضافة الى 3) تقليل انحدار الخروج لتفادي حصول حالة انجراف التربة في نهاية السد. ان تغيير زاوية انشاء الجدار القاطع له تاثير على العوامل التي تم ذكرها بشكل مباشر والتي من المطلوب تقليلها.

في هذا البحث، تمت دراسة تاثير تغيير زاوية الجدار القاطع من 0 حتى 180 درجة باستعمال برنامج حاسوبي متخصص (GeoStudio 2007 SEEP/W) وتم تحليل نتائج تغير الزاوية على العوامل المذكورة.

اسفرت النتائج عن تقليل جريان المياه الى اقل ما يمكن بزاوية 60 درجة وتقليل ضغط المياه اقل ما يمكن تحت السد بزاوية تتراوح بين 120 حتى 135 درجة وتقليل انحدار الخروج اقل ما يمكن بزاوية تتراوح بين 45 حتى 75 درجة.

تمت تحليل حالة وجود جدارين قاطعين الاول بزاوية 60 درجة والثاني بزاوية 120درجة. اسفرت النتائج عن الحصول على اقل قيم ممكنة للعوامل المدروسة جميعا.

Keywords: Flow under dams, optimization, cutoff walls, uplift pressure, exit gradient.

INTRODUCTION

Dams are constructed mainly to keep water in reservoirs, and to function for long times, hence the factors that may affect the functionality of these dams and may reduce it must be studied carefully and minimized to obtained a proper function of the dam.

Flow under concrete dams can create uplift pressure that could affect the dam and may cause it to fail to function properly; also the exit gradient can cause piping and quick condition at the toe of the dam, so, it is required to reduce the effect of water seepage by using cutoff walls, like slurry wall.

Slurry walls are non-structural barriers (Cutoff Walls, Slurry Trenches) that are constructed underground to impede groundwater flow. Slurry walls have been used for decades to provide cost-effective, long-term solutions for many groundwater control and groundwater remediation problems (www.geo-solutions.com, 2010)".

Seepage analysis of cutoff walls is useful in order to determine if high gradients develop at the base of the cutoff wall or on the downstream exit point.

The objective of this paper is to examine the effect of cutoff walls angle under a dam on the flow quantity, pore water pressure and the exit gradient, this will help to minimize flow quantity, the uplift forces under the dam and prevent quick condition at the exit points of the downstream flow for different angles of cutoff walls.

LITERATURE AND THEORY

The problem of seepage under dams was considered by many authors (Harr, 1962, Lambe and Whitman, 1979, Das, 2008, Craig, 2004) and many others.

In case of concrete dams, water flows under these dams. The line along which a water particle will travel is called flow line, and the line joining the points that show the same piezometric elevation called equipotential line.

A set of flow lines and equipotential lines is called a flow net; the flow lines intersect the equipotential lines at right angles. The flow and equipotential lines are usually drawn in such a way that the flow elements are approximately squares, as shown in figure 1.

A flow net is a graphical solution to the Laplace equation for two-dimensional flow for flow through a homogenous soil, it is an orthogonal network of flow lines and equipotential lines (approximately square for homogeneous, isotropic media).

$$\frac{\partial^2 H}{\partial x^2} + \frac{\partial^2 H}{\partial y^2} = 0 \quad (1)$$

There are several problems involving a concrete dam, prior to conducting an analysis, the problem to be studied must be defined in terms of:

a. Aquifer and concrete dam dimensions.
b. Coefficients of permeability of the dam and foundation soils.
c. Horizontal to vertical permeability ratios.
d. Boundary conditions (impermeable and symmetrical).
e. Exits and entrances (fixed potential areas).
f. Head versus time relationships for unsteady flow.

To solve these problems, there are approximate solutions as mentioned (Harr, 1962):

1) Graphical flow net.
2) Solution by Analogies (electrical analogue).
3) The flow tank.
4) Viscous flow models (Hele shaw model).
5) Relaxation method.
6) Method of fragments.
7) Others.

Flow nets and the method of fragments are two techniques that have long been used with limited success in furnishing seepage under hydraulic structures. The method of fragments is an approximate analytical method for the computation of flows and pressure heads for any ground-water system.

CASE STUDY

An example of flow under dam (after Craig, 2004) is taken to show the effect of cutoff wall on the flow quantity, pore water pressure, as calculated by hand. The section through a dam is shown in Figure 2. It is required to determine the quantity of seepage under the dam and plot the distribution of uplift pressure on the base of the dam. The coefficient of permeability of the foundation soil is 2.5×10^{-5} m/s.

The flow net is shown in figure 2. The downstream water level is selected as datum. Between the upstream and downstream equipotentials the total head loss is 4.00 m. In the flow net there are 4.7 flow channels and 15 equipotential drops. The seepage is given by:

$$q = kh\frac{N_f}{N_d} = 2.5 \times 10^{-5} \times 4.00 \times \frac{4.7}{15}$$
$$= 3.1 \times 10^{-5} \mathrm{m^3/s} \quad (\text{per m})$$

where N_f= Number of flow lines , N_d= Number of equipotential lines.

The pore water pressure is calculated at the points of intersection of the equipotentials with the base of the dam. The total head at each point is obtained from the flow net and the elevation head from the section. The calculations are shown in Table 1 and the pressure diagram is plotted in Figure 2.

This example will be used as a verifying case for the computer program Geostudio 2007 SEEP/W to study the objective of this paper and examine the effect of cutoff wall angle on the seepage under the dam.

COMPUTER PROGRAM

The computer program Geostudio 2007 SEEP/W was used as the software to examine the effect of cutoff walls on the flow, exit gradient, and pore water pressure under dam.

The same data used for the example in the case study are used here in the computer program.

Figure 3 shows the complete flownet of the example mentioned in case study with the flow lines and equipotentional lines distribution, where figure 4 shows the pore water pressure distribution under the dam.

The flow quantity is found to be 3.1231×10^{-5} m^3/sec, which is very close to the value obtained using hand calculations. The difference is:

$$\frac{3.1231\times10^{-5} - 3.1\times10^{-5}}{3.1\times10^{-5}} = 0.00745 = 0.745\%$$

This is considered an identical value to the one obtained in the example. The pore water pressure distribution is shown in figure 5(a) (B-C on fig. 3) to be the same as obtained from hand calculations, varying from 43 kPa under the beginning of the dam just after the cutoff wall, to the

value of 22 kPa just before the toe of the dam.
In addition, the exit gradient at the toe (A-B on fig. 3) was also obtained to be 0.36 at the toe at ground level and 0.215 at –0.8m. This is shown in figure 5 (b).
From the aforementioned results, the computer program GeoStudio 2007 SEEP/W is verified to be used for studying the effect of varying the cutoff wall angle on the flow quantity, pore water pressure, and the exit gradient.
The angle of the cutoff wall will vary from 0° to the horizontal ground level and this angle will increase in the clockwise direction (as shown in figure 6) in increments of 15° till the angle of 180° is reached. (angle 180° assumes no cutoff wall presence).

RESULTS AND DISCUSSION

The results of many runs of the computer program using various angles of cutoff wall are obtained. Starting from 0° to 180°, graphs showing total head, flownet (flow lines and equipotential lines), pore water pressure distribution, and exit gradient are shown for each case. Those results are shown in figures 7-42.
The results of flow quantities are summarized in table 2. This variation is also shown in figure 43. The flow quantity decreases as the angle increases from 0° to about 60°, after that the flow quantity increases with the increase of the angle.
A trend line can be drawn describing this relation between flow quantity and cutoff angle and could be described by equation 2:

$$y = -4\times10^{-14}x^4 + 1\times10^{-11}x^3 - 6\times10^{-10}x^2 - 4\times10^{-8}x + 3\times10^{-5} \quad (2)$$

This polynomial gave a regression value R^2 of 0.9981 which is considered very good as this equation could describe this variation. The pore water pressure under the base of the dam is also considered here in this paper; as it is important to examine this value to describe the uplift pressure exerted on the base of the dam to ensure stability of the dam. Table 3 shows the values of the pore water pressure under the base of the dam.

The data are also represented in graphical form as shown in figure 44. The pore water pressure is shown to decrease as the angle increase till the angle reaches about 120° to 135° then the pore water pressure increases with reshaping as shown in figure 44. Figure 45 is a magnification of the right end portion of figure 44, where the change on pore water pressure is shown more clearly.

Figure 46 is a magnification of the middle portion of fig. 44 where the base of the dam changes in thickness by an angle of 45°, this effect is shown clearly to affect the pore water pressure at the base of the dam, with an average value taken for an arbitrary angle (say 120°) to be:
37 – 28 = 9 kPa within about 20.5 – 19 = 1.5m
That is about 9 / 1.5 = 6 kPa / m
Compared to other portions of the graph in fig. 44 for the same angle where the reduction is about:
42.42– 38.02 = 4.4 kPa within about 28.9 – 21.48 = 7.42 m
And that is about 4.4 / 7.42 = 0.593 kPa / m
This demonstrates the big influence of the inclination of the base of the dam on the pore water pressure hence the uplift pressure.
The exit gradient is also studied at the end of the dam at two points, the first point is

at ground level (0 m), the second point is at (–0.8 m).

The data also represented graphically in figure 47 where the variation of the exit gradient is shown for the two points at the toe of the dam.

It is obvious from the graph that the value of the exit gradient for the point at –0.8 m is less compared to the exit gradient at the ground level (0 m). But both curves have approximately the same trend of variation. By that we mean that starting from angle 0°, the exit gradient decreases in value till we reach a minimum value at about 45°–75° then the exit gradient rises with the increase of the angle.

A trend line of a polynomial was found to describe this relationship for both points:

a- for point (0 m)

$$y = -6\times10^{-10}x^4 + 2\times10^{-7}x^3 - 1\times10^{-5}x^2 - 0.0001x + 0.3862 \quad (3)$$

$R^2 = 0.9953$

b- for point (–0.8 m)

$$y = -3\times10^{-10}x^4 + 1\times10^{-7}x^3 - 7\times10^{-6}x^2 - 0.0002x + 0.229 \quad (4)$$

$R^2 = 0.9967$

As shown from the aforementioned results, we conclude that the cutoff wall angle of around 60° gave the minimum flow quantity and minimum exit gradient, whereas the cutoff wall angle around 120° to 135° gave the minimum uplift pressure under the base of the dam.

According to these conclusions, an additional run of the computer program was conducted with two cutoff walls the first with an angle of 60° and the other with an angle of 120°.

The results are shown in figures 48 to 50, where figure 48 shows the total head distribution and the flownet, figure 49 shows the pore water pressure distribution, and figure 50 shows the pore water pressure under the base of the dam and the exit gradient.

Water quantity was found to be 3.089×10^{-5} m^3/sec which is very near to the minimum value obtained previously (3.06×10^{-5} m^3/sec) with difference of 0.948% only.

Pore water pressure of 41.08 kPa at the beginning of the dam was found to be even less than the value obtained previously 42.42 kPa with difference of 3.16%.

The exit gradient was found to be 0.361 and 0.215 at level 0m and -0.8m respectively, which are the same values that were obtained previously with negligible difference.

So it is concluded that using two cutoff walls gives the best results considering the three factors under study (flow quantity, pore water pressure, and exit gradient).

CONCLUSIONS AND RECOMMENDATIONS

From the results obtained previously, many conclusions are found and could be summarized as follows:

1- There is a direct relation between the angle of cutoff wall and the flow quantity of water under the dam. This relation could be described as shown in equation 2.
2- Minimum value of flow was found to occur at an angle of about 60° of cutoff wall.
3- Pore water pressure, hence uplift pressure under the dam was shown to have direct relation with the angle of cutoff wall.
4- The minimum value of pore water pressure was found to be at an angle of about 120° to 135°.
5- Exit gradient also has a direct relation with cutoff wall angle. This could be described by equations 3 and 4.

6- Minimum value of exit gradient was found to take place at an angle of about 45°–75°.

7- Using two cutoff walls with two different angles (60° and 120°) gave minimum values of the factors under study.

It is recommended that:

1- Further study of the effect of angle of cutoff wall on flow quantity, pore water pressure, and exit gradient is needed for many soil types.
2- Different geometry also should be investigated to examine the relations mentioned earlier.
3- Anisotropic condition is recommended to be investigated also.

REFERENCES

1. Craig, R. F., 2004, “Craig’s Soil Mechanics”, Spon Press, seventh Edition.
2. Das, B. M., 2008, "Advanced Soil Mechanics", Taylor & Francis.
3. Harr, M. E., 1962, “Groundwater and Seepage”, McGraw-Hill Book Company.
4. Lambe, T. W., and R. V. Whitman, 1979, “Soil Mechanics”, John Wiley & Sons.
5. www.geo-solutions.com, 2010, “Soil Stabilization and Slurry Wall Technologies”.

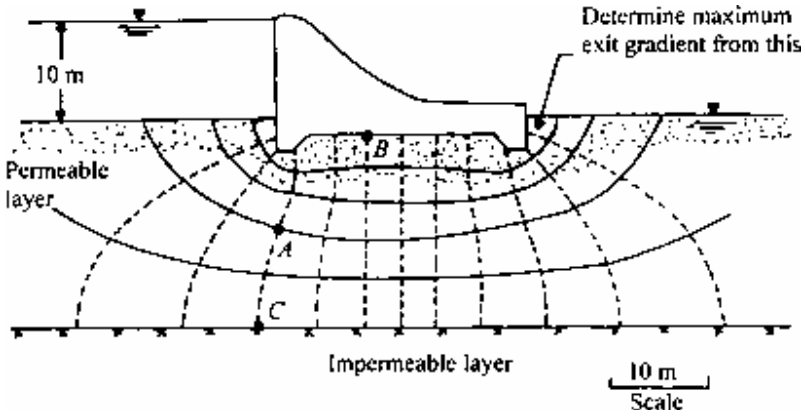

Figure 1 Typical flownet under a concrete dam

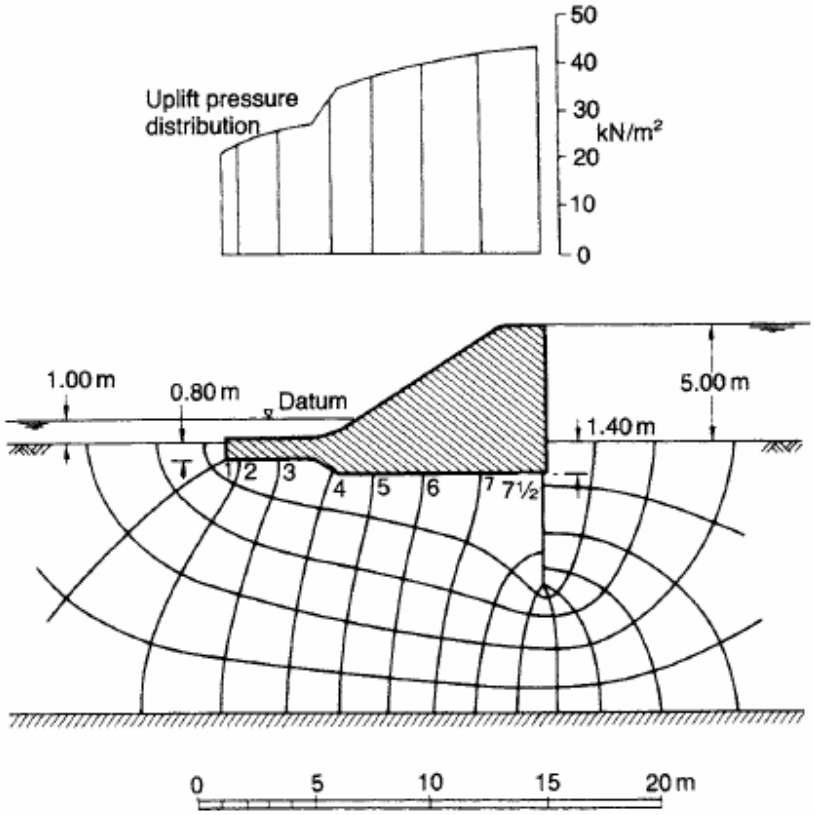

Figure 2 geometry and flow net of the example

Table 1

Point	h (m)	z (m)	$h - z$ (m)	$u = \gamma_w(h - z)$ (kN/m^2)
1	0.27	−1.80	2.07	20.3
2	0.53	−1.80	2.33	22.9
3	0.80	−1.80	2.60	25.5
4	1.07	−2.10	3.17	31.1
5	1.33	−2.40	3.73	36.6
6	1.60	−2.40	4.00	39.2
7	1.87	−2.40	4.27	41.9
$7\frac{1}{2}$	2.00	−2.40	4.40	43.1

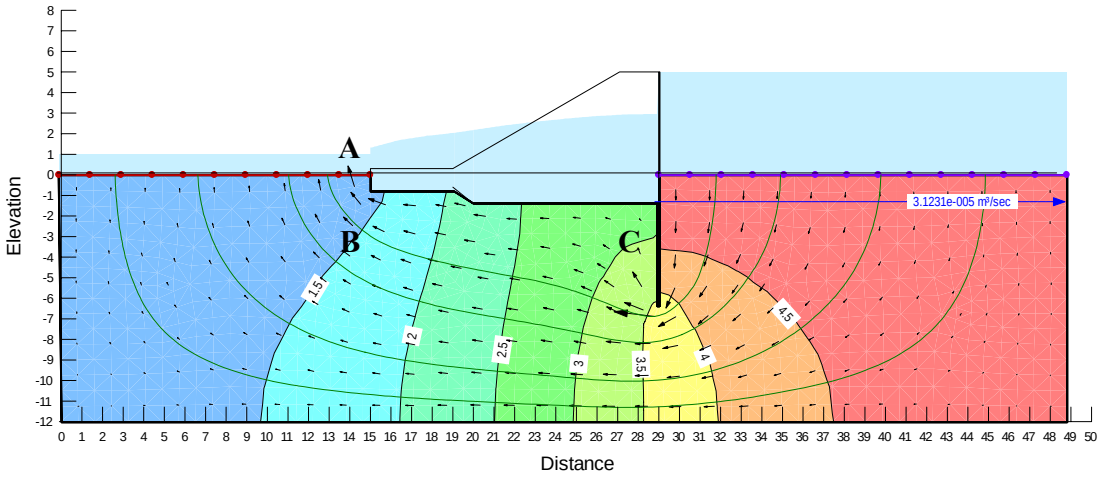

Figure 3 Flow net, flow quantity, and total head under the dam for the example

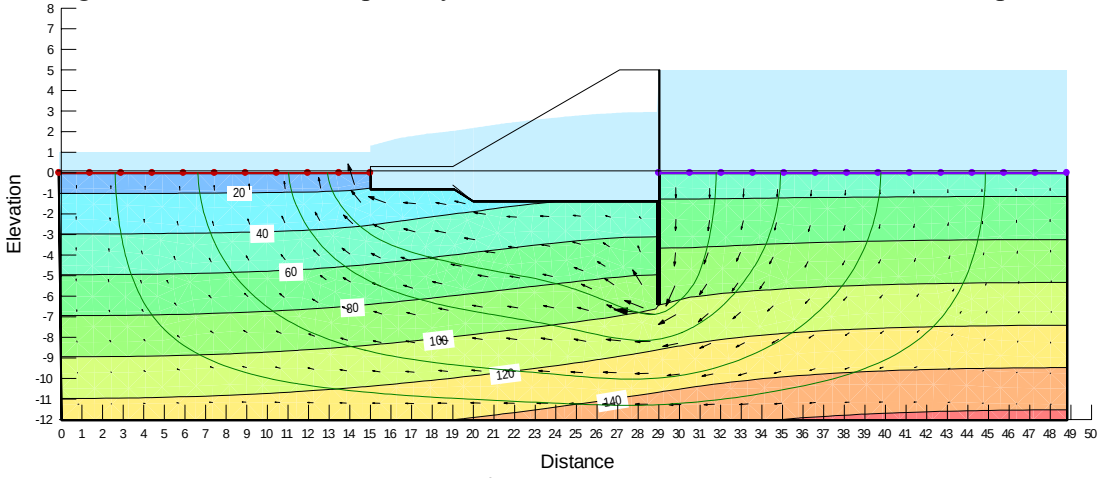

Figure 4 Pore water pressure (kN/m^2) distribution under the dam for the example

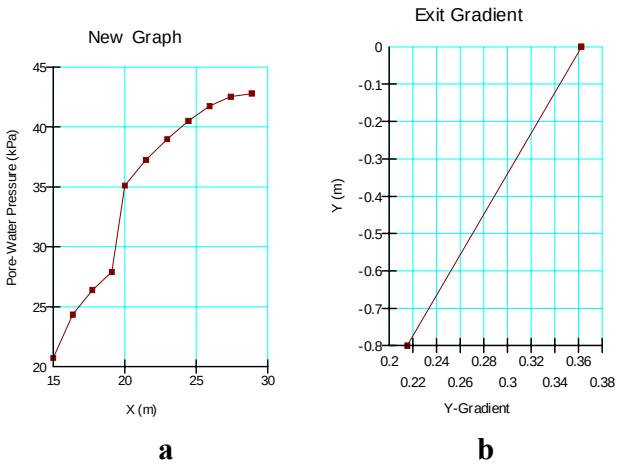

Figure 5 a) Pore water pressure distribution (**BC**), b) Exit gradient at toe (**AB**)

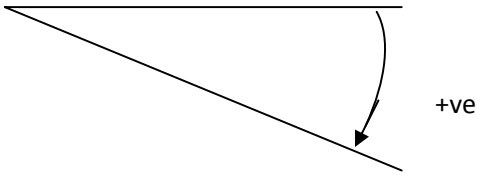

Figure 6 Positive direction for angle of cutoff wall

Case 0°

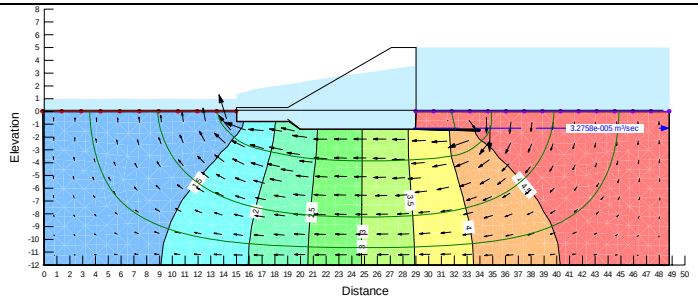

Figure 7 Flownet, flow quantity, and total head distribution for angle 0°

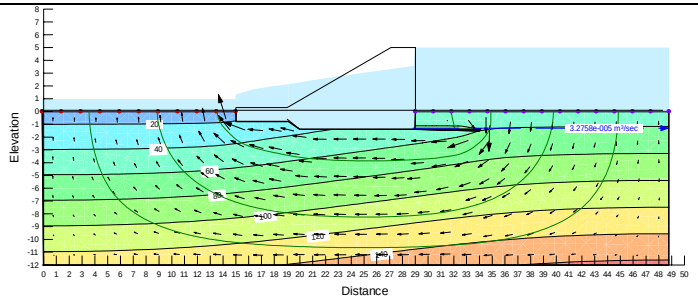

Figure 8 Pore water pressure distribution under the dam for angle 0°

Case 15°

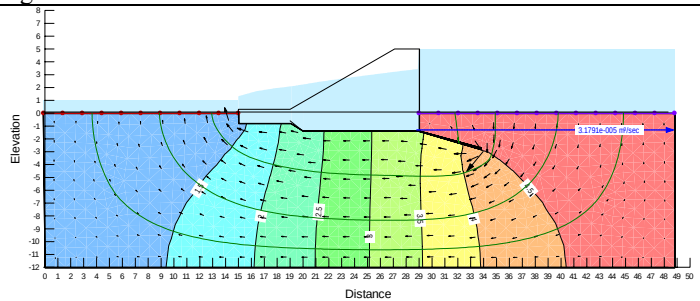

Figure 9 Flownet, flow quantity, and total head distribution for angle 15°

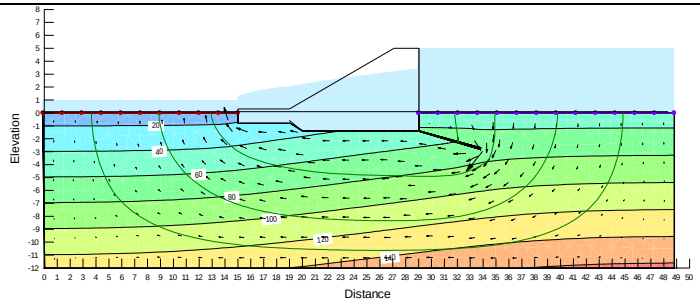

Figure 10 Pore water pressure distribution under the dam for angle 15°

Case 30°

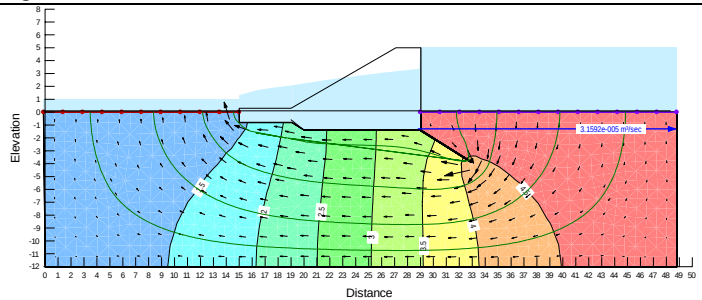

Figure 11 Flownet, flow quantity, and total head distribution for angle 30°

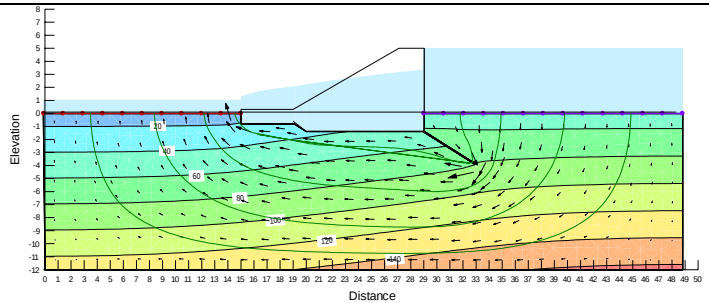

Figure 12 Pore water pressure distribution under the dam for angle 30°

Case 45°	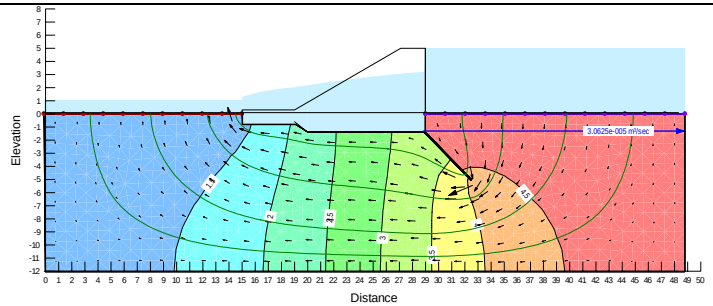 Figure 13 Flownet, flow quantity, and total head distribution for angle 45°	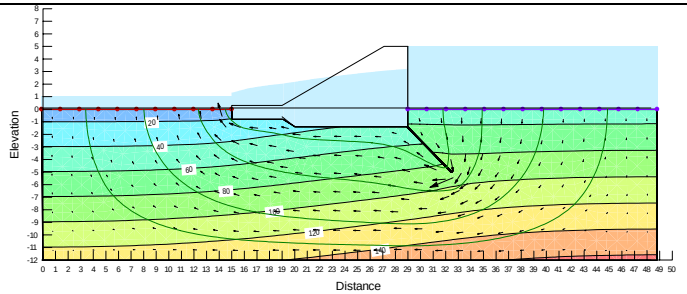 Figure 14 Pore water pressure distribution under the dam for angle 45°
Case 60°	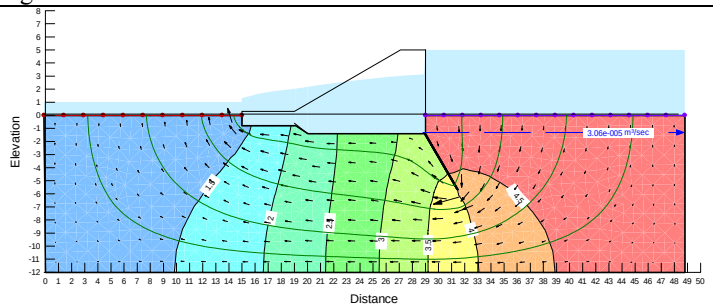 Figure 15 Flownet, flow quantity, and total head distribution for angle 60°	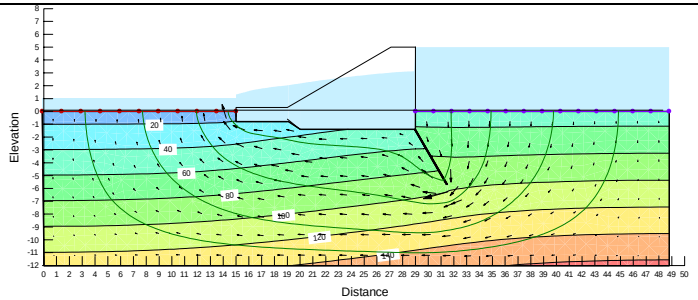 Figure 16 Pore water pressure distribution under the dam for angle 60°
Case 75°	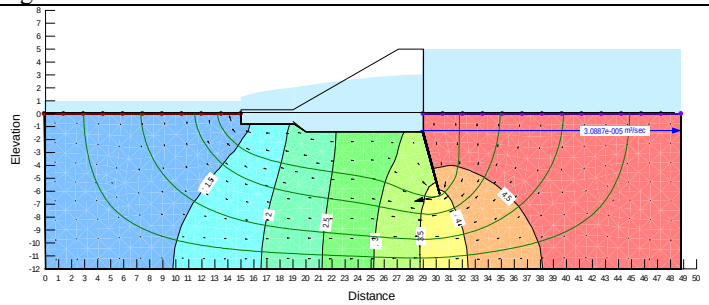 Figure 17 Flownet, flow quantity, and total head distribution for angle 75°	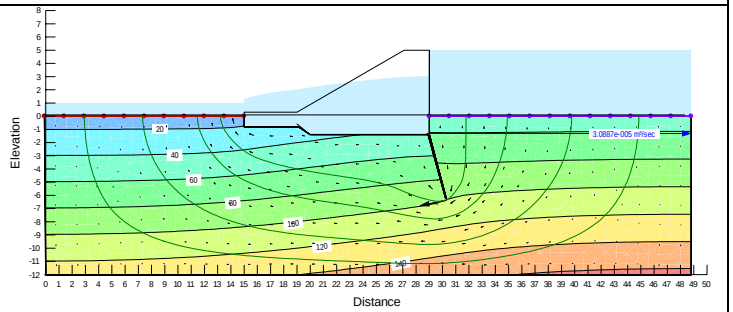 Figure 18 Pore water pressure distribution under the dam for angle 75°
Case 90°	See figure 3	See figure 4

Case 105°

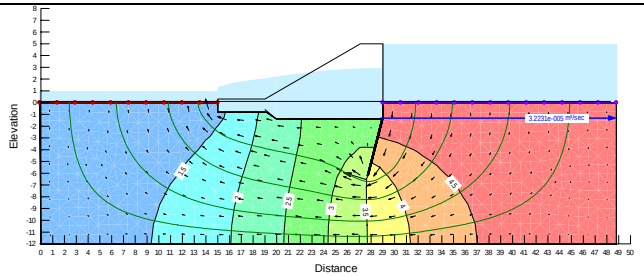

Figure 19 Flownet, flow quantity, and total head distribution for angle 105°

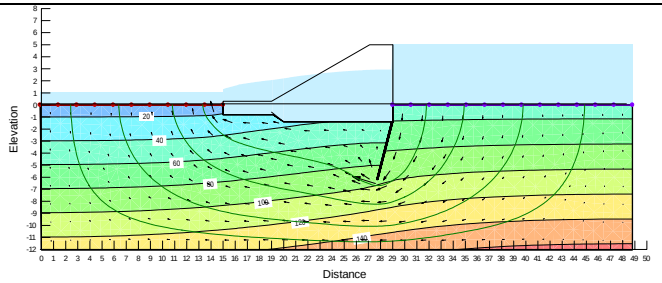

Figure 20 Pore water pressure distribution under the dam for angle 105°

Case 120°

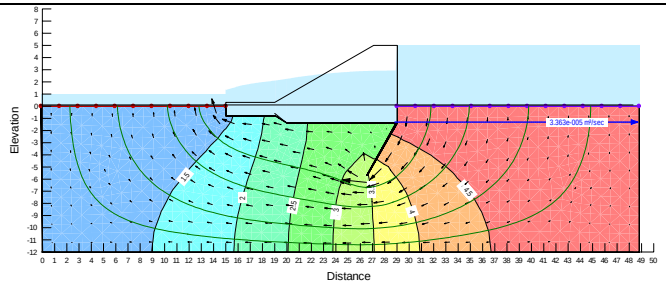

Figure 21 Flownet, flow quantity, and total head distribution for angle 120°

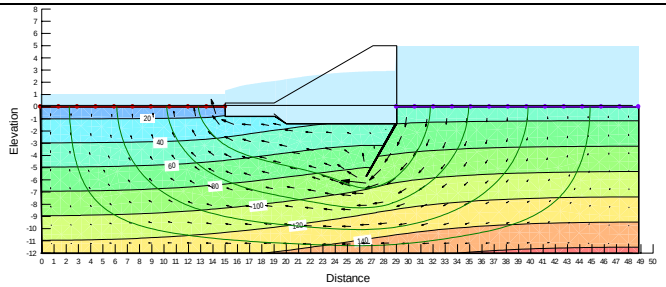

Figure 22 Pore water pressure distribution under the dam for angle 120°

Case 135°

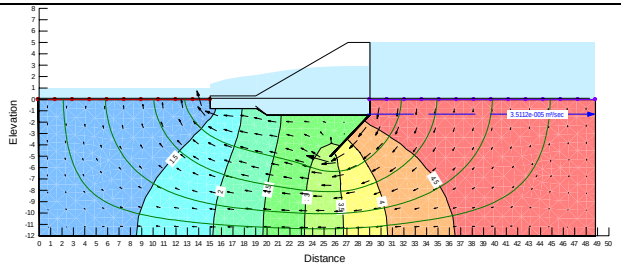

Figure 23 Flownet, flow quantity, and total head distribution for angle 135°

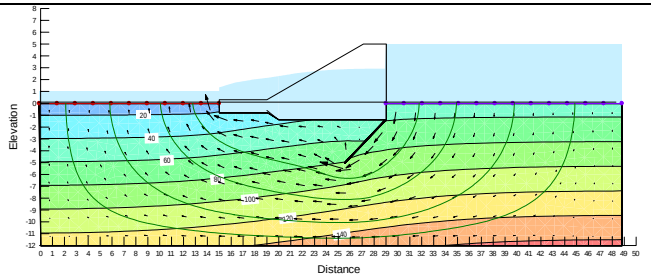

Figure 24 Pore water pressure distribution under the dam for angle 135°

Case 150°	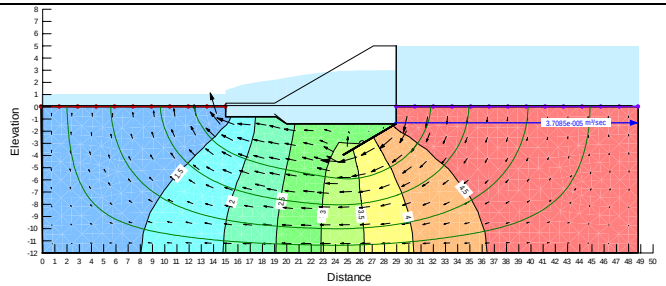 Figure 25 Flownet, flow quantity, and total head distribution for angle 150°	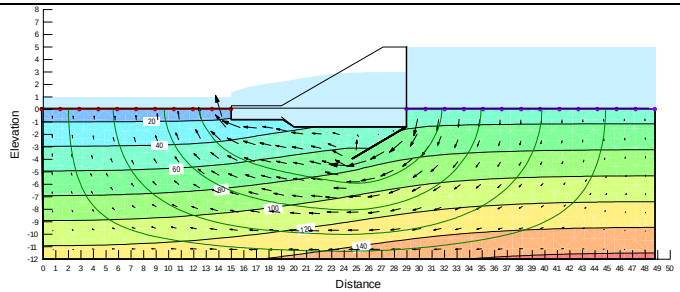 Figure 26 Pore water pressure distribution under the dam for angle 150°
Case 165°	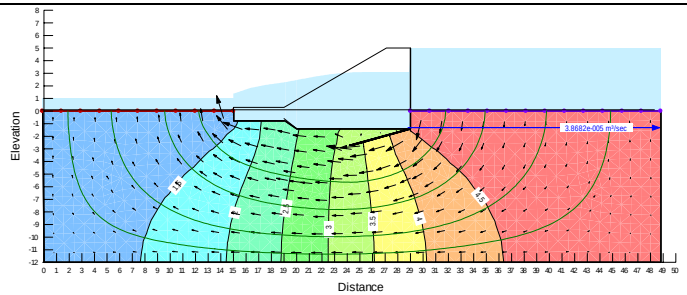 Figure 27 Flownet, flow quantity, and total head distribution for angle 165°	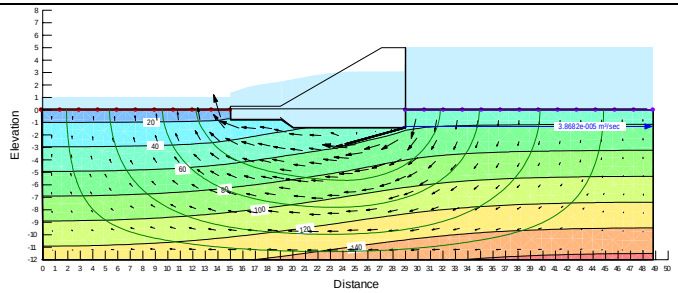 Figure 28 Pore water pressure distribution under the dam for angle 165°
Case 180°	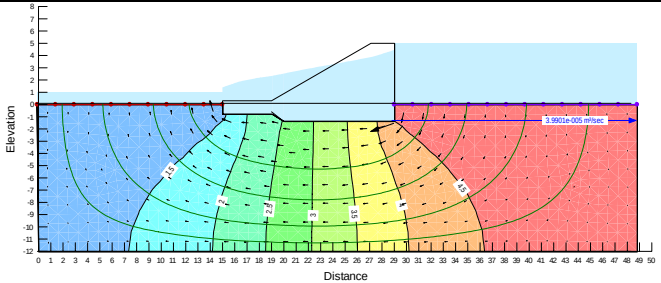 Figure 29 Flownet, flow quantity, and total head distribution for angle 180°	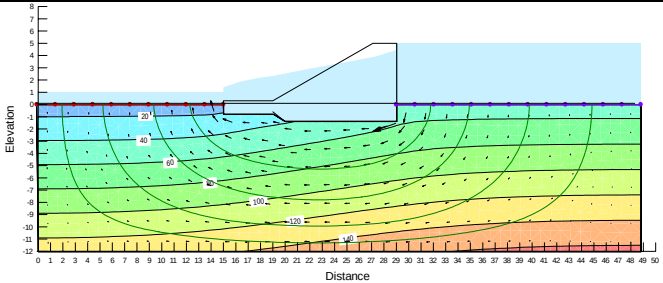 Figure 30 Pore water pressure distribution under the dam for angle 180°

Case 0°

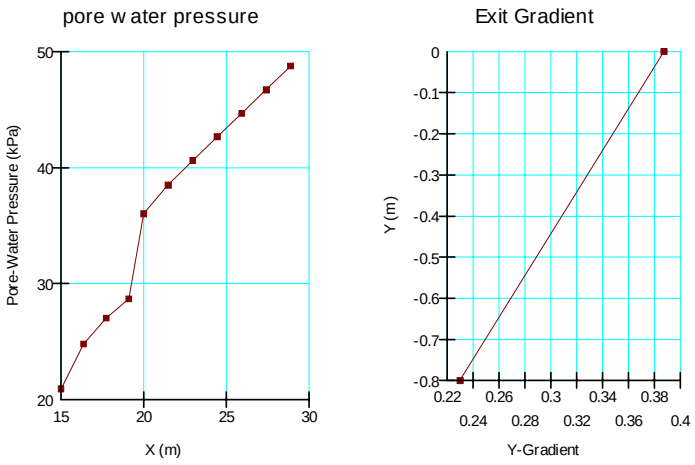

a b

Figure 31 a) Pore water pressure distribution, b) exit gradient at toe angle 0°

Case 15°

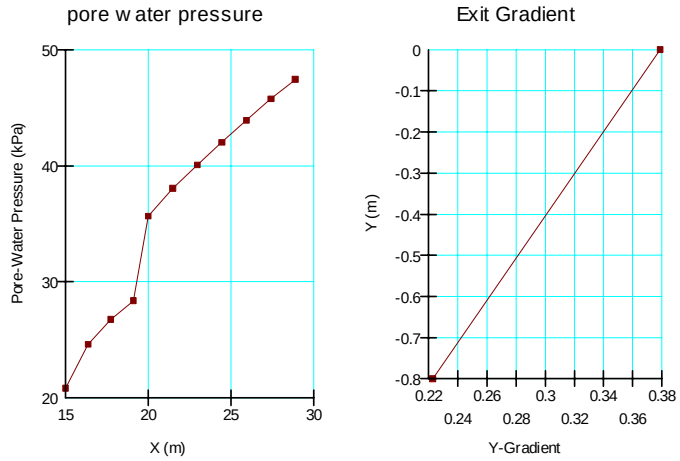

a b

Figure 32 a) Pore water pressure distribution, b) exit gradient at toe angle 15°

Case 30°

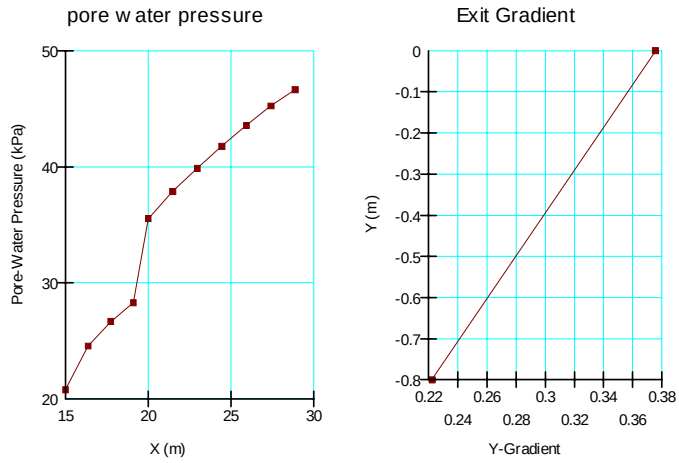

a b

Figure 33 a) Pore water pressure distribution, b) exit gradient at toe angle 30°

Case 45°

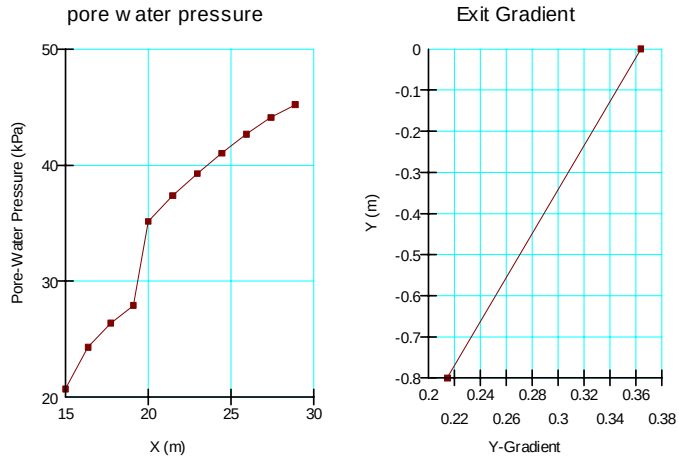

a b

Figure 34 a) Pore water pressure distribution, b) exit gradient at toe angle 45°

Case 60°	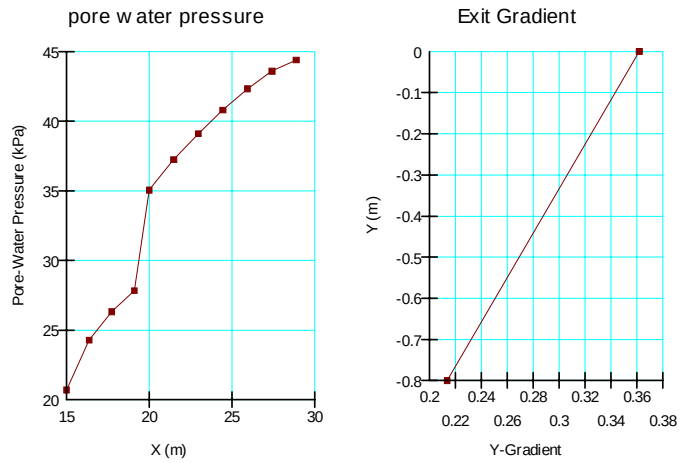 a b Figure 35 a) Pore water pressure distribution, b) exit gradient at toe angle 60°
Case 75°	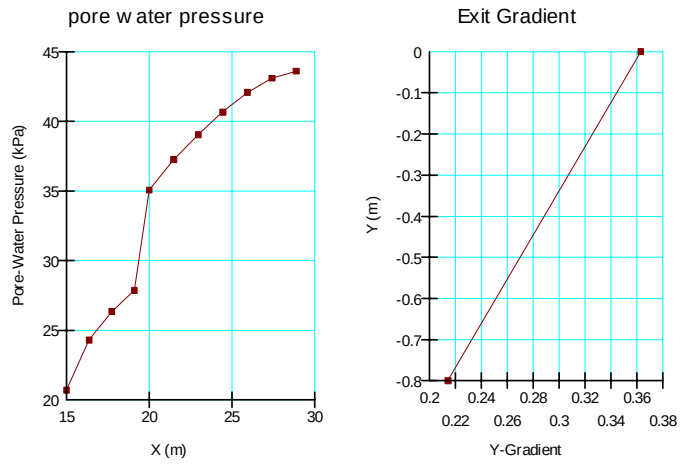 a b Figure 36 a) Pore water pressure distribution, b) exit gradient at toe angle 75°
Case 90°	See figure 5

Case 105°

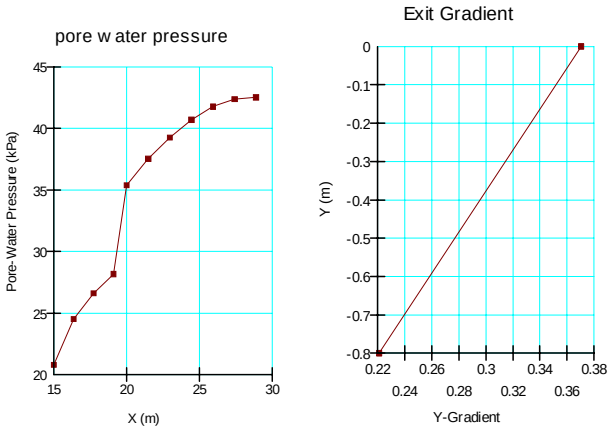

a b

Figure 37 a) Pore water pressure distribution, b) exit gradient at toe angle 105°

Case 120°

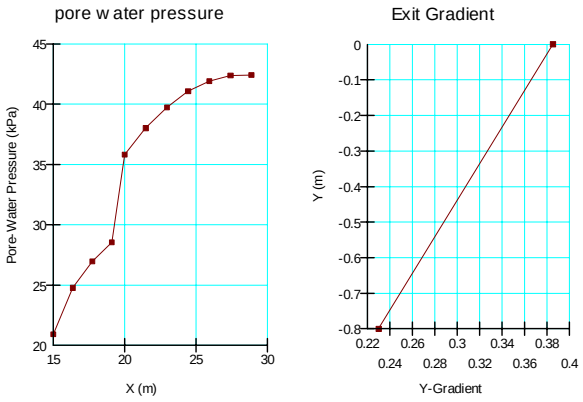

a b

Figure 38 a) Pore water pressure distribution, b) exit gradient at toe angle 120°

Case 135°

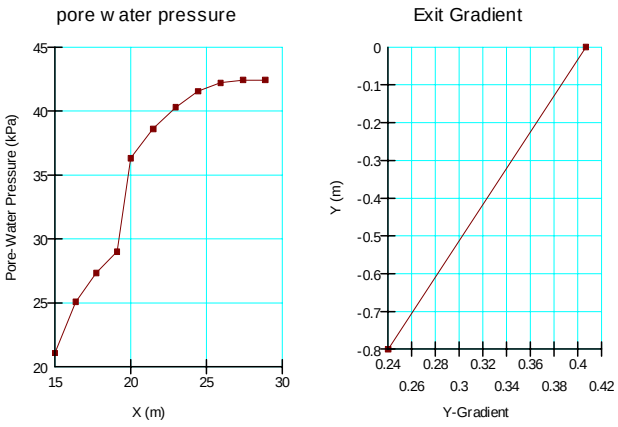

a b

Figure 39 a) Pore water pressure distribution, b) exit gradient at toe angle 135°

Case 150°

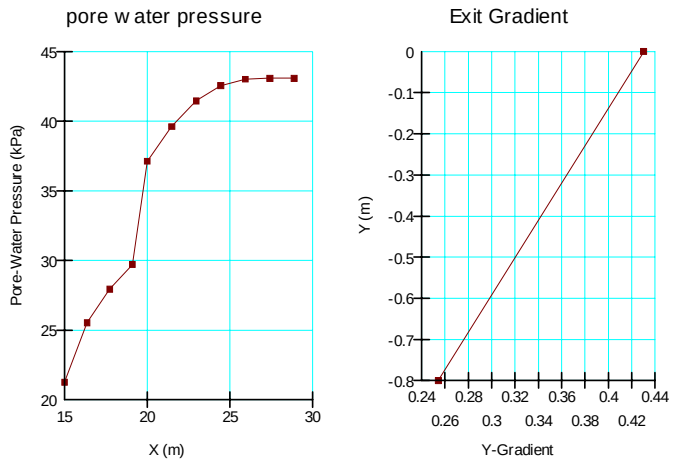

a b

Figure 40 a) Pore water pressure distribution, b) exit gradient at toe angle 150°

Case 165°

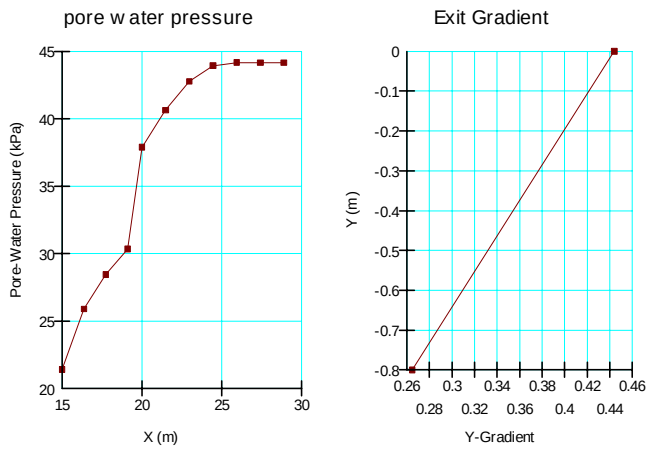

a b

Figure 41 a) Pore water pressure distribution, b) exit gradient at toe angle 165°

Case 180°

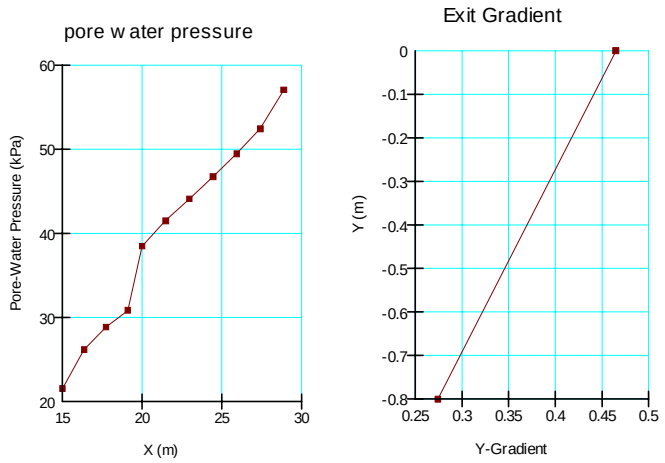

a b

Figure 42 a) Pore water pressure distribution, b) exit gradient at toe angle 180°

Table 2 Variation of flow quantity vs. cutoff wall angle

cutoff wall angle	Flow Quantity m^3/sec
0	3.2758E-05
15	3.1791E-05
30	3.1592E-05
45	3.0625E-05
60	3.0600E-05
75	3.0887E-05
90	3.12E-05
105	3.2231E-05
120	3.3630E-05
135	3.5112E-05
150	3.7085E-05
165	3.8682E-05
180	3.99E-05

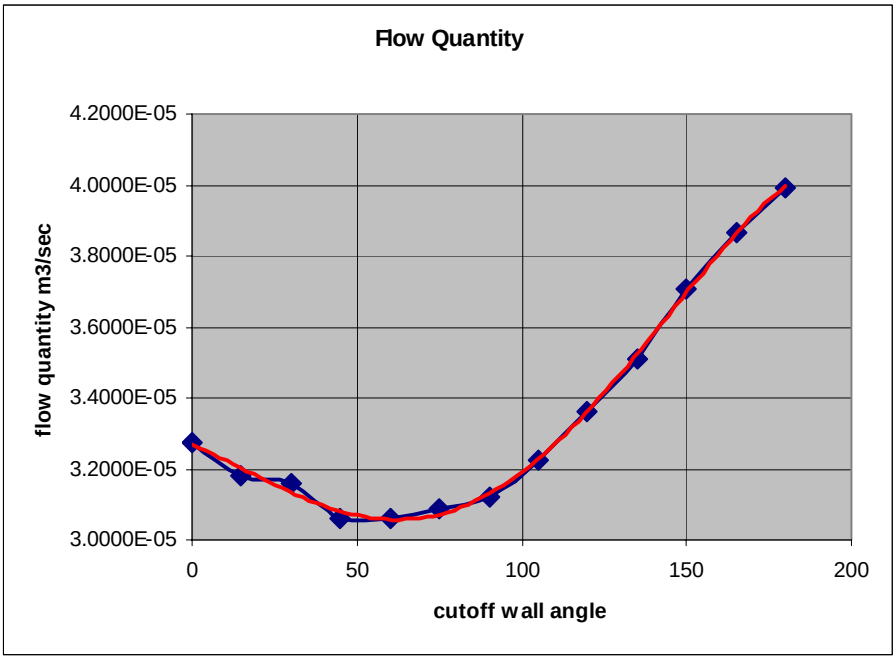

Figure 43 Variation of flow quantity vs. Cutoff wall angle

Table 3 pore water pressure under the base of the dam (kPa)

distance / angle	15	16.37	17.73	19.1	20	21.48	23	24.45	25.93	27.42	28.9
0	20.93	24.82	27.04	28.69	36.03	38.49	40.6	42.65	44.67	46.69	48.75
15	20.84	24.61	26.77	28.37	35.66	38.05	40.1	42.02	43.92	45.77	47.44
30	20.81	24.57	26.67	28.29	35.54	37.88	39.9	41.76	43.56	45.24	46.65
45	20.71	24.32	26.38	27.91	35.14	37.37	39.3	41.03	42.67	44.11	45.21
60	20.69	24.28	26.33	27.84	35.05	37.25	39.1	40.79	42.32	43.6	44.4
75	20.71	24.31	26.35	27.87	35.07	37.26	39.1	40.67	42.08	43.1	43.61
90	20.72	24.35	26.39	27.91	35.1	37.25	39	40.5	41.73	42.52	42.79
105	20.8	24.52	26.62	28.16	35.38	37.54	39.3	40.69	41.77	42.39	42.53
120	20.92	24.78	26.96	28.56	35.82	38.02	39.7	41.07	41.91	42.38	42.42
135	21.08	25.09	27.36	29.01	36.33	38.61	40.3	41.56	42.21	42.44	42.43
150	21.27	25.53	27.95	29.71	37.13	39.61	41.5	42.55	43	43.08	43.08
165	21.43	25.9	28.46	30.34	37.89	40.64	42.8	43.93	44.18	44.16	44.15
180	21.57	26.2	28.87	30.85	38.49	41.49	44.1	46.73	49.45	52.44	57.07

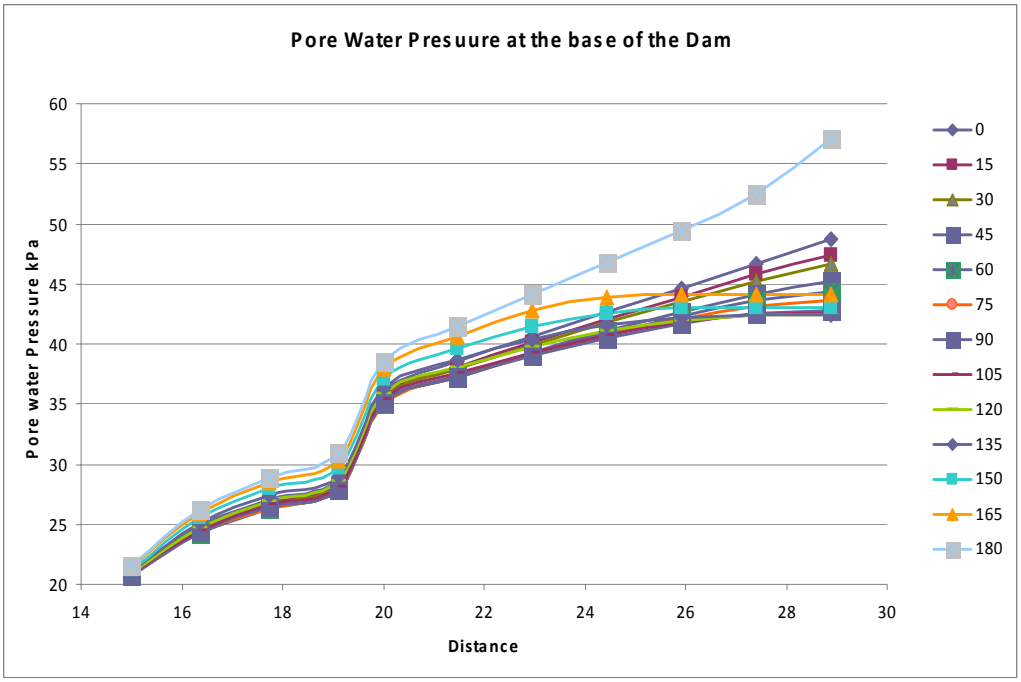

Figure 44 Variation of pore water pressure with the cutoff angle (kPa)

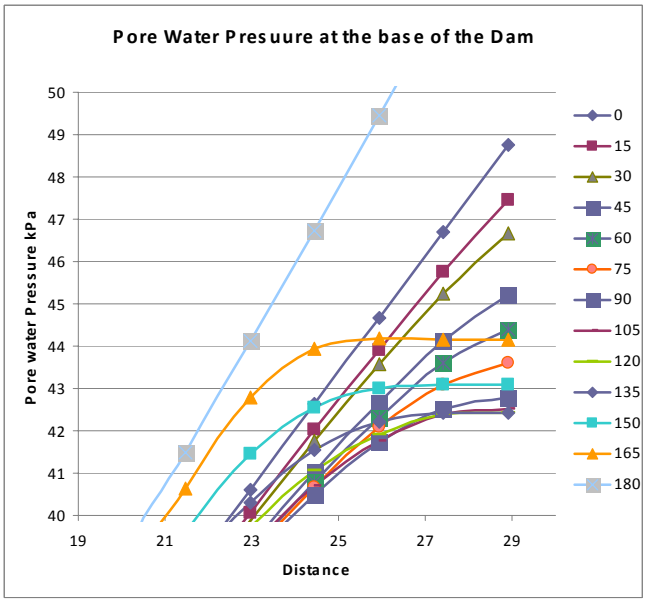

Figure 45 pore water pressure magnified end portion

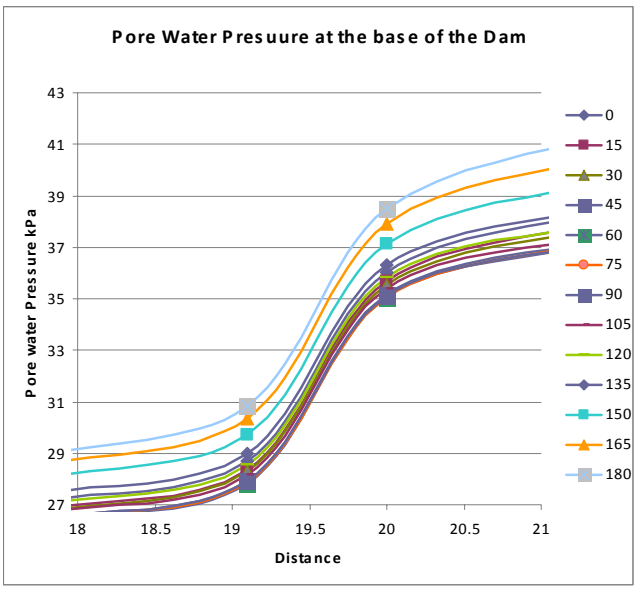

Figure 46 pore water pressure magnified middle portion

Table 4 Exit gradient vs. dam toe level

Angle / Level	0	15	30	45	60	75	90	105	120	135	150	165	180
0	0.39	0.38	0.38	0.36	0.36	0.36	0.36	0.37	0.39	0.41	0.43	0.44	0.46
-0.8	0.23	0.22	0.22	0.21	0.21	0.21	0.22	0.22	0.23	0.24	0.25	0.26	0.27

Figure 47 Graphical representation of exit gradient for the two points at dam toe

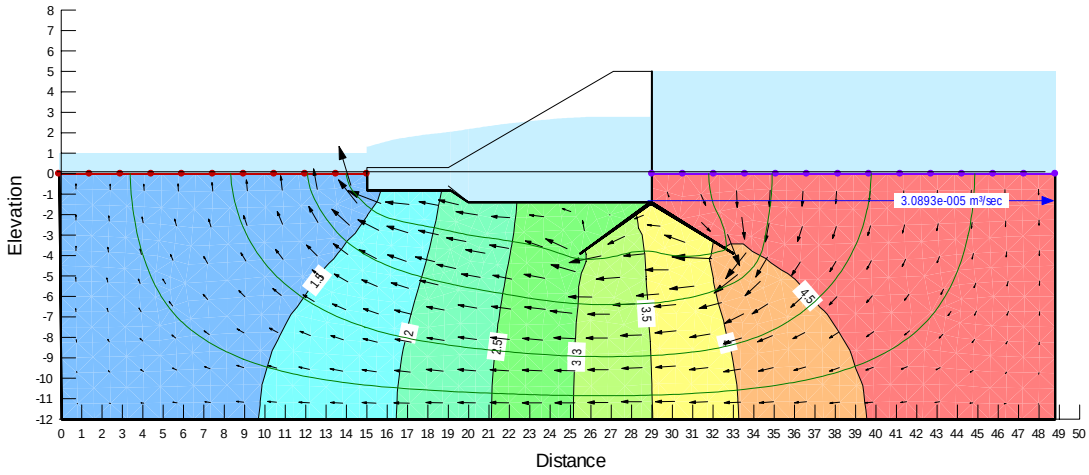

Figure 48 Flownet, flow quantity, and total head distribution (m) for angle 60° and 120°

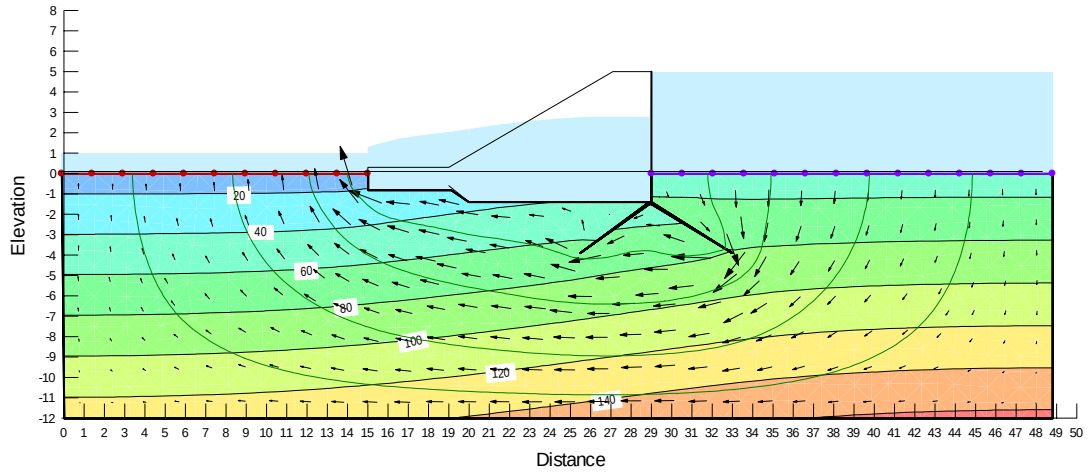

Figure 49 Pore water pressure (kN/m^2) distribution under the dam angle 60° and 120°

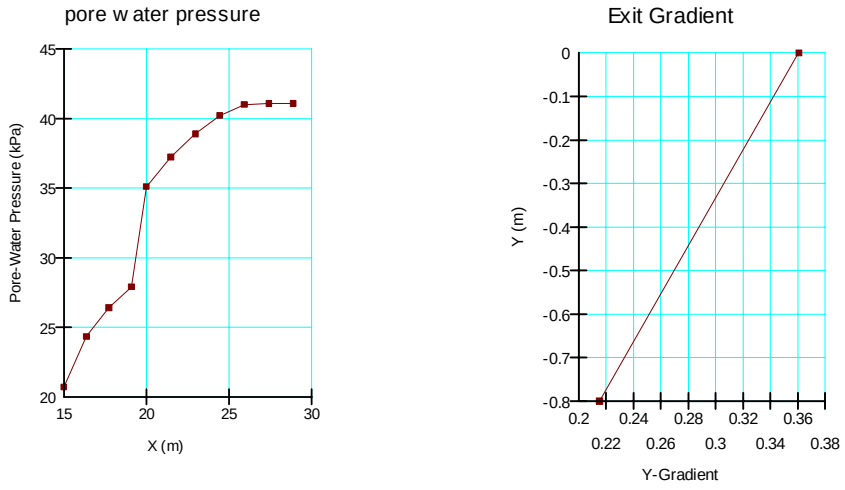

a b

Figure 50 a) Pore water pressure distribution, b) exit gradient at toe angle 60° and 120°

REMOVAL OF CHROMIUM(VI) FROM AQUEOUS SOLUTIONS USING SAWDUST AS ADSORBENT

Dr. najwa S. Majeed
Chemical Engineering Department, College of Engineering, University of Baghdad

ABSTRACT :

In the present study, a low cost adsorbent is developed from the naturally available sawdust which is biodegradable. The removal capacity of chromium(VI) from the synthetically prepared industrial effluent of electroplating and tannery industrial is obtained.

Two modes of operation are used, batch mode and fixed bed mode. In batch experiment the effect of Sawdust dose (4- 24g/L) with constant initial chromium(VI) concentration of 50 mg/L and constant particle size less than1.8 mm were studied.

Batch kinetics experiments showed that the adsorption rate of chromium(VI) ion by Sawdust was rapid and reached equilibrium within 120 min. The three models (Freundlich, Langmuir and Freundlich-Langmuir) were fitted to experimental data and the goodness of their fit for adsorption was compared. In the fixed bed isothermal adsorption column, the effect of particle size (dp) (1.09-1.8) mm, influent flow rate (Q) (1- 4) L/hr, bed depth (H) (25- 35) cm and the pH(1-7)of the solution were studied .The results show that Sawdust is an efficient adsorbent for the removal of Cr(VI) from wastewater. Percent removal of chromium reaches (100%) with increasing of contact time and decreasing the pH.UV- Spectrophotometer was used to determine the metal ion concentration.

ازالة الكروم من المياه الملوثة باستخدام نشارة الخشب كمادة مازة

الخلاصة :

امكانية استخدام المواد الفائضة والرخيصة الثمن مثل نشارة الخشب المطروحة من ورش النجارة كمواد مازة لبعض الايونات المعدنية الموجودة في المياه الملوثة مثل ايونات الكروم (VI) تمت دراستها.

تم استخدام نمطين من التشغيل في هذا البحث وهي تجارب النمط الدفعي (batch experiments) وتجارب النمط المستمر (fixed bed experiments). تم اجراء تجارب دفعية (batch experiments) لدراسة تأثير كمية نشارة الخشب (4-24)غم/ لتر بثبوت التركيز الابتدائي لايون الكروم(50 ملغم/ لتر) وحجم ثابت لجزيئات المادة الممتزة الذي هو اقل من 1.8 mm أظهرت النتائج ان نسبة ازالة المعدن تزداد بزيادة كمية نشارة الخشب و الزمن. كذلك أظهرت النتائج ان الوصول الى حالة التعادل تستغرق تقريباً (120)دقيقة، تم تحليل النتائج باستخدام موديلات (Langmuir, Freundlich and Langmuir-Freundlich) وأظهرت النتائج ان جميع الموديلات ذات تقارب جيد. كذلك اجريت تجارب النمط المستمر (fixed bed experiments) وتم دراسة حجم جزيئات المادة الممتزة (1.09 -1.8) بمعدل جريان داخل (1-4) لتر/ ساعة وارتفاع عمود الامتزاز (25-35) سنتمتر وحامضية المحلول (1-7). لقد أظهرت النتائج نشارة الخشب هي فعالة في امتزاز المعادن من مياه الصرف وكانت اعلى نسبة ازالة الكروم تصل (100%) بزيادة زمن العملية والمساحة السطحية وفعالية المادة الممتزة .

KEY WORDS :

Wastewater, Adsorption, Chromium(VI), Heavy metals removal, Sawdust, Low cost adsorbent.

INTRODUCTION :

Environmental contamination by toxic metal is of great concern because of health risks on humans and animals.Among the toxic metal ions , chromium is one of common contaminants which gains importance due to its high toxic nature even at very low concentrations(Vinodhini and Das, 2010).

Chromium(VI) is a cancer-causing agent and can pose health risk such as liver damage (Dokken et al.,1999).

Waste waters such as those generated during dyes and pigments production ,film and photography,galvanometry,metal cleaning, plating and electroplating may contain undesirable amounts of chromium(VI) anions(Venkateswaran ,2007 ;Bhattacharya ,2008).

Concentration of Cr(VI) present in industrial effluent streams are in the range of 50-200 mg/l(Contreras ,2004 ; Kumar and Bishnoi,2007).The permissible limit of Cr(VI) in potable water is 0.05 mg/l(Selvaraj and Manonmani ,2003).

In order to comply with the permissible limit,it is essential that industries treat their effluents to reduce the Cr(VI) concentration in water and wastewater to the acceptable level before its disposal or recycling into the natural environment.

There are various treatment technologies available to remove Cr(VI) from waste water such as chemical precipitation (Uysal and Irfan ,2007)Ion-exchange(Uysal and Irfan ,2000) , membrane separation(Kozloovski and Walkowiak, 2002),electrocoagulation(Roundhill and Koch ,2002),solvent extraction(Chen ,2004),reduction(Chen and Hao ,1998)reverse osmosis, and adsorption(Baral et al. , 2007 ; Mohan et al. , 2005). These techniques are economically expensive for the removal of Cr(VI) from wastewater.The above mentioned removal techniques have many disadvantages such as incomplete metal removal,high reagent and energy requirements, and generation of toxic sluge or waste products which require proper disposal without creating any problem to the invironment(Aliadadi et al. , 2006). Therefores , there is a dire need of a treatment method for Cr(VI) removal from wastewater which is simple,effective and inexpensive(Babu and Gupta , 2008).Adsorption when combined with an appropriate step of desorbing the Cr(VI) from adsorbent and avoiding the problem of disposal of adsorbent is a cost effective and versatile method for the removal of Cr(VI) (Kumar et al. , 2007).

The cost associated with commercial adsorbents make adsorption process very expensive which has led to the search for new stratgies for developing low-cost materials with a good capacity for Cr(VI) removal(Aggarwal et al. , 1999).In the recent years ,several studies have been reported on various low-cost adsorbents such as wool(Dakiky et al. ,2002) used tyers, seaweed, fungal biomass, green algae, maple sawdust(Shukla et al. , 2003),sugar industry waste,rad mud,tea factory waste(Malkoc and Nuhoglu,2005).

However,many of these naturally available adsorbents have low chromium adsorption capacity. Thus, there is a need to develop or find innovative low-cost adsorbents with an affinity towards metal ions for the removal of Cr(VI) from aqueous solution which leads to high adsorption capacity(Kumar and Bishnoi ,2008).

The objective of the present study is to investigate the possible use of sawdust as alternate adsorbent material for the removal of Cr(VI) from wastewater. Continuous adsorption experiments were conducted to understand and quantify the effect of influencing parameters such as flowrate, bed depth, partical size, pH of the solution.

Batch experiments are carried out for kinetic studies on the removal of Cr(VI) from aqueous solution. The Langmuir,Freundlich, Langmuir-Freundlich,equation models are used to fit the experimental equilibrium isotherm data obtained in this study.

EXPERIMENTAL WORK

Materials :

Adsorbent: Sawdust is collected from the Iraqi workshops.It is washed repeatedly with distilled water to remove the dust and soluble impurities.It is then kept for drying at room temperature for 8 hr.

The sawdust were sieving to produce a particle size(1.09,1.59,1.8mm).

Adsorbate : A stock solution of 1000mg/l of Cr(VI) is prepared by dissolving 2.828 gm of 99.9% Potassium dichromate(K_2 Cr_2 O_7) in 1000 ml of solution .This solution is diluted as required to obtain the standard solutions containing 10-100mg/l of Cr(VI),pH adjustment is carried out by using 0.5N HCl and 0.05N NaOH solutions.

EXPERIMENTAL MODES :

1) Batch Experiments

Batch experiments were used to obtain the equilibrium isotherm curves and then the equilibrium data. In batch mode effect of sawdust dose on adsorption process and equilibrium isotherm experiments were studies.

All experiments were carried out at 25C^o ±1 ,rpm=120 and pH=1 . Five of 1 liter flasks were used for all experiments conducted with an initial chromium (VI) concentration of 50 mg/L, sawdust dose was of (4,8,12,16,20,24) g/L. Samples were collected from the flasks and tested using (Shimadiza UV – 160) by determining the absorbance of the chromium ions with 1cm cell width (1cm layer thickness).

Data obtained from batch tests fitted to Freundlich, Langmuir and Freundlich-Langmuir adsorption isotherm equations.

2) Fixed Bed Column Experiments

Column experiments were carried out at various particle size (dp), flow rate (Q), bed depth (H), pH of the solution , to measure the breakthrough curves for the systems.

The fixed bed adsorber studies were carried out in Q.V.F. glass column of 3.5 in. (8.75cm) I.D. and 50 cm in height. The sawdust was confined in the column by fine mesh at the bottom to avoid loss the adsorbent. The influent solution was introduced to the column through a small water distributor and class balls to ensure a uniform distribution of influent through the adsorbent, fixed at the top of the column.

The experimental procedure as follow: The sawdust was placed in the adsorption column for the desired bed length and particle size.

- The wastewater with the desired concentration was prepared in the feed container, using distilled water.
- The wastewater was pumped to the adsorption column through the calibrated rotameter at the desired flow rate.
- Samples were taken periodically for concentration of metal measurment using UV-Spectrophotometer.
- The breakthrough curves were determined by plotting relating effluent concentration (C/Co) against time (t).

The schematic representation of experimental equipment is shown in **Fig 1**.

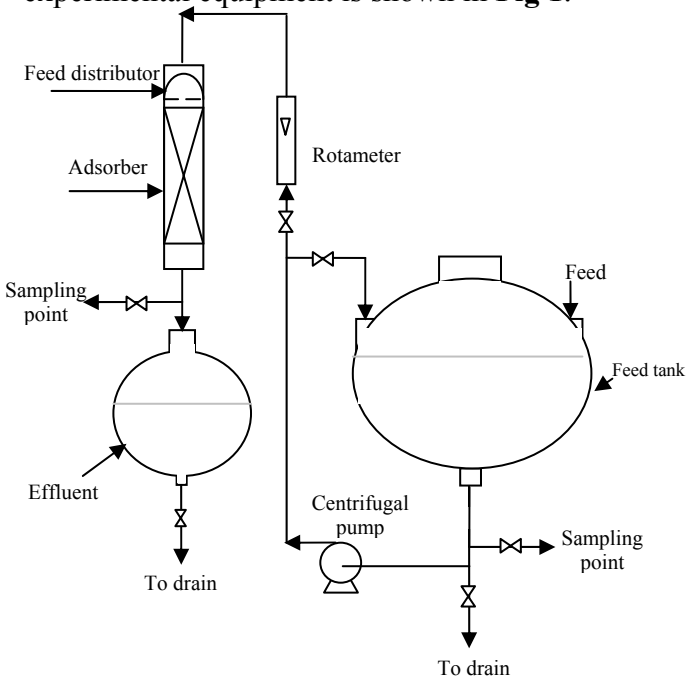

Fig. (1) Schematic representation of fixed bed experimental

RESULTS AND DISCUSSION:

Batch Experiments:

(i) Adsorption Isotherms:

Adsorption isotherm studies were performed to obtain equilibrium isotherm curves and data required for the design and operation of fixed bed adsorber. The adsorption isotherm curves were obtained by plotting the weight of the solute adsorbed per unit weight of the adsorbent (q_e) against the equilibrium concentration of the solute (c_e). **Fig. 2** shows the adsorption isotherm curve for adsorption of Cr(VI) on sawdust at 25 C^o .

The obtained data was correlated with Langmuir, Freundlich and Langmuir-Freundlich models. The Langmuir model describing adsorption can be described in **eq. (1)**as (Weber and Walter , 1972):

$$\frac{x}{m} = \frac{abC_e}{1 + aC_e} \qquad (1)$$

The Freundlich adsorption model in **eq. (2)** of the form (Weber and Walter, 1972):

$$\frac{x}{m} = kC_e^{1/n} \qquad (2)$$

Combination of Langmuir-Freundlich Isotherm Model, i.e. the Sips model for single component adsorption (Sips, 1984)as in **eq.(3)**:

$$q_e = \frac{bq_m C_e^{1/n}}{1 + bC_e^{1/n}} \qquad (3)$$

The parameters for each model obtained from non-linear statistical fit of the equation to the experimental data. All parameters with their correlation coefficients are summarized in **Table 1**.

From the statistical analysis (high values of the correlation coefficients) it was found that adsorption of metal by sawdust could be well described by the three isotherm models. The correlation coefficients were in the range of (0.956-0.9591 %) for initial chromium concentration 50 mg/l.

The correlation coefficient value was higher for Freundlich than the other correlations. This indicates that the Freundlich isotherm is clearly the better fitting isotherm to the experimental data.

Table 1 : Isotherm parameters for chromium(VI) Adsorption onto sawdust with the Correlation Coefficient.

Chromium solution		
Model	**Parameters**	**Values**
Langmuir eq.(1)	a,	0.006961
	b,	33.76436
	Correlation coefficient (R^2)	0.956
Freundlich eq.(2)	K,	0.279032
	n,	1.113541
	Correlation coefficient (R^2)	0.959166
Combination of Langmuir-Freundlich eq.(3)	q_m,	110.5533
	b,	0.002475
	n,	2.1842
	Correlation coefficient (R^2)	0.95851

FIXED BED EXPERIMENTS:

(i) Effect of Volumetric Flow Rate:

In a design of fixed bed adsorption column, the contact time is the most significant variable and therefore the bed depth and the metal solution flow rate are the major design parameters . The effect of varying the volumetric flow rate was investigated at constant concentration (50 ppm) and constant particle size (1.59) mm and bed depth (30) cm and solution pH(2), the breakthrough curves are presented in **Fig.5**. It is obvious that increasing the flow rate decreases the volume treated until breakthrough. This is due to the decreased contact time between the metal and the adsorbent at higher flow rate.

Increasing the flow rate may be expected to make reduction of the surface film. Therefore, this will decrease the resistance to mass transfer and increase the mass transfer rate. Also, because the reduction in the surface film is due to the disturbance created when the film of the bed increased resulting of easy passage of the adsorbate molecules through the particles and entering easily to the pores, this decreased contact time between metal and sawdust at high flow rate. These results agree with that obtained by(Kim et al. 2003) .

(ii) Effect of Bed Depth:

The effect of bed depth was investigated for metal adsorption on sawdust; the experimental breakthrough curves are presented in **Fig. 6.** The breakthrough curve was obtained for different bed depth of sawdustat constant flow rate (2 l/h),pH(2), constant particle size (1.59) mm and constant chromium(VI) concentration (50 ppm). **Fig.7** shows the effect of using bed depth of 60 cm. at pH=7, flow rate(2l/h) , and particle size (1.59) mm on breakthrough curve,it was clear that increasing the bed depth causes to increase the metal removal and can reach that obtain with pH=2 and bed depth of (30)cm at flow rate(2l/h), and particle size (1.59) mm. The increase in bed depth increases the breakthrough time and the residence time of the solute in the column, due to provide greater surface area(Malkoc and Nuhoglu,2006).

.

(iii) Effect of Particle Size:

In case of using an adsorbent particles of much smaller size to an extent, that will eliminate inter particle mass transfer resistance, so that the rate determining step is diffusion through film around each particle. The effect of varying the particle size was investigated; the experimental breakthrough curves are presented in **fig.8 t**he breakthrough curves were obtained for different particle size (1.8,1.59,1.09) mm at constant initial concentration of chromium(VI)(50ppm),bed depth of Sawdust (30 cm) ,pH (2) and constant flow rate(2l/h).The experimental results showed that fine particle size (1.09mm) showed a higher metal removal than others particle sizes as illustrated in the figure. This was due to large surface area of fine particles.

(iv) Effect of pH of the solution:

Earlier studies on heavy metal adsorption have shown that solution pH is the most important parameter affecting the adsorption process .

In order to establish the effect of pH on the adsorption of chromium(VI) ions,fixed bed adsorption studies at different pH values were conducted in the range of 1 to 7 **Fig.(9)** reveals that maximum adsorption capacity of Cr(VI) ions at pH =1 and significantly decrases with increase in pH values up to 7.

At lower pH, the biosorbent is positively charged due to protonation and dichromate ion exists as anion leading to an electrostatic attraction between them.Thus the uptake of Cr(VI) increased markedly with deceasing pH.Clear decrease in adsorption above pH 4 may be due to occupation of the adsorption sites by anionic species like $HCrO^{-2}{}_4$;$Cr_2O_7{}^{-2}$;$CrO_4{}^{-2}$ **;** etc. Which retards the approach of such ions further towards the sorbent surface(Boddu et al.,2003).

COMPETITIVE SEPARATION OF COPPER AND CHROMIUM(VI) :

The main objective of this part was to investigate the effect of other metals on chromium adsorption onto Sawdust.

Copper and Chromium were chosen due to their presence in several industrial wastewater and their toxicity.

Fig.10 show the breakthrough curves of copper and chromium(VI) on Sawdust ,it was clear that copper was higher removed than chromium(VI) at the early period of the adsorption process in a solution of 50% chromium and 50% copper at(pH 2),bed depth of(30 cm),particle size of (1.59mm),flowrate(2 l/h).

CONCLUSIONS :

The present study has led to the following conclusions:

1. Sawdust was effective in adsorbing heavy metal from wastewater.
2. In batch experiment the percent removal of Cr(VI) increases (66- 86 %) with increasing Sawdust dose (4 - 24 g/l).
3. Batch kinetics experiments showed that equilibrium time was about (120 min) with mechanical mixing by gar test at 120 rpm and at an initial concentration 50 ppm and adsorbent dose 8 gm/l.
4. The isotherm models (Langmiur, Freundlich and Langmiur- Freundlich) gave good fitting for the adsorption of Sawdust versus equilibrium concentration of chromium (VI). The correlation coefficients (R) obtained by "Statistica program" for these models were in the range of (95.6-95.91%).
5. In fixed bed experiment, the percent removal of chromium (VI) increases with increasing contact time, bed height, decreasing flow rate, reducing the pH of the solution.
6. The adsorption of chromium in the presence of copper ,showed that copper was higher affinity than chromium (VI) at the early period of the adsorption process in a mixture of (50% copper, 50% chromium (VI) at (pH=2,dp=1.59mm,flowrate=2l/h,bed depth=30cm).

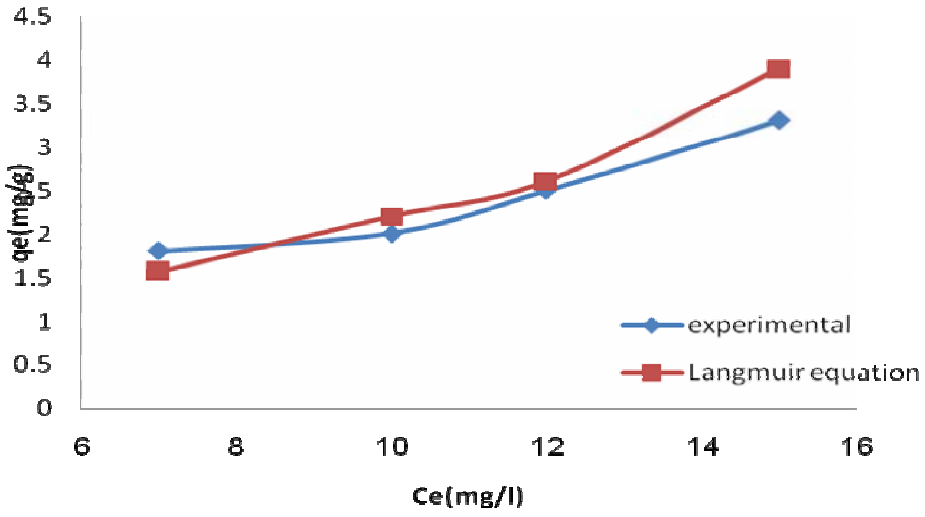

Fig. 2 Adsorption isotherm for Chromium on sawdust
(C_o=50mg/L, Temp. =25C^o,dp=1.59 mm)

Fig.3 Change in Chromium(VI) Concentration with Time of Batch Tests (C_o=50mg/L, Temp. =25C^o, particle size=1.59 mm)

Fig. 4 The Effect of Sawdust on Chromium(VI) Removal (Co=50mg/L, Temp. =25C^o, particle size=1.59mm)

Fig.5 Experimental Breakthrough Curves for Adsorption of chromium(VI) on sawdust at different flow rates (H=0.35 cm, d_p=0.35 cm,C_0=50 ppm)

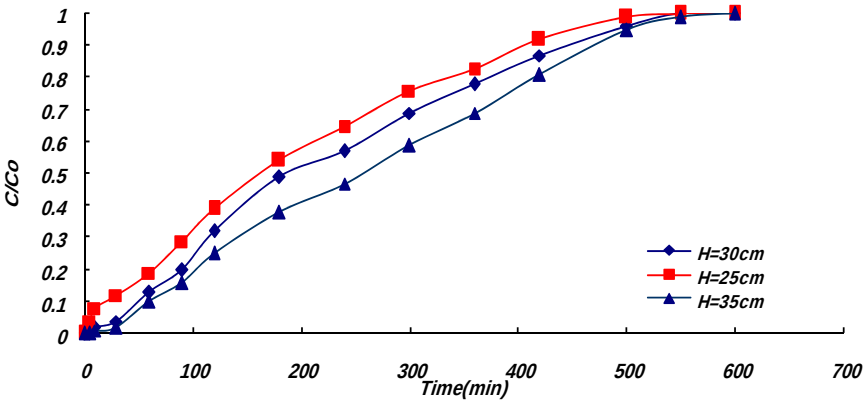

Fig.6 Experimental Breakthrough Curves for Adsorption of chromium(VI) at different bed depths (Q=2 l/hr, d_p=1.59mm,C_0=50 ppm)

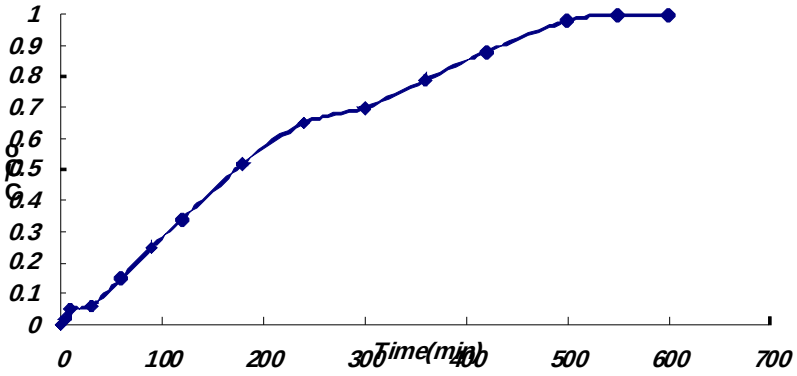

Fig.7 Experimental Breakthrough Curves for Adsorption of chromium(VI) at bed depth=60cm (Q=2 l/hr, d_p=1.59mm,C_0=50 ppm)

Fig.8 Experimental Breakthrough Curves for Adsorption of chromium(VI) on sawdust at different particle sizes(Q=2 l/hr, H=30 cm,C_0=50 ppm)

Fig.9 Experimental Breakthrough Curves for Adsorption of chromium(VI) on Sawdust at Different pH value (Q=2 l/hr, H=30 cm ,d_p=1.59 cm)

Fig.10 Experimental Breakthrough Curves for Adsorption of chromium(VI) and copper on Sawdust at (pH =2,Q=2 l/hr, H=30 cm ,d_p=1.59 cm)

REFERENCE :

- Aggarwal D., Goyal M., Bansal R.C.; Adsorption of Cr(VI)by activated carbon from aqueous solution , carbon 37 (1999) 1989-1997.

- Aliadadi M., Morshedzadeh K., Soheyli H. ; removal of Cr(VI) from aqueous solution by lignocellulosic solid wastes , Int. J. Environ . Sci.Technol.3(2006)321-325.

- Babu B.V., Gupta S. ; Adsorption of Cr (VI) using activated neem leaves as an adsorbent ; Kinetic studies , Adsorption 14(2008)85-92.

- Baral S ,Das S.N.,Rath P., chaudhury R.; Cr(VI)removal by calcined bauxite , Biochem , Eng.J. 34(2007)69-95.

- Bhattacharya ,A.K. ;"Adsorption , kinetics and equilibrium studies on removal of Cr(VI)from aqueous solutions using different low-cost adsorbents".Chem.Eng.J.,137(3), .(2008)529-541.

-Boddu V. M.;Abburi K,Talbott J.L.,Smith E.D.,Removal of Cr(VI) from water using a new composite chitosan biosorbent.Environ.Sci.Tech,37(19),4449-4456(2003)

- Chen H.; Adsorptive removal of Cr(VI)by Fe modified steam exploded wheat straw , Proc. Biochem.39(2004)541-545.

- Chen J.M.N., Hao O .J.N. ; Microbial Cr(VI) reduction , Critical reviews , Environ. Sci, Tecchnol.28(1998)219-251.

- Contreras S.M.,(2004)"Composting of tannery effluent with cow manure and wheat straw,Bioresour.Technol.94,223-228.

- Dakiky M., Khamis M., Manassra A.M. ;"Selective adsorption of Chromium(VI) in industrial wastewater using low-cost abundantly available adsorbents,Environ.Res.6(2002)533-540.

- Dokken K. ; Gamez G; Herrera I. ; Tiemann K. ; Pingitore N.E.;Chianelli R.R. ; Gardea Torresdey S.L;"Characterization of Chromium Cr (VI) bioreduction and Chromium (III)binding to alfalfa biomass'. In proccedings of 1999 conference on hazardous waste research, Snowbird , Utah, (1999)101-113.

- Jianlong W., Xinmin Z,;Removal of Cr(VI)from aqueous solution by macro

porous resin adsorption , J. Environ .Sci. Health A35(2000)1211-1230.

- Kim J.G., Kim J.H., Moon H.S., Chon C.M. and Ahn J.S.; "Removal Capacity of Water Plant Alum Sludge for Phosphorus in Aqueous Solutions", Chemical Speciation and Bioavailability, 14, 2003, pp 67-73.

- Kozloovski A. , Walkowiak; removal of Cr(VI)from aqueous solution by polymer inclusion membrances, Water Res.36(2002)4870-4876.

- Kumar R., Bishnoi N.R.; Biosorption of Cr(VI) from aqueous solution and electroplating wastewater using fungal biomass, Chem. Eng.135(2008)202-208.

- Kumar P.A. , Manabenra R. , Chakraborty S.; "Cr(VI) Removal from wastewater using aniline formaldehyde condensate coated silica gel,J.Hazard.Mater.143(2007).

- Roundhill D.M., Koch H.F.;Methods and techniques for the selective extraction and recovery of oxo-anions,Chem.Soc.Rev.31(2002)60-67.

- Malkoc E. and Nuhoglu; "Fixed Bed Studies for the Sorption of Chromium (VI) onto Tea Factory Waste", Chemical Engineering Science,V.61 (2006)pp4363-4372.

- Mohan D.,Singh K.P.,Singh V.K. ; removal of Cr(VI)from aqueous solution using low-cost activated carbons derived from agricultural waste materials and activated carbon fabric cloth , Ind.Eng.Chem.Res.44(2005)1027-1042.

- Selvaraj ,K. ,Manonmani, S.(2003)"Removal of Cr(VI)using distillery sluge". Bioresour. Technol. 89, 207-211.

- Shukla S.S., Kenneth L.D., Shukla A., Margrave J.L.;Adsorption of Chromium from aqueous solutions by maple sawdust,J.Hazard.Mater.B 100(2003)53-63.

- Sips R., 1984, J. Chem. Phys., 16, pp 490-495.

- Uysal M, Irfan A.;Removal of Cr(VI)from industrial wastewaters by adsorption , J. Hazard. Mater.149(2007)482-491.

- Venkateswaran , P. ; "Speciation of heavy metals in electroplating industry sludge and wastewater residue using inductively coupled plasma" Int.J.Environ.Sci.Tech.,4(4), (2007)497-504.

- Vinodhini V. ; N. Das "Relvant approach to assess the performance of sawdust as adsorbent of Chromium (VI) ions from aqueous solutions. , Int. J. Environ. Sci Tech.,7(1),85-92,(2010).

- Weber, J. R. and Walter, J., 1972, "Physicochemical Processes for Water Quality Control", Wiley-Interscience, New York.

NOMENCLATURE :

a Langmiur constant (L/mg)
b Langmiur constant (mg/g)
C Concentration of solute in solution at any time (mg/l)
C_e Concentration of solute in solution at equilibrium (mg/l)
C_0 Initial concentration of adsorbate (mg/l)
k Freundlich equilibrium constant indicative of adsorption capacity
m Mass of solute adsorbent (g)
n Freundlich constant indicative of adsorption intensity
H Bed depth (m)
Q Flow rate (l/h)
q_e Amount of metal ion adsorbed at equilibrium (mg/g)
R Correlation coefficient
t Time (min)
x Mass of solute adsorbed (mg)

MECHANICAL DEGRADATION OF HIGH MOLECULAR WEIGHT POLYMER WITH SURFACTANT ADDITION IN A ROTATING DISK APPARATUS

Izzat N. Slaiman [1], Haidar M. Al-Qamaje [2], Marwa F. Abdul-Jabbar [3], Hala S. Al-shifee [4]

Petroleum Eng. Department, Kirkuk University [1],Chemical Engineering Department, Collage of Engineering, Nahrain University, Baghdad, Iraq [2,3] , Ministry of oil, state company of oil projects, Chemical Eng. Department[4]

ABSTARCT

Mechanical degradation hampers the practical usage of polymers for turbulent drag reduction application. Mechanical degradation refers to the chemical process in which the activation energy of polymer chain scission is exceeded by mechanical action on the polymer chain, and bond rupture occurs. When a water-soluble polymer and surfactant are mixed in water solution, the specific structures (aggregates) are formed, in which polymer film is formed around micelle. In this work, Xanthan gum (XG) – Sodium lauryl ether sulfate (SELS) complex formation and its effect on percentage viscosity reduction (%VR) was studied. It was found that SELS surfactant reduced the mechanical degradation of XG much more efficiently than this polymer alone. Xanthan Gum (XG) has been tested for its shear stability and degradability. 0.5% and 1.0 % by weight concentration solutions were exposed to shear stirring at different speeds and time; also 0.5% through 1.5% by weight concentration solutions of SELS were added to XG solutions to determine the ability of SELS to reduce the mechanical degradation of XG. It has been noticed by measuring the percentage viscosity reduction (%VR) of the mixture of XG-SELS that the % VR decreases when added this surfactant to XG polymer.

الخلاصة

يحد الانحلال الميكانيكي للسلاسل البوليمرية من الاستخدامات العملية في تطبيقات تقليل الاعاقة في الجريان المضطرب. كما أن الانحلال الميكانيكي يعمل على تقليل الطاقة الموجودة في سلاسل البوليمر الطويلة عن طريق تكسير وتحطيم هذه السلاسل. أن إضافة المواد النشطة سطحيا إلى محاليل البوليمر في وسط مائي يعمل على تكوين جزيئات تسمى التجمعات أو (الاركيت) بحيث أن سلاسل البوليمر تحيط بجزيئات المواد النشطة سطحيا المسماة بالمذيلات في هذه التجمعات أو (الاركيت) وان هذه التجمعات أو (الاركيت) هي التي تعمل على تقليل الاعاقة أو تقليل الانحلال الميكانيكي في الجريان المضطرب. في هذا البحث تم حساب تأثير إضافة المواد النشطة سطحيا المسمى (صوديوم ليورال أيثر سلفيت) على بوليمر (صمغ الزانثان) عن طريق حساب النسبة المئوية لنقصان اللزوجة، حيث تم استخدام تركيزيين من بوليمر (صمغ الزانثان) وهما 0,5 و 1 نسبة وزنيه ومعاملتهما مع تركيزيين آخرين من المواد النشطة سطحيا وهما 0,5 و 1,5 نسبة وزنيه لمعرفة مدى تأثير المواد النشطة سطحيا على تقليل الانحلال الميكانيكي للبوليمر (صمغ الزانثان) ، فقد تم ملاحظة أن إضافة المواد النشطة سطحيا يعمل على تقليل الانحلال الميكانيكي للبوليمر المستخدم.

Keywords: Mechanical degradation, Polymer–surfactant aggregates, Viscosity reduction

INTRAODUCTION

The phenomenon in which drag of a dilute polymer solution is drastically reduced in turbulent flow by minute amounts of suitable additives has been well documented (**C.A. Kim et.al. 2001**). This implies that fluid containing these additives requires a lower pressure drop than pure solvent to maintain the same flow rate in a pipe. Although the mechanism for drag reduction has been the subject of extensive research, a complete and satisfactory explanation has not been reported. Nonetheless, drag reduction applications can be found in various engineering areas including the transportation of crude oil, increasing speed of boats and water supply and irrigation systems (**H.J. Choi et.al. 1999**), (**H. J. Choi et.al 2000**).

Among various additives such as polymers, surfactant solutions, and fiber particles, polymers are considered the most effective drag reducing agent. High-molecular-weight poly (ethylene oxide) (PEO) and polyisobutylene have been widely used as drag reducers. However, the use of these polymers in practical applications has been severely limited due to their poor mechanical stability in turbulent flow. The search for shear-stable drag reducing polymers continues to be a challenging task (**J.I. Sohn et.al. 2001**).

Drag-reducing polymers are found to lose their effectiveness when subjected to an intense turbulence field for sufficient amounts of time. These losses are usually associated with chain scission. However, if aggregation enhances drag reduction, it follows that degradation should also occur because of the breakup of agglomerates. Several studies used intrinsic viscosity measurements to infer that changes in the average molecular weight accompanies changes in the effectiveness of a polymer. However, the use of intrinsic viscosity to measure molecular weight when entanglements or aggregates are present has been questioned (**Matthew W. Liberatore et.al. 2004**).

Origins and mechanisms of degradation discussed in the literature depend on an insight into the nature of polymeric liquids. In modern polymer science, it is widely believed that attractive forces of cohesion between macromolecules in polymeric liquids and possibilities for the occurrence of supermolecular structures owing to these forces may be neglected. When considering concentrated systems, as a rule the attention is focused on the geometrical entanglements of chains. It is assumed that destruction is determined by high stress concentrations and, hence, an increased probability of breaking chemical bonds at sites of the entanglements. For dilute solutions, within the framework of this concept destruction is associated with deformations and stresses in a separate polymer chain. It is assumed that destruction occurs even for an arbitrarily small polymer concentration. Theories of destruction considering a behaviour of single chain in flow were proposed in works. Neglecting the cohesive forces which exist between the molecular chains results in an inadequate description of structure of the polymeric liquids. As a result, inferences which follow from this simplified consideration are in contradiction with experimental data (**V.N. Kalashnikov 2002**).

As has been shown in recent investigations (**V.N. Kalashnikov 2002**), for an understanding of the behaviour of polymeric liquids taking into account the forces of cohesion between the chains and study of self-assembly formations arising due to these forces are essential. It was shown that degradation is directly connected with specific supermolecular structures and does not occur in solutions with discrete macromolecules. As it turned out, even for very small concentrations the polymer solutions may represent two phase fluids. When, at a constant concentration, the molecular weight of the dissolved polymer increases, one of the two phases—namely, the phase rich in polymer—separates out in the form of dispersed globules. It then forms a three-dimensional network whose elements are liquid–crystalline fibrils. Abicontinuous structure is formed in which each phase occupies a connected space. With the appearance of the fibrillar network there arises the possibility for destruction of polymer molecules in response to shear flow, under

ultrasonic action, freezing, molecular fluctuations (**V.N. Kalashnikov 2002**).

The objective of the present work is concerned with the ability of Sodium lauryl ether sulfate (SELS) to reduce the mechanical degradation of high molecular weight Xanthan gum in water turbulent flow using a rotating disk apparatus. Therefore, dilute solutions of Xanthan gum with different concentrations in addition to different concentrations of Sodium lauryl ether sulfate (SELS) were exposed to shear degradation of a mechanical stirrer with blades. Furthermore, the relations between the increasing in percentage viscosity reduction with shearing time in a rotating disk apparatus were also studied.

EXPERIMENTAL WORK

The water soluble Xanthan Gum (technical grade) of molecular weight about $5.0*10^6$ g/mole was supplied from local market in Baghdad and Sodium lauryl ether sulfate (SLES) which were supplied by the general company of vegetable oil industries, Baghdad. SELS of general formula ($CH_3(CH_2)_{10}CH_2(OCH_2CH_2)_3OSO_3^-Na$) is a white gel material with a molecular weight of 372 g/gmol with an active material of 76% . Tap water was used for dissolving of Xanthan gum polymer and Sodium lauryl ether sulfate (SLES) surfactant. The total dissolved salts of tap water was 394 mg/l as tested in laboratory of Environmental ministry, Baghdad. The method of solution preparation adapted here was to make 0.5 %, 1 % and 1.5 % g/ml concentrations in a separate container. Thus 2.5, 5 and 7.5 gram of corresponding polymer or surfactant was placed in a one litter conical flask and mixed with 500 ml of the corresponding solvent (tap water).

The polymeric solutions of different concentrations were exposed to high speed stirred at different time. The viscosity of the solutions was measured as function of time and stirring speed, to evaluate the degree of polymeric degradation. The stirrer used has a sharp edge and rotating speed range 250–5000 rpm. Solutions of concentrations, 0.5 and 1.0 g/ml percent for Xanthan gum and 0.5 and 1.5 g/ml percent for Sodium lauryl ether sulfate were exposed to such shear degradation at 1000 , 2000 and 3000 rpm stirring for different time up to 1h (15, 30, 45 and 60 min).

The apparatus for shear degradation experiments consists of a 1000 ml beaker. The operated procedure was carried out by placing 300 ml of corresponding polymeric-surfactant solution (150 ml polymer + 150 ml surfactant) in the beaker. The stirring device was started at a fixed rotation speed. After each time period, the stirring was stopped, and raise the container from stirring device. Samples were taken to measure the viscosity of the solution. After that, the stirring was continued for further time period at the fixed rotation speed. All experiments were taken place at room temperature, 20–25°c.

The viscosity was measured by using Fungi lab viscometer, which measures fluid viscosity at a given shear rate. The principle of operation of the Fungi lab viscometer is to rotate a spindle, which is immersed in the test fluid until the fluid is at the immersion groove on the spindles shaft through calibrated spring. The viscous drag of fluid against the spindle is measured by the spindle deflection. The viscosity measurements of Fungi lab viscometer is in centipoises or milli Pascal seconds.

The percentage viscosity reduction %RV was calculated using the solution viscosity before and after degradation as in eq. (1):

$$\%RV = \frac{\mu_b - \mu_a}{\mu_b} *100 \quad (1)$$

Where:

μ_b = viscosity of solution before degradation

μ_a = viscosity of solution after degradation

RESULTS AND DISCUSSION

Due to a broad range of applications of surfactants and polymers, enormous amount of work has been done on the characterization and properties of surfactant and polymer solutions. Due to a wide variety of molecular structures, polymer and surfactant when mixed together in aqueous solution display a wide variety and sometimes even very strange pattern of properties (**Ketan Prajapati 2009**).

Xanthan Gum (XG) as a water soluble polysaccharide polymer is considered to be an effective drag–reducer agent in turbulence flow of hydrocarbons and water solvents (**Marwa F. Abdul Jabbar 2008**). Hence, it was worthy to investigate the shear stability of XG toward mechanical forces and its effect on drag reduction performance. Therefore, XG water solutions of 0.5% and 1.0 % concentrations were exposed to shear degradation by mechanical stirring at 1000, 2000 and 3000rpm. The results of time dependence of viscosity changes at different conditions are illustrated in figures 1, 2. Figure 1 shows a gradual decrease of the viscosity with exposure time and stirring speed due to degradation of XG polymers.

While, figure 2 indicates the combined effect of exposure time and stirring rate on percentage lowering of the viscosity. The original viscosity of 1 % solution was 401.3 cp decrease to 385.8, 353.8 and 300.9 cp at shearing with 1000, 2000 and 3000 rpm stirring rate respectively at 1hr exposure time. These are equal around 3.86, 11.91 and 25.0186% decrease respectively. These indicate that the degradation increases as exposure time and stirring speed increases.

A gradual decrease of viscosity was observed at time progress due to the degradation of polymer molecules under turbulent flow (high turbulent flow means high stirring speed). The viscosity behaviour in turbulent flow is appeared to be related to shearing force (stirring speed) in which these cause the breakage of main chain of the polymer by the mechanical energy. Therefore viscosity decrease with time as a consequence of scission of polymeric chain caused by turbulence flow (**Marwa F. Abdul Jabbar 2008**).

The polymeric solutions of different concentrations were exposed to high speed stirred at different time. The viscosity of the solutions was measured as function of time and stirring speed, to evaluate the degree of polymeric degradation. The stirrer used has a sharp edge and rotating speed range 250–5000 rpm. Solutions of concentrations, 0.5 and 1.0 g/ml percent for Xanthan gum and 0.5 and 1.5 g/ml percent for Sodium lauryl ether sulfate were exposed to such shear degradation at 1000 , 2000 and 3000 rpm stirring for different time up to 1h.

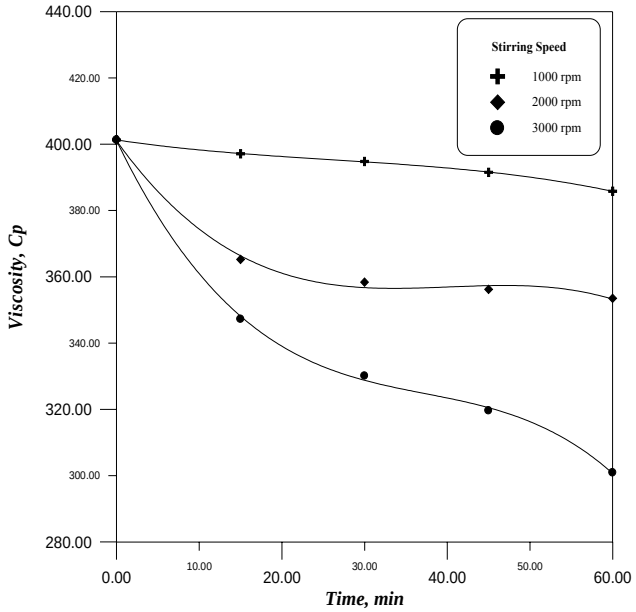

Fig. 1 Effect of exposure time and stirring speed on the viscosity of 1 % XG solution

Figures 3, 4 and 5 show the effect of concentration of SELS surfactant to modify the percentage of degradation (percentage viscosity reduction) for 0.5 % concentration XG polymer for different stirring speed and up to 1h exposure time.

For an absolute quantity of SLES surfactant, it was found that the percentage viscosity reduction of 0.5 % concentration XG polymer was found to be within the range of (0 to 2.7), (0 to 2.89) and (0 to 4.5) for 1000, 2000 and 3000 stirring speed respectively, while the percentage viscosity reduction of 0.5 % concentration of SELS surfactant added to 0.5 % concentration of XG polymer was found to be within the range of (0 to 0.90), (0 to 2.37) and (0 to 4.01) for 1000, 2000 and 3000 stirring speed respectively. It was found that the percentage viscosity reduction for the addition of 0.5 % concentration of SELS surfactant reduced the %RV within the range of (2.7 to 0.91), (2.89 to 2.37) and (4.5 to 4.01) for 1000, 2000 and 3000 stirring speed respectively, and up to 1h exposure time. Therefore, it can be concluded that surfactant additives substantially prevent the degradation of XG polymer, also helped to slow down the degradation effect (**Nam-Jin Kim et.al. 2000**).

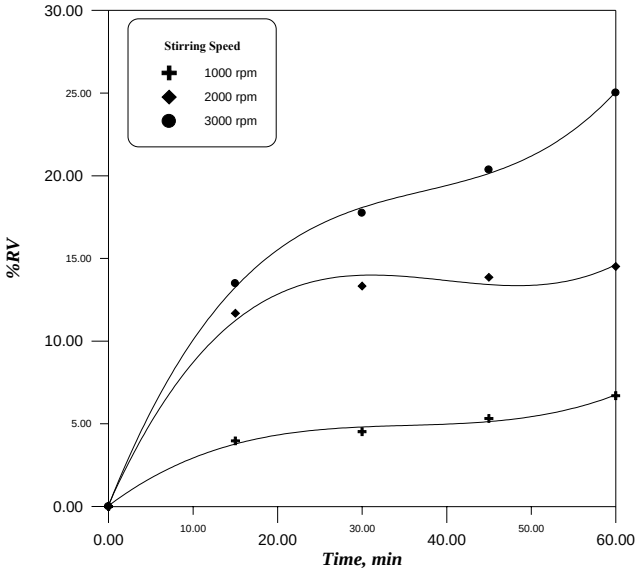

Fig. 2 Effect of exposure time stirring speed on Percentage viscosity reduction for 1 % XG solution

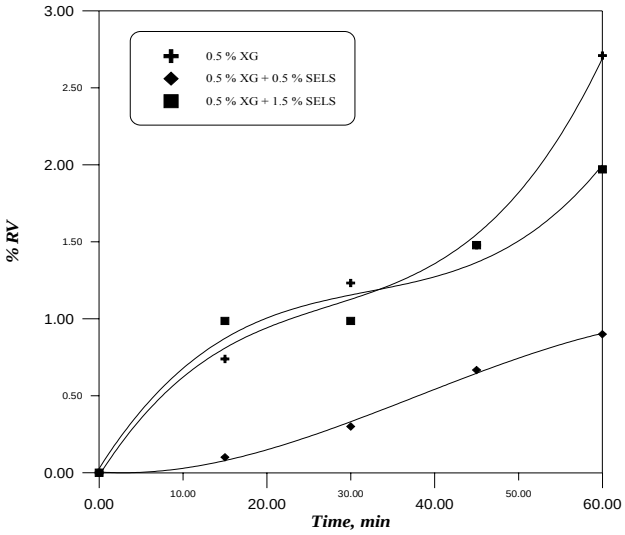

Fig. 3 Percentage viscosity reduction Vs. time for the system of 0.5 % XG solution and SELS for 1000 rpm stirring speed

Also it was found that the percentage viscosity reduction of 1.5 % concentration of SELS surfactant added to 0.5 % concentration of XG polymer to be within the range of (0 to 1.97), (0 to 2.75) and (0 to 4.617) for (1000, 2000 and 3000) rpm stirring speed respectively. Therefore, the addition of 1.5 % concentration of SELS surfactant decrease the %RV within the range of (2.7 to 1.97), (2.89 to 2.75) and (4.5 to 4.317) for (1000, 2000 and 3000) rpm stirring speed respectively, and up to 1h exposure time.

Also when the concentration of SELS added to 0.5 % concentration XG polymer increase from 0.5 to 1.5 the percentage viscosity reduction increase from (0.90 to 1.97), (2.37 to 2.75) and (4.01 to 4.317) for (1000, 2000 and 3000) rpm respectively, stirring speed and up to 1h exposure time.

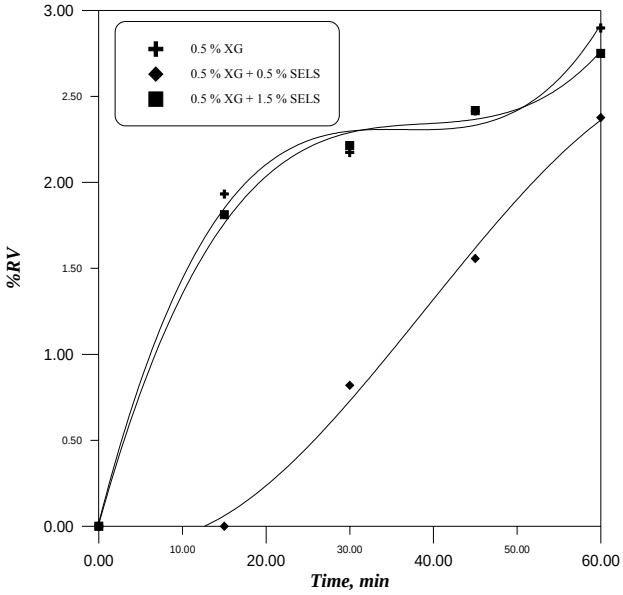

Fig. 4 Percentage viscosity reduction Vs. time for the system of 0.5 % XG solution and SELS for 2000 rpm stirring speed

It is generally concluded from figures (3, 4 and 5) and the data included in these figures, that the addition of 1.5 % concentration of SELS surfactant to 0.5 % concentration of XG polymer for different stirring speed, approximately don't effect of the rate of degradation of XG polymer or reduce the rate of degradation with small amount.

This because the amount of surfactant in the solution higher than the amount of polymer, this large amount of SELS compare with the amount of XG mean that the amount of micelles in the solution is higher than the amount of chains of the polymer (the amount of free micelles is high) . In other words, after the solution of polymer – surfactant formed aggregation structure the free micelles come from the excess concentration of surfactant that not formed aggregation form making the degradation more rapid. Because this free micelles broke down the advantage of aggregation form (increase the degradation) by broken its.

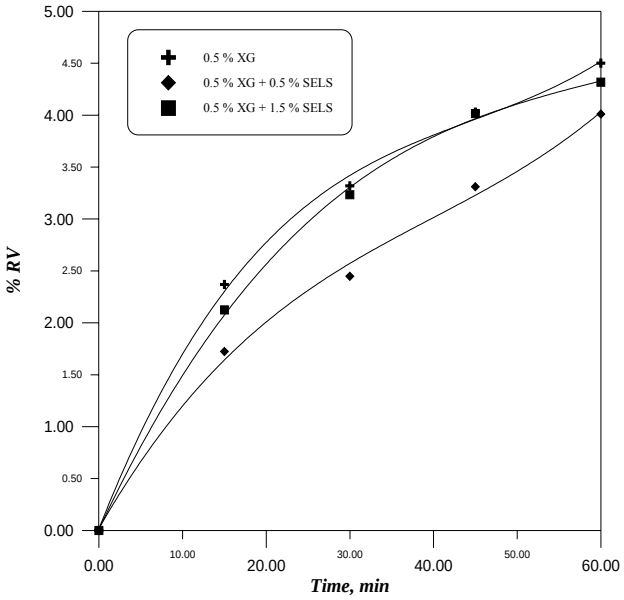

Fig. 5 Percentage viscosity reduction Vs. time for the system of 0.5 % XG solution and SELS for 3000 rpm stirring speed

Also, It is generally concluded from figures (3, 4 and 5) and the data included in these figures, that the addition of 0.5 % concentration of SELS surfactant to 0.5 % concentration of XG polymer for different stirring speed, decrease the rate of degradation of the polymer, but this degradation decrease with increase the stirring speed (shearing rate), as shown in figures 4 and 5 for 2000 and 3000 stirring speed. Therefore, the percentage viscosity reduction for an absolute amount of SELS is 0.91 for 0.5 % XG at 1000 rpm stirring speed and up to 1 hr exposure time, reduce to 0.91 when added 0.5 % SELS, while the percentage viscosity reduction decrease within the range (2.89 to 2.37) and (4.5 to 4.01) for 2000 and 3000 stirring speed respectively, for the same concentration of SELS added and exposure time.

Figures 6, 7 and 8 show the effect of concentration of SELS surfactant to modify the percentage of degradation (percentage viscosity reduction) for 1 % concentration XG polymer for different stirring speed and up to 1h exposure time.

For an absolute quantity of SLES surfactant, it was found that the percentage viscosity reduction of 1 % concentration XG polymer was found to be within the range of (0 to 6.69), (0 to 14.5102) and (0 to 25.0186) for 1000, 2000 and 3000 stirring speed respectively, while the percentage viscosity reduction of 0.5 % concentration of SELS surfactant added to 1 % concentration of XG polymer was found to be within the range of (0 to 2.83), (0 to 4.24) and (0 to 3.84) for 1000, 2000 and 3000 stirring speed respectively. It was found that the percentage viscosity reduction for the addition of 0.5 % concentration of SELS surfactant reduced the %RV within the range of (6.69 to 2.83), (14.5102 to 4.24) and (25.01 to 3.84) for 1000, 2000 and 3000 stirring speed respectively, and up to 1h exposure time. Therefore, it can be concluded that the addition of 0.5 % concentration SELS to 1 % concentration polymer reduce the rate of degradation higher than that the reduction of degradation come from the addition of 0.5 % concentration SELS to 0.5 % concentration polymer for different speed and exposure time.

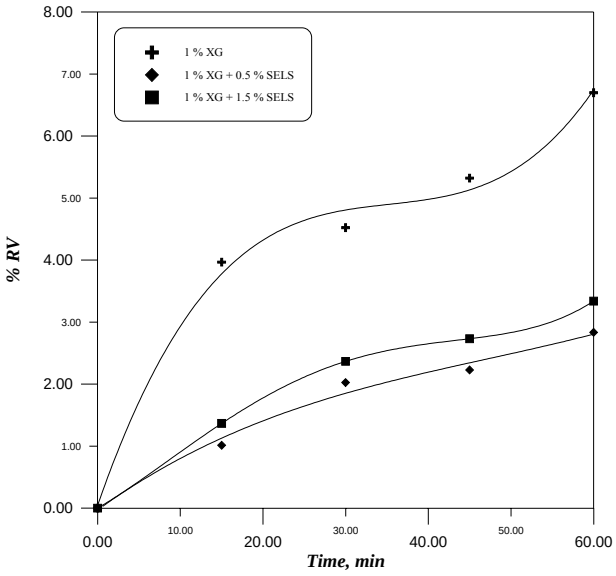

Fig. 6 Percentage viscosity reduction Vs. time for the system of 1 % XG solution and SELS for 1000 rpm stirring speed

Also it was found that the percentage viscosity reduction of 1.5 % concentration of SELS surfactant added to 1 % concentration of XG polymer was found to be within the range of (0 to 3.33), (0 to 11.342) and (0 to 5.55) for (1000, 2000 and 3000) rpm stirring speed respectively. Therefore, the addition of 1.5 % concentration of SELS surfactant decrease the %RV within the range of (6.69 to 3.33), (14.51 to 11.34) and (25.0186 to 5.55) for (1000, 2000 and 3000) rpm stirring speed respectively, and up to 1h exposure time. Also when the concentration of SELS added to 0.5 % concentration XG polymer increase from

0.5 to 1.5 the percentage viscosity reduction increase from (2.834 to 3.33), (4.241 to 11.342) and (3.846 to 5.55) for (1000, 2000 and 3000) rpm respectively, stirring speed and up to 1h exposure time.

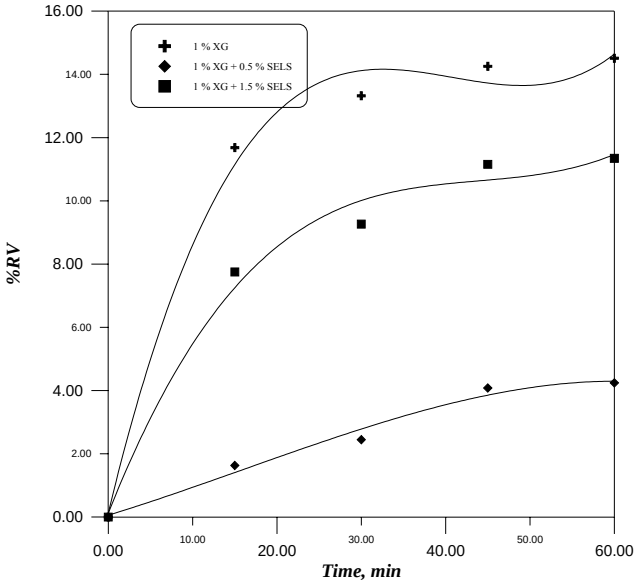

Fig. 7 Percentage viscosity reduction Vs. time for the system of 1 % XG solution and SELS for 2000 rpm stirring speed

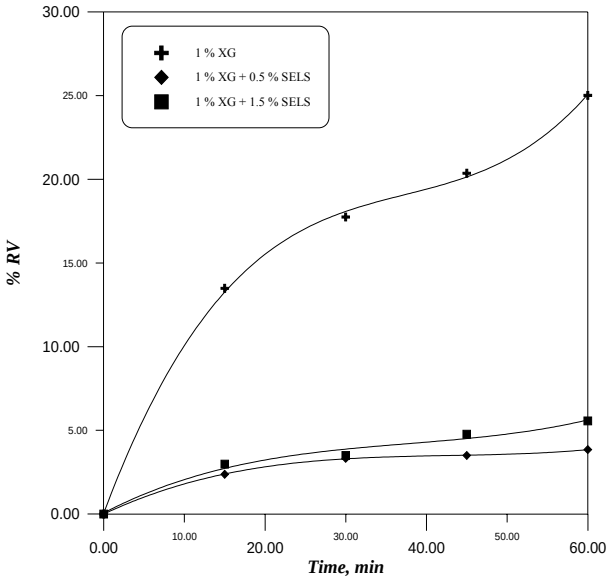

Fig. 8 Percentage viscosity reduction Vs. time for the system of 1 % XG solution and SELS for 3000 rpm stirring speed

It is generally concluded from figures (6, 7 and 8) and the data included in these figures, that the addition of 0.5 % or 1.5 % concentration of SELS surfactant to 1 % concentration of XG polymer for different stirring speed and exposure time, reduce the rate of degradation more than the addition of 0.5 % or 1.5 % concentration of SELS to 0.5 % concentration of polymer and this return to the effect of the amount of aggregation form in each case. In other words, the equilibrium amount between the micelles of surfactant and the chains (coiled or straight) of the polymer that's has the ability to form aggregation structure.

Figures 9 and 10 show the effect of stirring speed on the rate of degradation (percentage viscosity reduction) for different concentration of polymer and surfactant and up to 1 hr exposure time. It was shown that the mechanical degradation increased with increase the stirring speed. Therefore, Form figure 10 and at 1000 rpm, the percentage viscosity reduction for pure XG, 0.5 % SLES and 1.5 % SELS are (2.7, 0.9 and 1.97) while the percentage viscosity reduction at 3000 rpm become (4.5, 4.01 and 4.31). Therefore, increase the stirring speed mean that the rate of shear force increase and the polymer or surfactant is degraded more rapid than low stirring speed.

Also, from figure 9 and at 1000 rpm, the percentage viscosity reduction for pure XG, 0.5 % SLES and 1.5 % SELS were (6.69, 2.83 and 3.33) while the percentage viscosity reduction at 3000 rpm become (25.01, 3.846 and 5.55).

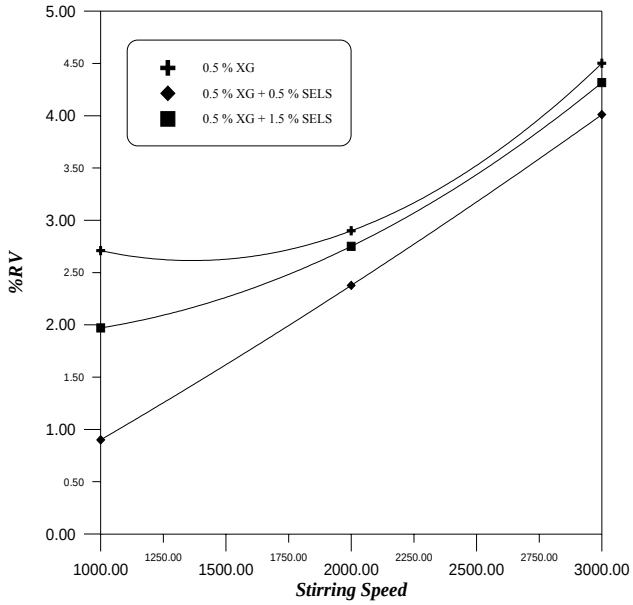

Fig. 9 Effect of stirring speed on Percentage viscosity reduction of 0.5 % XG solution and SELS for 1 hr exposure time

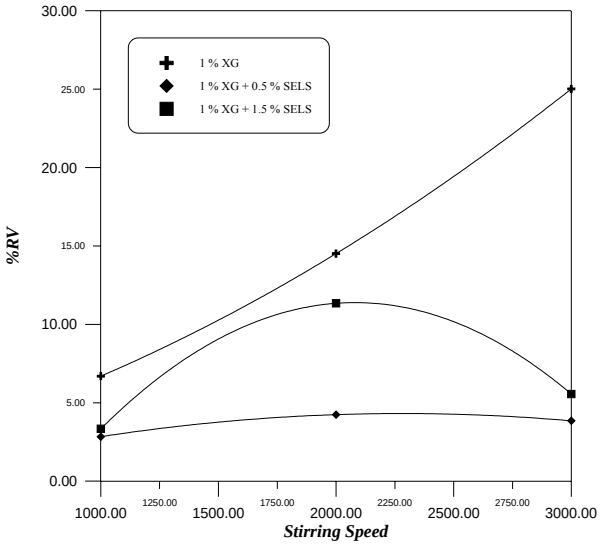

Fig. 10 Effect of stirring speed on Percentage viscosity reduction of 1 % XG solution and SELS for 1 hr exposure time

But also from figure 10 it was found that the rate of degradation (percentage viscosity reduction) for 3000 rpm is smaller than that for 2000 rpm for both (0.5 % and 1.5 %) concentration of SELS added to XG. This may be explained by the fact that the formation of aggregation (polymer + surfactant) is become better at high Reynolds number (high rate of stirring speed).

CONCLUSIONS

The results of the present investigation on the mechanical degradation effect in a synthetic polymer solution with surfactant additives can be summarized as follows;

1- When SELS is added to a XG, the mixture would appear to be more effective in the preventing the effect of mechanical degradation.
2- The addition of 0.5 % concentration of SELS surfactant to both (0.5 % and 1 %) concentration of polymer is considered the best concentration of surfactant that added to polymer at different stirring speed and exposure time.
3- Degradation at high stirring speed occurs more rapidly than that at low stirring speed, thereby indicating that when the stirring speed increases, mechanical degradation plays an important role.

References

1- C.A. Kim, D.S. Jo, H.J. Choi, C.B. Kim and M.S. Jhon, " A high-precision rotating disk apparatus for drag reduction characterization", Polymer Testing 20 (2001) 43–48.

2- J.-I. Sohn, C.A. Kim, H.J. Choi and M.S. Jhon, " Drag-reduction effectiveness of Xanthan Gum in a rotating disk apparatus", Carbohydrate Polymers 45 (2001) 61-68.

3- H.J. Choi, C.A. Kim and M.S. Jhon, " Universal drag reduction characteristics of polyisobutylene in a rotating disk apparatus", Polymer 40 (1999) 4527–4530.

4- H. J. Choi, C. A. Kim, J. H. Sung, C. B. Kim, W. Chun and M. S. Jhon, " Universal drag reduction characteristics of saline water-soluble poly(ethylene oxide) in a rotating disk apparatus ", Colloid Polym Sci 278 (2000).

5- Ketan Prajapati, “Interactions between drag reducing polymers and surfactants”, M.Sc thesis, Waterloo, Ontario, Canada, 2009.

6- Marwa F. Abdul Jabbar, “The Influence of Mechanical Effects on Degradation of Drag Reducing Agents”, M.Sc thesis, Nahrain University, Baghdad, Iraq, 2008.

7- Matthew W. Liberatore, Seunghyun Baik, Anthony J. McHugh and Thomas J. Hanratty, " Turbulent drag reduction of polyacrylamide solutions: effect of degradation on molecular weight distribution", J. Non-Newtonian Fluid Mech. 123 (2004) 175–183.

8- Nam-Jin Kim, Jae-Yong Lee, Seok-Mann Yoon, Chong-Bo Kim and Byung-Ki Hur,

"Drag Reduction Rates and Degradation Effects in Synthetic Polymer Solution with Surfactant Additives", Journal of industrial and engineering chemistry Vol. 6, No. 6, November 2000, 412-418.

9- V.N. Kalashnikov, "Degradation accompanying turbulent drag reduction by polymer additives", J. Non-Newtonian Fluid Mech. 103 (2002) 105–121.

NOMENCLATURE

cac: critical aggregation concentration

SDS : sodium dodecyl sulfate

SELS : Sodium lauryl ether sulfate

PEO : poly ethylene oxide

psp : polymer saturation point

XG : Xanthan gum

% VR : Percentage viscosity reduction

IMPROVED IMAGE COMPRESSION BASED WAVELET TRANSFORM AND THRESHOLD ENTROPY

*** Akeel abdual aziz mohammed**
***Assistant Lecturer \ Baghdad University\ College of Engineering\ Electronic and communication**

ABSTRACT

In this paper, a method is proposed to increase the compression ratio for the color images by dividing the image into non-overlapping blocks and applying different compression ratio for these blocks depending on the importance information of the block. In the region that contain important information the compression ratio is reduced to prevent loss of the information, while in the smoothness region which has not important information, high compression ratio is used .The proposed method shows better results when compared with classical methods(wavelet and DCT).

تحسين ضغط الصور بالاعتماد على محول المويجة وعتبة الانتروبي

***عقيل عبد العزيز محمد**
***مدرس مساعد\جامعة بغداد\كليه الهندسة\قسم الهندسة الالكترونية والاتصالات**

الخلاصة

في هذا البحث، تم أقتراح طريقة لزيادة نسبة الضغط للصور الملونة عن طريق تقسيم الصورة الى كتل غير متداخلة وتطبيق نسب ضغط مختلفة إلى هذه الكتل بالاعتماد على المعلومات المهمة في هذه الكتل. في المنطقة التي تحتوي على معلومات هامة يتم تخفيض نسبة الضغط لمنع فقدان المعلومات، بينما في المنطقة الناعمة(خالية من الترددات العالية) التي لم يتم استخدام معلومات هامة نسبة الضغط عالية. الطريقة المقترحة تظهر نتائج أفضل بالمقارنة مع الطريقة الكلاسيكية (wavelet and DCT).

INTRODUCTION

Image compression is the process of encoding information using fewer bits (or other information-bearing units) than an un-encoded representation would use through use of specific encoding schemes. Compression is useful because it helps to reduce the consumption of expensive resources, such as hard disk space or transmission bandwidth (computing) [Baluram, MHD.Farukh,and Pradeep Dhakad 2011]. These methods reduce the space necessary to store or transmit the image data by changing the way these images are represented. There are numerous methods for compressing digital image data and each has its own advantages and disadvantages [K.Somasundaram and I.K. Raj 2006].

One of the most commonly used lossy compression methods is that of transform coding using one of the many image transforms available [Panagiotacopulos,K. Friesen and S. Lertsuntivit 2000]. Recent years, many studies have been made on wavelets. An excellent overview of what wavelets have brought to the fields as diverse as biomedical applications, wireless communications, computer graphics or turbulence, is given in Image compression is one of the most visible applications of wavelets. A typical still image contains a large amount of spatial redundancy in plain areas where adjacent picture elements (pixels) have almost the same values. It means that the pixel values are highly correlated[S.Grgic, M.Grgic., and B. Zovko-Cihlar 2001].

During the past few decades , several kinds of transforms have successively been developed for image compression, such as the Karhunen–Loève transform(KLT) , discrete cosine transform (DCT) , and discrete wavelet transform(DWT)[Bo Li, Rui Yang, and Hongxu Jiang 2011] . The blocking artifacts and mosquito noise are absent in a wavelet-based coder due to the overlapping basis functions[Mandal, S. Panchanathan and T. Aboulnasr 1995].The redundancy (both statistical and subjective) can be removed to achieve compression of the image data. The basic measure for the performance of a compression algorithm is compression ratio (CR), defined as a ratio between original data size and compressed data size. In a lossy compression scheme, the image compression algorithm should achieve a tradeoff between compression ratio and image quality. Higher compression ratios will produce lower image quality and vice versa. Quality and compression can also vary according to input image characteristics and contents. Transform coding is a widely used method of compressing image information. In a transform-based compression system two-dimensional (2-D) images are transformed from the spatial domain to the frequency domain. An effective transform will concentrate useful information into a few of the low-frequency transform coefficients [S.Grgic, M.Grgic., and B. Zovko-Cihlar 2001].

PREPROCESS

The main purpose of the apply preprocess is to generate the wavelet transform blocks from the raw image data. One possible optimization, in order to achieve better compression ratio, is to apply color spaces transform. The proposed method takes advantage of the fact that small color changes are perceived less accurately than small changes in brightness. The human eyes are much more sensitive to brightness variations than to hue variations [H.Gu, D. Hong, and M. Barrett 2003].

Therefore, the hue data can be compressed more heavily than the brightness data[K. R. Castleman 1996]. RGB is a way that a computer defines a color in terms of the extensions of red, green, and blue components on CRT. YCbCr color space [R.Steinmetz and K. Nahrstedt 1997] was used internally in the MinImage. The following are the RGB to YCbCr and YCbCr to RGB conversion equations[R.Steinmetz and K. Nahrstedt 1997].

$$
\begin{aligned}
Y &= 0.2989R + 0.5866G + 0.1145B \\
Cb &= -0.1688R - 0.3312G + 0.5B \\
Cr &= 0.5R - 0.4184G - 0.0816B \qquad (1) \\
R &= Y + 1.4022Cr \\
G &= Y - 0.3456Cb _ 0{:}7145Cr
\end{aligned}
$$

$$B = Y + 1.7710Cb \quad (2)$$

The color space transform is necessary for compressing the true color images since the Y space contains more information than the Cb and the Cr spaces. Thus, the compressor can treat these color spaces differently in order to get greater compression ratio. By comparing the three color spaces, the Cb and Cr color spaces are easier to be compressed than the Y color space. The Cb and Cr color spaces contain less important information [H.Gu, D. Hong, and M. Barrett 2003].

PROPOSED METHOD

In the proposed method, the input image is transformed and then truncated according to a given threshold. The basic steps for implementing this procedure are outlined in the following steps:

Step 1: Load the image

Step 2: Applying color transformation, by converting the image from RGB into y CbCr.

Step 3: Each component in the image(y ,Cb ,and Cr) is subdivided into non-overlapping Mx M blocks.

Step 4: The 2D wavelet transform is applied to each block of the image.

Step 5: Compute the combination entropy (**CE**) of the current block according to the following equation [A. Tinku,., and K.Ajoy 2005]:

$$C.E = -\sum_n P_n \log_2(P_n), \text{bit/block} \quad (3)$$

Where, p_n is the combination probability of the nth pixel in i^{th} block. The larger combination entropy of an image mean richer information and low redundancy in the current block .The value of threshold is small to keep this important information .A lower combination entropy means fewer information and high redundancy in the current block .Therefore the value of a threshold is big because the information of this block has few coefficient. The wavelet transformation coefficients are truncated such that all the coefficients whose values are less than a given threshold (**TH**) are set to zero. The threshold takes percentage of the minimum and maximum coefficient values throughout the whole block coefficients. Threshold of current block is based on its entropy. There are two types of threshold operator called threshold transform, $T(.,\lambda)$ associated with the threshold λ, the hard threshold operator $T_h(.,\lambda)$ and the soft threshold operator $T_s(.,\lambda)$.

The hard threshold operator is defined as[C. Perrin, B. Walczak, and D. s. Massart 2001]:

$$S = T_h(Y_W,\lambda) = \begin{cases} Y_W & \text{if } |Y_W| \geq \lambda \\ 0 & \text{otherwise} \end{cases} \quad (4)$$

The soft threshold operator is defined as [A. Tinku,., and K.Ajoy 2005]:

$$S = T_s(Y_W,\lambda) = \begin{cases} \text{sign}(Y_W)(|Y_W| - \lambda) & \text{if } |Y_W| > \lambda \\ 0 & \text{otherwise} \end{cases} \quad (5)$$

Where, Y_W is the transform coefficient, and S are the threshold coefficients obtained after applying the threshold operator $T(.,\lambda)$. The transfer functions of the hard and soft threshold schemes are shown in Fig .1. Note that, hard threshold is a "keep or set to zero" procedure and is more intuitively appealing. On the other hand, soft threshold shrinks coefficients above the threshold in absolute value. While at first sight hard threshold may seem to be natural, the continuity of soft threshold has some advantages. In this paper the hard threshold is used and the type of threshold is quintile. In this method a percentage ratio of entries to be eliminated are selected. The smallest (in absolute value) ratio percent of entries are set to zero.

Step 6: Finally, quantization of each blocks in the image.

By applying a 2D inverse wavelet transform on compressed image, the decompressed image (reconstructed) will be obtained. The additive white Gaussian noise is added to image. Fig. 2 shows the proposed method flowcharts.

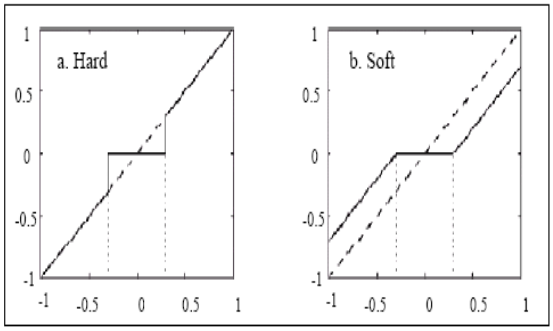

Figure1 Threshold (Shrinkage) functions

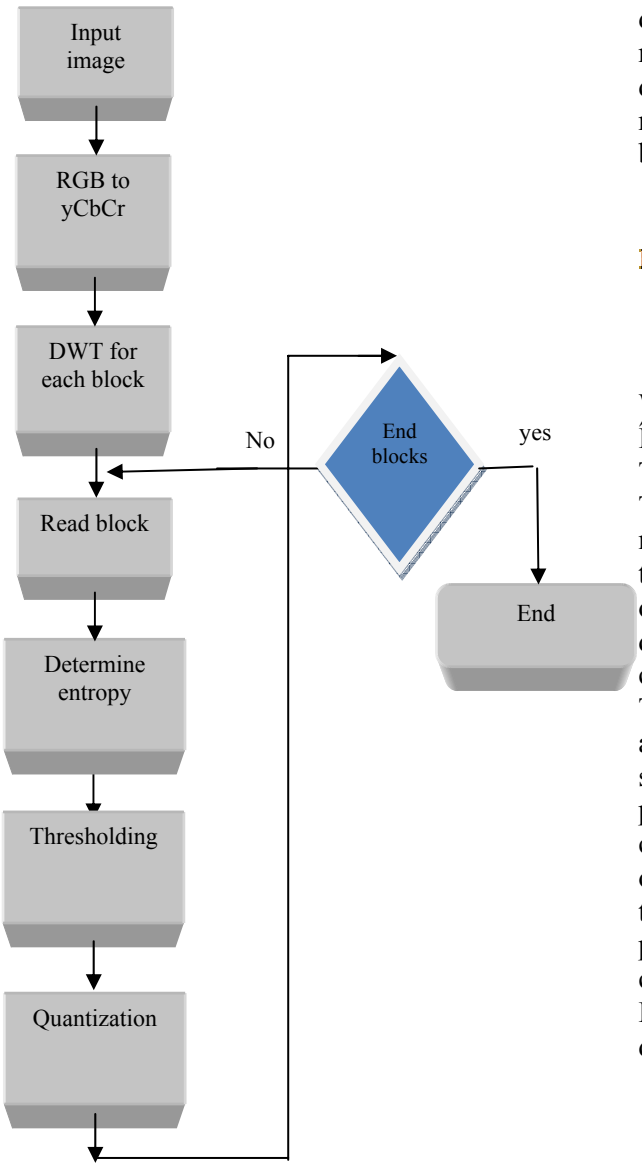

Figure 2 Proposed algorithm flowcharts

SIMULATION RESULTS

The proposed model is tested for compressing some images. The proposed method is realized using Matlab 7 R2010a package, with different test images of size 256*256 pixels as shown in the Fig.3. The proposed method was compared with standard DCT and wavelet methods.

Table 1 shows different compression ratio (92%,95%,97%)and the PSNR in dB obtained using the proposed method and wavelet and DCT based compression for different color images. Fig. 4 shows the reconstructed (decompressed) images based different methods. The peak signal to noise ratio, is defined as[K. S. Thyagarajan 2006] below:

$$PSNR=10\log\left\{\frac{(255)^2}{\frac{1}{N}\sum_{r=0}^{N-1}\sum_{c=0}^{N-1}[\hat{I}(r,c)-I(r,c)]^2}\right\} \quad (6)$$

Where I(r,c) represents original image and Î(r,c) represents decompressed image[K. S. Thyagarajan 2006].

The most popular metric of performance measure of a data compression algorithm is the compression ratio. It is defined as the ratio of the number of bits to represent the original data to the number of bits to represent the compressed data.

The compression performance of the new approach is assessed through computer simulation. Considering various compression parameters such as the percentage of compression ratio and the PSNR in decibels of different images, it is, in general, observed that the accuracy of the reconstruction of the proposed method gives good results as compared with the other methods. Exhaustive computer simulation results on different images indicate this trend.

Table 1:PSNR in dB obtained using different compression ratios for different images.

Image	Method	compression 92%	compression 95%	compression 97%
1	Proposed Method	25.8 dB	24.90 dB	23.12 dB
	Classical Method (Wavelet)	23.8 dB	22 dB	20.4dB
	Classical Method (DCT)	23.2db	21.4 dB	18.3 dB
2	Proposed Method	31.3 dB	29.4 dB	27.6 dB
	Classical Method (Wavelet)	28.2 dB	26.4 dB	23 dB
	Classical Method (DCT)	25.2 dB	24.1d B	20 d B

CONCLUSION:

This paper presents image compression technique. Instead of compressing all image with one compression ratio by selecting one threshold value for all pixels of the image, A threshold value is determined for each block in the image after dividing the image into M*M blocks .therefore getting different threshold values.

Based on the simulation results obtained in this study, the proposed approach can achieve high-compression ratio with high SNR. According to the results in **Table 1**, the obtained subjective tests show the superiority of the proposed algorithm when compared to the classical approaches. An important advantage of this method appears at edge region, because the proposed method keep the information at these region by reducing the compression ratio by selecting low threshold value.

RFERENCES

Baluram Nagaria, MHD.Farukh Hashmi ,and Pradeep Dhakad, " Comparative Analysis of Fast Wavelet Transform for Image Compression for optimal Image Quality and Higher Compression Ratio", International Journal of Engineering Science and Technology (IJEST),Vol. 3 No. 5 May 2011 ,ISSN : 0975-5462.

K.Somasundaram and I.K. Raj,"Low Computational Image Compression Scheme based on Absolute Moment Block Truncation Coding " Transactions On Engineering, Computing And Technology VO.13 MAY 2006 ISSN 1305-5313

N. D. Panagiotacopulos,K. Friesen and S. Lertsuntivit," Lossy Image Compression Using Wavelets", Journal of Intelligent and Robotic Systems 28: 39–59, 2000. © 2000 Kluwer Academic Publishers. Printed in the Netherlands

.

S.Grgic, M.Grgic., and B. Zovko-Cihlar," Performance Analysis of Image Compression Using Wavelets" *IEEE* Transactions On Industrial Electronics, Vol. 48, NO. 3, JUNE 2001 pp(682-695)

Bo Li, Rui Yang, and Hongxu Jiang," Remote-Sensing Image Compression Using Two – Dimensional Oriented Wavelet Transform" , IEEE Transaction on Geoscience and Remote Sensing, Vol.49, NO.1, JANUARY 2011

M. K. Mandal, S. Panchanathan and T. Aboulnasr . "Choice of Wavelets for Image Compression " , Lecture Notes in Computer Science Vol. 1133, pp. 239-249,1995

H.Gu, D. Hong, and M. Barrett ," Wavelet Image Compressor—MinImage ",Journal of Computational Analysis and Applications, Vol. 5, No. 1, January 2003 (# 2003)

K. R. Castleman, "Digital Image Processing". Prentice Hall, New Jersey, 1996.

R.Steinmetz and K. Nahrstedt, "Multimedia Computing, Communications and Applications", Prentice Hall, New Jersey, 1997.

A. Tinku,., and K.Ajoy, " Image Processing Principles and Applications " A John Wiley & Sons, Inc. ,Publication 2005.

C. Perrin, B. Walczak, and D. s. Massart, "The Use of Wavelets for Signal Denoising in Capillary Electrophoresis", Analytical Chemistry, Vol. 73, No. 20, pp.4903-4917 , October 15, 2001.

K. S. Thyagarajan," Digital Image Processing with Application to Digital Cinema", Focal Press 2006.

Figure 3 Testing images

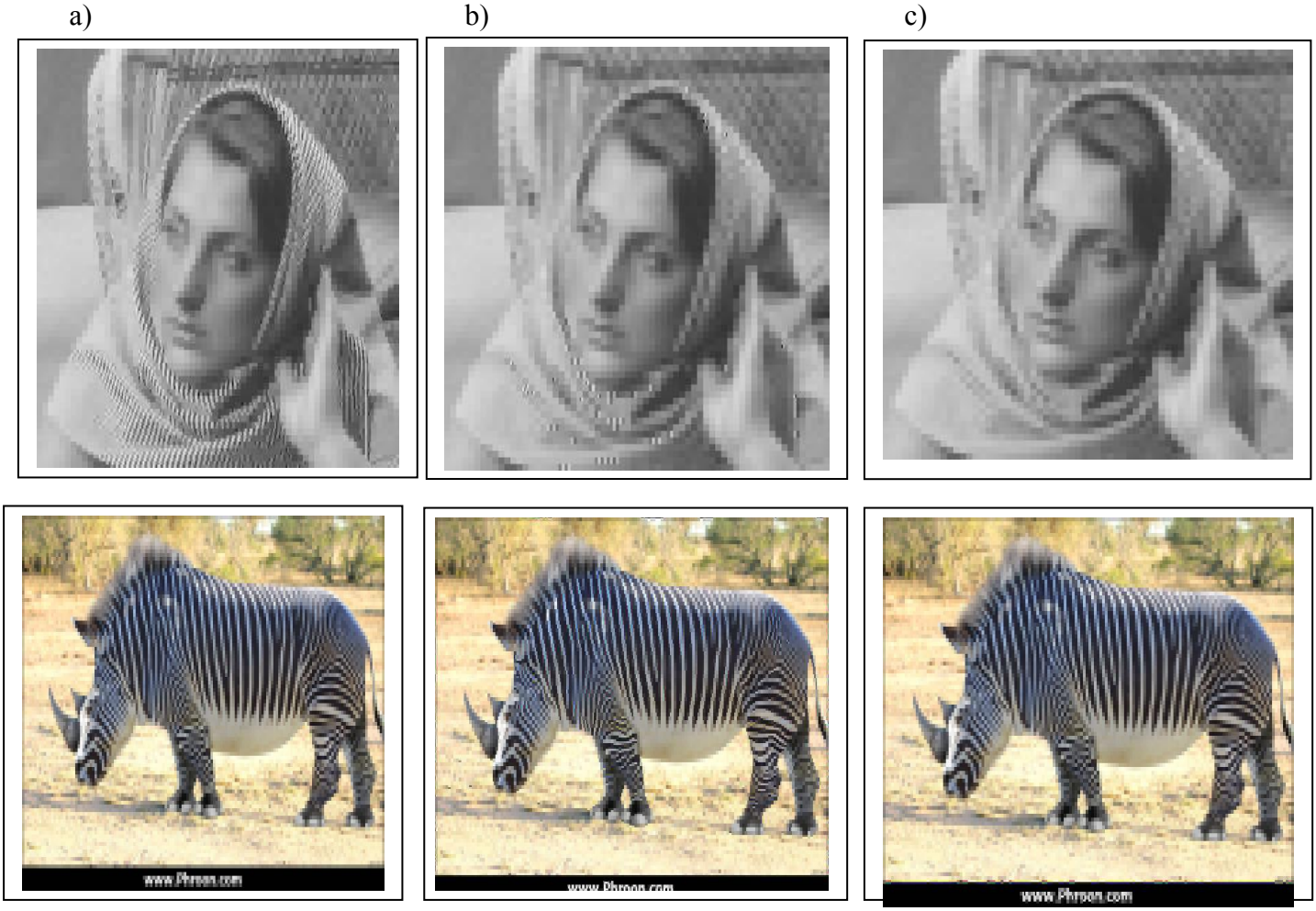

Figure 4 Reconstructed Images. a) Proposed method. B) Wavelet. C) DCT Method.

POLLUTION OF MINING INDUSTRY SULFUR PURIFICATION PLANT AT AL MISHRAQ

Dr. Jathwa A. Ibrahim

ABSTRACT

The Al Mishraq site has been the subject of many scientific studies for the period before and after the fire in 2003. Five visits to the site were conducted twice in 2003 for general fact-finding, twice in 2004, and once in 2005 for detailed sampling and monitoring.

Desk-based research and laboratory analysis of soil and water samples results indicate that surface water and groundwater pollution from Al Mishraq site was significant at the time of its operation. The primary pollution source was the superheated water injection process, while the principal receptor is the River Tigris. Now that the plant is idle, this source is absent.

Following the June 2003 sulphur fire, initial investigations indicate that short damage to vegetation was severe close to the plant but there is no evidence of widespread or significant long-term damage. Rainwater and drainage ponds and gullies close to the sulphur processing and acid contain hazardous levels of acid. Runoff from these areas may be affecting local water quality. There is regional moderate groundwater contamination by sulphate and hydrogen sulphide, but much of this may be naturally sourced.

The site in its current state represents a low risk to human health and the environment principally due to the acidic surface water ponds, but in the absence of corrective action, the hazard levels may be elevated after some decades.

الخلاصة:

كان موقع المشراق عنوانا لكثير من البحوث العلمية التي اجريت للفترة قبل وبعد حرب العراق في 2003. فقد تم اجراء خمسة زيارات الى موقع كبريت المشراق اثنتان في 2003، كزيارة استطلاعية واثنتان في 2004، وواحدة في 2005 لسحب عينات الفحص والتحري الدقيق.

بينت الدراسة المكتبية ونتائج التحاليل المختبرية على نماذج التربة والمياه السطحية والجوفية في الموقع ان التلوث ملحوض في المنطقة اثناء اشتغال المعمل وان المصدر الاساس للتلوث كان من حقن المياه الساخنة في باطن الارض وان المستلم الاساسي (principal receptor) هو نهر دجلة، وبتوقف المعمل يغيب مصدر التلوث.

بينت التحريات الابتدائية التي اعقبت الحريق الهائل الذي شب في الموقع في حزيران 2003 حدوث تدهور للغطاء النباتي لمنطقة محدودة محيطة بالمعمل ولايوجد اثر لانتشار التدهور للغطاء النباتي على مساحات ابعد او تدهور مستمر (long-term damage). ان انسياب وجريان مياه الامطار والمياه المتجمعة في الاحواض وقنوات المياه القريبة من مناطق تكدس الكبريت وانتاج الحامض وما تحتويه من نسب عالية وخطرة من مستوى الحامضية تكون ذات تاثير على نوعية المياه المحلية . وكما تبين الدراسة هناك تلوث في المياه الجوفية بالكبريتات وكبريتيد الهيدروجين ، ولكن معظم هذا التلوث يعزى الى مصادر طبيعية لها علاقة بطبيعة المنطقة. واخير ان كان لابد من الحكم على الموقع فان الموقع يمثل مستوى واطئ من الخطورة حاليا بسبب تواجد المياه الحامضية في البرك والاحواض ولكن بغياب الاجراءات التصحيحية قد يتفاقم الخطر الى مستويات عالية بعد بضعة عقود

Keywords: Sulphur, Sulphate, Al Mishraq site, Sulphur fire, Hydrogen sulphide, **AL-control Geochem. Laboratories**

INTRODUCTION

Broader industrial development began in the 1970s when the Iraqi government started a development programme largely funded from oil export revenues; the focus was on medium technology industries such as textiles, food production, construction materials and heavy industry including iron, steel and basic petrochemicals(Iraq Country Analysis, 2005). Higher technology goods were, and still are, largely imported.

The minerals industry grew gradually with a focus on sulphur, phosphate and potash, including post-processing of ores to produce sulphuric acid, alum and fertilizers. At its peak in the 1980s, Iraq was one of the world's largest producers of fertilizer (Mobbs, 2000).

Yet the UN sanctions, which were in place from 1990 to 2003, the 1991 conflict and other problems either curtailed or prevented the export of minerals and finished materials. As a result, large stockpiles of unsold material built up at some mining and mineral processing sites. As an example, up to 500,000 tonnes of sulphur were stockpiled at the Al Mishraq mining complex pending export (Marr, 2004)

The mining sector in Iraq was completely state owned and is dominated by two large complexes; Akashat/Al Qaim and Al Mishraq (UNEP, 2005), both of which are currently shut down due to looting, lack of spare parts, power, security and other problems.

The Al Mishraq sulphur mine and associated chemical works supplied raw sulphur, sulphuric acid, and alum (aluminum sulphate). The mining operations commenced in the 1970s and by 1983 had reportedly resulted in pollution of the Tigris River. An incident at the site (looting or sabotage) in June 2003 caused a catastrophic sulphur fire.

The present work focused on the area of the 2003 fire, sulphur storage, waste areas, and groundwater wells outside the site.

In 2004, the alum plant operated intermittently using up existing stocks of raw materials before closing down. In July 2005, the entire site was shut down and secured. As a result of the looting and under-investment, the facility is semi-derelict

SITE DISCRIPTION

The Al Mishraq sulphur mining and processing complex is located 50 km south of Mosul, in northern Iraq close to the west bank of the River Tigris, and 1.5 km west of village of Al-Safinah . Figure 1 shows the site location and surrounding land uses. The complex is spread over a 17-km^2 area and consists of a sulphur mine, a sulphuric acid plant, an alum (aluminum sulphate) plant, and associated facilities for power generation, water treatment, injection, administration and engineering. The plant operated from 1972 to April 2003 and is currently idle and partly derelict (Center of Environmental Surveys and Pollution Control, 1998).

The complex is located in an undeveloped sparsely vegetated hilly area. The open sulphur storage and waste storage areas are located in the southern compound area and is surrounded on all sides by undeveloped land. The western outskirts of the small village of Al-Safinah is approximately 1,100m east of the waste piles (Mahmood and others, 2005).

Figure 1: Al-Mishraq site location and surrounding lands

The site appears to be as an area of undulating hills and shallowly incised valleys with moderate gradients on the western half of the complex area and flat gently falling plains on the eastern half. The general topography falls from 250m above sea level to the west of the complex area down to 200m on the banks of the Tigris to the east (Carn & Krueger, 2004).

GEOLOGY AND HYDROLOGY

The ore body (the area of commercial mineralization) is over 10 km^2 in area and located at a depth of 50 - 300m. It is composed of a mixture of sulphur, gypsum and bitumen contained within limestone bedrock and is below the groundwater table (Mobbs, 2000). Groundwater flows through the ore body from the hills to the north-west into the River Tigris. Natural hydrogen sulphide springs were observed in the river prior to the start of mining (Al-Bassam, , 1984).

Rainfall generally infiltrates into the unpaved soil, stockpiles, and waste piles, recharging groundwater. Rainfall -run off when generated discharges into natural channels and eventually into the River Tigris (Ma'ala, and others, 1989).

PROCESS DISCRIPTION

The sulphur was mined by the Frasch process, where superheated water, steam and compressed air are injected into a sulphur-bearing deposit where sulphur is stripped from the returned water. Sulphuric acid was used to clean bitumen and other minerals from the sulphur and the resultant waste solids and liquids were deposited on-site to form large mounds dispersed in an area of more than 1 km^2. The waste piles contained up to 70% sulphur in various mineral forms (Center of Environmental Surveys and Pollution Control, 1998)

The purified sulphur was stockpiled next to a rail yard for export. In March 2003, the stockpile volume was approximately 500,000 m^3. Production effectively ceased in March 2003 and the site was comprehensively looted over the period April to July 2003.

In June 2003, a fire started by looters destroyed a large volume of the purified stockpile and the adjacent waste piles.

The fire was started by arsonists on June 25th 2003 and burned continuously for a month, although it was largely under control by 8th July. Reports of the sulphur volumes burnt range from 300,000 to 400,000 tones (Mahmood and others .2005).

The fire was eventually contained by a combination of isolation by earth man-made embankments burial with earth and foam smothering. The state of the sulphur stockpile after the fire indicates an approximate 70% loss in area (GEOSURV. 2005).

Burning of pure sulphur produces corrosive and toxic sulphur dioxide gas and because of the high concentrations of that gas generated by the fire, it was present as an aerosol (white smoke/fumes), forming acid rain.

Satellite image tracking of the smoke plume showed the sulphur dioxide (SO_2) cloud dispersing generally to the southeast; however, on some days it was also dispersed northwards. Elevated SO_2 concentrations detected over 200 km distant (Mahmood and others 2005)

At the local level, 25 villages and 3 towns were badly affected, with many hospital reports of respiratory problems and at least two deaths. Media reports at the time of the fire indicate that extensive damage occurred to wheat crops near the fire. It is believed that this was a result of acute acid burns to the exposed plants, resulting in plant death and stunted growth (Riadh. et al, 1983).

During the mining operations, a portion of the superheated water mixture was not recovered and instead leaked laterally underground and into the river as sulphur springs, thereby polluting the river. In a 1983 report, the sulphur springs were reported as fountains springing from the riverbank and reaching a height of up to 50m, indicating very high flow rates and pollution loads. Later changes in mining methods and the installation of subsurface cut-off walls reduced but did not eliminate the flow of sulphurous water into the Tigris (Al-Bassam,, 1984).

SITE CHEMICALS

The most important chemicals and material present at the Al Mishraq complex are;

- Pure sulphur
- Aluminum sulphate
- Asphaltenes (bitumen)
- Sulphuric acid
- Hydrogen sulphide

Sulphur, aluminum sulphate and bitumen have relatively low toxicity to humans. Sulphur is present naturally in food and in low concentrations; it is an important element for human health. Aluminum sulphate is used in food preservatives, cooking and water clarification and purification (Ma'ala, and others, 1989). Bitumen, whilst toxic to ingest, is used universally in road construction (Center of Environmental Surveys and Pollution Control, 1998).

Sulphuric acid is of concern primarily due to its corrosive effects. The acid plant is expected to contain significant quantities of residual acid in pipes, tanks and basins. Acid may also be present in surface water drainage and leachate from the sulphur waste piles (Ma'ala, and others. 1989).

Hydrogen sulphide is a toxic gas, which is naturally present in the groundwater of Al Mishraq. Desk studies reported that at least four local village wells are no longer used due to elevated hydrogen sulphide levels (UNEP, 2005). Hydrogen sulphide may also be present in the waste sulphur piles if anaerobic conditions prevail (Ma'ala and others, 1989).

SAMPLING

Five visits to the site were conducted twice in 2003 for general fact-finding, twice in 2004, and once in 2005 for detailed sampling and monitoring.

The work focused on the area of the 2003 fire, sulphur storage and waste areas. Groundwater wells outside the site were sampled and monitored with a portable instrument.

a. Soil Sampling

The sampling techniques used generally involved the collection of surface soils and substances. A total of 22 soils were collected. Sampling depths recorded range from surface with no depth range specified (but assumed to be 0-0.3m), to a maximum depth of 3m below ground level. Five of the 22 samples were taken from depths of approximately 1m and more.A lithological description of the

samples submitted to the laboratory is given in table 1.

b. Water Sampling

A single water sample was collected from water well on site. A further 9 water samples were collected including one from the river. A number of duplicate water samples were also submitted. Five samples from local village wells outside the site at a distance of 1-5 km from the site boundary. Four out of five wells were reported by the local population as unusable wells due to high sulphate or hydrogen sulphide levels. Table 2 summarizes ground water analyses activities.

LABORATORY ANALYSIS

Samples collected during the site investigations were put into separate containers and labeled with a unique sample number. Plastic tubs of 500 gm or 1kg capacity were used for the collection of soil and hazardous substance samples to be analyzed for metals and inorganic parameters. Wide neck glass jars of 250gm capacity were used for the storage of samples destined for the analysis of organic parameters.

Water samples destined for metals and most inorganic analysis were collected in 250ml plastic bottles. Samples for organics analysis were collected in 500ml amber glass bottles. Where practicable each sample bottle was filled completely to the brim with no headspace in the field to minimize losses through volatilization from the sample (Iraq Digest - Mishraq fire, 2008)

On completion of the fieldwork, samples were shipped by courier to the project contract laboratory, ALcontrol Geochem Laboratories, Chester, England with the completed Analysis Request Form and Sample Custody Sheet.

In line with current best practice, all testing methods employed by the laboratory have a quality control component, which is dependent upon the type of analysis and any specifications as required by the client. The Quality Control protocols routinely employ blanks, sample spikes, and replicates within the analytical procedure.

Where possible, ice packs were added to the cool box before the courier collected the box for shipment.

. The analytical parameters determined and the numbers of samples analyzed by sample type were as follows:

Soils

A total of 22 soil samples from the site were analyzed as indicated in figures 2 through 4 for the following analysis:

-Metals (antimony, arsenic, beryllium, cadmium, chromium, copper, lead, mercury, nickel, selenium, silver, thallium and zinc).

-Extractable Petroleum Hydrocarbons (EPH) (formerly known as Diesel Range Organics (DRO) carbon range: C10-C40)

-Gasoline Range Organics (GRO) carbon range C4-C10

-GRO carbon range C10-C12

- Volatile Organic Compounds (VOC): benzene, toluene, ethyl benzene,

m & p xylene, oxylene & methyltert-butyl ether (MTBE)

-Total sulphur, and -Total sulphate

-pH, and conductivity

-Anions: carbonate, chloride, fluoride, nitrate, nitrite and phosphate.

-Cations; calcium, magnesium, potassium and sodium, as shown in figure 4(a) and 4(b)

Waters

A total of 10 water samples including 1 groundwater sample and 1 duplicate were analyzed as in figures 5 through 7 for the following analysis:

-Metals (antimony, arsenic, beryllium, cadmium, chromium, copper lead, mercury, nickel, selenium, silver, thallium and zinc)

-Extractable Petroleum Hydrocarbons (EPH) (formerly known as Diesel Range Organics (DRO) carbon range: C10-C40)

- -Gasoline Range Organics (GRO) carbon range C4-C10; - GRO carbon range C10-C12.

-Total sulphate, -Soluble sulphate, and -Free sulphur

-Volatile Organic Compounds (VOC): benzene, toluene, ethyl benzene, m & p xylene, o xylene & methyltert-butyl ether (MTBE)

-Hardness, total dissolved solids and total suspended solids.

-Anions: carbonate, chloride, fluoride, nitrate and nitrite

-pH and conductivity.

-Cations: calcium, magnesium, potassium and sodium.

RESULTS

No guidance values have been published in Iraq. Yet tier 1 process guidance values from Netherlands (Lenore and others, 1999) and from Australia (Spatial Planning and the Environment, 2000) have been used.

a. Soil

Criteria are not set for sulphate or total sulphur in either the Dutch or Australian systems. However, the Australian jurisdiction has set "Interim Urban" levels for sulphate and total sulphur intended for the protection of built structures. The Interim Urban sulphate level of 2,000mg/kg was exceeded on 21 of 22 soil samples. The total sulphur Interim Urban level of 600mg/kg was exceeded on all occasions (22/22).

The soil in the Al Mishraq area contains naturally high levels of native sulphur and sulphate, primarily gypsum. In the mine area, elevated concentrations of bituminous compounds are also found naturally. Accordingly, it would be wrong to conclude that the site is contaminated because of these compounds are present. Laboratory analysis of soil indicates levels of sulphate of up to 265800mg/kg (figure 4 a). This is thought to indicate that the soils or the waste contain a high percentage of gypsum. Concentrations detected have been compared against the two sets of example Tier I screening criteria (guidance values). Those contaminants of concern that exceeded the screening criteria are presented in Table 3. None of the Australian Tier 1 screening criteria were exceeded.

b. Waters

Laboratory analysis of surface water indicated high levels of sulphates and carbonates. Water contamination by sulphur compounds is also a natural process in the Al Mishraq area. Sulphur compounds known to exist naturally including sulphates and hydrogen sulphide. Much of what was analyzed could therefore have occurred naturally.

The natural and induced contamination was differentiated on the basis of pH. What is not expected naturally is strongly acid water, i.e. pH 4 or below. The natural baseline for surface waters for the River Tigris was recorded as pH 8.4. In contrast, four surface water ponds and channels in the vicinity of the sulphuric acid plant and waste piles had pH values of 0.6, 0.7, 2.2 and 4.1 indicating highly acidic sources. The sample with a pH of 0.6 also had elevated levels of metals including copper, lead, arsenic, chromium and beryllium. This is to be expected in such an acidic sample as metals are liberated from soil minerals under acidic conditions.

The area of acidic surface water is located approximately 4 km from the River Tigris and is connected to the river by two steep sided gullies. The gullies appear to be mainly dry and the drainage rate during March 2005 visit was limited (less than 0.lm3/second). Significant short-term flows could however be expected during the rare rainy periods.

Sulphur and mineral deposits lining the

drainage canal indicate water pollution has been ongoing for many years. As the plant had been shut down for two years, the surface water sample is not effluent from ongoing operations.

The acid is therefore either residual effluent mixed with rainwater or ongoing acid drainage due to sulphide decomposition. In either cases, the surface water in the vicinity of the sulphur treatment complex is unlikely to regain a balanced pH in the short to medium term.

Water samples analytic results have been compared against the two sets of example Tier 1 screening criteria (guidance values) for groundwater. The contaminants of concern that exceeded the screening criteria are presented in tables 4 and 5.

Conclusions

- Mineral extraction industries may recover partially, if at all. The work done in this study provide firm evidence that the damage to the environment from the Al Mishraq fire was not permanent and natural recovery is very well advanced after two years. The temporary nature of the damage is probably due to the soil buffering capacity, which can neutralize episodic acidic rain and surface water and thereby protect plant root systems from permanent damage.

Leaves and stems exposed to the acidic aerosols will have been damaged at the time of the fire, but plants survived and grew back whilst future crops planted or sown will be largely unaffected.

- The maximum detected concentration of chromium in one soil sample exceeded the screening criteria 3-fold implying that a pocket or pockets of moderately high contamination are present. The very limited

- High concentrations of minerals occur naturally in the Al Mishraq area and any assessment of chemical contamination and wastes disposed at the site needs to consider this.
- Only a very small numbers of soils (1 of 26 samples: sample No.6) exceeded the Dutch Tier 1 screening criteria for their respective chemical parameters. The criteria are only exceeded for 2 of 13 metals (chromium and nickel). None of the hydrocarbon criteria is exceeded. None of the analytical parameters determined in the soils exceeded the Australian Tier 1 screening criteria.
  nature of the site investigation does not enable the lateral or vertical dimensions of such contamination sources to be delineated.
- A small number of water samples (1 of 10: sample WI) exceeded the screening criteria for 6 to 8 metals (Australian and Dutch respectively). The concentrations of the metals nickel and lead exceeded their Dutch screening criteria concentrations by more than 150-fold and 10-fold respectively.

- Acid drainage into the Tigris may affect local water quality but the scale of the river flow compared to the drainage gullies indicates that the impacts would be localized due to dilution and the buffering capacity of the river water.

Acronym and abbreviations

bgl : Below Ground Level

BTEX: Benzene, Toluene, Methylbenzene, and Xylem

DRO: Diesel Range Organics

EPH: Extractable Petroleum Hydrocarbons

GCMs: Gas Chromatography Mass Spectrometer

GRO: Gasoline Range Organics

IR: Infra Red

ISO: International Standards

PCBs: Poly Chlorinated Biphenyls

PID: Photo Ionization Detector

SVOCs: Semi Volatile Organic Compounds

VOCs: Volatile Organic Compound

XRD: X-Ray Diffraction

XRF: X-Ray Fluorescence spectroscopy

Table 1 Description of Soil Samples

Sample no.	Depth m bgl	Description
1	0-0.2	Loose dry grey sandy clayey SILT with a little gravel up to 20mm size
2	1.0	Loose damp light yellow-brown sandy SILT with brown inclusions of clay-like consistency
3	2.2	Loose fine silty orange-brown sandy clayey SILT with occasional small angular stones
4	1.5	Dry medium-dark brown clayey sandy slightly cohesive SILT with occasional gravel up to 25mm size
5	0.15	Light to medium brown sandy SILT
6	0.2	Light brown clayey sandy SILT
7	0.1	Light brown clayey sandy SILT with occasional vegetation
8	0.1	Light brown clayey sandy SILT with possible bitumen, occasional medium gravel and occasional vegetation
9	0.1	Medium brown clayey sandy SILT with occasional medium gravel
10	0.1	Light brown clayey sandy SILT with occasional medium gravel
11	3.0	Dark grey wet silty Clay
12	0.15	Medium grey green sandy SILT with occasional fine gravel
13	0.1	Light brown sandy clayey SILT with occasional medium gravel
14	2.3	Dark grey wet silty CLAY
15	0.15	Medium grey green sandy SILT with occasional fine gravel
16	0.1	Light orange brown sandy SILT
17	0.1	Light greenish grey sandy SILT
18	0.2	Light to medium grey silty clayey SAND with occasional fine to medium gravel
19	0.15	Orange brown silty SAND with occasional greenish grey fragments
20	0.15	Light brown clayey sandy SILT with occasional fine to medium gravel & occasional
21	0.2	Medium brown clayey sandy SILT
22	0.15	Medium brown clayey sandy SILT

Table 2: Al-Mishraq region groundwater field monitoring results

Sample	General sample location	Depth to water m	On-site monitoring results			
			Temp.(^{o}C)	pH	EC (m/s)	TDS (g/l)
W1	5 km from the S complex boundary in the south direction. Nasser village, unusable well, the location was affected by the 2003	10	19.8	8.2	2.47	1.23
W2	2 km from the complex boundary in the east. Al-Safina village. Unusable well	1.5	19.5	7.0	3.4	1.70

W3	2 km from the complex boundary in the southwest direction. Nasser village, well usable for irrigation.	20	23.8	6.7	7.01	3.46
W4	>3.5 km from the complex boundary in the west direction. Zahra village, well unusable for eight years.	5.7	19.1	7.7	11.23	5.6
W5	>1 km from the complex boundary in the west direction. Nina'a village, a new well unusable till now due to the high sulphur content and H_2S gas.	>50	23.7	7.6	6.06	3.02

Table 3: Contaminants of Concern in Soils- Dutch Criteria

Contaminant of Concern	Tier I Screening Criteria(mg/kg)	Maximum concentration (mg/kg)	Number above applicable criteria
Chromium	380	1082	1/26
Nickel	210	310	1/26

Table 4: Contaminants of Concern in Groundwater - Dutch Criteria

Contaminant of Concern	**Tier I Screening Criteria (µg/l)**	**Max. Concentration (µg/l)**	**Number above applicable criteria**
Arsenic	60	143	1/10
Beryllium	15	84	1/10
Cadmium	6	21.5	1/10
Chromium	30	7287	1/10
Copper	75	2704	1/10
Nickel	75	11470	1/10
Lead	75	123	1/10
Zinc	800	10320	1/10

Table 5: Contaminants of Concern in Groundwater - Australian Criteria

Contaminant of Concern	**Tier I Screening Criteria(µg/l)**	**Max. Concentration (µg/l)**	**Number above applicable criteria**
Arsenic	7	143	1/10
Cadmium	2	21.5	1/10
Copper	2000	2704	1/10
Nickel	20	11470	1/10
Lead	10	123	1/10
Zinc	3000	10320	1/10

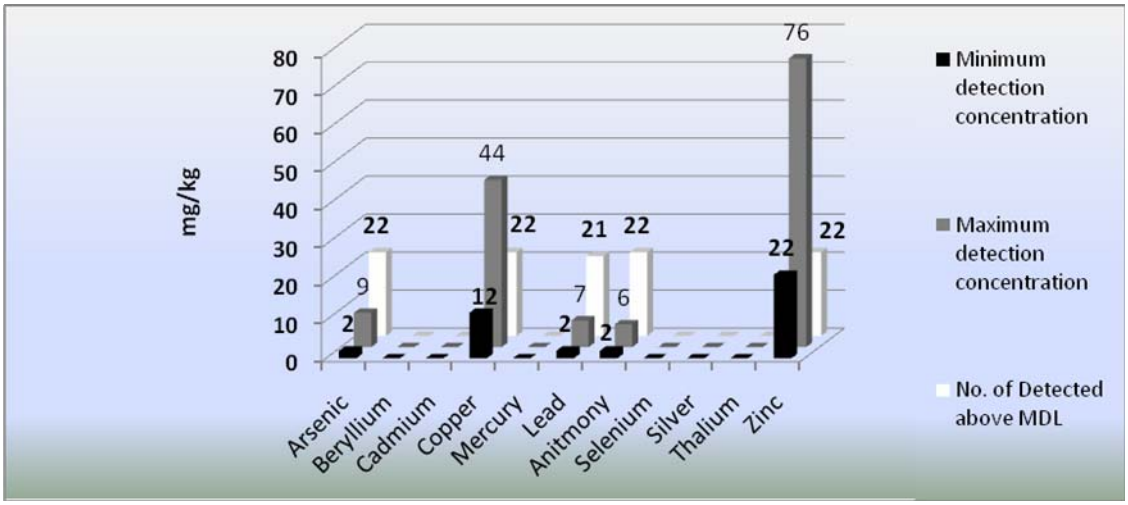

Figure 2 (a) Maximum and minimum detected heavy metal concentrations in soil, and number of samples detected above the minimum detection level of the analytical equipment used.

Figure 2 (b) Maximum and minimum detected heavy metal concentrations in soil, and number of samples detected above the minimum detection level of the analytical equipment used.

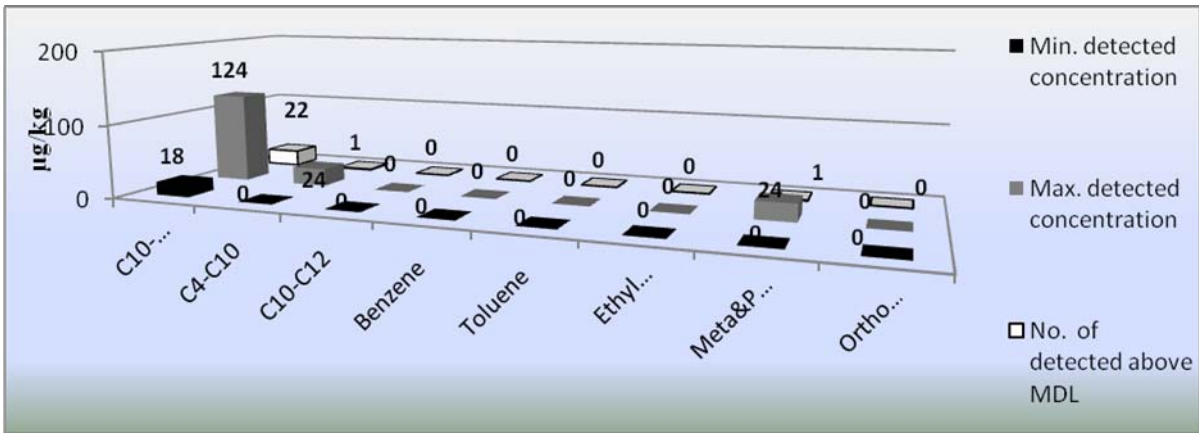

Figure 3 Maximum and minimum detected Volatile Organic Compounds (VOCs) and hydrocarbons concentrations in soil

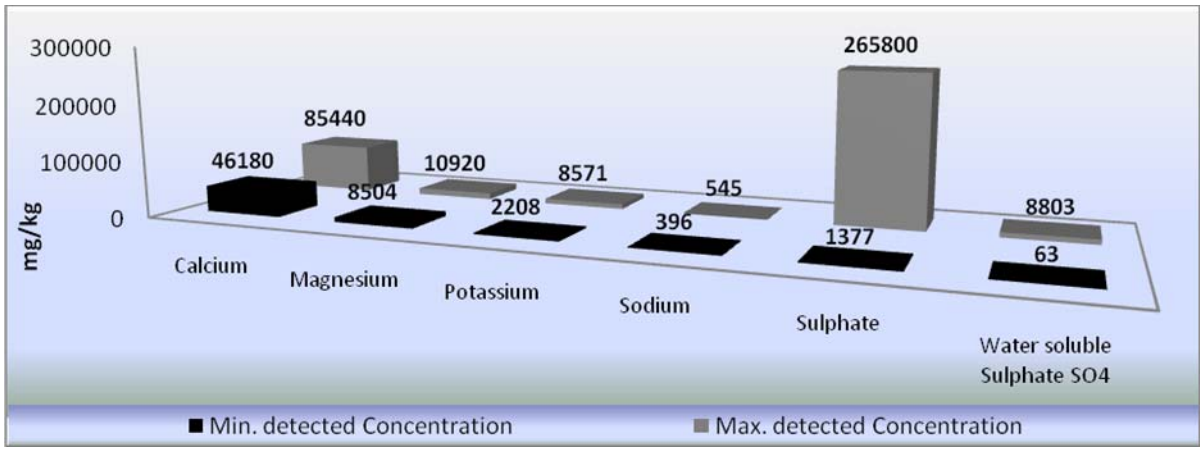

Figure 4 (a) Maximum and minimum detected Concentrations of other parameters in soil

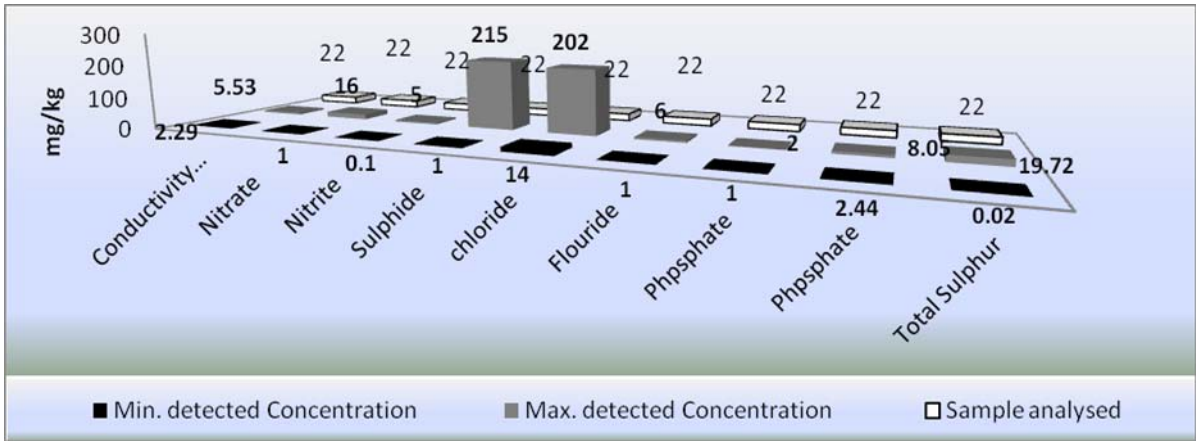

Figure 4 (b) Maximum and minimum detected Concentrations of other parameters in soil

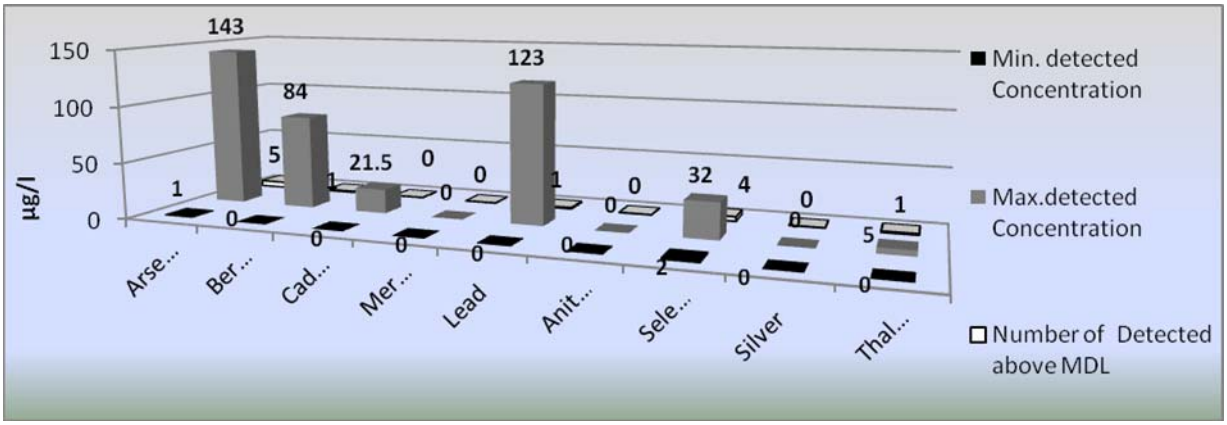

Figure 5 (a) Maximum and minimum detected heavy metal concentrations in water and number of samples detected above the minimum detection level of the analytical equipment used.

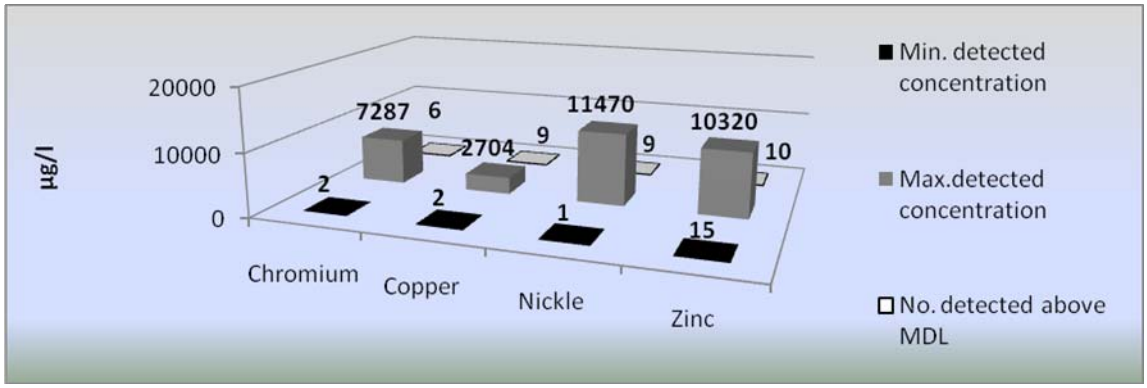

Figure 5 (b) Maximum and minimum detected heavy metal concentrations in water and number of samples detected above the minimum detection level of the analytical equipment used

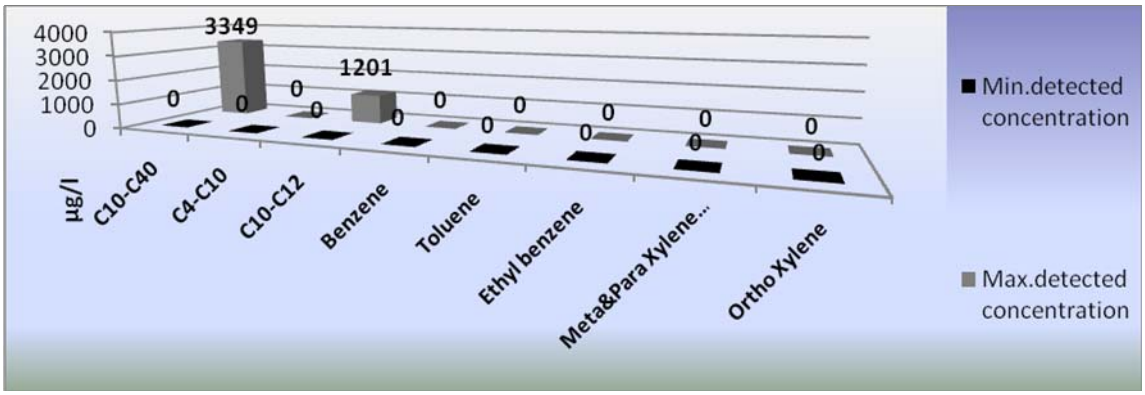

Figure 6 Maximum and minimum detected Volatile Organic Compounds (VOCs) and hydrocarbons concentrations in water

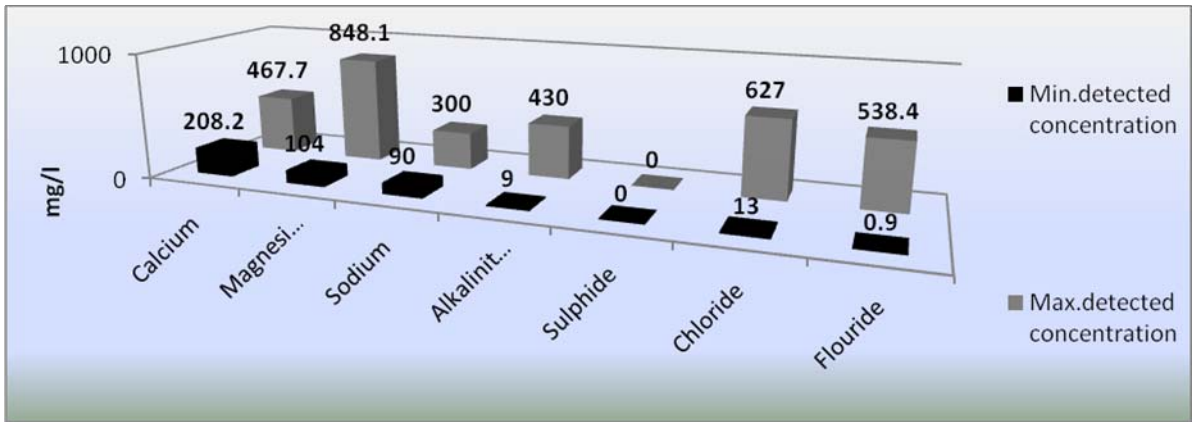

Figure 7 Maximum and minimum detected concentrations of other parameters in water

References

1. USA government Energy Information Administration - Iraq Country Analysis Brief. http://www.eia.doe.gov/emeu/cabs/iraq.html.
2. Mobbs P. 2000. The mineral industry of Iraq.US Geological Survey Minerals Yearbook 2000.
3. Marr P. 2004. " The Modern History of Iraq 2nd Ed" West view Press 2004.

Mining Pro files - Iraq. http://www.miningprofiles.com.

4. UNEP (2005). Assessment of Environmental Hot Spots in Iraq - UNEP Technical Report. Geneva, Switzerland, United Nations Environment Programme.
5. Center of Environmental Surveys and Pollution Control / Al-Mussel University, Sep., 1998, " The General Complex of Al-Mishraq Sulphur , Environment Evaluation".
6. Mahmood and others (2005). Industrial discharge from Al-Mishraq sulfur mines and their environmental effects, The General complex of geologic survey and mining , Interior report, no. 2920
7. Carn S.A & Krueger A.J 2004. Fire at Iraqi sulfur plant emits SO2 clouds detected by Earth Probe TOMS. Geophysical research letters Volume 31, 2004 L19105.
8. Al-Bassam, K.S., 1984. Final Report on the Regional Geological Survey of Iraq, Vol.5: Economic Geology. GEOSURV, int. rep. no. 1449.
9. Riadh. H. et al 1983. The regional effects of the effluents from the Mishraq sulphur mines in Iraq on the hydrological system. Hydrological Sciences Journal V28, 2 6/1983.
10. Ma'ala, K.A., Mahdi, A.H., Fouad, S.F., Lawa, F.A., Philip, W. and Al-Hassany, N., 1989. Report on geological investigation for native sulfur in the northern section of the Fatha
11. Mosul Sulfur District. GEOSURV, int. rep. no. 1938.
12. Iraq Digest - Mishraq fire. 2008, http://www.iraqdigest.corn/newsreview-jul-l.htm
13. Lenore S. Clesceri, Arnold E. Greenberg, Andrew D. Eaton, 1999 "Standard Methods for the Examination of Water and Wastewater" 20th edition
14. Spatial Planning and the Environment, 4 February 2000. Circular on Target Values and Intervention Values for Soil Remediation, Dutch Ministry of Housing, Spatial Planning and the Environment, 4 February 2000.
15. National Environment Protection (Assessment of Site Contamination) Measure: Schedule B(l) Investigation Levels for Soil and Groundwater, Australian National Environment Protection Council, 1999.

MEASUREMENT OF GROUND LEVEL OZONE IN SELECTIVE LOCATIONS IN BAGHDAD CITY

Yasmen A. Mustafa; Environment Eng.Dep.
Adnan H. Afaj; Ministry of Science and Technology
Sinan J. Mohammed Environment Eng.Dep.

ABSTRACT

The ground level ozone concentration at different locations in Baghdad city was identified. Five different sites have been chosen to identify the ground level ozone concentration. Al- Dora and Al-Za'afarania were chosen as areas contained point source (power plant station) in addition to high traffic load , while Al –Uma park, Aden square and Al-Mawal square were chosen as area contained heavy traffic only (line source). The measurement focuses on spring and fall because these periods display favorable meteorology to ozone formation. During the research period the maximum values (peaks) for ground level ozone concentration were observed at fall: at Al-Za'afarania area 101ppb as an average, at Al-Dora 87 ppb as an average and at line source areas 48 ppb as an average. Among the line sources area Al-Mawal square represent the highest peak value at fall 68 ppb. At spring the peaks of ozone concentration observed to be at the same height, 50 ppb for all sites. The downwind sites from the power plant stations at Al-Dora and Al-Za'afarania areas record higher ozone peaks compared with up wind sites. It can be concluded that the effect of power plant stations in forming ozone is larger than traffic load.

The comparison between the ground level ozone concentrations that measured during the research period in spring and fall, and the ambient air quality standards (AAQS) shows that:

- No exceeded levels were observed in spring for all sites.
- In fall the AAQS for ozone was exceeded in Al-Za'afarania area at 12: PM, 1: PM, 2: PM and 3: PM, and in Al-Dora at 2: PM.

الخلاصة

يهدف البحث الى تعيين تراكيز غاز الاوزون عند المستوى الارضي لعدة مناطق في مدينة بغداد . تم اختيارخمسة مناطق وهي منطقة الدورة و منطقة الزعفرانية والتي تمثل مصدر للتلوث النقطي (بسبب وجود محطات توليد الطاقة الكهربائية) اضافة الى انها مناطق مزدحمة بالمركبات. وتم اختيار حديقة الامة وساحة عدن وساحة الموال كمناطق مزدحمة بالمركبات
(مناطق ذات مصدرخطي للتلوث). القياسات تمت في فصل الربيع والخريف لان هذي الفترة تمثل افضل فترة لتكون الاوزون. خلال فترة البحث تبين ان اعلى قيمة لتركيز الاوزون ظهرت خلال فصل الخريف: في منطقة الزعفرانية 101 جزءاً بالبليون كمعدل ، في منطقة الدورة 87 جزءا بالبليون كمعدل ، وفي مناطق التلوث الخطي 48 جزءا بالبليون كمعدل. ساحة الموال سجلت اعلى قيمة لتراكيز الاوزون لمناطق التلوث الخطي في الخريف والبالغة 68 جزءا بالبليون .اما في الربيع اعلى تركيز للاوزون كان متساوياً تقريبا لكافة المناطق ,50 جزءاً بالبليون . في منطقة الدورة والزعفرانية خلال فصل الخريف، القياسات التي تمت في المناطق التي هي باتجاه الريح السائدة اظهرت قيم اعلى من القياسات التي تمت بعكس اتجاه الرياح السائدة . هذا يعطي مؤشر الى ان تأثير محطات توليد الطاقة الكهربائية على تكون الاوزون اكبر من تأثير حمل المركبات. ان المقارنة بين تراكيز الاوزون عند المستوى الارضي خلال فترة البحث مع المحددات القياسية للهواء المحيط بينت انه لا يوجد تجاوز في فصل الربيع ، كما بينت انه تم تجاوز المحددات في منطقة الزعفرانية في الساعة الثانية عشر،الواحدة ،الثانية والثالثة بعدالظهر خلال فصل الخريف. وكذلك تم تجاوز المحددات في منطقة الدورة في الساعة الثانية بعد الظهر.

KEY WORDS : Ozone; Photochemical smog; Air pollutant; secondary air pollutant.

1. INTRODUCTION

Tropospheric ozone is an important secondary air pollutant in the atmosphere that has received extensive attention in the literature (Abdul-Wahab, et al., 2005; Al-Alawi et al., 2008; Al-Khalaf, 2006; Bader, et al., 2008).It has been reported that ozone is a major oxidant, and it is the most important index substance of photochemical smog which has been recognized as one of the key pollutants degrading the air quality (Arya, 2002). There are no significant primary emissions of ozone into the atmosphere and all the ozone found has been formed by chemical reactions that occur in the air. Ozone produced when the primary pollutants, nitrogen oxides (NO_x) and the volatile organic compounds VOCs (often called non-methane hydrocarbons (NMHC), which are referred as ozone precursors, interact under the action of sunlight. Meteorological parameters (temperature, wind speed and direction, solar radiation, humidity, boundary layer depth) highly influence the formation and dispersion of ozone. Radiation, temperature and humidity drive the chemical reactions producing ozone, while boundary layer characteristics and the absence of wind are the factors which respectively lead to the build-up of precursors and limit their dispersion. The concentration varying widely from region to region, with the time of year, and the time of the day.(Lengyel, 2004; San Jose´ et al., 2005; Al-Alawi et al., 2008).

Both NO_x and VOCs are emitted from a large pool of sources. These sources are typically classified into four categories: area, point, mobile, and biogenic. Emissions of NO_x are produced primarily by motor vehicle engines, power plants, industrial plants, boilers and burning of fossil fuels. VOCs emissions are motor vehicle emissions, gasoline vapors, and chemical solvents. Biogenic volatile organic compounds(BVOCs) which almost emitted from forest and marshland like terpenes and isoprene are also contribute to ozone formation (Pfister et al.,2008). High concentration of ozone and other photochemical oxidants are observed over most large cities and metropolitan areas during warm months. Considerable levels of ozone are also found to exist over large rural regions in which ozone gets transported from large urban and industrial areas. Thus, tropospheric ozone is not merely an urban air pollution problem, but also a regional problem (Arya, 2002).

The impact of biogenic emissions on surface O_3 has been examined by many studies, biogenic volatile organic compounds is a source of hydroperoxy and organic peroxy radicals, which can react with NO_x to stimulate O_3 production and react with peroxy acetyl nitrate (PAN) which influence the global distribution of nitrogen oxides (NO_x) and thus indirectly impact O_3 production (Pfister et al., 2008).

Unlike the “bad” tropospheric ozone there is also the “good” stratospheric ozone. Most of the stratospheric ozone resides with its maximum concentration around 20km above the surface of the earth (Jacobson, 2002).

Stratospheric ozone plays a beneficial role by absorbing ultra violet radiation from the sun. So it protects the life on earth from the

destructive effects of such radiation. The large amounts of ozone produced in the stratosphere are inhibited from entering the troposphere by a sharp increase in atmospheric stability at the tropopause. Specific meteorological conditions may cause the descent of ozone rich air of stratospheric origin to the lower troposphere. The background ozone concentration is not easily measured. However, it has been estimated that the average ozone concentration on the earth's surface caused by such natural processes is between 20 and 50 ppb depending on the geographical location and latitude (Derwent et al., 1978).

Ozone is well known as strong oxidant. It has direct effect on human, vegetation and materials. Inhalation of air mass containing 1 ppm by volume ozone causes severe irritation and headache. Ozone irritates eyes, upper respiratory system, and lungs. Inhalation of ozone can sometimes cause fatal pulmonary edema which is an abnormal accumulation of fluid in lung tissue. Ozone generates free radicals in tissue. These reactive species can cause lipid peroxidation, oxidation of sulfhydryl (–SH) groups, and other destructive oxidation processes (Manahan, 2000; Schlink et al., 2006; Palli et al., 2008).

Phytotoxicity of ozone is characterizing the yellow and black spots on a green leaf. Wang et al., (2007) show that ozone effects on corn and soybeans in both quality and productivity in Linan, China. Quijano et al., (2009), show that phytotoxicity increased with altitude, substantial ozone injury symptoms were found at all altitudes on tobacco plants exposed to the ambient air, although, damage was more intense in the plants at greatest altitudes. Ground level ozone may cause reduced resistance to fungi, bacteria, viruses and insect (OTA, 1989). These impacts on sensitive species may result in declines in agricultural crop. Ramo et al., (2006), verify that ozone (40-50 ppb) reduced the total community biomass production and the growth of three species out of seven.

Ozone has direct effect on materials by reduction for its virtual life. Ozone attacks synthetic rubbers causing deterioration of rubber by cracking. The mechanism appears to be an attack at the double bonds in the hydrocarbon polymer used in the rubber (Boubel, 1994). Some of rubber manufacturers make test to their product by the exposure to high ozone concentration they call it ageing rubber tests. Ozone also attacks the cellulose in textiles, reducing the strength of such items and changing white color of fabric to the yellow (Brown, 2001).

Because ozone has those harsh effects on both life and material, the United States Environmental Protection Agency (USEPA) considered ozone as criteria pollutant. USEPA ozone standards have been change according to the development of research on life requirement. To attain the ozone standard, the 3-year average of the fourth-highest daily maximum 8-hour average ozone concentration measured at each monitor within an area over each year must not exceed 0.075 ppm (Bailar, 2008).

The aim of this research is to identify the ground level ozone concentration in Baghdad city at different locations. Five locations are chosen, Al- Dora and Al-Za'afarania sites are chosen to show the effect of the thermal power plant (as point source), and AL-Uma Park, Aden square and AL-Mawal Square are chosen to represent line source

2. FIELD WORK

2.1 Site Description

Five different sites have been chosen to evaluate ground level ozone in Baghdad city. Figure (1) and Table (1) show the description of these five sites. Different measuring points at Al Dora and Al-Za'afarania sites were chosen to show the

effect of the power plant (as point source) while Aden square in Al-Kadhemia area , Al-Mawal square in Al-Mustansiriya area and Al-Uma park in Bab Al-Sharqi area were chosen to represent line sources.

2.2 Data collection

Ozone monitor (S-500) from Aeroqual New Zealand Company used to measure ozone concentration in (ppb), the sensor head for ozone monitor is working on Gas Sensitive Semiconductor (GSS) principle,
The geographical positioning system (GPS) is of Taiwan production with Garmin trade mark model "etrex, Vista" it has been used to define the location in term of longitude and latitude with accuracy limit of about 5 meters. The ozone meter was fixed on aluminum bare at 1.6 m height to simulate respiratory system intakes. Care must be taken that no high buildings or trees were present near the measuring site. Values of day-light time period were used i.e. from 8: AM to 4: PM (LST) local standard time, since this documented as the most important photochemical production period. The measurement focus on spring and fall, these periods display favorable meteorology to ozone formation in Baghdad city, as indicated by Kanbour et al., (1987) and AL-Quzweny,(1990). Other researchers also indicate that these periods display favorable meteorology to ozone formation as in central Makkah ,Saudi Arabia (Al-khalaf, 2006) and in Rabia Area, Kuwait city (Bader et al.,2008).

3. RESULTS AND DISCUSSIONS

3.1 Al-Dora Area

Al-Dora area was considered as a case study, the area was expected to be affected by the pollutants which are emitted continuously from Al-Dora Power Plant and the traffic load at that area. Al-Dora Power Plant located in the south west of Baghdad city and to the west of the Al-Dora Refinery and the South Baghdad Power Plant Fig. (1). The wind rose over a period of one full year (2008) is constructed Fig. (2), using wrplot V.5.9 program. The wind rose shows that the majority of the prevailing wind is from the west, therefore the measurement points were selected at different locations (D1, D2, D3, D4, D5, D6, and D7) down wind and upwind from Al-Dora Power Plant, Fig. (3).

Figure,(4- a, b and c) shows the diurnal variation of ozone concentration at spring, early summer and fall downwind from Al-Dora Power Plant , while Fig. (4-d) shows the diurnal variation of ozone concentration upwind from Al- Dora Power Plant. Figure (4-e) represents the comparison between spring, early summer and fall.
From Fig. (4) it can be notice that:

- Almost two peaks were appeared in measuring sites with different heights.
- The same trend for ozone variation was observed at spring Fig. (4-a). The measurement was done at site D1, which was downwind from Al-Dora Power Plant, with south east wind direction at that date. The first peak (65 ppb average) was observed at 11:00 AM while the second (55 ppb) at 1:00 PM.
- In early summer Fig. (4-b), the measurements were done at three different locations downwind from Al-Dora power plant (D3, D4 and D5). At D4 two peaks were observed, the first 46.5 ppb at 11:00 AM and the second 57 ppb at 1:00 PM. At D3 and D5 one peak was observed, 40 ppb at 12:00 PM and 45 ppb at 1:00 PM respectively.

- In falls Fig. (4-c), measurement was done at two different locations D2 and D7 downwind from AL-Dora power plant. The highest peak of ozone concentration 236 ppb during the research period was observed at this area at point D7 at 2:PM .
- Multi lower peaks were observed up wind from Al-Dora power plant, Fig. (4-d) compared with downwind locations. The most probable source is the prevalent traffic load near by the road. The measurement applied at two locations D2 and D6. At location D2 the highest peak 37 ppb was recorded at October. It may be realized that the effect of Al-Dora Power Plant as point source in forming ozone is larger than the traffic load.
- It can be noticed that from Fig. (4-e) , fall represent a higher ozone peak 87 ppb compared with early summer 47 ppb and spring 50 ppb.

Figure,(4- a, b and c) shows the diurnal variation of ozone concentration at spring, early summer and fall downwind from Al-Dora Power Plant , while Fig. (4-d) shows the diurnal variation of ozone concentration upwind from Al- Dora Power Plant. Figure (4-e) represents the comparison between spring, early summer and fall.

From Fig. (4) it can be notice that:

- Almost two peaks were appeared in measuring sites with different heights.
- The same trend for ozone variation was observed at spring Fig. (4-a). The measurement was done at site D1, which was downwind from Al-Dora Power Plant, with south east wind direction at that date. The first peak (65 ppb average) was observed at 11:00 AM while the second (55 ppb) at 1:00 PM.
- In early summer Fig. (4-b), the measurements were done at three different locations downwind from Al-Dora power plant (D3, D4 and D5). At D4 two peaks were observed, the first 46.5 ppb at 11:00 AM and the second 57 ppb at 1:00 PM. At D3 and D5 one peak was observed, 40 ppb at 12:00 PM and 45 ppb at 1:00 PM respectively.
- In falls Fig. (4-c), measurement was done at two different locations D2 and D7 downwind from AL-Dora power plant. The highest peak of ozone concentration 236 ppb during the research period was observed at this area at point D7 at 2:PM .
- Multi lower peaks were observed up wind from Al-Dora power plant, Fig. (4-d) compared with downwind locations. The most probable source is the prevalent traffic load near by the road. The measurement applied at two locations D2 and D6. At location D2 the highest peak 37 ppb was recorded at October. It may be realized that the effect of Al-Dora Power Plant as point source in forming ozone is larger than the traffic load.
- It can be noticed that from Fig. (4-e) , fall represent a higher ozone peak 87 ppb compared with early summer 47 ppb and spring 50 ppb.

3.2 Al-Za'afarania Area

The measurements were located at four points (Z1, Z2, Z3 and Z4) Fig. (5), downwind and upwind from the south Baghdad Power Plant. Figure (6-a,b) represent the diurnal variation of ozone concentration at spring and fall while Fig. (6-c) illustrate the comparison between them.

From Fig. (6), it can be observed that:

- Two peaks were appeared in all locations. The peaks are nearly at same height in spring as well as in fall,
- In spring the measurements were applied at two locations Z1 and Z2 downwind from south Baghdad Power Plant. The first peak (50 ppb average) was appeared at 11:00 AM and the second (55 ppb average) appears at 1:00 PM, Fig. (6-a).
- In fall the measurements were applied at two locations, Z3 upwind and Z4 downwind from the south Baghdad Power Plant. The same trend was observed for the two locations Fig.(6-b), but a higher peaks can be noticed for location Z4 downwind the station. Downwind peaks 137 and 153 ppb appeared at 12: PM and 3: PM respectively, while up wind peaks 50 and 48 ppb appeared at 11: AM and 3: PM respectively.
- In spring there is a decline in ozone concentration at 12: PM while at fall the decline at 1: PM. No heavy traffic was observed at that time.
- It can be noticed that from Fig. (6-c), fall represent a higher average peaks (90 and 101ppb) compared with spring (50 and 55 ppb), also a shift in peak time can be noticed at fall. Kanbour et al.(1989) during their research period observed that the maximum value of ozone concentration, 285 ppb was recorded at Al- Za'afarania site in Baghdad city in October (1987).

3.3 Line sources

The measurements were located at three sites, Al-Uma Park, Aden Square and Al-Mawal Square, Fig. (7). Figure (8 -a, b, c, e, f, and g) shows the diurnal variation of ozone concentration during spring and fall for the three sites, while Fig. (8 -d, h) illustrates the comparison between these sites during spring and fall. From this figure it can be noticed that:

- Almost two peaks were appeared in all sites and in some times three peaks will appear.
- In spring a same trend for ozone concentration was observed in AL- Uma park, Aden square and Al–Mawal square. The highest peaks (45-58 ppb) were noticed after 12: PM for all sites.
- In fall many peaks were appears clearly. For Al-Uma park and Aden Square, the first peak (52 and 55 ppb average) noticed respectively at 11: AM and the second peak (44 and 50 ppb average) at 2: PM. For Al-Mawal square the first peak and the second peak appears earlier. The first 38 ppb at 10: AM and the second 68 ppb at 1: PM.
- A third peak occur at Aden square and Al-Mawal square after 4: PM, this was because these areas are commercial areas.
- The highest ozone peak at the present research period (84 ppb) in line source areas was recorded in Aden square at 1: PM.
- No clear difference in the peaks of ozone concentration between spring and fall were observed in these three areas, only clear peaks were appeared in fall, Fig. (6- d,h) .

4. COMPARISON BETWEEN POINT SOURCE,LINE SOURCE AND AMBIANT AIR QUALITY STANDARDS

It can be noticed from the previous results that line source areas had lower peaks for ground level ozone concentration compared with areas contained point source (as an average) at fall 87 ppb for Al-Dora, 101 ppb for Al- Za'afarania and 48 ppb for line source areas . While in spring the peaks were observed to be nearly equal 50 ppb in Al-Dora, 51 ppb at Al- Za'afarania and 51 ppb at line source areas,

The comparison between ground level ozone concentration for the period of the present research during spring and fall and the ambient air quality standards (AAQS) identify that:

- No exceeded levels were observed in spring for all sites Fig. (9-a).
- In fall the AAQS for ozone was exceeded in Al-Za'afarania area at 12: PM, 1: PM, 2: PM and 3: PM, and in Al-Dora at 2: PM Fig.(9-b).

5. CONCLUSIONS

The following conclusions can be considered from the present research:

1-Almost two peaks were appeared in all sites, a third peak was observed at afternoon in commercial areas (Aden square and Al-Mawal).

2-In all sites the peaks of ozone concentration appeared clearly in fall compared with spring. 3-The highest ground level ozone concentration was found during fall in all sites. 4 The highest peak of ground level ozone concentration was found during fall in Al-Za'afarania area (as an average) 101 ppb at 3: PM.

5- No clear variation in ozone concentration peaks between spring and fall in line source areas. 6- Area contained point source represent higher ozone peaks compared with areas contained line source only in fall, while in spring the peaks were observed to be approximately equal.

7- Upwind areas from Al-Dora Power Plant contained lower ozone concentration compared with downwind areas.

9-The AAQS for ozone concentration was exceeded in Al-Za'afarania areas at 12: PM, 1: PM, 2: PM and 3: PM and in Al-Dora at 2: PM in fall at the present research period.

References

- Abdul-Wahab, S. Bakheit, C. and Al-Alawi, M., (2005). Principal component and multiple regression analysis in modeling of ground-level ozone and factors affecting its concentrations. J. Environ Model. And Soft. Vol. 20, P.1263-1271.
- Al-Alawi, S., Abdul-Wahab, S. and Bakheit, C., (2008). Combining principal component regression and artificial neural networks for more accurate predictions of ground level ozone. J. Environ. Model & Soft., Vol. 23, P. 396- 403.
- Al-Khalaf, A., (2006). Influence of meteorological and related factors on surface ozone pattern at makkah station. J. Environ. Science, Institute of Environmental Studies and Research, Ain Shams University. Also available at www.kau.edu.
- Al-Quzweny, B. B., (1990). Measurement of air pollutant in Baghdad city: Nitrogen oxide and Ozone , M. Sc thesis ,University of Baghdad.
- Arya, S.,(2002). Air pollution: Meteorology and dispersion, Oxford University press, USA.

- Bader, N., Nassehi, V., Khan A.,(2008). Comparative assessment of ambient air quality in Rabia area year 2001 and 2004 in the state of Kuwait. J. Environ Sci. Vol. 4, P. 50-62.
- Bouble, R.W.,(1994). Fundamentals of Air Pollution .3 rd Ed. Elsevier. USA.
- Brown, R.P.,(2001). Ageing of Rubber: Accelerated Weathering and Ozone Test Results. UK. Rapra Technology Limited.
- Bailar, J. C.,(2008). Estimating mortality risk reduction and economic benefits from controlling ozone air pollution. National research council Washington, D.C.
- Derwent R. G., Eggleton, A., Williams, M. and Bell, C.,(1978). Elevated ozone levels from natural sources. J. Atmos. Environ., Vol. 12, P. 2173-2177.
- Jacobson, M. Z.,(2002). Atmospheric Pollution: History, Science and Regulation, Cambridge University Press USA.
- Kanbour, F., Faiq, S., Al-Taie, F., Kitto, A. and Bader, N.,(1987) variation of ozone concentrations in the ambient air of Baghdad. J. Atmos. Environ., Vol. 21, P. 72673-2679
- Langyel, A.,(2004). Prediction of ozone concentration in ambient air using multivariate methods. J. Chemosphere Vol. 57, P. 889-896.
- Manahan, S. E., (2000). Environmental Chemistry. 7th Ed.USA: Lewis publishers.
- OTA (US. Congress, Office of Technology Assessment).(1989). Urban ozone and the clean air act: Problems and proposals for Change. Washington, DC.: Government printing office
- Pfister, G. Emmons, K., Hees, P., Lamarque, J., Orlando, J., Walters, S., Guenther, A., Palmer, P., Lawrence, P., (2008). Contribution of isoprene to chemical budgets:A model tracer study with the NCAR CTM, MOZART. J. Geophys. Res., Vol.113, P. 21-33.
- Palli, D. Sera, F., Giovannelli, L., Masala, G., Grechi, D., Bendinelli, B., Caini, S., Dolara, P. and Saieva, C.,(2008). Enviromental ozone exposure and oxidative DNA damage in adult residents of Florence, Italy. J. Environ. Poll., Vol. 30, P. 1-5.
- Quijano, M. Peñuelas, J., and Ribas, A.,(2009). Increasing interannual and altitudinal ozone mixing ratios in the Catalan Pyrenees. J. Atmos. Environ., Vol. 43, P. 6049-6057.
- Ramo, K., Kanvera, T., Nikula S., Ojanpera, K., and Mannine, S.,(2006). Influences of elevated ozone and carbon dioxide in growth responses of lowland hay meadow mesocosms. J. Environ Poll., Vol.144, P. 101-111.
- San jose, R. Stohi, A., karatzas, K., Bohler, T., and Perez., J.,(2005). A modeling study of an extraordinary night time ozone episode over Madrid domain, J. Environ. Mod. & Soft. Vol. 20, P.587-593.
- Schlink, U., Herbarth, O., Richter, M., Dorling, S., Nunnari, G., Cawley, G. and Pelikan, E.,(2006). Statistical models to assess the health effects and to forecast ground-level ozone. J. Environ. Mod. and Soft., Vol. 21, P. 547-558.
- Wang X., Manning, W., Feng, Z. and Zhu, Y.,(2007). Ground level zone in china; Distribution and effects on crop yields. J. Environ. Poll. Vol.147, P. 394-400.

Table (1): Measuring sites descriptions

Site	Name and Location of Measuring Site	Code	Coordinate		Ozone source
1	Aden Square (North waste of Baghdad city)	A	N 33 21.764	E 44 20.007	Heavy traffic
2	Al Mawal Square (North east of Baghdad city)	M	N 33 22.194	E 44 24.201	Heavy traffic
3	Al Uma park (In the center of Baghdad city)	U	N 33 19.747	E 44 24.628	Heavy traffic
4	Al Za'afarania (South east of Baghdad city, located near South Baghdad power plant and to the north east of Al-Dora refinery)	Z1	N 33 17.692	E 44 27.265	South Baghdad power plant and heavy traffic
		Z2	N 33 17.127	E 44 27.785	
		Z3	N 33 17.294	E 44 26.893	
		Z4	N 33 17.061	E 44 27.314	
5	Al- Dora (South of Baghdad city near the Al-Dora power plant)	D1	N 3315 50.67	E 44 2144.7	Al-Dora power plant and heavy traffic
		D2	N 33 16.077	E 44 21.87	
		D3	N 3315 22.99	E 44 2156.13	
		D4	N 331530.31	E 44 2234.66	
		D5	N 33 15.348	E 44 22.698	
		D6	N 33 15.315	E 44 22.978	
		D7	N 33 15.281	E 44 22.524	

Fig.(1):Aerial photo for Baghdad city shows the measuring sites.

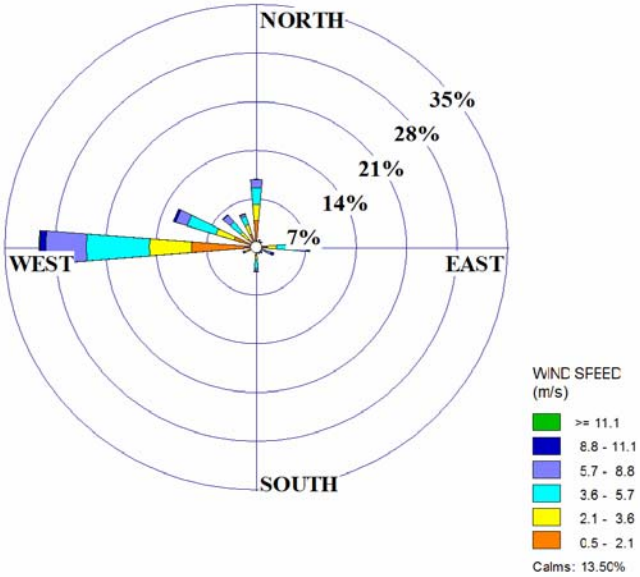

Fig.(2): Wind rose for Baghdad city one full year(2008).

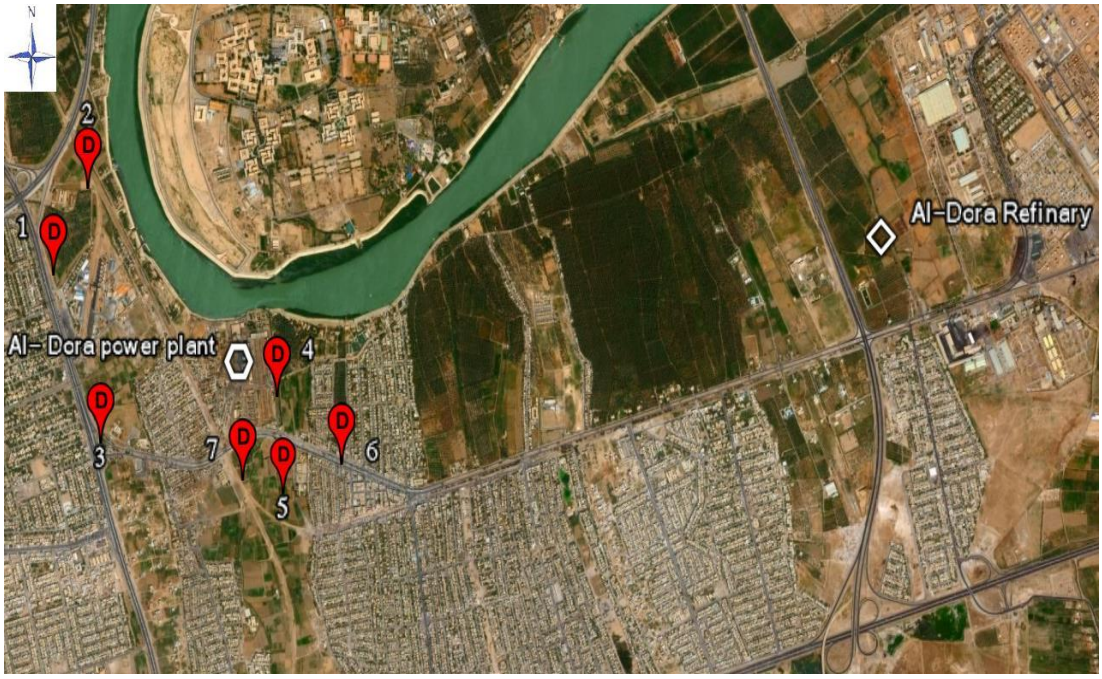

Fig.(3): Aerial photo for Al-Dora area shows the measuring sites around the power plant.

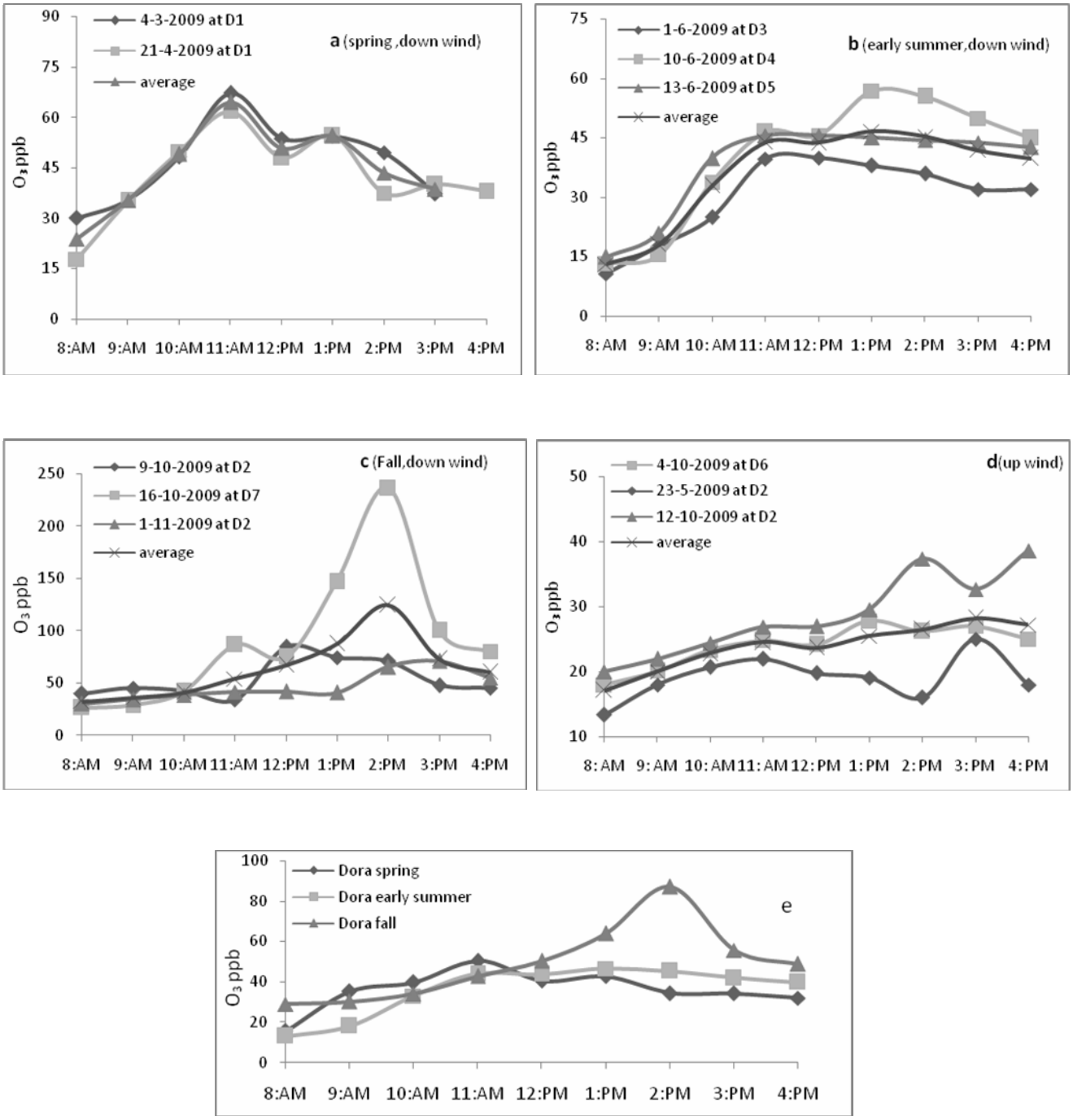

Fig. (4): Diurnal variation in ground level ozone concentration for Al-Dora site (a)at spring (b) at early summer (c) at fall (d) up wind (e) comparison between spring, early summer and fall (upwind and downwind measurements).

Fig.(5): Aerial photo for Al-Za'afarania area shows the measuring sits around the power plant.

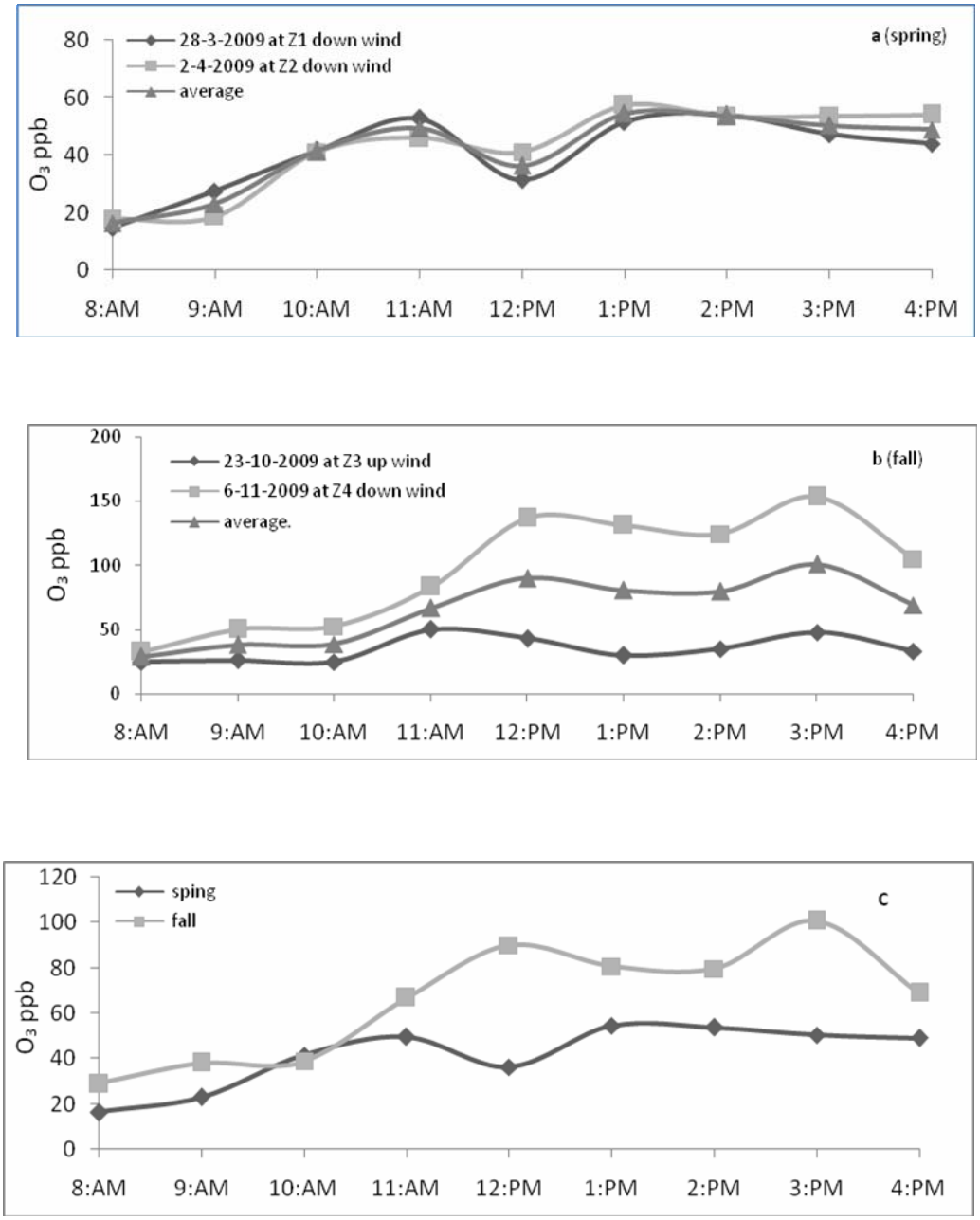

Fig. (6): Diurnal variation in ground level ozone concentration for Al-Za'afarania site (a) at spring (b) at fall (c) comparison between spring and fall.

Fig. (7): Aerial photos for line Source Area (U) Uma park (A) Aden square and (M) Al-Mawal Square.

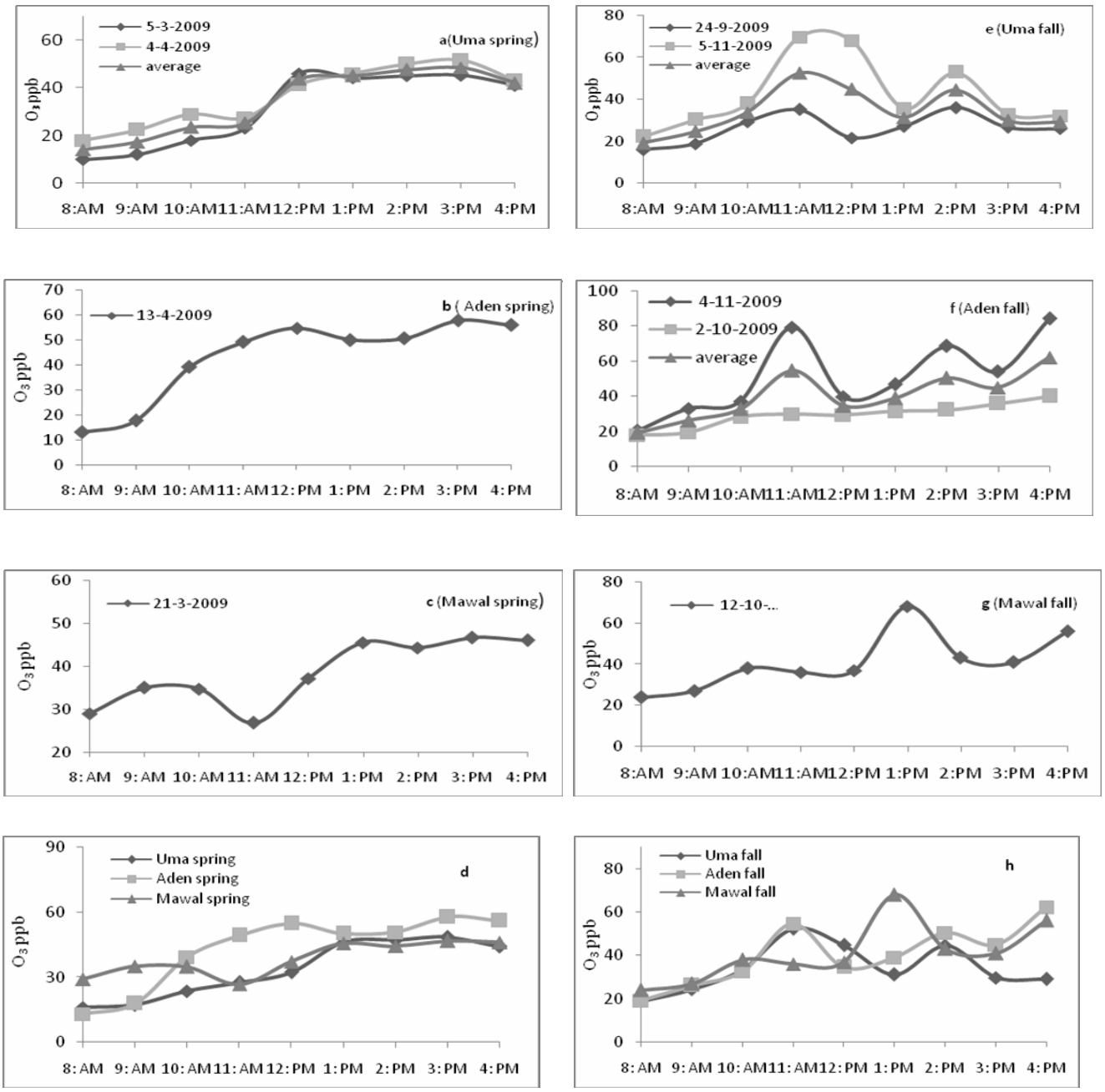

Fig.(8): Diurnal variation in ground level ozone concentration for line source sites (a) in Uma park at spring (b) in Aden square at spring (c) in Al-Mawal square at spring (d) comparison between ine source sites in spring (e)in Uma park at fall (f)in Aden square at fall (g)in Al-Mawal square at fall (h)comparison between line source sites in fall

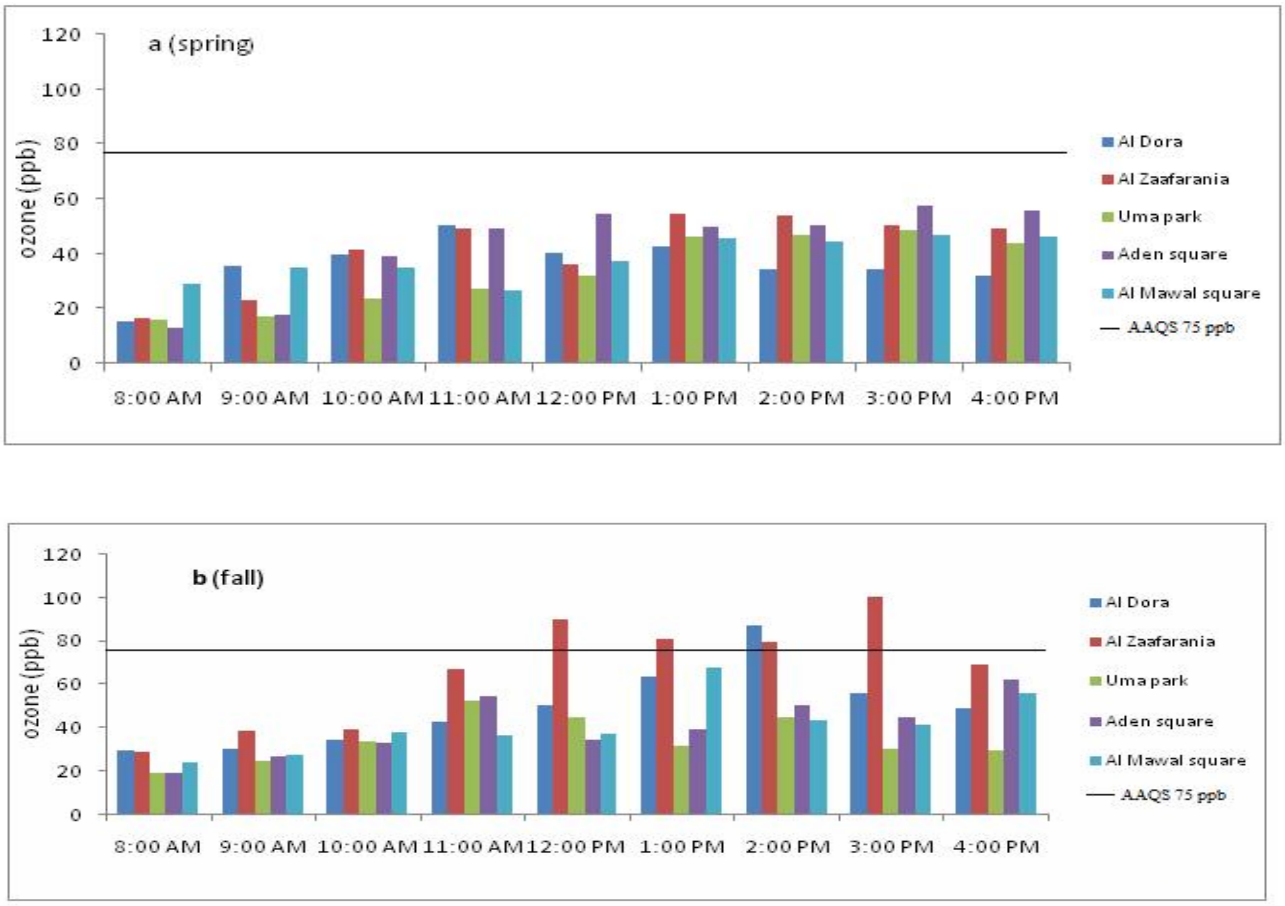

Fig.(9): Compression between measured value and AAQS

MAGNETO HYDRODYNAMIC NATURAL CONVECTION FLOW ON A VERTICAL CYLINDER WITH A PRESENCE OF HEAT GENERATION AND RADIATION

Asst. Prof. Manal H. AL-Hafidh
Mech. Engr. Dept
College of Engineering
University of Baghdad

Methaq T. Ali
Mechanical Engineer
msh_msh1977@yahoo.com.

ABSTRACT

The present work investigates the effect of magneto – hydrodynamic (MHD) laminar natural convection flow on a vertical cylinder in presence of heat generation and radiation. The governing equations which used are Continuity, Momentum and Energy equations. These equations are transformed to dimensionless equations using Vorticity-Stream Function method and the resulting nonlinear system of partial differential equations are then solved numerically using finite difference approximation. A thermal boundary condition of a constant wall temperature is considered. A computer program (Fortran 90) was built to calculate the rate of heat transfer in terms of local Nusselt number, total mean Nusselt number, velocity distribution as well as temperature distribution for a selection of parameters sets consisting of dimensionless heat generation parameter $(0.0 \le Q \le 2.0)$, conduction – radiation parameter $(0.0 \le N \le 10.0)$, and the dimensionless magneto hydrodynamic parameter $(0.0 \le M \le 1.0)$. Numerical solution have been considered for a fluid Prandtl number fixed at (Pr=0.7), Rayleigh number $(10^2 \le Ra_l \le 10^5)$. The results are shown reasonable representation to the relation between Nusselt number and Rayleigh number with other parameters (M, N and Q). Generally, *Nu* increase with increasing *Ra*, M, N and Q separately. When the MHD, N, and Q effect added to the heat transfer mechanism, the heat transfer rate increased and this effect increased with increasing in Ra, MHD, N, and Q. The effect of magneto hydrodynamic, heat generation and heat radiation on the rate of heat transfer is concluded by correlation equations. The results are found to be in good agreement compared with the results of other researchers.

الخلاصة

تمت دراسة تأثير الهيدروديناميكية المغناطيسية على الحمل الحر للجريان الطبـاقي علـى اسـطوانة عمودية بوجود تولد للطاقة الحرارية والإشعاع. المعادلات التي تتحكم بالبحث هـي الاسـتمرارية والـزخم ومعادلة الطاقة وتم تحويل المعادلات الى معادلات لا بعدية باستخدام دالـة الانـسياب الدواميـة وتـم حـل المعادلات التفاضلية الجزئية عدديا باستخدام طريقة الفروق المحددة والظروف الحدية الحرارية التي أخـذت بنظر الاعتبار هي ثبوت درجة حرارة الجدار. تم بناء البرنامج الحاسوبي (Fortran 90) لحـساب معـدل انتقال الطاقة الحرارية بدلالة رقم نسلت الموضعي ورقم نسلت الكلي وتوزيـع الـسرعة ودرجـة الحـرارة

للمعايير التي تتضمن مجموعة من القيم الابعدية.الطاقة الحراريـة المتولـدة اللابعديـة $(0.0 \le Q \le 2.0)$ والإشـعاع الحـراري اللابعـدي $(0.0 \le N \le 10.0)$ والهيدروديناميكيـة المغناطيـسية اللابعديـة $(0.0 \le M \le 1.0)$ اخذ بنظر الاعتبار الحل العددي لمـائع ذو رقـم برانـدتل (Pr=0.7) ورقـم رايلـي $(10^2 \le Ra_l \le 10^5)$. النتائج أعطت تمثيل مقبول لعلاقة رقم نسلت مع رقم رايلي بتأثير المعايير الأخـرى (M,N,Q) وبصورة عامة يزداد رقم نسلت بزيادة رقم رايلي وعند إضافة تأثير(M,N,Q)على ميكانيكيـة انتقال الطاقة الحرارية يزداد معدل انتقال الطاقة الحراريـة. النتـائج أعطـت تمثيـل لـرقم نـسلت ضـد الهيدروديناميكية المغناطيسية، التولد الحراري والإشعاع الحراري. . المقارنة مع البحوث الأخـرى أعطـت نتائج بتوافق جيد مع نتائج باحثين آخرين.

KEY WORDS: Natural Convection, Radiation, Magneto hydrodynamic, Vertical cylinder

INTRODUCTION

The problem of free convection due to a heated or cooled vertical cylinder provides one of the most basic scenarios for heat transfer theory and thus is of considerable theoretical and practical interest. The free convection boundary-layer over a vertical cylinder is probably the first buoyancy convective problem which has been studied and it has been a very popular research topic for many years**.**

Cooling of electronic devices to that of solar energy collectors, missile reentry, rocket combustion chambers, power plants for interplanetary flight and gas cooled nuclear reactors, have focused attention on thermal radiation as a mode of energy transfer and emphasized the need for an improved understanding of radiative transfer in these processes on the other hand magneto hydrodynamics is also motivated by its widespread application to the description of space (within the solar system) and astrophysical plasmas (beyond the solar system).

[Ganesan and Loganathan, 2002] analyzed the interaction of free convection with thermal radiation of a viscous incompressible unsteady flow past a moving vertical cylinder with mass and heat transfer. It was found that at small values of the Prandtl number and radiation parameter (N), the velocity and temperature of the fluid increased sharply near the cylinder as the time t increase, which is totally absent in the absence of radiation effects.

[Molla, 2005] describes the effect of magneto hydrodynamic natural convection flow on a sphere in present of heat generation. Results indicated that the local Nusselt number (Nu_x) decreases owing to increase the value of heat generation Q and the local rate of heat transfer Nu_x decreased slightly as the value of magnetic parameter M increased at different positions. The velocity distribution decreased slightly as the magnetic parameter M increased, but near the surface of the sphere velocity increased and became maximum and then decreased and finally approached to zero.

[Filar et.al., 2005] computed numerically three-dimensional convection of air inside a vertical cylinder isothermally heated and cooled from a side wall for both magnetic and gravity fields. A single electric coil was placed around the cylinder to generate a magnetic field. Convection was calculated for various coil level and magnetic strengths. The results indicated that effect of Magneto hydrodynamic increased and lead to increase the rate of heat transfer and this is clear at higher values of Rayleigh number and both coil elevation and Rayleigh number affect the heat transfer rate extensively. The maximum Nusselt number could be obtained for the coil located at about half of cylinder.

In the present study, the magneto hydrodynamic, effect was investigated for steady state laminar natural convection external flow with presence of heat generation and radiation on a vertical cylinder, for thermal boundary condition of constant wall temperature and for ($10^2 \leq Ra_l \leq 10^5$), ($0 \leq M \leq 1.0$), ($0 \leq Q \leq 2.0$) and ($0 \leq N \leq 10$).

To the best of our knowledge there is no previous work was found that studies the case of external flow on a cylinder taking the effect of MHD and the effect of all the parameters gathered a comparison was done between the result of the present study for the variation of Nu with Ra_l and the correlation of **[Mc Adams, 1954]** with deviation of 5% for the case of no

MHD, radiation and heat generation and another comparison between the present study and the work of **[Ganesan, 2002]** with and without radiation and for no MHD and no heat generation which gives a deviation of 1.7% with radiation and 1.5% without radiation..

MATHEMATICAL MODEL

The mathematical modeling will be set for laminar natural convection heat transfer on a vertical cylinder. The buoyancy effect caused by the density variation produces natural circulation resulting in the fluid motion relative to the bounding solid surface. The buoyancy forces behave as body forces and are included as such in the momentum equation. Under these conditions the continuity, momentum and energy equations are coupled.

The density is considered as linear function of temperature so that the usual Boussinesq's approximation is taken as **[Singh and Ajay, 2003]**:

$$\rho = \rho_o \left(1 - \beta \left[T - T_\infty \right] \right) \qquad (1)$$

$$g_r = 0 \qquad (2)$$

$$g_z = g\beta (T - T_\infty) \qquad (3)$$

Continuity Equation

The equation of conservation of mass in the cylindrical coordinates is given as:

$$\frac{1}{r}\frac{\partial}{\partial r}(r\,u) + \frac{\partial w}{\partial z} = 0 \qquad (4)$$

Momentum Equation

By using Navier-Stokes' equation in the cylindrical coordinates (r, z), the equation of conservation of momentum in the cylindrical coordinates (the radial (r) direction) is in the following form:

$$u\frac{\partial u}{\partial r} + w\frac{\partial u}{\partial z} = -\frac{1}{\rho}\frac{\partial P^*}{\partial r} + \nu\left(\frac{\partial}{\partial r}\left[\frac{1}{r}\frac{\partial}{\partial r}(ru) \right] + \frac{\partial^2 u}{\partial z^2} \right) + f_r \qquad (5)$$

Where (f_r) is the electromagnetic force in (r) direction **[Branover, 1978]**:

$$f_r = \frac{\sigma_o B_o^2 u}{\rho} \qquad (6)$$

The equation of conservation of momentum in the cylindrical coordinates (in the axial (z) direction) is in the following form:

$$u\frac{\partial w}{\partial r} + w\frac{\partial w}{\partial z} = -\frac{1}{\rho}\frac{\partial P^*}{\partial z} + \nu\left(\frac{1}{r}\frac{\partial}{\partial r}\left[r\frac{\partial w}{\partial r} \right] + \frac{\partial^2 w}{\partial z^2} \right) + g\beta(T - T_\infty) + f_z \qquad (7)$$

Where (f_z) is the electromagnetic force in (z) direction **[Branover, 1978]**:

$$f_z = \frac{\sigma_o B_o^2 w}{\rho}$$

Energy Equation

The energy equation in the cylindrical coordinates takes the following form:

$$u\ \frac{\partial T}{\partial r} + w\ \frac{\partial T}{\partial z} = \alpha \left(\begin{array}{l} \frac{1}{r}\frac{\partial}{\partial r}\left[r\ \frac{\partial T}{\partial r} \right] + \\ \frac{\partial^2 T}{\partial z^2} \end{array} \right) + \frac{q'''}{\rho\ cp} - \frac{1}{\rho\ cp}\frac{1}{r}\frac{\partial}{\partial r}\left(r\ q_r \right) \quad (8)$$

The volumetric rate of heat generation is given as:

$$q''' = Q_o(T - T_\infty) \quad (9)$$

Where Q_o is the heat generation/absorption and is a constant. **[Molla, 2005].**
The radiative heat flux q_r is given as: **[Brewster, 1992]**.

$$q_r = -\frac{4\sigma \partial T^4}{3K^* \partial r} \quad (10)$$

Where (K^*) is the mean absorption coefficient and (σ) is the Stefan-Boltzmann constant.

DIMENSIONLESS PARAMETERS AND EQUATIONS

$$\left(R = \frac{r}{l} \right), \left(Z = \frac{z}{l} \right), \left(U = \frac{u\ l}{\alpha} \right), \left(W = \frac{w\ l}{\alpha} \right), \left(\theta = \frac{T - T_\infty}{T_w - T_\infty} \right), \left(P = \frac{p l^2}{\rho\ \alpha^2} \right) \left(Q = \frac{Q_o l^2}{\rho cp\ \alpha} \right), \left(N = \frac{K^*\ K}{4\sigma T_\infty^3} \right), \left(M = \frac{\sigma_\circ B_\circ^2 l^2}{\rho\alpha} \right),$$

Dimensionless Continuity Equation

$$\frac{1}{R}\frac{\partial (RU)}{\partial R} + \frac{\partial W}{\partial Z} = 0 \quad (11)$$

Dimensionless Momentum Equation In (r) Direction

$$U\ \frac{\partial U}{\partial R} + W\ \frac{\partial U}{\partial Z} = -\frac{\partial P}{\partial R} + \Pr\left(\begin{array}{l} \frac{\partial}{\partial R}\left(\frac{1}{R}\frac{\partial (R\,U)}{\partial R} \right) + \\ \frac{\partial^2 W}{\partial\ Z^2} \end{array} \right) + MU \quad (12)$$

Dimensionless Momentum Equation In (z) Direction

$$U\ \frac{\partial W}{\partial R} + W\ \frac{\partial W}{\partial Z} = -\frac{\partial P}{\partial Z} + \Pr\left(\frac{1}{R}\frac{\partial}{\partial R}\left(R\frac{\partial W}{\partial R} \right) + \frac{\partial^2 W}{\partial\ Z^2} \right) + \Pr\ Ra_l\ \theta + MW \quad (13)$$

Dimensionless Energy Equation

$$U\frac{\partial\theta}{\partial R}+W\frac{\partial\theta}{\partial Z}=\left(1+\frac{4}{3N}\right)\left[\frac{1}{R}\frac{\partial}{\partial R}\left(R\frac{\partial\theta}{\partial R}\right)\right]+\frac{\partial^2\theta}{\partial Z^2}+Q\theta \quad (14)$$

Vorticity Transport, Stream Function and Energy Equations

The governing equations in dimensionless form above were written in terms of dependant variables (U, W, P and θ). It may be recommended to eliminate pressure term (because it will be a non linear term in momentum equation) **[Patanker, 1980]**. By converting momentum equations to vorticity transport equation by differentiate momentum equation in (r) direction with respect to (z) and momentum equation in (z) direction with respect to (r) and subtract them from each other and make use of continuity equation and vorticity definition:

$$\omega=\frac{\partial W}{\partial R}-\frac{\partial U}{\partial Z} \quad (15)$$

$$\frac{\partial(U\omega)}{\partial R}+\frac{\partial(W\omega)}{\partial Z}=\Pr Ra_1\frac{\partial\theta}{\partial R}+M\omega+\Pr\left(\frac{\partial}{\partial R}\left(\frac{1}{R}\frac{\partial(R\omega)}{\partial R}\right)+\frac{\partial^2\omega}{\partial Z^2}\right) \quad (16)$$

Also, by use of vorticity definition (15) and the definition of stream function, (ψ) which satisfy continuity equation, the vertical and radial velocities can be written as follows respectively:

$$W=-\frac{1}{R}\frac{\partial\psi}{\partial R} \quad (17)$$

$$U=\frac{1}{R}\frac{\partial\psi}{\partial Z} \quad (18)$$

So by substituting the velocity components (17) and (18) in equation (15), stream function equation resulted as:

$$-\omega=\frac{1}{R}\left(\frac{\partial^2\psi}{\partial R^2}-\frac{1}{R}\frac{\partial\psi}{\partial R}+\frac{\partial^2\psi}{\partial Z^2}\right)=\nabla^2\psi \quad (19)$$

The dimensionless energy equation (14) can be transformed to another form by substituting the continuity equation (11) in it as follows:

$$\frac{1}{R}\frac{\partial(RU\theta)}{\partial R}+\frac{\partial(W\theta)}{\partial Z}=\left(1+\frac{4}{3N}\right)\left[\frac{1}{R}\frac{\partial}{\partial R}\left(R\frac{\partial\theta}{\partial R}\right)\right]+\frac{\partial^2\theta}{\partial Z^2}+Q\theta \quad (20)$$

Boundary Conditions;

The imposed boundary conditions (illustrate in **Fig. (1)** and **Table (1)**), rewritten in terms of stream function and vorticity

(No slip condition)

$$\omega = \psi = U = W = 0$$

$\theta = 1$ (Constant wall temperatures)

NUMERICAL SOLUTION

The method of the numerical solution taken is the Finite Difference technique for solving the set of equations**[Patanker, 1980]**.

$$a_1\theta_{i-1,j} + a_2\theta_{i+1,j} + a_3\theta_{i,j} + a_4\theta_{i,j-1} + a_5\theta_{i,j+1} = 0 \quad (21)$$

Where:

$$a_1 = \frac{\left(U_b + |U_b|\right)\left(\Delta R(1-2i) - R_i\right)}{4\Delta R\left(R_i + i\Delta R\right)} + \left(1 + \frac{4N}{3}\right)\left(-\frac{1}{(\Delta R)^2} + \frac{1}{2\Delta R\left(R_i + \Delta R\right)}\right) \quad (22)$$

$$a_2 = \frac{\left(U_f - |U_f|\right)\left(R_i + \Delta R(1+2i)\right)}{4\Delta R\left(R_i + i\Delta R\right)} - (1 + \frac{4}{3N})(\frac{1}{\Delta R^2} + \frac{1}{2\Delta R(R_i + \Delta R)}) \quad (23)$$

$$a_3 = -Q + \frac{\left[\left(U_f + |U_f|\right)\left(R_i + \Delta R(1+2i)\right) + \left(U_b - |U_b|\right)\left(\Delta R(1-2i) - R_i\right)\right]}{4\Delta R\left(R_i + i\Delta R\right)} + \frac{\left(W_f + |W_f| - W_b + |W_b|\right)}{2\Delta Z} + \frac{2}{(\Delta R)^2} + \frac{2}{(\Delta Z)^2} \quad (24)$$

$$a_4 = \frac{\left(-W_b + |W_b|\right)}{2\Delta Z} - \frac{1}{(\Delta Z)^2} \quad (25)$$

$$a_5 = \frac{\left(W_f - |W_f|\right)}{2\Delta Z} - \frac{1}{(\Delta Z)^2} \quad (26)$$

$$b_1\omega_{i-1,j} + b_2\omega_{i+1,j} + b_3\omega_{i,j} + b_4\omega_{i,j-1} + b_5\omega_{i,j+1} + c = 0 \quad (27)$$

Where:

$$b_1 = -\frac{\left(U_b + |U_b|\right)}{2\Delta R} + \frac{1}{2\Delta R\left(R_i + i\Delta R\right)} - \frac{1}{(\Delta R)^2} \quad (28)$$

$$b_2 = \frac{\left(|U_f| - U_f\right)}{2\Delta R} - \frac{1}{2\Delta R\left(R_i + i\Delta R\right)} - \frac{1}{(\Delta R)^2} \quad (29)$$

$$b_3 = -M + \frac{\left[\left(U_f + |U_f|\right) - \left(U_b + |U_b|\right)\right]}{2\Delta R} + \frac{\left(W_f + |W_f| - W_b + |W_b|\right)}{2\Delta Z} + \frac{2\,\mathrm{Pr}}{(\Delta R)^2} + \frac{2\,\mathrm{Pr}}{(\Delta Z)^2} + \frac{\mathrm{Pr}}{\left(R_I + i\Delta R\right)^2} \quad (30)$$

$$b_4 = -\frac{\left(W_b + |W_b|\right)}{2\Delta Z} - \frac{\mathrm{Pr}}{(\Delta Z)^2} \quad (31)$$

$$b_5 = \frac{\left(W_f - |W_f|\right)}{2\Delta Z} + \frac{\mathrm{Pr}}{(\Delta Z)^2} \quad (32)$$

$$c = -\frac{\Pr Ra\left(\theta_{i+1,j} - \theta_{i-1,j}\right)}{2\Delta R} \tag{33}$$

$$\psi_{i,j}^{\,it+1} = (1-\Omega)\psi_{i,j}^{\,it} + \frac{\Omega}{4}\left[\begin{array}{l}\left(R_i + i\Delta R\right)\left(\Delta R\right)^2 \omega'_{i,j} + \\ \left(\frac{R_i + \Delta R(i-0.5)}{\left(R_i + i\Delta R\right)}\right)\psi_{i+1,j}^{\,it} \\ \left(\frac{R_i + \Delta R(i+0.5)}{\left(R_i + i\Delta R\right)}\right)\psi_{I-1,J}^{\,it+1} + \\ \left(\psi_{i,j+1}^{\,it+1} + \psi_{i,j-1}^{\,it+1}\right)\end{array}\right] \tag{34}$$

Where the parameter (Ω) is the over relaxation coefficient and its value is $(1 \le \Omega \le 1.5)$.

The local Nusselt number at the heated wall:

$$Nu_l = -\left(\frac{\partial\theta}{\partial R}\right) \tag{35}$$

The average Nusselt number along a single channel wall is defined by**[Schwab,1970]**:

$$N\bar{u} = -\frac{1}{l}\int_0^l Nu\ dZ \tag{36}$$

The overall heat transfer can be calculated by:

$$Q = 2\pi\ N\bar{u} \tag{37}$$

RESULTS AND DISCUSION

Effect of Different Parameters on Heat Transfer.

Streamlines and Isotherms.

Fig.(2a and b) show the streamlines and isotherms for different values of Ra_l without radiation, heat generation and magneto hydrodynamic (MHD). The mechanism of the flow occurs when the fluid near the hot wall is heated causing the density to be decreased and the fluid will be start to move upward nearby the hot wall towards the cold wall. It can be seen that the values of streamlines and isotherms at the cylinder surface increased when Ra_l increased. The isotherms will be closer to the cylinder and its value decreased from the surface to the ambient as Ra_l increased.
Fig. (3) and **Fig.(4)** show the effect of radiation for different values of Ra_l and with no heat generation and MHD. It is clear that the increase of radiation cause a distinct increase in the values of streamlines and a wide region of temperature distribution in the lateral direction for Ra_l (10^2) but for higher Ra_l the region of temperature distribution will be decreased and the streamlines will be closer to the cylinder.
A slight increase in streamlines and isotherms are shown in **Fig. (5)** and **Fig. (6)** when MHD increases for different values of Ra_l for the case of no radiation and heat generation. The flow exhibits a simple circulating pattern rising a long the hot wall and descending along the cold wall of the cavity. It is interesting to note that as the strength of the magnetic field increases the central streamlines are elongated horizontally and the temperature stratification in the core diminishes. The isotherms are almost parallel and are nearly conduction like and this is due to the suppression of convection by the magnetic field. For higher Rayleigh number and low MHD, the thermal boundary layers are well established along the side walls and the temperature stratification exists. This is because convection is the dominant mode of heat transfer at high Rayleigh number. From these figures, it is also observed that for higher Rayleigh number the effect of MHD on the temperature distribution is not prominent compared to that in the case of small Ra_l.

The Variation of Mean Nu with Ra_l.

The variation of total mean Nusselt number Nu with Ra_l is shown in **Fig.(7a)** with and without radiation for no heat generation and MHD. The increase of Nu is very clear when radiation effect is included and it is about 18%.
The variation of total mean Nusselt number Nu with Ra_l is shown in **Fig.(7b)** with and without heat generation for no radiation and MHD. The increase in Nu when the effect of heat generation is included and it is about 2.68 % for $Ra = 10^2$ and this percent continued until $Ra > 10^4$ then decreased and the curves coincides.
Fig.(7c) shows the variation of total mean Nu with Ra_l with and without MHD for no radiation and heat generation. The increase in Nu by 0.2% with MHD included is insignificant and the curves seem to be coincides.

The Effect of MHD on Nu Including Other Parameters

Fig.(8 a and b) show the variation of Nu with MHD for different values of Ra_l and heat generation with no radiation. When heat generation included the effect of MHD increased and cause to increase the rate of heat transfer and this is clear at higher values of Ra_l but for the situation of

applying radiation, Nu increase as the heat generation and Ra_l increase but MHD has no effect.

Fig.(9 a and b) show the variation of Nu with MHD for different values of Ra_l and heat radiation with no heat generation. For all values of Ra_l the effect of heat radiation to increase the rate of heat transfer when MHD increase.

The Variation of Dimensionless Temperature with Cylinder Radius.

Fig.(10a, b and c) shows variation of dimensionless temperature with R at center length of cylinder Z=0.5 and $Ra_l = 10^3$. **Fig (10a)** shows the effect of heat radiation on dimensionless temperature at no Q and MHD where increasing the value of heat radiation increase the dimensionless temperature and maximum increases at R=0.916 by 32.4% as N increases from 0.0 to 10.0. **In Fig (10b)** the effect of heat generation Q on dimensionless temperature is shown for no MHD and N. increasing the value of heat generation increase the dimensionless temperature and maximum increases at R=0.713 by 18.48% as Q increases from 0.0 to 2.0. **Fig (10c)** shows the effect of MHD on dimensionless temperature for no Q and N where the increase of MHD cause to increase the dimensionless temperature and maximum increases at R=0.651 by 11.83% as M increases from 0.0 to 1.0.

The Variation of Dimensionless Velocity profile with Cylinder Radius

Fig.(11a, b and c) shows the variation of velocity profiles with R at center length of cylinder Z=0.5 and $Ra_l = 10^3$. **Fig. (11a)** shows that the velocity profile is influenced considerably and increase when the value of the heat generation Q increases. But near the surface of the cylinder velocity increases significantly and then decreases slowly. The maximum values of the velocity are 0.652, 0.743, and 0.805 for Q=0.0, 1.0, and 2.0 respectively which occur at R=0.248, here it is observed that the velocity increases by 24.48% as Q increases from 0.0 to 2.0. In **Fig (11b)** the velocity distribution decrease slightly as the magnetic parameter M=(0.0,0.5,1.0), increase in the region $R \in \{0,2\}$ but near the surface of the cylinder velocity increases and become maximum and then decreases slowly to the end of the cylinder. The maximum value of the velocity are 0.652, 0.581, and 0.4808 for M=0.0, 0.5 and 1.0 respectively which occur at R=0.25, here the velocity decrease by 35.6% as M increases from 0.0 to 1.0. **Fig.(11c)** shows that the velocity profile is influenced considerably and increases when the value of heat radiation parameter N increases. But near the surface of the cylinder velocity increases significantly and then decreases slowly to the end of the cylinder. The maximum values of the velocity are 0.652, 0.252, and 0.154 for N=0.0, 5.0, and 10.0 respectively which occur at R=0.249, here it is observed that the velocity increases by 89.52% as N increases from 0.0 to 10.0.

A correlation has been set up to give the average Nusselt number variation with Ra, M and N and Q. This correlation is made by using the computer program (DGA v1.00).

$$Nu = 4.775\,Ra^{0.0575} + 0.0046\,M^{0.973} + 0.0346\,N^{1.487} +$$

For $Ra=10^5$ the correlation equation become.

$$Nu = 4.775\,Ra^{0.0575} + 0.013\,M + 0.0745\,N^{1.42} + 0.04\,Q$$

COMPARISON OF THE RESULTS

To the best of our knowledge there is no previous work studied the case of external flow on a cylinder taking the effect of MHD. A comparison was done between the result of the present study for the variation of Nu with Ra_l and the correlation of **(Mc Adams, 1954)** which is shown in **Fig.(12)** with a deviation of 5% for the case of no MHD, radiation and heat generation.

Fig.(13) shows a comparison between the present study and the work of **[Ganesan, 2002]** with and without radiation and for no MHD and no heat generation which shows an increase of Nu with Ra_l for a deviation of 1.7% with radiation and 1.5% without radiation. The results for all the previous figures show good agreement with other researches.

CONCLUSIONS

From the results of the present work and for the cylinder that described previously, the following conclusions can be obtained:

1. The totals mean Nusselt number (Nu) increases by 53.5% with the increase of Rayleigh number (Ra_l) from 10^2 to 10^5.
2. The totals mean Nusselt number (Nu) increases by 18 % with the increase of radiation parameter (N) from 0 to 10.
3. The total mean Nusselt number Nu increases by 0.2 % with increase MHD parameter M from 0 to 1.
4. The totals mean Nusselt number (Nu) increases by 2.68% with the increase of heat generation parameter (Q) from 0 to 2.
5. Dimensionless temperature θ increases by 18.48 % with increase heat generation parameter Q from 0 to 2 at R=0.5.
6. Dimensionless temperature (θ) increases by 11.83 % with the increase of (MHD) parameter (M) from 0 to 1 at R=0.5.
7. Dimensionless temperature (θ) increases by 32.4 % with the increase of radiation parameter (N) from 0 to 10 at R=0.5.
8. When Rayleigh number (Ra) increase the effect of MHD, radiation and heat generation decrease on total mean Nusselt number (Nu).

REFERENCES

Branover Herman, (1978), "Magneto hydrodynamic Flow in Ducts", The MIT Cambridge, Massachusetts, and London, England.

Brewster M.Q., (1992), "Thermal Radiative Transfer and Properties", John Willey & Sons. Inc., New York.

Filar P., Fornalik E. and Kaneda M., 2005 "Three Dimensional Numerical Convection of Air Inside a Cylinder Heated and Cooled Isothermally from a Side Wall", Int. J. Heat and Mass Transfer. Vol. 48, pp. 1858-1867.

Ganesan P., and Loganathan P., (2002) "Radiation and mass transfer effects on flow of an incompressible viscous fluid past a moving vertical cylinder", Int. J. Heat and Mass Transfer. Vol. 45. pp. 4281-4288.

Mc Adms, W. H. , (1954) "Heat Transmission", 3d ed. McGrew-Hill Book Company, New York.

Molla1 Md. M., Taher1 M.A., Chowdhury1 Md. M.K. and Hossain Md. A., (2005), "Magneto hydrodynamic Natural Convection

Flow on a Sphere in Presence of Heat Generation ", Int. J. Heat and Mass Transfer. Vol. 10, No. 4, 349–363.

Patanker, S. V., (1980) "Numerical Heat Transfer and Fluid Flow", Series In Computational Methods, McGraw-Hill, 1st Edition.

Schwab, T. H., and De Witt, K. J., (1970) "Numerical Investigation of Free Convection between Two Vertical Coaxial Cylinders", AICHE J., Vol. 16, pp.1005-1010.

Singh N. P. and Ajay Kumar Singh, 2003 "MHD Free Convection and Mass Transfer Flow Past a Flat Plate" the Arabian Journal for Science and Engineering, Vol. 32, number 1A .

Table (1) Boundary Conditions

Line	Θ	ψ	ω	W,U
AB	$\frac{\partial\theta}{\partial R}=0$	0.0	0.0	0.0
BC	1.0	0.0	$\omega=-\frac{1}{Z}\frac{\partial^2\psi}{\partial R^2}$	0.0
CD	1.0	0.0	$\omega=-\frac{1}{R}\frac{\partial^2\psi}{\partial Z^2}$	0.0
DE	1.0	0.0	$\omega=-\frac{1}{Z}\frac{\partial^2\psi}{\partial R^2}$	0.0
EF	$\frac{\partial\theta}{\partial R}=0$	0.0	0.0	0.0
FG	0.0	$\frac{\partial\psi}{\partial Z}=0$	0.0	0.0
GH	0.0	$\frac{\partial\psi}{\partial R}=0$	0.0	0.0
HA	$\frac{\partial\theta}{\partial Z}=0$	$\frac{\partial\psi}{\partial Z}=0$	0.0	0.0

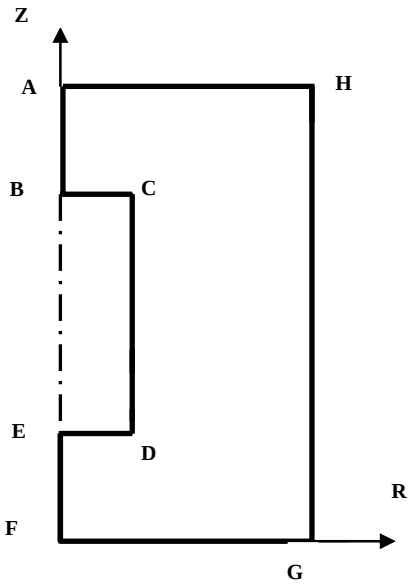

Fig. (1) Boundary condition of the problem

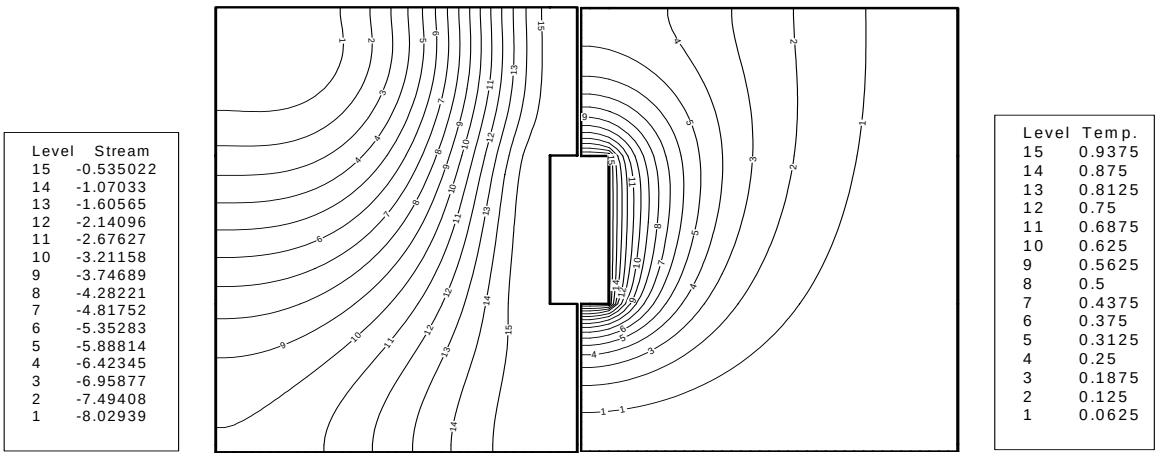

Fig. (2a) Streamlines and isotherm for $Ra_l=10^2$, M=0 , N=0 , Q=0

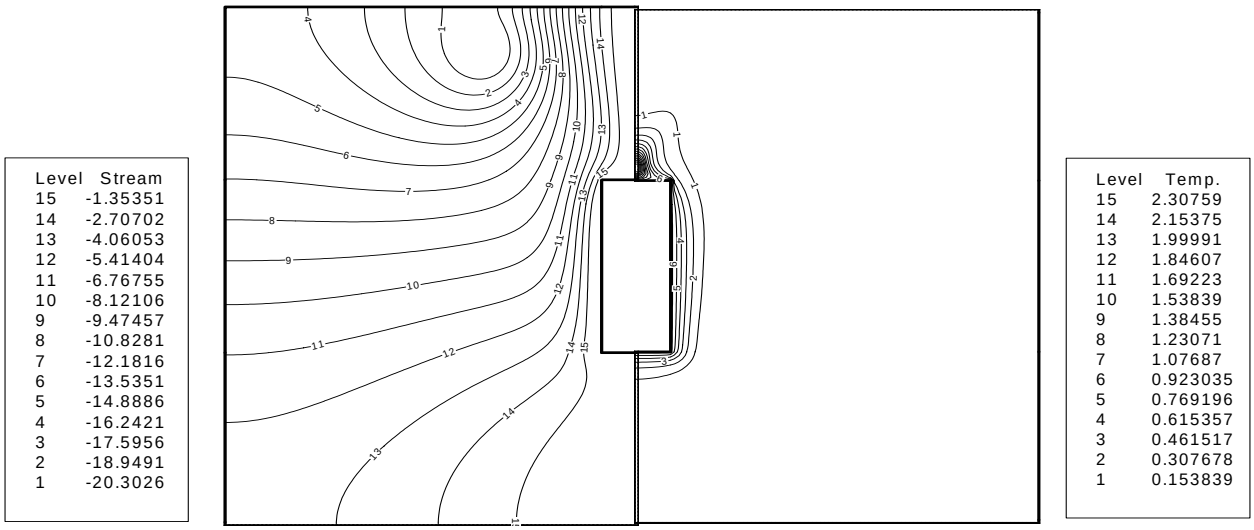

Fig. (2b) Streamlines and isotherm for $Ra_l = 10^5$, M=0 , N=0 , Q=0

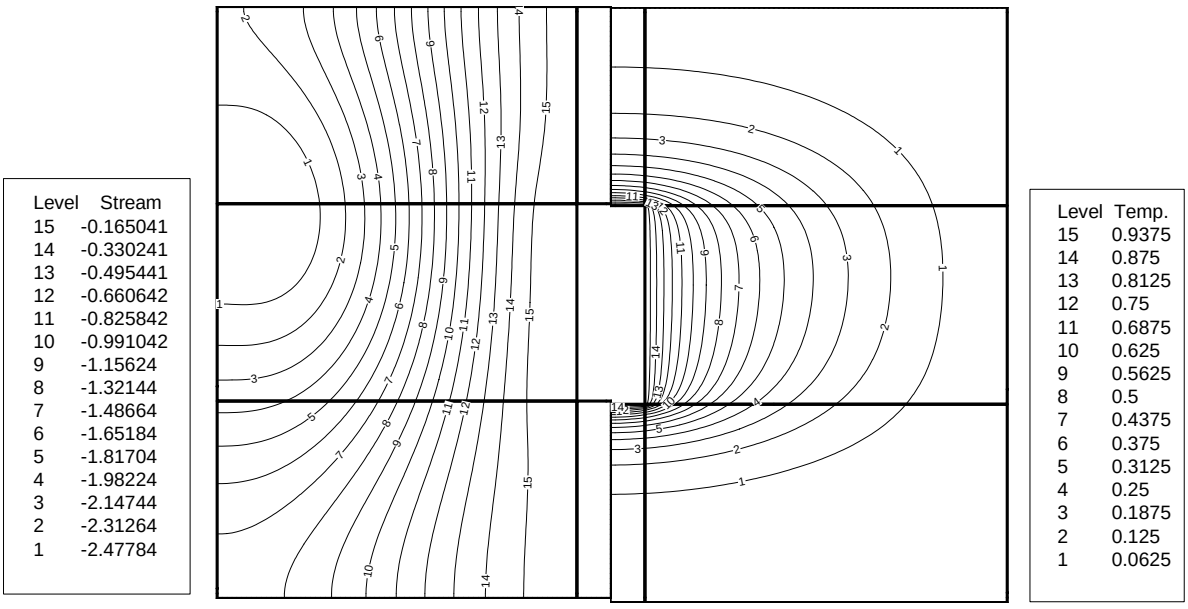

Fig. (3) Streamlines and isotherm for $Ra_l = 10^2$, M=0 , N=5 , Q=0

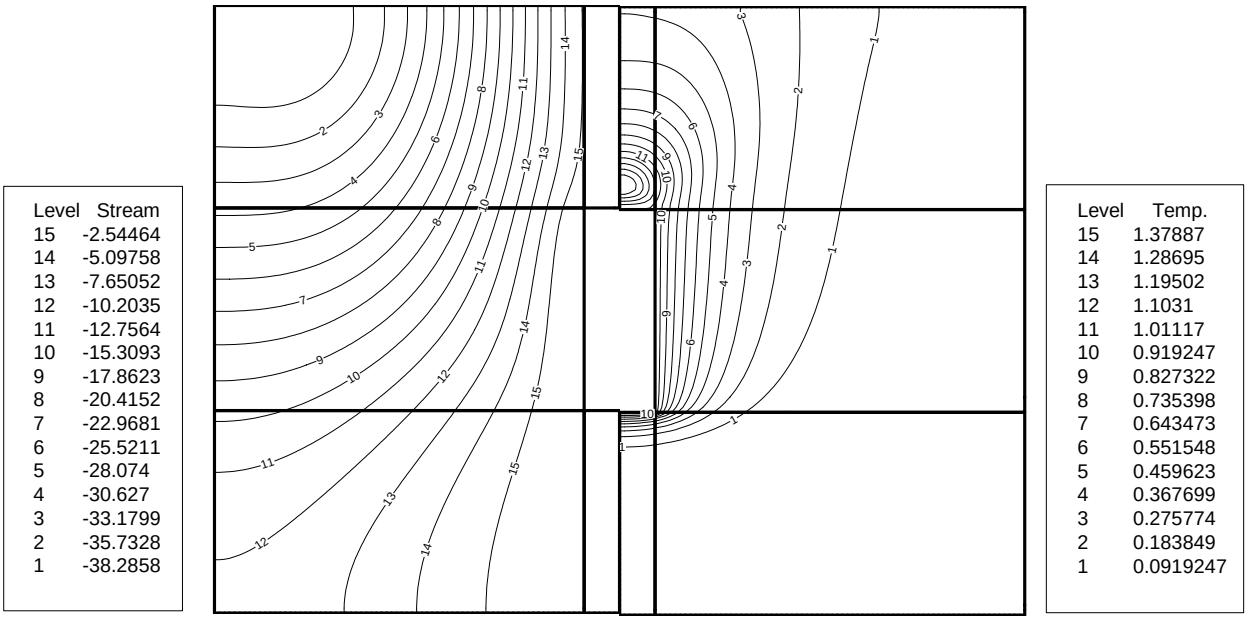

Fig. (4) Streamlines and isotherm for $Ra_l = 10^4$, M=0 , N=5 , Q=0

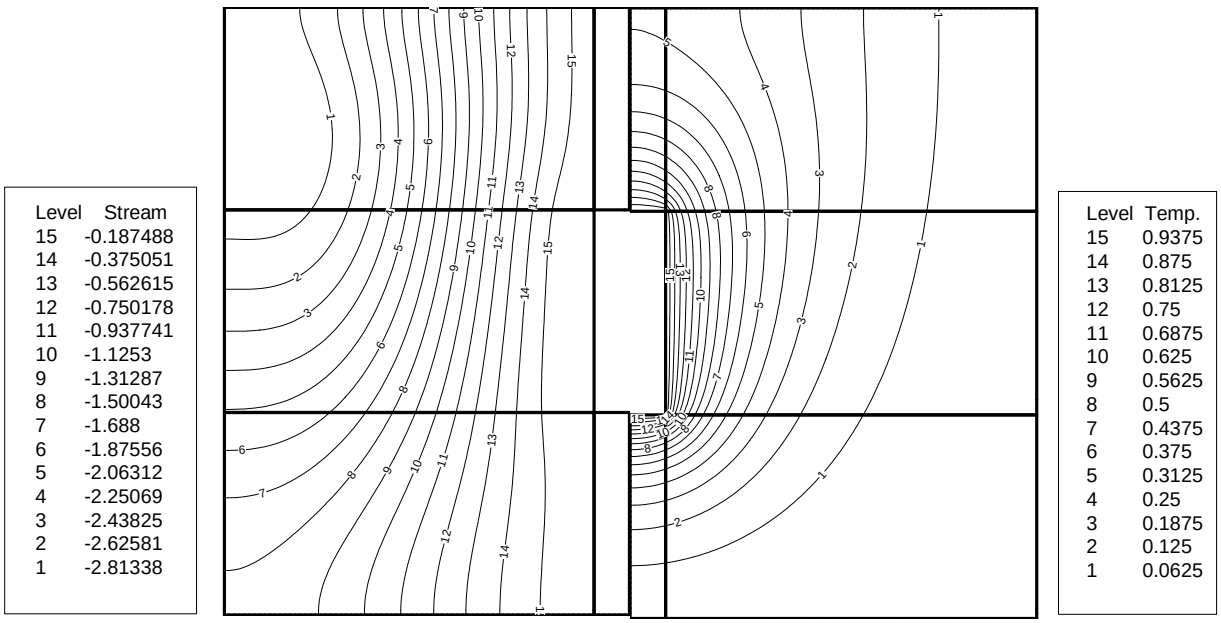

Fig. (5) Streamlines and isotherm for $Ra_l = 10^2$, M=1, N=0 , Q=0

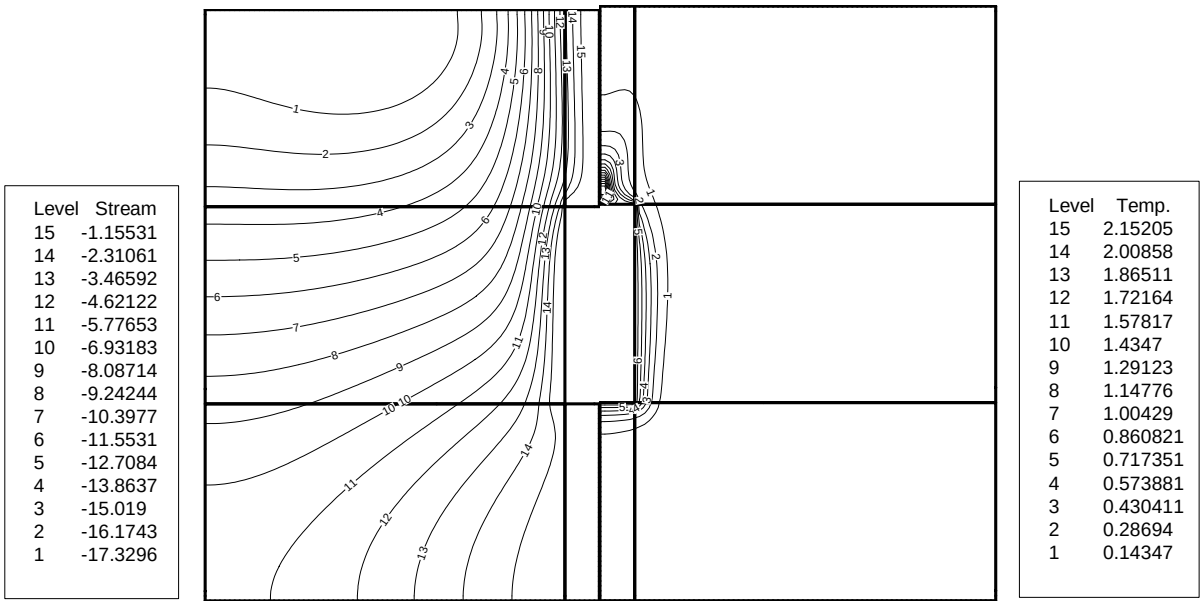

Fig. (6) Streamlines and isotherm for $Ra_l = 10^5$, M=1, N=0 , Q=0

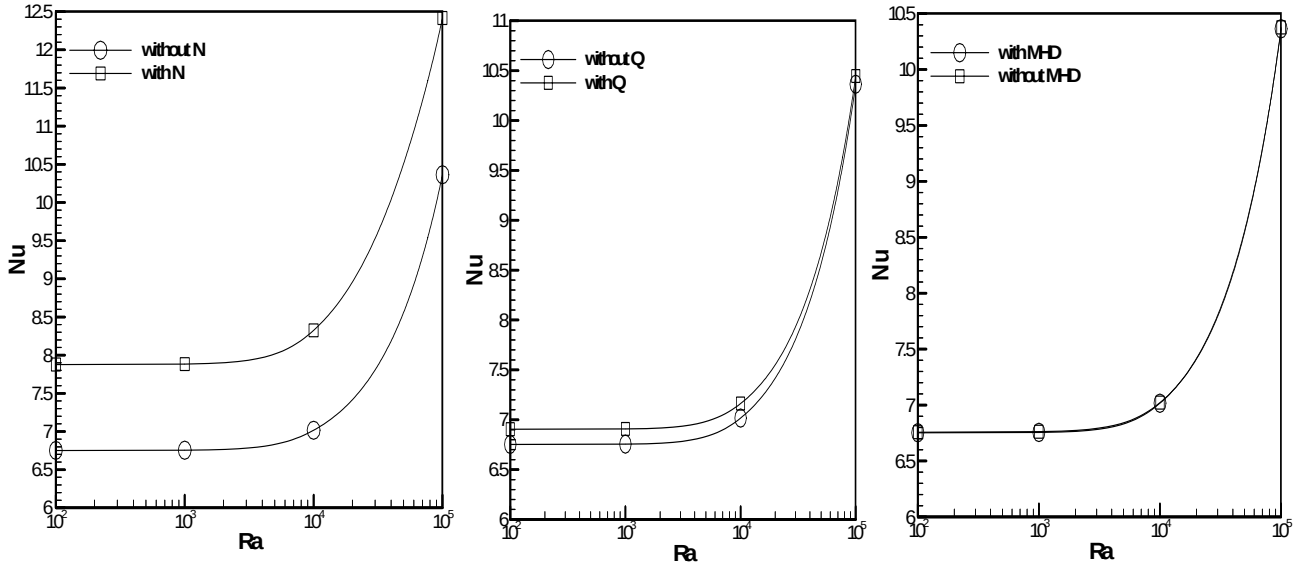

(a) (b) (c)

Fig. (7) Variation of total mean Nusselt number with Rayleigh number

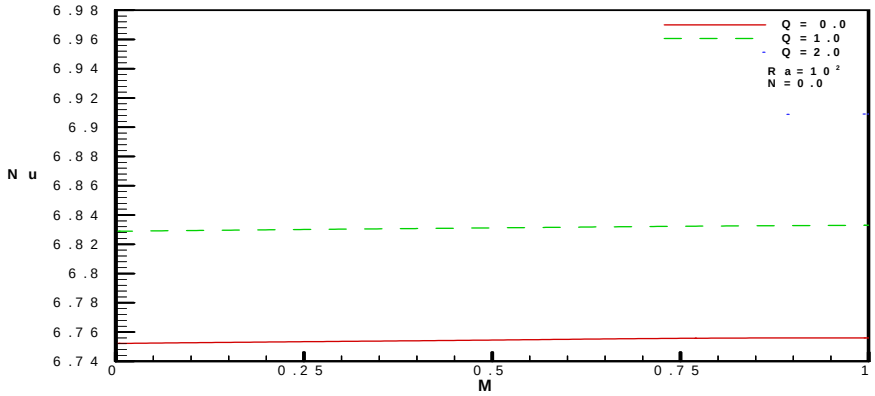

a. ($Ra_l=10^2$)

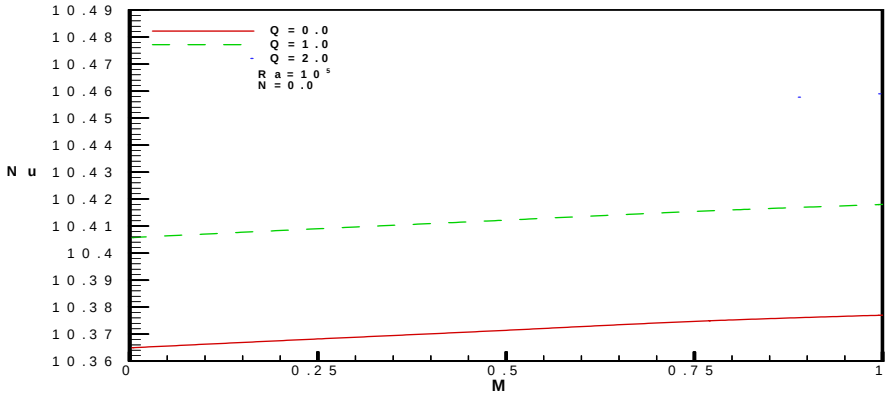

b. ($Ra_l=10^5$)

Fig (8) The variation of Nu with MHD for different values of Ra and Q

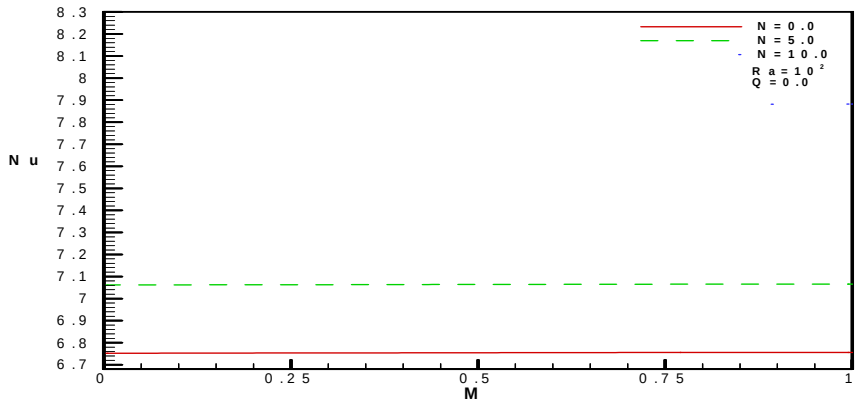

a. ($Ra_l=10^2$)

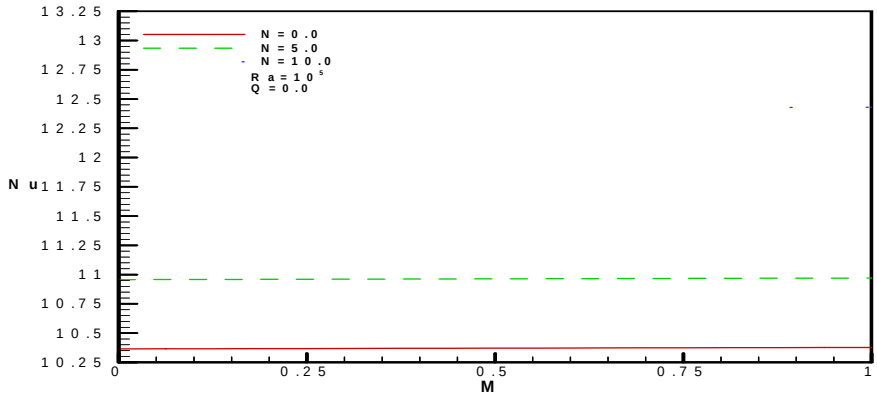

b. ($Ra_l=10^5$)

Fig (9) The variation of Nu with MHD for different values of Ra_l and N

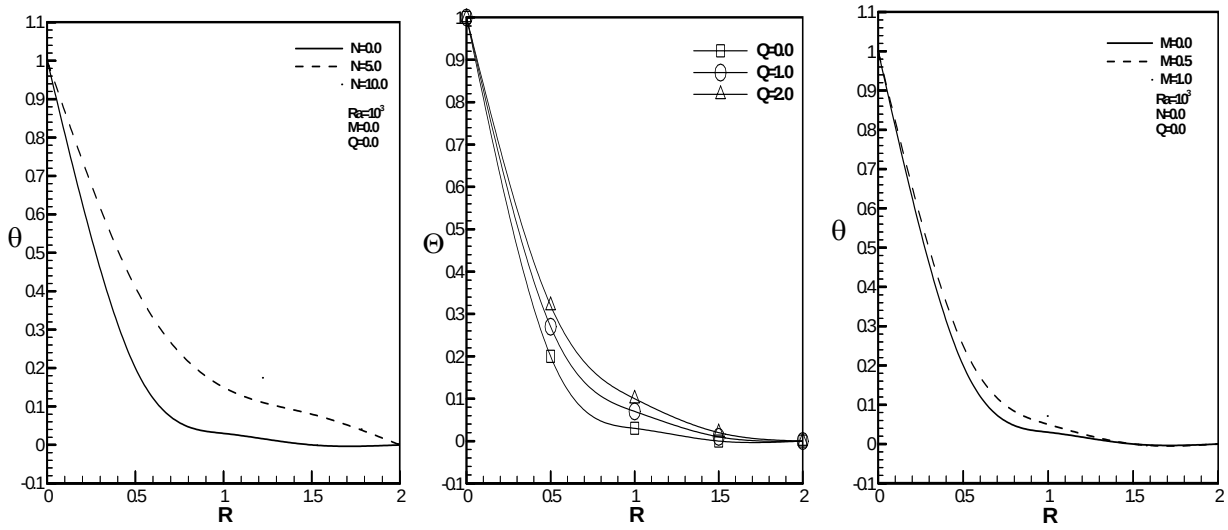

(a) (b) (c)

Fig. (10) Variation of dimensionless temperature with R at z =0.5, $Ra_l=10^3$

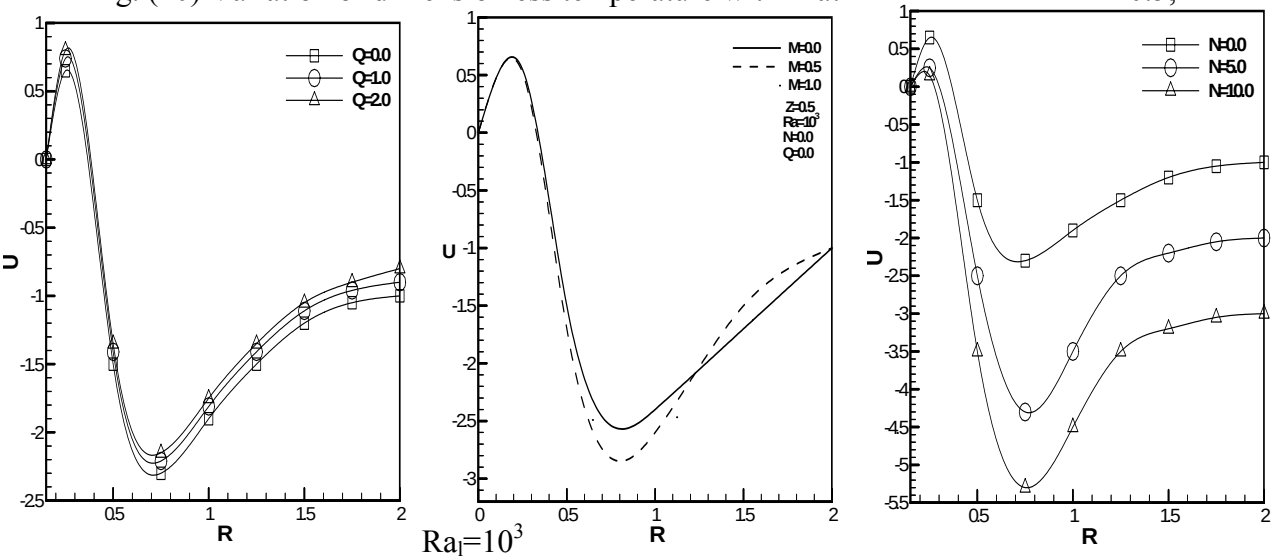

(a) (b) (c)

Fig. (11) Variation of velocity profiles with R at z =0.5, $Ra_l=10^3$

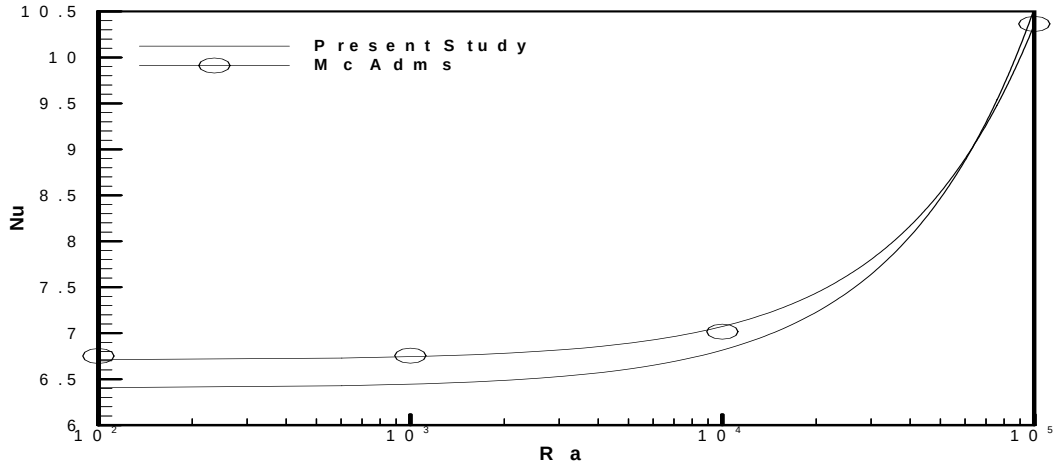

Fig. (12) Comparison of the present work with **[Mc Adam, 1954]**

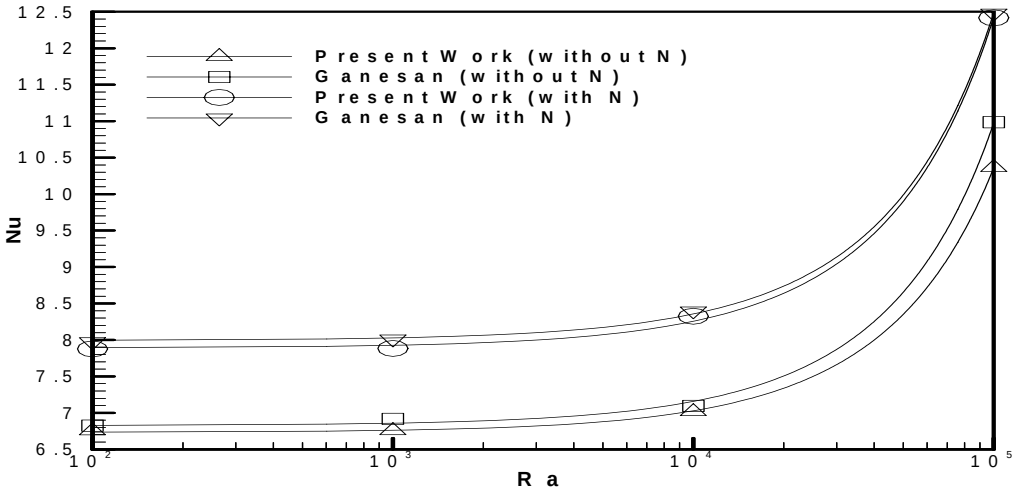

Fig. (13) Comparison of the present work with **[Ganesan, 2002]**

NOMENCLATUR

LATIN SYMBOLS

Symbol	Description	Unit
Cp	Specific heat at constant pressure	kJ/kg.K
f_r	Electromagnetic force in (r) direction	m/s^2
f_z	Electromagnetic force in (z) direction	m/s^2
g	Acceleration due to gravity	m/s^2
h	Heat transfer coefficient	$W/m^2.^oC$
i	R-direction directory	-
j	Z-direction directory	-
K	Thermal conductivity	$W/m.^oC$
K^*	Mean absorption coefficient	m^{-1}
l	Length of cylinder	m
M	Dimensionless Magneto hydrodynamic parameter	-
n	Indicate the unit vactor	m
N	Dimensionless Conduction-Radiation parameter	-
Nu	Average Nusselt number(Nu=hl/k)	-
P^*	Air pressure	N/m^2
P	Normalized air pressure	-
Pr	Prandtl number(Pr=ν/α)	-
q_r	Radiative heat flux	W
q	Overall heat transfer	W
Q	Dimensionless overall heat generation	-
Q_o	Heat generation/absorption	$W/m^3.^oC$
q'''	Volumetric heat generation	W/m^3
r	Radial direction	m
R	Dimensionless Radial direction	-
Ra_l	Rayleigh no. $\left(Ra_l = \frac{\Pr g \beta (T_w - T_\infty) l^3}{\nu^2} \right)$	-
T	Air temperature	K
T_∞	Ambient temperature	K
u	Radial velocity	m/s
U	Dimensionless Radial velocity	-
w	Vertical velocity	m/s
W	Dimensionless Vertical velocity	-
X	Nodes number in r-direction	-
Y	Nodes number in z-direction	-
z	Vertical direction	m
Z	Dimensionless Vertical direction	-

CREAK SYMBOLS

Symbol	Description	Unit
α	Thermal diffusivity	m^2/s
β	Coefficient of thermal expansion	K^{-1}
ε	Emissivity	-
θ	Dimensionless temperature	-
λ	Radii ratio	-
μ	Viscosity	kg/m.s
ν	Kinematics' viscosity	m^2/s
ρ	Air density	kg/m^3
σ	Stefan-Boltzmann constant	$W/m^2.K^4$
ψ	Dimensionless stream function	-
ω	Dimensionless vorticity	-

Subscript

Symbol	Description	Unit
(i,j)	Grid nodes in (r,z) direction	-

SOLAR WATER HEATER WITH SHELL AND HELICAL COILED TUBE HEAT EXCHANGER AS A STORAGE TANK

Dr. Karima E. Amori* **Dr. Faiz F. Mustafa**** **SAHAR MAJEED***
*Mech. Eng. Dep., Univ. of Baghdad **Manufacturing Dept. ,Al-Khwarizmi Engineering Univ.

ABSTRACT

In this work an experimental study is performed to evaluate the thermal performance of locally made closed loop solar hot water system using a shell and helical coiled tube heat exchanger as a storage tank. Several measurements are taken include inlet and outlet temperatures of both collectors and supply water and temperature distribution within the storage tank. This is beside the water flow rate in both collectors and load cycle. The main parameters of the system are obtained.

.

الخلاصة

يتضمن العمل الحالي دراسة عملية لتقييم الأداء الحراري لسخان شمسي مصنع محليا ذو خزان مكون من قشرة وأنبوب ملتف حلزونيا كمبادل حراري . أجريت عدة قياسات لدرجة حرارة دخول وخروج الماء لكلٍ من المجمع الشمسي والخزان و ماء الأستهلاك ، و توزيع درجات الحرارة داخل الخزان . هذا بالأضافة الى قياس معدل تدوير الماء في المجمع وماء الأستهلاك . تم التوصل الى تحديد المؤثرات الرئيسية المتحكمة بالمنظومة.

Keywords: Solar, Flat plate collector, Storage tank, coiled tube

INTRODUCTION

Solar hot water systems function as heat exchangers. They receive solar radiant energy and transfer it to the flowing fluid. The performance of solar systems varies as the design variables change, so it is necessary therefore to predict the parameters affecting this design and the operational variables.

Keltt et.al.(1984) studied experimentally the thermal performance of submerged coil heat exchangers for single wall coil and double wall coil for different tank sizes namely (300L and 450 L) for different load flow rates. Khalifa (1999) investigated a thermosyphon domestic hot water system to show the important variables that affect the performance of the solar system such as the temperature variation along the absorber fins, tubes and in the flow direction as well as the thermosyphonic mass flow rate. The design of an efficient heat exchanger has been investigated by Shokouhmand et.. al. (2008) with different coil pitches and curvature ratios. An enhancement in heat transfer rate is obtained due to the centrifugal force due to the curvature of the tube, results in the secondary flow development. The objective of the present work is to evaluate the thermal performance of a locally made solar hot water system for two cases; first the storage tank is of type shell and helical coiled tube heat exchanger and second a car radiator inserted inside a shell used as a storage tank

EXPERIMENTAL SETUP

The experimental apparatus shown in fig.(1) consist of a flat plate solar collector (2m *0.7m) in size made of mat black painted copper sheet (form the absorber plate) of thickness (0.7 mm). Seven copper tube risers of (3/8 " i.e 9.5 mm) diameter are welded to two copper headers of (7/8 " i.e 22.2 mm) diameter, and all welded to the absorber which in turn is fixed in wood box of (25 mm) thickness and covered by single glass panel of (4 mm) thickness. Glass wool insulation of (10 mm) is used to cover each side and back face of the absorber to minimize heat losses. The collector is mounted at a tilt angle of (33.3^o) from horizontal faces south. The storage tank is of type shell and helical coiled tube, the shell was a cylinder of (0.4 m diameter and 1 m height) made of Galvanized plate of 20 BWG have four ports (two inlets and two outlets), it is wrapped with (10 mm) glass wool insulation. To prevent pressure build up the tank was equipped with a pressure relief valve. A (0.6 m) height coiled tube is made by winding copper tube of (3/8 " i.e 9.5 mm) diameter around a cylinder to form (0.25 m outside coil diameter) , a spacer was placed between each two consecutive coil turns to ensure a uniform pitch along the coil which was (0.05 m). For all temperature measurements (18) copper constantan thermocouples are connected to a digital electronic thermometer with a resolution of ($0.1\ ^oC$) through (20) channel selector switch.

Test procedure

The experimental tests are carried out during July 2008 from (8:30 to 16:00). At the beginning of each test the rig should be drained out from air then the water is circulated at a flow rate of 0.2 m^3/hr (the minimum reading of the

flow meter used). All temperatures are recorded for different load flow rates: no load, 900 mL/hr and 450 mL/hr) which were measured by using graduated cylinder and stop watch. The selected load flow rates represent evacuating the storage tank once , twice and four times a day respectively.

THEORY

Thermal analysis is covered in many solar thermal engineering texts (Duffi & Beckman, and Lunde). Therefore, only equations which describe the thermal performance of the system will be described in this paper.

Actual Collector and supply Useful Energy Gain

For collector closed loop cycle the hourly useful energy gain can be calculated by:

$$Q_{coll} = m^{\bullet}_{coll}\ C_p\ (T_2 - T_1) \quad (1)$$

$$Q_{sup} = m^{\bullet}_{sup}\ C_p\ (T_{17} - T_{16}) \quad (2)$$

Where

Q_{coll} heat transferred in W, $m^{\bullet}$ mass flow rate (kg/s) , C_p water specific heat (J/kg.K)

and T_i measured temperature at location i (^oC) .

Effectiveness of Heat Exchanger

To define the heat transfer rate of the heat exchanger, the conventional definition of the effectiveness (ε) can be used , it can be written for the storage tank as:

$$\varepsilon = \frac{m^{\bullet}c_p)_{sup.} * (T_{17} - T_{16})}{m^{\bullet}c_p)_{min} (T_{13} - T_{16})} \quad (3)$$

Where $(m^{\bullet}c_p)_{min}$ is the lesser value of hot or cold fluid in the storage tank

In the case of no load (i.e. $m^{\bullet}c_p)_{min}$ is zero) this equation is not appropriate , Klett et. Al. (1984) defines the effectiveness for the storage tank in terms of an average tank temperature, T_{ST} computed as the average of several temperatures taken along the tank centerline (i.e.)

$$T_{ST} = (T_3 + T_4 + T_5 + T_6 + T_7)/5 \quad (4)$$

Hence the effectiveness can be defined as

$$\varepsilon = \frac{(T_{13} - T_{14})}{(T_{13} - T_{ST})} - 1 \quad (5)$$

RESULTS AND DISCUSSION

Several performance tests were obtained to investigate the collector alone and the SWH system. Fig. (2) shows the temperature difference (Δ**T**) across the collector obtained when it is

tested alone for two flow rates namely (450 mL/min and 1100 mL/min), it is clear that high flow rate leads to approximately uniform the temperature difference along the day, which is agrees with the enhancement of heat transfer due to the increasing of flow rate (Nusselt No. proportions with fluid velocity). The increase in water temperature across the collector was in the range of 10-54 ^{o}C as indicated by table (1) and Fig.(2). For solar water heater (collector and storage tank), Fig.(3) shows the variation of collector inlet, outlet and ambient temperatures which is found to follow with some time lag due to thermal capacity.

Stratification In The shell and coiled tube Storage Tank

The stratification phenomena is indicated in the storage tank in the present work, this phenomena demonstrate the conduction heat transfer mode of water when it is classified as not mixed thermal layers. Fig's (4, 5 and 6) show the stratification along the centerline of the storage tank at different times of the day for different continuous load flow rates namely zero , 450 mL/min and 900 mL/min respectively while the collector (closed loop) flow rate was (0.2 m^3/hr). It is clear that the temperature increases with time (reaches the peak after solar noon) then drops slowly. More heat is conserved in the storage tank as the rate of hot withdrawal reduces.

Effect of Load Flow Rate

Fig. (7) shows that increasing the load flow rate (which is the flow rate extracted by the user) decreases the inlet and outlet temperatures of the helical coiled tube for the same closed loop circulation flow rate which was (0.2 m^3/hr or 3333 mL/min). This means that the heat removed by the supply water is higher for high flow rates since heat transfer coefficient is increases with increasing Reynolds No. The same trend is shown in Fig's.(8) and (9) where the calculated heat removed by load is higher for higher flow rates but for the period after solar noon the lower flow rates remove higher values , this is due to the stratification effect in the storage tank which was higher (refer to Figs.(5 and 6)). The clear oscillations in the maximum and minimum values of the calculated useful heat gain in Fig's.(8 &9) are due to the oscillations in the hourly calculated temperature differences between collector's outlet and inlet temperatures for both load flow rates (refer to Fig.(3) and Eq.(1) for load flow rate of 900 mL/min).

Effectiveness of The Storage Tank

The effectiveness of the storage tank is shown in Fig.(10), it starts at high value and drops to rise again to the peak value then drops again rapidly. At the last day hour's the effectiveness rises rapidly due to the stratification effects in the storage tank.

Effect of Type of Heat Exchanger Type

Tests have been conducted when inserting a Brazilian car radiator in the storage tank instead of the helical coiled tube to examine the thermal performance of them in the solar hot water system. Fig.(11) shows the hourly inlet and exit temperature also the temperature difference of the circulating hot water for both coiled tube and radiator for no load , 0.45 L/min and 1.0 L/min load flow rate while the circulating flow rate was 0.2 m^3/hr . A valuable hourly temperature variations are obtained due

to the differences in the design configurations between the coiled tube and radiator. The later gives better results than the first, where larger temperature differences indicated for the same load flow rate.

CONCLUSION

This work shows that the system thermal behavior is sensitive to any part and can be enhanced further by investigating the design parameters and material selections. The following concluding remarks can be drawn during this work

- The stratification obtained in the storage tank is affected strongly on the collector inlet temperature.
- The stratification obtained in the storage tank is related strongly to the type of load rate (or load withdrawal pattern).
- Increasing the flow rate of the load decreases the stratification in the storage tank
- The effectiveness of the storage tank (shell and coiled tube) reaches approximately 78% for (450 mL/min) load flow rate.
- Using car radiator instead of the coiled tube enhances the thermal performance of the storage tank.

REFERENCES:

Duffi J. A.,and Beckman W. A. (1974)"Solar Energy Thermal Process ", John Wiley & sons Inc. New York.

Khalifa A. N.,(1999),"Thermal Performance Of Locally Made Flat Plate Solar Collectors Used As Part Of A Domestic Hot Water System", Energy Conversion & Management 40, PP. 1825-1833

Klett D.E.,Goswami D.Y.,and Saad M.T. (1984),"Thermal Performance Of Submerged Coil Heat Exchangers Used In Solar Energy Storage Tanks", Journal of Solar Energy Engineering, Aug., vol. 106, PP. 373-375

Lunde P. (1980) ,"Solar Thermal engineering, Space heating and hot Water Systems", John Wiley & sons Inc. New York.

Myrna Dayan, (1997),"High Performance In Low Flow Solar Domestic Hot Water Systems", MSc. Thesis Mechanical Engineering University of Wisconsin-Madison.

Shokouhmand H., Salimpour M.R. and Akhavan-Behabadi M.A.,(2008),"Experimental Investigation Of Shell And Coiled Tube Heat Exchangers Using Wilson Plots", International Communications In Heat And Mass Transfer, 35, PP. 84-92

Table (1): Measured Inlet And Outlet Temperature For Collector When Tested Alone on 14 - 15/7/2008

No.	Time	Circulation rate					
		$\dot{m}$ =0.45 l/min T_{amb}=36 °C 14-7-2008			$\dot{m}$ =1.1 l/min T_{amb}=38 °C 15-7-2008		
		T_{in}	T_{out}	ΔT	T_{in}	T_{out}	ΔT
1	11:00	32	53	21	29	43	14
2	11:15	33	63	30	30	43	13
3	11:30	34	65	31	30	43	13
4	11:45	35	66	31	30	44	14
5	12:00	38	83	45	30	44	14
6	12:15	40	93	53	31	45	14
7	12:30	42	96	54	31	45	14
8	12:45	42	97	55	31	46	15
9	13:00	42	97	55	30	46	16
10	13:15	42	96	54	30	45	15
11	13:30	42	96	54	30	44	14
12	13:45	42	96	54	30	42	12
13	14:00	42	96	54	30	42	12
14	14:30	36	89	53	30	41	11
15	15:00	36	82	46	30	40	10

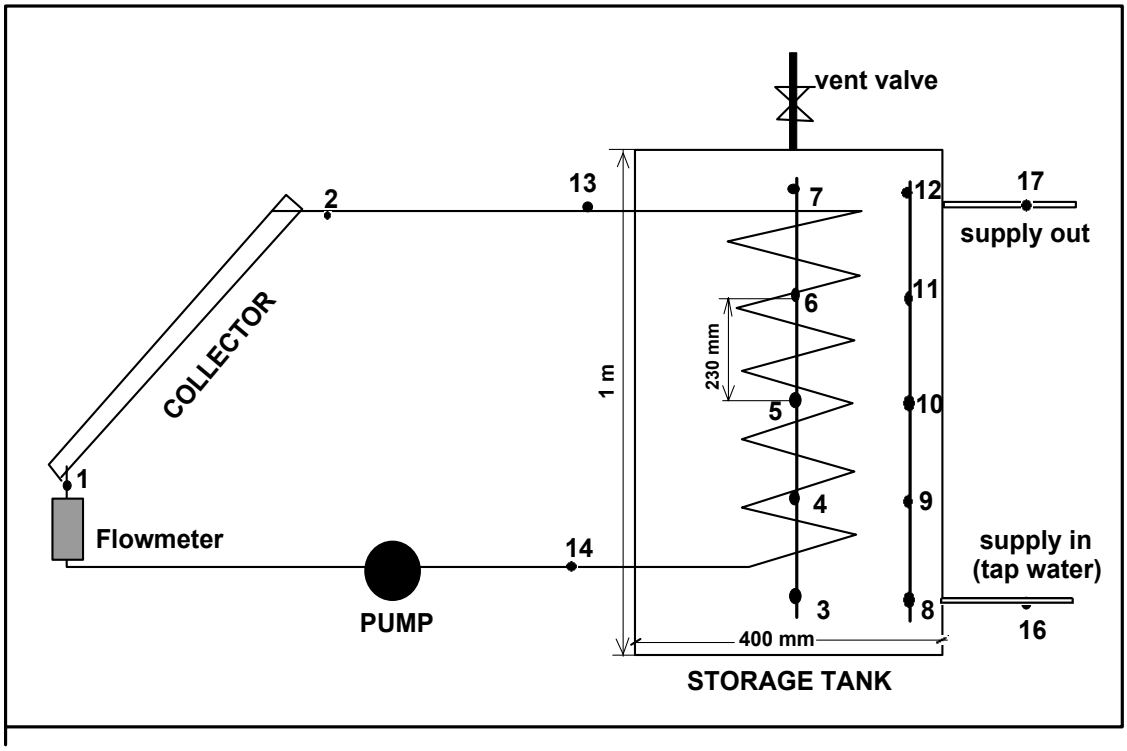

Fig.(1): Configuration of the Solar Water Heater

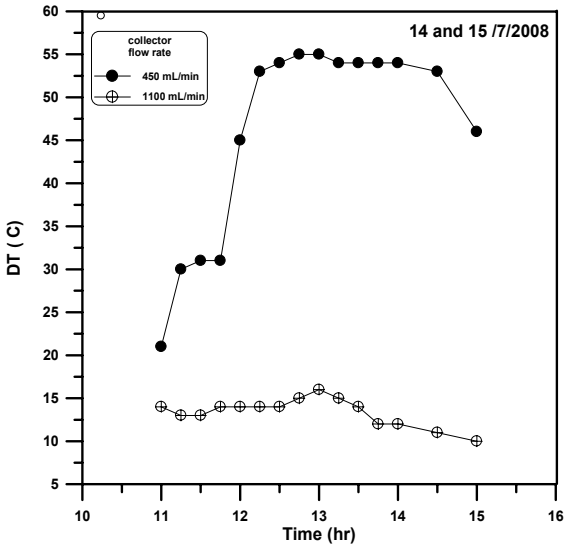

Fig.(2): Collector Outlet-Inlet Temperature Difference for different flow rates

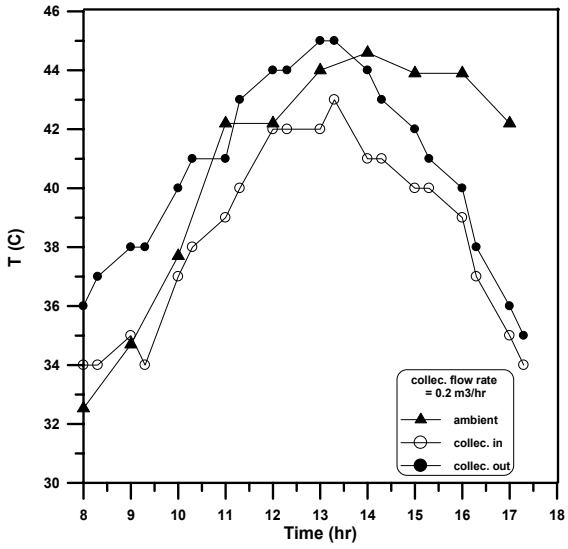

Fig.(3): Time Variation of Inlet, Outlet & Ambient Temperature for 900 mL/min supply load (18-7-2008)

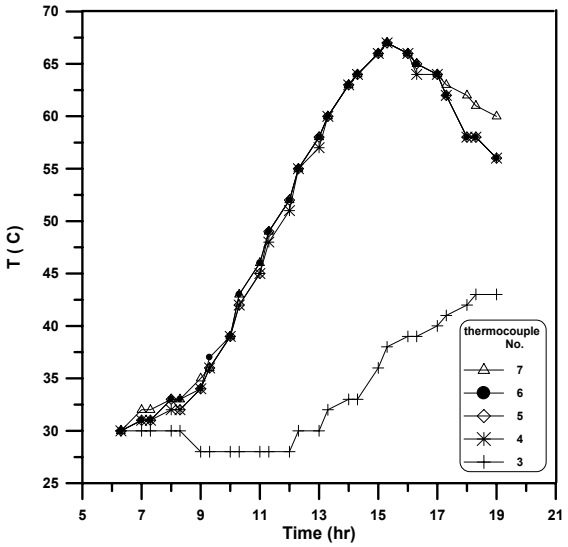

Fig.(4): Temperature Variation in Storage Tank With no Load of Water Supply on 19-7-2008 At Baghdad

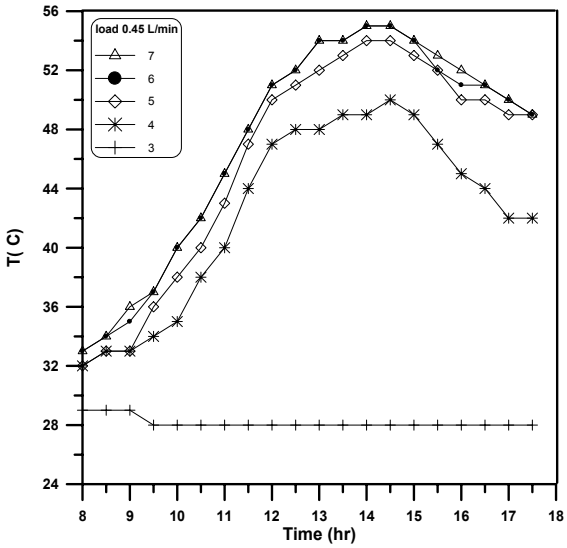

Fig.(5): Temperature Variation in Storage Tank With Load (450 mL/min) on 19-7-2008 At Baghdad

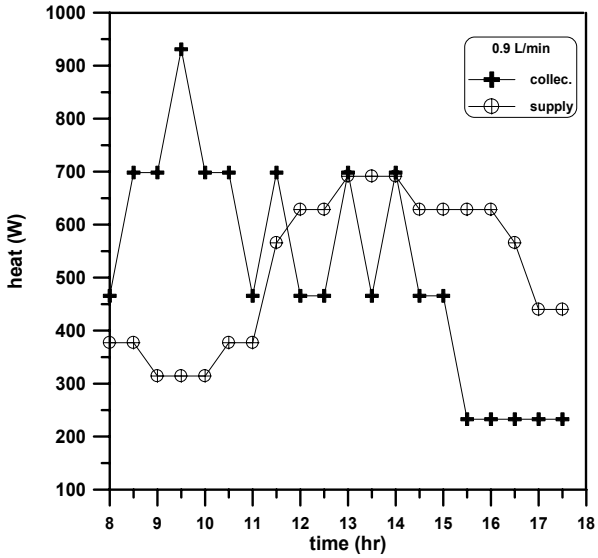

Fig.(8): Hourly Collector Useful Gain and Heat Transferred to Supply Water (900 mL/min Load)

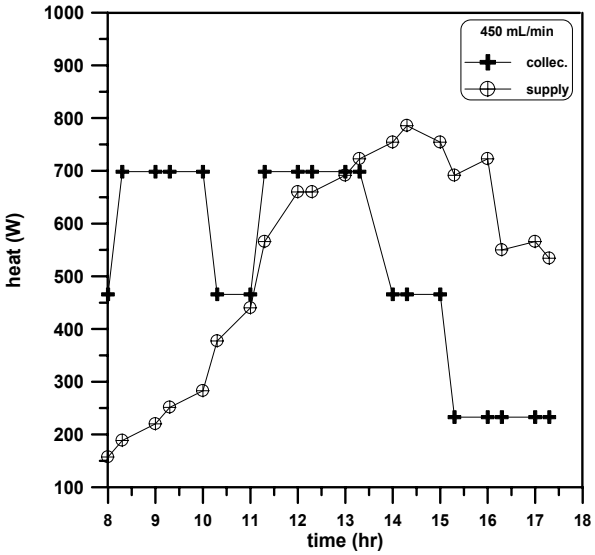

Fig.(9): Hourly Collector Useful Gain and Heat Transferred to Supply Water (450 mL/min Load)

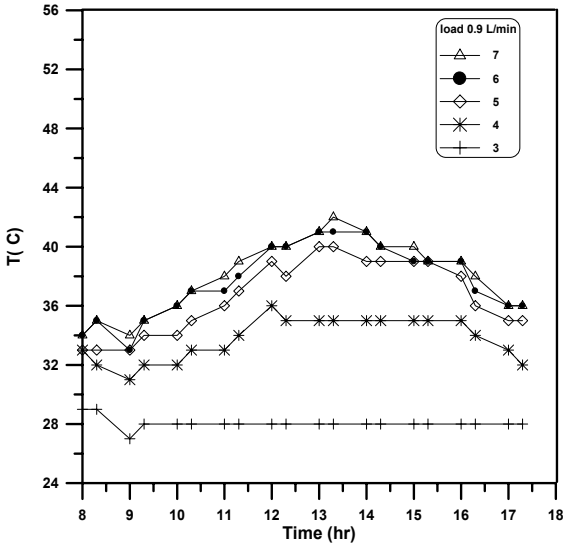

Fig.(6): Temperature Variation in Storage Tank With Load (900 mL/min) on (18-7-2008) At Baghdad

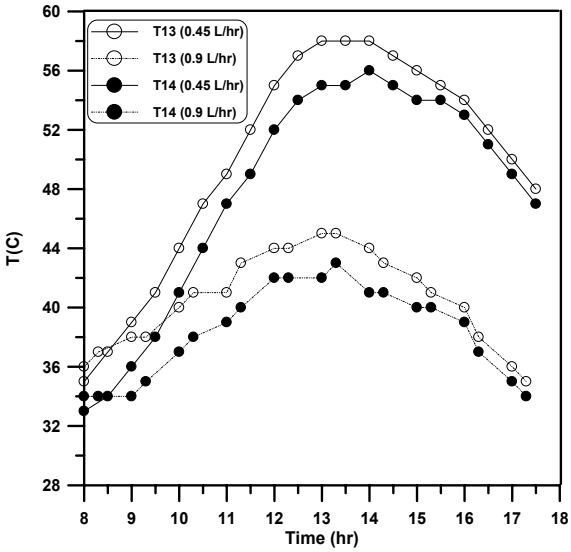

Fig.(7): Effect of Supply Water Load Flow Rate on Helical Coiled Inlet And Outlet Temperature Hourly Variation

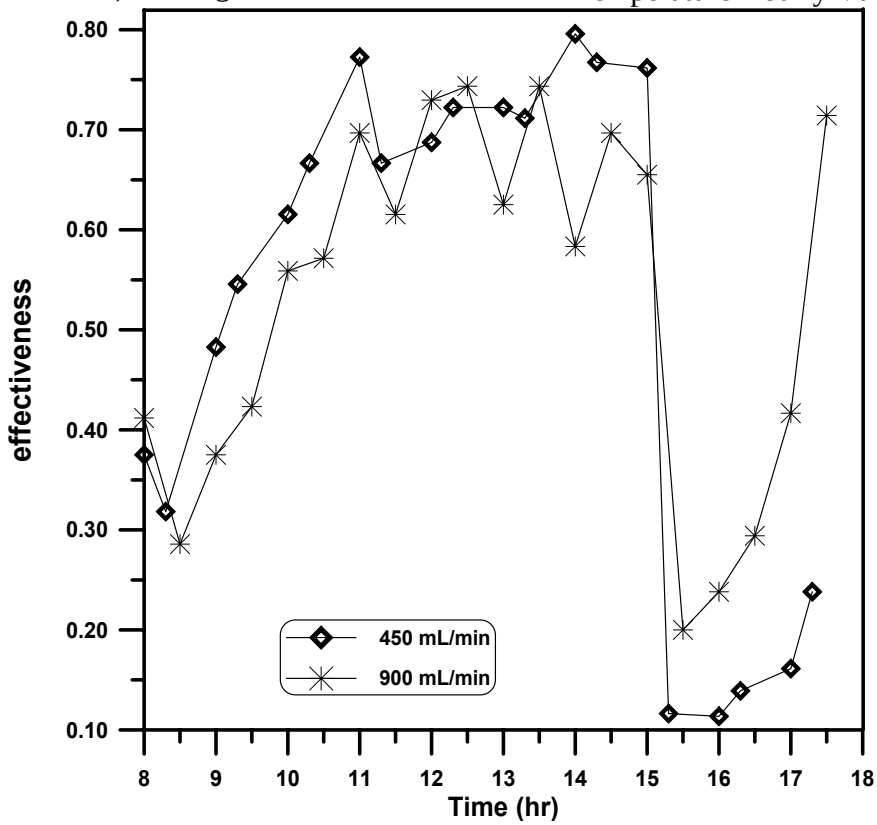

Fig.(10): Hourly Calculated Shell and Helical Coiled Tube Heat Exchanger (Storage Tank) Effectiveness

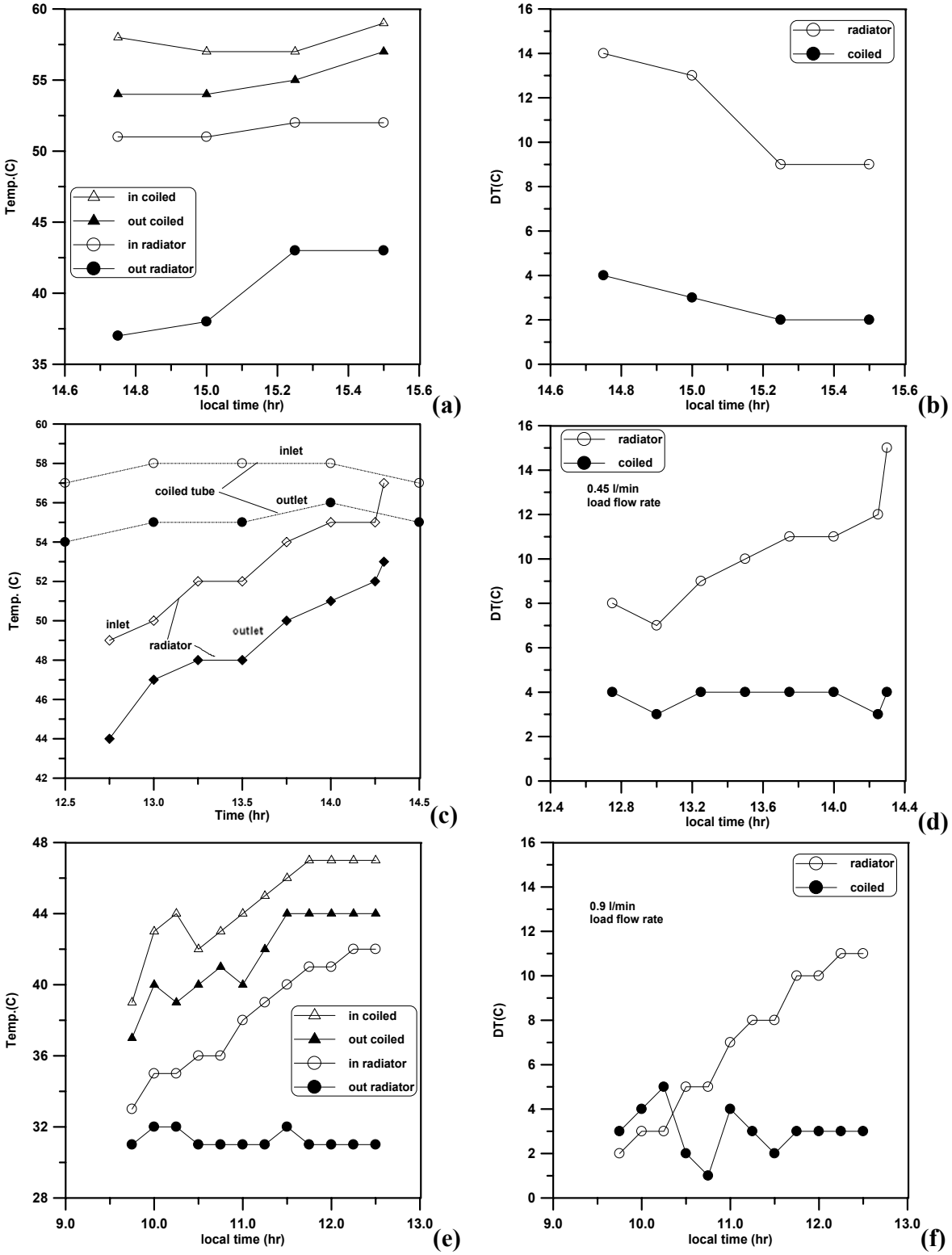

Fig.(11): Effect of Type of Inserted Tube In The Storage Tank on The Hot Water Inlet & Exit Temp. and Temp. Difference. a,b)no Load, c,d)0.45L/min e,f)1.0L/min load flow rate)

A GENERAL VELOCITY PROFILE FOR A LAMINAR BOUNDARY LAYER OVER FLAT PLATE WITH ZERO INCIDENCE

Qussai J. Abdul-Ghafour*
Department of Machines and Equipment, University of Technology, Baghdad, Iraq

ABSTRACT

A general velocity profile for a laminar flow over a flat plate with zero incidence is obtained by employing a new boundary condition to the other available boundary conditions. The general velocity profile is mathematically simple and nearest to the exact solution. Also other related values, boundary layer thickness, displacement thickness, momentum thickness and coefficient of friction are nearest to the exact solution compared with other corresponding values for other researchers.

الخلاصة

تم ايجاد معادلة عامة للسرعة خلال الطبقة المتاخمة للجريان الطباقي فوق السطح المستوي من خلال توظيف ظرف محيطي جديد بالاضافة الى الظروف المحيطية المتوفرة. المعادلة العامة المستحصلة ذات صيغة رياضية بسيطة واقرب ماتكون من الحل التام. تم استخدام المعادلة العامة للسرعة لايجاد القيم ذات العلاقة، سمك الطبقة المتاخمة و سمك الازاحة و سمك الزخم و معامل الاحتكاك وكانت النتائج هي الاقرب للحل التام مقارنة مع القيم المناظرة لها والمستحصلة من الباحين السابقين.

Keywords: Laminar Boundary Layer, Flat Plate, General Velocity Profile

INTRODUCTION

The boundary layer is a thin layer formed when a real flow passed over a solid surface. The velocity of the flow changes through this layer. At the surface, the velocity of the fluid relative to the surface is zero. The velocity of the flow then increases rapidly from zero and approaches the velocity of the main stream.

In 1904 German engineer Ludwig Prandtl (Schlichting 2000) suggested that the flow may be considered in two parts, the first part is at the boundary layer, where the shear stress is of prime importance, and the second is beyond the boundary layer where the velocity gradient is small and so the effect of viscosity is negligible. In this part the flow is essentially of an ideal fluid.

The boundary layer thickness (δ) is the value of height from the plate surface for which ($u \approx u_\infty$), and the boundary layer velocity profile refers to the manner which (u) varies with (y) through the boundary layer, as shown in **Fig.1** (Massey 2006).

The concept displacement thickness (δ*) (Massey 2006), allows us to consider the main flow as that of a frictionless fluid past a displaced surface instead of the actual flow past the actual surface. In other words, to reduce the total volume flow rate of a frictionless fluid by the same amount, the surface would have to be displaced outwards a distance (δ*). **Fig.2** shows observation of (δ*), where **Fig.2a** shows the corresponded behavior of ideal flow. The shaded areas in **Fig.2** are equal and can be presented mathematically as:

$$\delta^* = \int_0^{\delta} \left(1 - \frac{u}{u_\infty}\right) dy \qquad (1)$$

By similar conception, the total reduction in momentum flow rate equals the momentum flow rate under frictionless condition through thickness (θ) which called Momentum thickness (Massey 2006). Mathematically:

$$\theta = \int_0^{\delta} \left(\frac{u}{u_\infty}\right)\left(1 - \frac{u}{u_\infty}\right) dy \qquad (2)$$

The surface shear stress (τ_w) (Massey 2006) may be evaluated from knowledge of the velocity gradient at the surface that is,

$$\tau_w = \mu \left(\frac{\partial u}{\partial y}\right)_{y=0} \qquad (3)$$

From external flow, a dimensionless parameter from which the surface frictional drag may be determined, called skin friction coefficient (Massey 2006). In mathematical form,

$$C_f = \frac{\tau_w}{\frac{1}{2}\rho u_\infty^2} \qquad (4)$$

The momentum integral equation of the boundary layer, first derived by Von Karman (Eckert 1959) expresses the relation that must exist between the overall rate of flux of momentum across a section of the boundary layer, the frictional stress at the surface and the pressure gradient. It can be simply expressed as:

$$\frac{d\theta}{dx} = \frac{\tau_w}{\rho u_\infty^2} \qquad (5)$$

Many researchers employed different relations for the velocity profile through the boundary layer. Von Karman (Massey 2006) assumed that the velocity profile is a polynomial function of the vertical distance. Thus,

$$u = a + b(y) + c(y)^2 \quad (6)$$

Where a, b and c are constants.
The boundary conditions which are used to find the values of these constants are:

$$\text{at } y=0 \quad , u=0 \quad (7)$$

$$\text{at } y = \delta \text{ , } u = u_\infty \quad (8)$$

shear stress (τ) decreases linearly and becomes zero when $y= \delta$ (9)

Applying these conditions yields:

$$\frac{u}{u_\infty} = 2(\frac{y}{\delta}) - (\frac{y}{\delta})^2 \quad (10)$$

Another velocity profile derived by Von Karman (Eckert 1959), by using four conditions. These conditions are:

$$\text{at } y = 0, \quad u = 0 \quad (11)$$

$$\text{at } y = \delta, \quad u = u_\infty \quad (12)$$

$$\text{at } y = \delta, \quad du/dy = 0 \quad (13)$$

$$\text{at } y = 0, \quad d^2u/dy^2 = 0 \quad (\text{for constant pressure condition}) \quad (14)$$

The simplest function used to satisfy these conditions is a polynomial with four arbitrary constants. Thus:

$$u = a + b(y) + c(y)^2 + d(y)^3 \quad (15)$$

After applying these conditions, a velocity profile is obtained as:

$$\frac{u}{u_\infty} = \frac{3}{2}(\frac{y}{\delta}) - \frac{1}{2}(\frac{y}{\delta})^3 \quad (16)$$

Noting that, the forth condition in eqn.14 which is used in deriving eqn.16 is not used in deriving eqn.10.

(Pohlhausen 1921), suggested that the velocity profile is a polynomial of forth order. The profile is changed due to the variation in pressure gradient along the flat plate. For zero incidence case, the velocity profile becomes:

$$\frac{u}{u_\infty} = 2(\frac{y}{\delta}) - 2(\frac{y}{\delta})^3 + (\frac{y}{\delta})^4 \quad (17)$$

The most famous solution for the laminar boundary layer is obtained by (Blasius 1908), which is called the exact solution. This solution depends on obtaining new dependent and independent variables. A non-linear third order ordinary differential equation formed due to these variables then the solution achieved without the need of mathematical expression for the velocity profile. The result of this solution is agreed, and the results of other solutions are compared with it. **Table 1** shows the comparison between these solutions.

EVALUATION OF THE GENERAL VELOCITY PROFILE

The approach used in present work is a modified approach used by Von Karman (Eckert 1959). A new condition is employed in addition to the other four conditions described in eqn.11 to eqn.14. The new condition is,

$$\text{At} \quad y = 0 \qquad \frac{\tau_w}{\mu} = \left(\frac{\partial u}{\partial y}\right)_{y=0} \quad (18)$$

So the function which can be chosen to satisfy the five boundary conditions is a fifth order polynomial with five arbitrary constants. Thus,

$$u = c_1 + c_2(y) + c_3(y)^2 + c_4(y)^3 + c_5(y)^4 \quad (19)$$

Applying boundary conditions yields:

$$C_1 = 0 \tag{20}$$

$$C_2 = \frac{\tau_w}{\mu} \tag{21}$$

$$C3 = 0 \tag{22}$$

$$C_4 = \frac{4}{\delta^3} u_\infty - \frac{3}{\delta^2}\frac{\tau_w}{\mu} \tag{23}$$

$$C_5 = -\frac{3}{\delta^4}(u_\infty - \frac{2\delta}{3}\frac{\tau_w}{\mu}) \tag{24}$$

Substitute in eqn.19, yields:

$$u = \frac{\tau_w}{\mu}(y - \frac{3}{\delta^2}y^3 + \frac{2}{\delta^3}y^4) + 4u_\infty(\frac{y}{\delta})^3 - 3u_\infty(\frac{y}{\delta})^4 \tag{25}$$

For the assumed velocity profile in eqn.19, the first term is equal to zero (C1 = 0). The velocity gradient at the wall can be expressed as;

$$\frac{du}{dy})_{y=0} = A(\frac{u_\infty}{\delta}) \tag{26}$$

Where, (A) is the proportionality constant.

Substitute eqn.26 in eqn.3, to get:

$$\frac{\tau_w}{\mu} = A(\frac{u_\infty}{\delta}) \tag{27}$$

Substitute eqn.27 in eqn.25, to get:

$$\frac{u}{u_\infty} = A\left((\frac{y}{\delta}) - 3(\frac{y}{\delta})^3 + 2(\frac{y}{\delta})^4\right) + 4(\frac{y}{\delta})^3 - 3(\frac{y}{\delta})^4$$

Or

$$\frac{u}{u_\infty} = A(\frac{y}{\delta}) + (4-3A)(\frac{y}{\delta})^3 + (2A-3)(\frac{y}{\delta})^4 \tag{28}$$

This equation is the general equation for the velocity profile for laminar boundary layer over a flat plate with zero incidence.

In order to find an expression for boundary layer thickness (δ) we must use the momentum integral equation (eqn.5). Thus;

$$\frac{d}{dx}\int_0^\delta (\frac{u}{u_\infty})(1-\frac{u}{u_\infty})dy = \frac{\mu}{\rho u_\infty^2}(\frac{du}{dy})_{y=0} \tag{29}$$

Substitute eqn.27 and eqn.28 in eqn.29, integrate, to get:

$$(0.11428 + 0.06187A - 0.03015A^2)\frac{d\delta}{dx} = A\frac{\mu}{\rho u_\infty^2 \delta} \tag{30}$$

Eqn.30 is a differential equation, which can be solved by separating variables. The solution is:

$$\frac{\delta\sqrt{\mathrm{Re}_x}}{x} = \left(\frac{2A}{(0.11428 + .06187A - .03015A^2)}\right)^{0.5} \tag{31}$$

VALIDATION

Eqn.28 is an original and a general equation for the velocity profile. It can be reduces to many profiles obtained by other researchers.

Von Karman (Eckert 1959) suggested that the velocity profile is a polynomial of third order. Equating the coefficient of the forth power term in eqn.28 to zero, yields.

$$2A - 3 = 0$$

Or,

$$A = 3/2 \qquad (32)$$

Substituting this value in eqn.28, to get,

$$\frac{u}{u_\infty} = \frac{3}{2}(\frac{y}{\delta}) - \frac{1}{2}(\frac{y}{\delta})^3$$

Pohlhausen (Pohlhausen 1921) suggested that the velocity profile is a polynomial of forth order. It is clear that the coefficient of the forth power term in eqn.17 is equal to one. Equating the coefficient of the forth power term in eqn.17 and eqn.28, yields.

$$2A - 3 = 1$$

Or,

$$A = 2 \qquad (32)$$

Substituting this value in eqn.28, to get,

$$\frac{u}{u_\infty} = 2(\frac{y}{\delta}) - 2(\frac{y}{\delta})^3 + (\frac{y}{\delta})^4$$

This is exactly the velocity profile obtained by Pohlhausen (eqn.17)

EVALUATING OF BLASIUS VELOCITY PROFILE

In the exact solution, Blasius (Blasius 1908) found a numerical expression for (δ), (δ^*), (θ) and (C_f), with no explicit mathematical expression for the velocity profile. One of the consequences of Blasius solution is,

$$\frac{\delta\sqrt{Re_x}}{x} \approx 5 \qquad (33)$$

The result of the present work could be used for obtaining velocity profile agrees with exact solution. By comparing eqn.31 with eqn.33, simply result obtained:

$$\left(\frac{2A}{(0.11428 + 0.06187A - 0.03015A^2)}\right)^{0.5} \approx 5 \qquad (34)$$

Solving eqn.21 for (A), yields:

$$A = 1.67326 \qquad (35)$$

Substituting the value of (A) in eqn.28 to get the velocity profile for the exact solution,

$$\frac{u}{u_\infty} = 1.67326(\frac{y}{\delta}) - 1.01978(\frac{y}{\delta})^3 + 0.34652(\frac{y}{\delta})^4 \qquad (36)$$

Fig.3 shows the velocity profile for the present work and other profiles. It is clear that the profile of eqn.36 is the nearest one to the exact profile.

CONCLUTIONS

The result of this work is a new velocity profile for laminar boundary layer over a flat plate with zero incidence. This profile is nearest to the exact solution obtained by Blasius (Blasius 1908). Also the consequences of using the new profile in calculating (δ), (δ^*), (θ) and

(C_f) are mostly nearest to the corresponding values of the exact solution as shown in **table 1**.

The new profile is mathematically simple, accurate and including most conditions bounded the laminar boundary layer. Therefore it can be used in fluid mechanics and convective heat transfer fields.

REFERENCES

Duncan, W.J, Thomas, A.S. and Young, A.D. "Mechanics of fluid" Edward Arnold Ltd, (1970).

.

Eckert, E.R.G and, Drake, R.M "Heat and mass transfer" 2nd edition. McGraw Hill, Inc., (1959)

H. Blasius, Z. Math. Phys., 56, I (1908).

H. Schlichting, "Boundary Layer Theory". 8th edition. Springer, 2000.

K. Pohlhausen, Z. angew. Math. Mech., 1: 235 (1921)

Massey, B. S, "Mechanics of fluids". 8th edition. Tylor & Francis, 2006

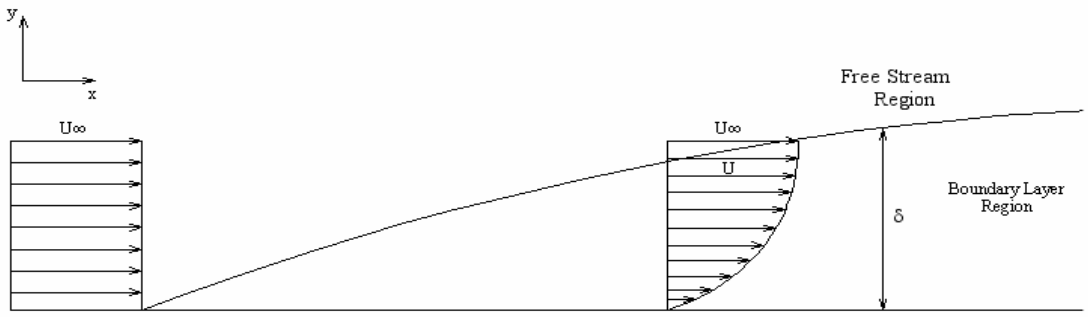

Figure 1: Velocity variation inside the boundary layer region

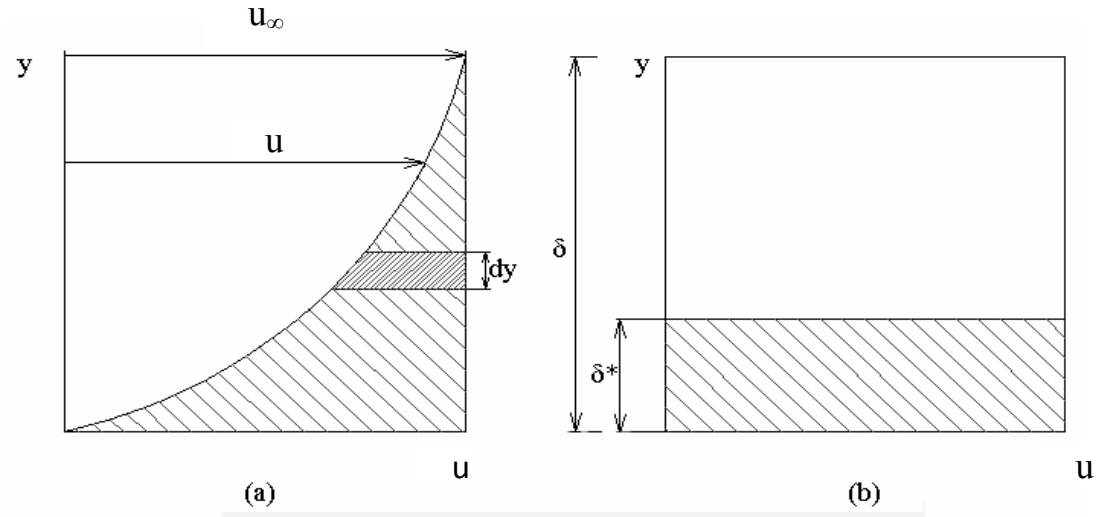

Figure 2: Observation of the displacement thickness (δ*)

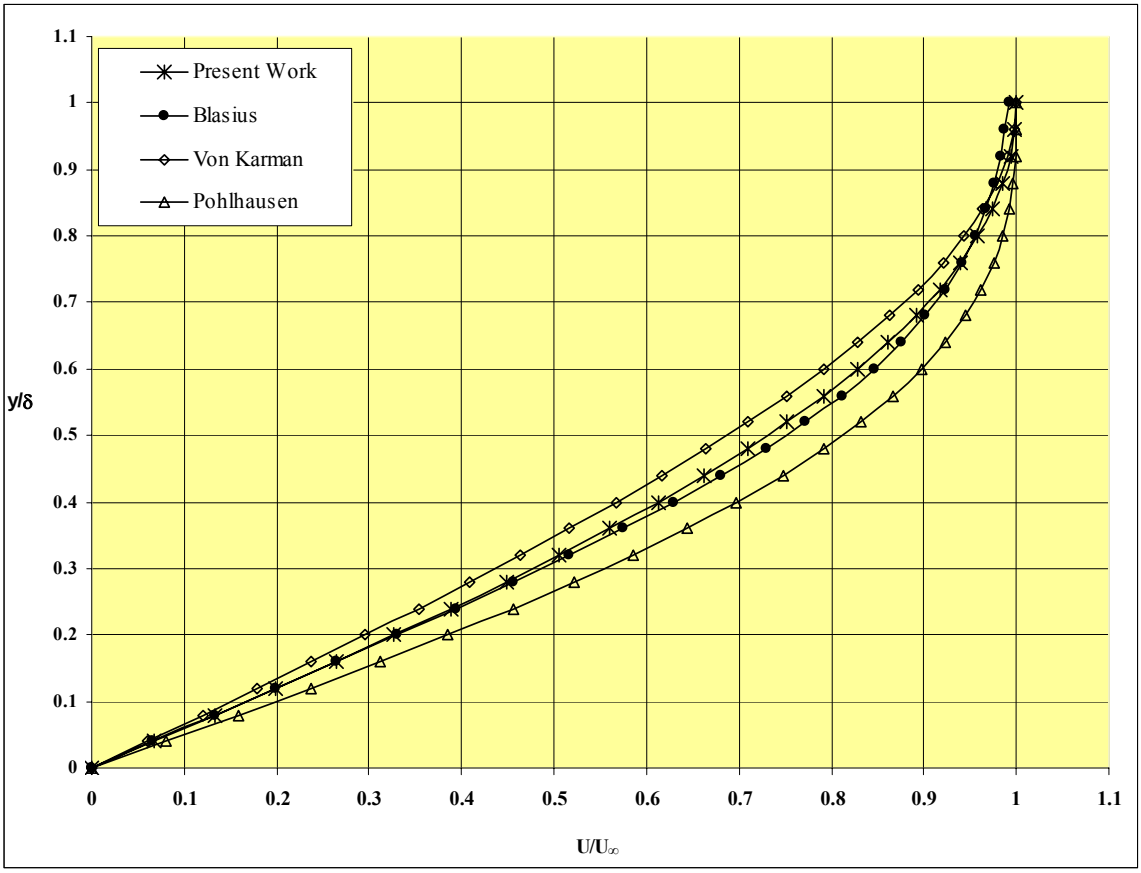

Figure 3: Velocity Profiles for the Present Work and Previous Studies Compared with Blasius Solution

Table 1: Results of δ, δ*, θ and C_f for Number of Obtained Velocity Profiles

$\frac{u}{u_\infty}$	$\frac{\delta\sqrt{R_{ex}}}{x}$	$\frac{\delta^*\sqrt{R_{ex}}}{x}$	$\frac{\theta\sqrt{R_{ex}}}{x}$	$\frac{C_f\sqrt{R_{ex}}}{2}$
$\frac{3}{2}(\frac{y}{\delta})-\frac{1}{2}(\frac{y}{\delta})^3$	4.64	1.74	0.646	0.323
$2(\frac{y}{\delta})-2(\frac{y}{\delta})^3+(\frac{y}{\delta})^4$	5.84	1.752	0.686	0.343
Blasius solution	5	1.721	0.664	0.332
Present work	5	1.745	0.667	0.334

Nomenclatures

Symbol	Meaning	Unit
C_f	Coefficient of friction	-
Re	Reynolds number	-
u	Flow velocity	m/s
u_∞	Free stream velocity	m/s
y	Vertical distance	m
ρ	Flow density	kg/m^3
δ	Boundary layer thickness	m
δ^*	Displacement thickness	m
θ	Momentum thickness	m
μ	Dynamic viscosity	$N.s/m^2$
τ_w	Wall sheer stress	N/m^2

THE EFFECT OF SPACE VOLUME ON FREE CONVECTION HEAT TRANSFER FOR ONGITUDINAL FINNED CYLINDER WITH DIFFERENT SLOPE NGLES

Lecture SALEEM KHALEFA KADHUM, M.Sc.

Computer and System Engineering Department

University of Technology

Baghdad, Iraq

ABSTRACT:

This study deals with free convection heat transfer for the outer surface of two cylinders of the shape of (Triangular & Rectangular fined cylinders with 8-fins), putted into two different spaces; small one with dimension of (Length=1.2m, height=1m, width=0.9m) and large one with dimension of (Length=3.6m, height =3m, width=2.7m). The experimental work was conducted with air as a heat transport medium. These cylinders were fixed at different slope angles (0°, 30°, 60° and 90°) .The heat fluxes were (279, 1012, 1958, 3005, 4419) W/m^2, where heat transferred by convection and radiation. In large space, the results show that the heat transfer from the triangular finned cylinder is maximum at a slope angle equals to 90° and is minimum at the slope of 0° angle whit the heat transferred from the triangular finned cylinder is maximum at slop angle of 30° and minimum at the slop of angle 60° in the small space with following range of the Raleigh number ($1.68*10^7$-$3.46*10^8$).

الخلاصة:-

يتناول البحث دراسة عملية لانتقال الحرارة بالحمل الحر من أسطوانتين ذات زعانف طولية مستطيلة المقطع ومثلثة المقطع بعدد(8 زعنفة) وذلك باستخدام الهواء كوسط ناقل للحرارة موضوعتين داخل حيزين مختلفين في الحجم أحداهما كبيربأبعاد (3m*3.6m*2.7m) والاخر صغير الحجم بأبعاد (1m*1.2m*0.9m)، ولمعرفة الخواص الحرارية تم وضع النموذجين اعلاة بزوايا ميل (90°,60°,30°,0°) عن الأفق ولمستويات فيض حراري(4419, 3005, 1958, 1012, 279) W/m^2 في حيز مفتوح إلى الهواء الخارجي حيث تنتقل الحرارة بالحمل والإشعاع. وقد وجد أن أعلى مقدار للحرارة المنتقلة بالحمل من الاسطوانة ذات الزعانف المثلثة المقطع في الحيز الكبيروبزاوية ميل مقدارها (90°) ولكلا النموذجين،أما بالنسبة للحيز الصغير فقد وجد أن أعلى مقدار للحرارة المنتقلة بالحمل يكون من الاسطوانة ذات الزعانف المثلثة المقطع وبزاوية ميل قدرها(30°)ولكلا النموذجين ولمدى عدد رايلي ($1.68*10^7 – 3.46*10^8$) .

Keyword: - Free Convection Heat Transfer , Longitudinal Finned Cylinder, Different Slope angle.

INTRODUCTION: -

The longitudinal fins with variable cross-sectional area are used in electronic and electrical devices and heat exchangers and in most applications of air-conditioning (condensers, and air heaters). The longitudinal fins have different cross-sectional areas like circular, triangle or other areas. Hence, cost factor should be considered especially if the product used commercially. It can be achieved by decreasing the heat exchanger size and weight by increasing its efficiency to maximize heat exchange.

There are many factors that increase the heat exchanger efficiency:-

- Decrease the size of fins by increase the surface area.
- Using high conductivity metals like Aluminum.
- Using forced convection heat transfer or counter current flow.
- Changing heat exchanger geometrical parameters.

Many researchers studied the free convection heat transfer and concluded empirical and numerical relations between Nusselt number and Raleigh number.

(Atipoang et al, 2008) presented an experimental study for the effect of slope angle on finned tube heat exchanger performance in free convection. The number of rows were with in the range of (1-4), with an inlet water temperature of (40, 60, and 80 ^{o}C), volumetric flow rate of (1.5 L/min), ambient temperature is (27°C) and slope angle with in the rang of (0° – 90°). They found that the best performance can be achieved for slope angle between (30°-45°) were heat exchanger efficiency decreased with increasing the number of rows.

***(Lkuo* 1983)** presented experimental studies for two cylinders of variable diameter at constant wall temperature. The Grashoff number ($4*10^4$ – $4*10^5$) depended on outside diameter of cylinder with different geometry ratios as (s/d=2-∞) and (x/d=2 – 10). The optimum ratios were (x/d=3) when (s/d= ∞), besides ($\frac{Nu_i}{Nu_o}$) equals one for all furthermore; an obvious enhancement obtained (x/d>3). In case of walls, the best geometrical ratio is (x/d=7).

The effect of the air space volume was studied upon the affects the free convection heat transfer coefficient. Also it was required to fined the optimum position of the fin and the appropriate space volume due to wide the application of fin tube in compact power plant, accurate electronic devices and heat exchangers design.

***(Sparrow* and Chrysler 1981)** studied the free convection heat transfer from a short cylinder conducted to a flat plate in constant heat flux condition and Raleigh number in the range of ($1.4*10^4$ – $1.4*10^5$). Three positions were investigated. They developed the following equation for Nusselt number for all cases:-

$$Nu = CRa^{m} \qquad (1)$$

(Yassen 1978) presented an experimental study on inclined flat cylinder. He used two cylinders of (38mm, 47mm) diameter. The slope angle was in the range of (0° – 90°). Constant heat flux was considered and Raleigh number was between ($0.28*10^6$ – $3.44*10^6$). He found that:-

$$Nu = \left[0.665 - 0.4885(\sin\theta)\right] Ra^{[1/4+(1/(12\sin\theta))]174} \qquad (2)$$

He also found that the vertical position is better and heat transfer coefficient

value increased to a certain value and then decreased.

(Young et al, 2005) presented a theoretical study for heat transfer for rectangular cross-section fin using one dimension analytical method and finite difference method. A comparison between two methods was done. This comparison deals with heat loss and temperature which was represented as equations interims of Biot number and non-dimensional length of fin. They found that finite difference gave better results with low error ratio by increasing number of nods.

TEST MODELS:-

There are two models used in the experimental work which were designed in standard same used for heaters. These models were made from hard aluminum (D_o=48mm, D_i=16mm), where the heater was positioned inside. Figure (1) shows triangular and rectangular longitudinal fins of dimensions (height =13mm, Length =300mm, number of fins=8). Electrical heater of 1kW was used the models were mounted on moving frame in order to obtain a range of angles (0° – 90°). The test model was positioned inside two spaces (inside thermally insulated wood) (Length=1.2m, height=1m, width=0.9m) and, then in room with dimensions (Length=3m, height=3.6m, width=2.7m).

CALCULATIONS:-

General equation ($Nu = CRa^m$) to calculate the Nusselt number and Rayleigh number as follows:-

$$\left.\begin{aligned} &Nu = h * D_o / k \\ &and \\ &Ra = \frac{\beta * g * D_o * (T_s - T_a)}{\nu^2} * \Pr \end{aligned}\right\} \quad (3)$$

The equations are used to calculate the heat generated and transferred by radiation and free convection

$$\left.\begin{aligned} &Q_g = I * V \\ &Q_g = Q_{conv} + Q_{rad} \\ &Q_{conv} = h * A_t * (T_s - T_a) \\ &Q_{rad} = \sigma * A_t * \varepsilon * (T_s^4 - T_a^4) \end{aligned}\right\} \quad (4)$$

and the film temperature and volumetric expansion coefficient are also calculated as follows:-

$$T_f = \frac{T_a + T_s}{2} \quad (5)$$

$$\beta = \frac{1}{T_f} \quad (6)$$

RESULTS AND DISCUTION:-

Rayleigh and Nusselt numbers were calculated for (Ra=$1.68*10^7$-$3.46*10^8$), variable heat flux (279, 4419 W/m^2). And slope angle (0°, 90°). (Fig. 2, 3, 4, and 5) respectively, the result shows that:-

1- (Fig. 2 , 3) show that the free convection heat transfer increased in large space with increasing, Rayleigh number and reach maximum value for slope angle of 90° and reach minimum value at $\theta = 0^o$. That is due to the longitudinal rectangular cross-section of the fin allowing the hot air with low density to flow upward uniformly. Moreover, the maximum lifting force for air is achieved, proportional with sin (θ) (upward effect), in the case of

slope angle (θ =30° and 60°). For the case of θ = 0°, the fins work as obstacles to block air flow which causes retardation of flow to be staffed. In addition, it adds thermal resistance on so, the loss from fin decreases. The heat lost from the test model of triangular fins is higher than rectangular fin, because of the large area of triangular cross – section.

2- (Fig. 4 , 5) show that the free convection heat transfer is increased in the small space by increasing the Rayleigh number. In cases the maximum value occurs when the slope angle equals to θ = 30° and minimum value when θ =60°.

For the case of test model inclination, the lifting force of air is proportional to sin(θ) and the normal component of buoyancy will be the effective force and reach the maximum value. In case of θ=90°, the longitudinal rectangular and triangular fins of the test model in vertical position allow the hot air to flow uniformly (maximum lifting force at θ=90°).

Due to this position in the small space, the distance between the fin and the upper surface of the space will be minimum at (θ=90°) and will equal to 25 cm. In this case, it causes an increase in the ambient temperature because of the thermal warming inside the small space. This will lead to lower temperature difference and heat transfer.

3- A comparison for free convection heat transfer of large space and small space are shown in (fig. 6, 7, 8, 9, 11, 12, 13, and 14) for different slope angles (0°, 30°, 60° and 90°) for both models. It was found that the free convection heat transfer will be much more than large space as compared with small space for different slope angles. That is due to the increase in the ambient air temperature which results from thermal warming in case of small space. As a result, the lower temperature difference and heat transfer will decrease, and vice versa for large space, large air draughts and higher heat transferred.

4-The relationship between Rayleigh and Nusselt numbers represented logarithmically and gave acceptable results according to the boundary conditions of each model.

Test model Triangular for small space

$\theta = 0^o \quad y = 0.03902 + 0.2008 \; x$

$\theta = 30^o \quad y = 0.377 + 0.165 \; x$

$\theta = 60^o \quad y = -1.024 + 0.282 \; x$

$\theta = 90^o \quad y = -0.3512 + 0.214 \; x$

Test model Rectangular for small space

$\theta = 0^o \quad y = 0.24097 + 0.1894 \; x$

$\theta = 30^o \quad y = -0.21475 + 0.2601 \; x$

$\theta = 60^o \quad y = -0.3075 + 0.249 \; x$

$\theta = 90^o \quad y = 0.01697 + 0.22315 \; x$

Test model Triangular in large space

$\theta = 0^o \quad y = 1.40399 \quad x - 2.25759$

$\theta = 30^o \quad y = 1.8083 \quad x - 2.40391$

$\theta = 60^o \quad y = 1.49397 \quad x - 2.42405$

$\theta = 90^o \quad y = 1.50816 \quad x - 2.44565$

Test model Rectangular in large space

$\theta = 0^o \quad y = 1.76686 \quad x - 3.03874$

$\theta = 30^o \quad y = 1.76417 \quad x - 3.0181$

$\theta = 60^o \quad y = 1.67471 \quad x - 2.82292$

$\theta = 90^o \quad y = 1.64845 \quad x - 2.75683$

Where:-

$$y = LogNu \quad , \quad x = LogRa$$

The deviation of this curved were treated by plotting the constant value C with their angles as shown in figs (10 and 15) where:-

$$C = m\,\theta^{n} \qquad (7)$$

The general equation for test model after substituting the value of constant C is $(1^{o} \le \theta \le 90^{o})$

a- Test model for rectangular cross – section small space:-

$$Nu = 1.828195 * \mathrm{Ra}^{0.230413} * \theta^{-0.1195} \qquad (8)$$

b- Test model for triangular cross – section small space:-

$$Nu = 1.491094 * \mathrm{Ra}^{0.144825} * \theta^{-0.133} \qquad (9)$$

C-Test model for rectangular cross – section in large space:-

$$Nu = 0.1477245 * \mathrm{Ra}^{1.713} * \theta^{0.46923} \qquad (10)$$

d- Test model for triangular cross – section in large space:-

$$Nu = 0.380609 * \mathrm{Ra}^{1.471} * \theta^{0.59543} \qquad (11)$$

The angle effect is included in the Nusselt number equation above. In addition, substituting the value of angle (θ), the error ratio does not exceeds 10%.

CONCLUSIONS:-

These results show that the free convection heat transfer coefficient of triangular cross – section is higher than the one with rectangular cross – section (for the same number of fins). The free convection heat transfer will be maximum at ($\theta=90^{o}$) and minimum at ($\theta=0^{o}$) in large space. In addition, the free convection heat transfer will be maximum at ($\theta=30^{o}$) and minimum at ($\theta=60^{o}$) in small space.

REFERENCES:-

Atipoang, Sanparwat, Tanongkiat and Chi-Chuan" Effect of inclination angle on free convection thermal performance of louver finned heat exchanger", Int. J. Heat. Mass transfer 40(3), PP.533 -544, 2008.

Lkuo Tokura and Others" An Experimental study of free convection heat transfer from a horizontal cylinder in a vertical array set in free space between parallel walls", Transaction of the ASME, Vol.105, PP.102 – 107, February 1983.

Sparrow E.M. and Chrysler "Natural Convection heat transfer coefficient for a short horizontal cylinder attached to a vertical plate", transaction of ASME, Vol. 103, PP. 630-637, 1981.

Yassen K. Salman "Laminar natural convection heat transfer from the outside surface of an inclined cylinder", M.Sc, thesis, University of Technology, 1978.

Young Min, Joo Suk and Hyung Suk"Analysis of a One-Dimensional method and the Finite difference

method", J .KSIAM, Vol.9, No.1, 91-89, 2005.

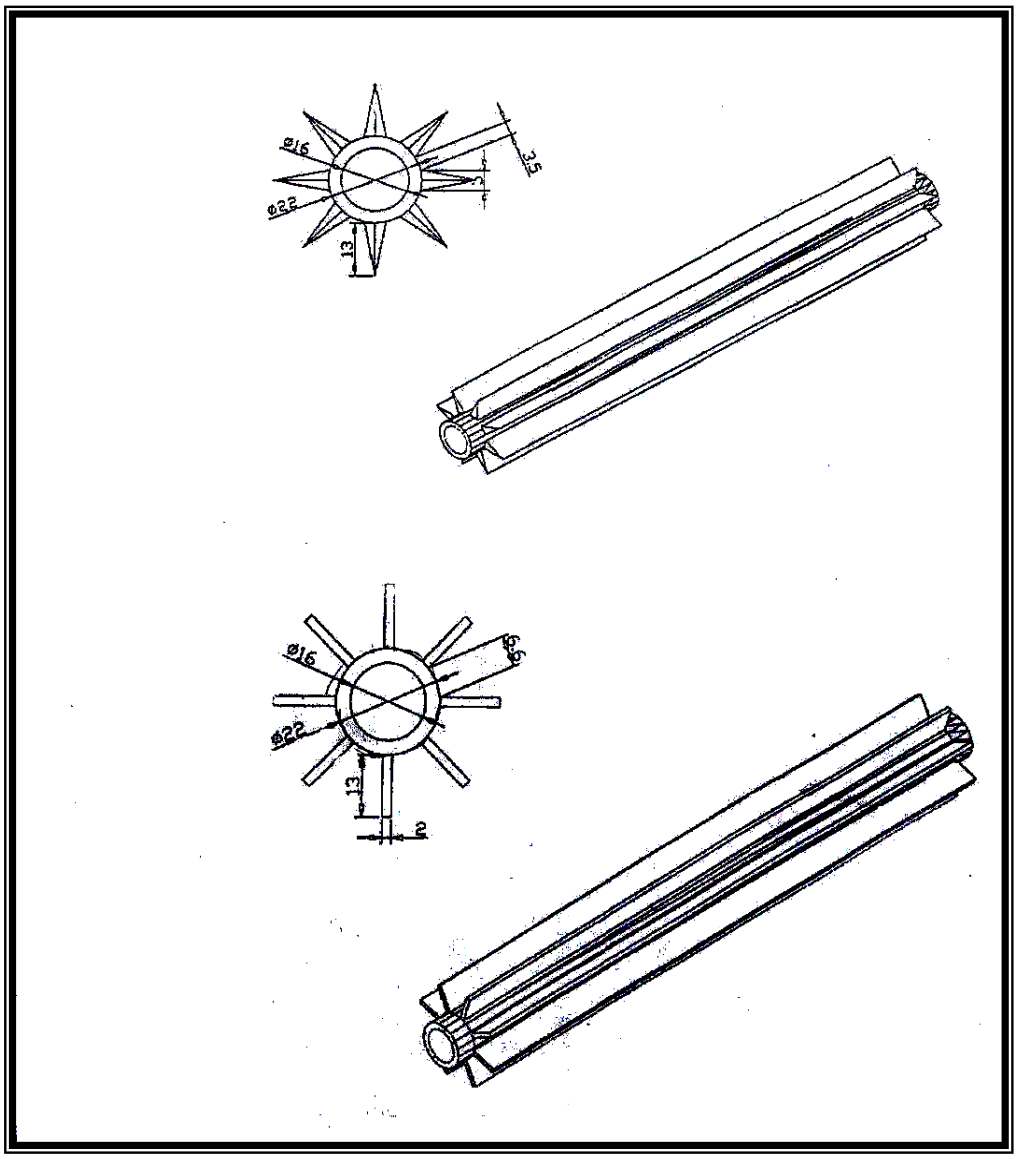

Fig (1) Isometric testing rig.

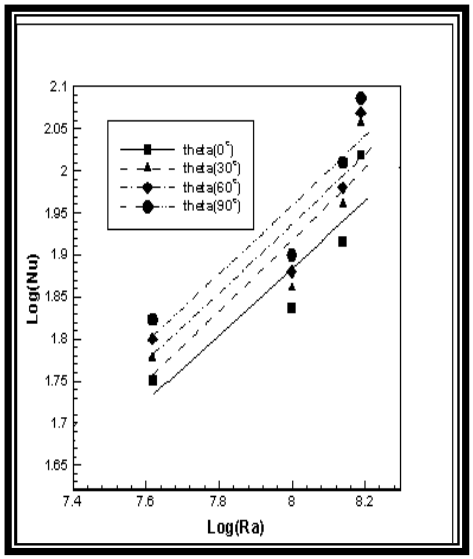

Fig (3) Relationships between Nu and Ra for longitudinally finned cylinder with different slope angles for rectangular cross – section in large space.

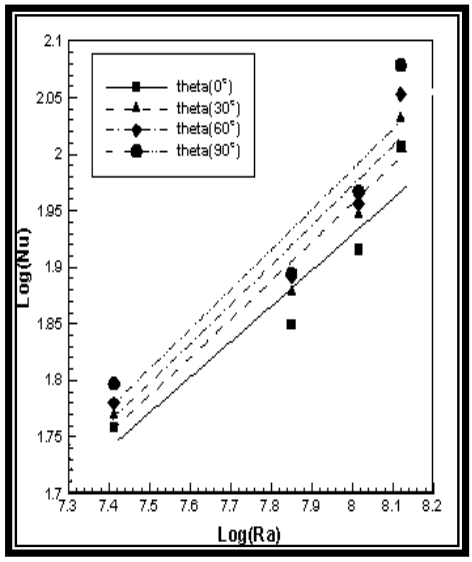

Fig (2) Relationship between Nu and Ra for longitudinal finned cylinder with different slope angles for triangular cross – section in large space.

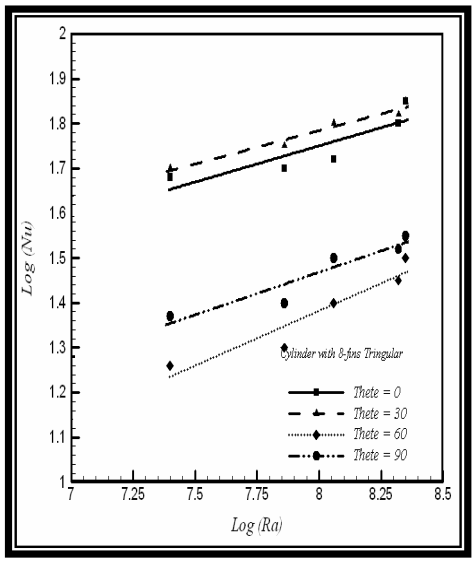

Fig (5) Relationship between Nu and Ra for longitudinally finned cylinder with different slope angles for rectangular cross – section in small. space

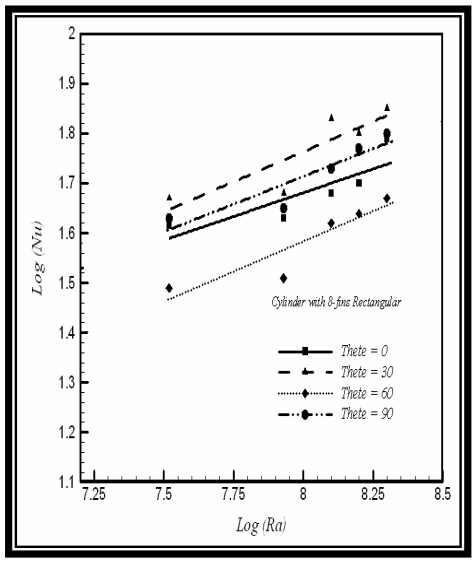

Fig (4) Relationship between Nu and Ra for longitudinally finned cylinder with different slope angles for triangular cross – section in small space.

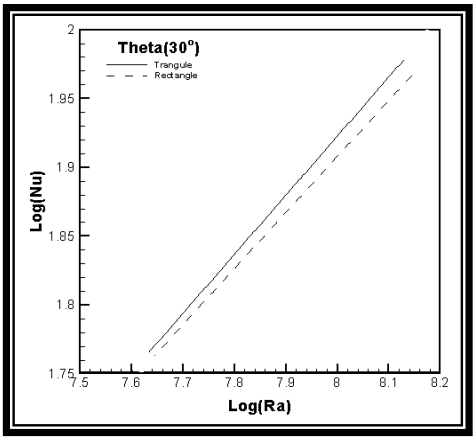

Fig (7) Relationship between Nu and Ra for test section at angle of 30° in large space.

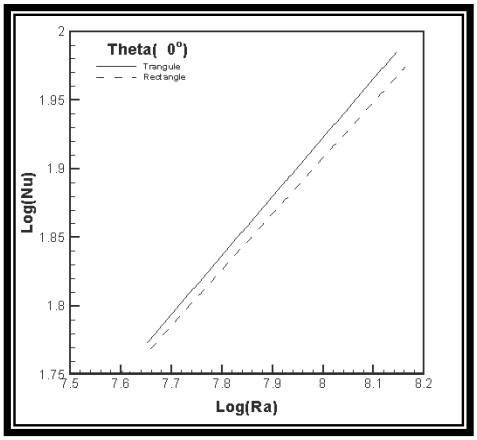

Fig (6) Relationship between Nu and Ra for test section at angle of 0° in large space.

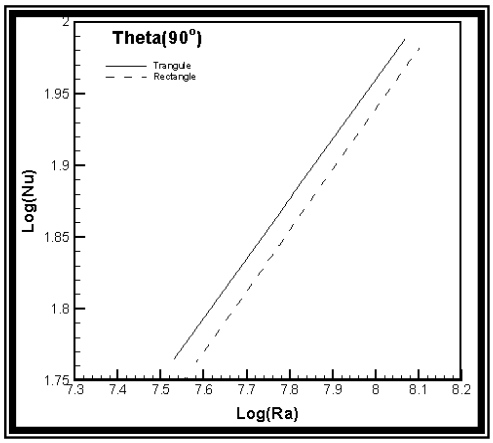

Fig (9) Relationship between Nu and Ra for test section at angle of 90° in large space.

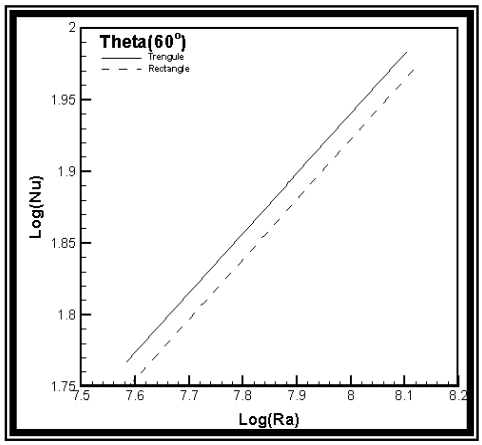

Fig (8) Relationship between Nu and Ra for test section at angle of 60° in large space.

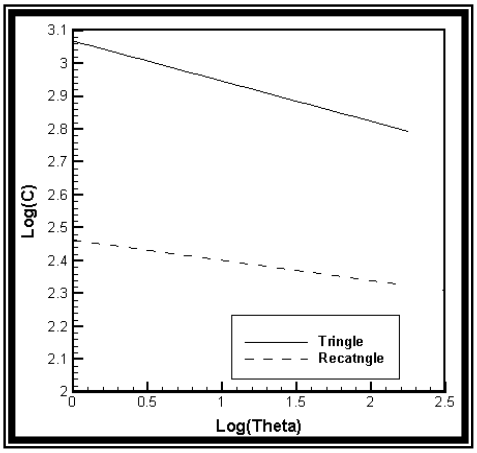

Fig (10) Relationship between slope angle and constant value (C).

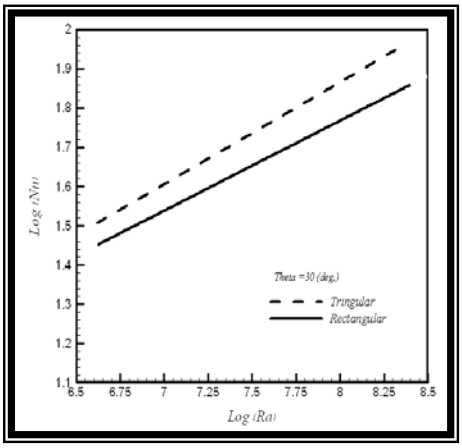

Fig (12) Relationship between Nu and Ra for test section at angle of 30° in small space.

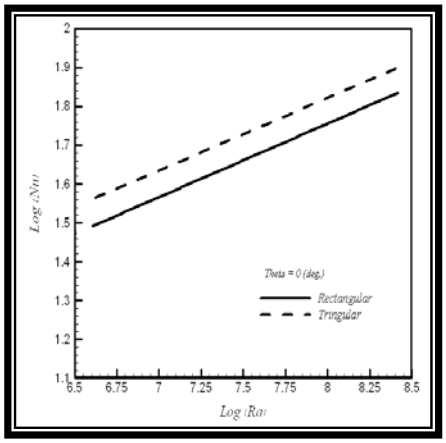

Fig (11) Relationship between Nu and Ra for test section at angle of 0° in small space.

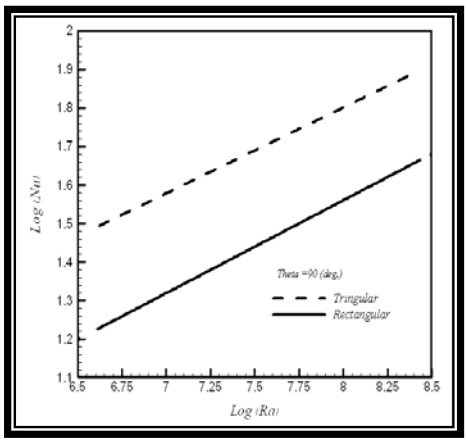

Fig (14) Relationship between Nu and Ra for test section at angle of 90° in small space.

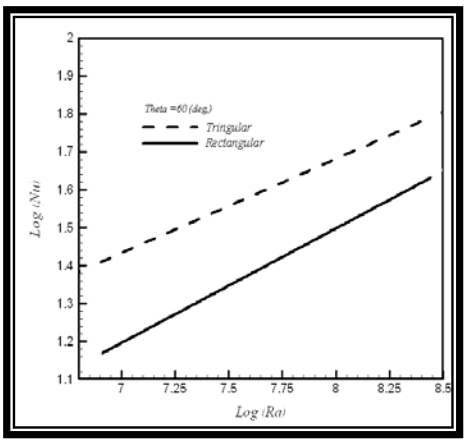

Fig (13) Relationship between Nu and Ra for test section at angle of 60° in small space.

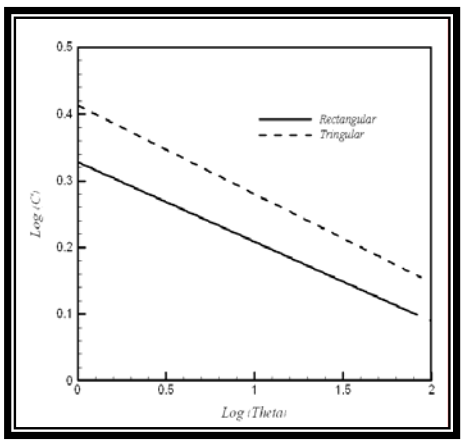

Fig (15) Relationship between slope angle and constant value (C).

NOMENCLATURE:-

A_t Total area in (m^2)
D_o Outer diameter in (m)
D_i Inner diameter in (m)
D_p Outer diameter tube with out fins in (m)
g Gravity acceleration in (m/s^2)
h Convection heat transfer coefficient in ($W/m^2.K$)
k Thermal conductivity in (W/m.K)
L Length of the cylinder in (m)
m Power of Rayleigh number
n The power of slope angle
Nu Nusselt number
Pr Parendtl number
Q_{conv} Heat transfer rate by convection in (W)
Q_q Heat generation in (W)
Q_{rad} Heat transfer rate by radiation in (W)
Ra Rayleigh number
T_a Ambient temperature in (^oC)
T_f Film temperature in (oC)
T_s Surface temperature in (^oC)
T_o Base temperature in (^oC)
T Tip of fin in (mm)
Lc Characteristic length in (m)
s distance between the cylinder and the wall (m).
x distance between two cylinder (m).

Roman symbols:-

β Volumetric expansion coefficient
ε Emmisivity.
σ Stefan - Boltzman constant in (W/m^2K^4)
υ Kinematic viscosity in (m^2/s)

THE INFLUENCE OF TOOL GEOMETRY OF FRICTION STIR WELDS ON MECHANICAL PROPERTIES AND MICROSTRUCTURE OF 2218-T72 ALUMINUM ALLOY

* Prof. Dr. Qasim M. Doos. * Samer J. Mahmood.
University of Baghdad, College of Eng.
Kasim_daws@yahoo.com , samerjasem@yahoo.co.uk

1- ABSTRACT

Friction stir welding (FSW) process is an emerging solid state joining process in which the material that is being welded does not melt. This process uses a non-consumable tool to generate frictional heat in the abutting surfaces. The welding parameters such as tool rotational speed, welding speed, axial force, etc., and tool pin profile play a major role in deciding the weld quality. In this investigation an attempt has been made to understand the effect of tool pin profile and rotation diameter on microstructure and mechanical properties in aluminum alloy (2218-T72).

Five different tool pin profiles (straight cylindrical, threaded cylindrical, triangular, square, and threaded cylindrical with flat), with three different rotation diameter (3, 4, 5) mm. have been used to fabricate the joint.

Effect of tool pin profile on mechanical properties of welded joints were investigated using different mechanical tests including (tensile, bending and microhardness tests). Microstructure characteristic during (FSW) process was studied and different welding joint were investigated using optical microscope. Based on the stir welding experiments conducted in this study the results show that aluminum alloy (2218-T72) can be welded using (FSW) process with maximum welding efficiency (86.95%) and (83.21%) in terms of ultimate tensile strength and bending force respectively using tool pin profile (threaded cylindrical with flat) with rotation diameter (5) mm, rotation speed (900rpm) and (30mm/min) welding speed.

Keywords: Aluminum Alloy, Friction Stir Weld, Tool Geometry.

الخلاصة

اللحام بالاحتكاك والخلط من الطرق التي تضهر الحالة الصلبة لطرق الربط والتي تكون حالة المعدن الملحوم ليست منصهرة.الطريقة تستخدم عدة غير مستهلكة لتوليد حرارة الاحتكاك في السطح المحاذي.أن عناصر اللحام مثل السرعة الدورانية لعدة اللحام وسرعة اللحام والقوة العمودية الخ.. بالأضافة الى شكل رأس العدة يلعب دور مهم بتحديد نوع اللحام. في هذا البحث محاولة لفهم تأثير شكل رأس العدة وقطر الدوران على الخصائص الميكانيكية والميتالورجية لسبيكة الألمنيوم

استخدمت خمس اشكال لرأس العدة(أسطواني عدل،أسطواني مسنن، مثلث، مربع، أسطواني مسنن مع شق منبسط) مع ثلاثة أقطار دورانية مختلفة (3,4,5)ملم لأنشاء الوصلات.

أن تاثير شكل رأس العدة لوصلات اللحام تم دراستها بالأعتماد على الفحوصات الميكانيكية الأتلافية مثل(فحص الشد،فحص الأنحناء،فحص الصلادة المجهرية) كذلك تم دراسة التغيرات الميتالورجية خلال عملية اللحام ودراسة مناطق اللحام المختلفة بأستخدام مجهر ضوئي. من التجارب المختلفة في هذة الدراسة اتضح بأن سبيكة الالمنيوم قابلة للحام بهذة الطريقة مع الحصول على اقصى كفائة لحام وصلت الى (86,95%)و(83.21) اعتماد على مقاومة الشد وقوة الانحناء بالتتابع بأستخدام شكل رأس عدة (أسطواني مسنن مع شق منبسط)وقطر دوران (5ملم).بسرعة دورانية 900 دورة بالدقيقة وسرعة لحام 30 ملمتر بالدقيقة.

2- INTRODUCTION

Friction stir welding (FSW) is a solid-state joining process, which uses a cylindrical rotating tool consisting of a concentric tool pin and tool shoulder. The strong metallurgical bonding during FSW is accomplished by (1) the severe plastic deformation caused by the rotation of the tool pin that plunges into the material and travels along the joining line and (2) the frictional heat generated mainly from the pressing tool shoulder. The key roles of the tool pin and the tool shoulder are to deform the material around the tool and to generate the frictional heating during the processing, respectively. Therefore, the tool geometry (i.e., the shapes and sizes of the pin and shoulder) is one of the most important processing parameters that determine the quality of the joint and the microstructure characteristics **[WANCHUCK WOO2006]**.

FSW offers several advantages over conventional fusion welding process because of its low heat input and absence of melting and solidification process. The most important benefits of FSW are its ability to weld the materials that was thought difficult to be welded such as aluminum alloy of 2xxx and 7xxx series. FSW is a solid state joining technology and gives better material properties: fewer weld defects, low residual stresses and improved dimensional stability **[YAN-HUA ZHAU2005]**.Other benefits include generally low defect compared with fusion welding and the ability to join dissimilar metals **[H.LOMBARD2007]**

3- EXPERIMENTAL WORK

The rolled plates of 3.8mm thickness, AA2218 aluminum alloy The chemical composition and mechanical properties of base metal are presented in **Table 1**, were cut into required size is (150mm×75mm×3.8mm) by power hacksaw cutting and grinding the plate edge to insure that there is no gap between the two plates as shown in **Fig. 1** was prepared to fabricate FSW joints. The initial joint configuration was obtained by securing the plates in position using mechanical clamps. The direction of welding was normal to the rolling direction. Single pass welding procedure was used to fabricate the joints.

Non-consumable tools made of law alloy steel were used to fabricate the joints. The tool dimensions are shown in **table 2.** Five different tools pin profiles (straight cylindrical, threaded cylindrical, triangular, square, and threaded cylindrical with flat), with three different rotations diameter (3, 4, 5) mm were used. Tool shoulder was constant for each tool 18 mm diameter, and used standard pitch screw for the threaded cylindrical, were used to fabricate the joints as shown in **Fig. 2.**

To obtain high quality of (FSW) welded joints with high mechanical properties, i.e. high welding efficiency; the main welding parameters (rotational speed and welding speed) must be carefully selected to balance the effect of each parameter on the amount of heat input during welding.

The rotation speed was chosen according to the self-optimized parameter suggested by **[Mohanad A .Al-Ani2007],** therefore tool rotation speed is kept constant at 900 rpm, and the welding speed was kept constant at 30 mm/min, the aluminum alloy use in Mohanad investigation was (7020-T6) aluminum alloy. The FSW trials are carried out on a vertical milling machine with square butt joint configuration.

Then the joints were visually inspected and X-Ray Photography **Fig. 3**. According to radiography inspection **Fig.4**, eight joints had internal defect in weld line. The type of defect is voids in the middle or root of the weld .from the table we find that, straight cylindrical and threaded cylindrical pin profile with (3,4,5 mm)rotation diameter containing void defect in weld line. The reason of this defect is insufficient heat input and flow of the plasticized metal. Triangular and square pin profile with (3 mm) rotation diameter containing void defect in weld due to the along the side of the shape is small and there is no effect on material flow.

4- TENSILE STRESS AND BENDING STRESS TEST RESULTS.

Flat weld specimens, are used to generate tensile and bending data perpendicular to the weld line. It includes the (NZ, TMAZ, HAZ and the base metal) represented along the gage length.

Tensile specimens were machined from the welds according to the American Society for Testing of Materials **[ASTM, 1988].**

Tensile test and bending test were done and until the failure take place and the result has been divided according to the tool pin profile. It should be noted that the values of the parent metal is (320**N/mm**^{2}, 915N) respectively.

A- Straight Cylindrical Pin Profile (T1-series):

T1-series are characterized by a change in pin diameter from 3mm to 5mm in steps of 1mm. The plastic metal flows around the pin, and there is no pulsating action in this series. The pin with 3mm, pin diameter produce welds with the lowest tensile strength **Fig. 5**. The increase in weld strength with 4mm rotation diameter is small compared to 5mm it is attributed to increasing heat Generation and plastic flow of metal. Bending stress reaches maximum value in this series with 5mm pin diameter. **Table 3** shows that the tensile strength, bending stress, and efficiency of weld joint increase with increasing pin diameter of the tool.

B- THREADED CYLINDRICAL PIN PROFILE (T2-SERIES):

T2-series explore the effect of thread and change in pin diameter on mechanical property, the screw thread will be beneficial to the heat generation under the same welding parameters, more heat input can improve the flow of the plastic material. There is no pulsating action. The Pitch on The pin is (o.5M, 0.7M, 0.8M). The thread on each pin was machined opposite to that of the spindle rotational direction to assist in plastic flow. The lowest values of tensile strength in this series were found with 3mm, and 4mm pin diameter tools. The highest tensile strength occurred with 5mm pin diameter **Fig 6** .The results of bending stress of welded joint also increased with increasing in pin diameter **Table 4**.

Comparing this series with (T1-series) it is found a small increasing in mechanical property due to the effect of thread.

C- Triangular Pin Profile (T3-series)

The triangular pin profiles produce a pulsating stirring action in the flowing material due to flat face. It produces 45 pulse/s when the rotates speed is 900 RPM. The tool with 3mm rotation diameter produces welds with the lowest tensile strength, increases

across tool with 4mm rotation diameter to reach maximum value on tool with 5mm rotation diameter **Fig 7.** The results of bending stress of welded joint also increases with increasing in pin diameter **Table 5** compared this series with previous series noted increas the mechanical properties (excepting the tool with 3mm rotation diameter) result from the impacted caused by the pulse during mixing the metal.

D- SQUARE PIN PROFILE (T4-SERIES):

Square pin profiles produce a pulsating stirring action in the flowing material due to flat face. it produces 60 pulse/s when the rotates speed is 900 RPM. The results show that tensile strength has been increased with increasing rotation diameter **Fig 8**. The joints fabricated using square pin have shown highest tensile strength compared to the joints fabricated using Triangular pin due to increase the pulse per Sec. Bending stress reaches maximum value in this series with 5mm rotation diameter. **Table 6** shows that the tensile strength, bending stress, and efficiency of weld joint increase with increasing pin diameter of the tool. The mechanical properties increase due to increase the pulses **[K. Elangovan, 2007].**

E- Threaded Cylindrical with Flat Pin Profile (T5-series)

This tool is characterized by flat; this series was designed to produce combined effects of improving the flow of the plastic material by the threaded and producing a pulsating stirring action by the flat side, the threaded cylindrical with flat pin produces 30 pulse/s when the tool rotates at 900 RPM speed. The maximum value of tensile strength in this series was found with 5mm rotation diameter see **Table 7**. Note there is large range in tensile strength between 3mm, and 4mm pin diameter this is due to increase area of the flat side. The maximum joint efficiency in (UTS FSW / UTS BM) is (86.95) for (G3T5) welded joint. The tensile strength, bending stress, and efficiency of weld joint increase with increasing pin diameter of the tool **Fig 9**.

4- MICROHARDNESS RESULTS.

Microhardness results show that small increase in hardness values toward the weld center **Fig 10**. The increased values found at the center of the weld are retained by the weld nugget and are probably related to the small grain size.

Another observation of the microhardness results is the hardness on one side of weld center differs from the other side (unsymmetrical weld). This difference can be explained as follows: In the leading side (advancing side) for the rotating tool where the rotational velocity vector and the forward motion vector are in the same direction and due to this there is higher heating on one side of the weld center and hence higher the hardness.

Of the 15 joints **Figs 11, 12, and 13**, the highest hardness value of 178 Hv has been recorded in the joint fabricated using threaded cylindrical with flat and rotation diameter (5mm) pin profiled tool and the lowest hardness value of 135Hv has been recorded in the joint fabricated using straight cylindrical rotation diameter (3mm) pin profiled tool, and the hardness increasing as the rotation diameter increased.

All the set of experiment joints increase in the hardness a cross the weld compared to the value of the base metal (HV_{500}=130) was due to equated structure or reprecipitation of the solid solution.

5- MICROSTRUCTURE.

The transition between the weld nugget and (TMAZ) is observed for all the joints fabricated using the tools with 5mm rotation diameter for comparison purpose.

Fig14 shows the sample of the joint produce by straight cylindrical pin profiled tool, it contains void formation on the root of the due to a sufficient heat generation and metal flow. **Fig15** shows the sample of the joint produce by threaded cylindrical pin profiled tool, it contains porous void formation on nugget zone and small cracks on the thermo-mechanically affected zone. **Fig 16** shows the sample of the joint produce by triangular pin profiled tool, it contains effects of pulse intervals and non-clear. **Fig 17** shows the sample of the joint produce by square pin profiled tool, it contains effects of clear and close due to the shape of square.

Fig 18 shows the sample of the joint produce by threaded cylindrical with flat pin profiled tool, it seen homogeneous structure of three regain (NZ,TMAZ,HAZ) are clearly.

6- CONCLUSIONS:

According to results of the present study of (FSW) process on selected Al-alloy, several conclusions can be written regarding alloy weldability, mechanical, microstructure.

1- Aluminum alloy (2218-T72) is wieldable using different (FSW) tool geometry giving different welding efficiencies. The shape of the pin with (3) mm rotation diameter has small effect on the mechanical properties (tensile, bending, hardness) , the shape of the pin with (4, 5) mm rotation diameter has a significant effect on the mechanical properties.

2- The maximum weld strength obtained in this study was (278.24 (N/mm2)) or (86.95 %) weld efficiency with (11.9 %) elongation is recorded in the weld using threaded cylindrical with flat pin profiled tool and 5mm rotation diameter.

3- In the stirred zone, fine equi-axed grains of size ranging are transformed from the parent metal grain structure.

4- Increasing tool pin diameter from (3mm to 5mm) step 1mm for a fixed other parameter causes increasing in mechanical properties of the welds joint.

7- REFRINCE

ASTM"Metals-Mechanical Testing Elevated and Low – Temperature Tests; Metallography"Annual Book of ASTM Standards, Volume 03.01, 1988.

ASM "Properties and Selection: Nonferrous Alloys and Special – Purpose Materials", ASM International, Volume 2.1988.

D.G. Hattingh, C. Blignault, T.I. van Niekerk, M.N. James "Characterization of the Influences of FSW Tool Geometry on Welding Forces and Weld Tensile Strength Using an Instrumented Tool", Materials processing technology,No.12, 2007.

H. Lombard, D.G. Hattingh, A. Steuwer, M.N. James "Optimizing FSW Process Parameters to Minimize Defects and Maximize Fatigue Life in 5083-H321 Aluminum Alloy ", Engineering Fracture Mechanics, Vol.75, No.14, PP.341-354, 2007.

K. Elangovan, V. Balasubramanian "Influences of Tool Pin Profile and Welding Speed on the Formation of Friction Stir Processing Zone in AA2219 Aluminum Alloy ", Materials processing technology, Vol.200, No.13,PP.163-175, 2007.

Mohanad Okab Yousuf Al-Ani "Investigation of Mechanical and Microstructure Characteristics of Friction Stir Welded Joints ", Ph.D thesis, University of Baghdad, 2007.

Wanchuck Woo, Hahn Choo, Donald W. Brown and Zhili Feng "Influence of the Tool Pin and Shoulder on Microstructure and Natural Aging Kinetics in a Friction-Stir-Processed 6061–T6 Aluminum Alloy ", Metallurgical and Materials Transactions A., Vol.38A, No.8, PP.69-76, 2006.

Yan-hua Zhao, San-bao Lin, Lin Wu, Fu-xing Qu "The Influence of Pin Geometry on Bonding and Mechanical Properties in Friction Stir Weld 2014 Al Alloy", Materials Letters, Vol. 59, No.5, PP.2948-2952, 2005

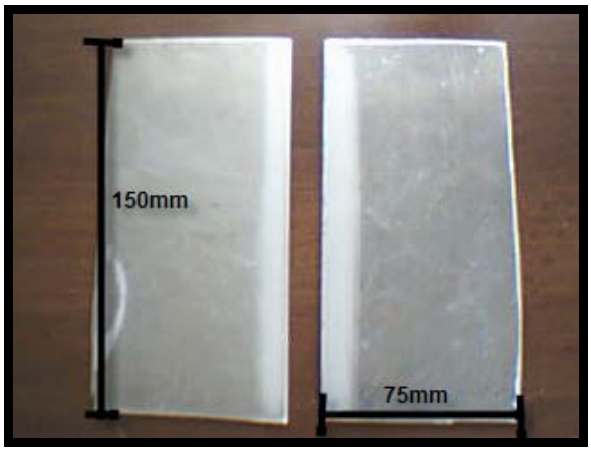

Fig. 1 Plates Preparation for welding.

Table 1 Chemical and Mechanical properties of Al alloy used in this study.

Material type and temper condition	2218-T72 Aluminum alloy (Measured)	2218-T72 Aluminum alloy (Standard)[ASTM]
Chemical Composition	Cu = 4.1% Ni = 2.0% Mg = 1.5%, Si = 0.8% Al=Rem	Cu = (3.5-4.5)% Ni = (1.7-2.3)% Mg = (1.2-1.8)%, Fe = 1.0%, Si = 0.9% Zn = 0.25%, Mn=0.2% Cr = 0.10%, Al=Rem
Mechanical properties	Ultimate strength = 320(N/mm^2) Yield strength =242 (N/mm^2) Elongation =14%	Ultimate strength = 330(N/mm^2) Yield strength = 255(N/mm^2) Elongation =11%

Fig. 2 Image of friction stir tools.

Table2 Different pin geometry of friction stir tools.

Description Of the pin	Rotation Diameter (mm)	Shoulder Diameter (mm)	Pitch on The pin (mm)	Pin length (mm)
straight cylindrical	3	18	non	3.5
	4	18	non	3.5
	5	18	non	3.5
threaded cylindrical (V –Thread)	3	18	0.5	3.5
	4	18	0.7	3.5
	5	18	0.8	3.5
triangular	3	18	non	3.5
	4	18	non	3.5
	5	18	non	3.5
square	3	18	non	3.5
	4	18	non	3.5
	5	18	non	3.5
threaded cylindrical (V –Thread) with flat	3	18	0.5	3.5
	4	18	0.7	3.5
	5	18	0.8	3.5

Fig (3) Samples of weld specimens.

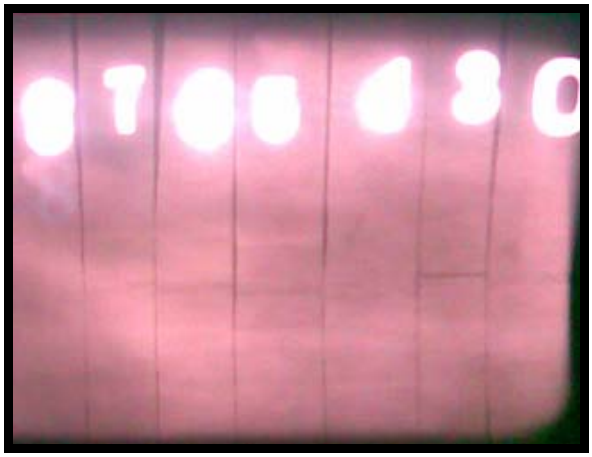

Fig (4) Samples of Radiography film.

Table 3 Results of Tensile and Bending Test of (T1-series).

FSW Exp.	Tensile Strength (N/mm^2)	Elongation (%)	Joint Efficiency in terms of tensile strength (%)	Maximum Bending Force (N).	Joint Efficiency in terms of Bending Force (%)
G1T1	144.24	5.5	45.07	337.8	35.52
G2T1	145.94	6.7	45.60	405.36	42.62
G3T1	244.6	8.8	76.43	511.53	53.78

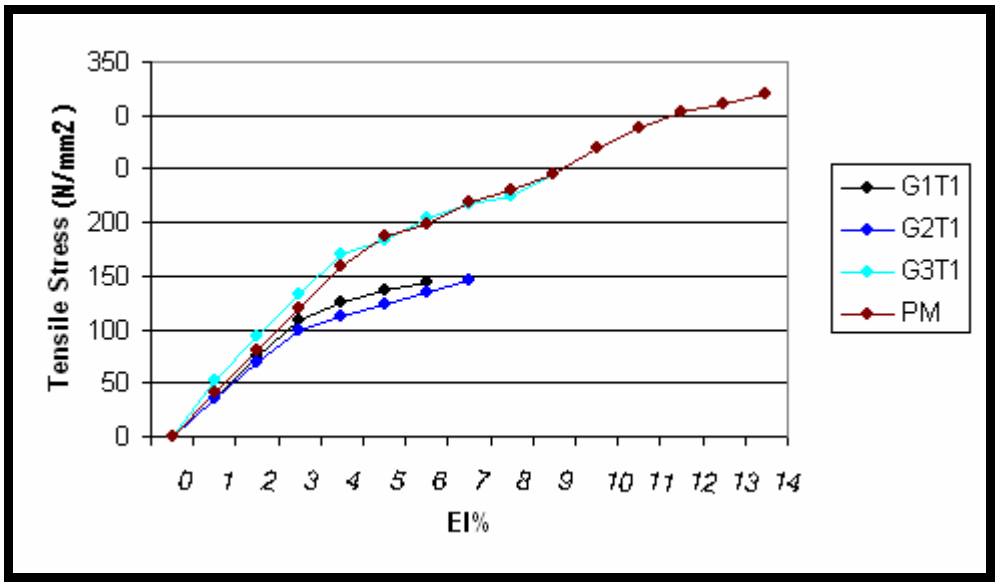

Fig. 5 Tensile strength change with rotation diameter for (T1-series).

Table 4 Results of Tensile and Bending Test of (T2-series).

FSW Exp.	Tensile Strength (N/mm^2)	Elongation (%)	Joint Efficiency in terms of tensile strength (%)	Maximum Bending Force (N).	Joint Efficiency in terms of Bending Force (%)
G1T2	152.06	5.7	47.51	550	57.83
G2T2	158.87	5.7	49.64	579.09	60.08
G3T2	258.09	10.8	80.65	685.25	72.05

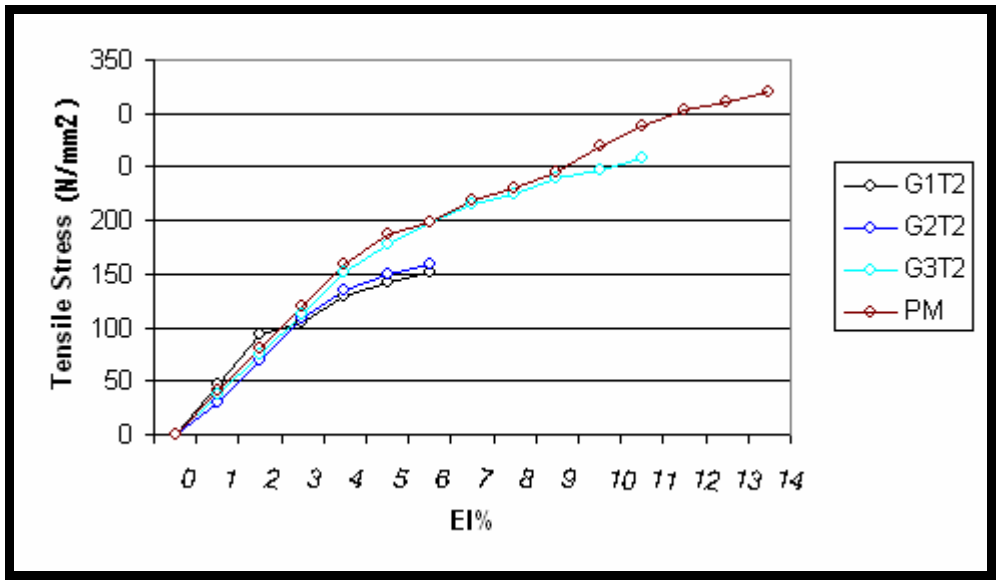

Fig 6 Tensile strength change with rotation diameter for (T2-series).

Table 5 Results of Tensile and Bending Test of (T3-series).

FSW Exp.	Tensile Strength (N/mm^2)	Elongation (%)	Joint Efficiency in terms of tensile strength (%)	Maximum Bending Force (N).	Joint Efficiency in terms of Bending Force (%)
G1T3	153.53	6.7	47.97	550.13	57.84
G2T3	191.19	9.8	59.74	694.09	72.98
G3T3	261.08	10.8	81.58	694.87	73.06

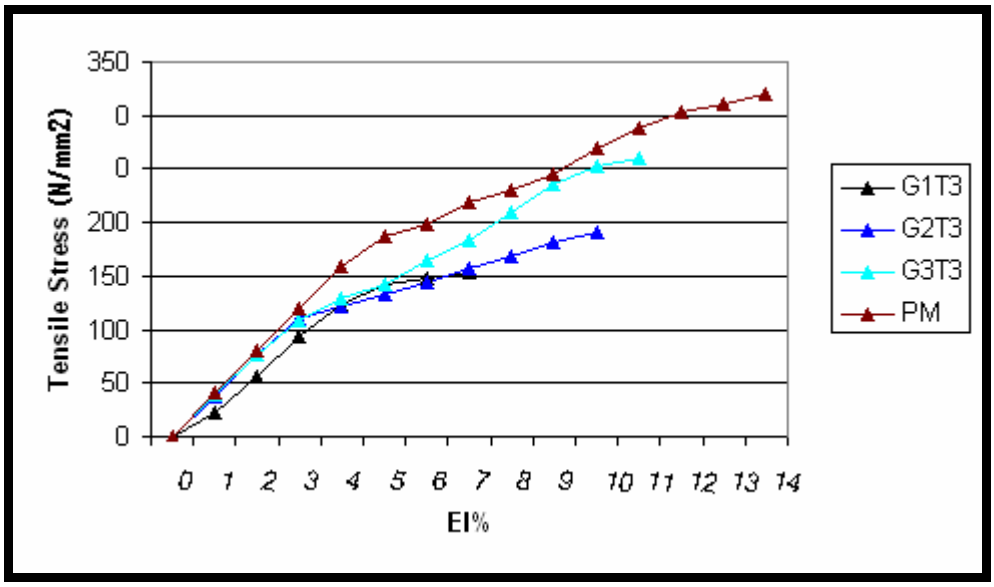

Fig 7 Tensile strength change with rotation diameter for (T3-series)

Table 6 Results of Tensile and Bending test of (T4-series)

FSW Exp.	Tensile Strength (N/mm^2)	Elongation (%)	Joint Efficiency in terms of tensile strength (%)	Maximum Bending Force (N).	Joint Efficiency in terms of Bending Force (%)
G1T4	166.5	7.7	52.03	617.6	64.94
G2T4	218.93	8.9	68.41	704.56	74.08
G3T4	265.05	10.9	82.82	762.46	80.17

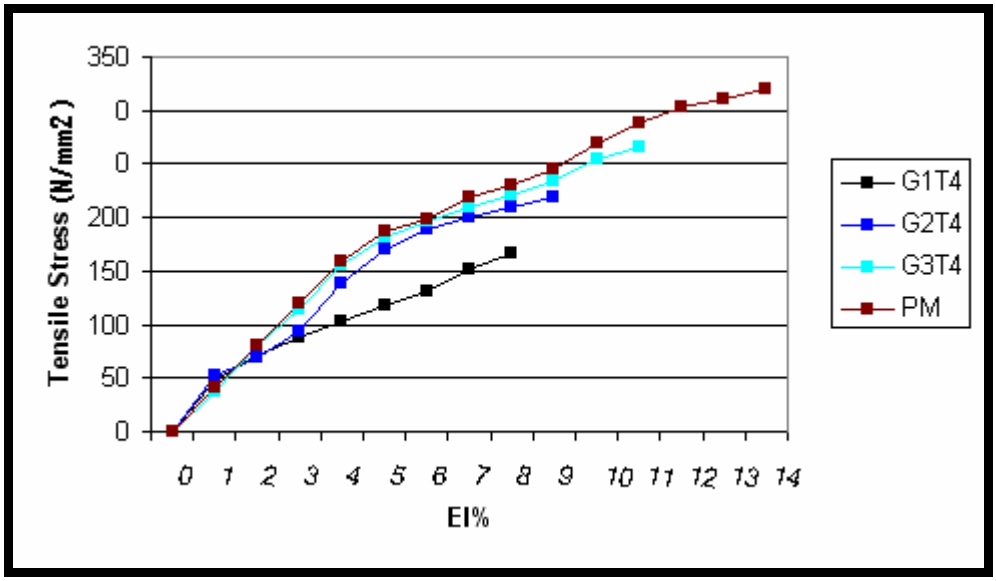

Fig 8 Tensile strength change with rotation diameter for (T4-serie

Table 7 Results of Tensile and Bending Test of (T5-series).

FSW Exp.	Tensile Strength (N/mm^2)	Elongation (%)	Joint Efficiency in terms of tensile strength (%)	Maximum Bending Force (N).	Joint Efficiency in terms of Bending Force (%
G1T5	166.55	5.8	52.04	598.39	62.92
G2T5	224.19	8.7	67.08	762.46	80.17
G3T5	278.24	11.9	86.95	791.42	83.21

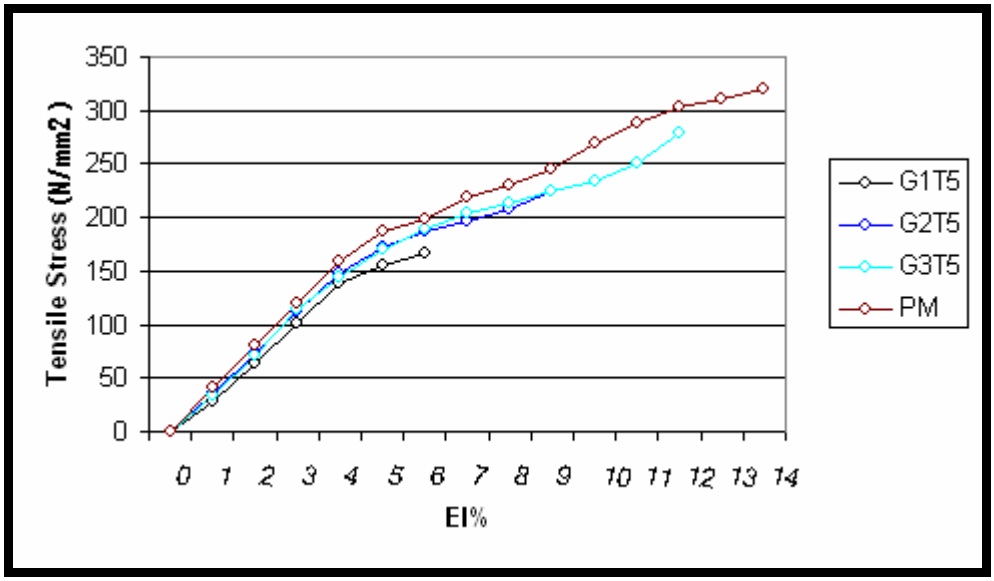

Fig 9 Tensile strength change with rotation diameter for (T5-series)

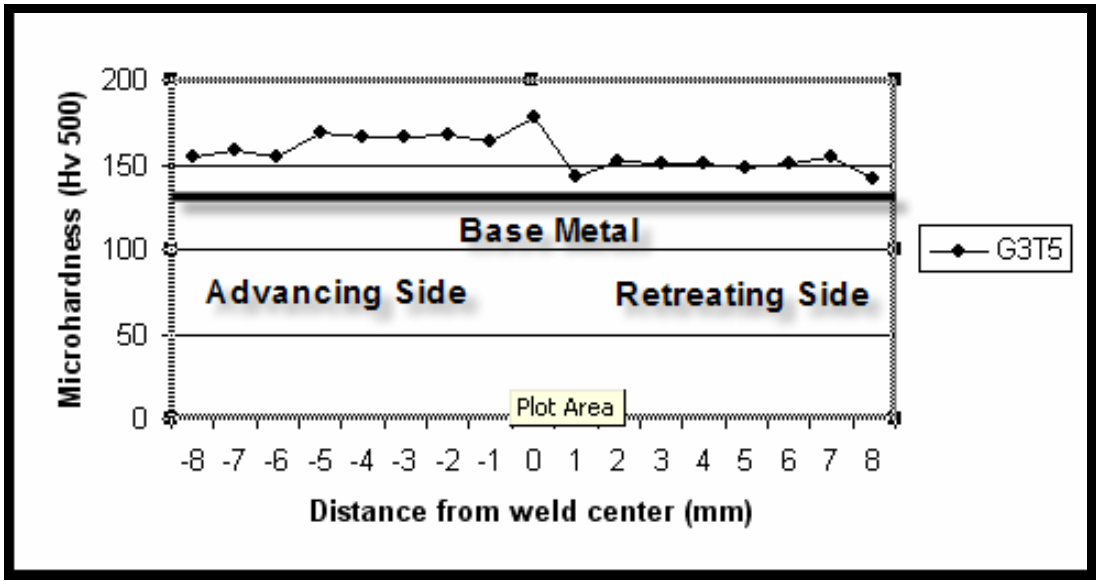

Fig 10 .Hardness distribution along (FSW) zone.

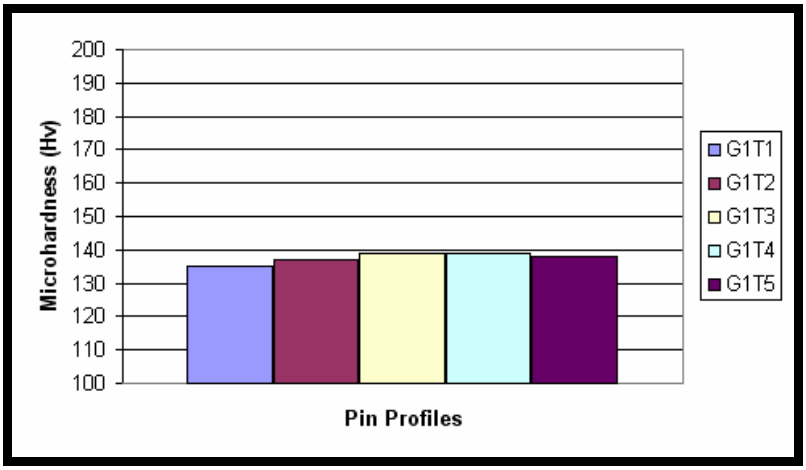

Fig 11 Effect of pin profiles with 3mm rotation diameter on (FSW) Zone Hardness.

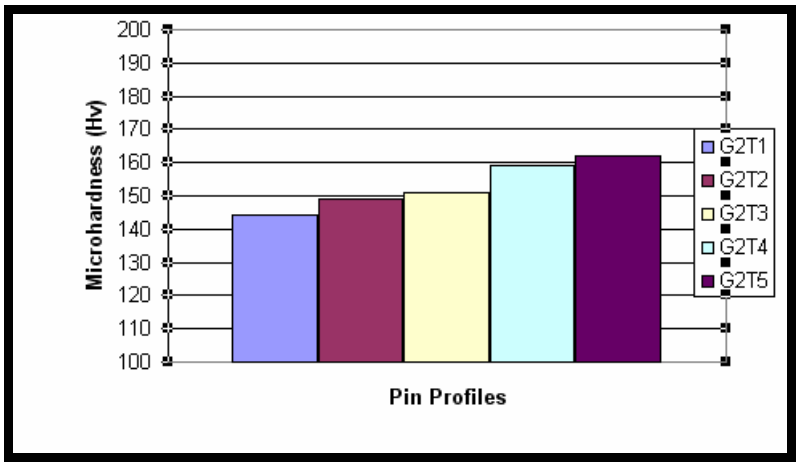

Fig 12 Effect of pin profiles with 4mm rotation diameter on (FSW) Zone Hardness.

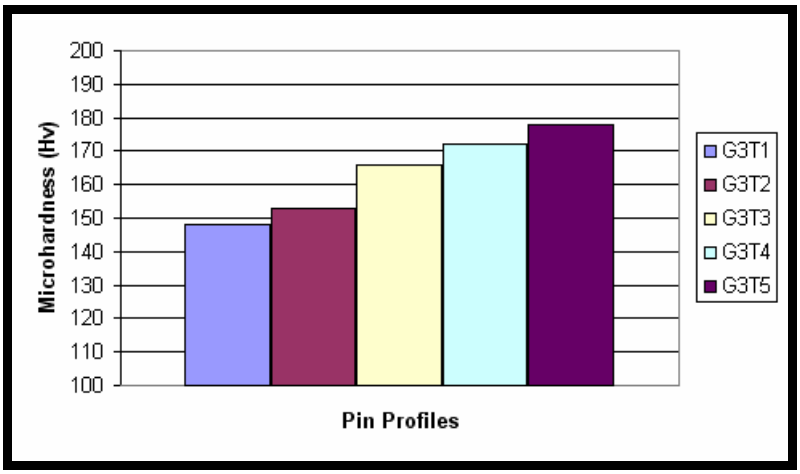

Fig 13 Effect of pin profiles with 5mm rotation diameter on (FSW) Zone Hardness.

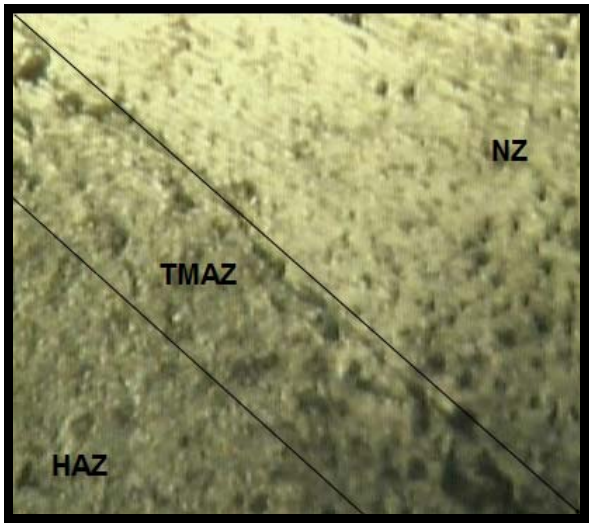

Fig (14) Microstructure observation of the joints fabricated by straight cylindrical pin profiled tool X125.

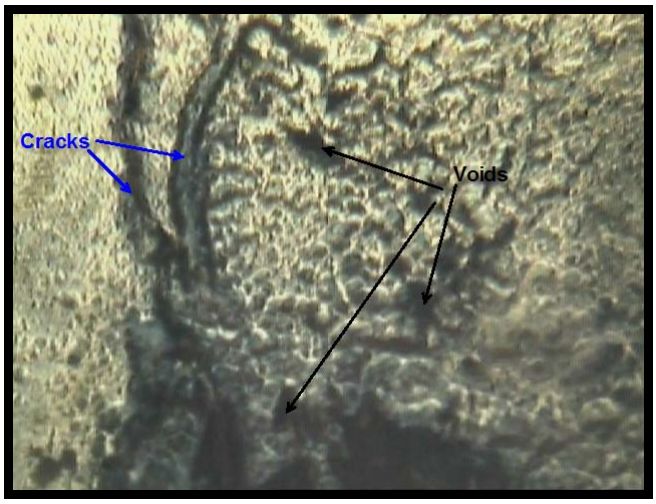

Fig (15) Microstructure observation of the joints fabricated by Threaded cylindrical pin profiled tool X125.

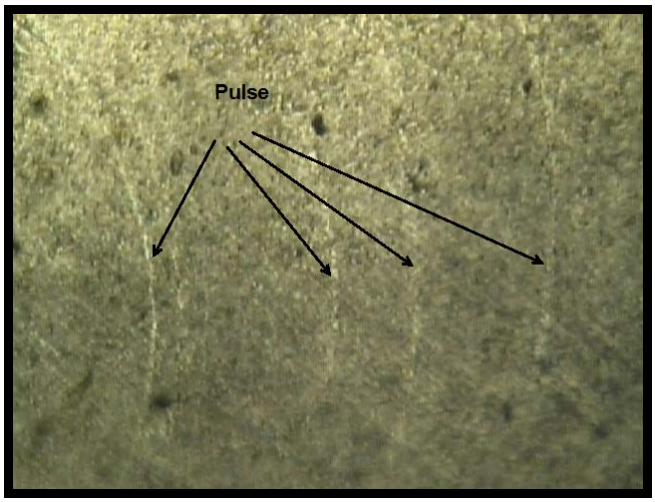

Fig (16) Microstructure observation of the joints fabricated by triangular pin profiled tool X125.

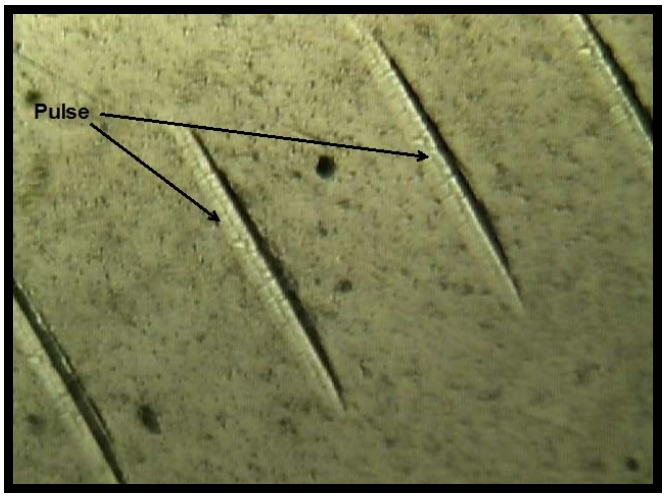

Fig (17) Microstructure observation of the joints fabricated by square pin profiled tool X125.

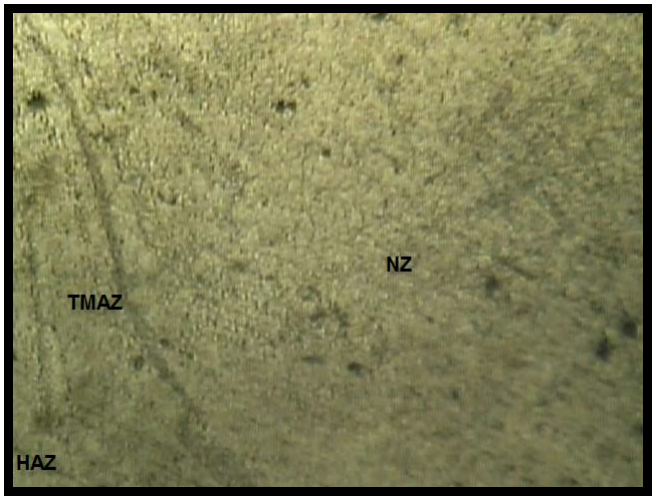

Fig (18) Microstructure observation of the joints fabricated by threaded cylindrical with flat pin profiled tool X125.

.

MEASUREMENT OF TRANSMITED VIBRATION TO TRACTOR SEAT

Dr.* Mudafer Kareem Abdullah
*** Ahmed Abd Ali Hamid AL-Mafraji**
*** Department of Agricultural Mechanization, Collage of Agriculture, Baghdad University, Iraq.**

ABSTRACT:

A field experiment was conducted at experimental field of Mechanization Agriculture , the College of Agriculture , Abu – Ghraib , University of Baghdad .To measure transmitted vibration to seat tractor during operation tillage , mold board plow with New Holland 66-S- 80 tractor as one machinery unit , Soil was treated at soil constant moisture (18 – 20 %) with two depths of plowing (15 and 20 cm) and three speed of tractor 2.0 , 3.5, 6.8 km / h . Three main dimensions in seat tractor measurement vertical, longitudinal and lateral acceleration. Split plot design under completes block design with three replicates .

قياس الاهتزازات المنقولة إلى مقعد جرار

الخلاصة :

التامة أجريت تجربة في حقل قسم المكننة الزراعية – كلية الزراعة – جامعة بغداد لقياس الاهتزازات المنقولة إلى مقعـد الجرار أثناء عملية الحراثة ، تم استخدام محراث مطرحي ثلاثي قلاب معلق مع الجرار نيوهولند ليصبح وحدة مكنية واحـدة . جرت معاملة التربة عند محتوى رطوبي ثابت 18 - 20 % وأستخدم الجرار نيو هولند ثنائي الـدفع ذو قـدرة حـصانيه متوسطة ، عند عمقين للحراثة هي 15 و 20 سم وأستخدم ثلاث سرع عملية للجرار هي 2.0 و 3.5 و 6.8 كم / ساعة. تم قياس التسارع المنقول إلى مقعد الجرار بثلاث اتجاهات رئيسية هي العمودي والطولي والجانبي ، نفـذت التجربـة بتـصميم الألواح المنشقة وتحت نظام القطاعات العشوائية الكاملة وبثلاث مكررات .

Key words: Ergonomics, Seat tractor, Vibration level, plow, Tillage.

INTRODUCTION

Recently, occupational health problems of agricultural workers have not received significant attention in developing countries. This is particularly important for tractor drivers who operate the tractor in unsuitable condition and high level of seat and tractor vibration .Tractors in high-income countries are very sophisticated and almost all have enclosed environment controlled suspended cabins and well design instrument and controls. These cabins are not likely to become common in countries like Iraq, because of economic reasons .Vehicle ride vibration is usually evaluated by acceleration value and its direction. In this regards, the acceleration can be divided into two groups, rotational and translational acceleration. Translational vibration is transmitted to a seat tractor along three perpendicular axes, longitudinal, lateral and vertical direction. Most of the tractor vibration occurs in the vertical plane, which is transmitted from wheels to the seat, whereas tractor drivers have more sensitivity to this type of vibration. On the other hand, vertical vibration level during field operation is usually exceeded from ISO standards levels (Maleki, 2008). Longitudinal and lateral vibrations occur due to tractor conditions. Vibration modes created by translational vibration on the human body caused discomfort, pain and injury. However rotational acceleration usually didn't cause any pain and injury (Griffin *et al*. 1982). The problems of tractor ride become more critical since the dominant natural frequency of the tractor (1-7 Hz) lies within most critical frequency range of human body (e.g. human trunk and lumbar vertebra have a natural frequency of 4-8 and 4-5 Hz, respectively) (Pop and Hansson, 1992 ; Troup, 1978; Klooster,2004) .

The vibration levels of tractors without cabins and suspensions have been extensively compared to the other road vehicles having suspension (Bovenzi and Betta, 1994). Moreover, many studies have been conducted on tractor seats in order to measure and compare the driver vibration with international health standards (ISO 2631-1:1997).

Many studies conducted to measurement levels vibration in seats tractor and the result was high levels combar with ISO 2631-1:1997 (Salakhe, 2007; Serudio, 2007; Muzammil, 2004). Vibration in tractor depends on many factors velocity of tractor, topography of field, tractor condition and design tractor and configuration which is by dynamic response (HSE, 2008).

The ride vibration of tractors with rear-mounted implements like mold board plow is frequently in excess of internationally accepted levels, especially during transport and plowing ,when the vibration level can be extremely high due to relatively high speed in combination with the roughness of the roads (Collins, 1991) .

The objective of this research is investigation of seat tractor vibration levels of common used tractor in Iraq and compared with ISO 2631- 1:1997.

MATERIALS AND METHODS :

A field experiment was conducted at experimental field of Mechanization Department - College of Agriculture, Abu – Ghraib, University of Baghdad. Soil type was clay – silt and unused to agriculture , Soil was treated at soil constant moisture (18 – 20 %) with two depths of plowing (15 and 20 cm) and three speed of tractor 2.0 , 3.5, 6.8 km / h , with constant revolution of engine at 2000 rpm by hand lever fuel .

Field area was 180 m length and 80 m width. Condition of tractor rebated be recommended(ISO 5008 : 2002) , the tractor shall be in working order with full tank and radiator , but without optional front and rear weight , tire ballast, The tire used in test was stander size for tractor . mold board plow with New

Holland 66-S- 80 tractor as one machinery unit figures (1) and (2) and tables (1) and (2) .Used vibration meter type VB-8201HA figure (3) , location of the measurement figures (4), (5) and (6), the acceleration was measured along three mutually perpendicular axes , define as follows :

Z – Vertical direction: sensor put under the seat.

X – Longitudinal direction: sensor put back to chest seat.

Y- Lateral direction: sensor put right side or to left side of the seat.

Result

The mean values acceleration $(m/\sec^2)$ for along three mutually perpendicular axes show in Table (3). From the table it can be observed that there was noticeable change in acceleration value in the kind of task undertaken in the present study. The transit acceleration to seat tractor increased with the increase in the velocity of tractor.

The vertical acceleration decrease with the increase depth plowing, Because velocity of tractor decrease with the increase depth plowing and cutting soil area for shears increase, that happen because slippage in tires tractor and increase resistance soil against shears plow, figure (7) .

Longitudinal acceleration increased with the increase velocity of tractor , high speed 6.8 km / h and depth plowing 20 cm was transit high vibration to seat tractor , while velocity 2.0 km / h and the same depth was less transit vibration to seat tractor, because different velocity both of them, figure (8) .

Lateral acceleration was increased with the increase velocity of tractor , high vibration transit to seat tractor with speed 6.8 km /h and depth plowing , while low vibration at 2.0 km /h and depth 15 cm figure (9)

DISCUSSION

Results of the study showed that the levels of vibration transmitted to seat tractor during the experiment was high compare with ISO 2631-1:1997 . Velocity of tractor was a strong statistical significant effect on transmitting vibration to seat tractor all three perpendicular axes. Like these values acceleration especially in vertical direction effect on operator and caused discomfort, pain and injury, tired, less performance and not completely control operation to the tractor by operator.

Therefore, we must reduce effect high levels vibration on the operator by:

1- Making full and proper use of seat position and suspension adjustments – drivers should be able
to easily reach the pedals, know how to use any back support, adjust the seat so it provides support
for their thighs and adjust the suspension mechanism correctly for their weight.

2- Choosing a speed appropriate for the ground they are driving over – control of whole body vibra-tion should be used to reduce the risk of injury, NOT increase productivity.

3- Selecting a course to avoid potholes, ruts, bumps etc as much as possible.

4- When conducted conventional tillage must the working time be 4 hour not more, and take period rest between the works.

5- Good stile operation can be reducing levels transit vibration to seat tractor.

SUMMARY

Results can be summarized as follows:

1- Transmitted acceleration to seat tractor in three dimension vertical, longitudinal and lateral Increasing with increased speed tractor.

2- Transmitted vertical acceleration to seat tractor decreasing with increase depth of plowing from 15 to 20 cm. Tractor operator was uncomfortable and incompletely control driving on tractor with high speed of tractor 6.8 km / h.

3- Levels transmitted acceleration to seat tractor was high and across levels safety compare with ISO 2631-1-1997

REFERANCES

Bovenzi M; Betta A (1994), Low back disorder in agricultural tractor drivers exposed to whole body vibration and postural stress. Applied Ergonomics, 25, 231}241.

Griffin, M. J., E. M. Whitham and K. C. Parsons .1982: Vibration and Comfort: translational seat vibration. Journal of Ergonomics. 5(7):603-630.

Collins, T. S. 1991, Loads in tractor linkages when transporting rear-mounted implements: Development of modeling and measurement techniques. J. Agric. Eng. Research 49: 165-188.

HSE, Health and Safety Executive 2008, Health and Hazards from Whole-body Vibration caused by Mobile Agricultural Machinery, HSE sheet no 20, UK.

International Standard Organization **ISO** 5008:2002, Agricultural Wheeled Tractors and Field Machinery - Measurement of Whole-Body Vibration of the Operator .

International Standard Organization ISO 2631-1:1997, Mechanical Vibration and Shock -Evaluation of Human Exposure to Whole-Body Vibration - Part 1: General requirements.

Klooster, Samuel J, 2004, Vibration Suppression and Safety Seat Motion Design of a Hyper Active Sea School of Mechanical Engineering Georgia Institute of Technology.

Maleki, A .Mohtasbi, S.S. Akram, A and Esfahanian, V. 2008, Investigation and Analysis of Driver Weight on His Health and Comfort in Three Commonly Used Tractors in Iran. Agricultural Engineering International: the CIGR Journal. Manuscript MES 07 007. Vol. X.

Muzammil M, Saad, S, Siddiqui and Faisal Hasan 2004, Physiological Effect of Vibration on Tractor Drivers under Variable Ploughing Conditions .46:403-409. Journal Occupational Health, India.

Pope MH; Hansson T H (1992), Vibration of the spine and low back pain. Clinical Orthopedics, 279, 49}59.

Salokhe, V. M .T. Niyamapa and Hiroshi Nakashima. 2007, Vibration Effects on the Performance of a Single-Shank Subsoiler. Agricultural Engineering International: the CIGR Journal. Manuscript PM 07018. Vol. IX.

Seruadio. P. Belfiore N.P. 2007, Analysis of driving seat vibration in high forward speed tractor; Journal Biosystems Engineering ISSN 1537-5110. Vol. 97, pp. 171- 180.

Troup . J. D. G (1978) . Driver's back pain and its prevention a review of postural, vibratory and muscular factors together with problem of transmitted road-shock. Applied Ergonomics 9, 207}214.

Figure. (1): Tractor new Holland and mold board plow as one machinery unit during measurement

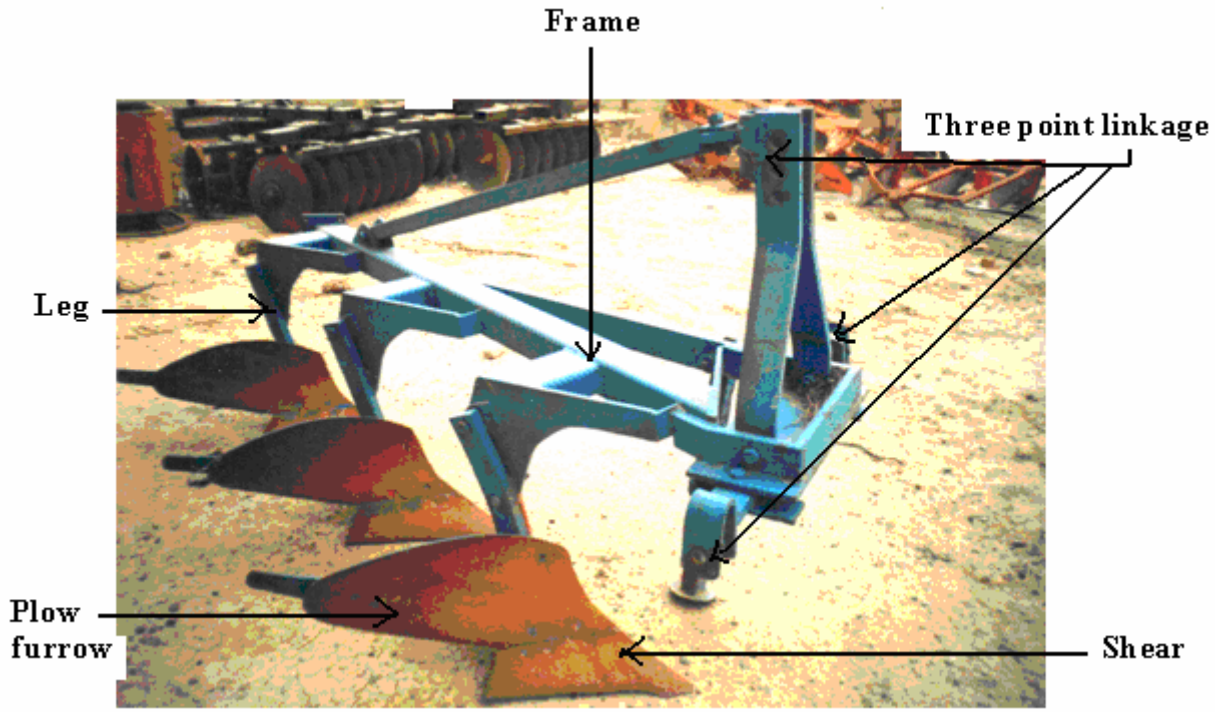

Figure. (2): Mold board plow

Table (1): Important specification of the tractor New Holland *

Model	New Holland 66 – S 80 2WD
Type engine	Iveco 4 stroke, direct injection, water cooled.
Number of cylinders	4
Diameter of cylinder (mm)	104
Long stroke (mm)	115
Engine power (horse mechanical)	80
Maximum revelation engine (rpm)	2600
Total weight (KN)	29.78
Tractor weight without ballast (KN)	25.80
Size rear tire	18.4 R 30
Pressure rear tire (Psi)	20 **
Size front tire	7.50 R16
Pressure front tire	30
Type suspension seat	Mechanical spring
Operator mass (kg)	65***
Made	Italy

*** Taken from NEW HOLLAND SERIES 66 SS**
*** * Pressures rear & front tire during experiment.**
***** Operator mass during experiment.**

Table (2): Specification of the mold board plow used in experiment.

Number shear	3
Type	Hanging by three linkage point
Working width (mm)	1050
Working depth (mm)	270
Total length (mm)	2880
Total width (mm)	1680
High (mm)	1155
Weight (kg)	280
Made	Iraq

.

Figure. (3) Vibration meter

Figure. (4) Measure transited acceleration to seat tractor in vertical direction.

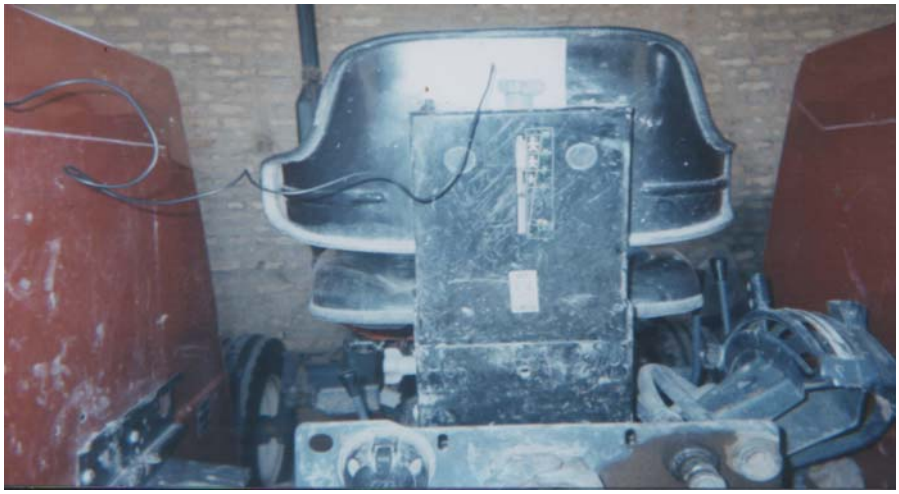

Figure. (5) Measure transited acceleration to seat tractor in longitudinal direction.

Figure. (6) Measure transited acceleration to seat tractor in lateral direction.

Table 3. The mean values acceleration $(m/\sec^2)$ for along three mutually perpendicular axes.

Depth plowing (cm)	speed tractor (km / h)	Vertical Z $(m/\sec^2)$	Longitudinal X $(m/\sec^2)$	Lateral Y $(m/\sec^2)$
15	2.0	4.8	11.1	2.8
15	3.5	4.9	11.8	5.6
15	6.8	7.0	12.7	5.7
20	2.0	4.5	10.5	2.9
20	3.5	4.7	12.8	5.2
20	6.8	6.3	14.6	7.7

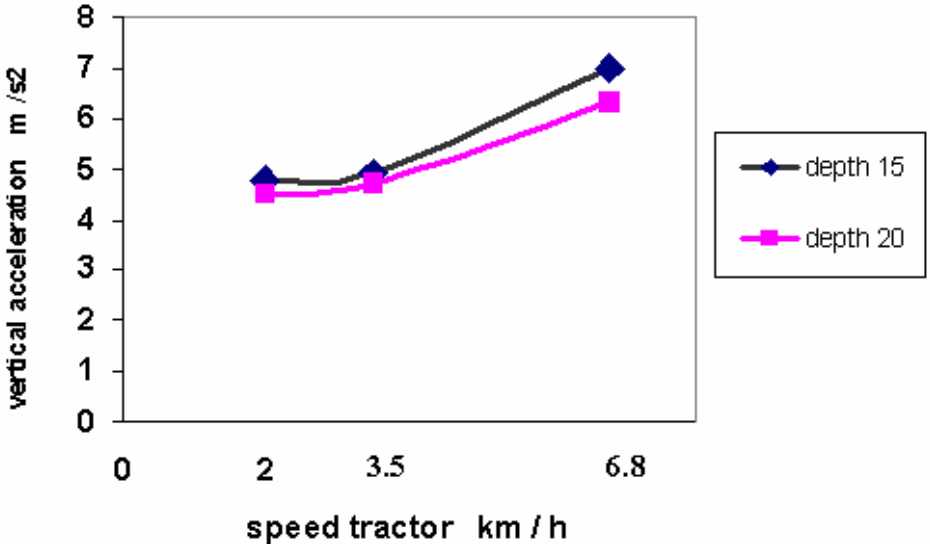

Figure 7. Relation transit vertical acceleration to seat tractor with speed and depth plowing

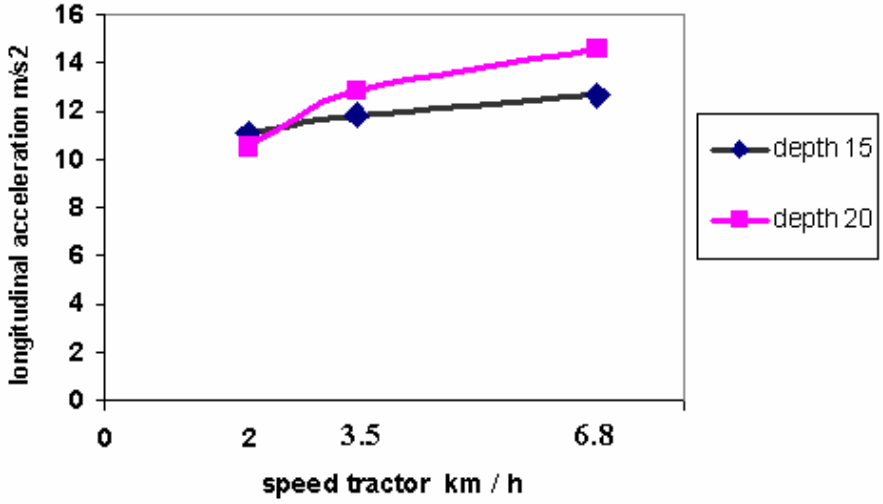

Figure 8. Relation transit longitudinal acceleration to seat tractor with speed and depth plowing

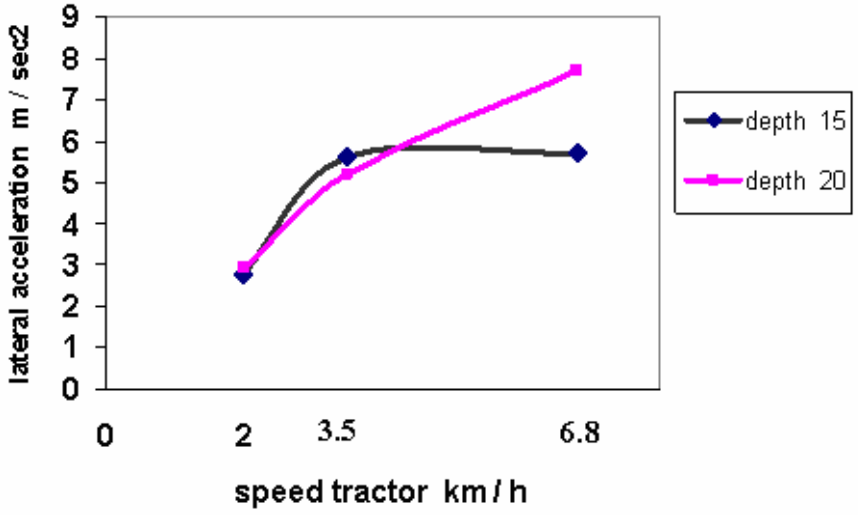

Figure 9. Relation transit lateral acceleration to seat tractor with speed and depth plowing

DEVELOPING LAMINAR MIXED CONVECTION HEAT TRANSFER THROUGH VERTICAL CONCENTRIC ANNULI WITH ADIABATIC INNER CYLINDER

Prof. Dr. Ihsan Y. Hussain Baghdad University Mech. Eng. Dep.
Dr. Akeel Abdullah Mohammed University of Technology Mech. Eng. Dep.
Ghada A. Sadiq Al-Mustansiriya University Mech. Eng. Dep.

ABSTRACT

Theoretical and experimental investigations have been carried out on developing laminar combined free and forced convection heat transfer in a vertical concentric annulus with uniformly heated outer cylinder (constant heat flux) and adiabatic inner cylinder for both aiding and opposing flows. The theoretical investigation involved a mathematical modeling and numerical solution for two dimensional, symmetric, simultaneously developing laminar air flows was achieved. The governing equations of motion (continuity, momentum and energy) are solved by using implicit finite difference method and the Gauss elimination technique. The theoretical work covers heat flux range from (200 to 1500) W/m^2, Re range from 400 to 2000 and ($1.36\times10^5 \le Ra \le 1.1\times10^7$) with radius ratio of 0.555 which is the same radius ratio used in the experimental part of this study and Pr=0.7. The experimental work includes construct a rig consists essentially of an annulus with uniformly heated outer cylinder and adiabatic inner cylinder to give clear insight into heat transfer process and compare its results with that obtained in theoretical part, the range of the study are (Re= 383, 724, 1000, 1500) and heat flux equal to (q =370, 422, 588, 980) W/m^2. Numerical results were represented by the temperature profile, axial velocity profile, outer surface temperature and the distribution of local Nusselt number along the dimensionless axial distance. The velocity and temperature profile results have revealed that the secondary flow created by natural convection have significant effects on the heat transfer process. Results reveal also that the experimental local Nusselt number along the annulus follows the same trend as present theoretical results with mean difference 10.23 %.

الخلاصة:

أجريتْ دراسة نظرية وعملية لانتقال الحرارة بالحمل المختلط لجريان الهواء المتطور الطباقي خلال تجويف حلقي عمودي ذو أسطوانتين متمركزتين؛ الخارجية مسخنة تسخين منتظم (فيض حراري ثابت) و الداخلية معزولة (لكلا الجريانين المساعد والمعاكس). البحث النظري تضمن عمل نموذج رياضي و دراسة عددية لجريان الهواء الطباقي المشكل تراكبيا ثنائي البعد. تم حل المعادلات الحاكمة للحركة (الاستمرارية ، الزخم ، الطاقة) باستخدام طريقة الفروقات المحددة و طريقة معكوس المصفوفة (طريقة كاوس). غطت الدراسة النظرية فيضا حراريا مداه من 200 واط\م^2 إلى 1500واط\م^2 ، معدل رقم رينولدز Re من 400 إلى 2000 و ($1.36\times10^5 \le Ra \le 1.1\times10^7$) مع نسبة نصف قطر تساوي 0.555 وهي نفسها المستخدمة في الجزء العملي من هذا البحث ورقم براندتل Pr =0.7. اشتمل الجزء العملي بناء جهاز تجريبي يتكون من تجويف حلقي متمركز بأسطوانة خارجية مسخنة تسخين منتظم و أسطوانة داخلية معزولة لاعطاء نظرة واضحة لعملية انتقال الحرارة ومقارنة نتائجها مع تلك التي تم الحصول عليها في الجزء النظري مدى الدراسة (Re= 383, 724, 1000, 1500) والفيض الحراري مساوي الى (q =370, 422, 588, 980) W/m^2 . تم تمثيل النتائج النظرية برسم توزيع درجة الحرارة، توزيع السرعة المحورية على طول التجويف الحلقي، درجة حرارة الاسطوانة الخارجية و توزيع رقم نسلت الموقعي مع المسافة المحورية اللابعدية. اظهرت نتائج توزيع السرعة و درجات الحرارة ان الجريان الثانوي الناتج من الحمل الحر(الطبيعي) له تاثير مهم على عملية انتقال الحراة. النتائج بينت بان قيم رقم نسلت الموقعي العملية تتخذ نفس سلوك قيم رقم نسلت الموقعي النظرية لكن أعلى تقريباً مع معدل فرق 10.23 %.

KEYWORDS: **Combined Convection, Concentric Annulus, Numerical and Experimental.**

INTRODUCTION

The convective heat transfer is of great importance in many engineering applications. A number of investigations have been carried out to study pure forced convection and pure natural convection in different geometries. However, mixed convection, i.e., combined free and forced convection is the most general single phase heat transfer phenomenon and has received considerable attention in recent years. Such a process occurs when the effect of the buoyancy force in forced convection or the effect of forced flow in free convection becomes significant. In mixed convection flows, the forced convection effects and the free convection effects may be of comparable magnitudes.

Mixed convection processes may be divided into external flows over immersed bodies, free boundary flows, and internal flows. In internal flows, mixed convective flows are quite common and there can be a variety of geometries, such as cylindrical, rectangular and triangular cross- sections. The concentric annular duct is of technical importance, as it represents numerous heat transfers and fluid flow devices. Mixed convection in concentric cylinders has been the subject of many investigations for quite some time, for example: Gas- cooled electrical cables, heat exchanger designed for chemical processes require the consideration of mixed convection in an annular flow, cooling of nuclear fuel rods where the results for the buoyancy-influenced convection in an annulus are useful and the collection of solar energy**.**

(El-Sharrawi and Sarhan 1980) studied mixed convection of upward and downward air flow in an annulus of radius ratio (0.5, 0.8, and 0.9) and Pr = 0.7. The flow with a flat velocity profile at the entrance was considered. The thermal boundary conditions of one wall being isothermal and other adiabatic. They noticed that when the free convection opposes the forced flow (heating with down flow or cooling with up flow) there exists a possibility of flow reversal near the heated boundary while such a flow reversal may occur near the insulated wall if the free convection is aiding the force flow. The axial velocity profiles development, pressure drop, mixing cup temperature and heat transfer coefficient along the annulus were calculated.

(Hashimoto et. al 1986) performed a numerical investigation of the mixed convection (both upward and downward helium gas flow with Pr = 0.671), with a simultaneously developing hydrodynamic and thermal boundary layer in a vertical annulus of (0.9) radius ratio. The flow was considered under isothermal or constant heat flux inner wall and adiabatic outer wall. The equations of the continuity, momentum, energy, and integral continuity were solved on the basis of the boundary layer approximation. The critical conditions effect on the flow which create a reversal flow and the effect of property variations on both Nusselt number and friction factor were obtained.

(Hanzawa et. al 1986) performed experiments to study the mixed convection of upward gas flow in vertical annulus of radius ratio range from (0.29 to 0.63) and hydraulic diameter to heating section length range from (0.34 to 1.4). A part of the inner tube was isothermally heated while the outer tube was kept adiabatic. The study covered Gr range from (1.5×10^6 to 2×10^8), Re range from (20 to 1000). The effects of operating conditions on the temperature profiles, flow pattern and heat transfer coefficient were investigated.

Numerical solutions for the problem of steady state laminar combined convection flows in vertical annular ducts were presented by **(Heggs et. al 1988)**. The axial diffusion terms were assumed to be negligible in the governing equations and the resulting parabolic equations were solved by using an implicit finite difference scheme and a marching solution technique. Constant wall temperature boundary conditions were used and investigations were restricted to the case Pr =0.72. Large ranges of values of the governing parameters Gr/Re and radius ratio were considered ($-90 \leq Gr/Re \leq 125$) and ($0.1 \leq N \leq 0.99$). For large values of the ratio

Gr/Re reverse flow was present in the fluid. A modified solution technique was used throughout the region of the annulus containing the flow reversal and complete solutions were presented for these situations for the first time. Heat transfer data in the form of flow average temperatures and local Nusselt numbers at both the inner and outer walls were presented. It was found that the behavior of the local Nusselt number on each wall was considerably different.

The laminar mixed convection in vertical channels was studied numerically by using an implicit finite difference method by **(Shaik 2005**) emphasis was devoted to analyze the hydrodynamic behavior of mixed convection flow under isothermal boundary conditions regarding. The pressure and pressure gradient variation along the channel (from the entrance till the fully developed region) was obtained numerically. Moreover, critical values of the buoyancy parameter Gr/Re were determined and the radius ratio (0.1, 0.3, 0.5 and 0.7). The hydrodynamic and heat transfer parameters of relevant importance were also presented.

The present work in its theoretical part includes a finite difference method using mesh grid point for vertical annulus mixed convection, the range of the work are ($400 \le Re \le 2000$),($1.36\times10^5 \le Ra \le 1.1\times10^7$) and the heat flux for aiding and opposing flow (200 to 1500) W/m^2 of radius ratio (0.555). The experimental investigation is made for simultaneously developing mixed convection laminar air flow in a vertical annulus of radius ratio (0.555) and with uniformly heated outer cylinder and adiabatic inner cylinder. The range of the work are (Re= 383, 724, 1000, 1500) and heat flux equal to (q =370, 422, 588, 980) W/m^2 with radius ratio (N=0.555).

MATHIMATICAL MODELING

The present analysis assumes incompressible fluid, steady state laminar air flow with two dimensional in the axial and radial directions for hydrodynamically and thermally developing flow see **Fig.1**. The assumptions were used are negligible viscous dissipation, no internal heat generation and heat dissipation, Cp and K are constants and the density ρ in the buoyancy term and the viscosity μ are varying with temperature in a quadratic equation. The governing equations become **(Kayes 1966)**:

$$\frac{\partial u}{\partial z}+\frac{v}{r}+\frac{\partial v}{\partial r}=0 \tag{1}$$

$$\rho_l\cdot\left(v\frac{\partial u}{\partial r}+u\frac{\partial u}{\partial z}\right)=-\frac{\partial p}{\partial z}\pm\rho g+\mu\cdot\left(\frac{\partial^2 u}{\partial z^2}+\frac{1}{r}\frac{\partial u}{\partial r}+\frac{\partial^2 u}{\partial r^2}\right)+2\left(\frac{\partial \mu}{\partial z}\cdot\frac{\partial u}{\partial z}\right)+\frac{\partial \mu}{\partial r}\cdot\left(\frac{\partial v}{\partial z}+\frac{\partial u}{\partial r}\right) \tag{2}$$

The sign ± ρg in the buoyancy term refers to downward or upward flow respectively.

$$\rho_l\cdot\left(v\frac{\partial v}{\partial r}+u\frac{\partial v}{\partial z}\right)=-\frac{\partial p}{\partial r}+\mu\cdot\left(\frac{\partial^2 v}{\partial z^2}+\frac{1}{r}\frac{\partial v}{\partial r}-\frac{v}{r^2}+\frac{\partial^2 v}{\partial r^2}\right)+2\cdot\left(\frac{\partial \mu}{\partial r}\cdot\frac{\partial v}{\partial r}\right)+\frac{\partial \mu}{\partial z}\cdot\left(\frac{\partial v}{\partial z}+\frac{\partial u}{\partial r}\right) \tag{3}$$

$$\left(v\frac{\partial t}{\partial r}+u\frac{\partial t}{\partial z}\right)=\frac{k}{\rho_i\cdot Cp}\cdot\left(\frac{\partial^2 t}{\partial z^2}+\frac{1}{r}\frac{\partial t}{\partial r}+\frac{\partial^2 t}{\partial r^2}\right) \tag{4}$$

The conversation of mass (continuity equation) can be expressed in the following integral form:

$$\rho_i\cdot\pi\cdot\left(r_o^{\,2}-r_i^{\,2}\right)\cdot u_i=\int_{r_i}^{r_o}2\pi\cdot r\cdot\rho\cdot u\cdot dr \tag{5}$$

The dynamic viscosity μ and density ρ are considered to be dependent on temperature according to the following relations **(Collins 1971);**

$$\mu = \mu_i\left(C_1 + C_2 t - C_3 t^2\right) \tag{6}$$

$$\rho = \rho_i\left(C_4 - C_5 t + C_6 t^2\right) \tag{7}$$

Dimensionless Equations

The physical properties, equations in dimensionless form become:

$$\mu = \mu_i\left(Co_1 + Co_2 T + Co_3 T^2\right) \tag{8}$$

$$\rho = \rho_i\left(Co_4 + Co_5 T/G + Co_6 T^2/G\right) \tag{9}$$

where

$$Co_1 = C_1 + C_2 t_i - C_3 t_i^{\,2},$$
$$Co_2 = \left(1/G.C_5\right)\left(C_2 - 2C_3 t_i\right)$$
$$Co_3 = -C_3/G^2 C_5^{\,2},$$
$$Co_4 = C_4 - C_5 t_i + C_6 t_i^{\,2}$$
$$Co_5 = \left(2C_6 t_i/C_5\right) - 1,$$
$$Co_6 = C_6/G C_5^{\,2}$$

$$\frac{\partial U}{\partial Z} + \frac{V}{R} + \frac{\partial V}{\partial R} = 0 \tag{10}$$

$$V\frac{\partial U}{\partial R} + U\frac{\partial U}{\partial Z} = -\frac{\partial P}{\partial Z} \pm \frac{4(1-N)^2}{Re^2}\left[G Co_4 + T(Co_5 + Co_6 T)\right] + \frac{2(1-N)}{Re}\left[\left\{Co_1 + T(Co_2 + Co_3 T)\right\}\cdot\left(\frac{\partial^2 U}{\partial Z^2} + \frac{1}{R}\cdot\frac{\partial U}{\partial R} + \frac{\partial^2 U}{\partial R^2}\right)\right] + \frac{2(1-N)}{Re}\left[\left\{Co_2 + 2TCo_3\right\}\left(2\frac{\partial T}{\partial Z}\cdot\frac{\partial U}{\partial Z} + \frac{\partial T}{\partial R}\left\{\frac{\partial V}{\partial Z} + \frac{\partial U}{\partial R}\right\}\right)\right] \tag{11}$$

$$V\frac{\partial V}{\partial R} + U\frac{\partial V}{\partial Z} = -\frac{\partial P}{\partial R} + \frac{2(1-N)}{Re}\cdot\left\{Co_1 + T(Co_2 + Co_3 T)\right\}\cdot\left(\frac{\partial^2 V}{\partial Z^2} + \frac{1}{R}\frac{\partial V}{\partial R} - \frac{V}{R^2} + \frac{\partial^2 V}{\partial R^2}\right) + \frac{2(1-N)}{Re}\cdot\left\{Co_2 + 2TCo_3\right\}\cdot\left(2\frac{\partial T}{\partial R}\cdot\frac{\partial V}{\partial R} + \frac{\partial T}{\partial Z}\left\{\frac{\partial V}{\partial Z} + \frac{\partial U}{\partial R}\right\}\right) \tag{12}$$

$$V\frac{\partial T}{\partial R} + U\frac{\partial T}{\partial Z} = \frac{2(1-N)}{Re\,Pr}\cdot\left(\frac{\partial^2 T}{\partial Z^2} + \frac{1}{R}\frac{\partial T}{\partial R} + \frac{\partial^2 T}{\partial R^2}\right) \tag{13}$$

$$\frac{1}{2}\cdot\left(1 - N^2\right) = \int_N^1 U\cdot R\cdot\left(Co_4 + Co_5\cdot T/G + Co_6\cdot T^2/G\right)\cdot dR \tag{14}$$

Boundary conditions in dimensionless form:

Entry condition

$$U = 1\ ,\ V = 0\ ,\ P = 0\ ,\ T = 0$$

Outer wall thermal condition

$$q = \left(k\cdot\frac{\partial t}{\partial r}\right)_{r=r_o} = \left(k\cdot\frac{\partial\left(T/G\cdot C_5 + t_i\right)}{\partial\left(R\cdot r_o\right)}\right)_{R=1}$$

$$\left(\frac{\partial T}{\partial R}\right)_{R=1} = \frac{q.r_o^{\,4}.g\cdot C_5}{k\cdot\nu_i^{\,2}}$$

Wall flow conditions

at R = N , U = 0 , V = 0 for all z

at R = 1 , U = 0 , V = 0 for all z

NUMERICAL SOLUTION

The numerical approximation method used is finite difference in the differential equations. The energy equation will be solved by a direct implicit method and the hydrodynamic part of the problem will be solved by means of an extension to the linearized implicit finite difference technique.

In the thermal length, problem of air flow with constant physical properties except the density in the buoyancy term is that the energy equation (11) is not couple with the equations of conservation of mass and momentum (8-10). This leads to special treatment for this problem by dividing it into two parts; the equation of energy can be solved to determine the temperature profile after which the equation of conversation of mass and momentum can be solved to determine the hydrodynamic characteristics of entry length using the temperature profiles previously obtained from the thermal calculations. Equation for temperature was written for each radial position at first axial step. This gives a set of M-1 equations for unknowns T's that were solved by Gauss elimination method. A rectangular grid was used with suffices m and n for the radial and axial directions, respectively. A uniform radial spacing was used, but the axial step size could be varied by doubling it at arbitrary axial locations. Basically, finite difference methods are used to give sets of linear equations for the variables U, V, P and T at the unknown axial position ("n+1"). Where the product of the two unknowns occurs, linearity is achieved by putting one unknown at its value of the previous known step ("n").

Numerical formulation

Continuity equation

$$\left(\frac{S\cdot x}{x-1}\right)V_{n+1,m}-S\cdot V_{n+1,m-1}+\frac{1}{2\Delta Z}U_{n+1,m}+\frac{1}{2\Delta Z}U_{n+1,m-1}=\frac{1}{2\Delta Z}\left(U_{n,m}+U_{n,m-1}\right) \quad (15)$$

$$R=\frac{x-1}{S}\quad,\quad x=F+m\quad,\quad N=\frac{F}{S}$$

F = number of the node at the inner surface from the center.

S = total radial mesh point from the center (S = F + M).

Momentum equations in axial and radial directions respectively:

$$\left[\frac{S^2(1-N)}{Re}\left\{T_A\frac{(2x-1)}{(x-1)}+\frac{T_B}{2}(T_{n+1,m+1}-T_{n+1,m-1})\right\}-\frac{S}{2}\cdot V_{n,m}\right]*(U_{n+1,m+1})+\left[\frac{2(1-N)}{Re}\cdot\left\{T_A\left(\frac{1}{\Delta Z^2}-2S^2\right)\right\}\right]*(U_{n+1,m})+\left[\frac{2(1-N)}{Re}\left\{\frac{2T_B}{\Delta Z^2}\cdot(T_{n+1,m}-T_{n,m})\right\}-\frac{U_{n,m}}{\Delta Z}\right]*(U_{n+1,m})+\left[\frac{S^2(1-N)}{Re}\left\{T_A\frac{(2x-3)}{(x-1)}-\frac{T_B}{2}(T_{n+1,m+1}-T_{n+1,m-1})\right\}\right]*(U_{n+1,m-1})+\left[\frac{S}{2}\cdot V_{n,m}\right]*(U_{n+1,m-1})-\left[\frac{P_{n+1,m}}{\Delta Z}\right]=+\left[\frac{4(1-N)}{Re^2}\{G\cdot Co_4+T_{n+1,m}(Co_5+Co_6T_{n+1,m})\}\right]+\left[\frac{4(1-N)}{Re\Delta Z^2}\cdot\{T_A+T_B(T_{n+1,m}-T_{n,m})\}\right]*(U_{n,m})-\left[\frac{2(1-N)\cdot U_{n-1,m}}{\Delta Z^2\cdot Re}\cdot T_A\right]-\left[\frac{P_{n,m}}{\Delta Z}\right]-\left[\frac{U^2_{n,m}}{\Delta Z}\right]-\left[\frac{S\cdot(1-N)}{\Delta Z\cdot Re}\cdot T_B\cdot(T_{n+1,m+1}-T_{n+1,m-1})\cdot(V_{n,m}-V_{n-1,m})\right] \quad (16)$$

where;

$$T_A=\left(Co_1+T_{n+1,m}(Co_2+Co_3T_{n+1,m})\right)$$

$$T_B=\left(Co_2+Co_3T_{n+1,m}\right)$$

$$\left[\frac{S^2(1-N)}{Re}\left\{T_A\frac{(2x-1)}{(x-1)}+T_B(T_{n+1,m+1}-T_{n+1,m-1})\right\}-\frac{S}{2}V_{n,m}\right]*(V_{n+1,m+1})+\left[\frac{2(1-N)}{Re}\left\{T_A\left(\frac{1}{\Delta Z^2}-\frac{S^2}{(x-1)^2}(2x^2-4x+3)\right)\right\}\right]*(V_{n+1,m})+\left[\frac{2(1-N)}{Re}\left\{\frac{T_B}{\Delta Z^2}(T_{n+1,m}-T_{n,m})-\frac{U_{n,m}}{\Delta Z}\right\}\right]*V_{n+1,m}+\left[\frac{S^2(1-N)}{Re}\left\{T_A\cdot\frac{(2x-3)}{(x-1)}-T_B(T_{n+1,m+1}-T_{n+1,m-1})\right\}+\frac{S}{2}\cdot V_{n,m}\right]*(V_{n+1,m-1})+\left[\frac{S}{12}\right]\cdot P_{n+1,m+2}-\left[\frac{2S}{3}\right]\cdot P_{n+1,m+1}+\left[\frac{2S}{3}\right]\cdot P_{n+1,m-1}-\left[\frac{S}{12}\right]\cdot P_{n+1,m-2}=\left[-\frac{U_{n,m}}{\Delta Z}\cdot V_{n,m}+\frac{4(1-N)}{Re\Delta Z^2}\cdot T_A\cdot V_{n,m}\right]+\left[\frac{2(1-N)}{Re\Delta Z^2}\cdot\left\{\frac{T_B}{2}\cdot(T_{n+1,m}-T_{n,m})-T_A\right\}\cdot V_{n-1,m}\right]-\left[\frac{S\cdot(1-N)}{Re\Delta Z}\cdot T_B\cdot(T_{n+1,m}-T_{n,m})\cdot(U_{n,m+1}-U_{n,m-1})\right] \quad (17)$$

Energy equation

$$\left[\frac{S}{2}\cdot V_{n,m}+\frac{S^2(1-N)}{\mathrm{Re}\cdot\mathrm{Pr}}\cdot\frac{(1-2x)}{(x-1)}\right]\cdot T_{n+1,m+1}+\left[\frac{U_{n,m}}{\Delta Z}+\frac{2(1-N)}{\mathrm{Re}\cdot\mathrm{Pr}}\cdot\left(2S^2-\frac{1}{\Delta Z^2}\right)\right]\cdot T_{n+1,m}+\left[\frac{S^2(1-N)}{\mathrm{Re}\cdot\mathrm{Pr}}\cdot\frac{(3-2x)}{(x-1)}-\frac{S}{2}\cdot V_{n,m}\right]\cdot T_{n+1,m-1}=\left[\left(U_{n,m}-\frac{4(1-N)}{\Delta Z\cdot\mathrm{Re}\cdot\mathrm{Pr}}\right)\cdot\frac{T_{n,m}}{\Delta Z}+\frac{2(1-N)}{\mathrm{Re}\cdot\mathrm{Pr}\cdot\Delta Z^2}\cdot T_{n-1,m}\right] \quad (18)$$

Integral continuity equation

$$\frac{3S^2(1-N^2)}{8}=\sum_{m=1}^{M}\left[(2m+F-1)U_{n+1,2m}\left(Co_4+\frac{Co_5}{G}T_{n+1,2m}+\frac{Co_6}{G}T^2{}_{n+1,2m}\right)\right]+\sum_{m=1}^{M-1}\left[(m+\frac{F}{2})\cdot U_{n+1,2m+1}\left(Co_4+\frac{Co_5}{G}T_{n+1,2m+1}+\frac{Co_6}{G}T^2{}_{n+1,2m+1}\right)\right] \quad (19)$$

The numerical calculations algorithm used is as follows:

Equation (18) for temperature was written for each radial position at first axial step. This gives a set of M-1 equations for unknowns T's that were solved by Gauss elimination method. Then equations (15-17) and with integral continuity equation (19) were similarly written and solved for the unknowns U,V and P and these gives (3M-2) equations for U,V and P unknowns. The known values of T, U, V and P were then used as input data to solve the next axial step.

The introduction of second derivative of velocity and temperature in the axial direction means that three axial positions were involved in the finite difference approximation, two positions (suffices "n-1" and "n") were known and one (suffices "n+1") was unknown. After solution of a given step, the old values at "n" and "n+1" become the new values at "n-1" and "n" respectively and old "n-1" data redundant.

Nusselt number

$$\mathrm{Nu}_z=\frac{2(1-\mathrm{N})\cdot\left(\frac{\partial \mathrm{T}}{\partial \mathrm{R}}\right)_1}{\mathrm{T}_{s_z}-\mathrm{T}_{b_z}} \quad (20)$$

EXPERIMENTAL APPARATS

The experimental apparatus, which has been designed and constructed to investigate combined convection heat transfer in an annulus where the outer cylinder is subjected to a constant heat flux while the inner cylinder is adiabatic. An open air circuit was used which included a blower (B), orifice plate section (C), settling chamber (D), test section and a flexible hose (E). The blower is driven electrically and the air flow rate can be regulated accurately by using a control The air induced by the blower, enters the settling chamber through a flexible hose (E). The settling chamber was carefully designed to reduce the flow fluctuation and to get a uniform flow at the test section entrance by using flow straightener (G). The air then passed through 1.2 m long test section. A symmetric flow and a uniform velocity profile produced by a well designed Teflon bell mouth (H) which is fitted at the annulus outer aluminum cylinder (I) and bolted inside the settling chamber (D). The inlet air temperature was measured by one thermocouple (J) located in the settling chamber (D) while the outlet bulk air temperature was measured by two thermocouples (Z) located in the test section exit as shown in **Fig.2**.

The test section consists of 4 mm wall thickness, 50 mm outside diameter and 1.2 m long aluminum cylinder (K) of inner cylinder located centrally in 5 mm thickness, 90 mm inside diameter and 1.2 m long aluminum of outer cylinder, by fitting it at the test section inlet with the 20 mm inside diameter, 50 mm

outside diameter and 15 mm long Teflon tube (N) and at the test section exit with the teflon piece (M). A ring (P) is used to hold and support the aluminum cylinder (K) with the teflon piece (N) centrally inside the settling chamber by adjustable screws (Q). The teflon was chosen because of its low thermal conductivity in order to reduce the heat loss from the aluminum cylinder ends.

The outer cylinder was heated electrically by using an electrical heater as shown in **Fig.3** section (A-A). The outer cylinder is covered by a 3 mm thickness asbestos layer (T), then a (2) mm in diameter nickel-chrome wire electrically isolated by ceramic beads (C) with diameter (6.5) mm, and then twenty layers of asbestos of thickness (25) mm to reduce the heat loss to minimum value. The temperature of outer cylinder was measured by fourteen asbestos sheath alumel-chromel (type K) thermocouples; there are three thermocouples (type K) on the outer surface of asbestos to calculate the conduction heat loss. The inner cylinder is insulated and it consists a teflon tube (S) and is covered by a 2 mm thickness asbestos layer (T), and the space between the asbestos and the inner cylinder wall is fitted with a fine grade sand (U) to avoid heat convection. The whole apparatus is designed with a view to obtain a good concentricity of the core cylinder and the containing cylinder. The measurements devices had been used including variac, digital voltmeter, clamp meter, two digitals thermometers.

RESULTS AND DISCUSSION

Theoretical results

Theoretical Results are studied mixed convection heat transfer to assisting and opposing air flow in a vertical annulus with adiabatic inner wall and uniformly heated outer wall. The ranges of governing parameters covered in the calculations are 400 $\leq$Re $\leq$ 2000, ($1.36\times10^5 \leq$ Ra $\leq 1.1\times10^7$), Pr=0.7 and N=0.555. The deviation in the average Nusselt number between the (12×48) grid sizes in r-z plane which has been used in all computations to a finer grid size (24×96) in r-z plane was found to be less than 0.5%. The temperature profile, velocity profile, variation of the outer tube surface temperature and local Nusselt number along the annulus has been investigated.

Temperature profile

The variation of temperature profiles along the vertical annulus is shown in **Fig.4** which are represented for Re = 1500 and heat flux q = 200 W/m^2, Ra=1.548×10^6. The figure shows a steep temperature gradient near the heated surface and the thickness of the thermal boundary layer gradually increases as the flow moves from annulus inlet towards annulus exit. It can be seen that there is a relatively high temperature variation near the heated surface causes an appreciable density change, which creates a rapid growth of thermal boundary layer along annulus length. **Fig.5** shows the effect of flow direction for various heat fluxes on the temperature profile at z = 0.72 m and Re=724. It can be seen that the temperature gradient with high heat flux is larger than that in low heat flux because of dominating natural convection. Also; it shows that the level of temperature profile with opposing flow is higher than that in aiding flow.

Velocity Profile

Development of the axial velocity profiles along the annulus axis in case of pure forced convection (i.e., buoyancy term is neglected), are shown in **Fig.6** for q $\approx$ 0 and Re =.724. Profiles reveal the limitation of the buoyancy effect and show approximately similar distribution about the middle of the annular space which is similar to pure forced convection behavior in agreement with **(Coney and El-Sharrawi 1975)**. The maximum axial velocity occurs at dimensionless radial distance ($r-r_i/r_o-r_i=0.5$). Figure shows also that the velocity increases with Re increasing because of the dominating pure forced convection in the heat transfer process.

Fig.7 shows the development of the axial velocity profiles for aiding and opposing flows at z = 0.72 m and Re=724 and for

various heat fluxes. It is clear from this figure that, when the free convection opposes the forced flow (i.e., for heating with down flow or cooling with up flow) the buoyancy force tends to retard the fluid near the heated boundary and accelerates it near the opposite adiabatic wall. In such case the maximum velocity profile distortion occurs when the slope of the profile at the heat transfer boundary reaches its minimum value. Therefore; in this case a possibility of flow reversal may occur near the heated wall if the natural convection is opposing the forced flow. On the other hand when the free convection aids the forced flow (i.e., upward flow) the fluid accelerates near the heated wall and decelerates near the opposite adiabatic boundary. But Fig.8 shows at z = 0.72 m and q = 1000 W/m^2 and various Reynolds number that the effect of forced convection is dominating with increasing Re. The velocities in aiding and opposing flows tend to approach to each other especially at the middle of annulus (at high Reynolds number).

Bulk Temperature

Fig.9 shows the variation of the bulk temperature (mixing cup temperature) with the axial distance z, corresponding to different heat flux and (Re =724) It is clear from this figure that the bulk temperature increases with increasing heat flux, the increase of local mixing causes an improvement in the local heat transfer process and reducing the heated surface temperature.

Surface Temperature

The outer cylinder surface temperature distribution along a vertical annulus is shown in **Fig.10** for constant heat flux (q = 700 W/m^2) and different Reynolds number (Re=400, 724, 1000, 1500, 2000). Figure shows that the outer tube surface temperature decreases as Reynolds number increases for the same heat flux.

Fig.11 shows the difference between aiding and opposing at the Reynolds number Re=724 and heat flux (370) W/m^2. It is clear from this figure that the outer tube surface temperature in case of opposing flow is higher than in aiding flow. This behavior can be attributed to that when the free convection aids the forced flow the density of the air near the wall decreases. The secondary flow assists main flow in removing heat from the outer tube surface and improving the heat transfer process because of the large velocity near the outer tube wall. On the other hand when the free convection opposes the forced flow, the velocities due to buoyancy flow and forced flow are in the opposite direction, in this case the buoyancy force tends to retard the fluid near the heated wall and accelerates it near the opposite adiabatic wall, so that the free convection effect will decrease in the case of the opposing flow causes the outer tube surface temperature distribution for opposing position to be higher than that for aiding position.

Local Nusselt Number (Nu_z)

The variation of local Nusselt number (Nu_z) with a logarithmic dimensionless axial distance (inverse Graetz number ZZ), is shown in **Fig.12**. The effect of heat flux variation (q=200, 370, 700, 1000, 1500) W/m^2 on the (Nu_z) along the dimensionless axial distance with constant Reynolds number (Re=1000). It is clear from this figure that the values of (Nu_z) is the same for different heat fluxes at the annulus entrance because of limitation of buoyancy effect at this region, then the values of (Nu_z) increases downstream as the heat flux increases. This behavior is due to the increase both thermal boundary layer thickness and the surface to bulk air temperature difference which accompanies with increasing the surface heat flux that accelerates the development of the secondary flow in the annulus down stream.

Fig.13 shows the effect of Reynolds numbers variation (400, 724, 1000, 1500, 2000) on the (Nu_z) along the dimensionless axial distance ZZ and constant heat flux (q=370 W/m^2). It is clear from this figure that the effect of secondary flow is small at the annulus entrance where the forced convection is dominant and the (Nu_z) values increase downstream of annulus as Reynolds number

decreases because of the dominant free convection.

Fig.14 shows the effect of aiding and opposing flow on the (Nu_z) values along the dimensionless axial distance ZZ for various values of heat transfer and constant Reynolds number (Re=724). It is clear from this figure that when the free convection aids the forced flow, the values of (Nu_z) are higher for the same logarithmic dimensionless axial distance (ZZ) than their corresponding values of the purely forced convection case ($q \approx 0$) and vice versa in the opposing direction. This is attributed to the higher velocities near the heated surface, and hence the decrease in the thickness of the developing boundary layer on that boundary, in case of an aiding free convection.

Experimental results

Surface temperature

The variations of surface temperature for different heat flux and Reynolds number equal to Re =1500 and for different Reynolds number and heat flux equal to 680 W/m^2 are shown in **Fig.15 & Fig.16;** respectively. **Fig.15** reveals that the outer surface temperature increases at the annulus entrance and attains a maximum value after which the surface temperature begins to decrease. The rate of surface temperature rises at early stage is directly proportional to the wall heat flux (422 to 980) W/m^2. The value of maximum temperature seems to move toward the annulus entrance as the heat flux increases. This can be attributed to the increasing of the thermal boundary layer faster due to buoyancy effect as the heat flux increases for the same Reynolds number. **Fig.16** shows the effect of Reynolds number variation (724, 1000) on the outer cylinder surface temperature. It is obvious that the increasing of Reynolds number reduces the surface temperature as heat flux kept constant.

Local Nusselt number (Nu_z)

The variation of the local Nusselt number with ZZ for Re=1500 and various heat flux is shown in **Fig.17**. It is clear from this figure that at higher heat flux, the value of local Nusselt number are higher than the results of lower heat flux. This may be attributed to the secondary flow superimposed on the forced flow effect increases as the heat flux increases that leading to higher heat transfer coefficient.

Verification of the results

Comparison with previous experimental

The experiments were done for heating outer tube annulus with radius ratio (0.555), (D_h=0.04 m), and (L/D_h=30) and air as a test fluid for present work. **Fig.18** reveals a comparison between the present experimental work for q=387 W/m^2 and Re=383 and the experimental work of (Falah 1993), who carried out it with internally heated inclined annulus of radius ratio (0.411), (D_h=0.043) and L/D_h=20.93, (q=283 W/m^2 and Re=300). It is clear from this figure that a convergence between the two curves is obtained.

Comparison with present theoretical results

Fig.19 shows a comparison between experimental and theoretical local Nusselt number in this work for Re=724 and q=370 W/m^2. Figure reveals that the experimental local Nusselt number follows the same trend and behavior as the present theoretical results but is approximately with means difference of 10.23 %.

Comparison with previous theoretical results

Fig.20 reveals a comparison between the local Nusselt number of the present work and the theoretical work of (Mohammed 2007), who carried out his work with internally heated vertical annulus of radius ratio (0.555), (Pr=0.72) and (q=95 W/m^2 , Re=500). It can be seen that the results have the same trend as that obtained in the present theoretical work.

CONCULUSIONS

The temperature profile along the annulus shows a steep profile near the heated

surface due to increasing of the thermal boundary thickness as the heat flux increases and decreasing of the Reynolds number at the same axial position, the increase in buoyancy effect causes an accelerate in the growth of the thermal boundary layer. Near the annulus entrance the velocity profiles for different heat flux were found to be similar to those for pure forced convection behavior. While the velocity profiles were distorted by the effect of the buoyancy force in downstream. The heat transfer process in the case of aiding flow is better than that in the case of opposing flow. The variation of the outer tube surface temperature along the annulus for both experimental and theoretical parts has the same trend and behavior. The buoyancy effect can be neglected at the annulus entrance for all Reynolds number and heat flux covered in this study. At constant Reynolds number the Nu_z value increases with increasing of the heat flux in the annulus downstream due to the increasing of buoyancy effect. At constant heat flux the Nu_z value increases at the annulus entrance as Reynolds number increases because of dominating forced convection, while the Nu_z value increases in the annulus downstream as the Reynolds number decreases due to free convection is dominant.

REFERENCES

Collins, "Combined convection in uniformly heated vertical pipe", Heat and mass transfer by combined forced and natural convection, (15th September 1971).

Coney J. E. R. and El-Shaarawi M. A. I. ,"Finite difference analysis for laminar flow heat transfer in concentric annuli with simultaneously developing hydrodynamic and thermal boundary layers " , Int. Journal for Numerical Method in Engineering, Vol. 9, pp. 17-38, 1975.

El-Shaarawi M. A. and Sarhan A., "Free convection effects on the developing laminar flow in vertical concentric annuli "J. Heat Transfer, Vol. 102, pp.617-622, November, 1980.

Falah A. Aboud, "Combined free and forced convection in an inclined Annulus"، M. Sc. Thesis, University of Basra, College of Engineering, Mechanical Department, 1993.

Hanzawa T., Sako A., Endo H., Kagwa M., Sunaga T**. and Koto K.,** "Combined free and forced laminar convective heat transfer from isothermally heated inner tube in vertical concentric annulus", J. Chemical Engineering of Japan ,Vol. 19 ,No. 1, pp. 78-81 , 1986.

Hashimoto K., Akino N., and Kawamura H., "Combined forced- free convection heat transfer to a highly heated gas in a vertical annulus" ،Int. J. Heat Mass Transfer, Vol.29, No.1, pp. 145-151, 1986.

Heggs and Ingham "Laminar flow combined in vertical annuli", Proceeding of the 8th Int. Heat Transfer Conference, Munchen, Fed. Rep.of Germany, Vol.2, pp. 941-956, 1988.

Kayes .W. M, "Advanced fluid dynamics and heat transfer"
Mc Graw-Hill, New York, (1966).

Mohammed. A. R. Nima, Developing laminar mixed convection heat transfer through concentric annuli" M. Sc. Thesis, University of Baghdad, College of Engineering, Mechanical Department, (2007).

Shaik Samivullah, "Laminar mixed convection in vertical channels" M. Sc. Thesis, King Fahd University of Petroleum and Minerals, Mechanical Engineering, 2005**.**

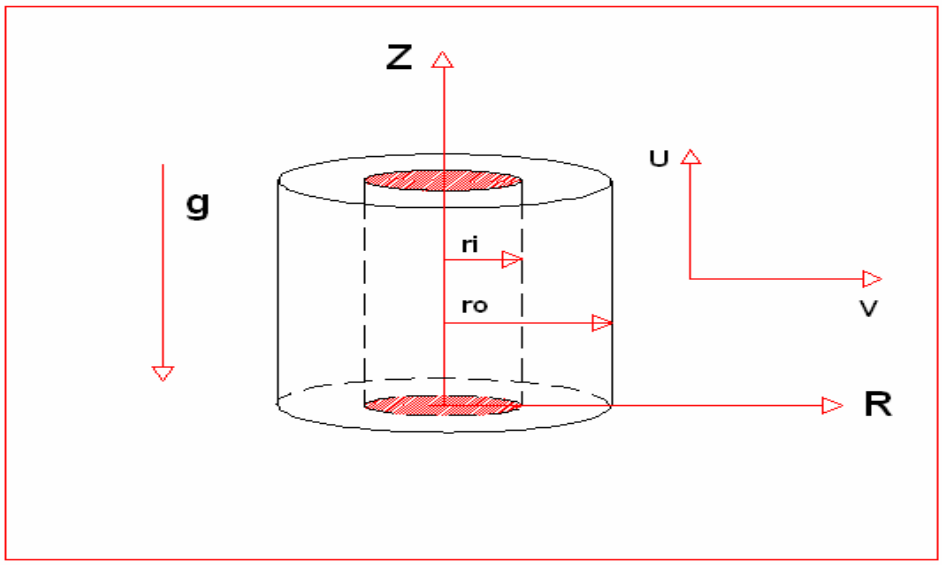

Fig. (1): Two- Dimensional Annular Geometry.

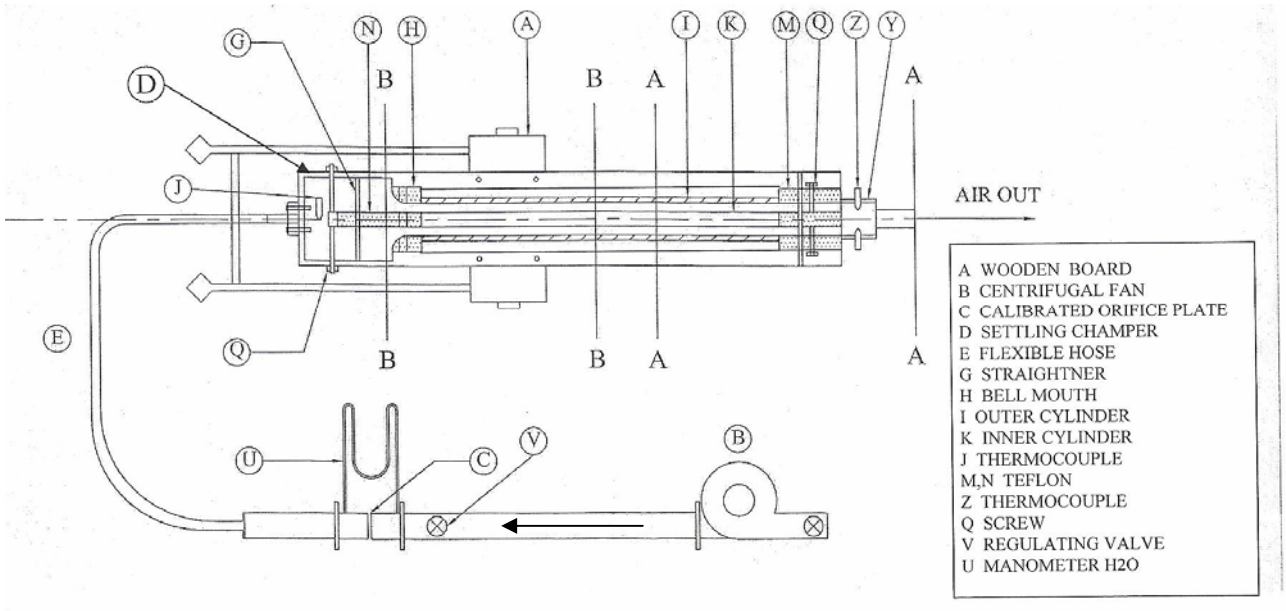

Fig. (2): Diagram of Experimental Apparatus.

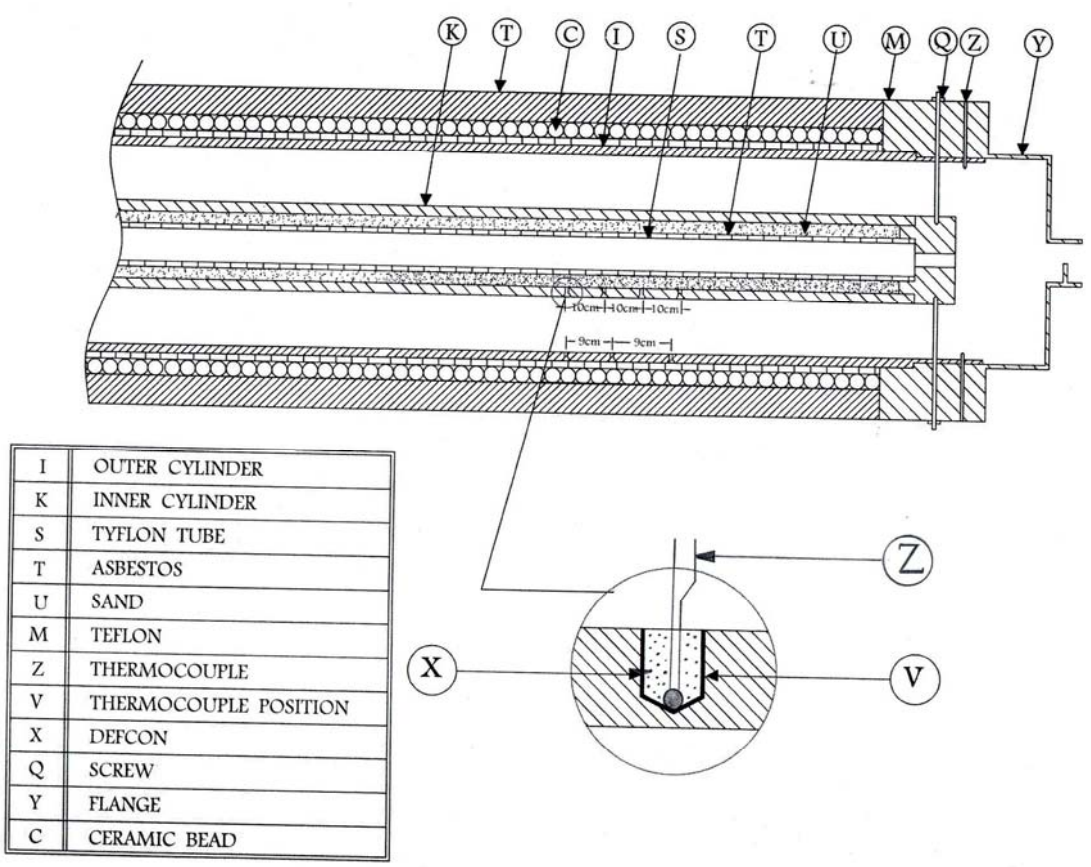

Fig. (3): Section A-A.

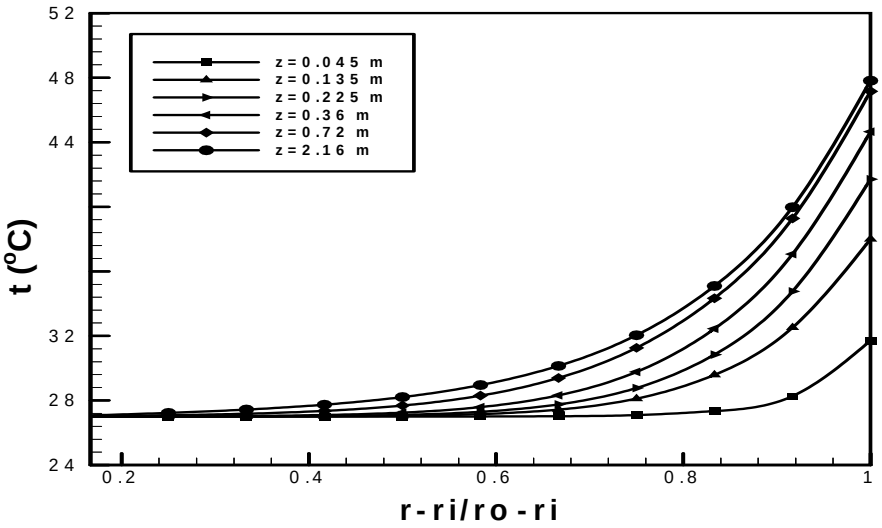

Fig. (4): Theoretical Development of the Temperature Profiles Along the Vertical Annulus for q=200 W/m^2, Re=1500 (aiding flow).

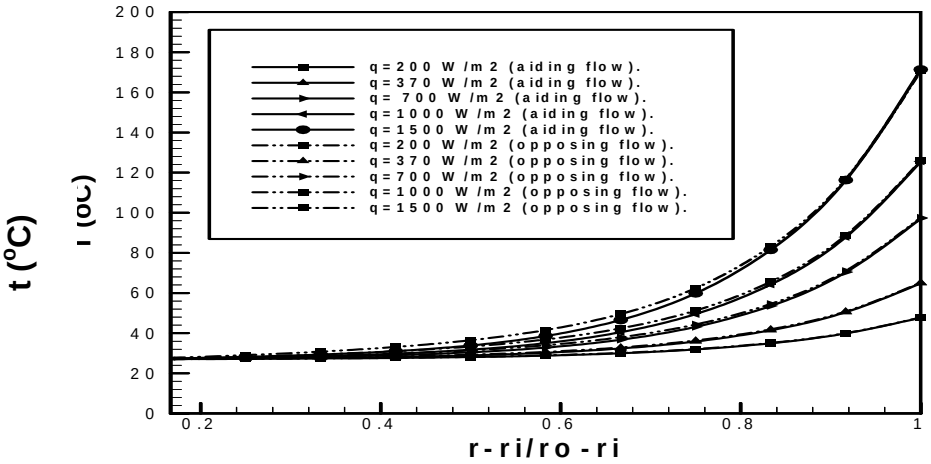

Fig. (5): Theoretical Development of the Temperature Profiles at (z = 0.72 m), Re=724 (aiding and opposing flow).

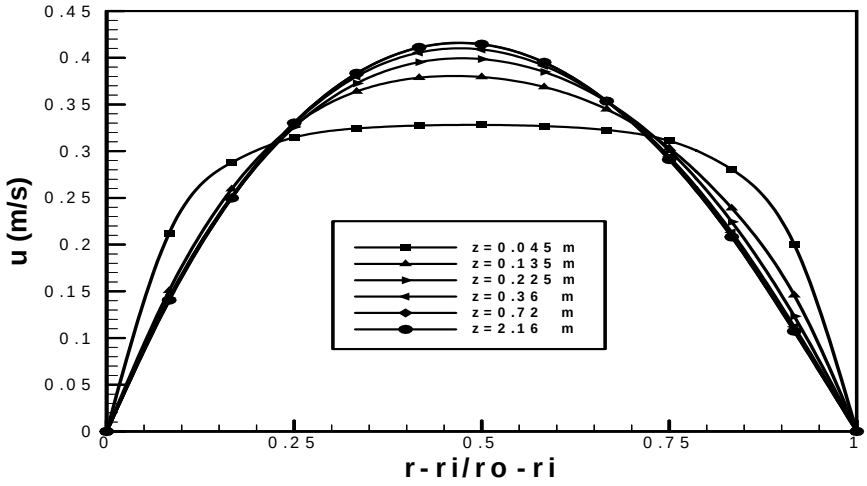

Fig. (6): Theoretical Development of the Axial Velocity Profiles Along the Vertical Annulus for q ≈ 0 W/m^2 , Re=724 (aiding flow).

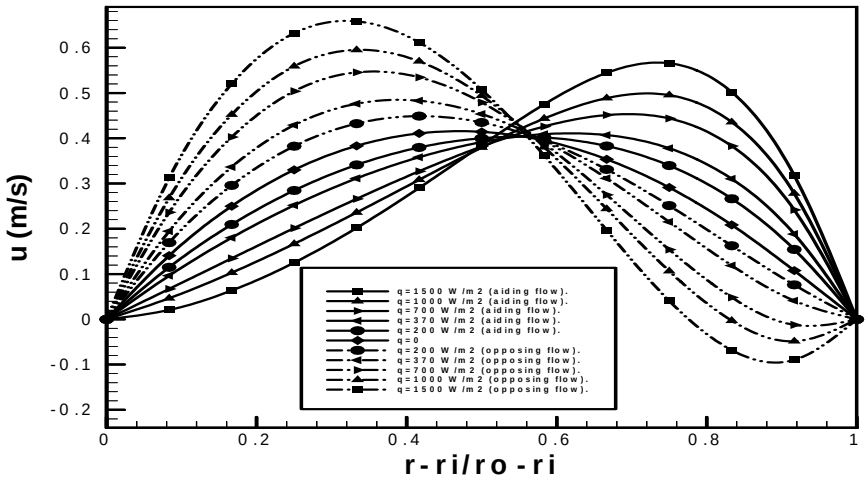

Fig. (7): Theoretical Development of the Axial Velocity Profiles at z =0.72 m, Re=724 for Various Values of q, (aiding and opposing flow).

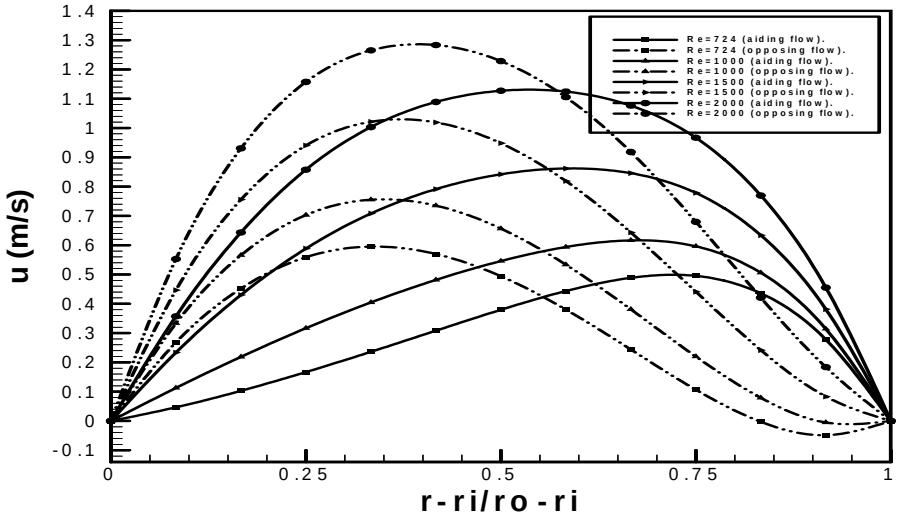

Fig. (8): Theoretical Development of the Axial Velocity Profiles at z =0.72 m, q = 1000 W/m^2 (aiding and opposing flow).

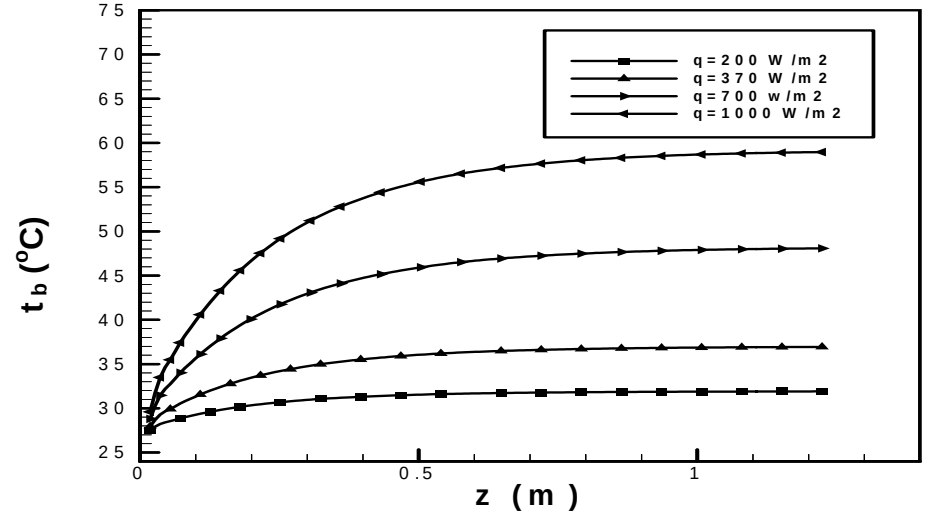

Fig. (9): Theoretical Variation of the Bulk Temperature Along the Axial Distance for Re=724.

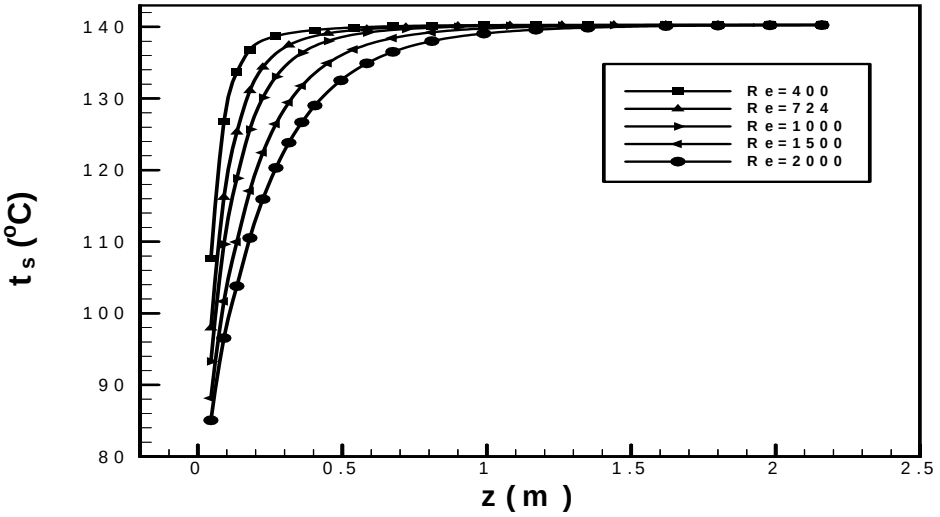

Fig. (10): Theoretical Variation of the Outer Tube Surface Temperature Along the Axial Distance for q =700 W/m^2.

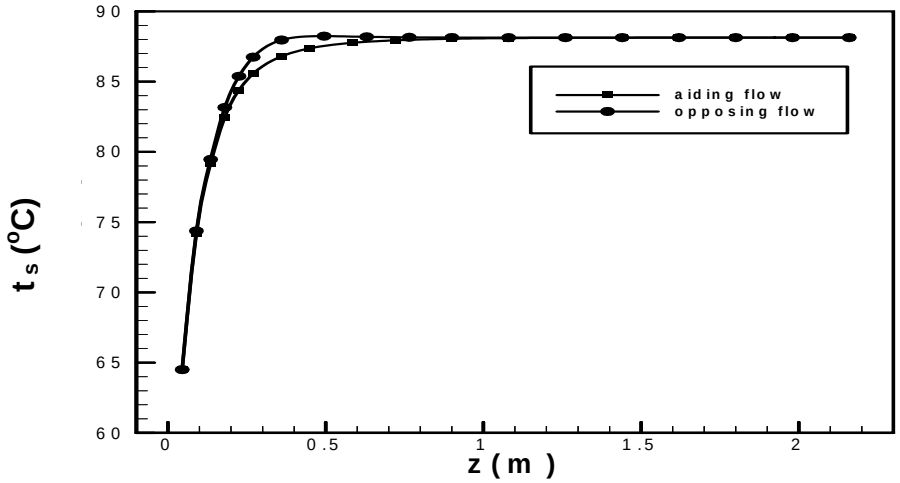

Fig. (11): Theoretical Variation of the Outer Tube Surface Temperature Along the Axial Distance for q =370 W/m^2, Re=724 (aiding and opposing).

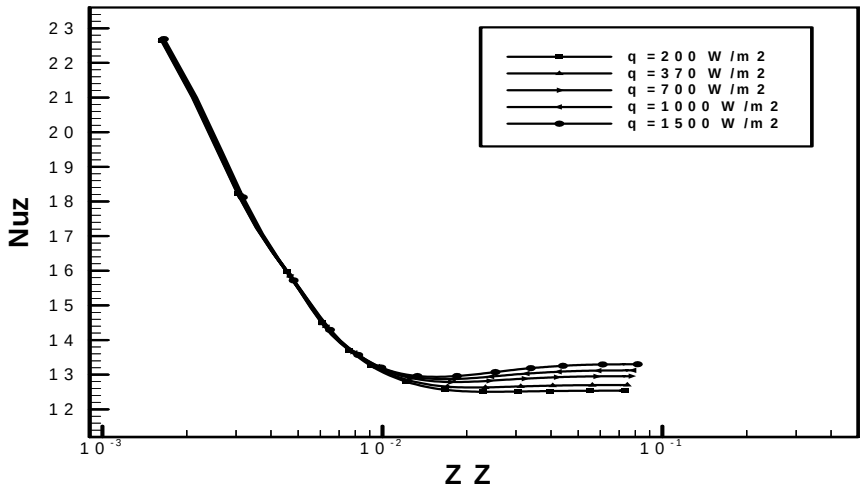

Fig. (12): Theoretical Local Nusselt Number Versus Dimensionless Axial Distance for Re=1000.

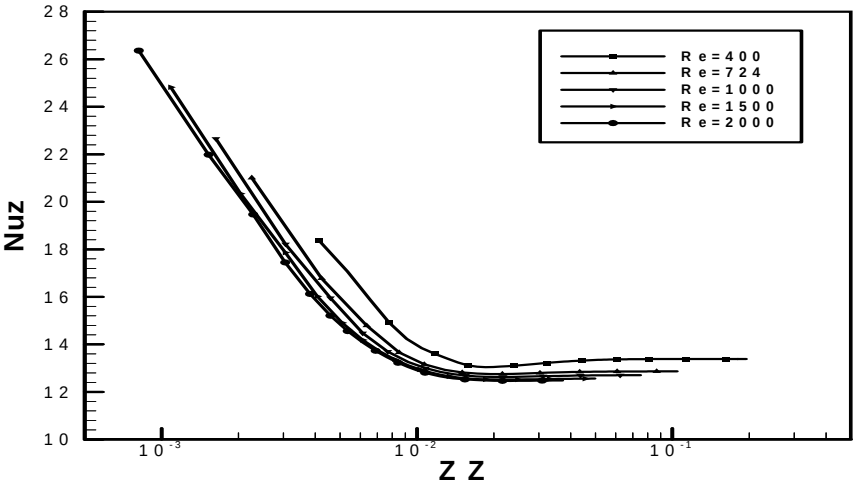

Fig. (13): Theoretical Local Nusselt Number Versus Dimensionless Axial Distance for q=370 W/m^2.

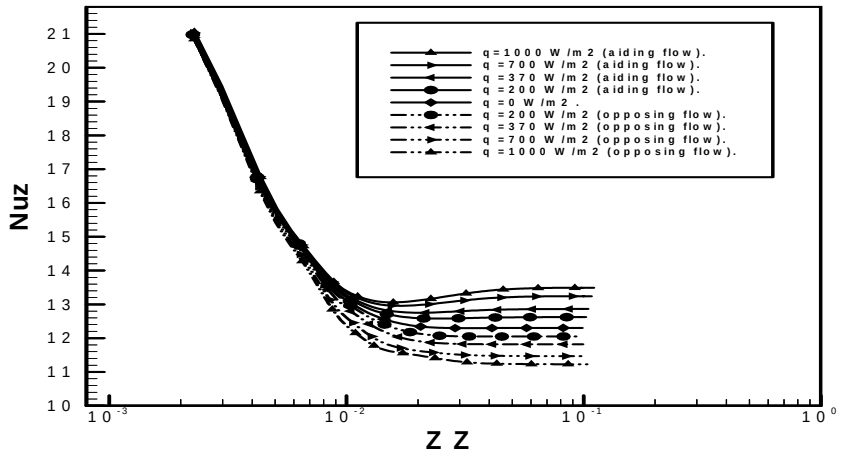

Fig.(14): Theoretical Local Nusselt Number Versus Dimensionless Axial Distance for Re=724 (aiding and opposing flow).

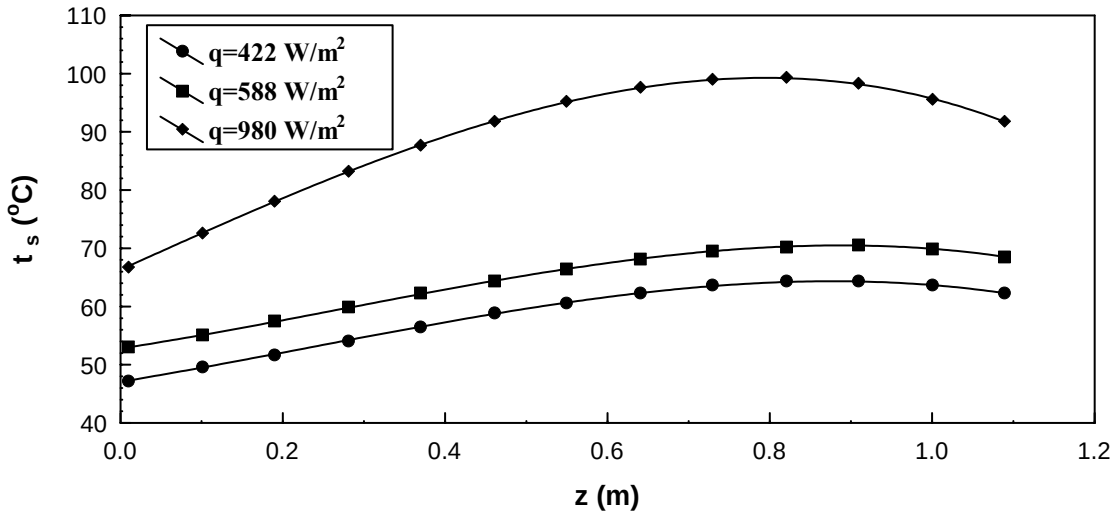

Fig.(15): Experimental Variation of the Surface Temperature with the Axial Distance, Re=1500.

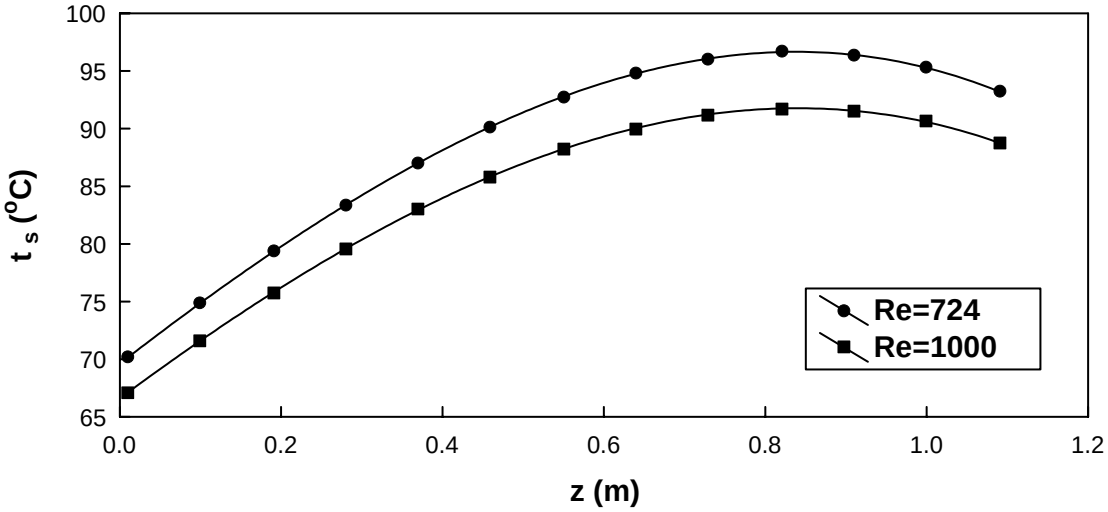

Fig. (16): Experimental Variation of the Surface Temperature with the Axial Distance, q=680 W/m^2.

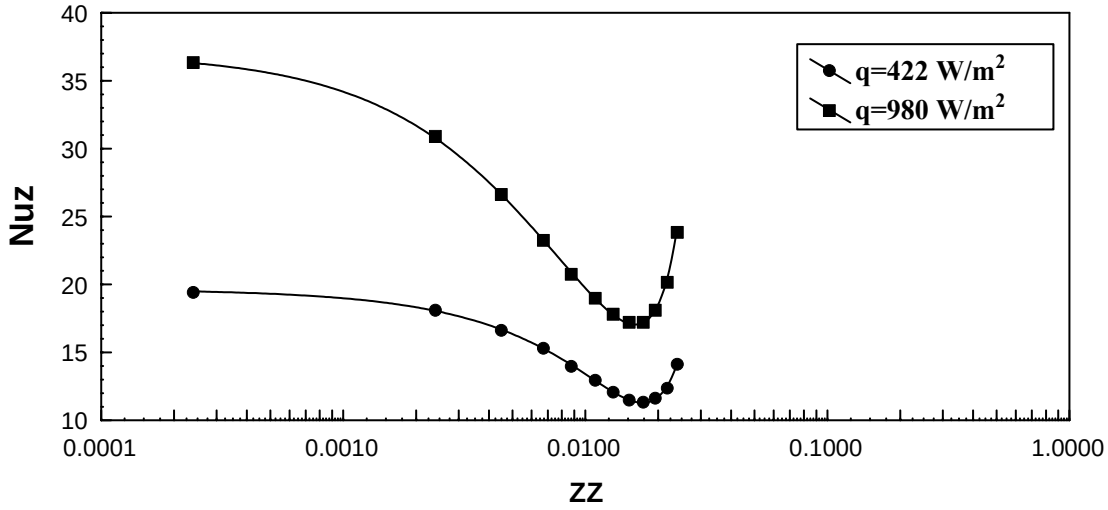

Fig. (17) Experimental Local Nusselt Number Versus Dimensionless Axial Distance, Re=1500.

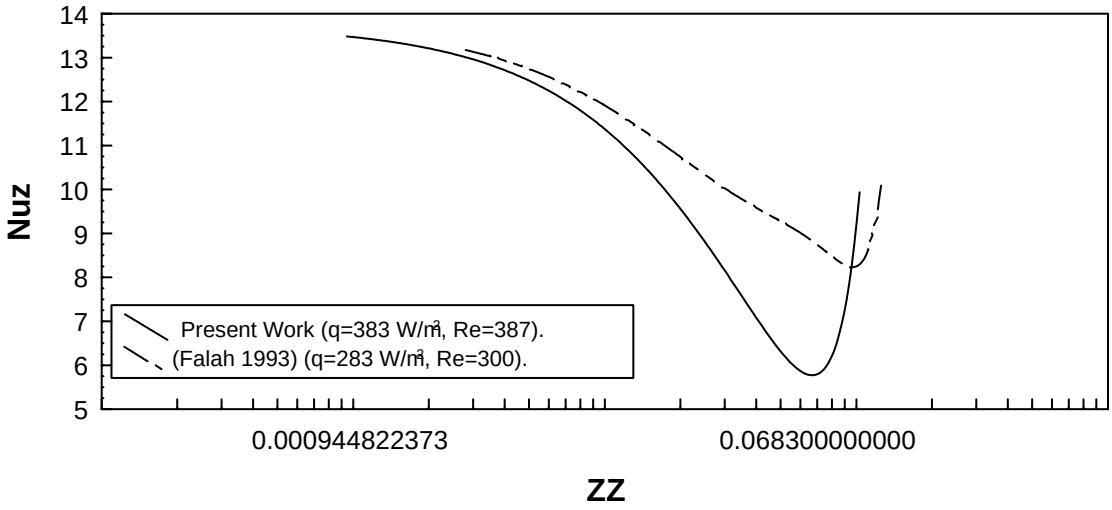

Fig.(18): Comparison of the Present Experimental Work with the Work of (Falah 1993).

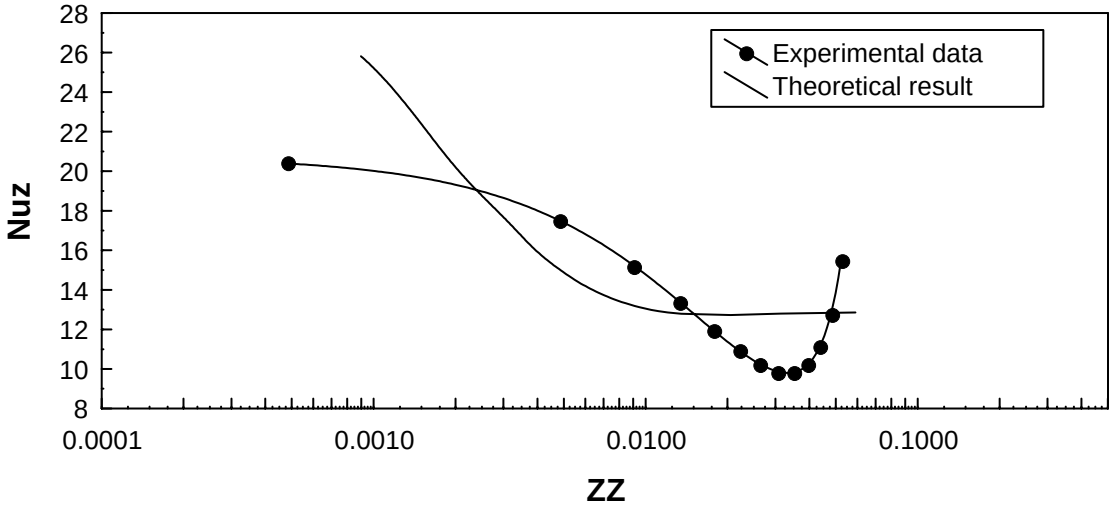

Fig.(19): Comparison of Experimental Nu_z with the Theoretical Result for Vertical Position, q=370 W/m^2 Re=724.

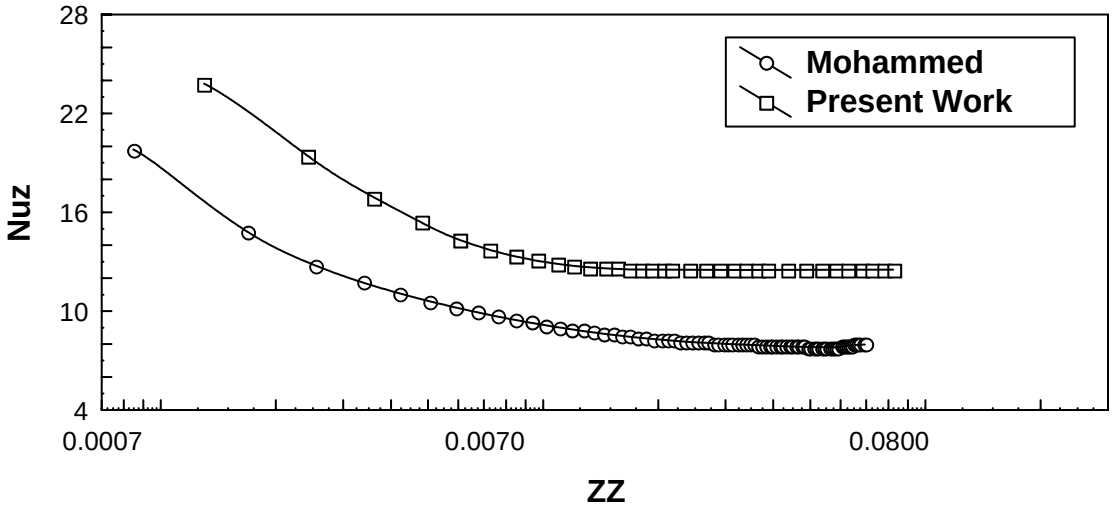

Fig. (20): Comparison of Theoretical Nu_z with the Theoretical Work of (Mohammed 2007) for Vertical Position, q=95 W/m^2, Re=500.

NOMENCLATURE
Symbols

$C_{1....}C_6$, Constants.
C_p, Specific heat at constant pressure.
D, Diameter
D_h= Hydraulic diameter= $2(r_o-r_i)$

$G = \frac{g\, r_o^{\,3}}{\nu_i^{\,2}}$ = Gravity acceleration

K, Thermal conductivity
M, Total radial mesh point
N, axial mesh point
N= Radius ratio=r_i/r_o

$P = \frac{p - p_i}{\rho\, u_i^{\,2}}$ = Pressure

q, Heat flux
r, Radial coordinate
r_i, Outer radius of inner cylinder
r_o, Inner radius of outer cylinder
t, Temperature
u, Axial velocity
v, Radial velocity
z , Axial coordinate

μ, Dynamic viscosity

υ, Kinematic viscosity

ρ, Density

ρ_i, Density at entrance

Nu, Nusselt number

$Pr = \frac{\mu \cdot Cp}{k}$ = Prandtl number

$R = \frac{r}{r_o}$ = Radial coordinate

$Re = \frac{u_i \cdot D_h}{\nu}$ = Reynolds number

$U = \frac{u}{u_i}$ = Axial velocity component

$V = \frac{v}{u_i}$ = Radial velocity component

$Z = \frac{z}{r_o}$ = Axial coordinate

$ZZ = z/Re.Pr.D_h$ = Inverse Graetz number

DIESEL PARTICULATE EMISSIONS EVALUATION FOR SINGLE CYLINDER ENGINE FUELLED WITH ETHANOL AND GAS-OIL SOLUTIONS

Dr. Mohammedali Abdulhadi
Lecturer
Department of Mechanical Engineering
University of Technology

ABSTRACT

Particulate matter (PM) emitted from diesel engine exhaust have been measured in terms of mass, using 99.98 % pure ethanol blended directly, without additives, with conventional diesel fuel (gas – oil),to get 10 % , 15 %, 20 % ethanol emulsions . The resulting PM collected has been compared with those from straight diesel. The engine used is a stationary single cylinder, variable compression ratio Ricardo E6/US. This engine is fully instrumented and could run as a compression or spark ignition. Observations showed that particulate matter (PM) emissions decrease with increasing oxygenate content in the fuel, with some increase of fuel consumption, which is due to the lower heating value of ethanol. The reduction in PM formation increased with load increase, maximum reduction were 58% at 1800 rpm. There was no significant reduction observed at low loads. It could be concluded from the test results that ethanol may be an alternative to / or partially substitute, fossil fuels.

KEYWORDS

Diesel engine, Ethanol – diesel blend, Particulate matter, Performance

الخلاصة :

الغرض من البحث دراسة تأثير زيادة نسبة الأوكسجين المضافة إلى وقود الديزل على معدل تكون (كثافة) المادة الدقائقية. تناول البحث القياس الكتلي لكمية المادة الدقائقية المنبعثة من عادم محرك ديزل يعمل بخليط من الكحول الأثيلي (نسبة نقاوته 99.98 %) ووقود الديزل الأعتيادي، بدون إضافة اي مادة مساعدة أخرى. المستحلبات (الخلائط) المستعملة في التجارب هي 10% ، 15 % ، 20 %، وقد قورنت كمية المادة الدقائقية الناتجة من هذه المستحلبات مع تلك الناتجة من تشغيل المحرك بوقود الديزل النقي بنفس الظروف. المحرك المستخدم في البحث أحادي الاسطوانة، ثابت، ذو نسبة إنضغاط متغيرة، من نوع ريكاردو(E6/US) وله امكانية التشغيل كمحرك انضغاطي الاشتعال أو بالشرارة.

وقد اظهرت النتائج أن إضافة الايثانول إلى وقود الديزل تؤدي إلى تناقص معدل تكون المواد الدقائقية ولمختلف ظروف تشغيل المحرك، مع زيادة طفيفة بمعدل استهلاك الوقود لتعويض انخفاض القيمة الحرارية للوقود. أظهرت النتائج أن معدل تكون المادة الدقائقية يتناقص بزيادة الكحول المضافة وبزيادة الحمل.أكبر معدل إنخفاض تم الحصول عليه هو بحدود 58 % عند إضافة 20 % كحول وعند سرعة 1800 rpm. بينت النتائج ان الكحول الأثيلي يمكن ان يحل محل وقود الديزل جزئيا على الأقل.

INTRODUCTION

The main advantages of diesel engine over gasoline engine are its fuel economy and durability, expectation are that diesel engine use will increase due to their superior performance characteristics. Diesel engine exhaust (DE), however, contains harmful pollutants in a complex mixture of gases and particulates.

Particulate matter (PM) is of concern because of its established relationship with human health and environmental contamination. PM penetrates through the respiratory systems damaging lunges and causing lunge cancer. When particulate settle on ground or water, it changes the nutrient balance in water depleting the nutrient in soil and damaging sensitive forests and farm corps.

In recent years many methods for the reduction of DE pollutants have been introduced, such as using alternative fuels and a variety of fuel additives and fuel blends **((Kowalewicz, 2005 & 2006)**, (**Lauerta, 2002), (Lu, et al, 2000))** development of new engine design (fuel injection optimization, modification of combustion chamber shapes **(Litzinger, et al 200))** , exhaust gas recirculation (EGR) technique **(Ladommatos, et al 1998)**, as well as improving the quality of the fuel (reducing sulphur content **(Huang, et al, 2007)**).

At present time ambient air quality standards around the world (e.g.: **USEAP, 2002, AQEG, 2005** and many others) have tighten the highest limit of fine particles in the ambient air. This makes reduction in DE emission a major research task in engine development.

Alternative fuels are becoming increasingly important due to environmental concern as well as replacing the conventional depleting fossil fuel. Ethanol is regarded as a kind of renewable fuel because it can be produced from agricultural sources, such as dates, sugar beets, barley, sugar cane, molasses and waste biomass materials etc., by using already improved and demonstrated technologies. In this frame bioethanol has the opportunity to contribute to the gradual substitution of fossil fuels, not only in the gasoline sector but even in the diesel one. Direct blending of ethanol with diesel fuel provides higher oxygen concentration, thus higher potential for particulate emission reduction.

One of the main reasons of PM formation is a local deficiency of oxygen during combustion of fuel in the engine combustion chamber. Hence enhancing the availability of oxygen in the combustion area would limit the intensity of PM formation. Increasing the amount of oxygen locally; can be done by supplying oxygen together with the fuel, this is achieved by: either using oxygenated additives or by dissolving oxygen in the fuel.

Oxygenated fuel additives are materials contain a high percentage of oxygen in their molecular structures, such as alcohols, ethers, carbonates, acetates, glycols and esters. Many researchers **(Litznger, et al, 2000), (Ladommatos, et al, 1998),** and **(Musculus & Diets, 2005)**) have investigated oxygenated additives, and their results indicate a dramatic reduction in PM emission. Oxygenation through gas dissolving in the fuel is also investigated; by dissolving air or diesel exhaust in the fuel **(Kowalewicze, et al, 2002), (Jerzy, et al, 2007).**

Jincheng Huang and co-workers conducted two sets of experiments at 1500 and 2000 rpm, and measured the opacity of diesel exhaust, they claim that they observed a decrease in smoke for the two sets of experiments; at 2000 rpm the reduction rates were from 16.7% to 65% for the 10% ethanol blend, and were from 45.2% to 82.9% for the 20% ethanol blend and 33.3% to 87.5% for the 25% ethanol; and similar trend for 1500 rpm. Their experiments were performed with 5% of n-butanol as a solvent. **Hassan and co-workers** indicated that for a 20% ethanol in diesel fuel cause a 14% reduction in smoke formation. **Lapuerta, et al**

also claim a reduction nearly 50% in smoke opacity for the loads covered in their experiments.

The results obtained in this work are in agreement with most of the literature reviewed, thereby confirming the results of this study.

EXPERIMENTAL INSTALLATION:

Testing was performed in a single cylinder variable compression ratio Ricardo E6/US engine, engine specifications are presented in **Appendix A**. The engine is four strokes, naturally aspirated and mounted on a common bedplate with an electric dynamometer and equipped with controls to regulate engine speed and load. The engine is adaptable to run as either a spark ignition or as a compression ignition engine. Alteration to ignition timing or injection timing can be made while the engine is running. **Figure (1)** shows a schematic diagram of the experimental test rig arrangement. **Figure (2)** shows a cross section of the engine. The fuel flow rate was measured by recording the time required for the consumption of 50ml of fuel, and intake airflow rate was measured using an orifice fitted to a 200 litre air tank connected with the induction manifold to reduce pressure pulsations.

Measurement of the pressure inside combustion chamber was performed by a pressure transducer, AVL 8QP 500C, pressure-time history inside the cylinder could be obtained with the use of a high speed measurement system (previous work (**Salman, 2005**)). **Figure (3)** shows examples of the pressure – crank angle diagrams obtained. Exhaust PM mass concentrations was measured by means of a gravimetric method **(Casati, et al, 2007)**, by sampling through a glass fibre filter fitted inside a specially developed support, shown in **figure (4).** The filters were weighed before and after sampling using an electronic balance to determine the total mass of PM collected on the filters. For each test a sample of exhaust gas (100ml) was carefully taken from the centre-line of the exhaust tail pipe by 100ml syringe and injected through the filter as indicated in **figure (4).**

TEST PROCEDURE:

Investigations were carried out at constant speed and varying load. Four different speeds (900, 1200, 1500, 1800 rpm) were selected to cover a wide range of engine operating conditions.

Four fuels of varying ethanol blend level were included in this work in order to study the effect of ethanol percent on particulate matter emission (the worst drawback on diesel engines). Ethanol blend concentration levels were specified on volume-percent bases and include 0, 10, 15, and 20%.

At each engine speed. The following parameters were recorded:

- Engine torque
- Fuel consumption
- Air consumption
- Intake air temperature
- Exhaust gas temperature
- Particulate matter

In the present study, first all measuring equipment were prepared and calibrated, then

the highest useful compression ratio and the best injection timing were determined for each type of fuel and they were found to be 17/1 and 38° BTDC respectively.

At each changes of fuel, lines were drained prior to filling them with the next fuel. Before beginning a new test, the sample syringe was cleaned in order to eliminate deposits of the previous test. After that, the engine was warmed up with the new fuel for at least 30 minutes to purge any of the remaining previously tested fuel. At each test several measurements of air and fuel consumption and three different particulate filters were taken. There were very little differences between the various measurements; however, in order to minimize any experimental inaccuracy averaged values were used for recording the results.

RESULTS AND DISCUSSION:

1) Engine Performance:

The effect of applying different loads on brake specific consumption (**bsfc**) at constant speed, was investigated for; 900, 1200, 1500, and 1800 rpm. **Figure (5)** represent the variation of **bsfc** at 1500 rpm, observation indicates that the more ethanol added in, the more fuel consumption, and generally straight gas-oil has the lowest fuel consumption is consistent in other tested speeds. The small increase of **bsfc** is expected due to the lower heating value of ethanol (26994 kJ/kg) compared to that of gas-oil (45144 kJ/kg), **Appendix B**. The 10, 15 and 20 percent blends have a drop in heating value of 4%, 6%, and 8% respectively. Increase in **bsfc** is not fixed for each blend. The test results show that at low to medium loads, up to 40 N, there was a negligible increase in **bsfc**, but it increases with load increase, and was at most 8% at 50 N load. A similar trend was observed in the other tested speeds.

The differences in **bsfc** reflect the differences in some of the physical properties of the fuel, such as: density, Oxygen content and heating value. **Figure (6)** represent the relation between maximum load and ethanol content, it shows that maximum load produced (power) reduced with increasing ethanol content for all tested speed. Moreover it can be concluded that highest reductions in load (power) were; 4%, 8%, 15%, and 15% for 900, 1200, 1500 and 1800 rpm respectively.

2) Particulate Matter:

It is well known that engine emissions are affected by the air/fuel ratio. In this study, the effect of ethanol content on air/fuel ratio is represented in **figure (7)** at medium load (40N) for the four tested speeds. It is clear that, differences in air/fuel ratio were very slight at each engine speed for as ethanol percentage increased; this was the case for other tested loads. Therefore, the production of emissions was due to different compositions of the fuel, but not to differences in air/fuel ratio.

Figures (8 – 11) show the relationship between PM mean concentration ($\mu g/m^3$) and loads applied in N at constant speed, when the engine fuelled with 0, 10, 15 and 20 percent ethanol blends, while **figures (12 – 15)** illustrates the relationship between PM mean concentration and ethanol contents percent by volume at constant load, for the same blends. Results show that the rate PM formation was decreasing as ethanol content (Oxygenate) in gas-oil increased. This was consistent in all four tested speeds. The observations are in accordance with that found in all literature reviewed **(Hassan, 2004)**, **(Lapuerta, 2008), (Huang, 2009), (Xing-cai, 2004)**. This behaviour can be mainly explained to the improvement in the combustion process due to the presence of oxygen, which leads to reduce

the probability of PM formation in locally rich zones. Moreover, it can be seen that PM formation decrease more in high loads than that at low loads. This is reasonable since more fuel is needed at high loads.

Adding oxygenates to diesel fuel (gas-oil) had a remarkable affect on the reduction of PM formation, especially at high load at any engine speed. When the engine ran with 10% ethanol blend on different engine speeds of 900, 1200, 1500 1800, PM formation rates were decreased by (7 – 50) %. For 15 % ethanol blend, the reductions were between (5 – 58) %, and for 20% ethanol blend, the reductions were up to 58%.

CONCLUSIONS:

Based on the experimental results of this study, the following can be drawn:

1) With reference to straight diesel fuel, it can be stated that PM collected on the filter decreases significantly as the ethanol content increases in the fuel.

2) The highest reduction in PM emission is at 1800 rpm and load of 45 N. Hence, it reaches about 58 % with 20 % ethanol addition.

3) The reduction in PM is low when the loads are at low level.

4) Ethanol could be used as alternative fuel to substitute diesel fuel partially or totally.

5) The bsfc was increased due to lower heating value of Ethanol.

6) The results obtained on performance and PM emission are in agreement with most of the literature viewed.

REFERENCES:

AQEG, Particulate matter in the United Kingdom, Defra, London, 2005.

Canackci M., Performance and emissions characteristics of biodiesel from soybean oil. Proc I MechE, vol. 219, Part D, 2005.

Casati R., Scheer V., Vogt, T. Benter, Measurement of nucleation and soot mode particle emission form diesel passenger car in real world and laboratory in situ dilution, Atmospheric Environment 41, 2007. pp 2125 – 2135.

Harrison R. and Yin J. Y., Characteristics of particulate matter in the United Kingdom, Report produced for Defra, March 2004.

Hassan A. M., Dawood Z. S. and Mahammed A. J., The effect of alternative fuel on the smoke limitation in diesel engine. Eng. And Technology, vol. 23, No. 8, 2004.

Huang X. Li, Z., Wang J., Zhang W., Particle size distribution from a GTL engine, Science of the Total Environment 382, 2007. pp 295 – 303.

Jerzy M., etal, Dissolving gas in diesel fuel as a may for fuel oxygenation and diesel exhaust emission reduction, SAE 2007 – 01 – 2049.

Jincheng Huang, etal, Experimental investigation on the performance and emission of a diesel engine fuelled with ethanol diesel blends. Applied Thermal Engineering 29 (2009), 2484-2490.

Kowalewicz A., and Wojtyniak M., Alternative Fuels and their application to combustion engines, Proc I MechE, Vol. 219, Part D, I MechE, 2005.

Kowalewicz A., Eco-diesel engine fuelled with rapeseed oil methyl ester and ethanol. Part 3 :

Combustion processes. Proc. I MechE vol 220, Part D, 2006.

Kowalewieze A., Pawlak G. and Pajaczek Z., Preliminary investigation of diesel engine with additional injection of ethyl alcohol, J. Of KONES Internal combustion engines, No.3 – 4, ISSN 1231 – 4005, 2002.

Ladommatos N., Abdelhalim S. M. and Zhao H., Effect of exhaust gas recirculation temperature on diesel engine combustion and emissions, Proc I MechE, vol. 212, Part 1998.

Ladommatos N., Abdelhalim S. M., Zhao H. and Hu Z., The effect of Carbon dioxide in exhaust gas recirculation on diesel engine emissions, Proc. I MechE, vol 212, Part D, 1998.

Lapuerta M, Armas D., Ballesteros R., Diesel particulate emissions from biofuels derived from Spanish vegetables oils. SAE, Vol. 1, 2002. pp 1657.

Lapuerta M, Armas O., Herreros J.M., Emission from a diesel-bioethanol blend in an automotive diesel engine, fuel 87(2008) 25 – 31.

Lapuerta M., Hernandez J. J., Ballesteros R. and Duran A., Composition and size of diesel particulate emissions from a commercial European engine tested with present and future fuels. Proc. I MechE, vol. 217, Part D, 2003.

Litzinger T., Stoner M., Hess H. and Boehman A., Effect of Oxygenated Blenging compounds on emissions from a turbo-charged direct injection diesel engine. Int. J. Engine Research, Vol. 1, No. 1, I MechE, 2000.

Lu X-C, Ma J-J, Ji L-B. and Hauang Z., Effect of premixed n-heptanes from the intake port on the combustion characteristics and emissions of biodiesel-fuelled engine, Proc. I MechE, Vol. 222, Part D, 2008.

Musculus M. P. B. and Diets J., Effect of diesel fuel combustion – modifier additives on in – cylinder soot formation in a heavy – duty D I diesel engine, Sandia report, SAN, 2005 – 0189, Sandia National laboratories, 2005.

Salman Y. K., Abdulhadi M. A. and Hassan A. M., Study of performance and prediction of heat release in compression ignition engine working on ethyl alcohol and gas – oil solution. Journal of Engineering, vol. 11, No. 1, 2005.

USEPA, Health assessment document for diesel engine exhaust, EPA/ 600/ 8 – 90/ 057F, 2002.

Xing – cai, etal Effect of cetane number improver on heat relax rate and emission of high speed diesel engine fuelled with ethanol – diesel blend fuel, fuel 83 (2004) 2013 – 2020.

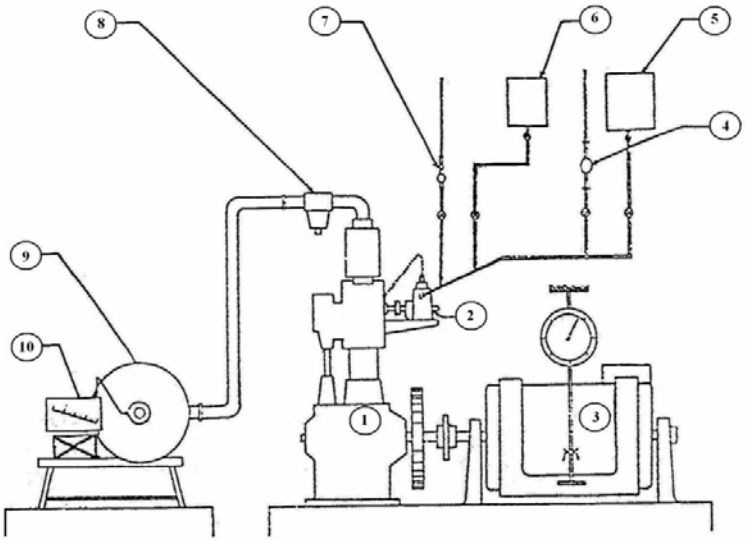

1- Engine
2- Fuel injection pump
3- Electric dynamometer
4- Gas oil fuel meter
5- Gas oil tank
6- Emulsified fuel tank
7- Emulsified fuel meter
8- Air filter
9- Air box
10- Inclined manometer

Fig.1: Schematic of the Engine and Fuel Supply System

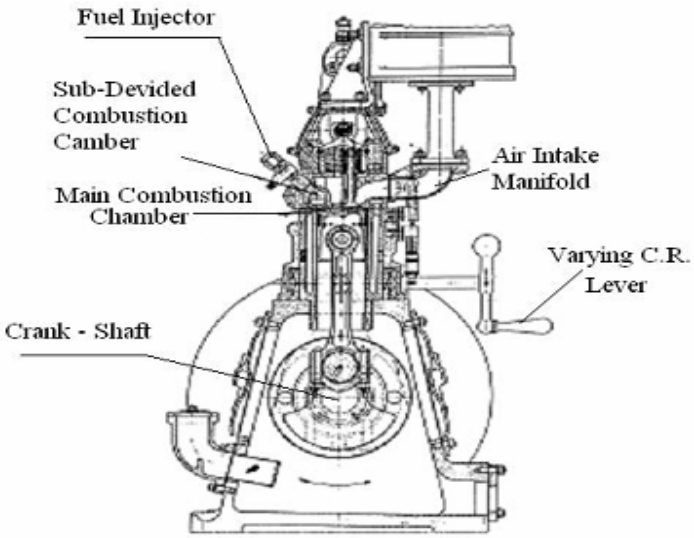

Fig. 2: Cross section of the engine used

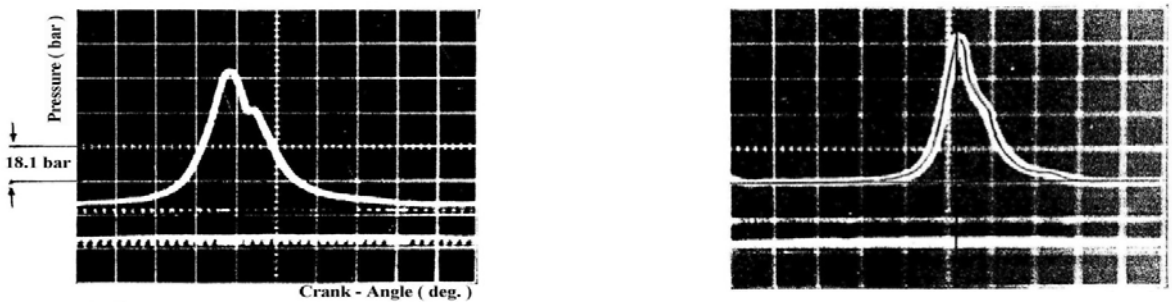

A) 900 rpm engine speed and 5.5 N Load Fuel : Straight Gas Oil

B) 1200 rpm engine speed and 32 N Load Fuel : 0.8 Gas Oil + 0.2 Ethanol

Fig. 3: Examples of pressure – crank angle curves obtained from oscilloscope screen for different speeds, Loads and fuel solutions (Salman, 2005).

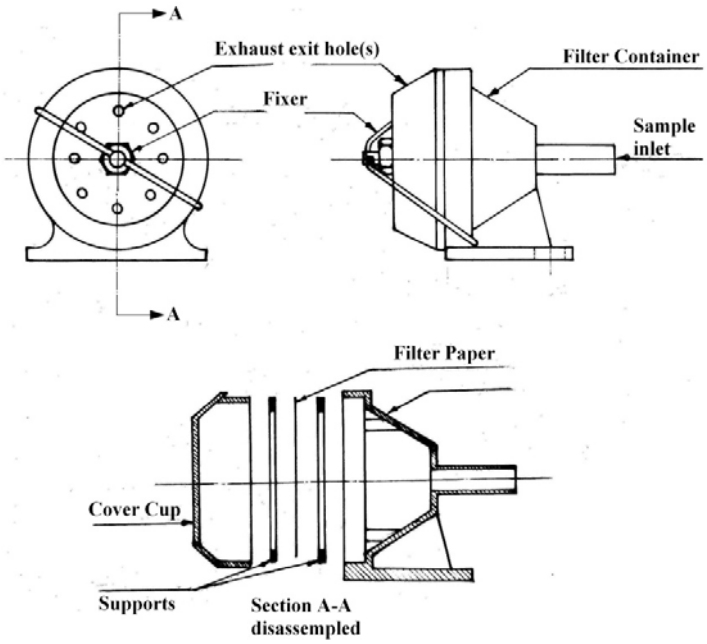

A) Filter

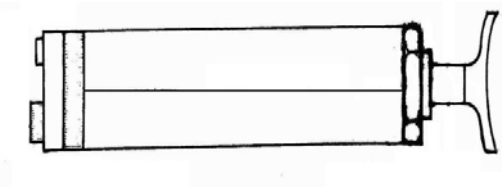

B) Syringe

Fig. 4: Particulate Matter Measurement equipment

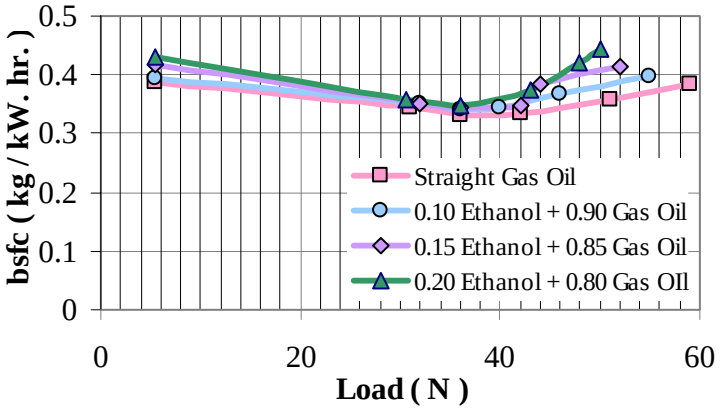

Fig. 5 : Effect of Ethanol Content on *bsfc* at Constant Speed (1500 rpm)

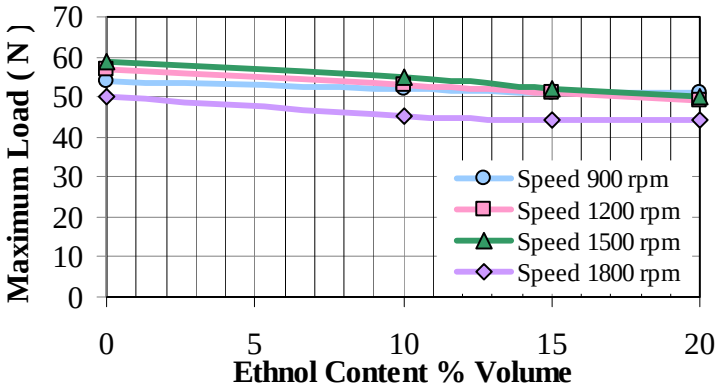

Fig. 6 : Maximum Load Variation with Ethanol Content For Different Speeds

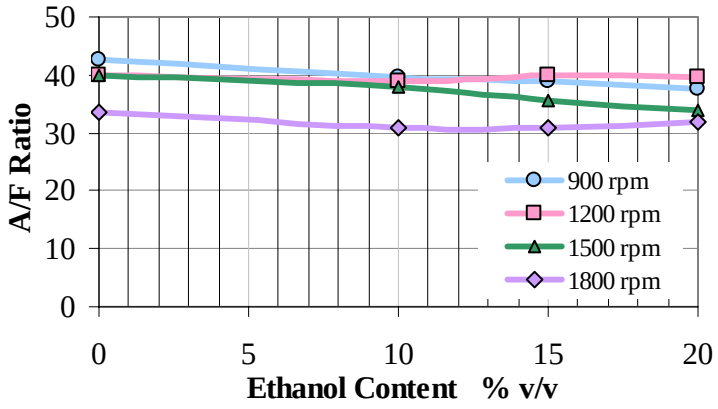

Fig. 7 : Effect of Ethanol Content on A/F Ratio at (25 N) Load for Different Speeds

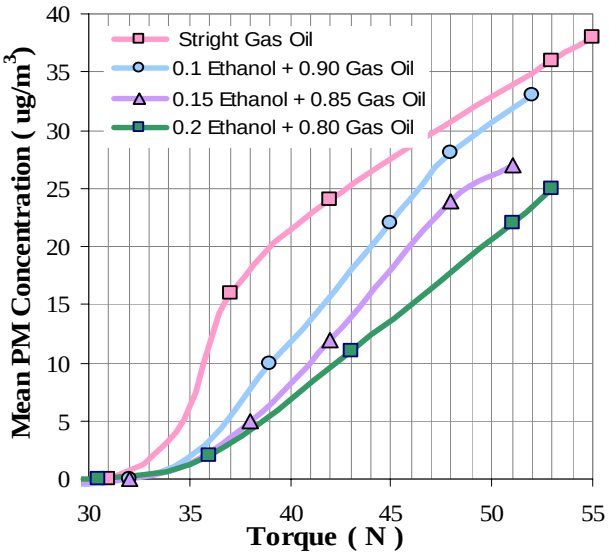

Fig.8:Effect of Ethanol Content on Mean Mass Particulates Concentration in the Exhaust Gasses for different loads at Engine Speed (900 rpm)

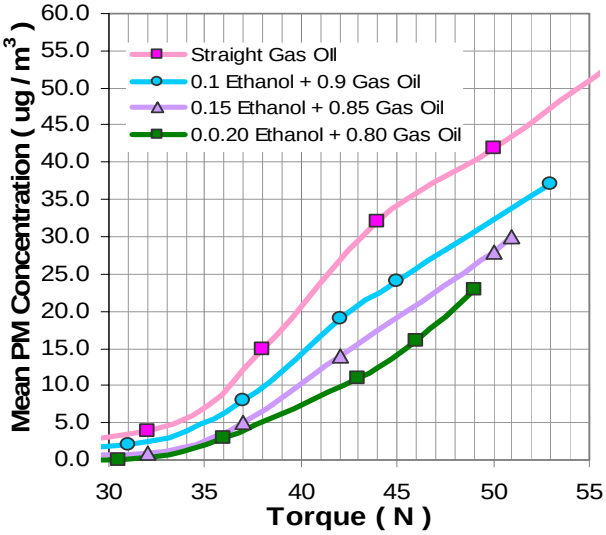

Fig.9: Effect of Ethanol Content on Mean Mass Particulates Concentration in the Exhaust Gasses for different loads at Engine Speed (1200 rpm).

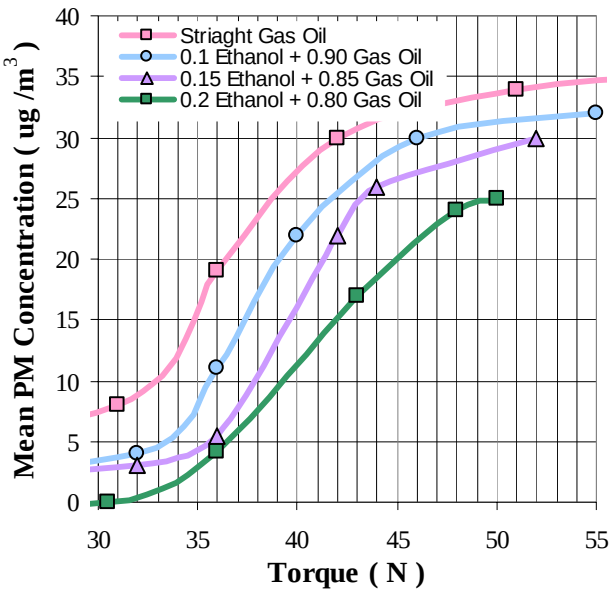

Fig.10: Effect of Ethanol Content on Mean Mass Particulates Concentration in the Exhaust Gasses for different loads at Engine Speed (1500 rpm).

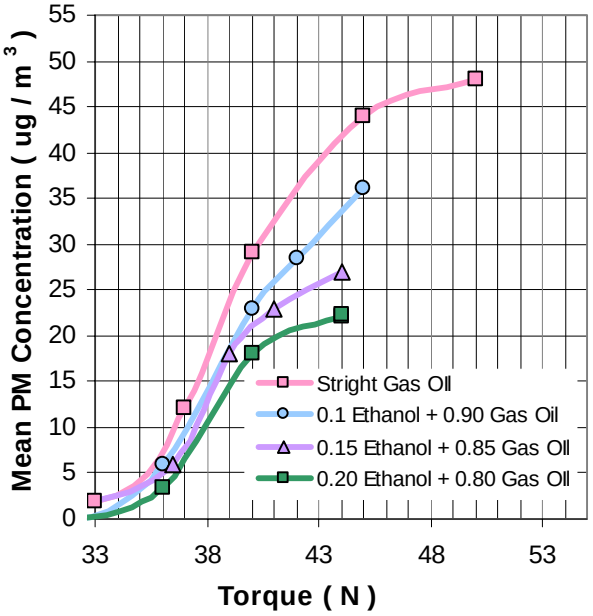

Fig.11: Effect of Ethanol Content on Mean Mass Particulates Concentration in the Exhaust Gasses for different loads at Engine Speed (1800 rpm).

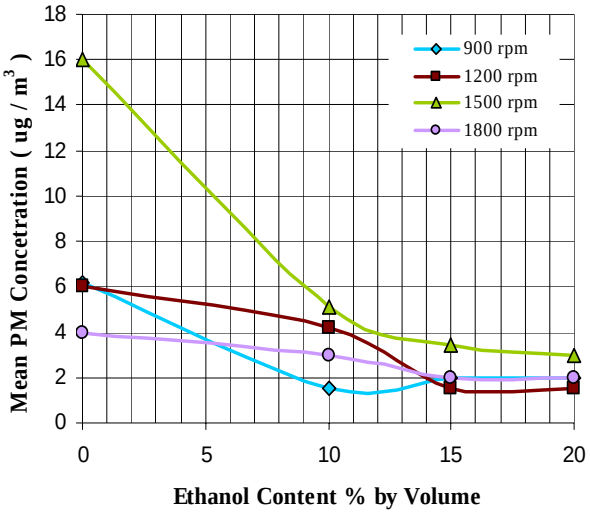

Fig.12:Effect of Ethanol Content on Mean Mass Particulates Concentration in the Exhaust Gases s for different speeds at constant load of 35 N.

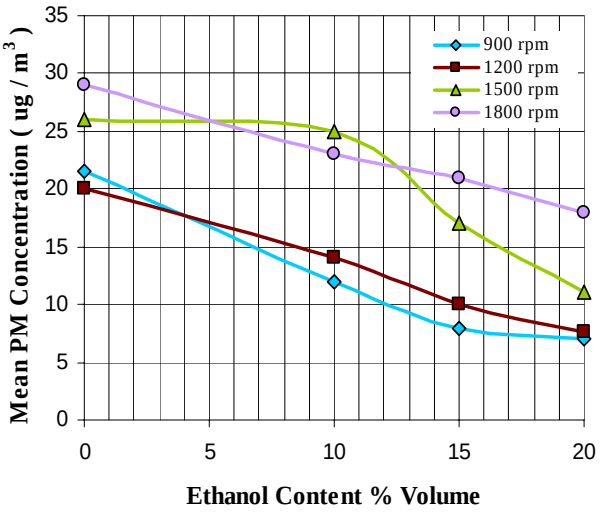

Fig.13:Effect of Ethanol Content on Mean Mass Particulates Concentration in the Exhaust Gases for different speeds at constant load of 40 N.

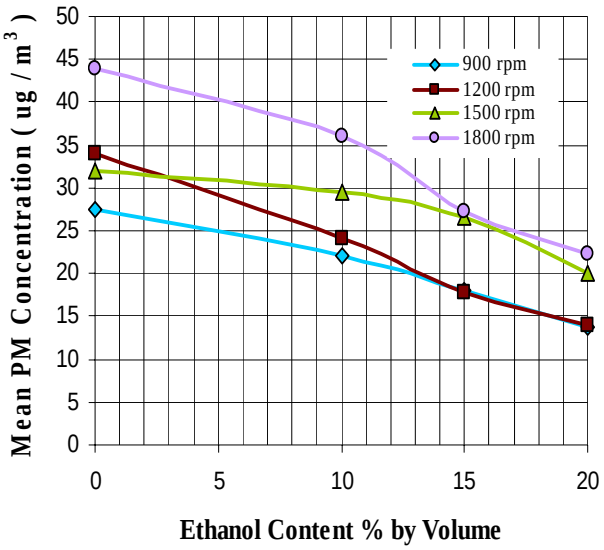

Fig.14: Effect of Ethanol Content on Mean Mass Particulates Concentration in the Exhaust Gasses for different speeds at constant load of 45 N.

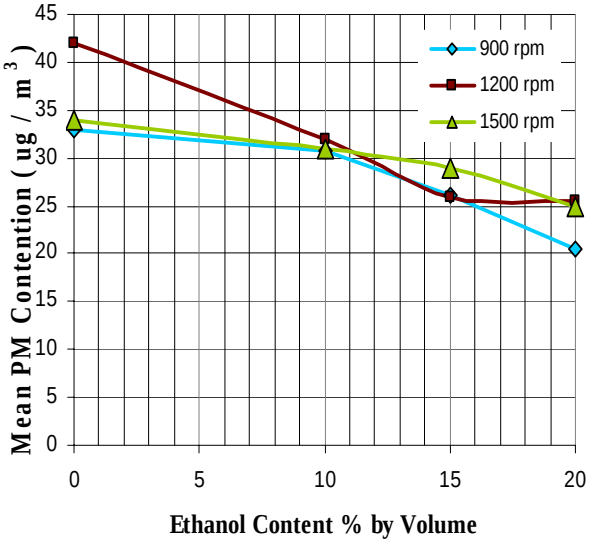

Fig.15: Effect of Ethanol Content on Mean Mass Particulates Concentration in the Exhaust Gasses for different speeds at constant load of 50 N.

APPENDICES:

Appendix – A

Specification of the Engine

No. of Cylinders	1
Bore	76.2 mm
Stroke	110 mm
Capacity	507 CC
Valve Timing	Inlet opens 9° BTDC
	Inlet closes 38° BTDC
	Exh. opens 44° BTDC
	Exh. closes 9° BTDC

Appendix – B

Properties of Gas Oil and Ethanol

1- Properties of Gas Oil

Chemical Formula	$C_{14}H_{24}$
Specific Gravity	0.84
Flash Point ^oC	54
Viscosity Cst at 38 ^oC	6
Sulphur Content % W	0.2
Diesel Index	55
Cetane No.	53
Calorific Value KJ/ Kg (Gross)	45144

2- Properties of Ethanol

Chemical Formula	C_2H_5OH
Specific Gravity	0.79
Flash Point ^oC	21
Viscosity Cst at 40 ^oC	1.1
Octane No.	89
Cetane No.	8
Calorific Value KJ/ Kg (Gross)	26994

INTERACTION EFFECTS OF HYDRODYNAMICALLY FULLY DEVELOPED PRIMARY FLOW AND SECONDARY FLOW IN THE THERMAL ENTRANCE REGION OF ANNULAR DUCT

Dr. Akeel A. Mohammed
University of Technology
Mechanical Eng. Dep.
Baghdad-Iraq

ABSTRACT

Experiments have been conducted to study the local and average heat transfer by mixed convection for hydrodynamically fully developed, thermally developing and fully developed laminar upward air flow in an inclined annulus with adiabatic inner cast iron tube and uniform heated outer aluminum tube with an aspect ratio ($\Omega = 0.72$) and ($L/D_h \approx 40$) for both calming and test sections). A wide range of Reynolds number from 859 to 2024 has been covered, and heat flux has been varied from 159 W/m^2 to 812 W/m^2 (these values of heat flux and Reynolds number gave Richardson number range from 0.03 to 0.38), with angles of annulus inclination $\phi=0^o$ (horizontal position), $\phi=60^o$ (inclined position), and $\phi=90^o$ (vertical position). The hydrodynamically fully developed condition has been achieved by using aluminum annulus (calming section) has the same dimensions as test section and has connected with it by Teflon piece. The average Nusselt numbers have been correlated with the product of (Richardson number and Reynolds number) and compared with available literature and showed satisfactory agreement. The temperature and local Nusselt number profiles results have revealed that the secondary flows created by natural convection have a significant effect on the heat transfer process.

الخلاصة:

أجريت تجارب لدراسة أنتقال الحرارة الموقعي والمعدل بواسطة الحمل المختلط لتمام التشكيل الهيدروديناميكي ولجريان الهواء الطباقي خلال مرحلة التشكيل الحراري وتمام التشكيل الحراري لتجويف حلقي بأنبوب داخلي حديدي المعدن معزول وأنبوب خارجي المنيومي المعدن مسخن تسخين منتظم بنسبة باعية 0.72 ونسبة ($L/D_h \approx 40$) لكل من مقطعي الخمد والأختبار . أمتد رقم رينولدز من 859 الى 2024 ويتغير الفيض الحراري من 159 W/m^2 الى 812W/m^2 (قيم الفيض الحراري ورقم رينولدز تعطي مدى لرقم ريجاردسن من 0.03 الى 0. 38) بزوايا ميل (وضع افقي $\phi=0^o$) ، (ϕ=60° وضع مائل)، (ϕ =90° وضع عمودي) . تم الحصول على حالة تمام التشكيل الهيدروديناميكي بوضع مخمد في مدخل مقطع الأختبار الحلقي ذو أبعاد مماثلة لأبعاد مقطع الأختبار ويرتبط معه بواسطة قطعة تفلون. تم استنباط معادلة تجريبية لمعدل أرقام نسلت مع حاصل ضرب كل من رقم ريجاردسن ورقم رينولدز و قورنت بعمل سابق و أعطت قبول مرضي. بينت نتائج توزيع درجة الحرارة و رقم نسلت الموقعي , بأن الجريان الثانوي المتولد من قبل الحمل الحر يمتلك تأثير مهم على عملية أنتقال الحرارة.

Key wards: Combined convection, thermally developing, and inclined annulus.

INTRODUCTION

Heat transfer takes place between a solid surface and a fluid whenever a temperature difference exists. Where mixing of the fluid particles occurs, the heat is transferred by convection. The latter may either be forced or natural depending on whether the fluid motion is imposed or whether it occurs because of a difference in density **[Holland and Moores 1970]**. Combined free and forced convection is known as mixed convection which is characterized by Richardson number (Ri) which represents the ratio of buoyancy force (Gr) and inertial force (Re^2).

The interaction of the natural and forced convection currents is very complex and difficult since it depends not only on all the parameters determining both forced and free convection relative to one another but also on a large number of interacting parameters including the relative direction of the natural and forced convection to each other (i.e. aiding or opposing flow), the geometry of the arrangement, the velocity profile at annulus entrance and the heating surface boundary conditions**[Bergles and Simonds 1971]**.There are many employments for heat transfer by combined convection in concentric annular tubes because of special importance in many industrial engineering applications for examples; double pipe heat exchangers designed for chemical process, food industrial, heating of process fluids, the cooling of electrical cables and nuclear fuel rods, and the collection of solar energy.**[Kotake and Hattori 1985]** studied numerically the mixed convection in a horizontal annulus by examining the similarity condition of fully developed laminar flows of fluid (Pr=1) over the range of($10^4 \leq Gr \leq 10^6$), with radius ratio (0.5). Results of the inner and outer tubes temperature along the annulus, the streamlines and isotherm, and the relation of Nu_m with Re_r , Gr were obtained. **[Nieckele and Patankar 1985]** presented a numerical study for fully developed region of the buoyancy affected flow with an axial laminar flow in a horizontal annular pipe with radius ratio of 0.2, 0.33, 0.5, and 0.66 and ($10^4 \leq Ra \leq 10^7$). The inner wall was heated isothermally while the outer wall was adiabatic. The axial velocity profiles, the temperature variation in the cross section along the annulus and the effect of the radius ratio on the circumferential variation of Nu_x were depicted. Steady-state, fully developed velocity and temperature fields in mixed convection through a horizontal annulus (radius ratio equals 0.8), with a prescribed constant heat flux on the inner cylinder and an adiabatic outer cylinder, were analyzed by (kaviany 1986), using finite difference approximation over the range ($10^5 \leq Ra \leq 10^9$) and (Pr=0.7, 7, 70). Results of inner surface temperature, development of axial velocity profiles, and the effect of the buoyancy on the radial temperature distribution along the annulus were calculated. Numerical calculations have been performed systematically by **[Ihsan and Akeel 2009]** to investigate the parametric influences on the heat and fluid flow patterns and heat transfer rate in the hydrodynamically and thermally fully developed region of inclined annulus of radius ratio fixed at 0.5 with uniformly heated inner cylinder and adiabatic outer cylinder. The ranges of governing parameters covered in the calculations are ($10^3 \leq Ra \leq 10^6$) and Pr=0.7&5. The results show that, for the two values of Prandtl numbers investigated, the transition from single-eddy pattern to the double-eddy pattern appears to occur between 10^5 and 10^6. Large temperature gradients and higher local Nusselt number attain at the bottom except at vertical position in which the angular variation of the Nusselt number remains constant because of symmetry about vertical axis. Only one available experimental work has the same thermal boundary conditions used in the present work. This work was presented by **[Gada**

2009] who studied simultaneously developing laminar mixed convection heat transfer in the entrance region of inclined concentric annuli with a radius ratio of o.555. The investigation covered Reynolds number range ($383 \leq Re \leq 1500$) and Rayligh number range from (1.005×10^5 to 1.52158×10^5) for horizontal position ($\phi=0^o$), vertical position ($\phi=90^o$), and inclined position with aiding and opposing flow ($\phi=\pm30^o,\pm60^o$) where the minus sign refers to opposing flow and the plus sign refers to aiding flow. Results show that the heat transfer process in the aiding flow is better than that in opposing flow and an empirical correlation has been deduced for each angle of inclination.

The present work is included using of entrance section (calming section) in which the upward flow is hydrodynamically fully developed at entrance of heat transfer cylindrical annulus with uniformly heated outer tube and adiabatic inner tube. From the experimental viewpoint, there are no available investigations have dealt experimentally to study the effect of laminar mixed convection to hydrodynamically fully developed, thermally developing and thermally fully developed for air flow in a concentric annulus on the heat transfer process. So , the present work is a step toward broadening the scope of experimental investigations and fulfilling the existing gap in the experimental data for laminar range so that more empirical correlation in a vertical, horizontal, and inclined circular concentric annulus can be developed for assisting flow since these correlations are limited .

EXPERIMENTAL APPARATUS

The scheme of experimental rig is shown in Fig.(1). Generally, it consists of a centrifugal fan (1) which has an air control valve (2) to regulate the air that push to the test section, orifice plate (2), manometer (3), flexible hose(4), settling chamber (5), calming section (8), and heating section (10). The test section (heating section) consists of 1.2m length concentric annulus with (21.9) mm outside diameter of inner tube made of cast iron and insulated from its inside by fiber glass, and heated outer tube made of aluminum with 52.3mm inside diameter and insulated from outside by 60 mm and 5.7mm as thickness for asbestos rope layer and fiber glass, respectively. To enable the calculation of heat loss through the lagging to carry out, eight thermocouples are inserted in the lagging as two thermocouples at four points along the heated section. Using the average measured temperature drop and thermal conductivity of lagging the heat losses through it can be calculated. The outer tube surface temperatures were measured by eighteen asbestos sheath thermocouples (type K) arranged along the outer tube. The calming section of concentric annulus with the same dimensions as test section and connected with it by a two Teflon connection pieces. The first piece has the same outer diameter of inner tube, and the other has the same inner diameter of outer tube. The air induced by the centrifugal fan, enters the orifice pipe section (14) (British standard unit) and then settling chamber through a flexible hose (4). The settling chamber was carefully designed to reduce the flow fluctuation and to get a uniform flow at the beginning of calming section by using flow straightener (6). A uniform velocity profile by a well designed Teflon bell mouth (7) which was fitted at the begging of outer tube of calming section (8). The inlet air temperature was measured by one thermocouple located in the settling chamber (5) while outlet bulk air temperature was measured by two thermocouples located in the test section exit. The local bulk air temperature was calculated by fitting straight line-interpolation between the measured inlet and outlet bulk air temperatures. The choice of linear distribution of the bulk air temperature is attributed to the following reason: for constant wall heat flux (q) boundary condition, the bulk temperature gradient is calculated from:

$$\frac{dt_b}{dx} = \frac{q.p}{m.c_p} = \frac{p}{m.c_p} h(t_s - t_b) \qquad \ldots(1)$$

Where p is the perimeter of outer tube = π d_2.

From eq.(1) the axial variation of t_b may be determined. The heat is transferred to the fluid and t_b increases with x. For constant heat flux (q) it follows that the right hand side of Eq.(1) is constant and independent of the distance (x), hence,

$$\frac{dt_b}{dx} = \frac{q.p}{m.c_p} \qquad \ldots(2)$$

By integrating and applying the boundary condition (at x=0 : t=t_i), it follows that:

$$t_b(x) = t_i + \frac{q.p}{\dot{m}.c_p} x \qquad \ldots(3)$$

Where t_i is the inlet bulk air temperature accordingly, the bulk temperature varies linearly with the distance (x) along the tube annulus. Moreover, from the following equation:

$$q = h(t_s _ t_b) \qquad \ldots(4)$$

The temperature difference (t_s - t_b) varies with the distance (x) **[Incropera and Dewitt 2003]**. The difference is initially small (due to the large value of the heat transfer coefficient at the tube entrance) but increases with increasing the distance (x) due to the decrease in heat transfer coefficient of the outer tube that occurs as the boundary layer develops **[Incropera and Dewitt 2003]**.

EXPERIMENTAL PROCEDURE

Voltage regulator (variac), accurate ammeter and digital voltmeter were used to control and measure the input power to the working outer tube of annulus. The flow becomes hydrodynamically fully developed, thermally developing and thermally fully developed at the entrance to the test section by using a calming section with the same ($L/D_h \approx 40$) as test section. The ratio is enough for the flow to reaches these conditions. The Reynolds number under consideration is ranged from 859 to 2024, actually this range has been selected after so many experimental attempts so as to ensure that the mixed convection regime has been covered and accordingly this range gives the thermally developing flow and the thermally fully developed flow conditions. Moreover, this range was selected since if any fluid enters the annular gap at a uniform temperature is less than the surface temperature, convection heat transfer will be occurred and a thermal boundary layer begins to develop. In addition, if the outer tube surface conditions is fixed by imposing either a uniform temperature is constant or a uniform wall heat flux q is constant a thermally fully developed condition is eventually reached. For both surface conditions, however, the amount by which fluid temperatures exceed the entrance temperature increases with increasing the distance (x). For laminar flow the thermal entry length my be expressed as **[Incropera and Dewitt 2003]**:

$$(X_{fd,t} / D_h)_{Laminar} \approx 0.05 \, Re \, Pr \qquad \ldots(5)$$

UNCERTAINTY ANALYSIS

The accuracy of experimental results depends upon the accuracy of the individual measuring instrument and the manufacturing accuracy of the circular inner and outer tubes. Also, the accuracy of any instrument is limited by its minimum division (its sensitivity). In the present work, the uncertainties in heat transfer coefficient (Nusselt number), Reynolds number and Richardson number were estimated following the differential approximation method **[Holman 1984]**. For a typical experiment, the total uncertainty in measuring the heater input power, temperature difference (t_s – t_b), the heat

transfer rate , the circular tube surface area and the air flow rate were ± 0.2%,± 0.33%, ± 1.8%, ± 1.5%, and ± 0.02%, respectively. These were combined to give a maximum error of 1.45 % in heat transfer coefficient (Nusselt number) and minimum error of ± 1.35% in Reynolds number and ± 1.41%, in Rayliegh number.

RESULTS

Generally, when Richardson number is kept constant, the effect of buoyancy forces in a horizontal annulus is larger than other annulus inclination angle. Therefore, it can be expected for the same conditions of flow rate and input heat flux, the distribution of surface temperature along the outer tube distance increases as the annulus inclination angle changes from horizontal to vertical position as shown in Fig.(2) for Ri=0.03.This behavior can be attributed to that in horizontal position, the direction of forced convection is perpendicular to the direction of secondary motion caused by natural convection, so a spiral vortex will be generated along the axial distance causes a reduction in the surface temperature. This vortex will be weak if the angle of inclination deviates from the horizontal position towards the vertical position in which it diminishes. If the behavior of temperature distribution is studied alone in this figure, it will be noticed that the temperature value increases with the axial distance because the free convection effects do not start at the annulus inlet but require a starting length before being established. Then, the temperature value begins to decrease down stream due to strong natural convection in this region and heat losses. Fig.(3) shows the effect of angle of inclination on the local Nusselt number with the inverse Greatz number $(Gz)^{-1}$ (dimensionless axial distance) for Ri=0.076. It is apparent from this figure that the values of Nu_L decrease as the angle of inclination moves from horizontal to vertical position. The general variation of Nu_L reveals that the Nu_L near the inlet of annulus heated region are very high values since at the onset of heating, the wall to fluid temperature difference is larger (i.e; the thickness of thermal boundary layer is zero) leading to no fluid thermal profile has developed (there is only hydrodynamically fully developed fluid profile which distorts continuously as the flow moves further downstream of the test section). As a result, there is no net buoyant force upstream. Then the value of Nu_L decreases continuously due to the thermal boundary layer develops, and then near the exit of annulus heated region, the Nu_L value slightly increases because the secondary flow resulting from the natural convection which accelerates the approach of the fluid to the wall temperature through enhancement of the convection process down stream. It is expect that the length to hydraulic diameter ratio of the test section would have some bearing on the heat transfer performance and it is enough in the present work ($L/D_h \approx 40$) to obtain thermally fully developed. Taking into account the stronger of secondary currents in the horizontal position which is coupled with primary flow to produce strong vortex, the heat transfer process in the horizontal position is batter that in other angles of inclination. The relation between average Nusselt number and Reynolds number with Rayleigh number as a parameter is shown in Fig.(4). The results of Nu_m obtained for Re between 859 to 2024 and for Ra varied from 7.3×10^4 to 1.9×10^5. As be shown, the mean Nusselt number increases as Re increases where Ra is kept constant, and as Ra increases where Re is kept constant. The same result is obtained in Fig.(5) which shows the relation between Nu_m and Ra with Re as a parameter. Fig.(6) shows the effect of angle of annulus inclination on the relation between Nu_m and Ra where Re equals 2024. It is noticed that the heat transfer process improves as the angle of inclination moves from vertical to horizontal position. The same result will be obtained if Ra is kept constant ($Ra=1.9 \times 10^5$) as shown in Fig.(7). The values of the average Nusselt number (Nu_m) for

horizontal (ϕ=0°), inclined (ϕ=60°), and vertical positions (ϕ=90°) are plotted in Figs.(8-10); respectively in the from of log(Nu_m) against log(Ri.Re) for the range of Re from 895 to 2024 and Ri from 0.03 to 0.38. The dashed line in this figure represents the empirical correlation that deduced by Gada. It was shown that the heat transfer equations for all the positions have the same following from:

$$Nu_m = c\,(Ri \,.\, Re)^m \qquad \ldots(6)$$

Where c and m are shown in table 1.

These figures show that the values of Nu_m in the present work are higher than in the work of Gada. This result leads to the important physical fact that the heat transfer process in the hydrodynamically fully developed region of annulus is better than that in the hydrodynamically developing region.

CONCLUSIONS

As a result from the experimental work conducted in the present work to study mixed convection heat transfer for thermally developing and hydrodynamically fully developed laminar air flow in an inclined annulus with uniformly heated outer tube, the following conclusions can be made:

1. The horizontal position gives a stronger spiral vortex along the axial distance of the annular gap causes a reduction in the surface temperature and increasing in the heat transfer coefficients.
2. The variations of surface temperature and the local Nusselt number were found to be strongly dependent on Richardson number and angle of inclination.
3. The heat transfer results for horizontal, inclined, and vertical position for mixed convection in laminar range were correlated as $Nu_m=c(Ri.Re)^m$
4. The mixed convection region has been bounded by the suitable selection of Richardson number (i.e., Reynolds number and Rayliegh number ranges) which is varied approximately from 0.03 to 0.38.
5. The present experimental results have been compared with the available literature and showed similar trend and important physical fact says the heat transfer process in the hydrodynamically fully developed region of duct (any geometry) is better than that in the developing region of this duct.

NOMENCLATURE

Cp Specific heat at constant pressure, (J/Kg.^{0}C)
D_h Hydraulic diameter, (m)
h Coefficient of heat transfer, (W/m^2.^{0}C)
L Annulus length, (m)
q Convection heat flux, (W/ m^2)
r_1 Radius of inner tube (m)
r_2 Radius of outer tube (m)
$\dot{m}$ Mass flow rate (Kg/sec)
κ Thermal conductivity of air (W/m.°C)
t Outer tube surface temperature (^{0}C)
x Axial distance

Greek

ϕ Angle of inclination, (degree)
μ Dynamic viscosity, (Kg/m.s)
ν Kinematics viscosity, (m^2/s)
ρ Air density at any point, (kg/m^3)
β Thermal expansion, (1/K)
Ω Aspect ratio= r_1/r_2-r_1

Dimensionless Gropes:

Gr Grashof number $= \dfrac{g\,\beta\,q r_1^{\,4}}{k\,\nu^{\,2}}$

Nu Nusselt number $= \dfrac{hD_h}{k}$

Ra Rayligh number = Gr.Pr

Re Reynolds number $= \frac{u_i D_h}{\nu}$

Ri Richarson number $= \frac{Gr}{\mathrm{Re}^2}$

Nu Nusselt number $= \frac{qD_h}{k(t_s - t_b)}$

G_Z Graetz number = $\mathrm{Re.Pr.D_h / x}$

Subscript:

L Local
b Bulk
f Film
i Inlet
s Surface
fd,t Thermally fully developed
m Average

REFERENCES

[Bergles A.E.and Simonds,R.R.]
"Combined forced and free convection for laminar flow in a horizontal tube with uniform heat flux". Int . J. Heat mass transfer Vol. 3, No. 14, PP-1989-2000 (1971).

[Holman J. P.]
"Experimental Method for Engineers", McGraw-Hill, Tokyo, Japan, 4th Edition (1984).

[Holland F.A. , M.moores R.M., Wastor F.A and wilkingson J. K]
"heat transfer" Heinemann Educational Books, Loondon,(1970).

[Gada A. Sadiq]
"Developing laminar mixed convection heat transfer through concentric annuli with adiabatic inner cylinder " M.SC. thesis, University of Baghdad , College of Engineering, Mars (2009).

[Ihsan Y. Hussain and Akeel A. Mohammed]
"Laminar combined convection in the fully developed region of concentric inclined annulus with uniformly heated inner cylinder ",the 6th engineering conference, university of Baghdad, collge of engineering. Vol.3: Mechanical and Nuclear Engineering, PP.19-35, 5-7 April (2009).

[Incropera F.P. and Dewitt D.P.]
Fundamentals of Heat and Mass Transfer, fifth ed.,John Wiley and Sons Inc. , (2003).

[Kaviany M.]
" Laminar combined convection in a horizontal annulus subjected to constant heat flux inner wall and adiabatic outer wall", J. Heat Transfer, Vol. 108, pp. 392-397, May, 1986.

[Kotake S. and Hattori N]
"Combined forced and free convection heat transfer for fully developed laminar flow in horizontal annuli" Int. J. Heat Mass transfer. Vol.28,No.11,PP.2113-2120, (1985).

[Nieckele A. O. and Patankar S. V]
"Laminar mixed convection in a concentric annulus with horizontal axis "J. heat transfer, Vol.107, PP.902-909, November, (1985).

Table 1: Constants in Eq.(6) for various angles of inclination

ϕ	Present work		Gada work	
	c	m	c	m
0°	3.991	-0.469	3.749	-0.487
60°	3.48	-0.495	3.172	-0.493
90°	2.8681	-0.481	2.402	-0.438

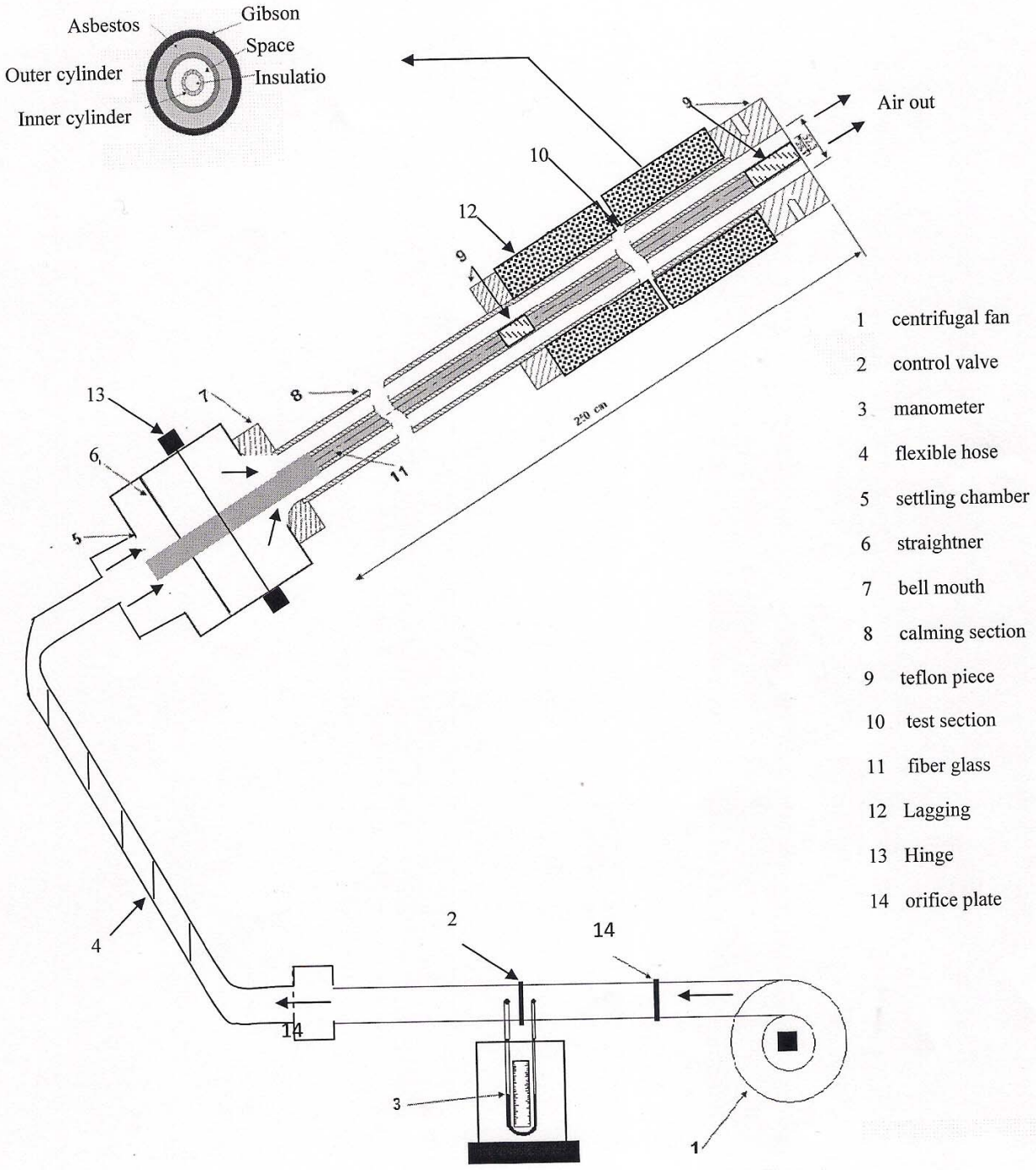

Fig .1: Diagram of experimental arrangement.

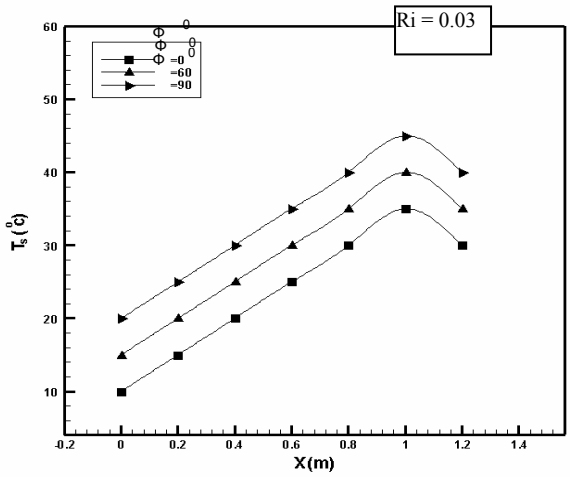

Fig.2: Variation of surface temperature along x-axis.

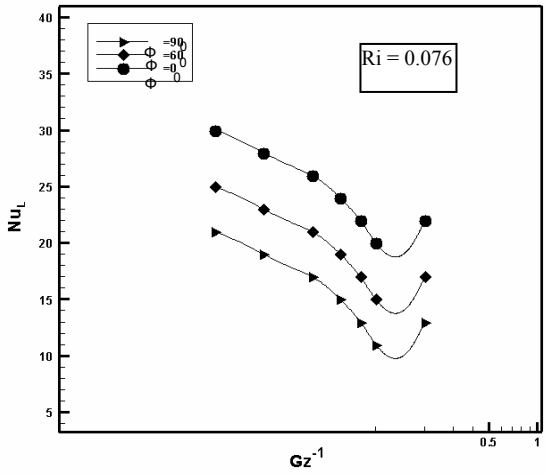

Fig.3: Local Nusselt number versus inverse Greatz number.

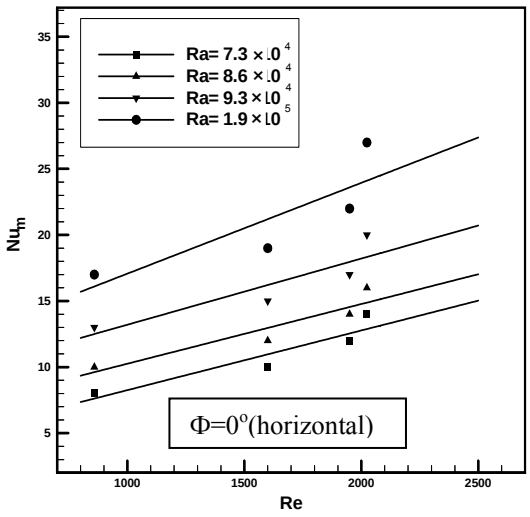

Fig.4: Mean Nusselt number versus Reynolds Number for various Rayliegh number.

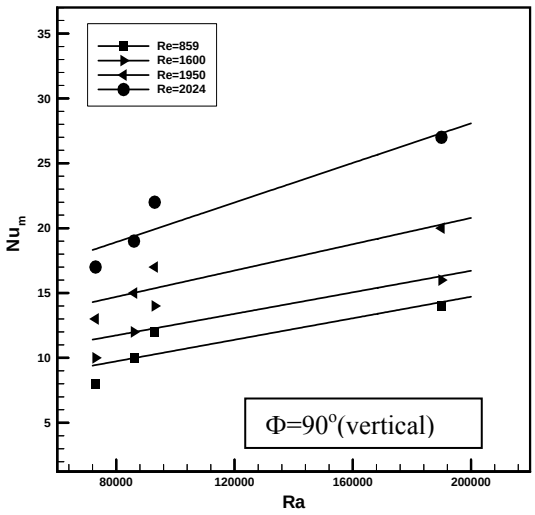

Fig.5: Mean Nusselt number versus Rayliegh number for various Reynolds number.

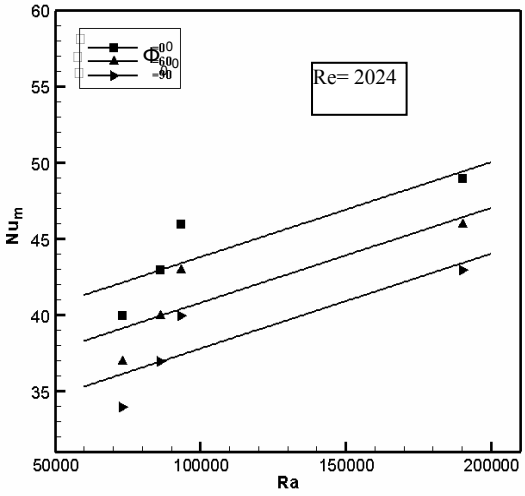

Fig.6: Mean Nusselt number versus Rayliegh numbe for various angles of inclination and Re=2024

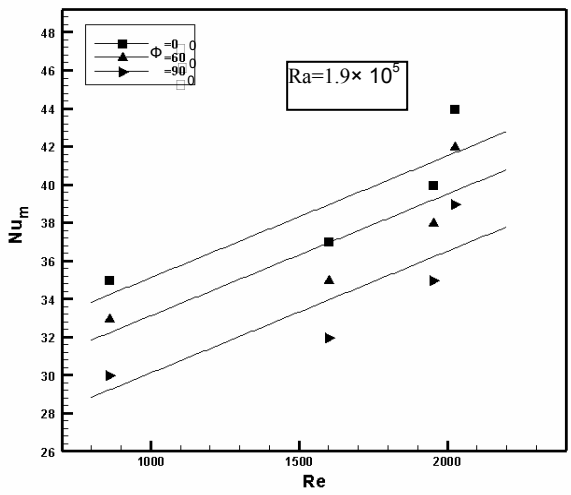

Fig.7: Mean Nusselt number versus Reynolds number for various angles of inclination and $Ra=1.9\times10^5$

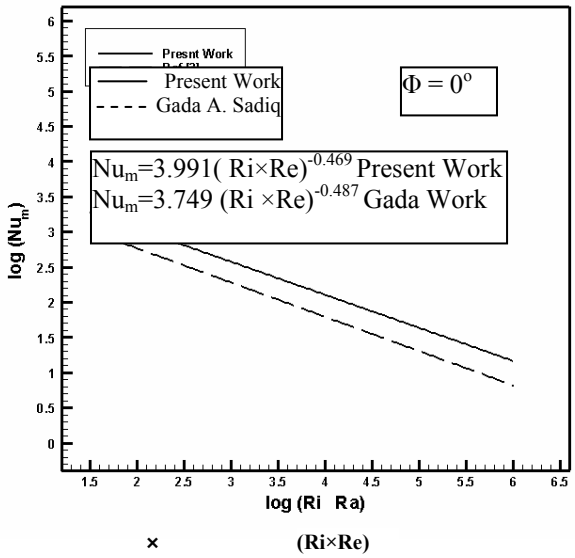

Fig.8: Log(Nu_m) versus Log(Ri.Re) for $\Phi = 0^o$

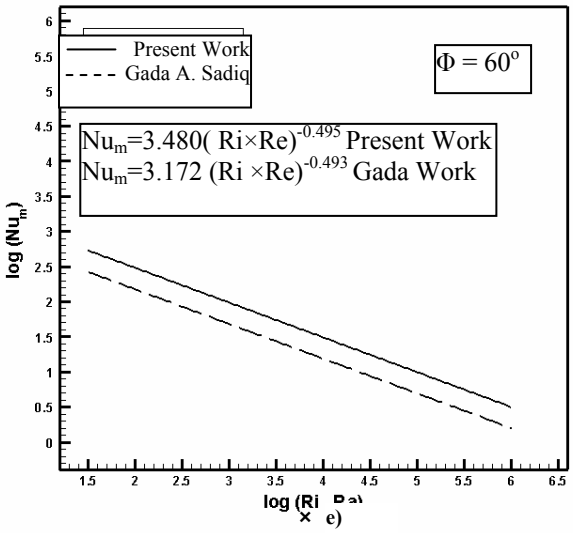

Fig.9: Log(Nu_m) versus Log(Ri.Re) for $\Phi = 60^o$

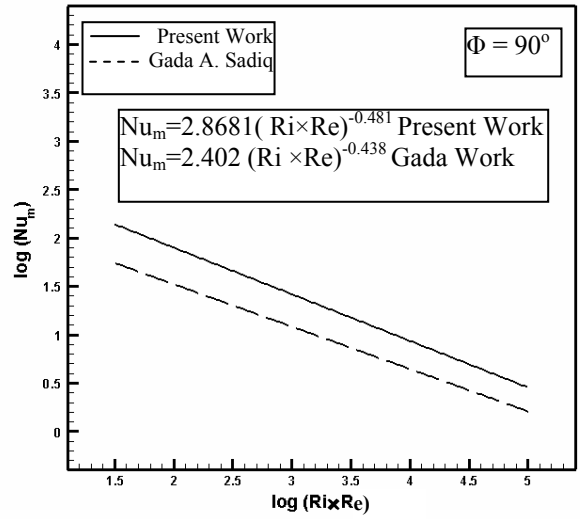

Fig.10: Log(Nu_m) versus Log(Ri.Re) for $\Phi = 90^o$

بناء نظام اداري لتسعير الفعاليات في العقود الانشائية باعتماد هيكلية تجزئة العمل في قطاع المباني في العراق

حسن كمال محسن الحلي، م.د. حاتم خليفة العجيلي ، أ.م.زهير ميخائيل ساكو

ملخص البحث

تعتمد فرضية البحث على وجود ظاهرة عامة في إعمال المقاولات لدى المقاولين وهي تجاوز الكلف الحقيقية المصروفة خلال مرحلة التنفيذ عن الكلف التخمينية للمقاولات الإنشائية في مرحلة تقديم العطاء مما يسبب العجز المالي والمشاكل الاقتصادية للمقاولين.تبنى البحـث دورة حياة بناء النظام التي تمر بمراحل مختلفة هي تحديد المشكلة وتحليلها وتصميم النظـام الإداري المقترح.ولانجاز ذلك تم دراسة النظم العالمية والمحلية المعتمـدة وبرمجـة النظـام الإداري المقترح بصيغة متناغمة مع بعض برامج الحاسوب الآلي المختلفة لتـشكل بأجمعهـا برنامجا حاسوبياً مطوراً يستخدم لتسعير فعاليات عقود الانشاء المختلفة وليكـون أكثـر دقـة وسرعة وعلمي وكفوء وبسيط يسهل على المقاولين استخدامه ويمتلك المرونة الكافية لغـرض التطوير والتكيف مع المتغيرات المستقبلية يعتمد على هيكلية تجزئة العمل ويتوافق مع الـدليل القياسي الموحد للمسح الكمي لإعمال المباني والهندسة المدنية.

The research hypothesis depends on the existence of a general phenomenon in the contracts business of the contractors represented in the fact that the actual costs of the contracts expended during the execution period exceed the estimated costs of the constructive contracts in the tender presentation phase , resulting in a financial shortage and economic problems for the contractors. The research has adopted the lifecycle of system building which goes through different phases: the problem identification, the problem analysis and the design of the proposed management system. To achieve this goal, both the standard local and international systems have been studied.Morover, the proposed management system has been programmed in accordance with the various computer programmes so that all of them form a developed computer program used for pricing the various activities of the construction contracts.A faster and more accurate program that is also characterized by being simple, scientific,efficient and easily used by the contactors. It is also flexible enough for being developed and adjusted to future changes. Furthermore, it depends on work breakdown structure and agrees with the united standard guide of quantity survey for civil engineering works.

كلمات رئيسية: ادارة كلف الانشاء ، هيكلية تجزئة العمل ، تسعير ، الدليل القياسي الموحـد للمسح الكمي لإعمال المباني والهندسة المدنية.

1- مقدمة

تعاني شركات ومؤسسات المقاولات العاملة في قطاع الإنشاء في العراق حاليا برغم خبرتها المكتسبة في مجال إدارة المشاريع من مشكلة قديمة في مجال تسعير الكلف ناتجة من عدم اختيار اليه مناسبة للتخمين والتسعير تعتمدها عند تهيئة العطاءات والدخول بها في المناقصات التنافسية على تنفيذ المشاريع والإعمال المعروضة في السوق الإنشائية مما يعرضها الى احتمالية الخسارة او الفشل في الحصول على ذلك العمل او قد تحصل عليه بسعر لا يتناسب والكلف المصروفة عليه ولا تمكنها من تغطية مصاريفها مما يعرضها لمخاطر الخسارة .

2- ادارة كلف مشاريع الانشاء

يعرف تقدير التكاليف او تقدير الميزانية بأنه (توقع الكلفة الحقيقية لعمل ما عند انتهائه) ويستخدم في ذلك (اليوسفي،2000) :

1. تكاليف حقيقية معروفة .(كلف سوق)
2. معلومات عن المنتج او المشروع المراد تقويمة .
3. دراسة وبحث عن معلومات وتكاليف من مشاريع سابقة .(معلومات تاريخية)

تتضمن عمليات ادارة كلفة مشروع الانشاء (PMBOK,2004) تخمين الكلفة وانشاء ميزانية الكلفة والسيطرة على الكلفة وتخطيط الموارد.

يمكن أن تصنف تخمينات الكلفة إلى ثلاثة اصناف رئيسة طبقا لوظائفها هي تخمينات التصميم وتخمينات العطاء وتخمينات السيطرة (Hendrickson &Tung,2003).

يعتقد الباحث ان التقسيم الذي جاء به اليوسفي هو الاقرب الى الواقع العملي في العراق ، حيث سمي الكلفة الكلية "تكلفة دورة الحياة" (اليوسفي، 2000) وتشمل الكلفة الاولية بالاضافة الى تكاليف الملكية ذلك ان قيمة أي شيء تشمل سعر الشراء بالاضافة الى تكاليف الاستخدام، وقد عرف التكلفة الاولية بانها(استثمارات راس المال وتشمل التصميم، التخطيط، الانتاج، الانشاء، تكاليف الاشراف، الاختبارات، الشحن، التخزين وتكاليف الادارة ،.....الخ). وحدد عناصر الكلفة الاولية بتكلفة الاعمال الانشائية.وتكلفة اعمال الموقع، وتكلفة التصميم والمراجعة والدراسات، والاحتياطي والطوارئ وتكلفة الادارة والاشراف، والربح .

اما تكاليف الملكية فهي (اجمالي الكلف التي تصرف على المشروع منذ امتلاك الارض وبدء استخدامها وتشمل: الطاقة، الوقود، التشغيل، الصيانة، الاصلاح، المساندة، التخزين، الامن، الخسارة، الاستبدال، التلف، الضمان، الارباح ..الخ)

3- هيكلية تجزئة العمل

يكمن مفتاح التخطيط السليم للمشروع في القدرة على تحديد نظم المشروع الرئيسية والثانوية بطريقة يرتبط كل منها بالاخر وترتبط كلها بالاطار العام للمشروع وتعرف هذه الطريقة بهيكلية تجزئة العملWork Breakdown Structure

تتكون المبادئ الاساسية لإنـشاء هيكليـة تجزئة العمل مما يأتي(Lessard,2007):

أ- وجوب ظهور أي وحدة عمل في مكان واحـد فقط في WBS.

ب- يمثل محتوى عمل اي فقرة في WBS مجموع الفقرات اسفل الهيكليه ويقصد بالفقرة جزء مـن الشجرة الهيكلية.

ت- فقرة WBS مسؤولية فرد واحد فقط.

ث- يخدم فريق المشروع في الحقيقـة تناسـق WBS مع طريقة العمل المعمول بها كمـا يخدم أغراض عملية أخرى.

ج- يجب ان يشترك أعضاء فريق المشروع في تطوير WBS لضمان التناسق.

ح- ضمان توثيق كل فقرة من فقـرات WBS لتكوين فهم دقيق لمجال العمل الكلي ولـيسَ ذلك الجزء المتضمن في تلك الفقرة فقط.

يتضمن WBS عملية موجهـه لاكمـال المهـام الرئيسة في السلسلة بينما يَتطور المشروع بمـرور الوقت. توجد ثلاث مداخل لبنـاء هيكليـة تجزئـة العمل (Wysocki,2007) :

أ-مدخل اسم- نوع(Noun–Type Approaches) ، هي تسليم عمـل المـشروعَ مـن ناحيـة المكونات (طبيعي أو وظيفي).

ب- مـدخل فعـل-نـوع(Verb-Type Approaches) هـي قابليـه تـسليم عمـل المشروع من ناحية الأعمال التي يجب عملهـا للإنتاج القابـل للتـسليم. وتتـضمن التـصميم والانشاء وفحص التنفيـذ ونظريـات أهـداف المشروع.

ت- مدخل الهيكلية التنظيمية (Organizational Approaches) هي قابلية تسليم عمل المشروعَ من ناحية الوحدات التنظيمية التي ستعمل علـى المشروع. يتضمن هذا النوع من النظرية القسم، العملية، الموقع الجغرافي.

توجـد ثـلاث مفـاهيم اساسـية لتطـوير هيكليـة تجزئـــــة العمـــــل وتحديـــــد الفعاليـــــات (Wysocki,2007)،(Lessard,2007):

أ- مفهـوم التنـاظر(Analogous Estimates): تساعد في أغلب الأحيان لمراجعة WBS للمشاريع المماثلة.

ب-مفهـوم مـن الأعلـى للأسـفل (Top-Down Estimates) : تكـــون البدايـــة بـــالفقرات الأكبرللمشروع ومن ثم يتم تجزئتها الى مستوى ادنـى. تبدأ نظريـة من الأعلـى للأسفل فـي مستوى الهدف وتتوالى تقسيمات عمل أسفل إلى المستويات الأدنـى مـن التعريـف حتـى يـصل الـى تقـسيم المشاركين في العملية.

ت- مفهوم من الاسفل الى الاعلى (Down-Top Estimates): يمكـن تحديـد فعاليـات البدايـة فـي المـشروع مـع تفاصـيل المهـام ومـن ثـم تجميعهـا لتكوين فعالية في مستوى أعلى.

4- تقييم النظم العالمية والمحلية المعتمدة:

حاول البحث دراسة وتقويم النظم العالمية والمحلية المعتمدة لما لذلك من اثر كبير على النظام الاداري المقترح باعتبار ان تلك النظم او تطويرها تـشكل العمود الفقري للنظام الاداري المقترح وفيما يلـي اهم النظم المحلية والعالمية:

اولا : النظم المحلية(الدليل القياسي الموحد):

تبين للباحث عدم وجود اي نظـام مهيـأ لهيكليـة تجزئة العمل على صعيد العـراق سـوى الـدليل القياسي الموحد ، ويعرف الدليل القياسي الموحـد مستند مكتوب عن ((SMM6)) كأسـاس حـساب الكميات لإعمال المباني و الهندسة المدنيـة ليحـل محل العرف الذي يسير علية المهندسون في الوقت الحاضر لاعداد جدول الكميات والذرعات النهائيـة بسبب عدم وجود مستند مكتوب وعدم تقييس طريقة الحساب والذي يؤدي دائما الى تفـسير شخـصي يحتمل توليد المنازعات بين صاحب العمل والمقاول او الى فروقات كبيرة بين الكلفة التخمينية الاوليـة والـذرعات النهائيـة(وزارة التخطـيط،1984)، ويتكون من سبعة عشر فصلا.

يمكن ملاحظة ان ترميز هيكلية تقسيم العمل في هذا الدليل رقمي مثلا(اعمـال الموقـع تأخـذ الرقم(3-2) واجزاء هذه الفقـرة تاخـذ الارقـام الشجرية وكما يلي تعليمات عامة(3-2-1) وحفـر الاختبـار(3-2-2) ومجـسات(3-2-3) وهكـذا بالنسبة للمستوى الثالث والرابع...الخ.

يرى الباحث ان الدليل القياسي الموحـد لـم تجري عليه اي محاولة تطوير على انه لا يتماشى مع الظرف الحالي عند اعـداد جـداول الكميـات للأسباب الاتية:

1. تم اعداده بصيغة نثرية متوافقة مع الـشروط المقاولة العراقية وهذا بدورة يصعب استخدامة في الحاسوب او البرامج الحاسوبية.
2. لايصل هيكلية تجزئة العمل في هذا الدليل الى مستوى العنصر وهذا مايسبب صعوبة في تخمين الكلفة او التسعير.
3. ينطبق هذا الدليل فقط على العقود التي تحتوي جداول الكميات ولا ينطبق على العقـود الحديثـة مثل عقود نظام (BOT).
4. يعتمده اغلب اصـحاب العمـل والمقـاولين كمواصفة وليس كمستند قابل للتسعير.

ثانيا : النظم العالمية

قام الباحث بدراسة وتحليل العديد من النظم العالمية المستخدمة لغايات مختلفة بهـدف الوصـول الـى مقترح نظام اداري يتوافـق مـع هيكليـة النظـام المقترح وكما يلي:

أ- نظام الطرق القياسية لقياس اعمـال المبـاني Standard Method of Measurement of Building Work (SMM7)

وهو من اصدار معهد مـساحة الكميـات الملكـي البريطاني. ويمثل الرقم (7) الطبعة السابعة. يكون ترتيب النظام اعتياديا وليس على شـكل تقـسيمات تقليدية. يتميز (SMM7) عن النسخ السابقة له مثل (SMM6) تحويله من النثر الى جداول تـصنيف وهذا من شأنه ان يجعل من مهمة استخدامه اسرع واكثر تنظيما من تفسير النسخة النثريـة ويمكـن استخدامها في المقايسة وفي التنفيذ عبر الحاسـوب الا ان هذا التغير لايمنع استخدام النثر التقليدي في كتابة جداول الكميات اذا ماكانـت هـذه الطريقـة مرغوبة، وبالاضافة الى هذه التغييرين الأساسـيين فقد بسطت القواعد بصورة عامة وحدثت الوثيقة بما يتلائم مع الممارسة الحديثة (SMM7,1992).

وعلى سبيل المثال فان نظام الترميز لاعمال الموقع اخذ الحرف (D) بينما اخذ تحـري التربـة المستوى الثاني (D10) و تثبيت التربة المـستوى الثاني أيضا (D11))

ومما يجدر بالذكر فان الدليل القياسي الموحد استند في تصميمة على (SMM6) اي الطبعة السادسة لسنة 1978.

ب- مباديء المقايسة لاعمال الانشاء(PMI)

Principles of Measurement for Works of Constrauction

من اصدار مؤسسة رويل. تطورت جداول الكميات كعامل مساعد للسيطرة المالية وعقود الانشاء في المملكة المتحدة عبر مدة زمنية طويلة وبسبب ممارسات مختلفة ونزاعات متتالية فقد تم اولا تحديد مجموعة من مبادئ الادارة على اساس قومي في 1922 ومن ذلك الحين تم اجراء تعديلات تعكس نمو الخبرات والتطورات في ممارسة الانشاء (PMI,1994). على سبيل المثال فأن ترميز هيكلية تجزئة العمل لاعمال الخرسانة (C) عام المستوى الثاني(C1) المستوى الثالث(C1.1) وهكذا)علما ان الهيكلية في هذا النظام تتوقف عند المستوى الثالث.

ت- الطريقة القياسية لمقايسة اعمال الهندسة المدنية (CESMM3) Civil Engineering Standard Method of Measurement

يهدف لإحداث تحسينات مع الاحتفاظ بالصفات الجيدة للطبعة السابقة ، وتكون التحسينات الاساسية والرئيسة المبتغاة كالتالي (CESMM3,1991) :

1. تحديد شكل ومحتوى جداول الكميات المهيأ وفقا للطريقة القياسية للمقايسة .
2. توفير هيكل نظامي لمفردات الجدول يؤدي الى وصف وتبنيد اكثر توحيدا .
3. طرح التقسيم الثانوي للعمل بصيغة بنود مما يمكن من توفير وصف اكثر دقة وتوازنا لقيمة العمل الموجودة في العقد.
4. الاخذ بنظر الاعتبار التقنيات الحديثة في انشاء وادارة الهندسة المدنية وتأثير هذه التقنيات على العمل نفسه وعلى ادارة العقود.

اما اهم التغيرات التي اجتمعت وسببت الحاجة الى الطبعة الثالثة فهي:

1. اجراء تعديلات تمكن من استخدامها مع شروط (ICE) الخاصة بالعقود.
2. يجعلها تتوافق مع تطورات تقنيات الهندسة المدنية.
3. اجراء تعديلات بسيطة وتصحيحات على نص الطبعة الثالثة.

لم يعد جدول الكميات الذي كان جوهريا في عقود جدول الكميات سوى مجرد قائمة تسعير للاعمال الدائمة ليعكس بصورة كافية عن المتغيرات العديدة في كلفة الانشاء لاعمال الهندسة المدنية والتي بدورها نتجت عن التطورات التي طرأت على تقنيات وطرق الانشاء ولذلك تقرر توفيرها للبنود الاضافية للعمل المقاس وللمفردات الاخرى التي يتم ادخالها حسب اختيار صاحب العطاء وتكون متصلة بشكل مباشر بطرائق الانشاء.

ج- النموذج الموحد والصيغة الاساسية Uniformat &MasterFormat

تعتبر الصيغة الأساسية (Master Format) احد اكثر صيغ البيانات شيوعا للاستخدام في صناعة الانشاء اليوم (Master Form ,2004). ظهرت هذه الصيغة بادئ الامر خلال 1960 كجهد مشترك لمعهد مواصفات الانشاء (The Construction

(CSI) Specifications Institute) بالاشتراك مع منظمات تجارية احترافية وانشائية اخرى. قامت المجموعة بعد الاشتراك مع المجموعات الكندية بنشر اصدار بعنوان ملحق (Uniformat) او النموذج الموحد والذي توفر في عام 1972. لاحقا تم اعادة تعريف (Master Format) كصيغة أساسية في 1978 وتم نشر النسخة المنقحة الاولى منه في عام 1983 وتعاقب اعادة تنقيحها 1988 و 1995 وفي عام 2004 (Dell'Isola,2002)

من الممكن التميز بين منافع وسلبيات كلا النظامين في الجدول (1) وكالاتي:

جدول (1) المقارنة بين (Master Format) & (Uniformat)(الباحث)

	الصيغة الأساسية (Master Format)	النموذج الموحد (Uniformat)
الايجابيات	1. مقبولة من المقاولين بالنسبة الى المواصفات والبرمجة الزمنية .	1. مقبولة من المصممين .
	2. ذات توجه تجاري للمواد وهي نظام مفيد جدا في تحديد وتنفيذ السيطرة النوعية على المواد واعمال التجارة.	2. تعتمد على وظيفة العناصر وتنظم حول المكونات الوظيفية والعنصرية .
	3. جيدة لكتابة المواصفات المفصلة.	3. ممتازة لاستخدام مواصفات الاداء
	4. جيدة لعمل التخمينات المفصلة .	4-1جيدة لعمل التخمينات المفاهيمية. 4-2تستخدم في التخمينات المفصلة بالرغم من ارتباطها بالمفاهمية.
	5. ممتاز في طور التنفيذ للسيطرة على الكلفة	5. ممتازة لسيطرة على الكلفة في مرحلة التصميم
		6. فعالة للمقارنة بين التصاميم المتنافسة.
		7. قيمه لجمع وحفظ معلومات المشروع التاريخية.
السلبيات	1. ذات استخدام محدود للميزانية والتخمينات المفاهيمية ولكنها من التخمينات المفصلة.	1. تزيد صعوبة جمع المقاولين لحصص المقاولين الثانوين ويفضل عطاء كاملا.
	2. صعوبة الاستخدام للسيطرة على الكلفة في مرحلة التصميم .	2. استخدام محدود للسيطرة على الكلفة في مرحلة الانشاء .
	3. صعوبة الاستخدام للمقارنة بين التصاميم المتنافسة .	

5- المسح الميداني

أ- تبين من خلال اجراء الاستبيان المغلق والمقابلات الشخصية والملاحظة المباشرة ان غالبية الجهات التي اختيرت كعينة للبحث تمتلك فرق عمل واقسام للتخمين والتسعير وتجري عملية التخمين في وقت مبكر من المشروع مستندة على المعلومات التاريخية السابقة في عملية التخمين وان تخمينات المهندس المستندة على المخططات والمواصفات وتخمينات العطاء هي اكثر انواع التخمين استخداما والذي اعتمده الباحث عند انشاء النظام الاداري المقترح. كما اكد المسح الميداني اعتماد عينة البحث بشكل رئيس على طريقة المسح الكمي وهذا مايؤكد ان التخمين يتم بعد اعتماد المخططات والمواصفات بشكل رئيس. تم دراسة وتحليل العوامل المؤثرة على التخمين وقد تم استبيانها باعتماد خمس درجات تقويميه لاخذها بنظر الاعتبار عند انشاء النظام المقترح وتم ايضاحها في الجدول (2)

جدول (2) معدل تكرار العوامل المؤثرة على التخمين

ت	العوامل المؤثرة على التخمين	معدل التكرار	التقويم	درجة الاهمية
1	عدم وجود او عدم وضوح جداول الانشاء والتصاميم	5,98	جيد	مهم
2	قلة الوقت المخصص لعمل التقديرات	5,93	جيد	مهم
3	عدم اكتمال المخططات والمواصفات المشروع	5,84	جيد	مهم
4	عدم دقة اعمال التخطيط الاولية وبرمجة التصميم	5,53	جيد	مهم
5	تغيير المواصفات	5,49	جيد	مهم
6	عدم معرفة متطلبات صاحب المشروع بشكل كامل	5,22	جيد	مهم
7	طرح العديد من المتطلبات بشكل اجمالي	4,73	جيد	مهم
8	توفر المواد الاولية والتكميلية	4,73	جيد	مهم
9	حجم او مجال عمل المشروع	4,69	جيد	مهم
10	جغرافية الموقع	4,56	جيد	مهم
11	عدم حصول القائمين على التقديرات على جميع المتطلبات في وقت واحد بل بشكل تدريجي .	4,47	جيد	مهم
12	عوامل خارجية	4,47	جيد	مهم
13	عدم وجود معلومات وبيانات موثقة للتكاليف من مشاريع سابقة	4,38	جيد	مهم
14	التخمين الاولي المنخفض	4,24	جيد	مهم
15	ضعف تعريف المجال	4,07	جيد	مهم
16	صعوبة تقنيات التنفيذ الغير المتوقعة	3,98	متوسط	غير مهم

ت	العوامل المؤثرة على التخمين	معـــدل التكرار	التقويم	درجة الاهمية
17	محاولة تكييف التكلفة الاجمالية لتلائم مبـالغ مـشاريع سـابقة بغض النظر عن المتطلبات الخاصة	3,84	متوسط	غير مهم
18	طبيعة التربة	3,67	متوسط	غير مهم
19	الاحوال الجوية الغير متوقعة .	3,62	متوسط	غير مهم
20	عدم تحديد النظم الخاصة للانشاء وللخدمات في البداية (نظـام الحريق ، نظام صوت ،....الخ)	3,44	متوسط	غير مهم

كما قد تبين من المسح الميداني ان مـشكلة التضخم وتذبذب الاسعار تؤثر كثيـرا فـي المواد الانشائية والعمالة والمعدات.

ب- محور هيكلية تجزئة العمل:

تبين للباحث من خلال المسح الميداني عـدم وجود ثقافة علمية في مواضيع حساسة فـي عملية التخمين والتسعير مثل هيكل تجزئـة العمل وهـذا مايؤكـد ان معظـم التـسعير والتخمـين يجـري علـى وفـق اسـلوب المعلومات التاريخية للمشاريع الـسابقة وان ذلك قد يعرض المقاول الى المخاطرة عنـد تقديم عطاءه.

ت- محور العقود واليات تسعيرها:

لقد تاكد للباحث من خلال المسح الميداني ان نمط التسعير الاكثر استخداما في العراق هو عقد جدول الكميات. كما تبين للباحـث مـن خلال المسح الميـداني ودراسـة المـشاكل المتولدة لدى القيام بتسعير جداول الكميـات ان تكلفة الأعمال التى لم تـرد فـي جـدول الكميات والمطلوب القيام بها هي مـن اهـم المشاكل المتولدة. وان العوامل المؤثرة فـي تسعير المقاوله ان العرض والطلب ومـدى تـوفر المـواد الأوليـة والأيـدي العاملـة والاستقرار السياسي والامني عوامل مؤثرة في تسعير المقاولة .

اعتمد الباحث طريقة التسعير الرصـين فـي بناء النظام الإداري لاعتباره اكثـر طـرق التسعير امانا للمقـاول وصـاحب العمـل والاوسع انتشاراً.

5. منهج تطوير تـصميم النظـام الاداري المقترح

يتطلب ايجـاد التـصميم الامثـل لاي نظـام مطلوب لمقابلة حاجة معينة الى اتباع مـنهج تحليلي ذو عمليات متتابعة ومتكررة يتمثل في المراحل الاتيه :

أ- التمهيد للنظام الاداري المقترح من خلال دراسة الحالة الراهنة للاحاطة بكافـة ابعـاد المشكلة وتعريف الحاجة الـضاغطة، وذلـك للوصول الى الحل الأمثل المتمثـل (بالنظـام المقترح) .

ب- تحليل وتعريف المشكلة والمتمثلة اعتماد صاحب العمل فـي المراحـل المبكـرة مـن المشروع الانشائي طرق مختلفة في تخمـين الكلفة ومن ثم تحديد الميزانية المرصودة لهذا

المشروع ، مما قد يؤدي الى المجازفه في ترسية العطاء على مقاول غير مؤهل في نهاية مرحلة تقديم العطاء نظرا لاختلاف دقة ونوع الطريقة المتبعة من قبل صاحب العمل . وتعقيد الفعاليات لمشاريع الابنية بشكل خاص وتداخلها مما يجعل من الصعوبة القيام بتسعيرة صحيحة للمقاولات خالية من وجود المخاطر او المجازفات التي يمكن ان يتحملها المقاول نتيجة لدخوله في المناقصه.

ت- تحديد الحاجة لبناء نظام إداري علمي وعملي شامل لتسعير الفعاليات الانشائية باعتماد هيكلية تجزئة العمل في قطاع المباني في العراق يمكن استخدامه من قبل صاحب العمل في مرحلة التخمين على ان يكون استخدامة الرئيس من قبل المقاول لاعداد العطاء وتقديمة في المقاولات التنافسية ومواكبة الحداثة والابتكار المطلوب للعقود وتسعيرها وفقا لمتطلبات واقع الحال والمستقبل بعد 2003.

ث- وضع المعايير التي تحدد الدخول الى النظام الاداري المقترح وقد حدد الباحث المعايير الأساسية التي يجب توفرها للدخول الى النظام الاداري المقترح:

1) اكتمال مخططات ومواصفات المشروع .
2) تسعير المواد الاولية حسب وحدة القياس المحددة في الدليل القياسي الموحد .
3) معرفة اجور عمل الايدي العاملة للفعاليات المختلفة والمعدات حسب وحدة قياس الفعالية .
4) كمية كل فعالية من فعاليات المشروع.
5) معرفة كلفة الخدمات الادارية والارباح والنثريات المطلوبه للعمل
6) نوع العقد المبرم او المراد ابرامة.
7) اختار الباحث نموذج حاسوبي تطبيقي للنظام الاداري يصلح لقطاع المباني لكونه النموذج الاكثر شيوعا.

7- تشكيل الهيكل العام للنظام الاداري المقترح

اعتمد الباحث من خلال نتائج التحري الميداني و دراسة النظم العالمية والمحلية المعتمدة انشاء الهيكل العام للنظام الاداري المقترح استنادا الى وحدات الدليل القياسي الموحد حيث يتكون من عشرة بنود رئيسة المتمثلة باعمال الموقع والاعمال الترابية والركائز والاعمال الخرسانية واعمال البناء والقواطع واعمال العزل الحراري وقطع الرطوبة والاعمال المعدنية والاعمال الخشبية واعمال الانهاء والصبغ واعمال التسطيح واعمال الصحيات وتجزء هذه البنود الى فعاليات ذات مستوى ادنى تصل في بعض التجزئة الى عشرة مستويات.

8- التصميم الاوفق

تم التدرج في بناء النظام الاداري المقترح من اجل الوصول الى نظام اداري علمي وعملي متكامل ، وقد كانت البداية مع تصميم مبسط للمشكلة المطروحة ثم الصعود بالتصميم حتى

الوصول الى التصميم الامثـل ، وذلـك دفـع الباحث الى مناقشة النظام عدة مـرات لتنقـيح النظام والوصول به الى الصياغة النهائية المبينة في المخطط الانسيابي(1) .

9-تطوير البرامج الحاسوبية للنظام الاداري المقترح

تبنى الباحث عدة برامج لتطـوير وتفعيـل النظام الاداري المقترح من خلال اسـتخدام البرامج التالية:

1. Microsoft office project professional 2003.
2. Microsoft office Excel 2003.
3. WBSPro.

10-متطلبـات البرنـامج المطـور للنظام الاداري المقترح

يتطلب البرنامج المطور للنظـام الاداري المقترح مايلي:

1. اعداد قائمة باسعار المواد الاولية فـي الاسواق المحلية واصلة الى موقع العمل.
2. اعداد قائمة بكميـات بنـود جـدول الكميـات علـى وفـق المخططـات والمواصفات المكتملة.
3. تحديد كلف العمالة والمعدات وفـرق العمل كمبلغ مقطوع او متر مربـع لكـل فعالية.
4. تحديد اجور تصنيع القالب الخشبي لكل متر مربع.
5. اجور اعمال الحدادة لحديد التسليح.لكل طن .
6. تحديد المبالغ المحددة للاعمال الاداريه والارباح على شكل نسبه مئوية او مبلـغ مقطوع.

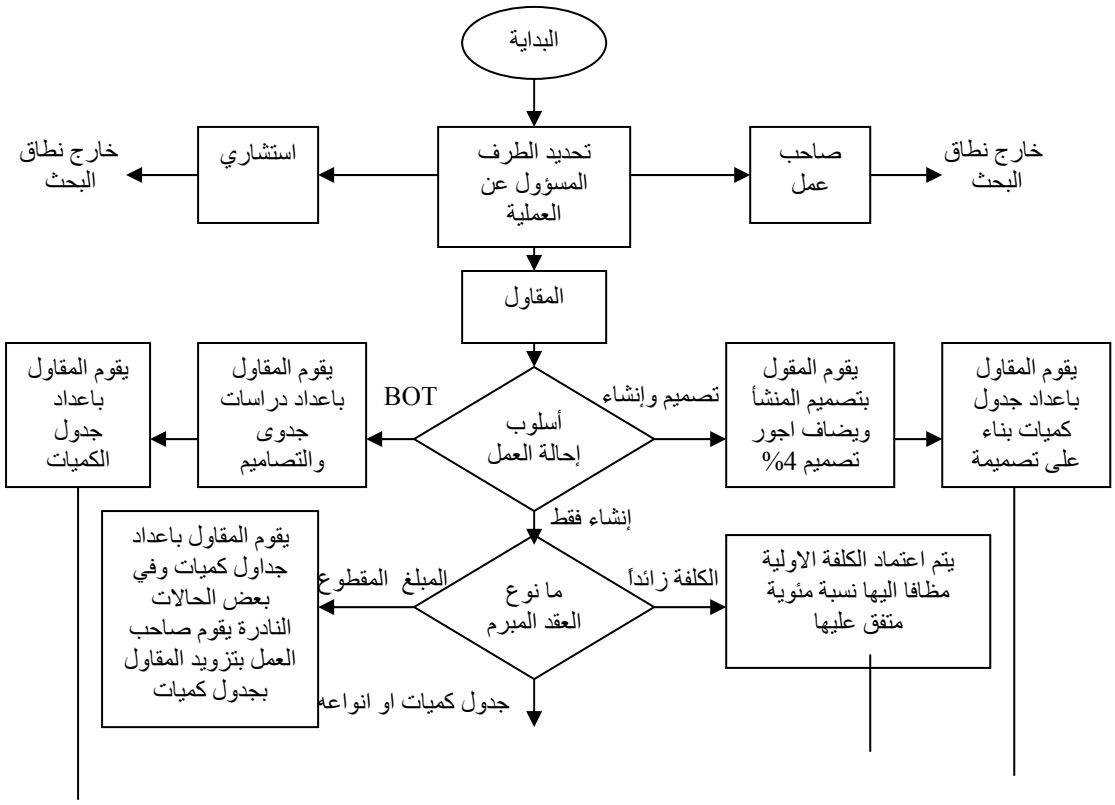

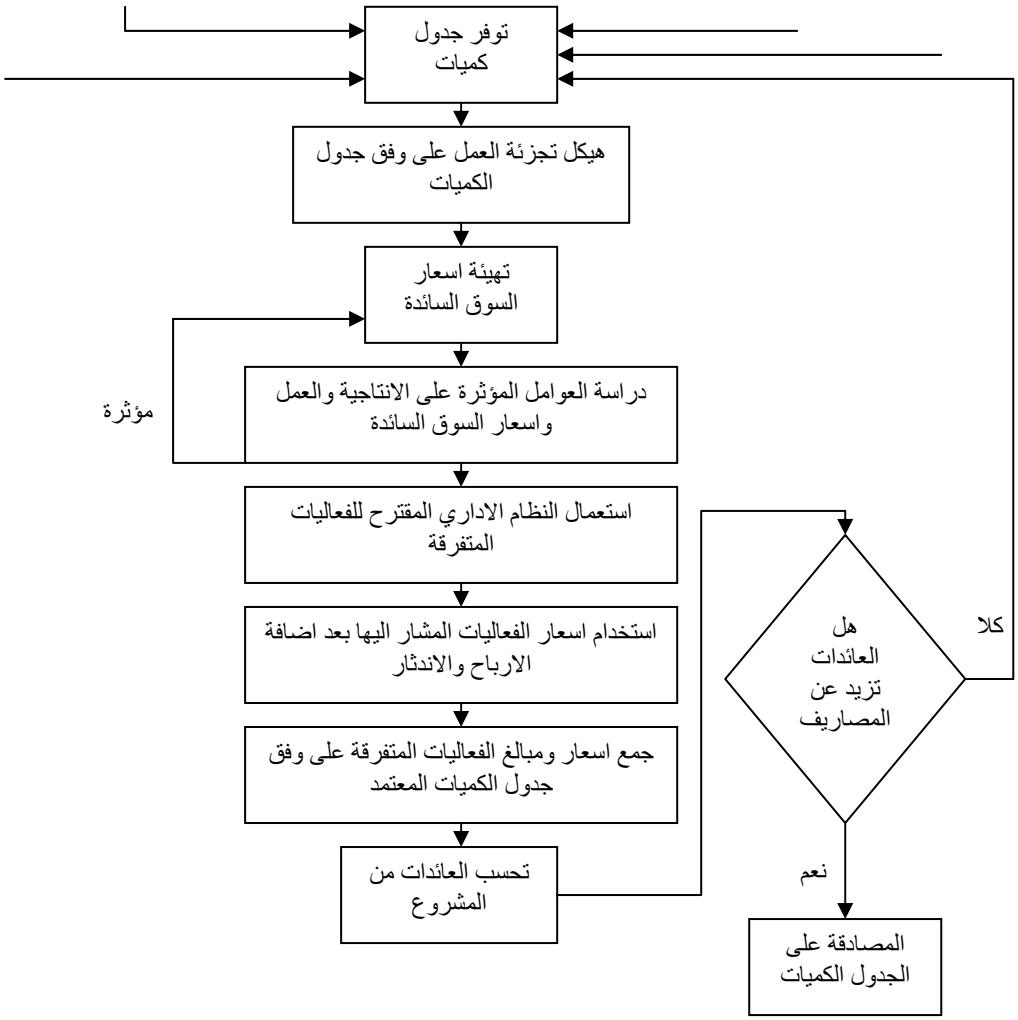

شكل (1) مخطط انسيابي للنظام الاداري المقترح

7. تخمين مقدار الاندثار والهدر والضياع الحاصل في المواد
8. اجور الخلط وصب الخرسانة لكل متر مكعب.
9. تهيئة الحاسوب والبرامج المطلوبة للعمل والقيام بالتسعير.

6. اسلوب عمل البرنامج المطور

يعمل البرنامج الحاسوبي المطور في بيئة ويندوز XP من خلال الضغط المزدوج على الملف(الدخول الى البرنامج.pps) وكالاتي:

1- يتم الدخول الى البرنامج نقرا منفردا على ايقونه (الدخول الى البرنامج) لتظهر القائمة الموضحة بالشكل (2).

2- يتم ادخال سعر الوحدة للمواد والنسبة المئوية للهدر والضياع في الحقول المخصص لها في الشكل(2) .

3- الضغط على المفتاح (Ctrl+m) لتشغيل (Macros) والانتقال الى النظام الاداري ليفتح نافذه جديدة موضحة بالشكل (3)

4- يمين كل تبويب رمز هيكل تقسيم العمل وتوجد كلمة (السابق) للرجوع الى

القائمة السابقة وللدخول الى اي تبويب يتم النقر علية ، وكمثال على ذلـك سـتظهر القائمة الموضحة بالشكل(5) عند النقر على تبويب(الحفريات والاعمال الترابية). حيث يتكون من احد عشر تبويب ويمثل المستوى الثالث من هيكل تقسيم العمل ويتكون مـن حقول الفعالية والوحدة التي تقـاس بهـا الفعالية وسعر الوحدة لهذه الفعاليـة (يـتم ادخاله من قبل المستخدم) والكمية (المحددة في جدول الكميات)والمبلغ الاجمالي لهـذه الفعالية كما وتظهر كلمة (السابق) للعـودة الى القائمة السابقة.

عند الضغط على تبويـب (اعمـال المجاري تحت الارض وتشمل الحفر الردم والقوالب والتوابع والاملائيـات) سـتظهر القائمة الموضحة بالشكل(6) عند النقر على تبويب (1.1.10.2خرساني(حوض تفتـيش) ملحقات انابيب المجاري) ستظهر القائمـة الموضح بالشكل (7) حيث تتكون القائمـة من حقل رمز هيكل تقـسيم العمـل حقـل الفعالية وشكل حوض التفتيش الذي يوضح انواع احواض التفتـيش وهـي دائريـة او مربعة او مستطيل وحقل (القطر او البعـد) وحقل (سمك جدار الحوض) و وحقل (عمق الحوض) وحقل (اجور العمل للصب للمتر المكعب) وحقل (اجور عمل القالب جملة) ونسبة الخلط(للاسمنت والرمل والحـصى) (كمية حديد التسليح تفتيش (طن)) وحقـل (اجور عمل الحديد لكل طن) وحقل (عـدد تفتيش) (المحدد في جدول الكميات) وجميع هذه الحقول يتم إدخالها من قبل المـستخدم ويتعامل البرنامج بهذه المدخلات لاظهـار النتـائج فـي الحقـلين (الـسعر لكـل وحده(عدد))(المبلغ الاجمالي للفقرة) ويوجد تبويب (مستطيل) يمكن التعامل معه عنـد النقر عليه.

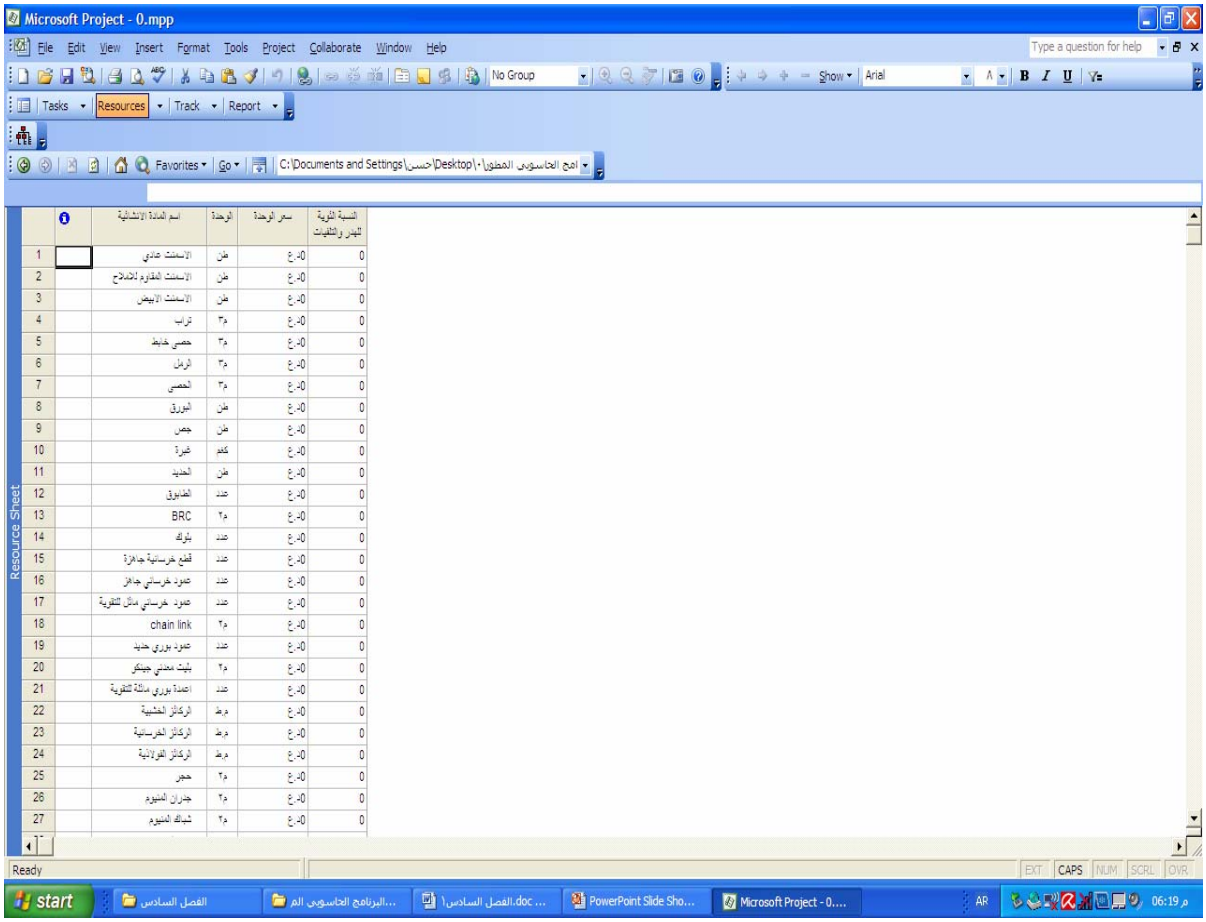

شكل(2) نافذة ادخال اسعار المواد والنسبة المئوية للهدر والاندثار

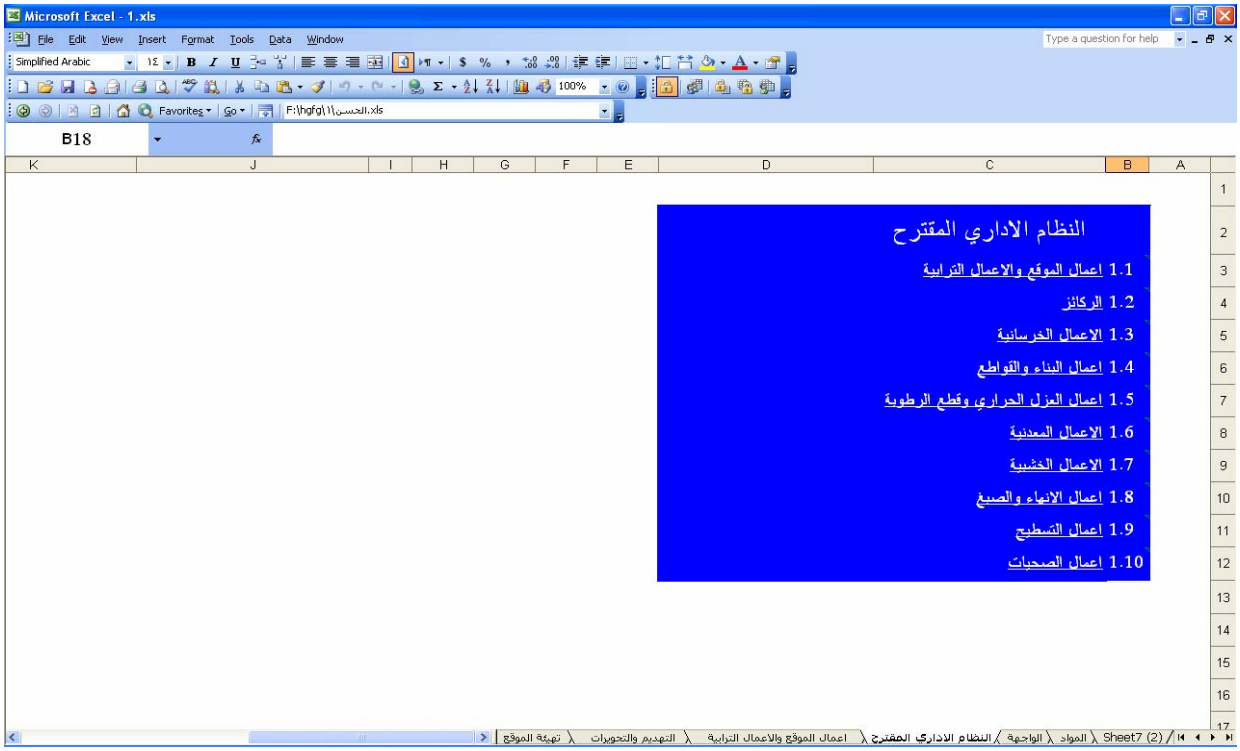

الشكل(3) نافذة النظام الاداري المقترح

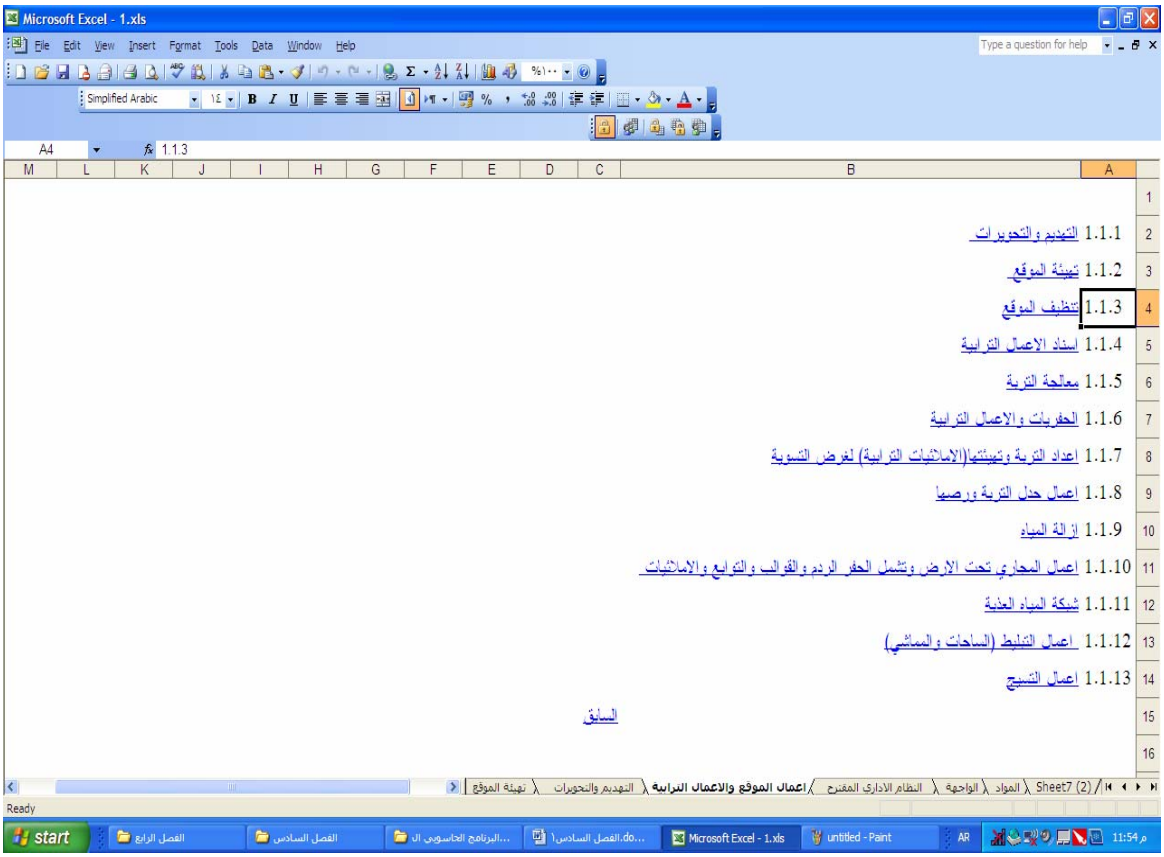

شكل (4) نافذة اعمال الموقع والاعمال الترابية

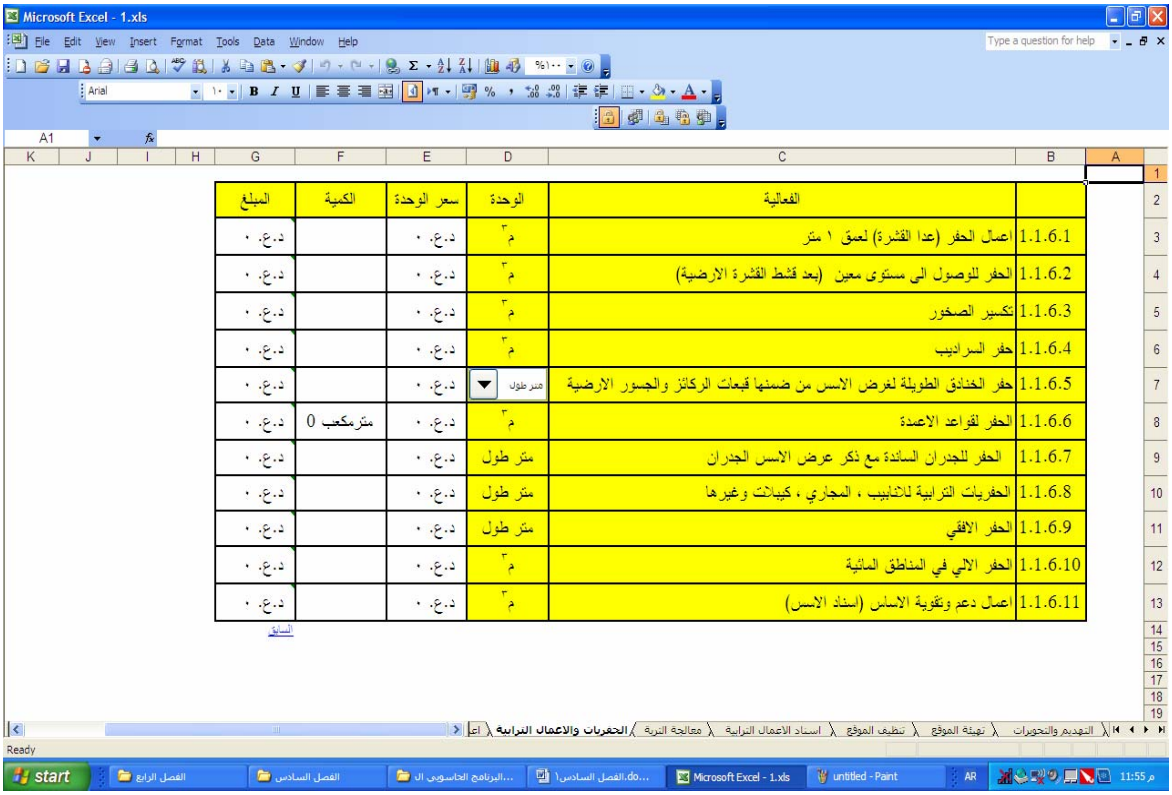

	الفعالية	الوحدة	سعر الوحدة	الكمية	المبلغ
1.1.6.1	اعمال الحفر (عدا القشرة) لعمق ١ متر	م٣	د.ع. ٠		د.ع. ٠
1.1.6.2	الحفر للوصول الى مستوى معين (بعد قشط القشرة الارضية)	م٣	د.ع. ٠		د.ع. ٠
1.1.6.3	تكسير الصخور	م٣	د.ع. ٠		د.ع. ٠
1.1.6.4	حفر السراديب	م٣	د.ع. ٠		د.ع. ٠
1.1.6.5	حفر الخنادق الطويلة لغرض الاسس من ضمنها قبعات الركائز والجسور الارضية	متر طول	د.ع. ٠		د.ع. ٠
1.1.6.6	الحفر لقواعد الاعمدة	م٣	د.ع. ٠	مترمكعب 0	د.ع. ٠
1.1.6.7	الحفر للجدران الساندة مع ذكر عرض الاسس الجدران	متر طول	د.ع. ٠		د.ع. ٠
1.1.6.8	الحفريات الترابية للانابيب ، المجاري ، كيبلات وغيرها	متر طول	د.ع. ٠		د.ع. ٠
1.1.6.9	الحفر الافقي	متر طول	د.ع. ٠		د.ع. ٠
1.1.6.10	الحفر الالي في المناطق المائية	م٣	د.ع. ٠		د.ع. ٠
1.1.6.11	اعمال دعم وتقوية الاساس (اسناد الاسس)	م٣	د.ع. ٠		د.ع. ٠

السابق

الشكل(5) نافذة الحفريات والاعمال الترابية

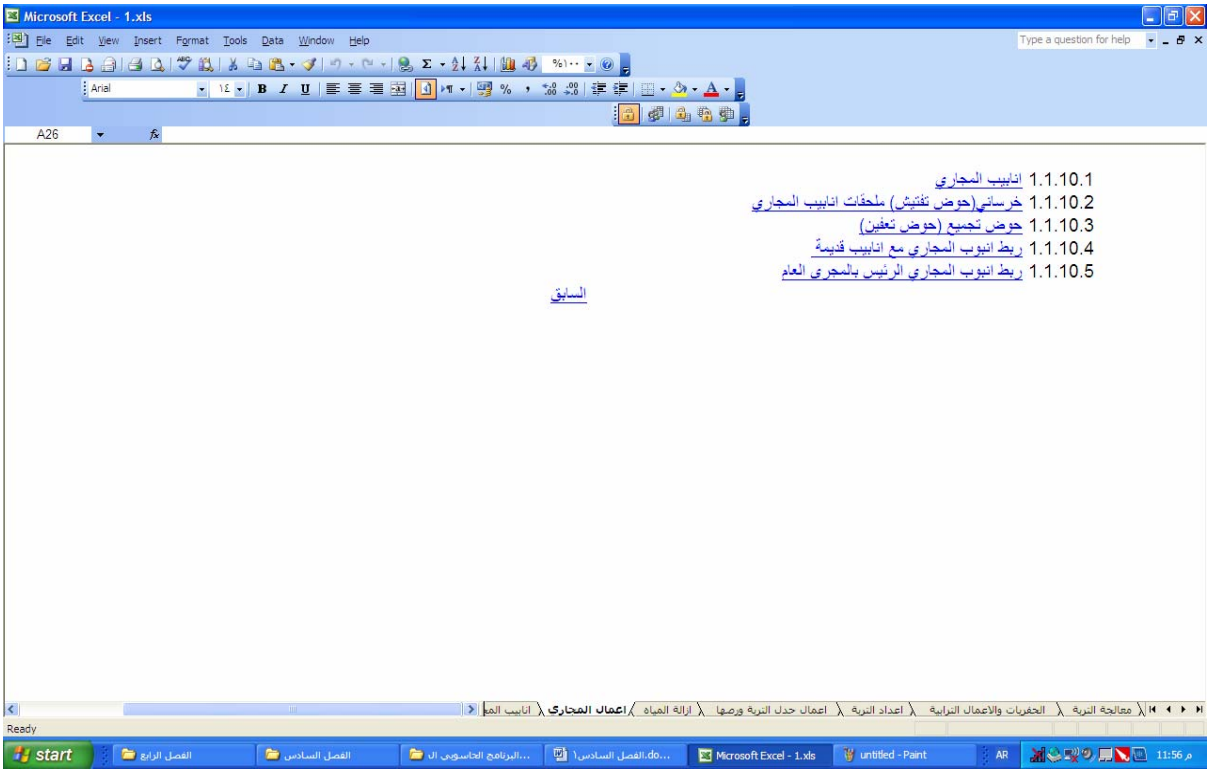

الشكل(6)نافذة للدخول خرساني(حوض تفتيش) ملحقات انابيب المجاري

5- بعد ادخال جميع البيانات المطلوبة يقوم البرنامج بتطبيق المعادلة الخاصة لاستخراج كميات الخرسانة المطلوبة للعمل والتي ينتج من تحليلها كمية المواد الاولية المطلوبة في الاسمنت والحصى والرمل وبجود رابط مع الاسعار يتم احتساب المبالغ الخاصة بالمواد االاولية يضاف اليها المبالغ الناجمه عن احتساب اجور العمالة ليظهر المبلغ الاجمالي للفقرة اولا ثم بتقسيمها على كمية المواد يظهر سعر الوحدة.لقد تم احتساب تلك المواد والاعمال بفرضية توفر الكهرباء والماء في الموقع العمل اللذين لم يتم احتساب كلفهما.على سبيل المثال فان المعادلات المستخدمة في تخمين مانهول خرساني مدور هي :

المبلغ =
(IJ10+L3*K3+G3+F3*IM10)*M3)

حيث

IJ10=IN10*IR9+IO10*IR10+
IP10*IR11+K3*IR12*MI10

MI10=2*C3*3.14*D3*E3+((2*C
3^2*3.14*D3)/4)

IN10=((IM10/(0.67*(H3+I3+J3)))
*1400)/1000

IO10=(IM10/(0.67*(H3+I3+J3)))*
I3

IP10=(IM10/(0.67*(H3+I3+J3)))*
J3

ويرمز

لمبلغ المواد IJ10 ، واجور عمل الحديد L3 ، ونسبة الخلط للاسمنت H3 ، ونسبة الخلط للرمل I3 ، ونسبة الخلط للحديد J3 ، وكمية الحديد بالطن (في م3 الواحد)K3 ، واجور عمل القالب G3 ، واجور عمل الصب F3 ، وكمية الخرسانة IM10 ، والكمية M3 ، وكمية الرمل C3 ، وسمك الجدار D3 ، والعمق E3 ، وكمية الاسمنت IN10 ، وسعر الاسمنت IR9 ، وكمية الرمل IO10 ، وسعر الرمل IR10 ، وكمية الحصى IP10 ، وسعر الحصى IR11 ، وسعر الحديد IR12

6- نفس الطريقة يمكن احتساب الفقرة الخاصة باعمال البناء بالطابوق فوق مستوى مانع الرطوبة للطابق الارضي .

7- ان عملية احتساب الاعمال الخاصة بالطابوق طابق (3,2,1) تختلف عن الطابق الارضي في فقرة اجور العمل التي تختلف من طابق الى اخر .

8- بعد ادخال جميع التبويبات والوصول الى القائمة الاخيرة(الصحيات / مرازيب) يكون قد انتهى عمل المستخدم في ادخال المعلومات والانتقال الى الطور الاخير من عمل البرنامج المطور والذي يتضمن استعراض النتائج.

9- عند النقر على زر التالي الواردة في القائمة ستظهر النافذة الموضحة بالشكل (9) التي تتكون من القائمة وعدة حقول منها حقل (هيكل تجزئة العمل) ويوضح رمز كل فعالية في هيكل تجزئة العمل وحقل (اسم الفعالية) وحقل الكلفة الإجمالية وحقل التحميلات (الادارية والإرباح) وقد ارتأى الباحث من ادخال هذه القيم من قبل المستخدم، لإمكانية تغيرها حسب رغبة المستخدم وحقل (المبلغ الاجمالية) للفعالية (حيث تتكون من التحميلات يضاف لها الكلفة الفعلية للفعالية). وبالضغط على المفتاح (Ctrl+E)لتشغيل (Macroo) سيتم اظهار الكلفة الاجمالية للمشروع الموضح بالشكل (10).

10- اعتمد الباحث في النظام الاداري المقترح شمولية جميع فعاليات مشروع المباني التقليدية ذات (اربعة طوابق) ولكنه ذلك لايمنع من اضافة بعض الفعاليات من قبل المستخدم اذا تطلب الامرفي القائمة الموضحة بالشكل(10)

لاظهار الهيكل الشجري لجميع الفعاليات ورمز هيكل تجزئة العمل الخاص بها والكلفة الاجمالية لكل فعالية يتم النقر على الايقونة (WBS Chart pro) اعلى يسار الواجهه الموضحة بالشكل(11) ليظهر الشكل (12) الذي يوضح الهيكل الشجري للنظام الاداري المقترح ورمز هيكل تجزئة العمل بها والكلفة الاجمالية لكل فعالية

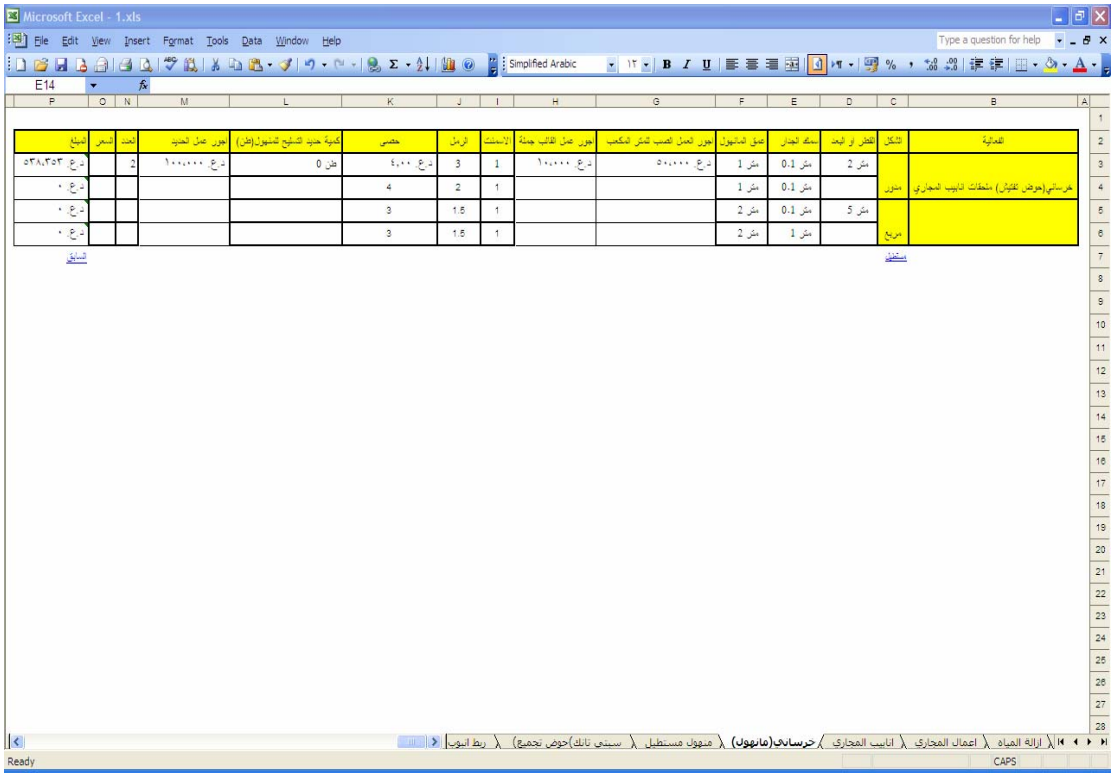

الشكل(7)نافذة خرساني(تفتيش) ملحقات انابيب المجاري

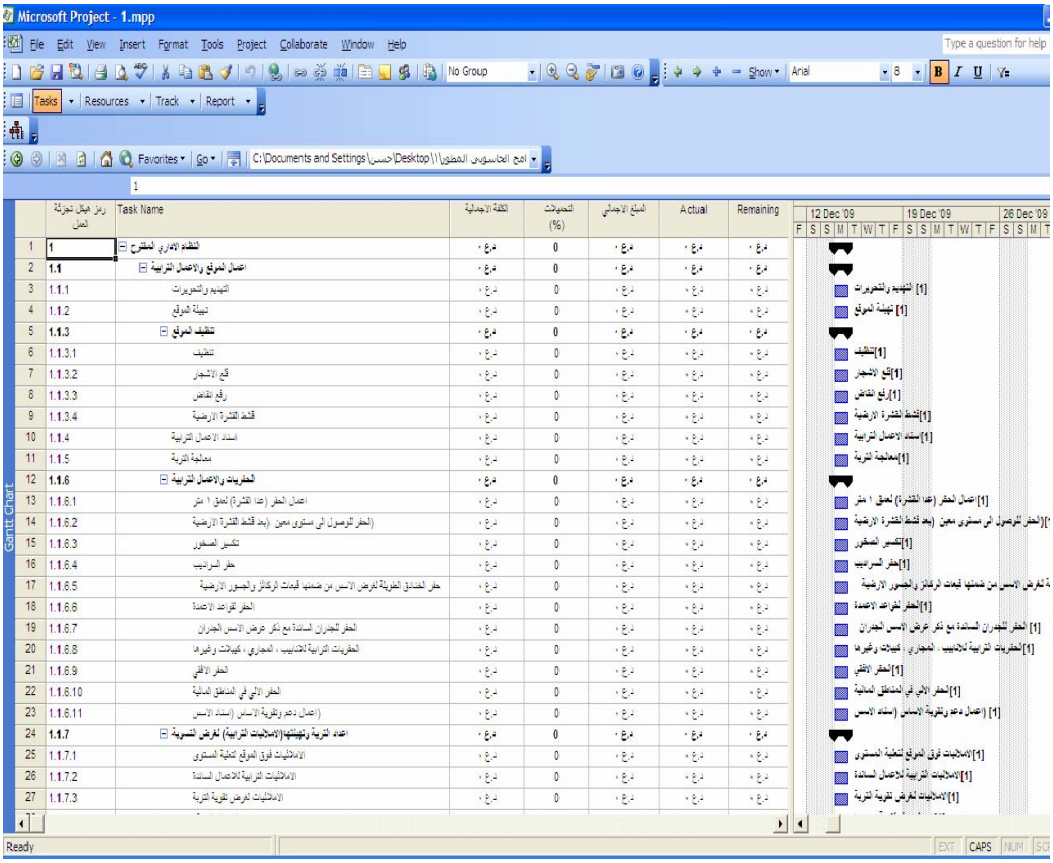

الشكل(8) الانتقال الى هيكلية تجزئة العمل

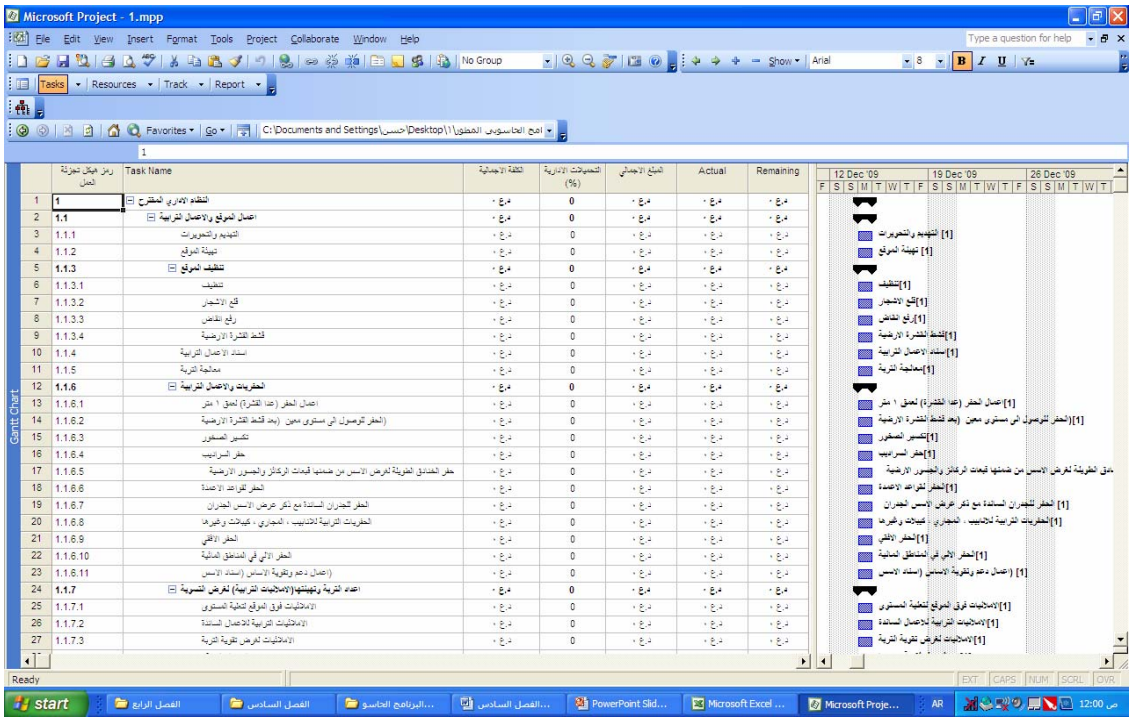

الشكل(9)الكلفة الاجمالية للمشروع

الذهاب الى WBS Chart pro

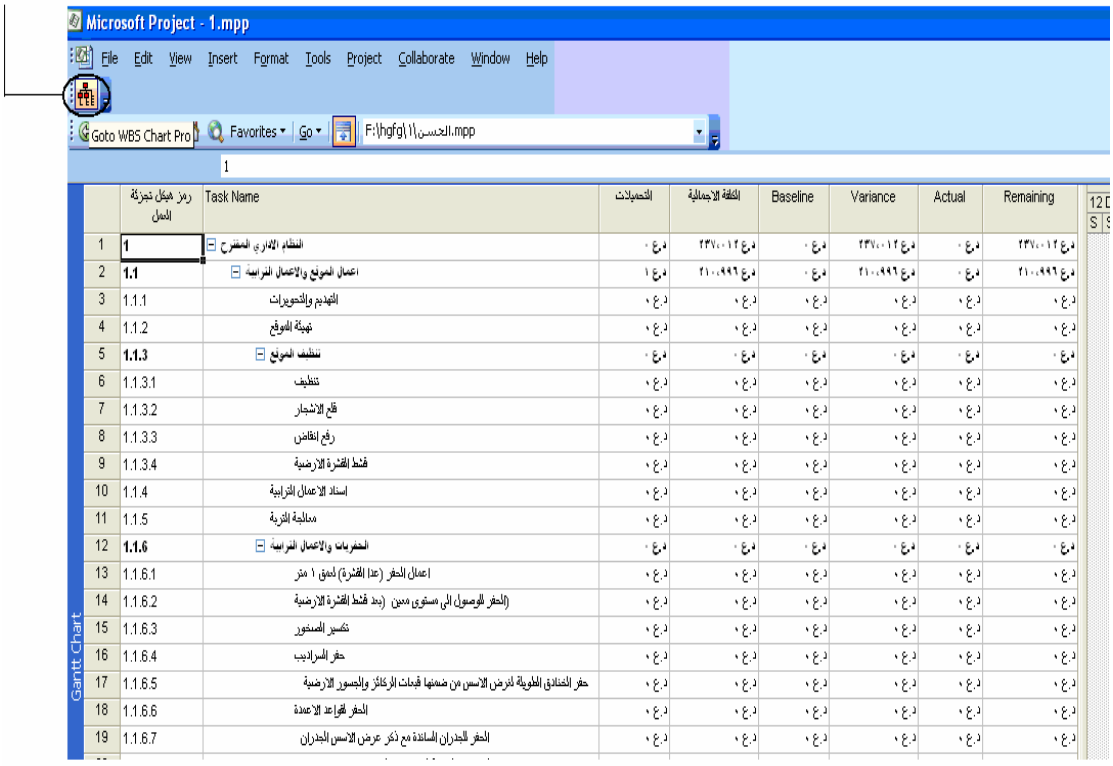

شكل (10)الدخول الى الهيكل الشجري للنظام الادراي المقترح

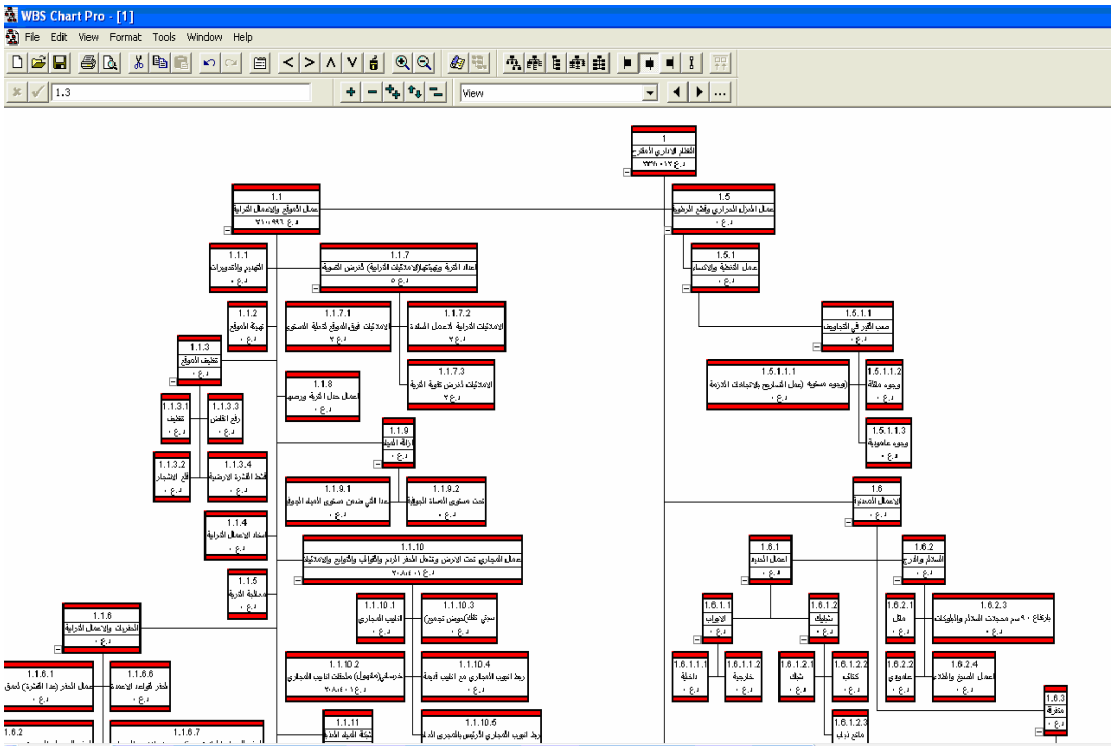

شكل(11) الهيكل الشجري للنظام الادراي المقترح

تقويم النظام الاداري المقترح

يتم ذلك عن طريقين:

1. تطبيق النظام الاداري المقترح على مشاريع الانشاء (مشروع تشييد شقق سكنية للأطباء التدريسيين في الجادرية ومشروع هدم وإعادة بناء مدرسة ثانوية تتكون من ثمانية عشر صف (آيلة للسقوط).
2. تقويم النظام الإداري المقترح عن طريق الاستبيان التقويمي المفتوح.

7. الاستنتاجات والتوصيات

توصل الباحث الى الاستنتاجات التالية:

1. تتوفر في معظم مؤسسات القطاع العام قسم خاص للتخمين والتسعير كما ان لديها فرق متخصصة في اعمال التخمين والتسعير و ادارة الكلفة.
2. تبدأ عملية التخمين في وقت مبكر من المشروع في اغلب المؤسسات وتكون هذه العملية مستندة في اغلب الاحيان وفقا الى معلومات تاريخية سابقة.
3. تخمينات المهندس المستندة على المخططات والمواصفات اكثر انواع التخمين المستخدمة في مؤسسات القطاع العام والخاص ويدل ذلك على الاهتمام بمرحلة ما قبل تقديم العطاء .

4. يتحدد اختيار نوع العقد بشكل رئيس على الرغبة في الحصول على اسعار منافسة و طبيعة العمل المراد انجازة و مدى اكتمال التصاميم ودرجة تعقيدها ،اما درجة العلاقة بين صاحب العمل والمقاول ليست ذات تأثير كبير على اختيار نوع العقد كما اوضحته عملية المسح الميداني.

يوصي الباحث بما ياتي:

1. تدريب الملاكات العاملة في مجال التخمين والتسعير مما ينمي فيهم الثقافة العامة والخاصة في النظم العالمية المختلفة المعتمدة لإعداد جداول الكميات و تسعير عقود التشييد بمختلف انواعها وعدم الاقتصار على بعض الانواع السائده.
2. أهمية التوثيق للمشاريع المنفذة وخاصة فيما يخص تحليل الكلفة والاستفادة من ذلك في عملية التسعير في المشاريع المستقبلية.
3. الاعتماد بشكل رئيس على البرامج الحاسوبية والاستخدام الامثل لها والابتعاد عن التسعير اليدوي الذي يسبب في اغلب الاحيان اخطاء تؤدي الى خوض مناقصات تسبب مخاطرة كبيرة.
4. توفير وقت كافي وملائم لاجراء التخمينات مع توفير جداول إنشاء وتصاميم واضحة لاعطاء نتائج تخمينية دقيقة يمكن الاعتماد عليها في توفير العطاء المناسب للمناقصة.
5. تطوير هيكلية تجزئة العمل المعتمدة في البحث والعمل على توفير هيكلية تجزئة عمل معتمدة في العراق تتناغم مع الدليل القياسي الموحد ولاتخرج على النظم العالمية مثل (Master Format) و(Uniformat)

المصادر

CESMM3, 1991 (*Civil Engineering Standard Method of Measurement*), 3rd Edition Copyright © by The Institution of Civil Engineering and The Federation of Civil Engineering Contractors, London.

Dell'Isola. Michael. D., PE, CVS 2002 (*Architect's Essentials of Cost Management*) Copyright © by John Wiley & Sons, Inc., New York.

Hendrickson. C. & Au. Tung, 2003 (*Project Management For Construction*) First Edition , Prentice- Hall , Inc , Abivision of Simon & Schuster Englewood Cliffs , New Jersey , USA

Lessard. Charles & Joseph, 2007 (*Project Management for Engineering Design*), Copyright © by Morgan & Claypool

Master Format, 2004 (E*dition – Numbers & Titles All Contents*) Copyright, The Construction Specifications Institute and Construction Specifications Canada.

PMBOK, 2004 (*A Guide to the Project Management Body of Knowledge*) , 3rd Edition © Project Management Institute, Inc.

PMI , 1994 (*Principles of Measurement For Works of Construction*), 1st Edition Copyright © by RICS.

SMM7 , 1992 (*Standard Method of Measurement Building Work*), Amendment -3- of Seventh Edition.

Venkataraman. Ray R. & Pinto. K. Jeffrey, 2008 (*Cost and Value Management in Projects*) Copyright John Wiley & Sons, Inc.

Wysocki Robert K., 2007 (*Effective Project Management: Traditional, Adaptive, Extreme*), 4th Edition Copyright © by Robert K. Wysocki.

وزارة التخطيط والتعاون الانمائي ،1984 (الدليل القياسي الموحد للمـسح الكمـي لإعمـال المباني والهندسة المدنية) ، الطبعة الأولى .

اليوسفي ، عبد العزيز سليمان ،2000 ،(إدارة القيمة المفهوم والاسـلوب) ،الطبعـة الثالثـة الجمعية الدولية لمهندسي القيمة الولايات المتحدة الأمريكية.

Production of Biodiesel Fuel from Used vegetable Oil

Hussain K. Hussain, Haider Abdul Kareem Al Jendeel, Tariq M. Naife
College of Eng./Chem.Eng.Dept.

Abstract

Used vegetable oil was introduced to transesterfication reaction to produce Biodiesel fuel suitable for diesel engines. Method of production was consisted of filtration, transesterfication, separation and washing. Transesterfication was studied extensively with different operating conditions, temperature range (35-80°C), catalyst concentration (0.5-2 wt. % based on oil), mixing time (30-120 min.) with constant oil/methanol weight ratio 5:1 and mixing speed 1300 rpm. The concentration of Fatty acid methyl esters (Biodiesel) was determined for the transesterficated oil samples, besides of some important physical properties such as specific gravity, viscosity, pour point and flash point. The behavior of methyl esters production and the physical properties of Biodiesel were studied with the different operating conditions. The results show that increasing methyl esters concentration with increasing temperature and catalyst concentration and the transesterfication is a second order reaction The research aiming to recycle spent cooking oils to prevent pollution of soil and water, and converting them to Biodiesel fuel with low emissions.

انتاج وقود الديزل الحيوي من الزيوت النباتية المستعملة

الخلاصة

تم ادخال الزيت النباتي المستعمل لتفاعل الاسترة التبادلية لانتاج وقود حيوي مناسب لمكائن الديزل. ان طريقة الانتاج تضمنت الترشيح، الاسترة التبادلية، الفصل والغسل. درست الاسترة التبادلية على نطاق واسع بمختلف الظروف التشغيلية، مدى درجة حرارة (35-80م) ، تركيز العامل المساعد (0.5-2 % نسبة وزنية) ، زمن خلط (30-120 دقيقة) بنسبة وزنية ثابتة زيت الى الميثانول 5:1 وسرعة خلط 1300 دورة بالدقيقة. حدد تركيز الديزل الحيوي لنماذج زيت الاسترة التبادلية ، اضافة الى بعض اهم الخواص الفيزياوية مثل الكثافة النوعية، اللزوجة، نقطة الانسكاب و نقطة الوميض. لقد تم دراسة سلوك انتاج الاسترات المثيلية والخواص الفيزياوية لوقود اليزل الحيوي بمختلف الظروف التشغيلية. اظهرت النتائج زيادة تركيز الاسترات المثيلية بزيادة درجة الحرارة وتركيز العامل المساعد وان حركية التفاعل الاسترى من الرتبة الثانية. البحث يهدف الى تدوير زيوت الطبخ المستهلكة لمنع تلوث التربة والماء، وتحويلها الى وقود الديزل الحيوي ذو الانبعاثات المنخفضة.

Key Word: Biodiesel Fuel, Transesterfication, used vegetable oils

Introduction

Biodiesel is a mono alkyl ester of long chain fatty acids biodegradable, nontoxic fuel oil that is essentially free from sulfur and aromatics derived from renewable lipid such as vegetable oils and animal fats. It can also be produced from recycled vegetable oil or animal fat, which is generally referred to as waste vegetable oil. Used cooking oils and animal fats and the general set of products can be an excellent feedstock for biodiesel production depending on their condition and quality attributes (Guo,Y.,2002, Mark Hall,2009).Used cooking oils or animal fats are may be collected after cooking in the home or restaurants as well as from the commercial food industry. Frequently, this oil is placed in the solid waste stream and is deposited in landfills. Unfortunately, some of the oil is poured into sinks and finds its way into the sanitary sewer system and eventually becomes a burden on the wastewater treatment system (Mark Hall, 2009). Waste cooking oil is mainly composed of triglycerides, and contains some free fatty acids (Shigashida M., 2009). Most common method to produce biodiesel is by transesterification which means the reactions of catalyzed chemical involving vegetable oil and an alcohol to yield fatty acid alkyl esters and glycerol. Figure 1 shows a schematic representation of the transesterification of triglycerides with methanol to produce fatty acid methyl esters (Biodiesel).

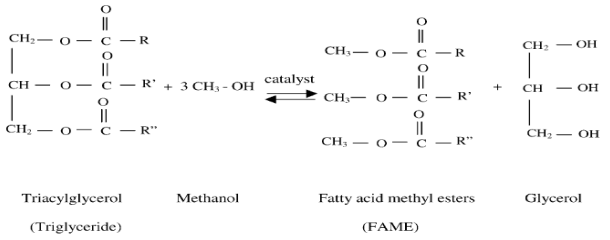

Fig.1.Transesterfication Sketch

Triacylglycerol is the main component of vegetable oil, consists of three long chain fatty acids. As shown in Figure 1 when triacylglycerol reacts with an alcohol the three fatty acids chains are released from the glycerol skeleton and combine with the alcohol to yield fatty acid methyl ester (Y.Zhang , 2003). The stoichiometric reaction requires 1 mol of a triglyceride and 3 mol of the alcohol. However, an excess of the alcohol is used to increase the yields of the alkyl esters and to allow its phase separation from the glycerol formed. Several aspects, including the type of catalyst (alkaline or acid), alcohol/vegetable oil molar ratio, temperature, purity of the reactants (mainly water content) and free fatty acid content have an influence on the transesterification (UlfSchuchardt,1998). Biodiesel is renewable with energy efficient and also displaces petroleum derived diesel fuel, it can be used in most diesel equipment and no or only minor modifications and reduce greenhouse gases emissions and tailpipe emissions, including air toxics and smogs(Pongsiri Jaruyanon,2007). The lifecycle production and use of biodiesel produces approximately 80% less carbon dioxide emissions, and almost 100% less sulfur dioxide. Combustion of biodiesel alone provides over a 90% reduction in total unburned hydrocarbons, and a 75-90% reduction in aromatic hydrocarbons. Biodiesel can be used alone or mixed in any ratio with petroleum diesel fuel. The most common blend is a mix of 20% biodiesel with 80% petroleum diesel (Douglas G., 2002).

This paper focused on production of Biodiesel fuel from used cooking vegetable oil to establish a concept for recycling spent vegetable oils by using small pilot plants for production as in Europe and southeast Asia where the production cost of one gallon Biodiesel Fuel from used oil is 1.09$. It is a fuel from a cheap source, has 90% of petroleum diesel fuel efficiency in addition to its features as fuel friendly to environments by preventing soil and water from direct pollution and gives low emission of combustion gases. The effect of catalyst concentration, temperature and mixing time were studied, and the purity of Biodiesel with its physical properties was determined at various operating conditions.

Experimental Work

Materials

1. Used vegetable oil collected from the kitchen frying oil with boiling point 200°C, free fatty acids less than 5% and free acid methyl esters less than 1%.

2. Methanol analytical reagent A.R. assay (GC) 99.8% supplied by LAB-SCAN analytical sciences

3. Sodium hydroxide 98% supplied by RIEDEL-DEHAENASEELZE-HANNOVER.

Biodiesel Production

In general, Laboratory transesterification was carried out in a conical flask equipped with a magnetic stirrer. Either low or high base concentration dissolved in methanol and added to vigorously stirred recycled vegetable oil at 35 to 45°C with stirring for 60 min. (Fröhlich A., 2005). In this work Biodiesel was produced at various operating conditions, temperature range 35-80°C, ,

catalyst concentration range 0.5-2 wt. % and mixing time range 30-120 minute with constant oil/methanol weight ratio 5/1 and fixed mixing speed 1300 rpm. The operating conditions at which obtained optimum production is 65°C, 1wt. % NaOH and 1 h mixing time. The procedure of production was divided to three stages:

1. Pre-treatment

Used vegetable oil was exposed to thermal treatment 120 °C for 2 h and filtered under vacuum filtration to remove the impurities and contaminants, medium speed filter paper was used in a Buchner funnel which equipped to vacuum filtration system consist of 1 liter vacuum flask, trap and vacuum pump.

2. Transesterification

The Transesterification reaction was carried out in a 250 ml three neck flask, the two side necks equipped to a high efficiency condenser and a separating funnel, while a thermocouple was attached to the middle neck. A digital magnetic stirrer with hot plate (STUART CD 163) was used, able to read and control temperature automatically. In addition to a chiller (GALLENKAMR REGD) supplied the condenser with cold water. A 150 g of used vegetable oil was poured in the flask which set in a constant reaction temperature (35-80°C) with intensive stirring 1300 rpm (Jon Van Gerpen, 2005). Sodium methoxide solution was prepared by dissolving sodium hydroxide in methanol according to fixed oil/methanol weight ratio 5:1 and sodium hydroxide (0.5-2 wt. % based on oil), solution was transferred to separating funnel and poured into oil gradually and mixed for 30-120 minute. Mixture was quenched to stop reaction at once.

3. Separation and washing

The transesterification mixture was placed in a separating funnel for at least 6 h to ensure complete separation of Biodiesel (yellow) from glycerol (red to orange). The upper layer (Biodiesel) was drained and then washed by mixing with one volume of distilled water for about 15 minute to remove remained unreacted catalyst. The foggy solution poured into a separating funnel and left for 3 h. Biodiesel was placed in a furnace at 120°C for 1 h to ensure removing the remaining methanol and water (Fröhlich A., 2005).

Feedstock and Products Tests

Gas Chromatography analysis

Fatty acid methyl esters (Biodiesel) composition of samples was determined by gas chromatography (UNITED TECHNOLOGIES-PACKARD) using a column SE-30, and flame ionisation detector. The initial column temperature, 200 °C, was held for 6 min, and then increased to 325 °C at 1°C/min. Injector temperature was 300 °C and detector temperature was 350 °C. The flow rates of gases helium (carrier gas), hydrogen and air were 30, 30 and 250 ml/min respectively (Nezihe Azcan, 2008). Figure 2 shows gas chromatography analysis of Biodiesel produced at 65°C, 1wt. % NaOH and 1h. mixing time. It is shows that the concentration of fatty acid methyl esters is 94%.

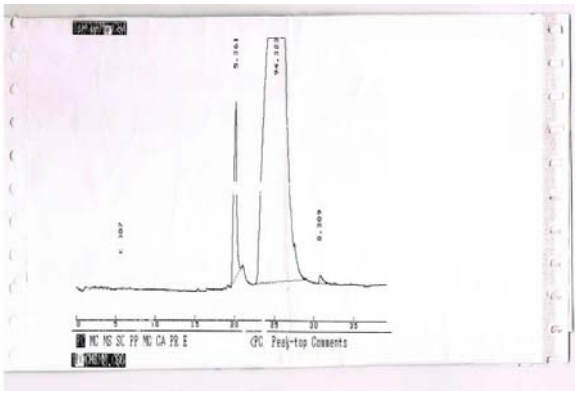

Fig.2. Gas Chromatography Analysis of Biodiesel

Density and Specific Gravity

The density and specific gravity of feedstock and products was determined by (ASTM D1217 - 93(2007).

Viscosity

The viscosity of feedstock and products was determined by (ASTM D445 - 09).

Flash Point

The flash point of feedstock and products was determined by (ASTM D93 - 08).

Pour Point

The pour point of feedstock and products was determined by (ASTM D97 - 09).

Results & Discussion

Effect of Catalyst Concentration

The present result shows the effect of catalyst concentration (NaOH wt. %) on Biodiesel volume percentage in the transesterficated oil with mixing time 30 minute at different temperatures.

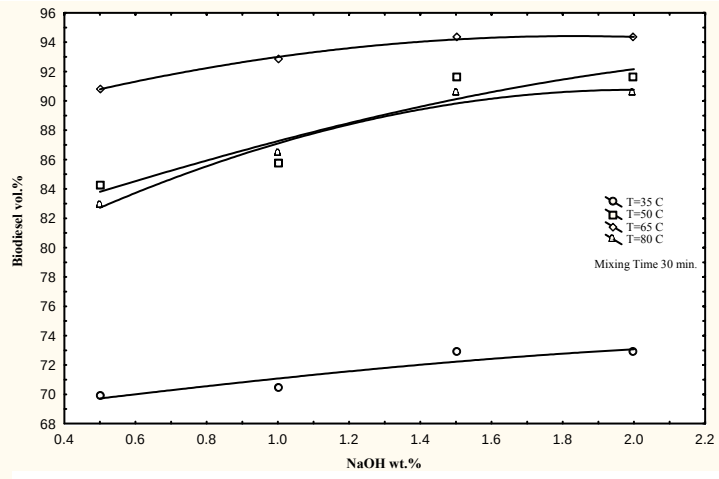

Fig.3. Effect of NaOH Concentration on Production of Biodiesel at Different Temperatures

Figure 3 results show that Biodiesel percentage (methyl esters) increased with increasing sodium hydroxide concentration at different temperatures. Catalyst concentration has an effective role in Biodiesel production, methyl esters increased with increasing sodium hydroxide concentration at different temperatures and that restricted according to the saturation level of NaOH in methanol if it above saturation or not. The concentration of methyl esters becomes constant beyond 1.5 wt. % NaOH and there is no significant increase, that matter qualifying this percentage to be the optimum, but some of NaOH was remained insoluble in the transesterfication mixture at this percentage and that never note at lesser concentrations, that because NaOH became above saturation in sodium methoxide solution so can consider the optimum is 1wt. %. In general, methyl esters increased with increasing temperature up to 65°C (Yong W,, 2007) at which maximum Biodiesel concentration was obtained 94 vol. %. At temperature 80°C the concentration of methyl esters was decreased which indicated that the optimum transesterfication temperature is reflux temperature. Solubility of sodium hydroxide in methanol increased with increasing temperature which creates an efficient homogeneous sodium methoxide solution responsible on converting the triglycerides to fatty acid methyl esters, which mean that at high temperature an efficient sodium methoxide produced, so high Biodiesel was yield.

Effect of Mixing Time

Figure 4 show the effect of mixing time on Biodiesel volume percentage in the transesterficated oil with sodium hydroxide concentration 1wt. % at different temperatures.

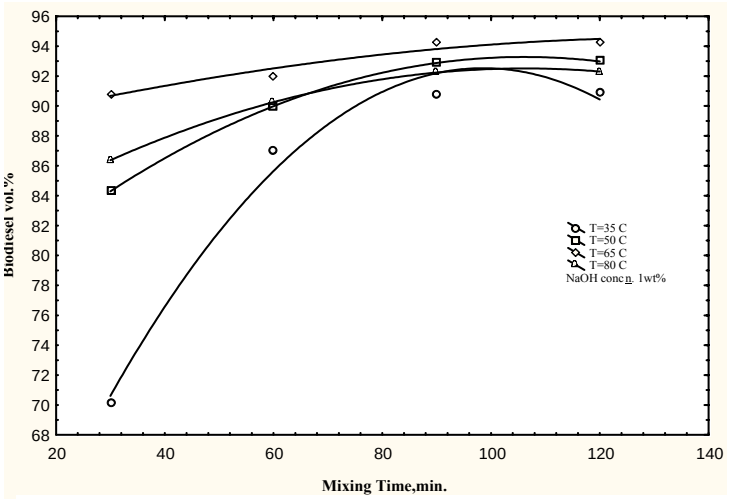

Fig.4.Effect of Mixing Time on Production of Biodiesel at Different Temperatures

Results show that methyl esters percentage (Biodiesel) increased with increasing mixing time at different temperatures (M.G.Devanesan, 2007). Biodiesel concentration increased clearly from 30 to 90 minute, and there is no significant increasing in Biodiesel concentration for longer extent of mixing time, this behavior was clear at minute 120. Mixing was necessary for commencement transesterfication reaction, where sodium methoxide begin attack the triglycerides of used oil, and residence time is one of the most important parameters affect reaction, which can be expressed by residence time and conversion, so the transesterfication is time dependence to get progressing in conversion until reaching equilibrium. From getting before, could be explain the reasons for increasing of Biodiesel concentration with increasing mixing time and the steadily concentration of methyl esters after 90 minute of mixing. Also, the concentration of methyl esters increased with increasing temperature at all times of mixing except at temperature 80°C where the Biodiesel concentration closed to concentration at temperature 50°C in mixing time 60 minute and then deviated to lesser concentration.

Effect of Catalyst concentration and mixing time on Biodiesel Physical Properties

1. Flash and pour Points

The flash and pour points are from the most important characteristics of engine fuel which restrict the safety and performance features of

fuel. Results show that biodiesel fuel had a flash point range between 180- 192°C, flash point decreased with increasing catalyst concentration, mixing time and triesterfication temperature but beyond 65°C was increased near to those at 50 °C caused by decreasing of methyl esters concentration at temperatures beyond 65°C as shown in figures 5 and 6 . While the pour point had a very narrow range begins from -9 to -12 °C and can say that no clear difference happened to pour point at different catalyst concentrations and transesterfication temperature. In general, pour point was recorded decreasing with increasing catalyst concentration and transesterfication temperature. From before, the produced Biodiesel fuel has high safety in storage and in engine combustion and can be workable even at low environment temperature (severe conditions).

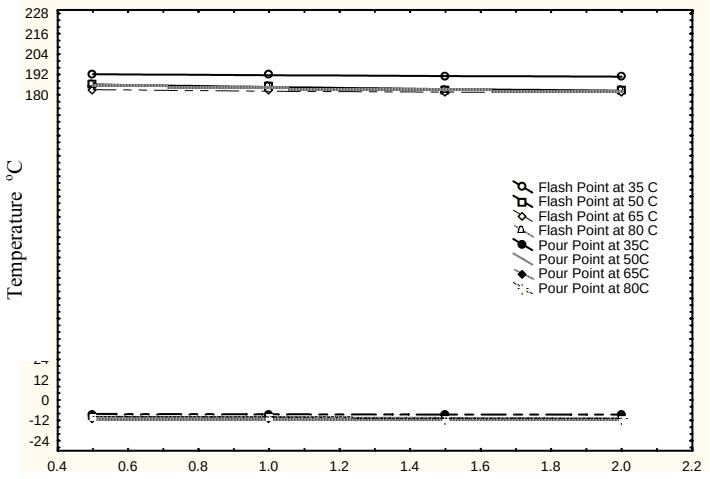

Fig.5. Effect of NaOH Concentration on Flash and pour points of Biodiesel

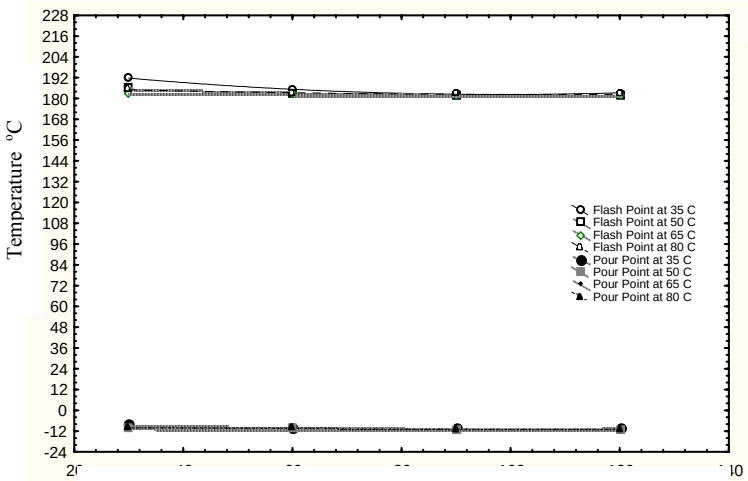

Fig.6.Effect of Mixing Time on Flash and pour points of Biodiesel

2. Viscosity and Specific Gravity

Figures 7 to 10 are showing the effect of catalyst concentration and mixing time on viscosity and specific gravity of Biodiesel fuel at different temperatures. Results show that viscosity and specific gravity decreased with increasing catalyst concentration, mixing time and transesterfication temperature. Increasing concentration of methyl esters with increasing catalyst concentration, mixing time and transesterfication temperature causes the decreasing in the viscosity and specific gravity of Biodiesel fuel, where long chains of triglycerides with high viscosity and high specific gravity converted to mono fatty acid methyl esters have viscosity and specific gravity lesser, which is responsible on this behavior. A viscosity range of Biodiesel fuel was distinguished from different operating conditions (1 - 2.6 cSt) at 100°C, but a very narrow specific gravity range was recognized (0.86 - 0.89).

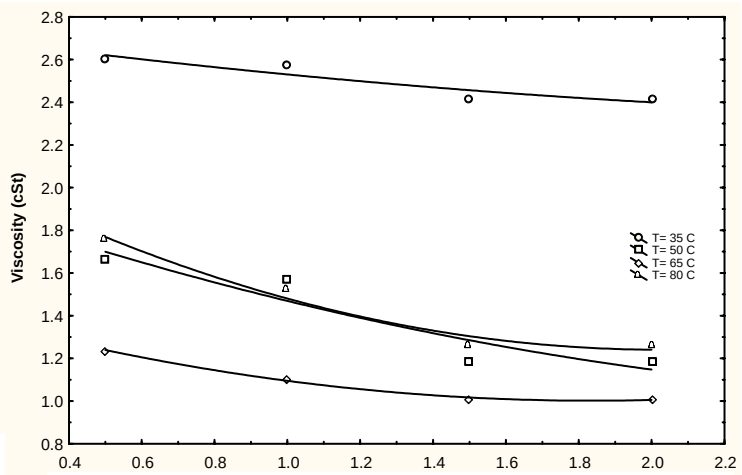

Fig.7. Effect of NaOH Concentration on Viscosity of Biodiesel at Different temperatures

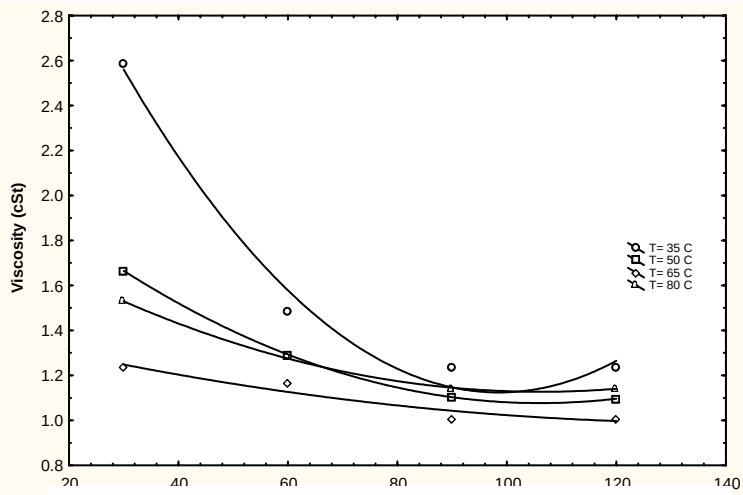

Fig.8.Effect of Mixing Time on Viscosity of Biodiesel at Different Temperatures

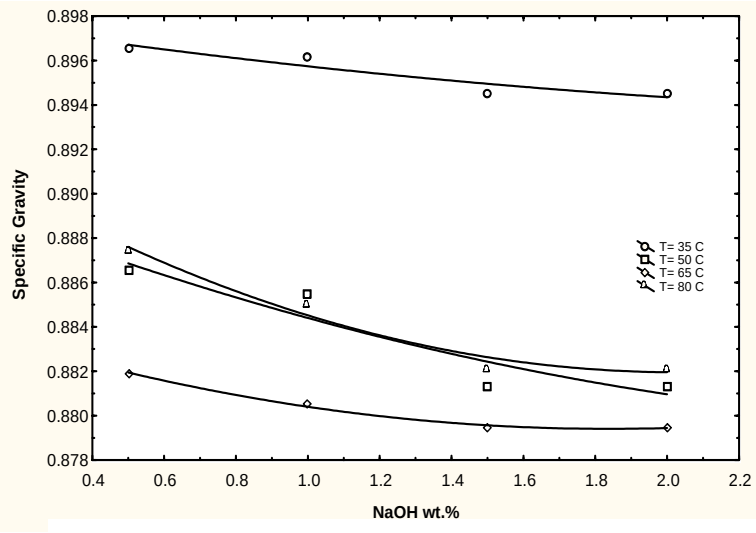

Fig.9. Effect of NaOH Concentration on Specific Gravity of Biodiesel at Different Temperatures

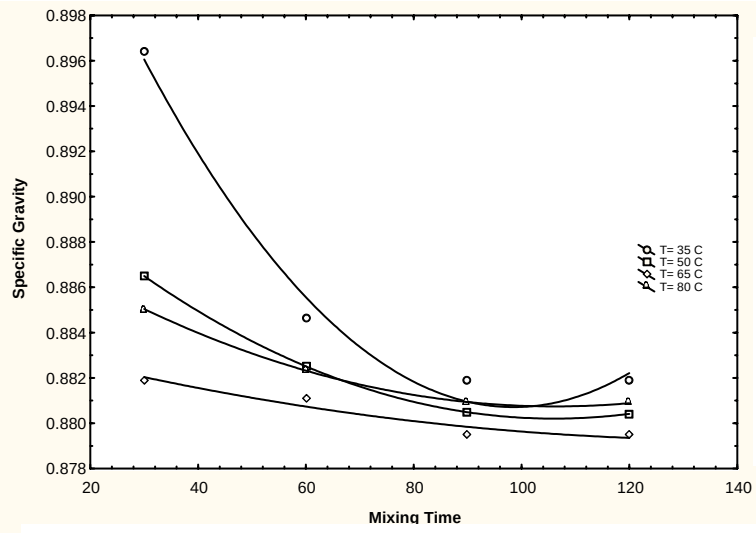

Fig.10. Effect of Mixing Time on Specific Gravity of Biodiesel at Different Temperatures

Kinetics of Transesterfiction Reaction

Transesterfication reaction of triglyceride (backbone of used vegetable oil) with methanol and in presence of sodium hydroxide to produce fatty acid methyl esters (Biodiesel) was studied. Transesterfication is a reversible reaction in which one molecule of triglyceride reacts with three molecules of methanol, the three fatty acids chains are released from the triglyceride skeleton and combine with the alcohol to yield fatty acid methyl esters and glycerol which is call "net reaction". In fact, triglyceride react with the first molecule of methanol to produce diglyceride and ester of first chain of fatty acid then the diglyceride molecule react with the second molecules of methanol to produce monoglyceride and ester of second chain of fatty acid, finally the monoglyceride molecule react with the third molecule of methanol to produce ester of third chain of fatty acid with glycerol. Transesterfication reaction was carried out in a constant volume batch reactor without flow and the integral method was used for analysis of data. Some assumptions decided for simplifying determination order of reaction such as neglecting the effect of decomposition reaction. Thus, the irreversible reaction is simply the special case of the reversible reaction in which C_A, = 0, or X_{Ae} = 1, or Kc = α (Octave Levenspiel, 1999). Results show that transesrefication is a second order reaction. A plot of ln[(1.875 - X) /(1.865(1-X))] vs. *t,* as shown in Fig.11, gives a straight line through the origin for this form of rate of equation. The experimental data seems to be better fitted by a curve than by a straight line as shown in Fig.12, which indicated that this reaction is not first order reaction.

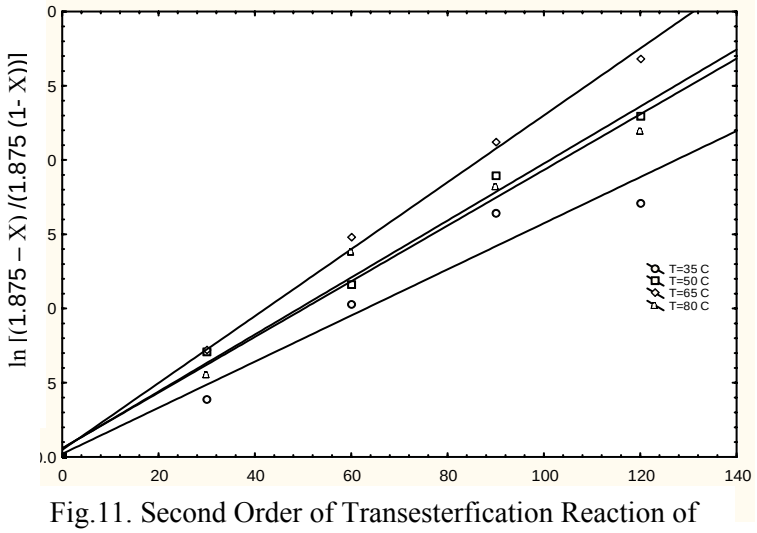

Fig.11. Second Order of Transesterfication Reaction of Biodiesel Production at Different Temperatures

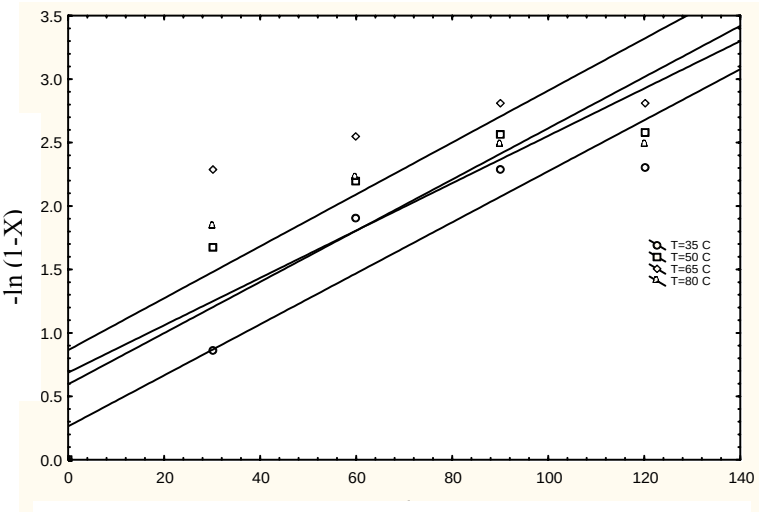

Fig.12. First Order of Transesterfication Reaction of Biodiesel Production at Different Temperatures

Conclusions

Biodiesel fuel produced from waste vegetable oil was affected by catalyst concentration, temperature of reaction and mixing time. Result show that biodiesel was increased with increasing catalyst concentration and the best concentration was 1 wt % where higher catalyst concentration led to above saturation state. Also, the biodiesel increased with increasing temperature of reaction up to 65°C (boiling point of methanol) at higher temperature biodiesel was decreased. Biodiesel was increased sharply with increasing mixing time from 30-60 minute and the increasing was taking steadily behavior as reaching 90 minute. The physical properties of the biodiesel fuel were compatible with the standard specifications as shown in Table 1. The kinetics of transesterfication reaction was examined and results indicated that this reaction is a second order.

Table 1 Physical properties of standard and obtained Biodiesel Fuel

Test	Standard	Obtained
Specific gravity@15.6 ^{o}C	0.86-0.90	0.88-.89
Kinematic Viscosity at 40°C,mm^{2}/s	3.5-5	4.5-5
Flash Point,^{o}C	minimum120	184-194
Pour Point,^{o}C	< 3	-9/-12

References

Douglas G. Tiffany,"The growth of alternative Fuels:Minnesota and US Prespectives,2002.

Fröhlich A. and Rice B.," Evaluation of recovered vegetable oil as a biodiesel feedstock", Irish Journal of Agricultural and Food Research **44:** 129–139, 2005.

Guo, Y., Leung, Y.C. and Koo, C.P.," A Clean Biodiesel Fuel Produced from Recycled Oils and Grease Trap Oils", Better Air Quality in Asian and Pacific Rim Cities (BAQ 2002) 16 Dec 2002 – 18 Dec 2002, Hong Kong SAR.

Jon Van Gerpen," Biodiesel processing and production", Fuel Processing Technology,86, 1097– 1107, 2005.

Mark Hall, Sushil Adhikari, Steve Taylor," Producing Biodiesel for Municipal Vehicle Fleets from Recycled Cooking Oil", report by the Auburn University Natural Resources Management & Development Institute and Alabama Cooperative Extension System, 2009..

M.G. Devanesan, T. Viruthagiri, and N. Sugumar," Transesterification of Jatropha oil using immobilized *Pseudomonas fluorescens",* Afr. J. Biotechnol., 6 (21), pp. 2497-2501, 2007

Nezihe Azcan and Aysegul Danisman," Microwave assisted transesterification of rapeseed oil", Fuel 87, 1781–1788, 2008.

Octave Levenspiel," Chemical Reaction Engineering", Third Edition (1999).

Pongsiri Jaruyanon and Wongkot Wongsapai, "Biodiesel Technology and Management from Used Cooking Oil in Thailand Rural Areas", Department of mechanical Engineering, Faculty of Engineering and Industrial Technology, Silpakorn University, Nakorn Prathom, Thailand,2007.

Shigashida M., Biodiesel Manufacturing Plant, Producing fuel from waste cooking oil, thereby contributing to solving problems of waste disposal and protecting the environment, Inquiries CDM Infrastructure & Environmental, Inc., 2009. http://www.cdmie.com

Ulf Schuchardt, Ricardo Sercheli, and Rogério Matheus Vargas, "Transesterification of Vegetable Oils: a Review", J. Braz. Chem. Soc., 9(1), 199-210, 1998.

Y. Zhang a, M.A. Dub_e, D.D. McLean, M. Kates, Biodiesel production from waste cooking oil: 1. Process design and technological assessment Bioresource Technology 89 (2003) 1–16.

Yong W, Shiyi O (2007). "Preparation of biodiesel from waste cooking oil via two- step catalyzed process", Energy conversion Manage, 48:184-188.

.

STATIC PERFORMANCE CHARACTERISTICS OF VORTEX RATE SENSOR

Dr .Ali Abdul AL-Muhsen AL-Asady
Asst .prof. Dept .of Mech .En
Baghdad University

Wisam Gasim Kadhum
Dept.of Mech .Eng.
Baghdad University

ABSTRACT

The vortex rate sensor is a fluidic gyroscope with no moving parts and can be used in very difficult conditions like radiation, high temperature and noise with minimum cost of manufacturing and maintenance. A vortex rate sensor made of wood has been designed and manufactured to study theoretically and experimentally its static performance .A rig has been built to carry out the study, the test carried out with three different air flow rates (100, 150, and 200 l/min).The results show that the relation between the differential pressure taken from the sensor pickoff points and the angular velocity of the sensor was linear.The present work involved theoretical and experimental study of vortex rate sensor static characteristics .Vortex rate sensor has been designed and manufactured with dimensions-:

Radius of vortex chamber= 140 mm, Radius of sink tube r_s= 4.5 mm, the pickoff hole diameter = 2mm, Height of vortex chamber b= 19 mm, Height of pickoff pipe h= 25 mm.

Keywords :Vortex rate sensor, Angular vortex rate sensor, Rate gyro

الخلاصة:

متحسس معدل التدويم هو جايروسكوب مائعي بدون اجزاء متحركة ويمكن استخدامه بظروف صعبة جدا كالاشعاع ودرجات الحرارة العالية والضوضاء وبأقل كلفة تصنيع وصيانة. متحسس معدل التدويم مصنوع من ماده الخشب تم تصميمه وتصنيعه واستخدامه لوضع دراسة نظريه وعمليه للأداء الاستاتيكي للجهاز. كذلك تم بناء منظومة خاصة لإجراء الدراسة، في هذه الدراسة تم تسليط ثلاثة قيَم مختلفة لمعدل تدفق الهواء وهي (100,150 و 200 لتر\دقيقه) ووجد من خلال هذه الدراسة ان العلاقة ما بين فرق الضغط المأخوذ من الجهاز والسرعة الزاوية للجهاز هي علاقة خطيه.يتضمن هذا البحث دراسه نظريه وعمليه للخواص الاستاتيكيه للمتحسس . حيث تم تصميم وتصنيع المتحسس بالابعاد التاليه:

نصف قطر حجرة الدوامه(R)=140 ملم ، نصف قطر مجرى الخروج (r_s)=4,5 ملم،قطر فتحه الpickoff=2ملم، ارتفاع حجرة الدوامه (b)=19ملم، ارتفاع انبوب pickoff (h) =25 ملم.

INTRODUCTION

General introduction

The vortex rate sensor is a pure fluidic device with no moving parts that senses angular velocity about its axis and provides a differential pressure proportional to that velocity it can be used instead of a gyroscope .The three basic parts of the sensor are the coupling element, the vortex chamber, and the signal pickoff .The vortex rate sensor utilizes the tendency of the swirling flow to conserve the angular momentum imparted to it as a means of amplification to sense small rates of rotation . The existing vortex rate sensor consists of two coaxial disks separated by cylindrical coupling ring, which are often a porous material, with outlet sinks and two suitable pickoffs .The gaseous fluid flows through the coupling element of uniform length and porosity and discharges at the sink tube .The radial flow between the two coaxial disks is modified by the viscous shear and by the vertical flow created by the rotation of the unit about an axis parallel to its axis of symmetry .Thus, the confinement of the real flow and the subsequent modification of the velocity distribution in the sink tube cause appreciable reduction in the angular momentum imparted at the coupling . Attention is given to sensitivity, accuracy, and response time and to sensor design and fabrication with emphasis on housing and manifold, null adjust and built-in test and temperature compensation .A number of applications of the vortex rate sensor are considered :aircraft flight controls, ejection seat stabilization, and helicopter gun turret stabilization.

Various analyses have been carried out in the past with varying degrees of success and different specific objectives on vortex rate sensor.

[Organ H.D. 1965] changed the porous with cylindrical outer screen member and inner cylindrical screen member has a slightly smaller diameter than outer screen member . Positioned intermediate inner screen member and outer screen member are a plurality of glass balls having a small diameter approximately (0.15) It is clear that coupling means is porous in nature and allows fluid to pass through with a minimum of restriction.

[Barrete Doyle 1966] made vortex rate sensor with the same geometry but with another kind of pickoff, this kind includes optical means for providing an output signal indicative of the rotation of coupling relative to the structure .Optical means comprises a light source and two reflecting mirrors attached to intermediate light source and reflecting surface .A pair of photocells is attached to contiguous mirrors.

[Camarata F.J. 1969] Invented a twin vortex rate sensor .The invention contemn plates the provision of two counter-moving or rotating vortices, each having its axis or center line coincident with the axis about which movement of the body is to be sensed . The output flow or pressure of each vortex is compared with that of the other, and the differential of such output pressure or flows provides a signal indicative of the rate and direction in which a body containing such vortices is turning on the said axis .Thus, it will be seen that this applicant provides a device generally similar in function to a gyroscope, and it can be said that it is general object of this applicant to provide a device

capable of sensing the rate and angular direction of movement of a body about a reference axis and capable also of producing a signal indicative of rate and direction so that the signal can be used in control of angular movement of the body.

[Hagiwara, etal.1973], studied the static characteristics of vortex rate sensor .A sensor probe is constructed of two stagnation pitot tubes whose setting gap and angle are determined to be 3.6 mm and 67.5 deg . respectively for a sink tube with inner diameter of 8 mm by the preliminary experiments .In case of 100 *l*/min supply, output signal is 8.3 mm water per r.p.m and is linear up to 10 r.p.m for a sensor with the outer diameter of 280mm.Sensor efficiency is deduced theoretically and the results of the analysis are verified to coincide very well with the experimental results.

[Peter Norton 2006] invented a vortex angular rate sensor for measuring yaw rate or roll rate of an automotive vehicle comprises a freely rotating inertial disk and an angular rate sensor responsive to the rotation of the inertial disk relative to housing .In one embodiment the inertial disk presents an alternating magnetic field at its circumference .The rate and direction of rotation of the inertial disk relative to its housing is determined by three magnetic field sensor such as a linear Hall Effect sensor responsive to the field presented by the inertial disk .In another embodiment electronic cameras measure movement of fiducially marks on the inertial disk .Air surrounds the inertial and air viscosity gradually brings rotation to a stop .For yaw rate measurement the disk axis is oriented vertically and the inertial disk is supported in the radial direction by low friction bearing such as ball bearing or magnetic bearings and the axial direction by substantially frictionless bearing such as magnetic bearings .In certain embodiments two magnetic poles operate as both axial and radial bearings .For the purpose of sensing incipient or actual vehicle rollover, the axis of the inertial disk is oriented in the direction of the roll axis of the vehicle .The angle of recent rotation and rate of rotation of the inertial disk relative to the housing indicate the angle through which the vehicle has recently rotated about its roll axis and the roll rate of the vehicle .

GEOMETRY OF THE SENSOR AND MEASURING CIRCUIT

The sensor shown in the fig.1 made of wood type (NDF) for ease of machining.

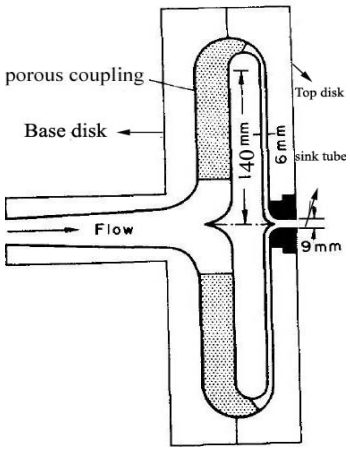

Fig.1 Schematic Drawing of vortex rate sensor

A series of slices and porous media made of sponge was inserted in the inlet region partly the purpose of the porous media and a slices

were partially to ensure uniform flow at the periphery of the pancake.A single hole of 9mm diameter was drilled at the center line of the outer disk; a sink tube was fitted into this hole and tightened on the outer disk .The pickoff tube used at the exit of the sink tube called cylindrical pickoff tube as shown in **fig.2** placed across the sink tube.

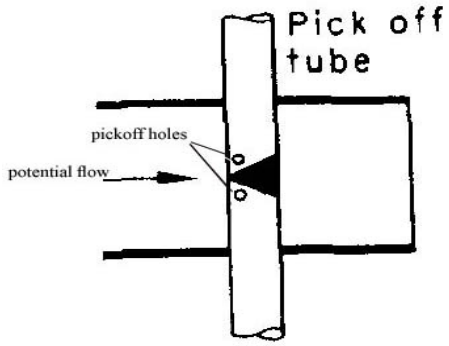

Fig.2 Schematic of Cylindrical Pickoff Element

The pickoff hole was positioned at 45 degree from the direction of flow in order to obtain maximum theoretical differential pressure across them .A straight forward analysis of potential flow about circular cylinder shows that whereas the rate of change of pressure with angular position is maximum at θ=45 degree .**Fig.3** shows the test rig, its consist of compressor to supply air, rotameter to measure the air flow rate and control it ,vortex rate sensor and pick off element, see **fig.4**, rate table for control and apply the angular velocity see **fig.5**, and U tube manometer to measure the output signal of vortex rate sensor

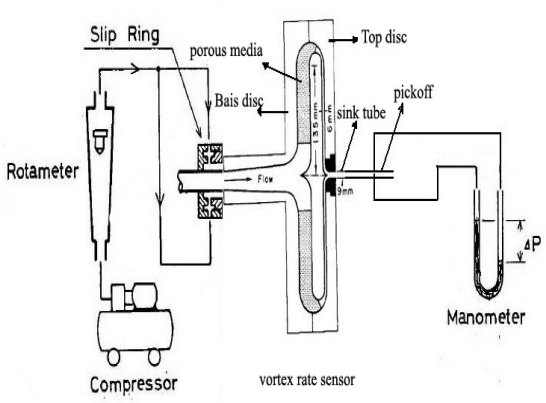

Fig.3 testing rig

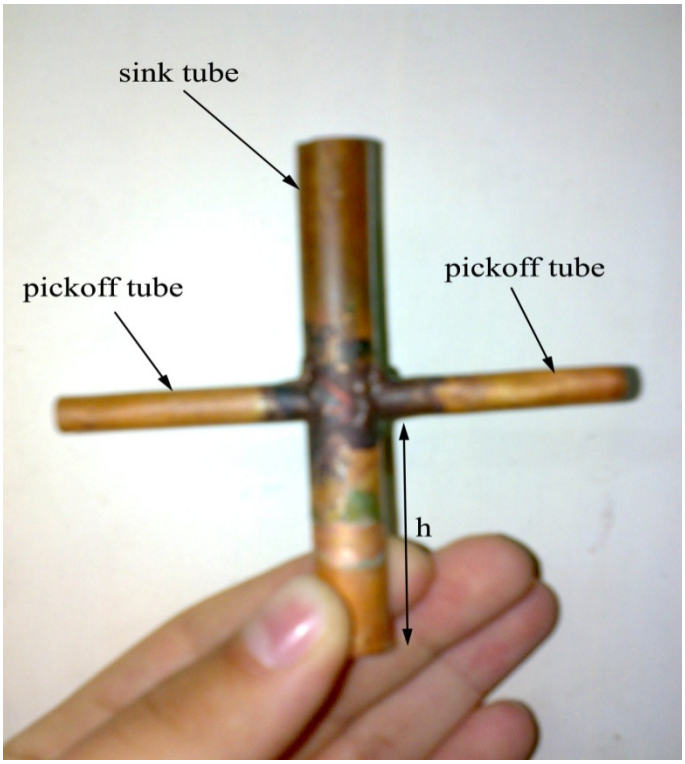

Fig.4 pickoff tube used in the test rig

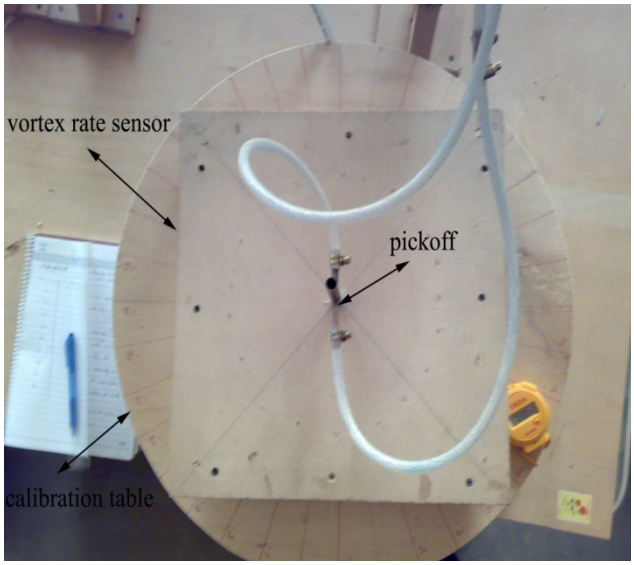

Fig.5 Calibration Table of vortex rate sensor

ANALYSES OF THE SENSOR OUTPUT

The principle work of pickoff element like the principle work of Pitot tube, because both of them determine the pressure at stagnation point(pickoff holes, pitot hole) which it's one of the application of Bernoulli's equation .It follow from Bernoulli's equation that the pressure at stagnation point (total pressure P) is equal to the sum of the static pressure (P = 0) the dynamic pressure ($\frac{\rho U^2 \sin^2\theta}{2}$) of the flow .Apply the following assumption:

1. Neglect the viscosity (invisced) i.e $\left(\upsilon\nabla^2 V\right)$ .Is small, because the boundary layer is small compared with the chamber height.
2. The flow is incompressible (M< 0.3)
3. Neglect the body force (g=0).
4. Steady state.

The pickoff holes are set at angle **θ** against the sink tube axis and those holes are located at symmetrical distance – r_p and $+r_p$ from the center of sink tube respectively .If the vortex rate sensor is stationary and supply flow rate is constant, the detecting pressures of pickoff holes (P1 = P2).

$$P_1 = P_2 = 0.5\rho\beta^2 U^2 \sin^2\theta \qquad (1)$$

Eq. (1) represents the pressure distribution at pickoff hole when the vortex rate sensor is stationary .Where :
(β=1.12 for turbulent distribution flow) **[Pavila, C. 1972]**.
As the vortex rate sensor rotates with angular rate ω_m, the jet from sink tube develops into spiral flow with the spiral angle Δθ .The differential pressure Δp between the pickoff holes (1) and (2) is produced.

$P_1 = 0.5\ \rho\ \beta^2\ U_s^2\ \sin^2\theta_1$ for pickoff hole (2)
$P_2 = 0.5\ \rho\ \beta^2\ U_s^2\ \sin^2\theta_2$ for pickoff hole (3)
$\Delta p = P_1 - P_2$ sub Eqs(2) and (3) that leads to:

$$\Delta p = 0.5\rho\beta^2 U_s^2 \Delta\theta \qquad (4)$$

Where $\Delta\theta \approx (\sin^2\theta_1 - \sin^2\theta_2)$
Noting that the swirling angle, resulting from the tangential velocity of fluid relative to the tangential velocity of pickoff hole; is given by **[Camarat, F. J 1996].**

$$\tan\Delta\theta = \frac{(U_{\theta rp} - r_p w)}{\beta U_s} \qquad (5)$$

$$\Delta\theta = \frac{U_{\theta rp}}{\beta U_s} \qquad (6)$$

Where $U_{\theta rp}$ is the maximum tangential velocity at radius $\mathbf{r_p}$ in sink tube, and that equal to:

$$U_{\theta rp} = \frac{E_2 \omega R^2}{r_p} \qquad (7)$$

r_p is The radial distance to the location of the pickoff hole which is also the radius where the tangential velocity is maximum.

$E_2=\Gamma_p$,Γ_0= 0.716**[pavilan. C.1972].**

Sub eq (7) in (6) and then in eq (8) we obtain:

$$\Delta p = 0.5\rho\omega\beta E_2 U_s\left(\frac{R^2}{r_p}\right) \qquad (8)$$

The maximum tangential velocity occurs at a radial distance ranging from $0.3\,r_s$ to $0.4\,r_s$

Multiplying eq (8) by $(\frac{Q}{Q})$

r_s: the radius of sink tube .

Thus, writing :r_p=J .r_s

Where; J=const=0.376 **[peter Norton, 2006].**

Q=π. r^2_s. U_s then eq (8) is:

$$\Delta p = 0.34\left(\frac{\rho\omega Q}{r_s}\right)\left(\frac{R}{r_s}\right)^2 \qquad (9)$$

It is evident from eq (9) that the differential pressure signal increases most rapidly with degreasing sink tube radius, secondly with increasing sensor radius, and thirdly with increasing rate of rotation, flow rate and fluid density.

The standard deviation for the eq. (9) between the theoretical and experimental results for (10) points curve at 100 l/min air flow rate is calculated as below;

$$\text{Standard deviation} = \frac{\sqrt{\frac{\sum(\delta(\Delta p))^2}{N-1}}}{\sqrt{N}} \qquad (10)$$

Where; N is the number of the corresponding points.

The standard deviation = 2.01108 mm water.

Obviously, there is a limit to the magnitude of each one of these parameters .The size of the pickoff element that in turn is limited by manufacturing difficulties, the flow rate is limited by the capacity of the available power source.

TEST PROCEDURE:

To collect and explain the relation between (Δp) and (ω) (static characteristics of vortex rate sensor) should follow the procedure bellow:

1) Turn on the compressor and start to press the air inside the container of compressor.
2) Open the valve of the rotameter and fix the float off on the flowmeter (50 L/min) firstly.
3) Before applying the angular velocity to the vortex rate sensor see that the signal in the differential manometer is zero.
4) Apply angular velocity started from (10, 20, 30, 40, 50, 60, 70, 80, 90) deg/sec respectively with no change in the value of the flow rate.
5) In each angular velocity has been applied on the vortex sensor, there is a signal produce as differential pressure measured in (mm water) on the differential manometer.
6) After that repeat the procedure again but with another flow rate (100, 150, 200) L/min respectively.

RESULTS AND DISCUSSIONS:

The experiment that carried out for vortex rate sensor with this dimensions (Radius of vortex chamber (R)=140 mm , Radius of sink tub r_s= 4.5 mm, pickoff hole diameter =2mm , Height of vortex chamber (b)=

19mm, Height of pickoff pipe (h) =25 mm). Fig.6 shows the static characteristics theoretically for various flow rate and angular velocities .Note from Fig.6 that the linearity of vortex rate sensor keep in linear for ω=90 degree/sec and the Δp increases when increase the angular rate ω and when increase the flow rate of the input. Fig.7 shows the results of the vortex rate sensor experimentally for various flow rates and angular velocities .The range of linearity of signal obtained from cylindrical pickoff element was limited to approximately 70 deg/sec as shown in Fig.7 .This was in part due to the fact that the total velocity vector in the vicinity of the pickoff element was not in the plane normal to the cylinder, in the part due to the constricting effect of pickoff element which in turn altered the velocity profile and accelerated the flow, and in part due to the separation and vortex shedding behind the cylindrical coordinates .Fig.8 shows comparison between experimental and theoretical static characters and shows the relation between the differential pressure and angular velocity .It is, however; apparent from a cursory examination of the data presented here, the cylindrical pickoff yields a differential pressure output very good. So the output remains linear up to an angular velocity of approximately 70 deg/sec .This is partly due to the fact that the swirling flow has not been distributed by cylindrical pickoff and that the signal transition line has resulted in relatively more stream lined body there by significantly eliminating the flow separation , vortex shedding and noise.

There are many reasons that effect on the relation between the differential pressure and angular velocity:

1. Experimental errors (like stop watch, calibration table.)
2. The effect of viscosity on the swirl and flow in the sink tube.
3. The effect of the porous media and slices and several other secondary effects lead to reduce
   The efficiency.

The linearity of the vortex rate sensor to the differential pressure or between Δp and ω is also calculated from measuring the maximum input deviation and the maximum full scale input:

Non-linearity = ((max. input dev.)/(max. full scale input))*100 (11)

The non-linearity of the sensor is 5%, and form **fig.7** the curves make a line with a regression factor **0.9955** so we can say that the vortex rate sensor is linear to differential pressure Δp.

Resolution is the smallest measurement a sensor can reliably indicate .The resolution of the vortex rate sensor is 9 mm water differential pressure.

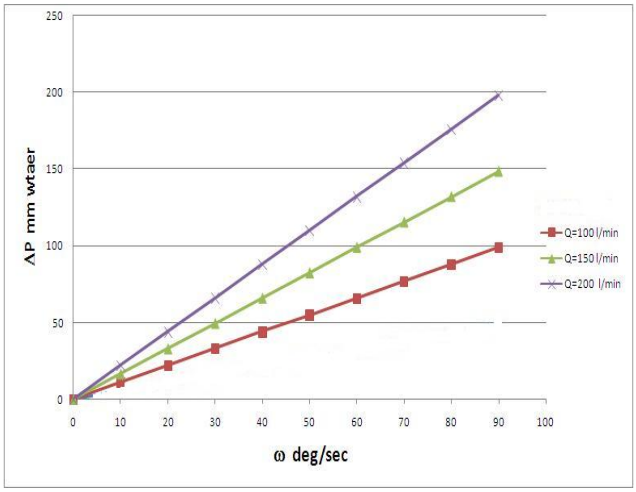

Figure.6 Theoretical Static Characteristics.

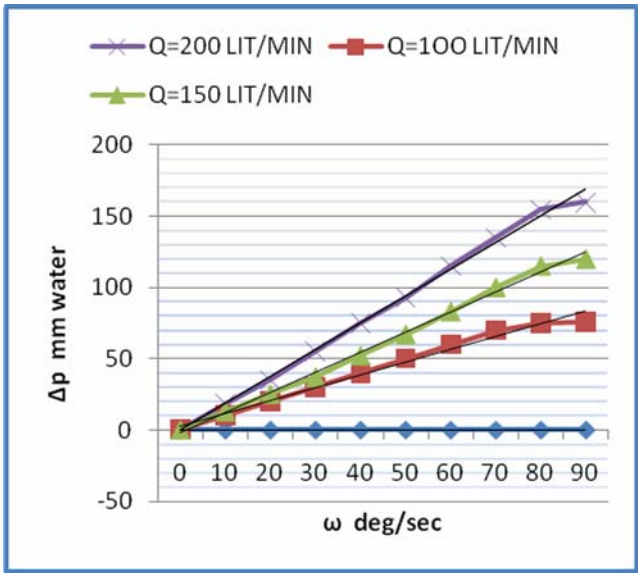

Figure.7 Experimental Static Characteristics.

CONCLUSIONS:

The static performance characteristics of vortex rate sensor are presented in fig (6, 7 and 8).from the figures it can be concluded that relation between the differential pressure and angular velocities is linear and the sensitivity of the instrument is increases as the flow rate increase.

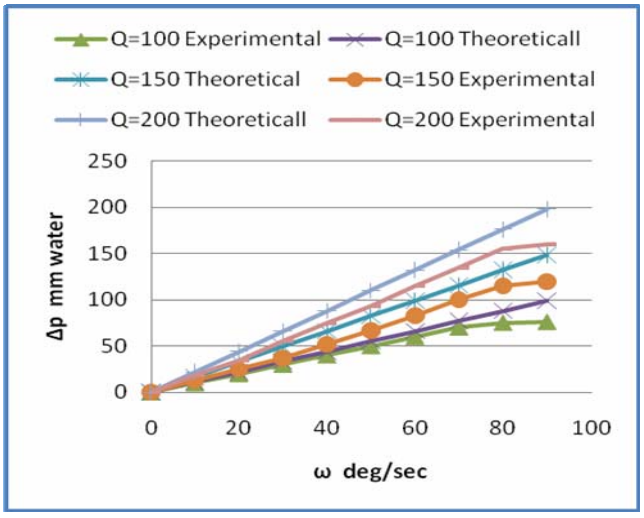

Figure.8 Comparison between theoretical and experimental static characteristics.

REFRENCESES

Barrett Doyle, “Vortex Rate Sensor", U.S Patent 3,240,060 (Mar 1966).

Camarata, F.J.”Twin vortex angular rate sensor”, U.S patent 3,447,383 (June 1996)

Foster. K .&Parker, G.A,"Fluidics Components and Circuits", McGraw-Hill Company, 1970

Ogren .H .D, “vortex rate sensor” ,U.S patent 3,203,237 (Aug 1965).
Aeronautics and Space A demonstration, Washington, D.C, July 1969.

Paviln..,”Theoretical Analysis of Angular Momentum Conservation and Signal Transition in a Constant Speed Rate Sensor", Journal of fluid mechanics, Vol.8, pp 433-443, pergamon presses 1972.

Peter Norton, "Angular Rate Sensor ", U.S Patent 7,132,936 B1, (Nov 2006).

Sarpkaya. T, "A Theoretical and Experimental Study of Vortex Rate Gyro", advance in fluidics, ASME, 1967.

.Sarpkaya.T,"A Pneumatic Vortex-Angular Rate Sensor-Analysis and Experiments", second IFAC symposium on fluidics, Vol.9, pp.29-34, pergamon press, 1973.

Tatsaya, Chiaki Iwadare,”On a vortex angle ratesensor” J.S.M.E, vol.12, no.7, 1973

Wilton P .Lock and Sbu W.Gee, "Flight Investigation of A Fluidic Auto Pilot System", National

Tatsuya Hagiwara, Shoji Kamimura and Chiaki Iwadare. "On A Vortex Angular Rate Sensor", J.S.M.E, Vol.12, No.7, 1973.

NOMENCLATURE

SYMBOL	MEANING
E_2	viscous efficient within sink tube
G	Acceleration due to gravity (m/ s^3)
M	mach number
P	Pressure distribution for potential flow across cylinder (mm water)
R	The effective radius of vortex rate sensor (mm)
r_p	The radial distance to the location of the pickoff hole (mm)
U_s	the average velocity in sink tube (mm)
$U_{\theta rp}$	Maximum swirl velocity in sink tube (mm/s)
B	coefficient depending on a velocity distribution in the sink tube
Γ	Kinematics viscosity (m^3 / s)
Θ	The swirl angel (degree)
P	The density of fluid (kg / m^3)
Ω	The angular viscosity (rad/s)
Γ_0	Circulation retained by the flow prior to the entrance into sink tube (m^2 / s)
Γ_p	Core circulation (m^2 / s)

AGENT BASED MONITORING FOR INVESTIGATION PROCESS AND MAINTENANCE IMPROVEMENT

Ameer Hussein Ali, Zouhair I. Ahmed, Soroor K.Hussain

ABSTRACT

Agent technology has a widespread usage in most of computerized systems. In this paper agent technology has been applied to monitor wear test for an aluminium silicon alloy which is used in automotive parts and gears of light loads. In addition to wear test monitoring، porosity effect on wear resistance has been investigated. To get a controlled amount of porosity, the specimens have been made by powder metallurgy process with various pressures (100, 200 and 600) MPa. The aim of this investigation is a proactive step to avoid the failure occurrence by the porosity.

A dry wear tests have been achieved by subjecting three reciprocated loads (1000, 1500 and 2000)g for three periods (10, 45 and 90)min. The weight difference after each test is immediately measured to find the losing weight and wear rate for each specimen. Wear test was monitored online by two sensors, force sensor to control the applied load, find friction force and coefficient of friction. The sensor is an acoustic emission to detect crack initiations of the worn surface by transfers the emitted ultrasonic waves from crack initiations to electric signals. Scanning electron microscope has been used to examine the worn surfaces. The overall results include that the effect of pores depends on pore shapes, sizes and concentrations.

Keywords: Agent Technology, Aluminium Silicon Alloys, Monitoring Process, Acoustic Emission Sensor, Wear, Scanning Electron Microscope and Predictive Maintenance.

الخلاصة:

تقنية العميل لها استخدام واسع في معظم الأنظمة المسيطر عليها بواسطة الحاسوب. في هذا البحث تم تطبيق تكنلوجيا العميل لمراقبة فحص البليان لسبيكة الأمنيوم سليكون التي تدخل في صناعة اجزاء السيارات ومنتجات اخرى كتروس اللأحمال الخفيفة. بالاضافة الى مراقبة فحص البلي، تم التحقيق من تأثير المسامية على مقاومة البليان. للحصول على كمية مسيطر عليها من المسامية تم تصنيع العينات بواسطة عملية مساحيق المعادن مع ضغوطات متغيرة (100، 200 و600) ميكا باسكال. الهدف من هذا الفحص هو الخطوة الاستباقية لتجنب حدوث الفشل الناتج من المسامية.

اختبارات البلي الجاف قد انجزت عن طريق تسليط ثلاثة احمال تبادلية (1000، 1500 و2000) غم لثلاث فترات (10، 45 و 90) دقيقة. تم قياس الفارق بالوزن مباشرة بعد اختبارات البلي الجاف قد انجزت عن طريق تسليط ثلاثة احمال تبادلية (1000، 1500 و2000) غم لثلاث فترات (10، 45 و 90) دقيقة، وتم قياس الفارق بالوزن مباشرة بعد كل عملية فحص لإيجاد فقدان الوزن ومعدل البلي لكل عينة. اما فحوصات البلي تم مراقبتها بصورة مباشرة بواسطة متحسسين، احدهما متحسس القوى واستخدم لضبط الحمل المسلط ، ايجاد قوة الإحتكاك و معامل الاحتكاك. اما المتحسس الاخر هو متحسس الانبعاثا ت الصوتية لكشف بدايات التصدع في السطح المبلي عن طريق تحويل الموجات فوق الصوتية المنبعثة من بداية التصدع الى اشارة كهربائية. تم استعمال المجهر الماسح الألكتروني لفحص السطوح البالية. تضمنت النتائج بشكل اساس ايجاد تأثير المسامية على مقاومة البليان الذي يعتمد على شكل وحجم وتراكيز المسامات على في المعدن.

1. Introduction:

Agents could be designed to work with uncertain and/or incomplete information and knowledge. Hence, many tasks related to manufacturing - from engineering design to supply chain management - could be conducted by agents, small and large, simple and sophisticated, fine- and coarse-grained that were enabled and empowered to communicate and cooperate with each other [11]. An agent is just something that acts (agent comes from the Latin agere, to do). But computer agents are expected to have other attributes that distinguish them from mere "programs" such as operating under autonomous control, perceiving their environment, persisting over a prolonged time period, adapting to change, and being capable of taking on another's goals[14]. An abstract view of an agent is shown in Fig.1. In this paper agent system is represented by Universal Material Tester machine which is shown in Fig. 2. Sensors are represented by acoustic emission sensor and strain gage which is involved in the load cell while the action is represented by monitoring results of agent environment which is the wear test environment.

Measurement of wear is one of big importance not only in tribology research but also in practical applications, such as engineering surface inspection, coating failure detection, tool wear monitoring and so on. Due to the complexity of a wear analysis process, measurement of wear is usually conducted offline. Reliable online measurement or monitoring of wear remains a challenge to tribology research as well as to the industry [21]. Signals of acoustic emission sensor is useful to detect the level of degradation for the part which is made by type of the alloy which is subjected for the wear test by making comparison between the signals at the work with those come from the wear test. Agent monitoring will give the report of the wear resistance behavior as acoustic emission sensor signals with a description represents by wear track depth data. That report will be the reference to know the state of the product which is made from the same alloy which is used in the test by compare the output signals from that product with the signals of the test by using acoustic emission sensor similar to that which is used in the test.

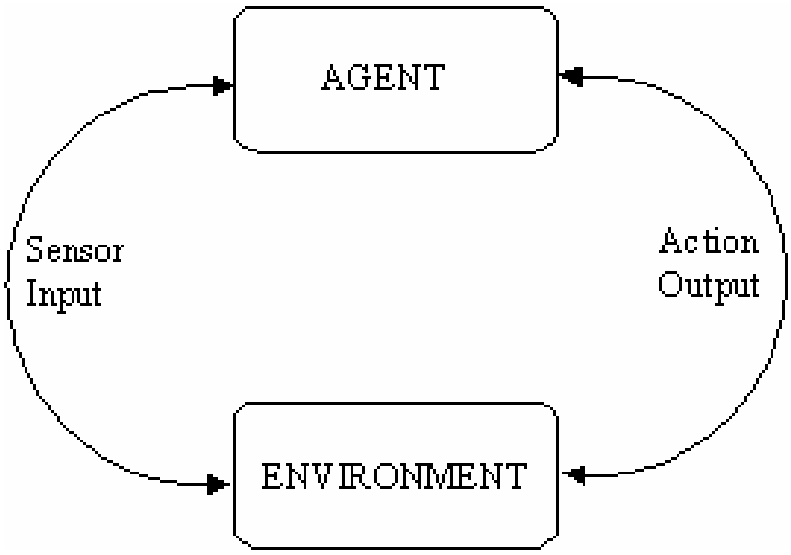

Fig. (1): An agent in its environment [5].

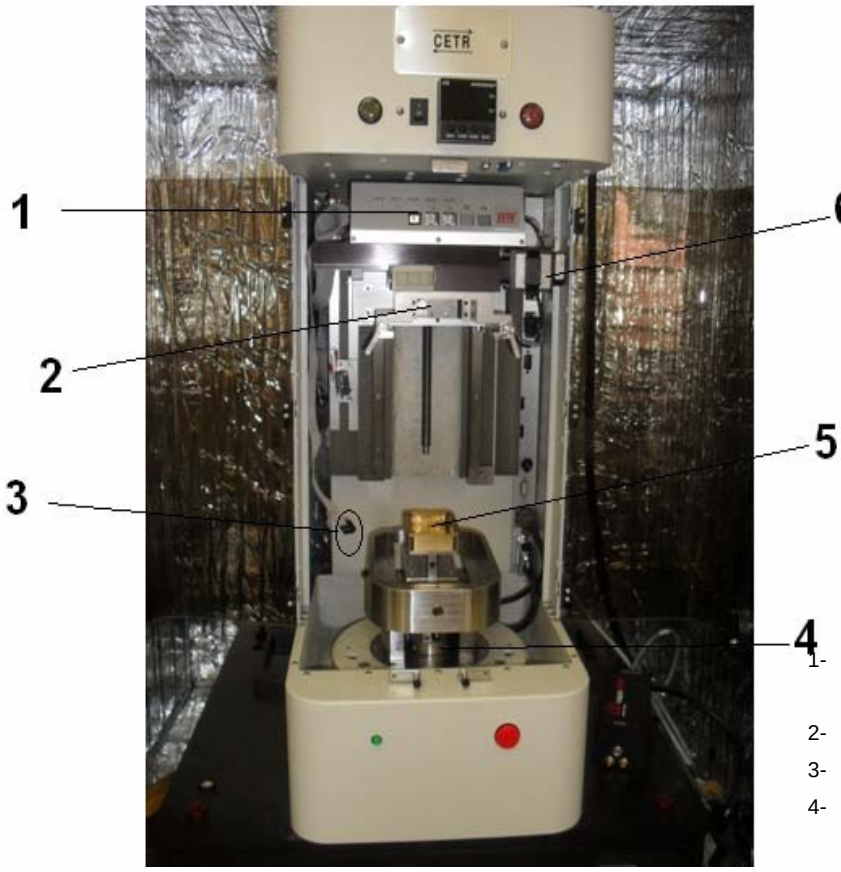

1- AE sensor and load cell manual reset.
2- Holder of the load cell.
3- Data bus cable of the load cell.
4- The reciprocator and AE sensor place.
5- Specimen holder.
6- Servo motor which move the holder of load cell up/down.

Fig. (2): Universal Material Tester machine

2. Aluminium Silicon Alloys:

The characteristic property of aluminium alloys is relatively high tensile strength in relation to density compared with that of other cast alloys, such as ductile cast iron or cast steel. The high specific tensile strength of aluminium alloys is very strongly influenced by their composed polyphase microstructure. The silicon content in standardized commercial cast aluminium silicon alloys is in the range of 5 to 23 wt. %. The structure of the alloys can be hypoeutectic, hypereutectic, or eutectic, as can be seen on the equilibrium phase diagram Fig.3. Aluminium–Silicon alloys are a common choice for such applications, and their applicability in gears and structural parts subjected to wear is well established. A higher amount of silicon increases hardness and wear resistance [13] [10]. The alloy which is used in this research contains (88.8% Al, 6% Si, 4.5% Cu, 0.5% Mg and 0.2% Sn) this type of alloys is used to make some of automotive parts such as clutch housing, pistons and sliders.

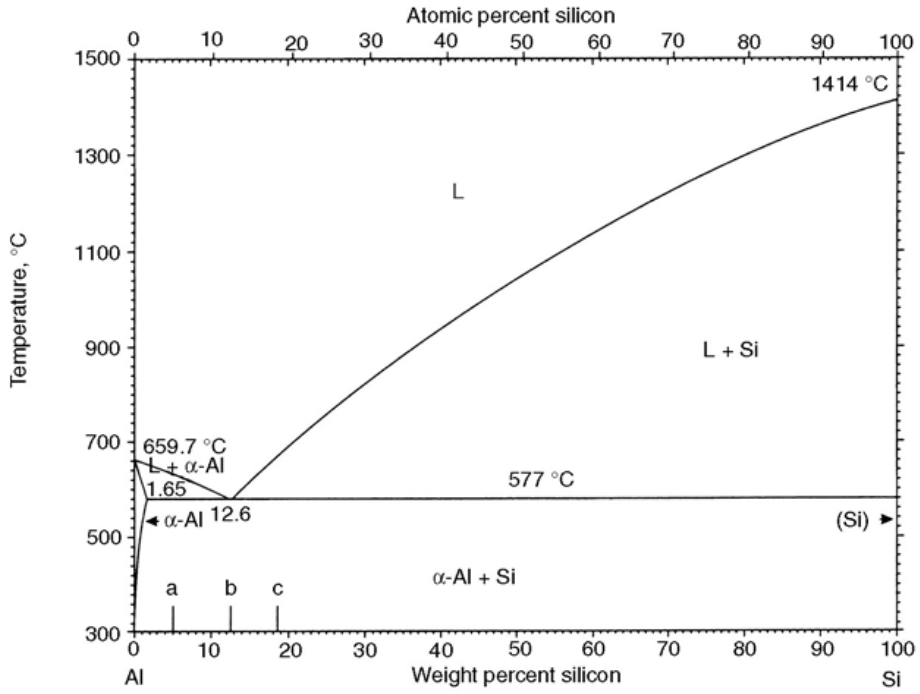

Fig. (3): Al-Si equilibrium diagram [10].

3. Predictive Maintenance:

Predictive maintenance attempts to detect the onset of a degradation mechanism with the goal of correcting that degradation prior to significant deterioration in the component or equipment based on the severity of the condition and the consequence of failure, it possible to determine an appropriate priority and course of action to minimize the risk and consequence of the pending failure [15]. The diagnostic capabilities of predictive maintenance technologies have increased in recent years with advances made in sensor technologies. A comprehensive predictive maintenance management program uses the most cost effective tools (e.g., Vibration Monitoring, Thermograph, Tribology) to obtain the actual operating condition of critical plant systems and based on this actual data schedules all maintenance activities on an as-needed basis. Including predictive maintenance in a comprehensive maintenance management program optimizes the availability of process machinery and greatly reduces the cost of maintenance. It also improves the product quality, productivity, and profitability of manufacturing and production plants.

There are three basic techniques of predictive maintenance:

1. Existing sensor – based maintenance techniques.
2. Test sensor – based maintenance techniques.
3. Test signal-based maintenance techniques.

The first one consists of maintenance methods that use data from existing process sensors such as pressure sensors, thermocouples, and resistance temperature detectors that measure variables like temperature, pressure, level, and flow. The second uses data from test sensors such as accelerometers for measuring vibration and acoustic sensors for detecting crack initiations of materials or other sound sources for failures caused these sounds such as leaks in vessels. The third one represents the active techniques while the previous are passive techniques. One form of test signal–based predictive maintenance involves injecting a signal into the equipment to measure their performance [7]. A significant amount of work has been done by NASA to measure the range when journal bearings emit ultra-sonic noise when wear has developed [3].

4. Experimental:

4.1 Specimens Preparation:

Specimens in this research are prepared by powder metallurgy. Powder metallurgy provides porosity with homogeneously distribution. The powder which have been used for making the specimens pressed at (100, 200 and 600) MPa to make a variety of porosity volume percentages and porosity percentage for the load subjected surface area. A Lico wax C used as a pressing lubricant and the specimens sintered in a tube furnace in the presence of Nitrogen gas at 560°C for 20 minutes then slow cooled to 480°C. The difference compaction pressures make samples with variable densities.

The green and sintered densities of samples were determined according to Metal Powder Industries Federation standard. The un-sintered (green) density of the samples was calculated for each sample by weighing the samples in air (W**air**) and in water (W**water**). The green density calculated using eq. (1)

$$\rho_{Green} = \frac{W_{air} * \rho_{water}}{W_{air} - W_{water}} \quad (1)$$

The temperature of the water was 20.6°C while the temperature of specimens about 20° C. The sintered density was performed by weighing the samples in air (W_{air}) prior to infiltrating them with ESSO-NUTO H46 hydraulic oil then weighing the samples in air (with oil impregnation) then measuring weight of the samples which are impregnated by the oil in the water. Finally the sintered density is calculated by eq. (2)

$$\rho_{sintered} = \frac{W_{air} * \rho_{water}}{W_{so} - W_{wo}} \quad (2)$$

The volume percentage of porosity is calculated using eq. (3)

$$P_V = 100 - \left(\frac{\text{sintered density}}{\text{theoritical density}} * 100\right) \quad (3)$$

The results of volume percentage of porosity are shown it table 1

Table (1) green and sintered density values

Specimen	Green Density (g/cm³)	Sintered Density (g/cm³)
Pressed at 100 MPa	2.13	2.3
Pressed at 200 MPa	2.3	2.47
Pressed at 600 MPa	2.57	2.59

The theoretical density of the alloy calculated to be 2.75 (g/cm³) according to the rule of mixture.

4.2 Hardness Test:

The difference of compaction pressures for the specimens gives them a different hardness. Measuring hardness of the specimens before preparation have been made, because the image analysis of the specimens requires high quality surface, destructive method of hardness test (Rockwell Hardness Test) have been used. The tool used was a diamond cone with a 60 kg load. Twelve measurements at twelve different places were taken for each sample to insure that any irregularities in the surface can't affect the hardness value. The total penetration depth is consisted of a plastic component and an elastic recovery component which have been evolved during the period of unloading. The hardness values of the specimens are (34, 49 and 58) HRA for the specimens (100, 200 and 600) MPa.

4.3 Preparation for Image Analysis:

First of all, each specimen has been divided into three sub-specimens because nine specimens are needed in this work, and then put them again into a furnace to evaporate the oil which used during cutting them. The specimen surface should be prepared very well with less possible number of scratches. The reason of that, is to get an accurate determination of the surface porosity percentage, and then each specimen is grounded by using 240, 320, 400 and 600 grit SiC abrasive papers then polished by using a billiard pad cloth, which is suitable for Aluminium Silicon polishing, with water contained of (1, 0.3 and 0.05) μm grains of Gamma Alumina powder. After polishing, the specimens have been washed properly and put in a cup of water in an ultrasonic device to remove the residual grains of polishing powder then the sample was subjected to a hot air to drying them. The measured surface roughness for the specimens (100, 200 and 600) MPa around (1.40, 1.34 and 1.28)μm respectively.

4.4 The Image Analysis:

The purpose for image analysis is to calculate the surface porosities by using the software Image Pro Plus. In this research, the Metallurgical Microscope BX51 equipped with bright-field objectives have been used to take images at high resolution. According to the ASTM (E 1245) standard test, 36 images have been taken for each sample with same magnification equal to 100x such as the pictures in figure (22). Porosities have been identified based on the variation of their grey-level intensity compared to the matrix. Grey-level threshold settings were selected to allow autonomous detection of porosity using the "flicker method" of switching back and forth between porosity and the matrix. The grey-level thresholds in addition to boundary conditions such as(aspect ratio, minimum radius and area) were set to avoid second phase particles and dendrites detection Counting method has been chosen to correct the edge effects, so the porosity lying across the boundary field is counted only once. For each field the area fraction of the detected area of porosity was measured by dividing the detected area of porosity by the area of the measurement field. The results of percentage of porosity surface area are (7.21± 0.156, 4.6 ± .0133 and 3.2± .011) for (100, 200 and 600) MPa respectively.

4.5 Application of The Loads:

The loads have been applied by using the UMT according to ASTM (G 133-5) 2010. Dry, reciprocating test is done by utilizing the upper ball specimen which slides against a flat lower specimen in a linear, back and forth, sliding motion having a stroke length of 5.03 mm. All the tests have been applied at room temperature and relative humidity of 40-55%. The load has been subjected downward through the ball contour-face against a flat specimen mounted on a reciprocating drive. The tester allows for monitoring the dynamic normal load, friction force and depth of the wear track during the test. The weight of the specimen was measured before and after each wear test to determine individual weight loss at selected time intervals. Three different loads of (1000, 1500 and 2000) g have been subjected to 10 Hz frequency or velocity (100.6 mm/s) and three different time intervals (10, 45 and 90) minutes. After wear tests, the worn surfaces and cross sections of wear tracks are examined using Scanning Electron Microscope.

5. Results:

The results monitored by the Universal Material Tester machine which is used for testing the specimens which have been discussed. The weight loss, wear rate, coefficient of friction, wear track depth and acoustic emission sensor results have been monitored for wear test of the specimens.

5.1 Effect of Applied Load:

Weight loss increases by increasing of the applied load due to high stresses leading to the yielding and subsequent fragmentations and oxidation during sliding, the applied load also causes the strain hardening for the metals depends on the property of the metal which is under the load [8,6,5]. In the fig. 4 (a, b and c) weight loss raised for the specimen 100MPa from 1.9mg at the load 1000g and 60.36m sliding distance to 3.6mg at the load 2000g with same sliding distance this increasing occurred for all the specimens but with different ratios depend on the load and the

porosity volume for the specimen. Wear rate will increase as a result of the increasing of weight loss for example the specimen of 600MPa compaction got increasing in wear rate from (0.00883 to 0.01472)mg/m for the load 1000g and 2000g respectively and at period 90min.

5.2 Effect of Porosity:

The presence of porosity clearly effects on the abrasive wear and other wear mechanisms due to the role of pore with its capacity to catch the fragments or debris of the worn surfaces. The filling of pores by the debris or oxides will improve wear resistance for the material according to prevent oxides debris to take the role of abrasives also it'll prevent the detachment of pores edges. Pores will reduce the micro contact between the two mating surfaces which is leading to reduce the friction and the wear. Shape of pore plays a significant role in filling the pore by the debris also in term of crack initiations and stress concentration the circular shape it's the best one because it's easier to fill and the less in term of stress concentration [14].

In fig. 5 (a, b and c) the wear rate decreases markedly during the increasing of sliding distance specially at load 1000g for the highest porosity volume which is the specimen 100MPa also at load 1500g, the value of wear rate at the 540.24m of sliding is convergent in spite of the difference by hardness values. At load 2000g the effect of the porosity lowered in term of wear rate improvement due to the lower magnitude of hardness for a specimen which has high porosity volume percentage. In addition to that the scanning electron microscope images for debris of this load show big size for debris of worn surfaces at load 2000g consequently big size of debris with small pores lower the probability of entrapping the debris in pores so the debris of worn surface and oxide of Al would be as abrasives for the surface in addition to the applied load.

5.3 Coefficient of Friction:

Coefficient of friction increases by increasing the applied force but it's also affects by the geometry of the surfaces [20]. Surface has complex effect on COF due to the valleys and grains orientation [4]. Friction causes energy dissipation as heating leading to softening of the metal and thermal oxidation of the surface. Aluminium oxide is has high hardness and so adhesive to the surface so it will need high load to penetrate [12]. Figures In this research the surface finish for the specimens is treated to be good for reducing the effect of surface roughness. Pores presence will increase surface roughness specially the big sizes but when debris settle down in the pores COF will decrease or get more stable [11]. All the specimens in this research COF got slight increasing by increasing the load but specimens of 100MPa compaction got more COF increasing than other due to lower hardness so it's easy to penetrate. the specimen 100MPa with load 1000g COF decreased to the half in addition to lower wear track depth while that didn't appear with other loads because 1500g and 2000g overcame the presence of the oxide layer and strain hardening for the specimens. COF trends for the specimens of 200MPa are stable but with clear increasing for loads 1500g and 2000g due to detachment of the oxide layer which causes adhesion with the tool and surface as observed by naked eye exam for the tool and SEM for the wear track. Specimens of 600MPa compaction high hardness with the oxide layer give the stability for COF trends except for the load 2000g a slight increasing was observed.

5.4 AE Results:

The sources of AE sensor of sliding test come from plastic deformation, initiation and growth of cracks, appearance of wear debris, of new surfaces because of wear and energy liberation at repeated deformation or phase hardening-weakening and damage of surface layer. Characteristics of AE are sensitive to the wear mode. Higher AE intensity values are typical with abrasive wear in comparison with adhesive and fatigue wear.

When studying the shape of AE signals at steady-state friction it was found that materials damaged by adhesion and fatigue produced a continuous signal with a small amplitude while materials damaged by adhesion with seizure yield a signal of explosive type. When the abrasive wear becomes dominate the amplitude of signals increase approximately 2–3 times [21]. Specimens which are compacted under 100MPa have lowest AE intensity with continues stability and little amplitudes relatively to the others as shown in Fig. (9). According to the trends of 200MPa and 600MPa specimens, AE intensity is relatively high and abrasive wear appeared more effective than adhesive, also it is easier to detach the surface of lower compaction metal due to it has relatively low hardness.

5.5 Wear Track Depth:

The figures give same trend which is the increasing of depth value by increasing the applied load. In addition to that, the monitoring process for the test shows the changes of depth's value during the test and the differences among specimens. In figure (10 a) the changes in the trend is less than of figure (10 b), this is because the specimen 100MPa has more pores than 200MPa and its pores are bigger in the size. The changes in trend of figure (10 c) is less than of figure (10 b), here the effect of hardness takes part to make the test value seems more stable. There is another explanation for depth trend changes caused by the porosity, where debris of worn surfaces for a specimen which has high number and big size of pores has no effect on the depth trend such as the specimen which has less number and smaller size of pores, will be between the two contacting surfaces so debris reduces the depth then it will increase the value of the depth when debris leave away the contact area. SEM images show the size of debris at load 2000g and load 1000g. At 2000g size the debris is bigger than at 1000g; this prevents pores to be contained, so changes in trend of depth have been noticed. The depth value of specimen 100MPa at period 90 min is less than of the specimen 200MPa at the same period of time; this is because of small size of debris which enables the pores to entrap it.

5.6 Scanning Electron Microscope Images:

Fig. (13 a, b, c and d) shows the drift of metal at the edge of wear track for each specimen also the detached particles which migrated due to adhesive wear or penetrated the surface by the applied pressure and surface softening as a result of frictional heat. Figure 14 (a, b, and c) shows the worn surface under 1000g and 90min, surface damage of the specimens is clear for 200MPa and 600MPa but it isn't for one of 100MPa specimens because of the role of porosity. Pores effect is not enough to reduce damage of the surface for higher loads. Surface damage for the worn surface by load 1500g appears in figure (16 a) which reveals micro cracks nearby pores in spite of filling by debris while other images of other specimens for the same conditions depict less surface damage due to their high hardness. Same thing repeated with the load 2000g the specimens which are compacted by high pressure resisted and have more wear than others but they got more damage than specimens which are subjected to load of 1000g as shown in figure (15) and (17). Higher magnification of SEM images in figure (5.30) enables us to see the effect of pore size and shape. For 100MPa the pore is large and contains large debris size in addition to small size of debris while for 200MPa pore is relatively small and contains small size debris. Figure (5.30 c) clarifies the effect of pore shape, that pore has sharp edges which are considered as stress concentrations and the place of crack initiations.

Figure (5.31) shows the effect of delamination for some grooves of 90min period, this period has a highest number of cycles so delamination occurred for this period more than others. The cracks extended from the pores under the groove to the surface have been observed. Also it's observed that specimens of 100MPa are affected by delamination more than the others.

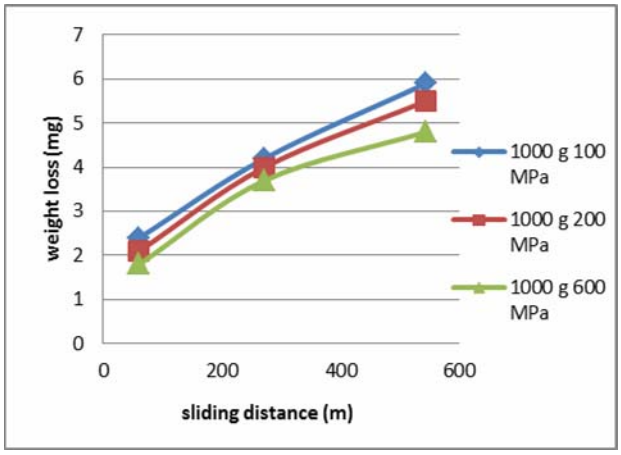

a

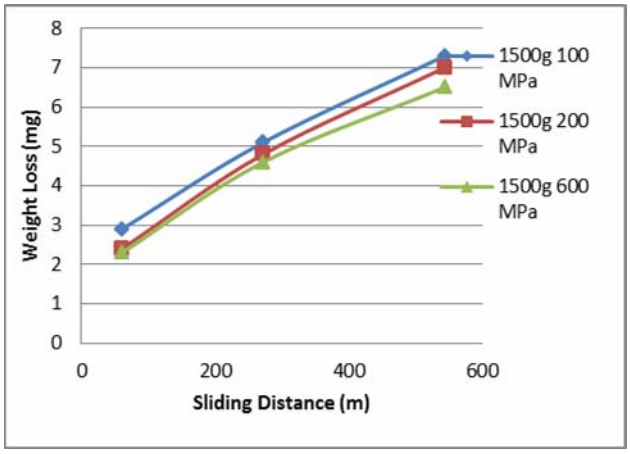

b

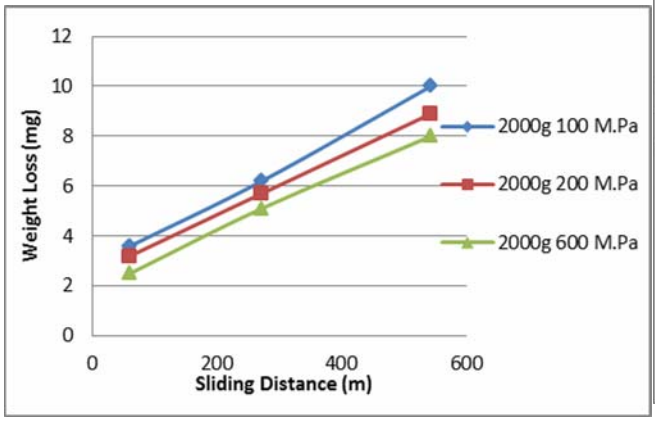

c

Fig. (4) Weight loss vs. sliding distance for the three loads and three types of compaction (a, b and c)

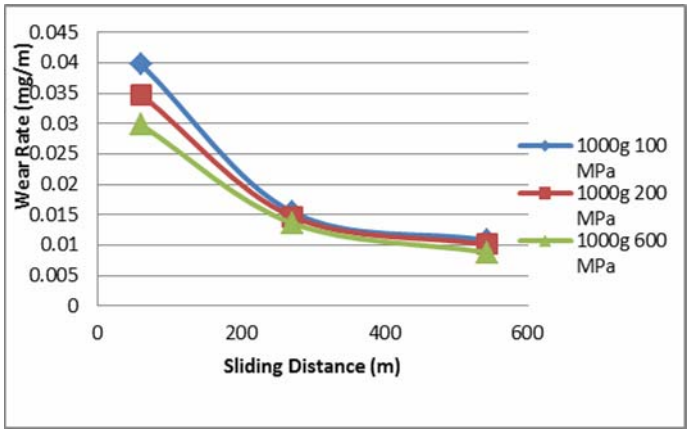

a

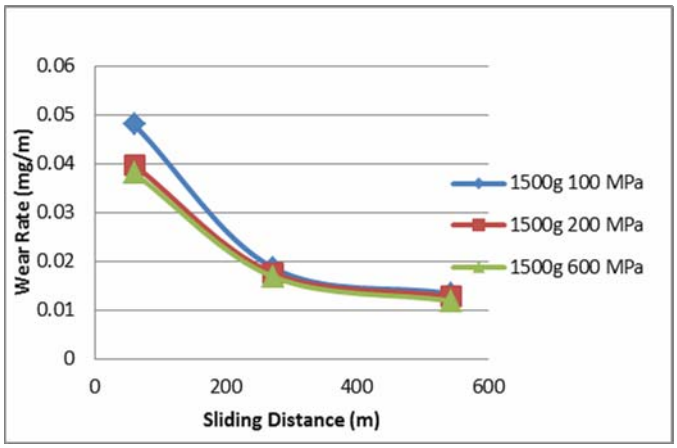

b)

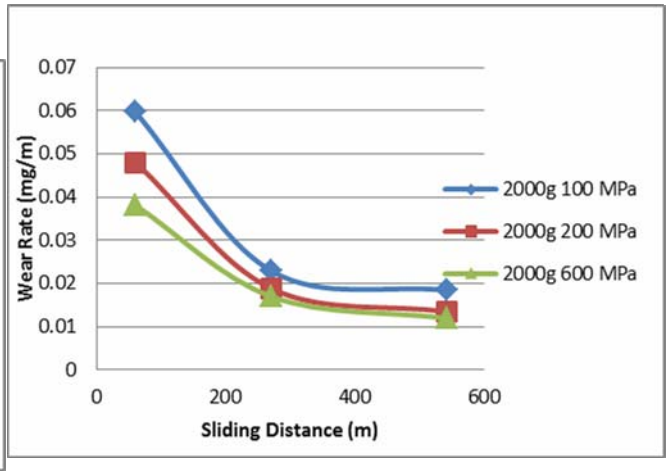

c)

Fig. (5) Wear rate vs. sliding distance for the three loads and three types of compaction (a, b and c)

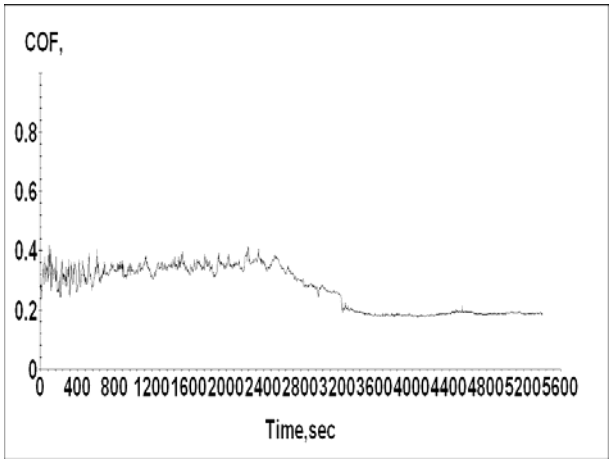

a

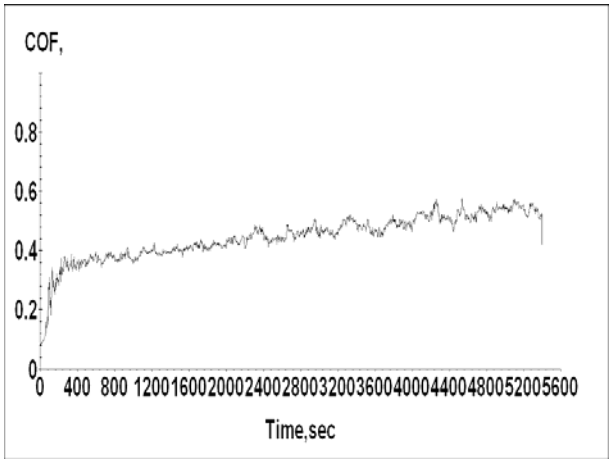

b

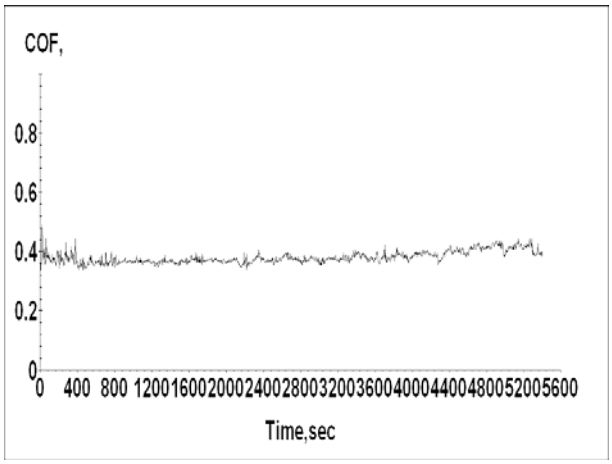

c

Fig. (6) COF 1000g 90 min (100, 200 and 600) MPa (a, b and c) respectively.

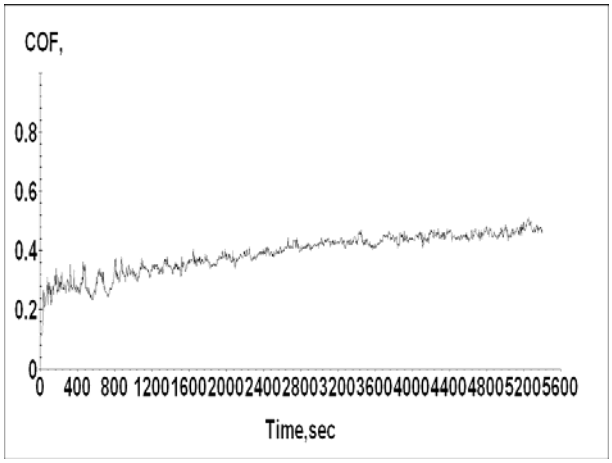

a

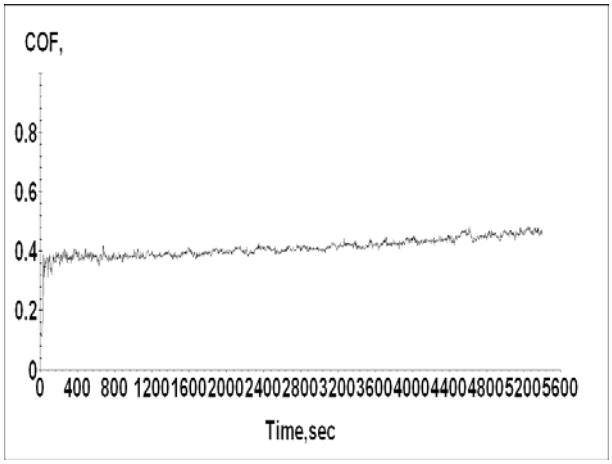

b

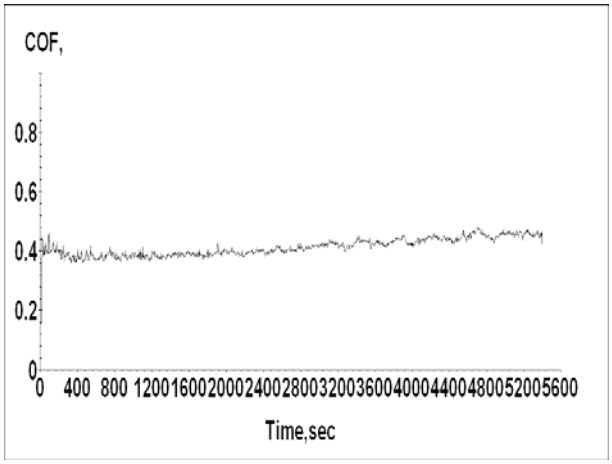

c

Fig. (7) COF 1500g 90 min (100, 200 and 600) MPa (a, b and c) respectively.

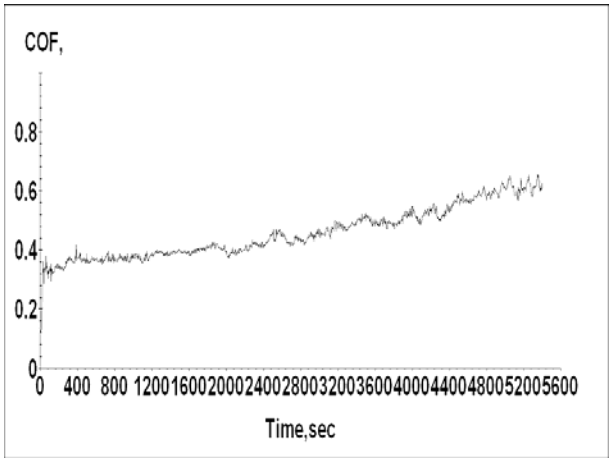

a

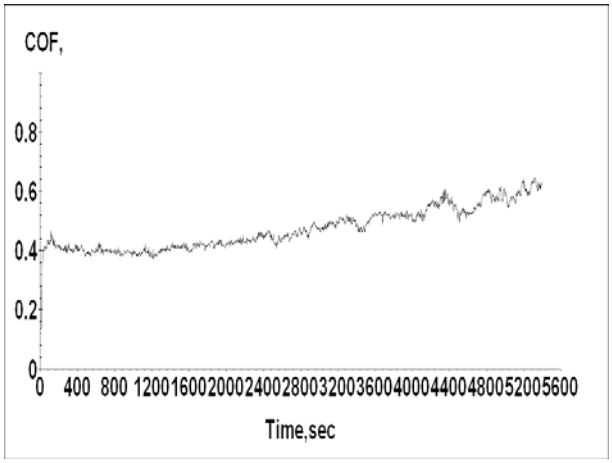

b

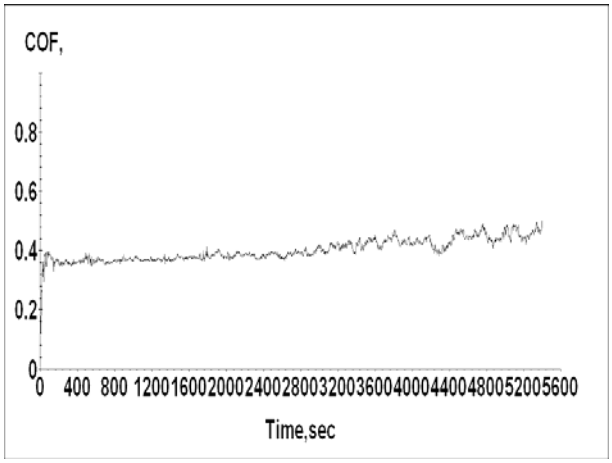

c

Fig.(8) COF 2000g 90 min (100, 200 and 600) MPa (a, b and c) respectively.

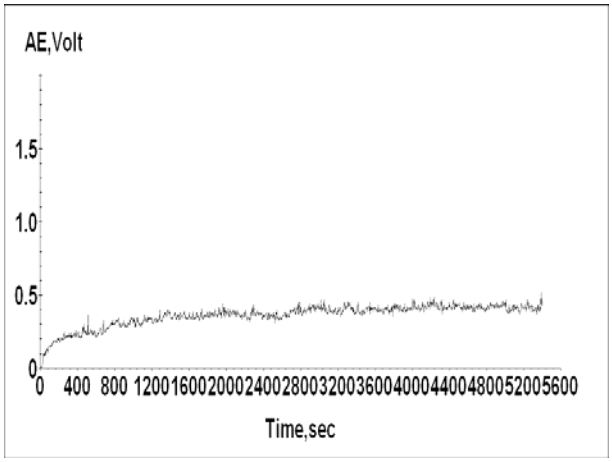

a

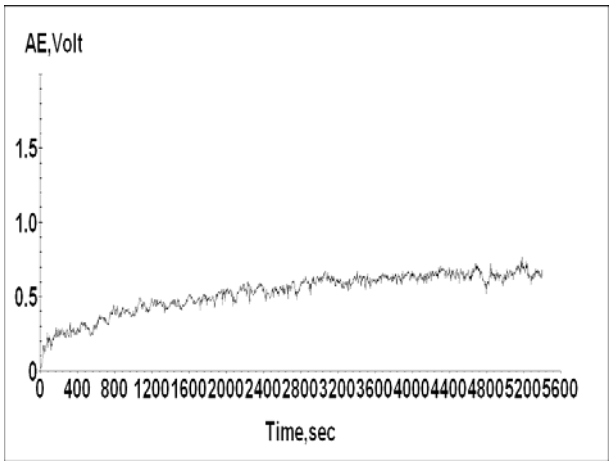

b

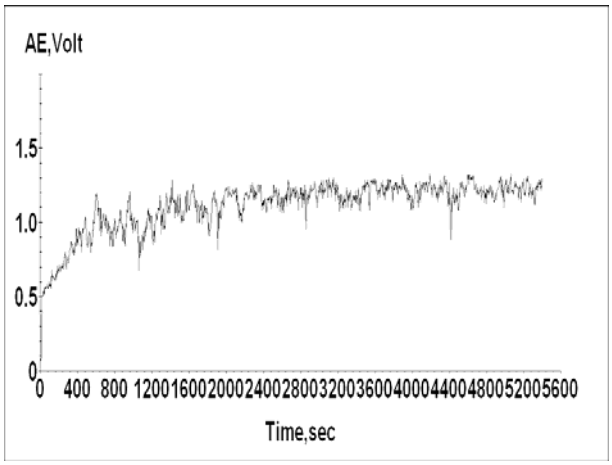

c

Fig. (9) AE 1500g 90 min (100, 200 and 600) MPa (a, b and c) respectively.

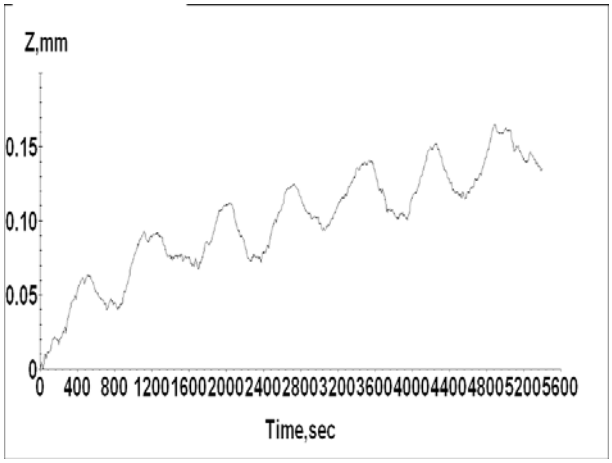

a

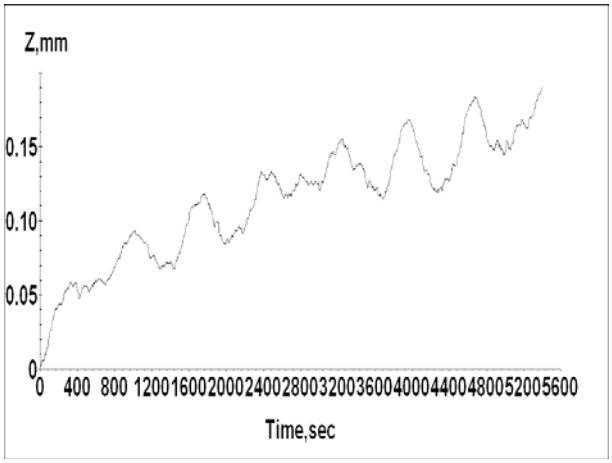

b

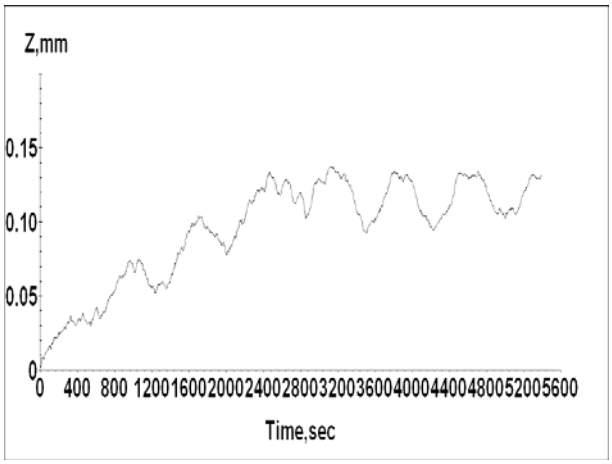

c

Fig. (10) Wear track depth 1000g 90 min (100, 200 and 600) MPa (a, b and c) respectively.

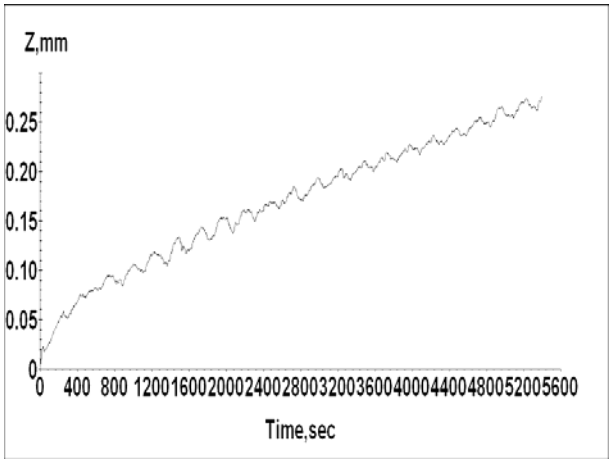

a

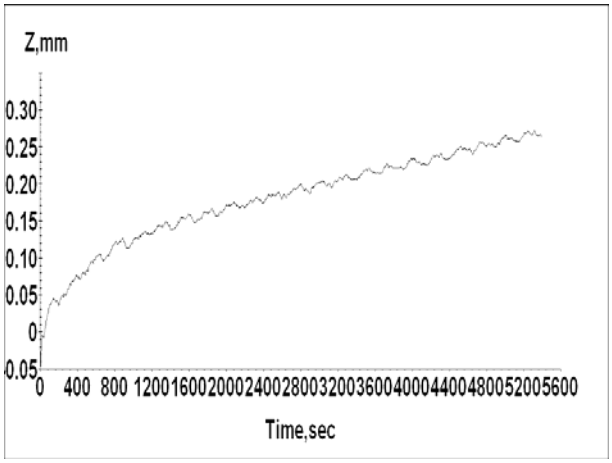

b

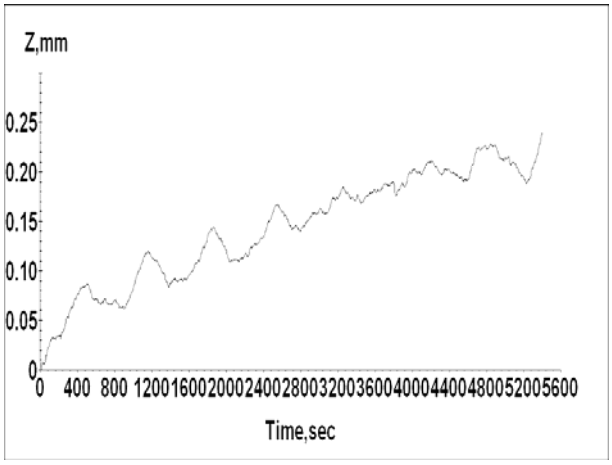

c

Fig. (11) Wear track depth 1500g 90 min (100, 200 and 600) MPa (a, b and c) respectively.

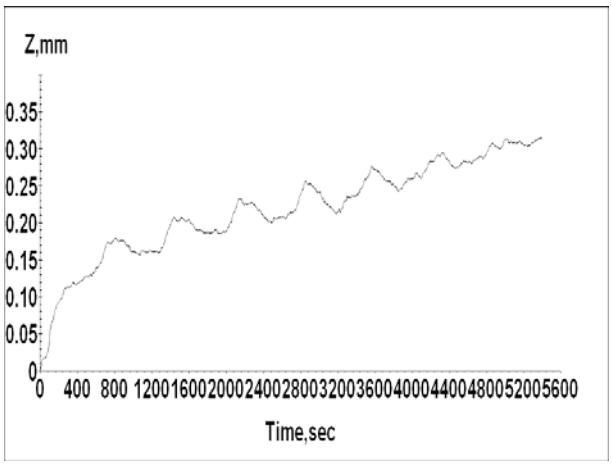

a

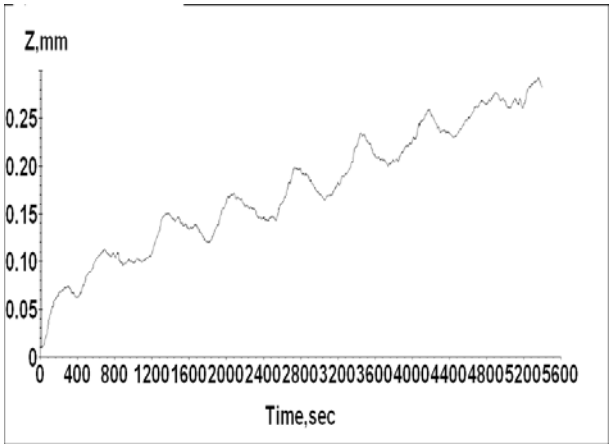

b

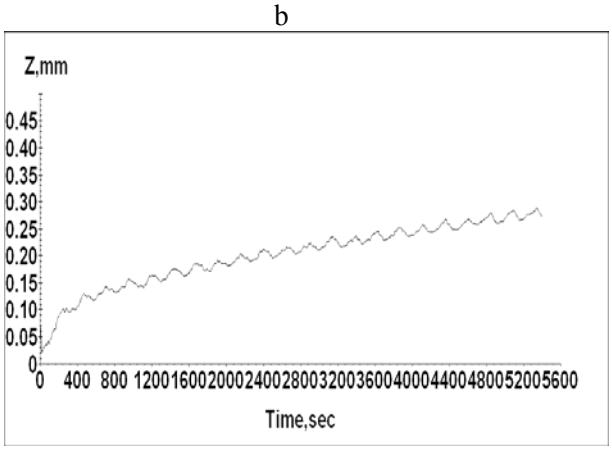

c

Fig. (12) Wear track depth 2000g 90 min (100, 200 and 600) MPa (a, b and c) respectively.

a) 100 MPa 1000g 10 min

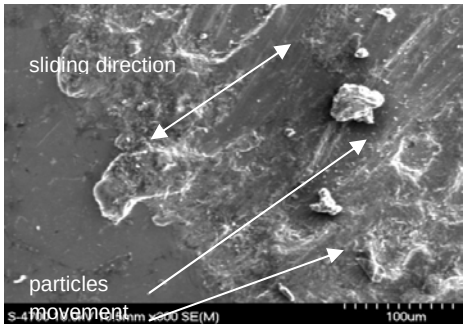

b) 200 MPa 1000g 10 min

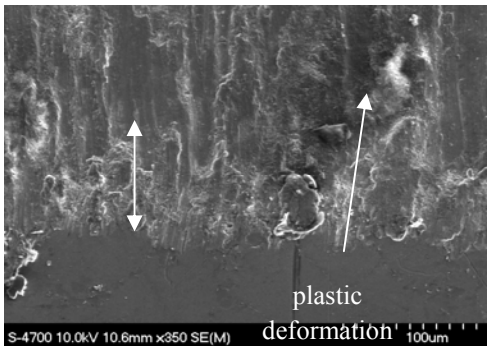

c) 600 MPa 1000g 10 min

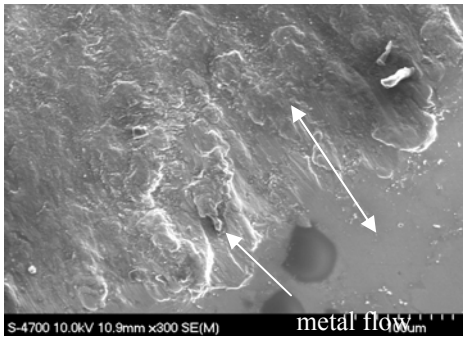

d) 100 MPa 1000g 90 min

Fig. 13 (a, b, c and d) edge of the wear track.

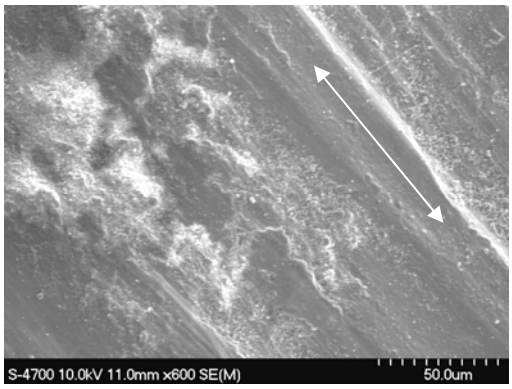

a)

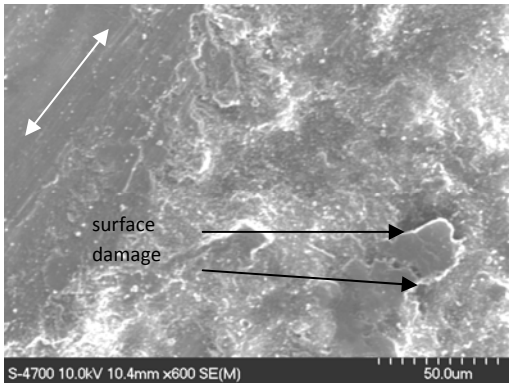

b)

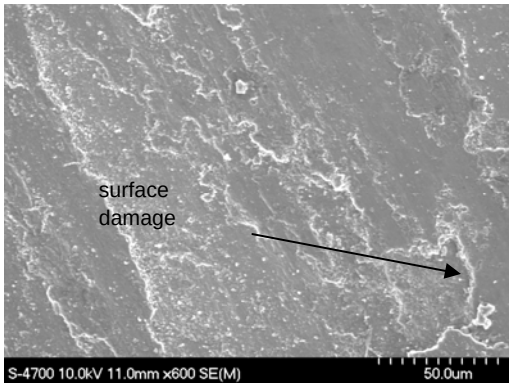

c)

Fig. (14) Wear track of 1000g after 90min for (100, 200 and 600)MPa. (a, b and c) respectively.

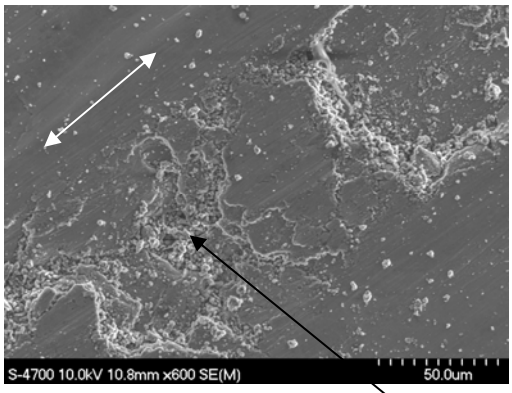

a)

pore filled by debris

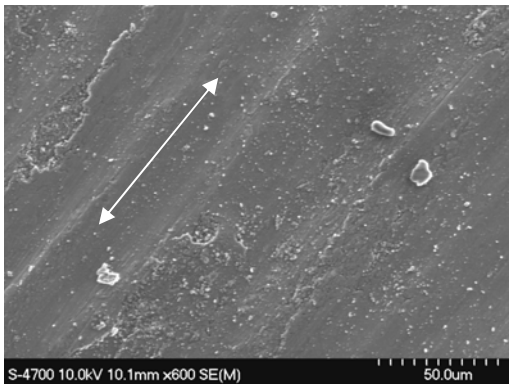

b)

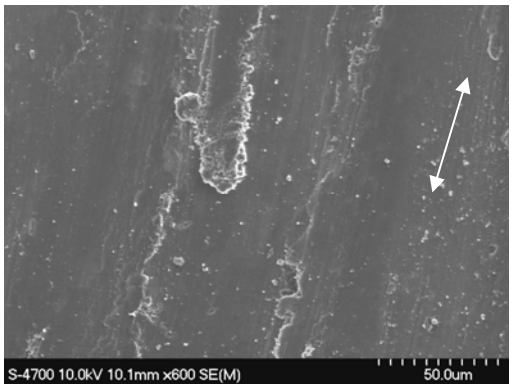

c)

Fig. (15) Wear track of 1500g after 45min for (100, 200 and 600) MPa. a, b and c respectively.

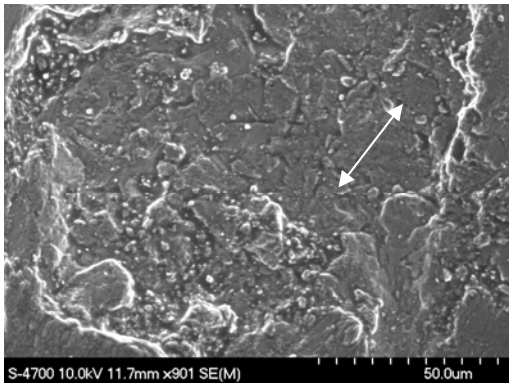

a)

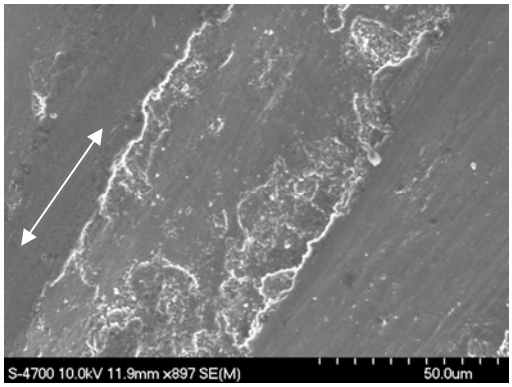

b)

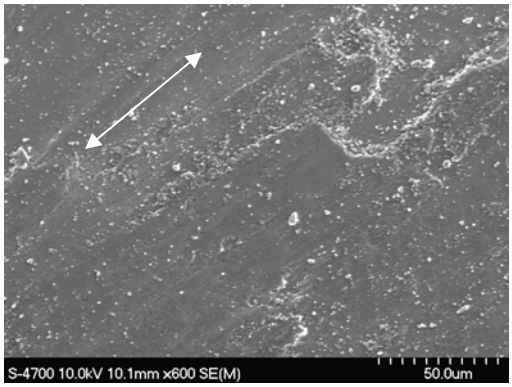

c)

Fig. (16) Wear track of 2000g after 45min for (100, 200 and 200 and 600) MPa (a, b and c respectively).

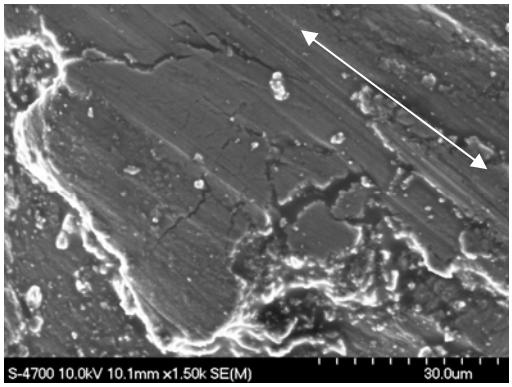

a)

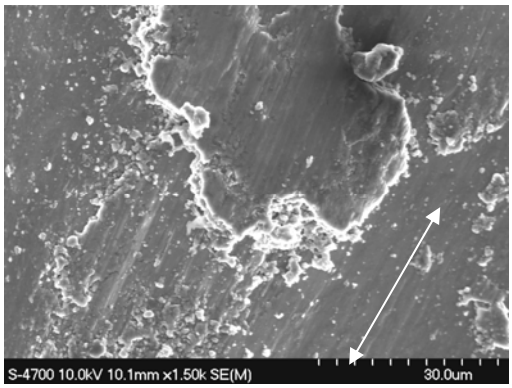

b)

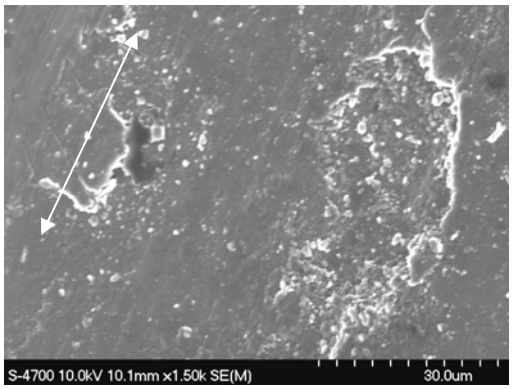

c)

Fig. (17) Wear track of 2000g after 90min for (100, 200 and 600) MPa (a, b and c) respectively.

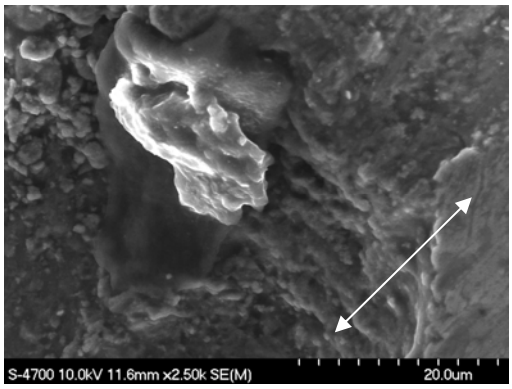

a)

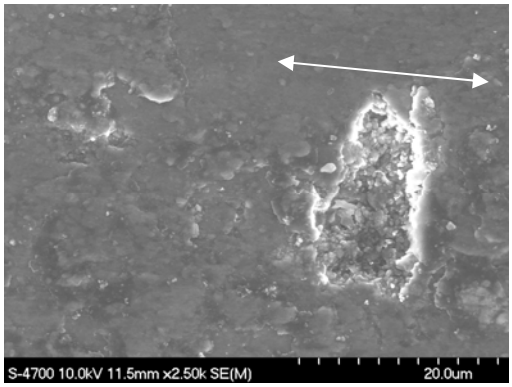

b)

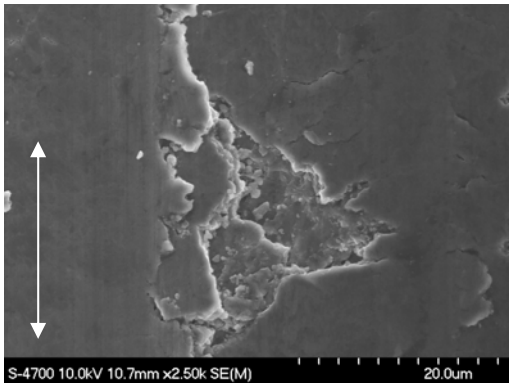

c)

Fig. (18) Wear track of 1000g after 90min for (100, 200 and 600)MPa (a, b and c) respectively.

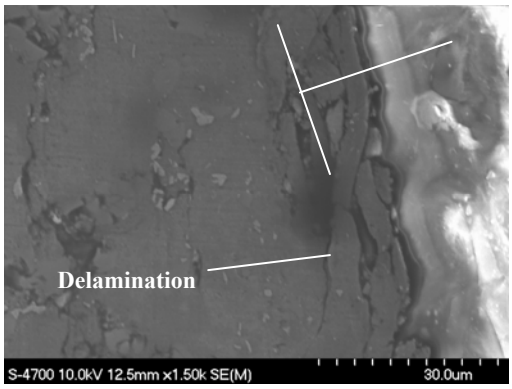

a)

Siding direction is perpendicular to the specimen

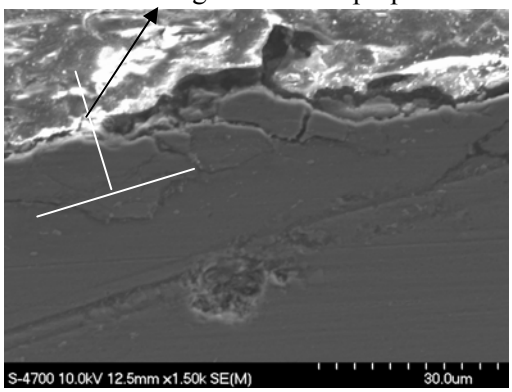

b)

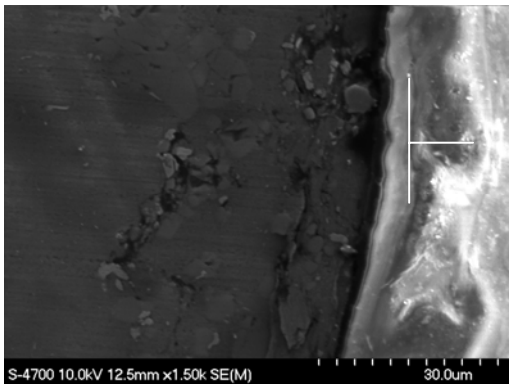

c)

Fig. (19) Cross sectional image of 2000g 90min for (100, 200 and 600)MPa (a, b and c) respectively.

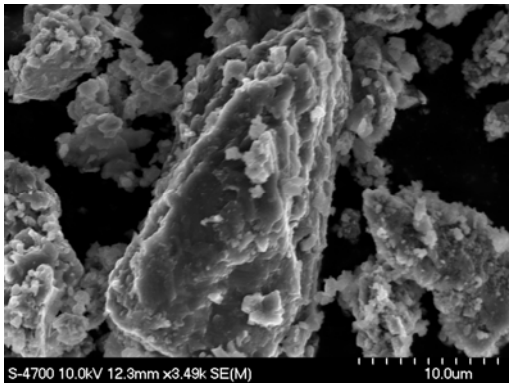

a)

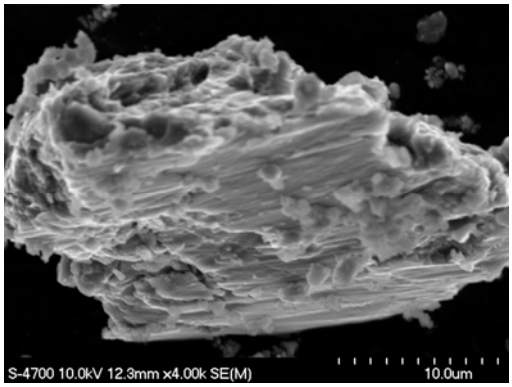

b)

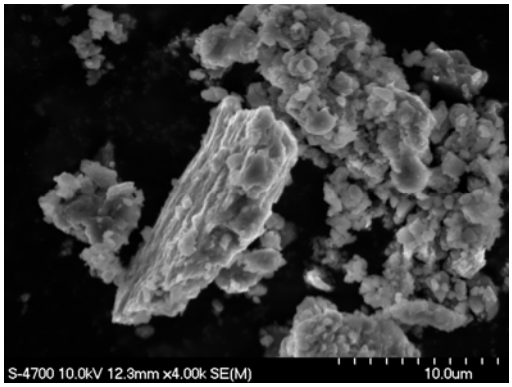

c)

Fig. (20) Debris of the specimens under 1000g for 90min (100, 200 and 600)MPa (a, b and c) respectively.

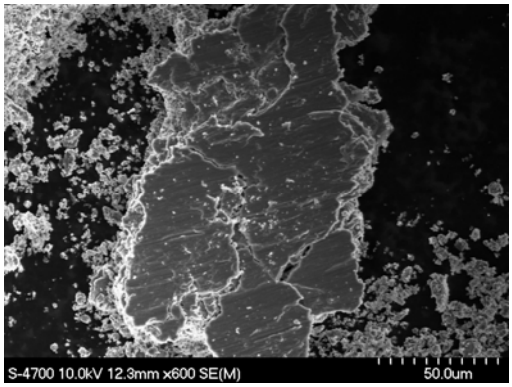

a)

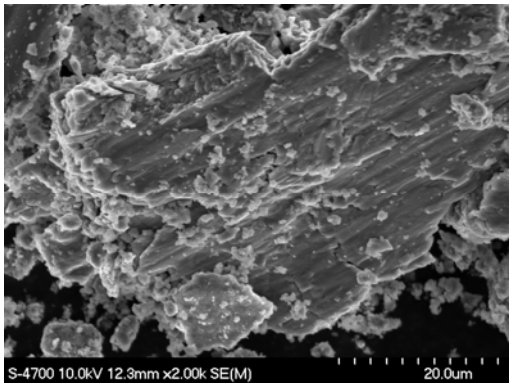

b)

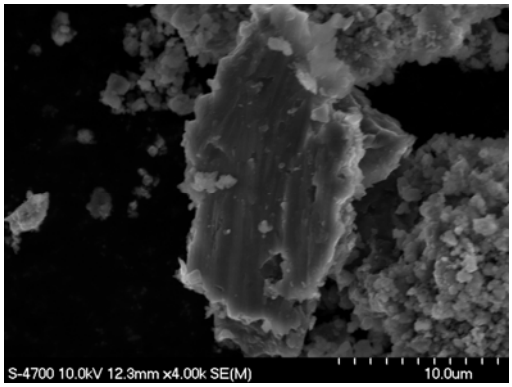

c)

Fig (21): Debris of the specimens under 2000g for 90min.

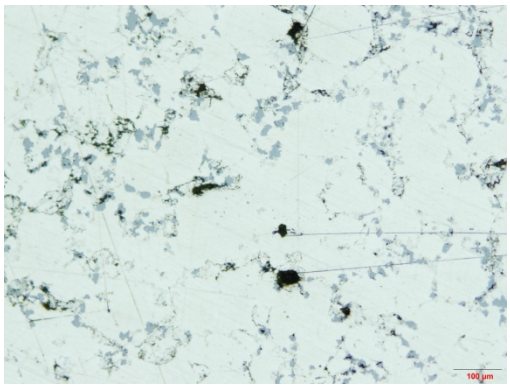

a

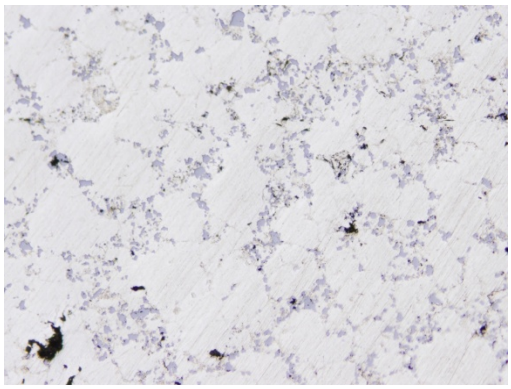

b

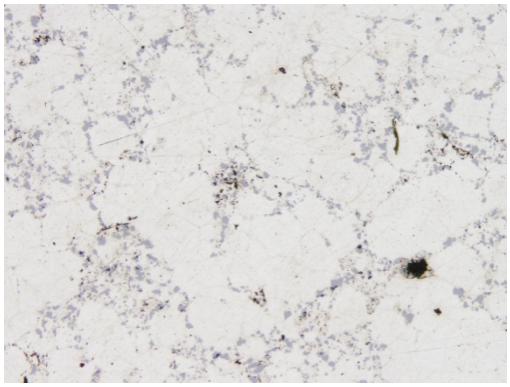

c

Fig. (22) Pictures for image analysis to measure the porosity surface area percentage for (100, 200 and 600)MPa (a, b and c) respectively.

Conclusions:

1. Wear test has a dynamic environment represented by strain hardening of the surface metal after load application, softening due to heat generation because of friction; friction changes as a result of roughness changes in addition to pores presence in this research so on line monitoring results give a clear picture about wear test and its dynamic changes.
2. Porosity has a significant effect on wear resistance this appeared clearly from the results of the test. Pore size and shape play the role of porosity effect, porous surface with a relatively big size pores has better wear resistance if the applied load is low but it has worse if the load is high.
3. Agent technology has the flexibility to monitor such a dynamic environment like a dry sliding wear test and give a brief report to the individual events during the test.
4. AE results can be transferred to detect faults for any product made by the tested material depending on the similarity of test conditions because it represents on material properties and the media of sound transfer.

References:

1. Abdulhaq A. Hamid, S.C. Jain, P.K. Ghosh, and Subrata Ray "Characterization and Tribological Behavior of Cast In-Situ Al (Mg,Mo)-Al2O3 (MoO3) Composite", Metallurgical and Materials Transaction B, Vol. 37, No. 4, pp. 519-529, (2006).

2. A.S. Anasyida, A.R. Daud, M.J. Ghazali "Dry Sliding Wear Behaviour of Al–12Si–4Mg alloy with Cerium Addition", Materials & Design, Vol. 31, No. 1,p.p 365-374, (2010).
3. Anderson, M. L. (1994) "Predictive maintenance: its present state and future potential for the mobile equipment industries", In Proc of the Conference Equipment resource management into the 21st century, Nashville, Tennessee, ASCE, New York. 210 p.

4. B. Bhushan "Introduction to Tribology", Wiley N.Y. (2002).
5. B. Dubrujeaud , M. Vardavoulias and M. Jeandin, "The role of

porosity in the dry sliding wear of a sintered ferrous alloy", journal of wear, Vol. 174, Issues 1-2, pp.155-161, (1994).

6. B.K. Prasad, "Influence of Some Test Parameters on Dry Sliding Wear Characteristics of a Zinc-11.5% Aluminium Alloy", Journal of Materials Engineering and Performance Volume, Vol. 11,No. 4, pp. 461-468, (2002).

7. Hashemian, H. M, "State-of-the-art predictive maintenance techniques", IEEE Transactions on Instrumentation and Measurement ,Vol. 60, Issue 1, pp. 226-236, (2010).
8. H.Z. Ye, D.Y. Li, and R.L. Eadie "Influences of Porosity on Mechanical and Wear Performance of Pseudoelastic TiNi-Matrix Composites", Journal of Materials Engineering and Performance, Vol. 10, No. 2, p.p 178-185,(2001).

9. Jianbo Zhang, Regtien, Paul P.L. and Korsten, Maarten " Monitoring of Dry Sliding Wear Using Fractal Analysis". In: 10th IMEKO TC10 International Conference on Technical Diagnostics, Budapest, Hungary, (2005).
10. Małgorzata Warmuzek "Aluminium-Silicon Casting Alloys Atlas of Microfractographs ", ASM, (2004).
11. M. G. GEE, E. A. ALMOND "The Affect of Surface Finish on the Sliding Wear of Alumina", Journal of Materials Science, Vol. 25, No. 1, pp. 296-310, (1990).
12. Michael F. Ashby And David R. H. Jones "Engineering Materials 1 An Introduction to their Properties and Applications", Butterworth-Heinemann, 2nd Ed., (1996).
13. Myer Kutz, "Handbook of Materials Selection", John Wiley & Sons, (2002).
14. Piao Zhong-yų, Xu Bin-shi, Wang Hai-dou, Pu Chun-huan " Investigation of fatigue failure prediction of Fe-Cr alloy coatings under rolling contact based on acoustic emission technique", Applied Surface Science, V. 10, 1016, (2010).
15. Ron Moore, " Selecting The Right Manufacturing Improvement Tools", Elsevier, (2007).
16. V.K. Gupta, S. Ray2, O.P. Pandey, "Dry Sliding Wear Characteristics of 0.13 wt. % Carbon Steel", Materials Science-Poland, Vol. 26, No. 3, (2008).
17. Russell, S. and Norvig, P. "Artificial Intelligence: A Modern Approach", Prentice Hall Series in Artificial Intelligence. Englewood Cliffs, New Jersey, (2003).
18. Teppo Pirttioja, Antti Pakonen, Ilkka Seilonen, Aarne Halme and Kari Koskinen" Multi-Agent Based Information Access Services for Condition Monitoring in Process Automation ", 3rd International Conference on Industrial Informatics IEEE, (2005).

19. Woolderidge. M "An Introduction to Multiagent Systems", John Wiley & Sons Ltd., (2002).
20. Valentin L. Popov, "Contact Mechanics and Friction Physical Principles and Applications", Springer-Verlag Berlin Heidelberg (2010).
21. Victor Baranov, Evgeny Kudryavtsev ,Gennady Sarychev and Vladimir Schavelin, "Acoustic Emission In Friction" , Moscow State Engineering Physics Institute Kashirskoe sh. 31, Moscow, first edition, Elsevier, (2007).

List of Symbols		
Symbol	Meaning	Unit
ρ_{Green}	Green Density	g/cm^3
$\rho_{sintered}$	Sintered Density	g/cm^3
ρ_{water}	Water Density	g/cm^3
AE	Acoustic Emission	Volt
COF	Coefficient Of Friction	
HRA	Rockwell Hardness	
W_{water}	Sample weight on water	g
W_{air}	Sample weight on air	g
W_{wo}	Sample weight on water after impregnation with oil	g
W_{ao}	Sample weight on air after impregnation with oil	g
Vs.	Versus	

*(⟷) This shape always refers to the sliding direction on SEM images.

RELATION BETWEEN STANDERD PENETRATION TEST AND SKIN RESISTANCE OF DRIVEN CONCRETE PILE IN OVER-CONSOLIDATED CLAY SOIL

Zuhair Kadhim JahanGer, M. Sc. (C. E.)
Assistant Lecturer, Baghdad University, Department of Water Resources Engineering
زهير كاظم جهان كير،(ماجستير هندسة مدنية،جيوتكنك)، مدرس مساعد،قسم هندسة الموارد المائية، جامعة بغداد

ABSTRAC

In this research the relation between skin resistances and standard penetration test of over consolidated clay soils has been studied. The research includes doing boreholes at Babil governorate in Iraq to get undisturbed samples and standard penetration test. Determination skin friction from direct shear test between smooth concrete and soil was explored in laboratory for design purposes and correlated with standard penetration test values. In many foundation design problems, the shear strength between soil and foundation materials were estimated or correlated without any direct methods for measurement.

Twelve strain controlled direct shear tests were performed simulate the shear strength interaction between smooth concrete and undisturbed over consolidated silty clay, determine the soil – foundation interface friction, considering the following variables :(1) over consolidation ratio OCR between 1.4 to 2.4 (2) Concrete, smooth surface, (3) Undisturbed samples, (4) Variation of the normal load between the friction surface. The results showed that both cohesion and internal friction should be considered in evaluating skin friction. The results of cohesion and angle of internal friction were correlate with the standard penetration test SPT –N . Interface friction angle was 14.5° , while the adhesion was 15.5 kPa. The ultimate shear strength was mobilized through 10%- 16% strain in the direction of shear surface. .

A fairly good correlation between the N_{70}-value and the interface friction parameters were established for determination unit skin friction for driven piles. Finally, based on the test results, a simple relation was proposed to relate the N_{70} value and interface friction of silty clay soils for a range of N_{70} between 12 and 20.

Keywords: undisturbed, O.C., silty clay، soil-concrete skin friction, direct shear test, SPT.

ألخلاصه

تضمن البحث إيجاد علاقة بين مقاومة الاحتكاك وقيمة ضربات فحص الاختراق القياسي لتربة طينية مفرطة الانضمام.حيث تم عمل حفر أختبارية لأستخراج نماذج تربة غير مشوشة من محافظة بابل –العراق وفحص الاختراق القياسي . حسب احتكاك التماس من تجارب القص المباشر بين الخرسانة (مواد الأساس)وتربه طينية لإيجاد علاقة مع قيمة ضربات فحص الاختراق القياسي N_{70} لأغراض تصميمية . غالباً ما تخمن معاملات مقاومة القص بين التربة ومواد الأسس في معظم مشاكل تصميم بدون طرق مباشِره للحساب.

أجري في هذا البحث اثنا عشر اختبار لمقاومه القص المباشر مسيطر الانفعال أخذين بنظر الاعتبار المتغيرات والظروف التالية: (1) تربه طينية عرينيه مفرطة الانضمام (نسبة الانضمام الأسبق OCR بين 1.4-2.4) (2) خرسانة ناعمة السطح (3) نماذج غير مشوشة (4) تغيّر الحمل العمودي على سطح التماس . عكست الاختبارات بشكل اعتيادي معاملات القص كما في تجارب التربة الطبيعية (التلاصق وزاوية الاحتكاك الداخلي)، كانت زاوية احتكاك التماس $14,5^{\circ}$ وبينما كان الالتصاق 15,5kPa ، تأهبه مقاومة القص العظمى للتماس من 10- 16% انفعال أزاحه باتجاه سطح القص.

تم استخلاص علاقة ملائمة بين قيمة ضربات فحص الاختراق القياسي -N_{70} ومعاملات احتكاك الالتصاق لحساب احتكاك التماس لركائز الدق،أخيرا وبالاعتماد على نتائج الفحص تم استخلاص علاقة بين احتكاك التماس ضربات فحص الأختراق القياسيN_{70} لتربة طينية غريني ، لقيم ضربات فحص الأختراق القياسي N_{70} بين (12-20).

الكلمات ألمفتاحيه:غير مخلخلة،مفرطة الانضمام،طين غريني، احتكاك التماس التربة – الخرسانة، ،فحص القص المباشر،فحص القص القياسي .

INTRODUCTION

A relation between SPT and skin friction have no direct relationships .Recent developments in civil engineering, especially in soil mechanics and foundations engineering , take a great step forward from "design by experience" to design by a well-established theory verified by experiment(Site and lab Test). In the case of skin friction(between soil and foundation) , is the stress-strain relation if one starts to move in relation to another? This mutual effect of soils and structures in the transmission of the forces through the contact surface is called skin friction.

Until recently the values of skin friction used for design purposes were the average values obtained by field tests, with only qualitative reference to such factors influencing their magnitude as type of soil, type of construction material, and surface finish, moisture content of the soil, etc. The modern trend is to establish skin shear strength coefficients throughout laboratory experiments in which the factors influencing the results may be controlled quantitatively (Potyondy, 1961).

The soil parameters needed for static analysis of single and group piles capacity consist of the angle of internal friction(ϕ)and the cohesion (c). The strength parameters have been determined from laboratory triaxial tests on undisturbed samples with experience used to extrapolate this data to obtain the design parameters. Also , used in situ parameters of cone penetration test or pressure meter test and probably most pile design still relies heavily on standard penetration test N values in sand and field tests for shear strength in cohesive soil deposits (Bowles, 1997).

In the field of geotechnical engineering, it's well known that the designs of piles foundation depend upon end bearing and /or skin friction between the piles and soil. When a load is applied to the soil surface , the soil resists the applied loads by developing contact forces wherever they touch at their asperities. At each contact, the particles respond by deforming in three ways: compressing, bending, and sliding. Deformation due to sliding is usually the most significant and is non linear and irreversible, making the load – deformation behavior of soil non linear and irreversible as well (Lambe and Whitman, 2000).

There are various ways to determine the pile capacity and most of them rely on full scale field tests using full size piles, but such tests are expensive and the results may apply only to the site where the test was performed. The value of skin friction factor to use in determining the load capacity of piles is a subject of much debate and testing (Budhu, 2008).

Chandler, and Martins(1982) doing Load tests on a modal pile installed in speswhite kaolin, based on tests on nine normally consolidated and one over consolidated sample, show that the angle of shaft friction is independent of the stress ratio in the soil before loading and is only just less than the triaxial effective angle of shearing resistance of soil for normally and over consolidated kaolin. When loaded axially the lateral stresses on the pile shaft decrease with increasing shaft load for normally consolidated soil, and increase on loading in over consolidated soil

Many geotechnical problems involve estimation of stresses transferred along the interface between soils and solid surfaces. Considerable work have been done on the interfacial friction between cohesion-less soils (sands) and solid surfaces. The interfacial shear resistance between fine grained soils and solid surfaces depends on whether its mobilization takes place in drained or in undrained condition. Also most of these studies are on normally consolidated soils, the influence of over-consolidated soils has received little attention (Acar et. al 1982, Ampera and Aydogmus, 2005)

Several kinds of apparatus have been used to investigate the interfacial friction between fine-grained soil and solid surfaces, for example the direct shear apparatus and the simple shear apparatus. Model pile tests have also been used for this purpose.

The results may be valuable and provide some rationale for reported correlations between N and skin friction from piles.

The objective of this study is correlate the evaluate results of adhesive and angle of internal friction skin friction using direct shear test box with the standard penetration test results on undisturbed over consolidated silty clay soil .

TEST PROGRAM

The test program consist of doing boreholes at Babil governorate in Iraq to get undisturbed samples and in-situ standard penetration test. Conducted classification test and determination skin friction from direct shear test between smooth concrete and native soil was explored in laboratory for design purposes and correlated with Standard penetration test blows values .Conducted 12 direct shear box tests on specimens of over consolidated cohesive silty clay soil and smooth concrete slice (foundation materials). The soil was placed in the bottom part of the direct shear box

test and the concrete was placed above it (in the upper part of the box) as shown in **Fig.1**. Test series (S1 – S5) were performed on five undisturbed cohesive silty clay soils, a total of twelve Direct Shear Tests were carried out , **Table 1** shows the details of the test series performed.

These 12 tests were conducted in such a way that in the first six tests the rate of strain was higher than the second group, **Table 2** shows the details values of shear strength and interface friction parameters of the test series performed.

The shear strength along the surface of contact of the soil and the foundation are given by Coulomb equation (Ampera and Aydogmus, 2005) as in eq. (1) below :

$$InterfaceFriction = f_c c + \sigma \tan(f_\phi \phi) \qquad (1)$$

Where $f_c = \frac{c_a}{c}$ (mean= 0.25)

$f_\phi = \frac{\delta}{\phi}$, (mean= 4.4)

σ' = Effective normal stress.
c = Cohesion of soil
C_a = Adhesive bet. Soil and clay
ϕ = Angle of internal friction of soil
δ = Angle Interface friction

It's worth to mention that all soil tests were carried out in accordance with (ASTM standards). For the determination of physical properties of soil well-known standard equipment was used. It is worth to mention that laboratory , field ,and in situ tests of the study conducted in 2007 .

SAMPLE PREPARATION FOR ITERFACE TEST

The soil part of the specimen was undisturbed cohesive silty clay soil extracted directly from Shelby tube to prepare the test sample, for the direct shear test, (Five undisturbed samples were obtained from various locations and different depths . The boring equipment used in carrying out the field work was rotary drills rigs, with thin wall tube samplers Shelby tube for taking undisturbed samples .Disturbed samples were obtained to determine the classification of soils, the samples that were secured by the Standard Split Spoon Sampler were also used as disturbed samples. The water table was found at the time of boring be 3-4 m deep) using extruder sampler (6 × 6× 2 cm) specified for direct shear test as shown in **Fig. 1 and Fig.2** . The other part was a slice of concrete cube which was cast using job mix (1:1.5:3) and cured for 28 days. Then the soil pushed to the bottom half of the Direct Shear Box before tighten the two halves of box. Later the concrete slice (foundation material) was put in the upper half of the shear box . Finally the test was conducted in the usual manner (Das, 2002, and Lambe and Whitman, 2000).

Slices of concrete cubes made to fit the Shear Box device dimension by making projection of 6 mm in the direction of applied shear and less than 1 mm in the opposite direction. Note that the soils are denoted by series symbols (S1 – S5).

ANGLE OF ITERFACE FRICTION δ

The angle of wall friction δ can be estimated from **Table 3** or directly measured for important projects. Any direct measurements between the soil and wall material should use pressure that is on the order of what is expected in the prototype, since δ is some what pressure dependent.

If ϕ < δ, you assume a frictionless interface (but there may be adhesion, since a ϕ <δ soil would have cohesion).Interface friction apparently depends not only on the soil properties but also on the amount and direction of foundation movement. Indications are that maximum wall friction may not occur simultaneously with maximum shearing resistance along the rupture surface and that wall friction is not a constant along the wall—probably because the relative soil-wall movement is not constant as shown in **Fig.3**.

Considerable engineering judgment must be applied to obtain realistic values of wall friction since they are pressure-dependent. Values of δ = 0.6ϕ to 0.8ϕ are reasonable for concrete walls where forms are used giving a relatively smooth back face. **Table 3** gives several values of δ for other wall-to-soil materials (Bowels, 1997) .

For steel, concrete, and wood the values shown are for a normal pressure an of about 100 kPa. Decrease the values about 2 degrees for each 100 kPa increase in sand (Acar et al. ,1982).

ITERFACE ADHESION C_a

Interface adhesion develops from any

cohesion in the soil. In the upper region it is expected a tension crack may form (or form during dry periods as the ground naturally shrinks). The value of adhesion C_a below the tension crack depth is usually taken at from 0.5 to 0.7 s_u with a maximum value not much over 50 kPa (Bowels, 1997).

THE STANDARD PENETRATION TEST (SPT)

The standard penetration test, developed around 1927, is currently the most popular and economical means to obtain subsurface information (both on land and offshore). It is estimated that most conventional foundation design in world is made using the SPT. The method has been standardized as ASTM D 1586 since 1958 with periodic revisions to date. The test consists of the following: (ASTM D 1586-99)

1. Driving the standard split-barrel sampler a distance of 460 mm into the soil at the bottom of the boring.
2. Counting the number of blows to drive the sampler the last two 150 mm distances (total = 305 mm= 1 ft) to obtain the N number.
3. using a 63.5-kg driving mass (or hammer) falling "free" from a height of 760 mm. Several hammer configurations are available.

The exposed drill rod is referenced with three chalk marks 150 mm apart, and the guide rod is marked at 760 mm (for manual hammers).

The assemblage is then seated on the soil in the borehole (after cleaning it of loose cuttings). Next the sampler is driven a distance of 150 mm to seat it on undisturbed soil, with this blow count being recorded (unless the system mass sinks the sampler so no N can be counted). The sum of the blow counts for the next two 150-mm increments is used as the penetration count N unless the last increment cannot be completed. In this case the sum of the first two 150-mm penetrations is recorded as N.

The boring log shows refusal and the test is halted if

1. 50 blows are required for any 150-mm increment.
2. 100 blows are obtained (to drive the required 300 mm).
3. 10 successive blows produce no advance.

When the full test depth cannot be obtained, the boring log will show a ratio as

70/100 or 50/100

Indicating, that 70 (or 50) blows resulted in a penetration of 100 mm. Excessive equipment wear, as well as greatly reduced daily drilling meterage, results when blow counts are high. Standardization of refusal at 100 blows allows all drilling organizations to standardize costs so that higher blow counts result in a negotiation for a higher cost/length of boring or a requirement for some type of coring operation.

The standard blow count N_{70} can be computed from the measured N as follows:

$$N_{70} = C_N \times N \times \eta_1 \times \eta_2 \times \eta_3 \times \eta_4 \qquad (2)$$

Where

η_i = adjustment factors from (bowels, 1997)

N_{70} = adjusted N

C_N = adjustment for effective overburden pressure p'$_o$ (kPa) computed, $C_N = \left(\frac{95.76}{p'_\circ}\right)^{1/2}$

Meyerhof (1976) produced correlations between base and frictional resistances and **N**-values. It is recommended that **N**-values first be normalized with respect to effective overburden stress:

Normalized **N** = $\mathbf{N}_{mea.} \times 0.77 \log (1920/\sigma'_v)$ (3)

the influence of over- consolidated soils has received little attention

Pile type	Soil type	Ultimate base resistance q_b (kPa)	Ultimate shaft resistance q_s (kPa)
Driven	Gravelly sand Sand	40(L/d) **N** but < 400 **N**	2 $\mathbf{N}_{avg}$
	Sandy silt Silt	20(L/d) **N** but < 300 **N**	
Bored	Gravel and sands	13(L/d) **N** but < 300 **N**	$\mathbf{N}_{avg}$
	Sandy silt Silt	13(L/d) **N** but < 300 **N**	

DIRECT SHEAR TEST

The direct shear test is the oldest and simplest form of shear test arrangement. The test equipment consists of a metal shear box in which the soil specimen is placed. The box is split

horizontally into halves. Normal force on the specimen is applied from the top of the shear box. Shear force is applied by moving one –half of the box relative to the other to cause failure in the soil specimen. A conventional strain controlled direct shear box machine with specimen dimensions of (6×6×2 cm) was used. Series of shear strength test on 12 samples were conducted in such a way that the soil is placed in the bottom part of the Direct Shear Box device and the concrete (foundation material) is placed above it, i.e. in the top part of the shear box. The test were carried out at two constant rate of strain 1.2 mm/min and 0.3 mm/min. to make two different condition.

The tests were carried out in soaked condition using normal pressure ranging from 26.2 kPa to 349 kPa, as illustrated in **Table 2**.

Typical results of sample number five are shown in **Fig. 4**. and **Fig. 5** shows typical strain-shear stress for over consolidated clay.

RESULTS AND DISCUSSION

The soil was classified as over consolidated silty clay soil of firm to stiff strength $s_u \cong 30-60kPa$.

Fig. 6 show the results of direct shear test between an over consolidated cohesive soil and smooth concrete (foundation material) in soaked conditions at a stain rate of 1.2 mm/min.

The results showed that both cohesion and internal friction should be considered in evaluating skin friction , as illustrated in **Table 4**. The ultimate shear strength was mobilized at about 10 % strain of sample dimension. From the results shown in **Fig. 7** the following best relationship was obtained according to R^2:

$$\text{Linear equation(kPa)} \quad C_a = 0.2802(\sigma_n) + 14.196 \qquad (4)$$

By using the linear equation and putting two different normal stresses(σ_n =50 & 100 kPa) to get two adhesion shear stresses(C_a). determine from the slope of the line the angle of interface friction. and by putting zero normal stress we get the adhesion shear stresses for **Fig. 7**.

Fig. 8 and, illustrates the results between shear stress and normal stress for the group B six specimens, the results show a friction angle and adhesion between the tested soil and concrete. The adhesion achieved from the cohesion properties of soil and angle of friction (interface friction) obtained from rough surface of concrete (foundation material). The ultimate shear strength was mobilized at about 10 % strain of sample dimension . From the results shown in **Fig.9** the following best relationship was expressed according to R^2:

$$\text{Linear equation(kPa)} \quad C_a = 0.301(\sigma_n) + 13.72 \qquad (5)$$

Comparison of results of **Figs. 6 and 7** with the results shown in **Figs. 8 and 9** indicates that tests at lower rate of strain ,i. e ,0.3 mm/min had increased the adhesion and decreased the angle of internal friction slightly. This is due to the low applied strain that permits the soil to consolidate and to increase the contact area with the concrete face.

Fig.10 shows the scatter of the results graph of all twelve tests. From the results the friction angle and adhesion between the tested soil and concrete can be expressed by best relationship :

$$\text{Linear equation(kPa)} \quad C_a = 0.301(\sigma_n) + 13.72 \qquad (6)$$

A list of possible relationships for estimating the interface friction parameters using various equations developed in this study is summarized in **Table 5**. During this study, all possible relationships were tried; however, naturally in some of these relationships the evaluated adhesion stress were low, high or negative value. The equations given in **Table 5** are the ones which had correlation coefficient (R^2> +0.5).

Figs. 11and **12** illustrate the relations among standard penetration test blows value (N_{70}), adhesion ,and interface friction angle. They can be used to relate the N_{70} value and interface friction of silty clay soils for N_{70} between 12 and 20,such relations can be expressed by:

$$\text{Adhesion, kPa} \quad C_a = 1.12 \times N_{70} \qquad (7)$$

$$\text{Interface friction angle, (°)} \quad \delta = 0.964 \times N_{70} \qquad (8)$$

The shear strength parameters between a soil and a foundation material can be conveniently determined by a direct shear test. Normal pressure

is the most effective parameter on the shear between the soil and concrete.

The direct shear test is simple to perform, but it has some inherent shortcoming .The reliability of the results may be questioned because the soil is not allowed to fail along the weakest plane but is forced to fail along the plane of split of the shear. This shortcoming is related to the original test for soil only to determine their strength parameters.

Despite of this shortcoming, this is a great advantage of the direct shear test; where the shear strength between the soil and the foundation material can be obtain during ordinary site investigation for pile foundation construction.

CONCLUSIONS

This work has presented the results of an experimental Laboratory and in-site work on five different soil samples used as underneath soil for a construction site. From the results of this work, the following conclusions can be withdrawn:

1. Interface angle of friction is $\delta^{\circ} \cong 4.4\phi$, and $\delta = 0.964 \times N_{70}$.
2. The adhesion between over consolidated clay and concrete is C_a=0.25 c ,and $C_a, (kPa) = 1.12 \times N_{70}$.
3. In cohesive soils it's preferable to use standard penetration test together with other tests as direct shear test to estimate the pile load capacity or the length of pile proposed.
4. In the case of over consolidated cohesive soils the adhesion and interface friction part should be taken and is mobilized at a 10 % strain into in evaluating interface shear strength.
5. The shape of stress-strain curve of soil concrete interaction is without peak value.

REFERENCES

- Acar, Y. B., Durgunoglu, H. T. and Tumay, M. T. (1982) "Interface Properties of Sand." Journal of Geotechnical Engineering, ASCE, Vol. 108, No. 4, 648-654.
- Ahmad, A.A. and JahanGer, Z. K. (2008)" Skin friction between Undisturbed Over consolidated silty Clay Soils and Concrete," University of Baghdad, Journal of engineering, No.4, Vol.14, pp.3068-3076.
- American Society for Testing and Materials, ASTM. (1988). Annual Book of Standards, sec. 4, Vol. 04.08, West Conshohocken, Pa.
- Ampera, B. and Aydogmus, T. (2005) "Skin Friction between Peat and Silt Soils with Construction Materials." Ejge Paper, http://www.ejge.com/2005.
- Bowles, J, E. (1997)."Foundation Analysis and Design." 5th edition, McGraw-Hill, Inc.
- Budhu, M. (2008)."Soil Mechanics and Foundations." 3rd edition, John Wiley and Sons, Inc, New York.
- Chandler, R. J. and J. P. Martins. (1982) "An experimental study of skin friction around piles in clay" Géotechnique, 32, No. 2, pp. 119-132
- Das, B. M. (2007)."Principles of Geotechnical Engineering." 5th edition, Brooks/Cole, pp315-322.
- Lambe, T.W. and Whitman, R.V. (2000) "Soil Mechanics." John Wiley and Sons.
- Meyerhof, G. G. (1976), "Bearing Capacity and Settlement of Pile Foundations," JGED, ASCE, vol.102, GT 3, March, pp. 195-228.
- Potyondy, J. G. (1961) "Skin friction between various soils and construction materials." Géotechnique, , 11, No. 4, pp. 339-353
- Winterkorn,H.F.,Fang,H.F.(1975)"Foundation engineering handbook" Litton educational publishing ,Inc.

LIST OF SYMBOLS

C: Cohesion.
C_a: Adhesion between soil and concrete.
d :Shaft diameter.
G_s : Specific gravity
e_o :Void ratio.
L: Embedded length.
L.L: Liquid limit.
N_{70}: Corrected blows of SPT.
$\mathbf{N_{avg}}$: Average value along shaft .

OCR: Overconsolidation ratio= $\frac{P'_c}{P'_\circ}$

P□c: Maximum preconsolidation pressure.
P□◦ : Effective average geostatic pressure.
P.L: Plastic limit.
P. I: Plasticity Index.
SPT: Standard penetration test (in-situ test).
s_u:Undrained shear strength.
w: Water content %.

Ø: Angle of internal friction.
δ: Interface friction angle between soil and concrete.
τ_s : Interface Shear strength.

Table 1 Properties of the soil used *

Soil Series	Depth (m.)	Sample No.	LL %	PI %	*w* %	γ_d kN/m^3	G_s	** OCR= $\frac{P'_c}{P'_\circ}$	Consolidation Test				Sieve Analysis % Passing No. 200	Soil Type	Triaxial compression UU-test		SPT N-Value
									e_o	P'_c kPa	c_c	c_r			C kPa	Ø Deg	
S1	2.0-3.0	1	40	18	17.2	15.7	2.69	2.6	0.739	120	0.18	0.031	97.4	CL	95	4.0	14
		2															
S2	2.5-3.0	3	55	28	24.6	15.2	2.71	1.72	0.835	90	0.19	0.034	98.3	CH	149	5.5	18
		4															
S3	3.0-4.0	5	48	25	27.2	13.9	2.69	1.4	0.851	85	0.16	0.031	96.3	CL	112	1.5	16
		6															
S4	2.0-3.0	7	44	21	21.5	15.4	2.68	2.05	0.824	95	0.14	0.026	85.5	CL	56	4.5	12
		8															
		9															
S5	5.5-6.5	10	43	23	25.9	14.4	2.68	1.4	0.738	125	0.17	0.031	97.0	CL	83	5.5	15
		11															
		12															

***Adopted from (Ahmad and JahanGer, 2008)**

$$**OCR = \frac{P'_c}{P'_\circ}$$

$$S1 \Rightarrow \sigma'_{v\circ} = P'_\circ = \sum \gamma' \times Z_{a\,var\,ege} = 2.5 \times (15.7 \times 1.172) = 46.001 kPa$$

$$P'_c = 120 kPa$$

$$\Rightarrow OCR = \frac{120}{46} = 2.6$$

$$S5 \Rightarrow \sigma'_{v\circ} = P'_\circ = \sum \gamma' \times Z_{a\,var\,ege} = [4 \times (14.4 \times 1.259) + 2 \times (14.4 \times 1.259 - 9.81)] = 89.11 kPa$$

$$\Rightarrow OCR = \frac{125}{89.11} = 1.4$$

Table 2– Values of shear strength and interface friction parameters

Sample No.	Normal Stress (kPa)			Rate of Strain (mm/min)	Shear Strength		Average Interface coefficients used	
	1	2	3		Adhesion C_a (kPa)	Angle of interface friction δ′ (°)	C_a(kPa)	δ′(°)
1	41.9	71.0	129.3	1.20	36.13	14.86	14.5	15.5
2	41.9	71.0	129.3	1.20	13.2	17.43		
3	41.9	71.0	129.3	1.20	16.35	10.5		
4	45	76.4	139	1.20	5.15	17.9		
5	45	76.4	139	1.20	4.0	18.53		
6	45	76.4	139	1.20	5.2	17.6		
7	45	76.4	139	0.30	12.93	16.4		
8	114	192.4	349	0.30	39.85	13.4		
9	114	192.4	349	0.30	21.49	15.10		
10	114	192.4	349	0.30	24.13	15.4		
11	114	192.4	349	0.30	45.8	8.3		
12	26.2	40.8	70	0.30	3.1	13.6		

Table 3 Friction angles between various materials and soil or rock (Bowels, 1997)

Interface materials	Friction angle, δ, degrees†
Mass concrete or masonry on the following:	
Clean sound rock	35°
Clean gravel, gravel-sand mixtures, coarse sand	ϕ
Clean fine to medium sand, silty medium to coarse sand, silty or clayey gravel	ϕ
Clean fine sand, silty or clayey fine to medium sand	ϕ
Fine sandy silt, nonplastic silt	ϕ
Very stiff and hard residual or preconsolidated clay	ϕ
Medium stiff and stiff clay and silty clay	ϕ
Steel sheet piles against the following:	
Clean gravel, gravel-sand mixture, well-graded rock fill with spalls	22°
Clean sand, silty sand-gravel mixture, single-size hard rock fill	17
Silty sand, gravel, or sand mixed with silt or clay	14
Fine sandy silt, nonplastic silt	11
Formed concrete or concrete sheetpiling against the following:	
Clean gravel, gravel-sand mixtures, well-graded rock fill with spalls	22–26
Clean sand, silty sand-gravel mixture, single-size hard rock fill	17–22
Silty sand, gravel, or sand mixed with silt or clay	17
Fine sandy silt, nonplastic silt	14
Various structural materials	
Masonry on masonry, igneous and metamorphic rocks:	
Dressed soft rock on dressed soft rock	35°
Dressed hard rock on dressed soft rock	33
Dressed hard rock on dressed hard rock	29
Masonry on wood (cross grain)	26
Steel on steel at sheet-pile interlocks	17
Wood on soil	14–16‡

*May be stress-dependent (see text) for sand.

†Single values ±2°. Alternate for concrete poured on soil is $\delta = \phi$.

‡May be higher in dense sand or if sand penetrates wood.

Table 4 Values of shear strength and skin friction for silty clay material

Sample No.	c kPa	Adhesion C_a (kPa)	$f_c = \frac{c_a}{c}$	Mean f_c	Ø Deg	Angle of interface friction δ′ (°)	$f_\phi = \frac{\delta}{\phi}$	Mean f_ϕ
1	95	36.13	0.39		4.0	14.86	3.7	
2	95	13.2	0.13		4.0	17.43	4.2	
3	149	16.35	0.11		5.5	10.5	1.9	
4	149	5.15	0.04		5.5	17.9	3.25	
5	112	4.0	0.04		1.5	18.53	12.3	
6	112	5.2	0.05		1.5	17.6	11.7	
7	56	12.93	0.24	0.25	4.5	16.4	3.64	4.4
8	56	39.85	0.72		4.5	13.4	2.9	
9	56	21.49	0.39		4.5	15.10	3.3	
10	83	24.13	0.29		5.5	15.4	2.8	
11	83	45.8	0.55		5.5	8.3	1.5	
12	83	3.1	0.04		5.5	13.6	2.4	

Table 5 Summary of relationships developed to evaluate interface friction parameters

Relations developed to evaluate interface friction parameters			
Equation	**R^2**	**Regression Equation**	**For example σ_n =100 kPa**
Group A			
Linear	0.513	$C_a = 0.280262 * \sigma_n + 14.19$	C_a= 42.19 kPa
Log	0.501	$C_a = 22.6933 * \log(\sigma_n) + -60.42$	C_a= -14.62 kPa(Neglect Eq.)
Exponential	0.549	$C_a = \exp(0.00771 * \sigma_n) * 18.26$	C_a= 39.51 kPa
Power	0.542	$\log(C_a) = 0.628 * \log(\sigma_n) + 0.835$	C_a= 123 kPa(over estimated)
Group B			
Linear	0.884	$C_a = 0.301289 * \sigma_n + 13.72$	C_a= 43.82 kPa
Log	0.914	$C_a = 44.320 * \log(\sigma_n) + -151.69$	C_a= - 63 kPa(Neglect Eq.)
Exponential	0.689	$C_a = \exp(0.00579 * \sigma_n) * 19.42$	C_a= 34.67kPa
Power	0.910	$\log(C_a) = 0.964 * \log(\sigma_n) + -0.759$	C_a=14.75 kPa(under estimated)
Scatter graph, Group A&B			
Linear	0.861	$C_a = 0.302 * \sigma_n + 12.901$	C_a=43.17 kPa
Log	0.833	$C_a = 40.039 * \log(\sigma_n) + -133.12$	C_a= -53kPa(Neglect Eq.)
Exponential	0.678	$C_a = \exp(0.00571 * \sigma_n) * 20.62$	C_a= 36.5kPa
Power	0.822	$\log(C_a) = 0.845 * \log(\sigma_n) + -0.143$	C_a= 35.3kPa

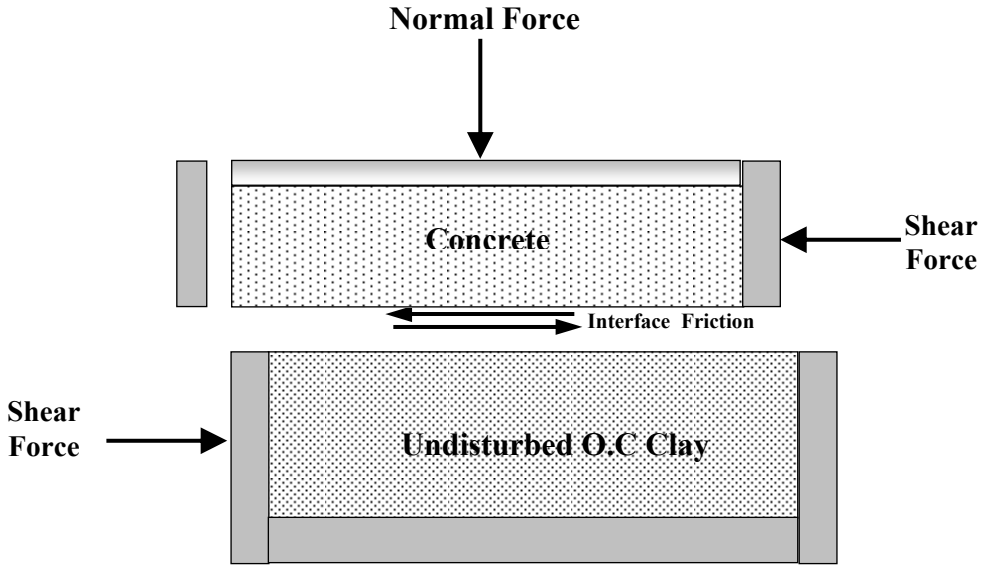

Fig. 1 Schematic diagram of direct shear test During test

a) DST sampler extrude

b) DST box assembly

c) Concrete and Soil Interaction

Fig. 2 Direct shear test plate

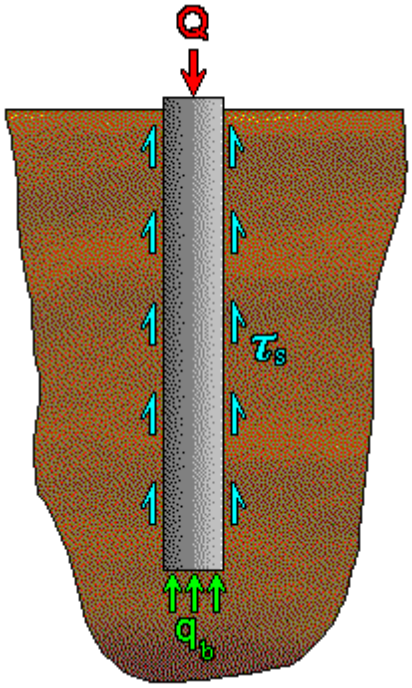

Fig. 3 Schematic diagram of pile load capacity shows interface friction stress

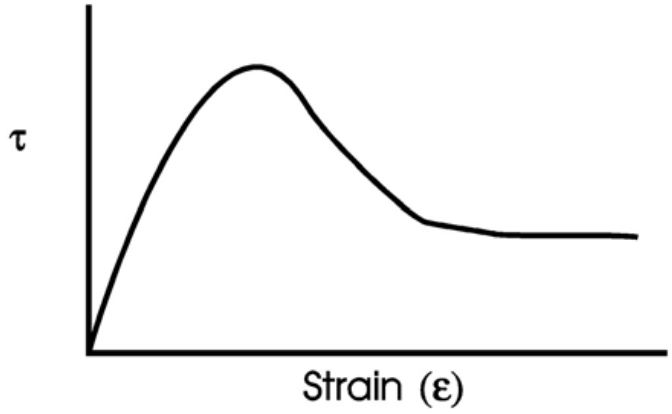

Fig. 4 Strain for over consolidated clay (Winterkorn and Fang, 1975)

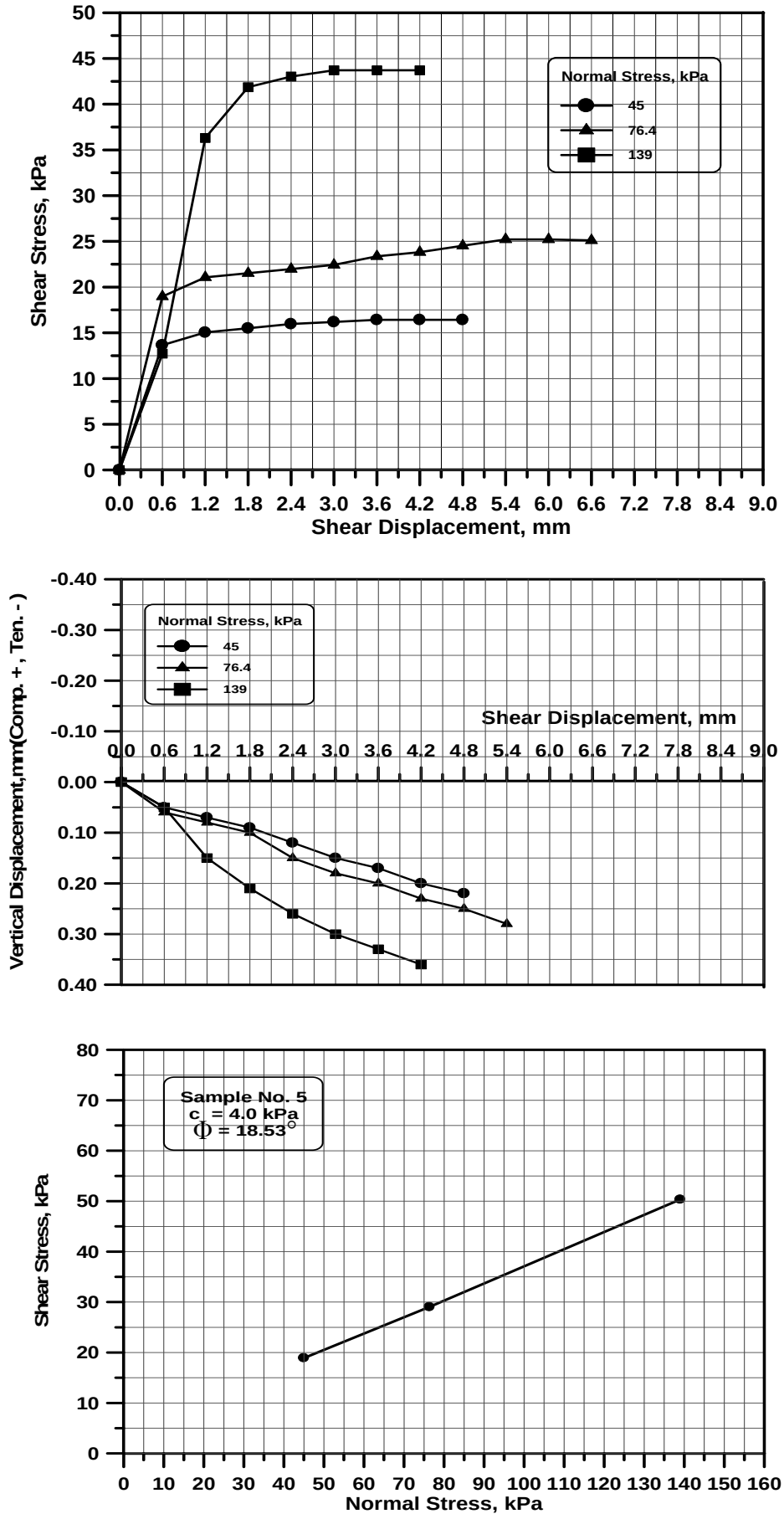

Fig. 5 Results of direct shear test for sample number 5

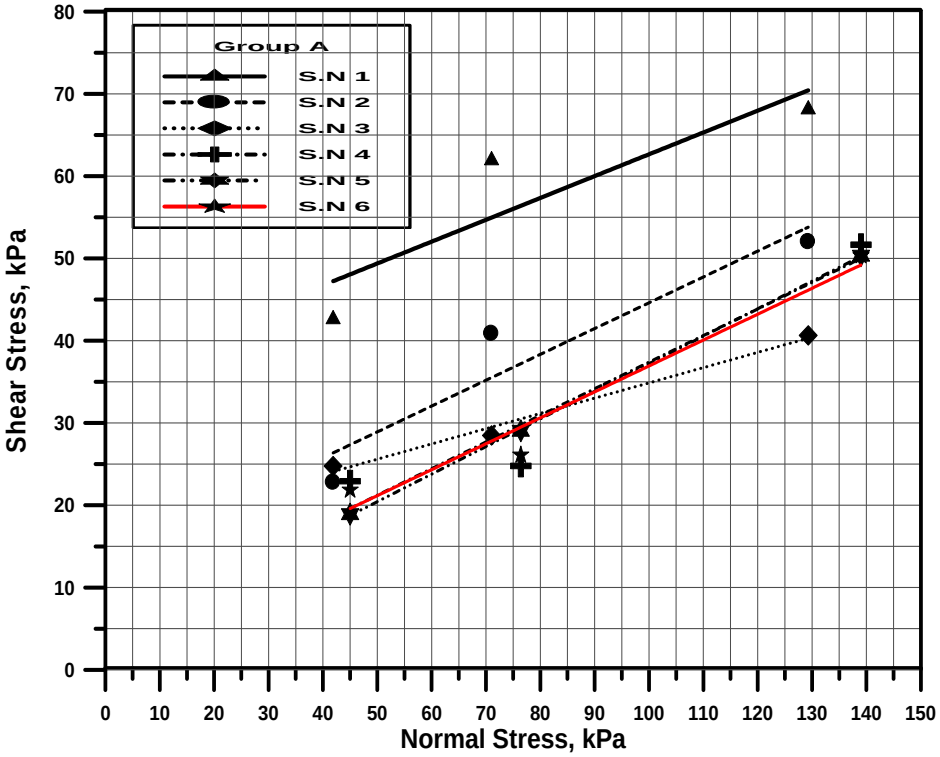

Fig. 6 Results of six direct shear test of O.C clay soil-Precast concrete in undrained condition group A

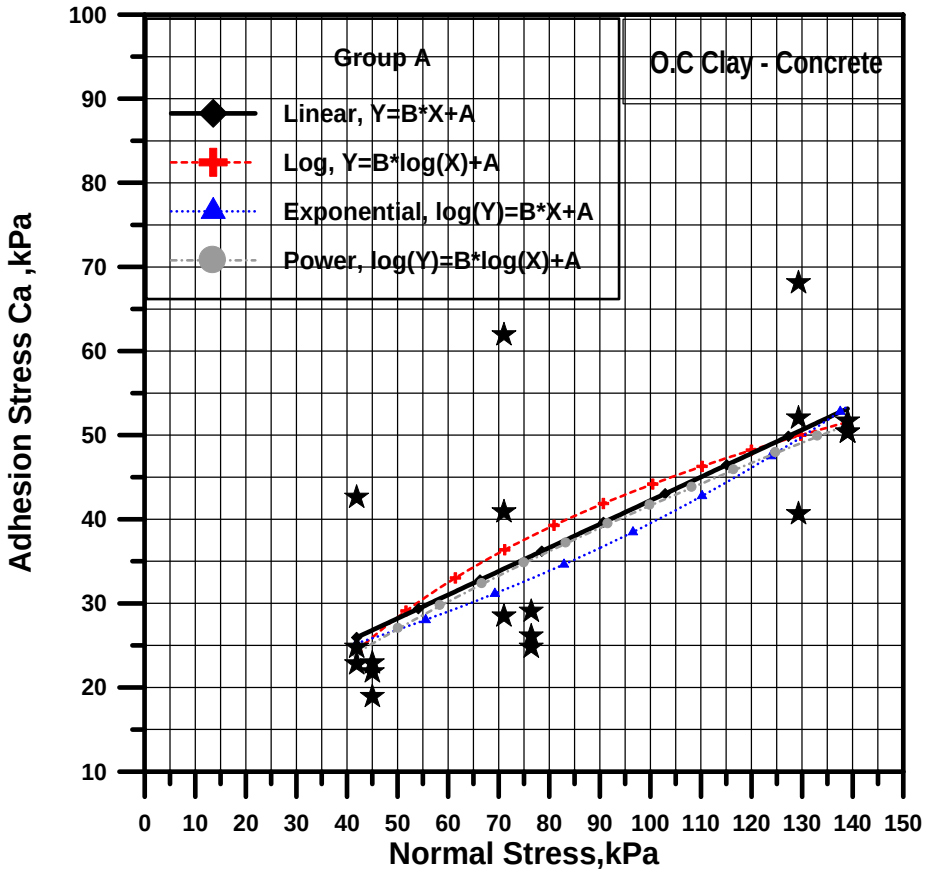

Fig. 7 Determination of skin friction parameters (C_a & δ) of O.C clay – Precast concrete group A

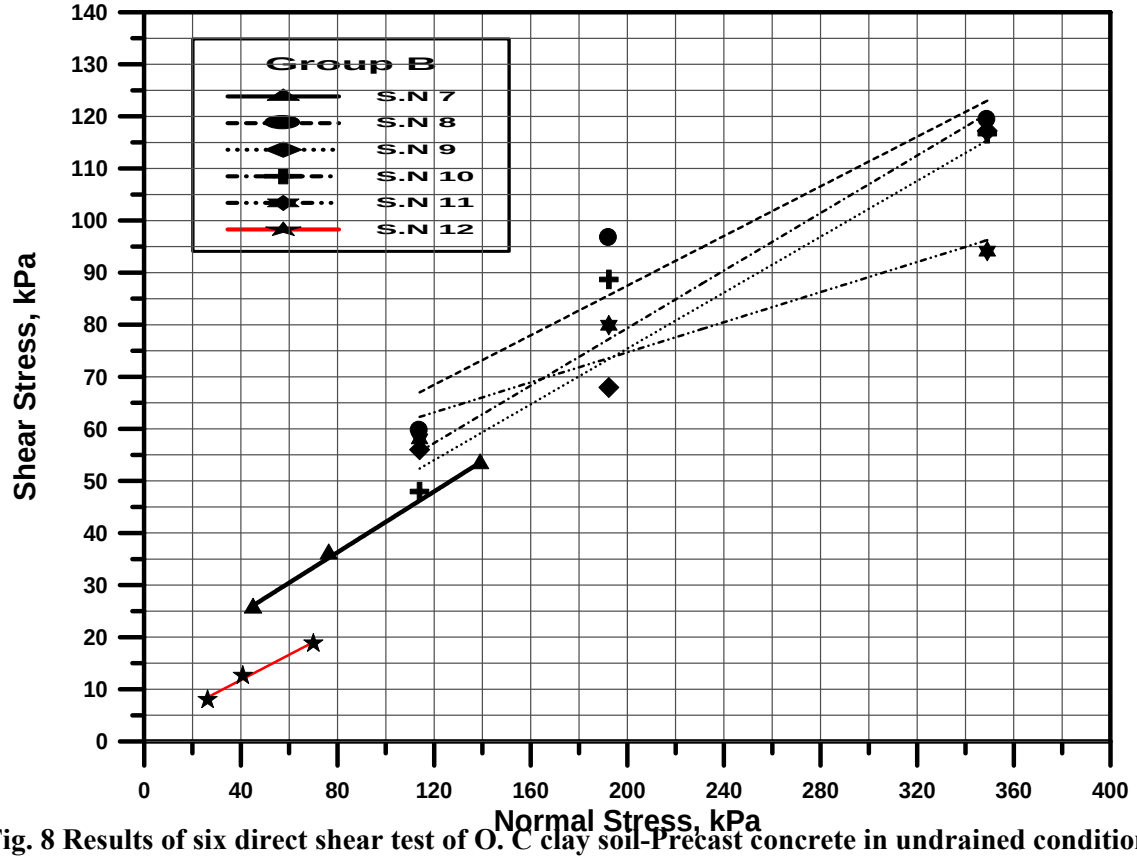

Fig. 8 Results of six direct shear test of O. C clay soil-Precast concrete in undrained condition group B

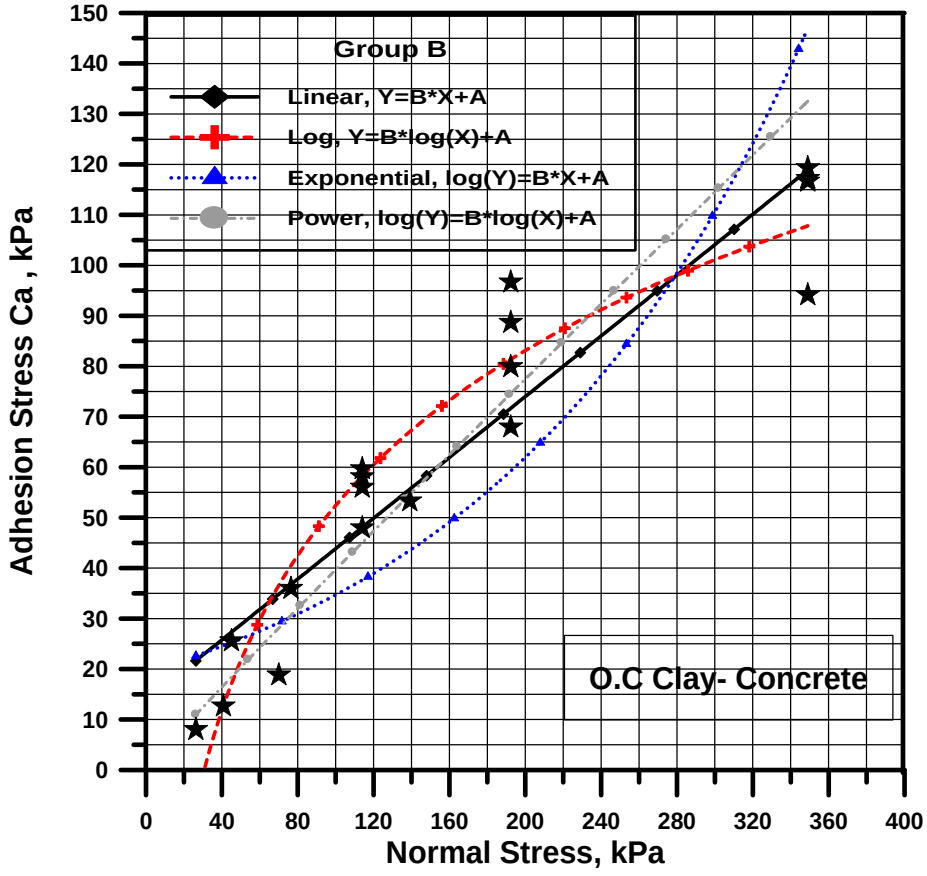

Fig. 9 Determination of skin friction parameters (C_a & δ) of O. c Clay – Precast concrete in group B

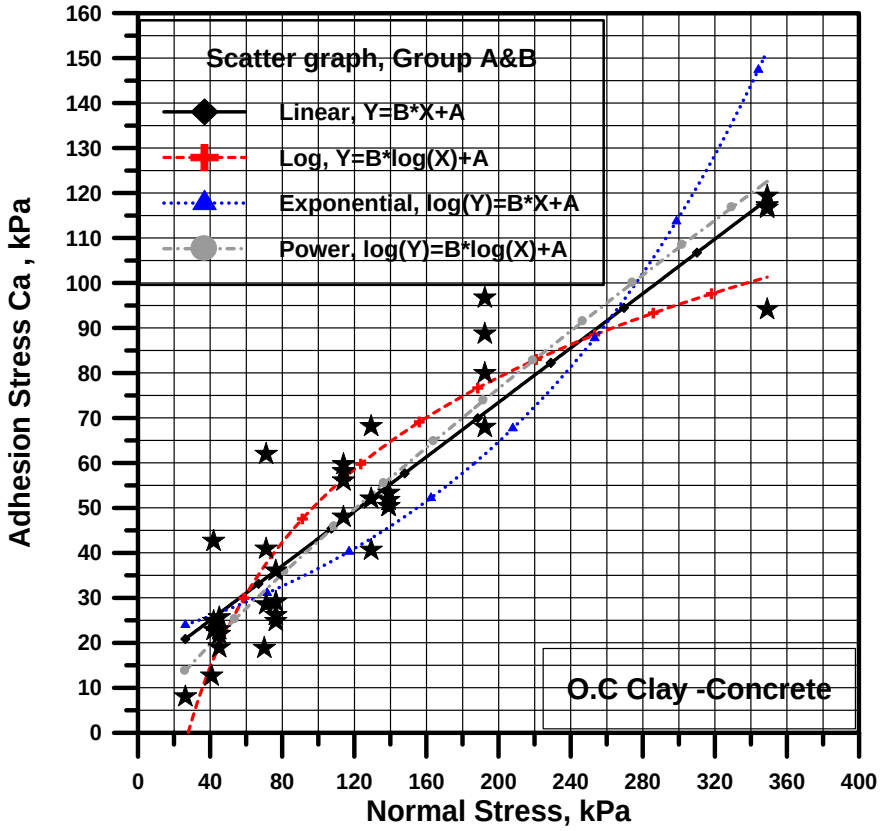

Fig. 10 Determination of skin friction parameters (C_a & δ) of O. C clay – Precast concrete (all test) Scatter graph

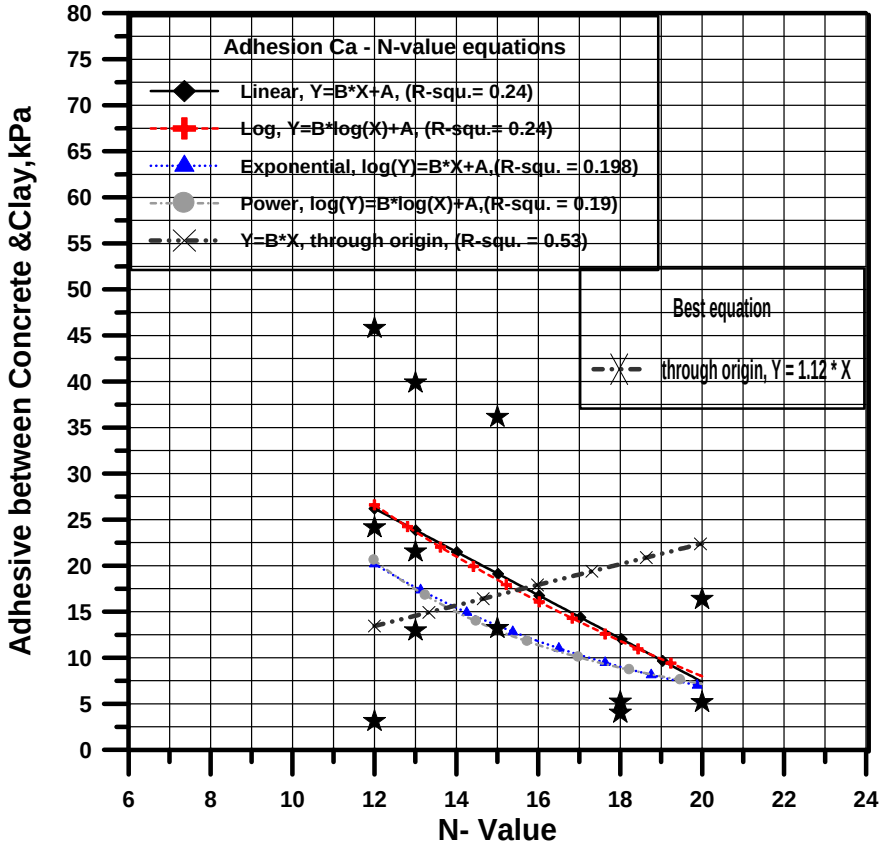

Fig. 11 Adhesive C_a versus N.value of O. C clay – Precast concrete

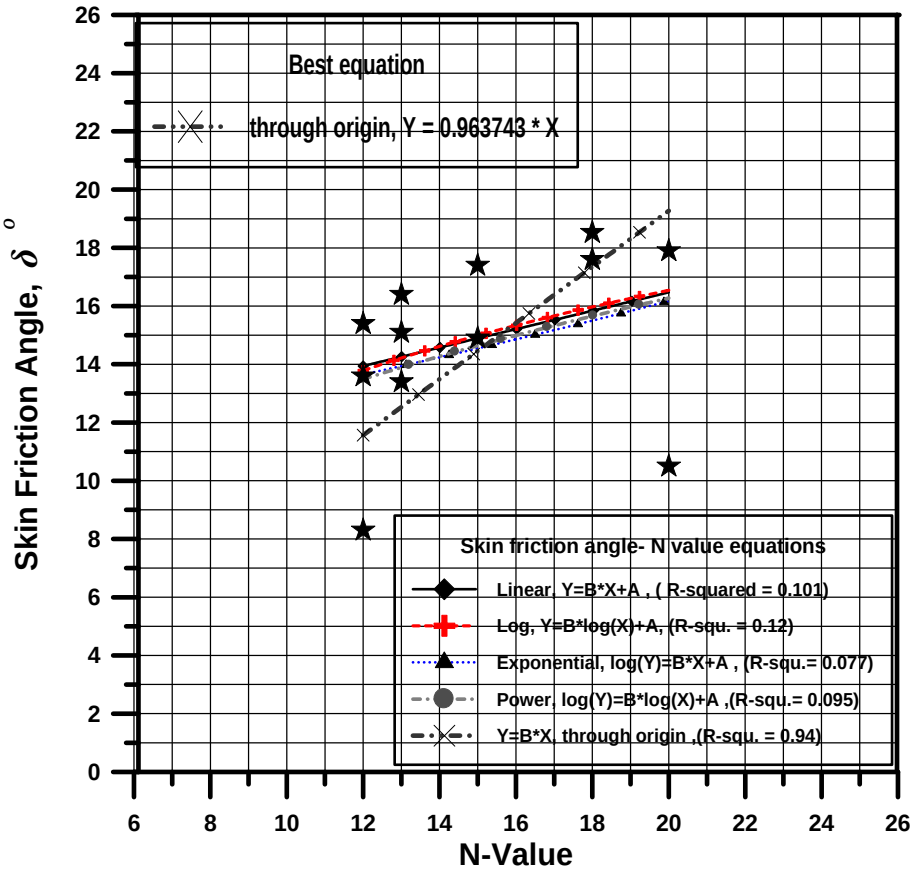

Fig. 12 skin friction angle δ versus N_value of O. C clay – Precast concrete

MODIFIED TRAINING METHOD FOR FEEDFORWARD NEURAL NETWORKS AND ITS APPLICATION in 4-LINK SCARA ROBOT IDENTIFICATION

Dr. Nadia A. Shiltagh

Computer Engineering/ University of Baghdad

Prof. Dr. Kais Said Ismail

Computer Engineering/ University of Baghdad

Dina A. Abdul Kadeer

Computer Engineering/ University of Baghdad

ABSTRACT

In this research the results of applying Artificial Neural Networks with modified activation function to perform the online and offline identification of four Degrees of Freedom (4-DOF) Selective Compliance Assembly Robot Arm (SCARA) manipulator robot will be described. The proposed model of identification strategy consists of a feed-forward neural network with a modified activation function that operates in parallel with the SCARA robot model. Feed-Forward Neural Networks (FFNN) which have been trained online and offline have been used, without requiring any previous knowledge about the system to be identified. The activation function that is used in the hidden layer in FFNN is a modified version of the wavelet function. This approach has been performed very successfully, with better results obtained with the FFNN with modified wavelet activation function (FFMW) when compared with classic FFNN with Sigmoid activation function (FFS) .One can notice from the simulation that the FFMW can be capable of identifying the 4-Links of SCARA robot more efficiently than the classic FFS.

الخلاصة

في هذا البحث نتائج تطبيق الشبكات العصبية الصناعية ذات الدالة المحفزة المطورة لتعرف على أداء الروبوت المكون من أربع درجات من الحرية (4 - DoF) لذراع الروبوت (SCARA) سيتم وصفها. النموذج المقترح لإستراتجية التعرف يتكون من شبكة التغذية العصبية ذات الدالة المطورة التي تعمل بالتوازي مع نموذج الروبوت SCARA. تم تدريب الشبكات العصبية ذات التغذية الأمامية (FFNN) على الروبوت ، دون الحاجة إلى أي معرفة سابقة عن النظام المراد التعرف علية.الدالة المحفزة المستخدمة في الطبقة المخفية من الشبكات العصبية الأمامية هي نسخة مطورة من دالة الموجات. وقد نفذ هذا التحوير بنجاح كبير ، مع الحصول على نتائج أفضل عند استخدام FFNN ذات الدالة المحفزة المطورة (FFMW) بالمقارنة مع FFNN الكلاسيكية . من خلال النتائج من الممكن ملاحظة أن FFMW قادرة على تحديد 4 - روابط الى الروبوت نوع SCARA أكثر كفاءة من الشبكات العصبية ذات الدالة المحفزة من نوع Sigmoid.

Key index: **4-link SCARA robot, Identification , FFNN, wavelet activation function, modified wavelet activation function**

1. Introduction

In general, SCARA (Selective Compliance Assembly Robot Arm) robot, is a type of horizontal drive, and is used as the arrangement of parts to a printed wiring board and a product assembly; it is usually controlled by PID compensator to attain an exact movement. In controlling the SCARA robot, the arm head is moved by motors and the system is a Multiple-Input Multiple-Output (MIMO) system, so each link is required its accuracy and incoherency [Akamatsu S and et. al.,2009]. Recently the soft computing methodologies such as fuzzy logic, neural networks, and genetic algorithms have been used to solve the control problems of dynamic systems that are characterized with uncertainties in terms of structure and parameters. These uncertainties cannot adequately be described by deterministic models and therefore conventional control approaches based on such models are unlikely to result in the required performance. In the past two decades, a large number of research results in modeling and parameter identification have been reported. The intensive research in this area has focused on the torque-controlled robots with the dynamics being formulated on the basis of joint torque vs. joint motion [Hui J,2009- Abiyev and et.al.,2008]. System identification is a critical part of system analysis and control. Nonlinear system identification can be roughly divided into two categories, known structure and unknown structure. If the system structure is available a priori, the nonlinear system identification becomes a nonlinear parameter estimation problem [Er-Wei B. and et. al.,2007]. Some of researches use the recurrent neural networks for identification [Jiang Z. 2006- Khireddine M. S. and et. al. 2010- Passold F. 2009].

2. The Proposed Structure

The feed-forward neural network that is used in the non-parametric identification of the SCARA robot as shown in **Fig.1** consists of:
Input layer (12-nodes) each three combination representing position, Velocity, and acceleration.
The Hidden layer (40 nodes)
Output layer (4 nodes). Each node representing the torque of each link in the SCARA manipulator. The proposed model is shown in **Fig. 2**. The activation function that is used in the training algorithm is the modified of the wavelet function which is known as Superposed Logistic Function **(SLOG)** [Kuraz, Y,2005] and is described as equ. (1)

$$f(net) = \left[\frac{1}{(1+e^{(-net+1)})} - \frac{1}{(1+e^{(-net+0.5)})} - \frac{1}{(1+e^{(-net-0.5)})} + \frac{1}{(1+e^{(-net-1)})}\right] \quad (1)$$

While a modified SLOG function **(MSLOG)** is described in the form as shown in equ. (2)

$$f(net) = K * \left[\frac{1}{(1+e^{(-net+a)})} - \frac{1}{(1+e^{(-net+b)})} - \frac{1}{(1+e^{(-net-b)})} + \frac{1}{(1+e^{(-net-a)})}\right] \quad (2)$$

Where $net = \frac{(X*V)-b}{a}$

And $X = input\ vector$ and $V = weights\ of\ hidden\ layer$

The parameters K,a,b are selected by trial and error (K=2.5) in order to scale the data between (-1 and 1), and (a=b=5).

The derivative of equ. (2) is described in equ.(3)

$$f'(net) = K * \left[\frac{e^{(-net+a)}}{(1+e^{(-net+a)})^2} - \frac{e^{(-net+b)}}{(1+e^{(-net+b)})^2} - \frac{e^{(-net-b)}}{(1+e^{(-net-b)})^2} + \frac{e^{(-net-a)}}{(1+e^{(-net-a)})^2}\right] \quad (3)$$

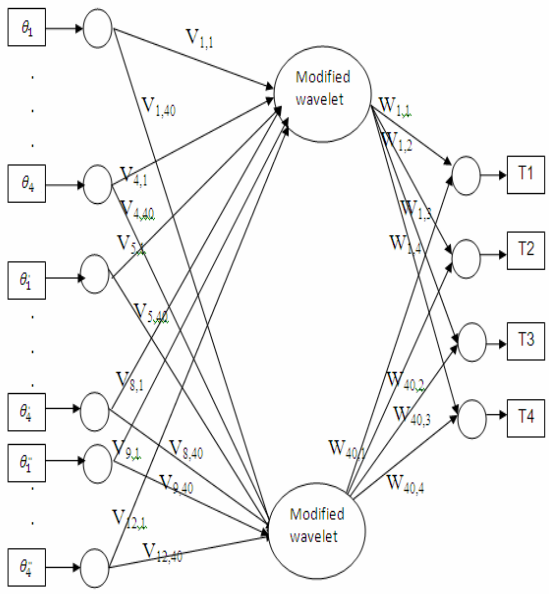

Figure 1 : FeedForward Neural Network With MSLOG

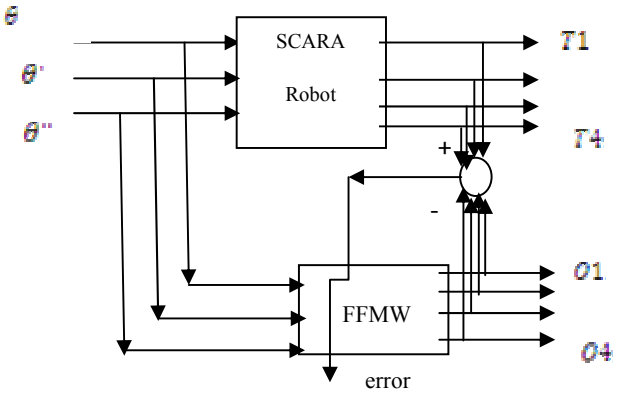

Figure 2 : Identification Model

The behavior of the MSLOG with different values of K is explained in the **Fig. 3**

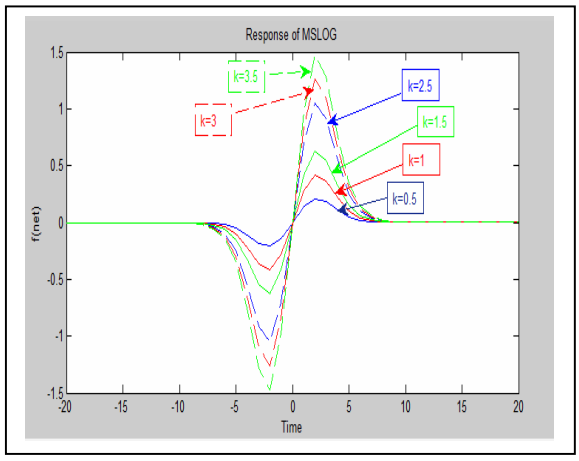

Figure 3 : Behavior of the MSLOG with different values of K

3. The Training Algorithm

The traditional Back-propagation training algorithm [Chaturvedi D., 2008] is used to train the FFS. The FFMW is trained using the modified training algorithm (Modified Back-propagation) which is shown in flow chart (1) the activation function that is used in the hidden layer is MSLOG, while the activation function of output layer is linear. This approach in training method is different from the traditional Back-propagation algorithm that is used sigmoid or tangential activation function in the hidden layer. The training algorithm is shown in flow chart (1). The simulation results are implemented using MATLAB (m-file).

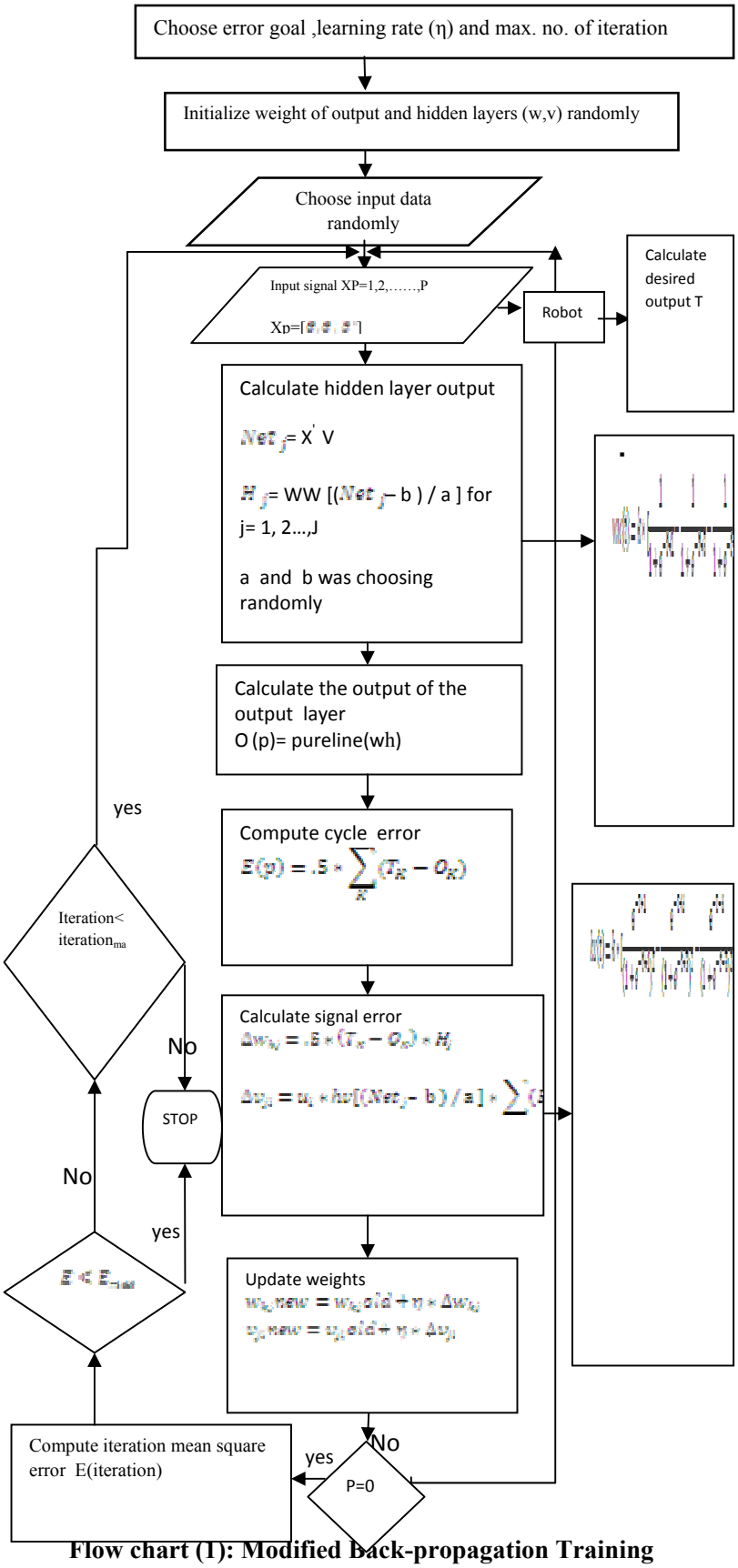

Flow chart (1): Modified Back-propagation Training Algorithm for FFMW

4.The Robot Architecture:

Consider the SCARA manipulator of **Fig. 4**; this manipulator, which is an abstraction of the Calibration of SCARA Manipulator robot of **Fig. 5** [Spong M. W.,2004], consists of an Revolute Revolute Prismatic (RRP) arm and a one degree-of-freedom wrist, whose motion is a roll about the vertical axis. The first step is to locate and label the joint axes as shown. Since all joint axes are parallel, some freedoms are available in the placement of the origins. The origins are placed as shown for convenience using the Denavit -Hartenberg convention (D-H). The x_o axis is established in the plane of the page as shown in **Fig. 4**. This is completely arbitrary and only affects the zero configuration of the manipulator, that is, the position of the manipulator when the joint parameters are given Table (1).

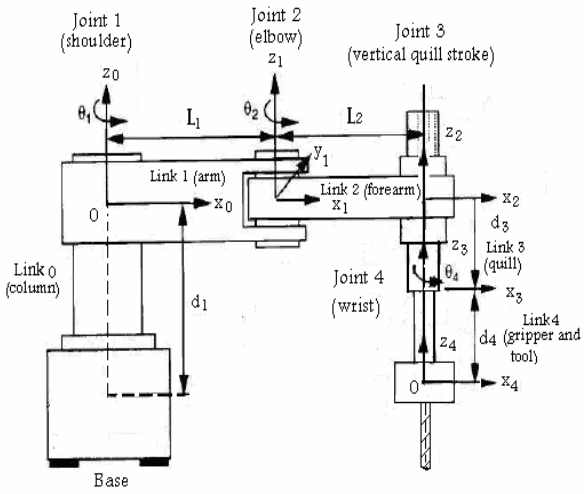

Figure 4: DH coordinate frame assignment for the SCARA manipulator.

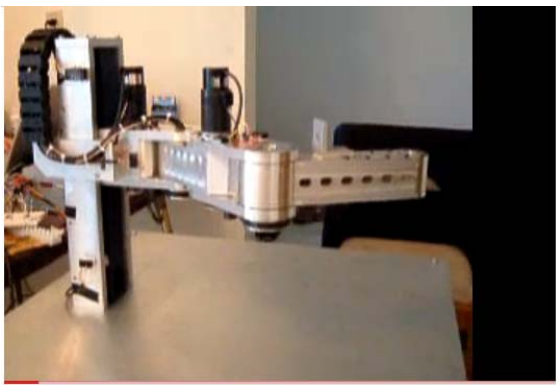

Figure 5: The SCARA Robot.

Table1: D-H parameters of the SCARA robot

i	θi	di	ai	αi
1	θ1	0	L1	0
2	θ2	0	L2	0
3	0	d*	0	0
4	θ4	d4	0	0

The ability to control a robot end effector in three-dimensional space requires the knowledge of a relationship between the robot's joints and the position and orientation of the end effector. The relationship requires the use and an understanding of the rotation matrix (Rot) and the translation vector (Trans). In this convention, each homogeneous transformation A_i is represented as a product of four basic transformations

$$A_i = Rot_{z,\theta_i}\ Trans_{z,d_i}\ Trans_{x,a_i}\ Rot_{x,\alpha_i}$$

$$= \begin{bmatrix} c\theta_i & -s\theta_i & 0 & 0 \\ s\theta_i & c\theta_i & 0 & 0 \\ 0 & 0 & 1 & 0 \\ 0 & 0 & 0 & 1 \end{bmatrix} \times \begin{bmatrix} 1 & 0 & 0 & 0 \\ 0 & 1 & 0 & 0 \\ 0 & 0 & 1 & d_i \\ 0 & 0 & 0 & 1 \end{bmatrix} \times \begin{bmatrix} 1 & 0 & 0 & 0 \\ 0 & c\alpha_i & -s\alpha_i & 0 \\ 0 & s\alpha_i & c\alpha_i & 0 \\ 0 & 0 & 0 & 1 \end{bmatrix}$$

$$= \begin{bmatrix} c\theta_i & -s\theta i c\alpha_i & s\theta i s\alpha i & a i c\theta_i \\ s\theta_i & c\theta_i c\alpha_i & -c\theta_i s\alpha i & a i s\theta_i \\ 0 & s\alpha_i & c\alpha_i & d_i \\ 0 & 0 & 0 & 1 \end{bmatrix} \quad (4)$$

where the four quantities θ_i, a_i, d_i, α_i are parameters associated with link i and joint i, and c denoting cosine and s for sine. The four parameters a_i, α_i, d_i, and θ_i in equ. (4) are generally given the names link length, link twist, link offset, and joint angle, respectively. These names derive from specific aspects of the geometric relationship between two coordinate frames [Spong M. W.,2004],.

For SCARA robot, the link parameters are shown in the Table 1, using the (D-H) convention, It is straightforward to compute the matrices A_i as shown below and the forward kinematic is given by equ. (5):

$$A_1 = \begin{bmatrix} c_1 & -s_1 & 0 & a_1 c_1 \\ s_1 & c_1 & 0 & a_1 s_1 \\ 0 & 0 & 1 & 0 \\ 0 & 0 & 0 & 1 \end{bmatrix}$$

$$A_2 = \begin{bmatrix} c_2 & s_2 & 0 & a_2 c_2 \\ s_2 & -c_2 & 0 & a_2 s_2 \\ 0 & 0 & -1 & 0 \\ 0 & 0 & 0 & 1 \end{bmatrix}$$

$$A_3 = \begin{bmatrix} 1 & 0 & 0 & 0 \\ 0 & 1 & 0 & 0 \\ 0 & 0 & 1 & d_3 \\ 0 & 0 & 0 & 1 \end{bmatrix}$$

$$A_4 = \begin{bmatrix} c_4 & -s_4 & 0 & 0 \\ s_4 & c_4 & 0 & 0 \\ 0 & 0 & 1 & d_4 \\ 0 & 0 & 0 & 1 \end{bmatrix}$$

$$T_0^4 = A_1 A_2 A_3 A_4 = \begin{bmatrix} c_{12}c_4 + s_{12}s_4 & -c_{12}c_4 + s_{12}s_4 & 0 & a_1 c_1 + c_{12} \\ s_{12}c_4 - c_{12}s_4 & -c_{12}c_4 + s_{12}s_4 & 0 & a_1 s_1 + a_2 s_{12} \\ 0 & 0 & -1 & -d_3 - d_4 \\ 0 & 0 & 0 & 1 \end{bmatrix}$$

(5)

It is well known that a robot manipulator can be modeled as a set of (*n*) rigid bodies connected in a serial chain with torques/forces acting at the joints. By applying the Lagrange equation of motion, the robot dynamic equation is derived as :

$$M(\theta)\ddot{\theta} + C(\theta)\dot{\theta} + F(\dot{\theta}) + G(\theta) + T_d = T$$

(6)

where θ is the *n*x1 vector of joint positions, T is the *n*x1 vector of applied joint forces/torques, $M(\theta)$ is the (*n*x*n*) symmetric positive-definite manipulator inertia matrix, $C(\theta,\dot{\theta})$ is the (*n*x1) vector of centripetal and Coriolis torques, $F(\dot{\theta})$ is the (*n*x1) vector representing torques due to friction acting at the manipulator joints, $G(\theta)$ is the (*n*x1) vector of gravitational torques and T_d is the (*n*x1) vector of unknown signals due to un modeled dynamics and external disturbances.

This robot dynamic equation can also be written in a more compact form:

$$M(\theta)\ddot{\theta} + H(\theta,\dot{\theta}) + T_d = T$$

(7)

where:

$$H(\theta,\dot{\theta}) = C(\theta,\dot{\theta})\dot{\theta} + F(\dot{\theta}) + G(\theta)$$

(8)

represents torques arising from centrifugal, Coriolis, gravity and friction forces.[Mosquera V., and Vivas A.,]

3. Simulation Results

The proposed model is implemented in 4-DOF SCARA manipulator. The torque of each link is shown in **Fig. 6-9** when the FFMW is used and **Fig. 10-13** when FFS is used. The results show that the proposed model gives excellent results in comparison with the results that the FFS give. The algorithm is implemented offline to identify torque of each link. The mean square error (MSE) of the proposed model is less than the MSE of the FFS, and the MSE when the neural networks with wavelet activation function (FFW) is used. This is shown in **Fig. 14**. The simulation also implemented online in order to show the efficiency of the proposed model. The results also show that the proposed model has good identification in terms with minimum error in comparison with the FFS and FFW. This is shown in **Fig. 15.** Table (2) and table (3) show that the FFMW reaches the error goal much faster than the FFW and FFS.

4. Conclusions

The simulation results show that the FFMW provides good results in comparison with FFS in terms of minimizing mean square error and training time, when offline and online training are used. This is because the nonlinear function that is used in the hidden layer is more efficient than the sigmoid function which the classic FFNN uses. The MSLOG has the capability of solving the nonlinearity of each link in the SCARA robot.

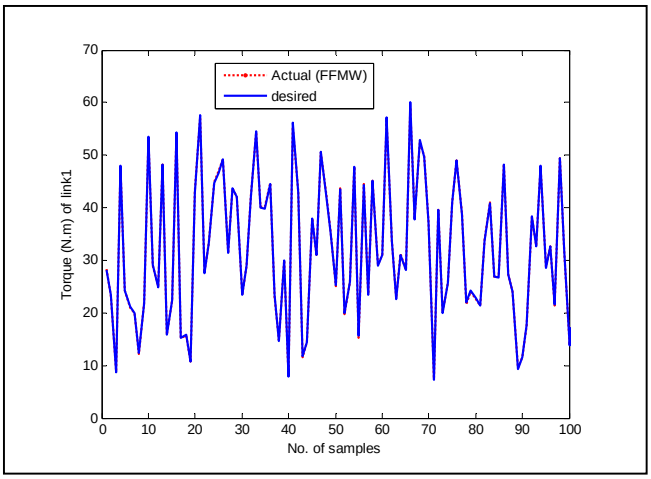

Figure 6 : **Torque of link1 when Neural Network with modified Activation function is used**

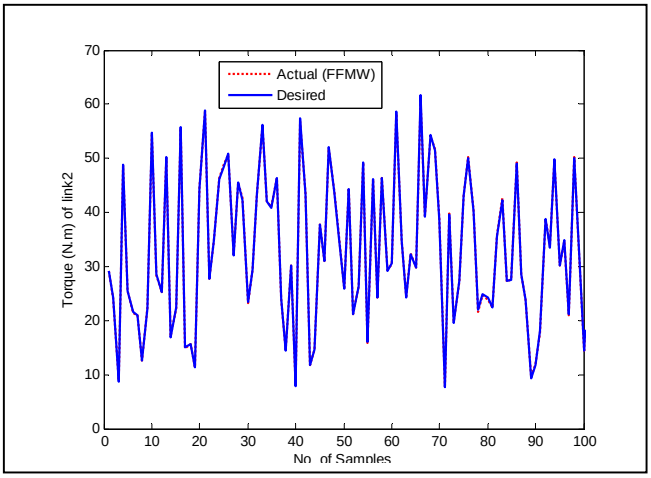

Figure 7 : Torque of link2 when Neural Network with modified Activation function is used

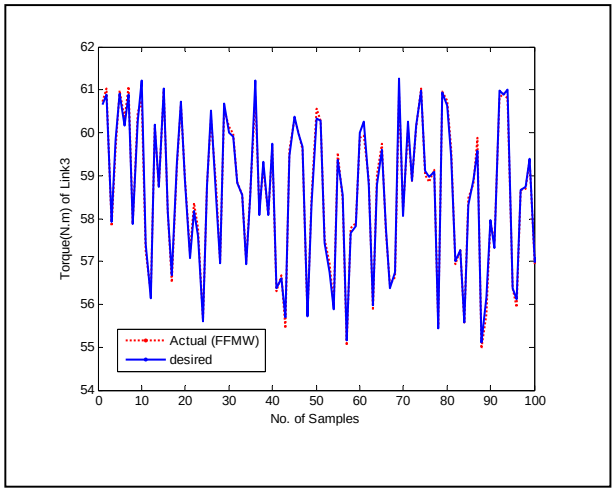

Figure 8 : Torque of link3 when Neural Network with modified Activation function is used

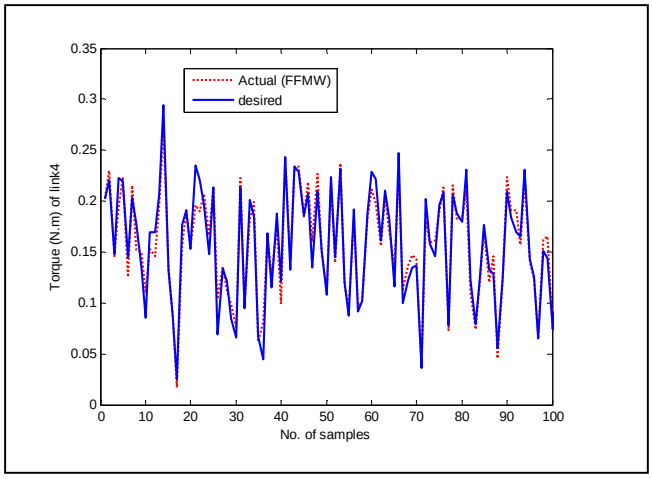

Figure 9: Torque of link4 when Neural Network with modified Activation function is used

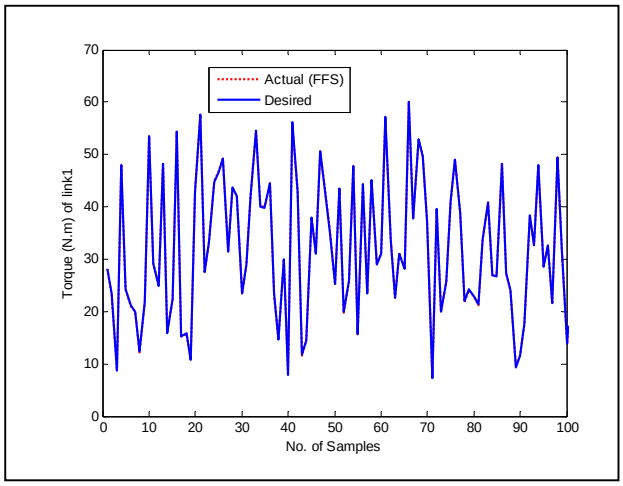

Figure 10: Torque of link1 when Neural Network with sigmoid Activation function is used

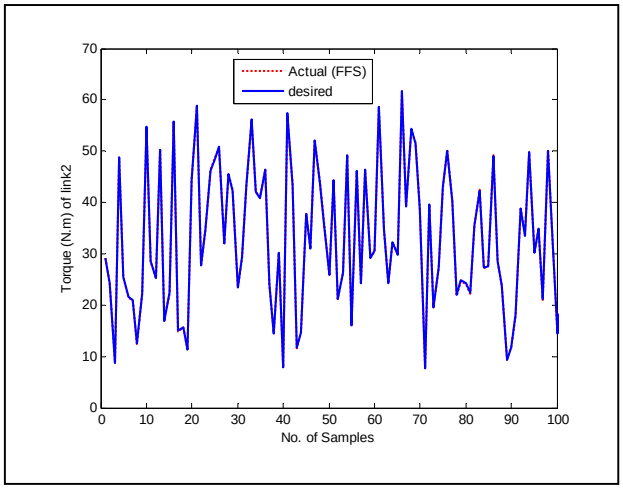

Figure 11: Torque of link2 when Neural Network with sigmoid Activation function is used

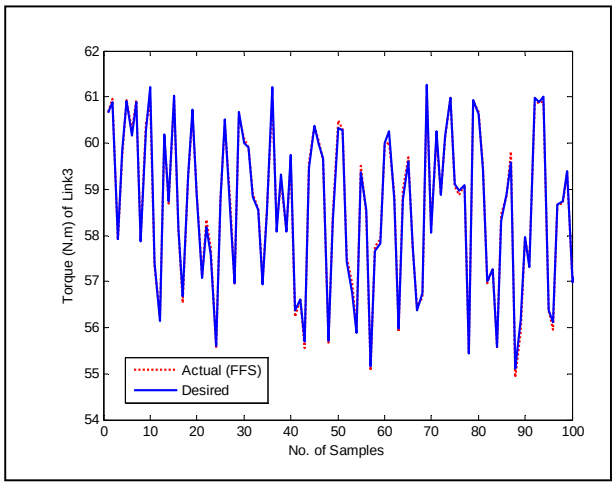

Figure 12: Torque of link3 when Neural Network with sigmoid Activation function is used

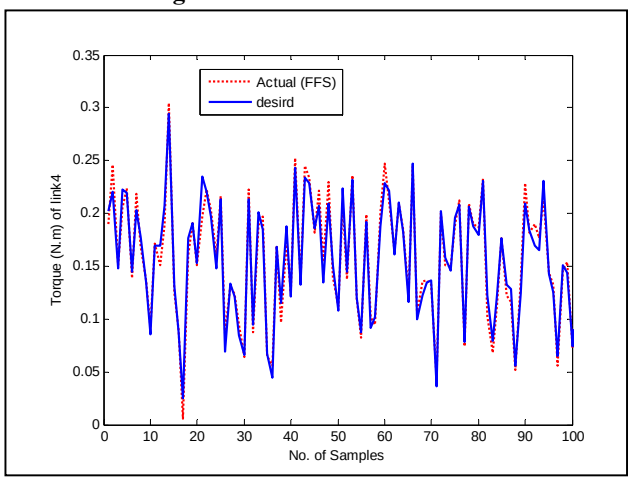

Figure 13: Torque of link4 when Neural Network with sigmoid Activation function is used

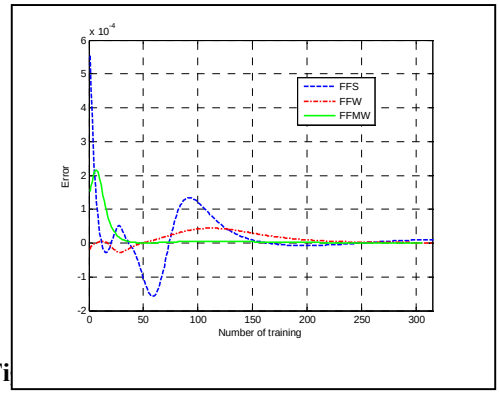

Fi

methods

Table 2: The mean square error when three methods are used

method	MSE	No. of Iteration
FFMW	8.3457e-010	315
FFW	1.0415e-006	315
FFS	9.1036e-006	315

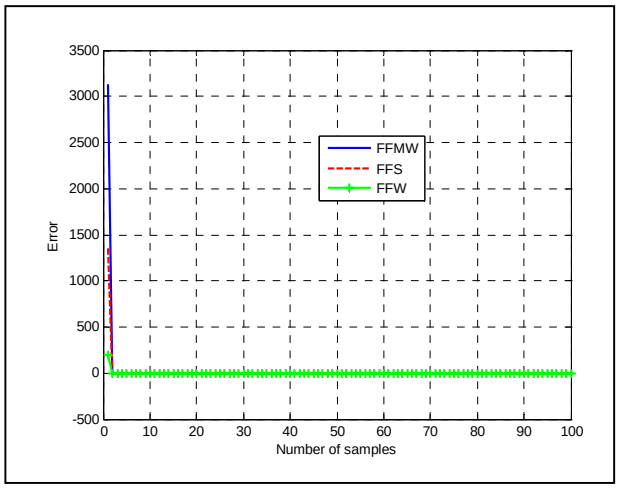

Figure 15: The error for three methods

Table 3: The error when three methods are used

method	Error	No. of samples
FFMW	4.3038e-006	100
FFW	1.3323e-004	100
FFS	3.7152e-005	100

References

Abiyev R. H., Kaynak O.“**Identification and Control of Dynamic Plants Using Fuzzy Wavelet Neural Networks”,** IEEE International Symposium on Intelligent Control Part of IEEE Multi-conference on Systems and Control San Antonio, Texas, USA, September 3-5, 2008.

Akamatsu S. Konishi M. and Imai J.,” **Position Control of 2-Link SCARA Robot by using Internal Model Control”,** Memoirs of the Faculty of Engineering, Okayama University, Vol. 43, pp. 49-54, January 2009

Chaturvedi D., **“Soft Computing Techniques and its Applications in Electrical Engineering”,** Springer-Verlag Berlin Heidelberg, 2008

Er-Wei B., Tempo R. and Liu Y.” **Identification of IIR Nonlinear Systems Without Prior Structural Information”,**IEEE Transection on Automatic Control, Vol. 52, No. 3, March ,2007.

Hui J. Z.,”**Dynamic Parameter Identification Of Robots Using A Neural Network as A Compensator”,** The ANNALS of "DUNAREA De Jos" University of Galati Fascicle Xiv

mechanical Engineering, ISSN 1224-5615 2009

Jiang Z., Ishida T. and Sunawada M." **Neural Network Aided Dynamic Parameter Identification of Robot Manipulators"**, IEEE International Conference on Systems, Man, and Cybernetics October 8-11, 2006, Taipei, Taiwan

Khireddine M. S. and Boutarfa A. " **Reconfigurable Control For A Scara Robot Using RBF Networks".** *Journal of* Electrical Engineering, Vol. 61, No. 2, 2010, pp. 100–106.

Kuraz, Y.**," Identification and Control of Robot Manipulator Using Adaptive Fuzzy Wavelet Network",** Ph.D. thesis**,** University of Baghdad, 2005**.**

Mosquera V., and Vivas A., **"Robust Control For A SCARA Robot With Parametric Uncertainty",** *University of Cauca, Popayán, Colombia Ustarth,2006.*

Passold F., "**Applying RBF Neural Nets for Position Control of an Inter/Scara Robot**", Int. J. of Computers, Communications & Control, ISSN 1841-9836, E-ISSN 1841-9844 Vol. IV (2009), No. 2, pp. 148-157.

Spong M. W., Hutchinson S., and Vidyasagar M.," **Robot Dynamics and Control**", Second Edition, January 28, 2004.

List of symbols

α_i	Angle of joint i
a	Constant of MSLOG
b	Constant of MSLOG
d_i	Offset of link i
K	Gain of MSLOG
θ	Position
$\dot{\theta}$	velocity
$\ddot{\theta}$	Acceleration
T	Torque of SCARA robot